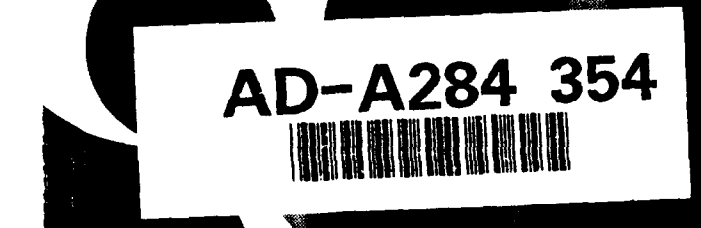

THE INSTITUTE OF MATERIALS

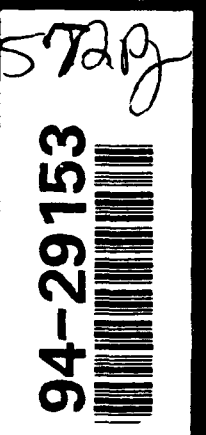

9th International Conference on

Deforma… Yield and … Fracture o… Polymers

Churchill College, Cambridge, UK
11–14 April 1994
Sponsored and Organised by
the Polymer Industry Division

PAPERS

9th International Conference on

Deformation, Yield and Fracture of Polymers

Churchill College, Cambridge, UK
11-14 April 1994

CONFERENCE PAPERS

The Institute of Materials
1 Carlton House Terrace, London SW1Y 5DB
(Registered with Charity Number 269275)

Printed by
The Chameleon Press Ltd, 5-25 Burr Road, Wandsworth, London SW18 4SG
Telephone: 081 870 7588

CHURCHILL CONFERENCE 1994

8th International Conference on

DEFORMATION, YIELD AND FRACTURE OF POLYMERS

11-14 April 1994: Churchill College, Cambridge, UK

The Churchill conferences on deformation, yield and fracture of polymers, held triennially since 1970, have established this event as the leading conference on its subject worldwide.

The 1994 conference reviews developments and identifies trends in the scientific understanding of the deformation, yield and fracture of polymeric materials.

CONFERENCE PRE-PRINTS

Extra copies of the conference preprints available for sale from the Conference Department of The Institute of Materials at the address shown below.

Published by:

The Institute of Materials
1 Carlton House Terrace
London SW1Y 5DB

Tel: 071 839 4071

CHURCHILL CONFERENCE 1994

ORGANISING COMMITTEE

A J Kinloch (Chairman)	Imperial College of Science Technology and Medicine
C P Buckley	University of Oxford
C B Bucknall	Cranfield University
A M Donald	University of Cambridge
R A Duckett	University of Leeds
K E Evans	University of Liverpool
J Hodgkinson	Imperial College of Science Technology and Medicine
N J Mills	University of Birmingham
D R Moore	ICI Advanced Materails
K Thomas	University of Aberystwyth
R E Wetton	Polymer Laboratories Ltd
J G Williams	Imperial College of Science Technology and Medicine
R J Young	Manchester Materials Science Centre

INTERNATIONAL SCIENTIFIC COMMITTEE

H R Brown	IBM Almaden Research Centre, USA
B Cherry	Monash University, Australia
M Dettanmaier	Max-Planck-Institut für Polymerforschung, Germany
R J Gaymans	University of Twente, The Netherlands
H H Kausch	EPFL, Switzerland
E J Kramer	Cornell University, USA
L Monnerie	ESPCI, France
A Pavan	Politecnico di Milano, Italy
K Takahashi	Kyushu University, Japan
V I Vettegren	Russian Academy of Science, Russia
A F Yee	University of Michigan, USA

ASSOCIATED BODIES

This conference is organised by The Institute of Materials, in association with the British Society of Rheology and the Polymer Physics Group of the Institute of Physics and Royal Society of Chemistry.

SPONSORS

The Organising Committee thank the following organisations for their generous support of the Conference.

Akzo Research Laboratories
Courtaulds Research
DSM Research
European Research Office, US Army
ICI Chemicals and Polymers Ltd
Polymer Laboratories Ltd

DEFORMATION YIELD AND FRACTURE OF POLYMERS
Churchill College, Cambridge, UK: 11-14 April 1994

PROGRAMME

Monday 11 April 1994

11.00 Registration

12.25 Lunch

13.45 **Opening Remarks by the Conference Chairman**
AJ Kinloch (Imperial College of Science, Technology and Medicine, London, UK)

Session A - TOUGHENED POLYMERS
Chairman: EJ Kramer (Cornell University, USA)

13.50 1 **Fracture in polymer alloys: mechanistic dependence on volume fraction and morphology**
AF Yee and BJ Cardwell (The University of Michigan, Ann Arbor, MI, USA)
J Wu and YW Mai (Sydney University, Australia)

14.15 2 **A model for particle cavitation and dilation band formation in rubber toughened plastics**
CB Bucknall (Cranfield University, Bedford, UK)
A Lazzeri (University of Pisa, Italy)

14.40 3 **Deformation micromechanics in rubber-toughened acrylic polymers**
PA Lovell, AJ Ryan, MN Sherratt and RJ Young (Materials Science Centre, University of Manchester and UMIST, Manchester, UK)

15.05 4 **Polyamide-rubber blends: influence of deformation speed on crack propagation process**
RJ Gaymans (University of Twente, Enschede, The Netherlands)
K Dijkstra (DSM Research, The Netherlands)
H Janik (Technical University of Gdansk, Poland)

15.30 5 **Real-time cryo-deformation of polypropylene and impact modified polypropylene in the transmission electron microscope**
RC Cieslinski (The Dow Chemical Company, Midland, MI, USA)

15.55 Tea

Chairman: AF Yee (University of Michigan, USA)

16.20 6 **Predictive models for the deformation and yield of toughened polymers**
FJ Guild (University of Surrey, Guildford, UK)
AJ Kinloch (Imperial College of Science, Technology and Medicine, London, UK)

16.45 7 **Ultimate toughness of amorphous polymers**
HEH Meijer and MCM van der Sanden (Eindhoven University of Technology, The Netherlands)

17.10 8 **The effect of rubber properties on the mode of deformation in rubber modified polystyrene**
A da Silva (Universidade do Minho, Portugal)
R Borggreve (DSM Research, The Netherlands)

17.35 9 **Role of the rubber particle in toughened polystyrene**
CB Bucknall, CA Correa, VLP Soares and XC Zhang (Cranfield University, Bedford, UK)

18.00 Close of Day 1

18.15 Welcome Reception - Sponsored by Polymer Laboratories Ltd

Tuesday 12 April 1994

Session B - CHAIN DOMINATED PROCESSES
Chairman: JG Williams (Imperial College of Science, Technology and Medicine, UK)

09.00 10 **Molecular deformation processes in polymers**
RJ Young (Materials Science Centre, University of Manchester and UMIST, Manchester, UK)

09.25 11 **Prediction of the molecular mechanical response of polymers and biopolymers**
R Pachter, PD Haaland, RL Crane and WW Adams (Wright-Patterson AFB, Ohio, USA)
R J Young (Manchester Materials Science Centre, Manchester, UK)

09.50 12 **Studying the deformation behaviour of high-performance fibres in tension and compression by spectroscopic-mechanical methods**
C Galiotis and C Vlattas (Queen Mary and Westfield College, London, UK)

10.15 13 **Aspects of the mechanical properties of spider dragline silk**
DV Mahoney (3M, Austin, Texas, USA)
RK Eby (The University of Akron, Ohio, USA)

10.40 Coffee

Chairman: CB Bucknall (Cranfield University, UK)

11.10 14 **Ultrastructural studies of the mechanism governing compressive deformation in high performance polymers**
DL Vezie and EL Thomas (MIT, Cambridge, MA, USA)

11.35 15 **Yielding and hysteresis of polymer fibers**
MG Northolt and JJM Baltussen (Akzo Research Laboratories, Arnhem, The Netherlands)

19.30 Conference Dinner

Thursday 14 April 1994

Session F - FRACTURE
Chairman: RJ Gaymans (University of Twente, The Netherlands)

09.00 32 **The evolution of cracks in brittle solids**
D Hull (University of Liverpool, UK)

09.25 33 **Fracture surface energy and craze fibril stress in PMMA in water**
R Schirrer and L Josserand (ICS(CRM-EAHP), Strasbourg, France)
P Davies (IFREMER, Plouzane, France)

09.50 34 **The relationship between slow crack propagation and tensile creep and behaviour in polyethylene**
P O'Connell, M Bonner, RA Duckett and IM Ward (IRC in Polymer Science and Technology, University of Leeds, UK)
LJ Rose and AD Channell (BP Chemicals, Grangemouth, UK)

10.15 35 **Statistics of atomic vibrations and fracture kinetics**
VI Vettegren and I I Ibrogimov (Physical Technical Institute, St Petersburg, Russia)

10.40 Coffee

Chairman: RJ Young (Materials Science Centre, University of Manchester and UMIST, UK)

11.10 36 **Plane-strain dynamic fracture resistance of polyethylene from tests on water pressurised pipe**
CJ Greenshields, SJK Ritchie and PS Leevers (Imperial College of Science, Technology and Medicine, London, UK)

11.35 37 **The effect of water on the mechanical properties of polystyrene bead foam**
NJ Mills and P Kang (The University of Birmingham, UK)

12.00 38 **Cyclic near-tip stresses for fatigue cracks in polymers: in-situ measurements, crack-tip microscopy and applications**
L Pruitt (University of California, Berkeley, CA, USA)
S Suresh (Massuchusetts Institute of Technology, Cambridge, MA, USA)

12.25 39 **Direct measurement of strain energy release rates during fatigue of reinforced nylon 66**
MG Wyzgoski and GE Novak (General Motors North American Operations, Warren, MI, USA)

12.50 **Closing Remarks by the Conference Chairman**
AJ Kinloch (Imperial College of Science, Technology and Medicine, London, UK)

13.00 Lunch

POSTER SESSION 1

P1 **The deformation of elastomeric O-rings compressed between flat rigid plates**
WE Warren and JA Weese (Texas A&M University, TX, USA)

P3 **Poly-conformers physics versus macromolecular physics: rubbery state deformation**
JP Ibar (Solomat Research Institute, New Canaan, CT, USA)

P4* **The concept of a common nature of the α and β relaxation transitions as a basis for predicting the anomalies in deformation behavior of multicomponent polymer systems**
VA Bershtein, VM Egorov and LM Egorova (Ioffe Physical Technical Institute of the Russian Academy of Sciences, St Petersburg, Russia)

P5* **New possibilities for study of deformation kinetics, microplasticity and relaxations in polymers using a laser interferometer**
NN Peschanskaya, PN Yakushev, AB Sinani and VA Bershtein (Ioffe Physical-Technical Institute of the Russian Academy of Sciences, St Petersburg, Russia)

P6* **The effect of inclusions and pores on viscoelastic behavior of a polymer**
X-M Wang, G Mei and Y-P Shen (Xi'an Jiaotong University, Xi'an Shaanxi, People's Republic of China)

P7 **Rubber-elastic deformation of PVC fatigue craze**
Y Imai, T Ohno and T Takase (Nagasaki University, Japan)

P8 **Crack-tip damaged zone, K_I values and propagation of a crack in rubber toughened PMMA**
C Fond, R Berthet and R Schirrer (ICS(CRM-EAHP), Strasbourg, France)

P9 **The long-term aging effects of viscoelastic polymers and its finite element method**
Feng ZhiGang and Zhou JianPing (National University of Defense Technology, HuNan, People's Republic of China)

P10* **Morphological, thermal and mechanical properties of polybutylene terephthalate and polypropylene blends**
ZA Mohd Ishak and JA Lee (Universiti Sains Malaysia, Penang, Malaysia)

P11 **A kinetic approach to the description of elasticity in a wide temperature range for oriented polymers**
SV Bronnikov (Institute of Macromolecular Compounds, Russian Academy of Sciences, St Petersburg, Russia)

P12 **Morphology and deformation/fracture behavior of PMMA ionomers and their blends**
X Ma, JA Sauer and M Hara (The State University of New Jersey, Piscataway, NJ, USA)

P13 **Fatigue failure in thermoplastic copolyesters**
EJ Moskala, TH Pecorini and LT Germinario (Eastman Chemcial Company, Kingsport, TN, USA)

P14 **The fatigue crack propagation behavior of cellulose esters**
TH Pecorini and EJ Moskala (Eastman Chemical Company, Kingsport, NJ, USA)

P16 **Deformation and fracture of polypropylene exposed to ultraviolet irradiation under stress**
Li Tong, B O'Donnell and JR White (University of Newcastle upon Tyne, UK)

P17 **A unified model of inelastic behaviour and fracture of polymers including second-order-effects**
H Altenbach (Otto-von-Guericke-Universität Magdeburg, Germany)
A Zolochevsky (Kharkov Polytechnical Institute, Ukraine)

P19* **Specific features of the thermoelastic effect in polymers**
VP Volodin (Institute of High Molecular Compounds of the Russian Academy of Sciences, St Petersburg, Germany)
AI Slutsker (AF Ioffe Physical Technical Institute of the Russian Academy of Sciences, St Petersburg, Germany)

P20 **Yield and fracture behaviour of epoxy networks modified with rubber or/and glass beads**
A Maazouz, H Sautereau and JF Gérard (Institut National des Sciences Appliquées de Lyon, Villeurbanne, France)
L Mercante, R Frassine and A Pavan (Polytecnico di Milano, Italy)

P21 **Fracture behaviour of polystyrene and rubber toughened polystyrene**
DG Cook, A Rudin and A Plumtree (University of Waterloo, Ontario, Canada)

P22 **Using the essential work of fracture method for studying physical aging in thin, ductile polymeric films**
JA Nairn (University of Utah, Salt Lake City, Utah, USA)

* Paper not available at time of Print

FRACTURE IN POLYMER ALLOYS: MECHANISTIC DEPENDENCE ON VOLUME FRACTION AND MORPHOLOGY

AF Yee*, BJ Cardwell*, J Wu‡, and YW Mai‡

The fracture toughness and toughening mechanisms in several polymer alloy systems consisting of pairs of rigid polymers have been studied. In all these materials the dispersed phase toughened the alloys by crack wake bridging and drawing, reaching remarkable levels of toughness. However, when further modified by elastomers capable of cavitating, some of these alloys achieved even higher levels of toughness by promoting shear plasticity. A bridging model originally proposed for ceramics containing ductile particles was modified and found to have excellent fit with data on an epoxy containing polyamide particles. An examination of the model reveals that controlled debonding at the particle matrix interface is essential to toughening. The particles must then be able to yield and strain harden. Surprisingly the size of the particle is also an important factor: larger particles can draw to larger dimensions and contribute proportionately to toughness. Elongated particles deeply anchored to the matrix are also more effective than spherical particles.

INTRODUCTION

The conventional approach to toughening of plastic materials is to incorporate a dispersed phase of elastomeric particles. By this approach the modulus, creep resistance, and often the tensile strength of the composite are compromised. These undesirable reductions suggest that an alternative strategy for toughening plastics is needed. One possibility is the development of polymer alloys consisting of two or more rigid components. Usually such alloys are brittle, but occasionally certain combinations produce alloys of surprising toughness without need for further toughening with rubber. The objective of this work is to understand and model the toughening mechanisms in these alloys and how they are related to the composition, morphology, interfacial adhesion, etc.

EXPERIMENTAL RESULTS

Fracture toughness and toughening mechanisms of alloys of pairs of rigid polymers were investigated. Some alloys were also further toughened with elastomeric materials capable of cavitation, a key conventional toughening mechanism. The results are summarized in the following.

A. DGEBA epoxy/piperidine/PA-12. Fracture toughness results for this series is shown in Fig. 1. This low Tg epoxy is capable of exhibiting extensive shear plasticity when toughened with liquid rubber or core/shell rubber[1]. But when it was toughened by the PA-12 particles the maximum toughness achievable was equal to that using rubber eventhough no significant shear plasticity was found. The majority of the toughening effect appear to be from crack wake particle bridging and stretching. (Fig. 2). Comparable toughening effects (K_{Ic} = 1.75 MPa$\sqrt{m}$) are obtained on a higher T_g brittle epoxy (K_{Ic} = 0.8 MPa$\sqrt{m}$)-- DGEBA cured with diamino-diphenyl-methane (DDM). This epoxy cannot be toughened effectively with rubber. The toughening is achieved with little sacrifice in modulus.

B. PA-66/PPE. A graft copolymer has been used to compatibilize the two phases producing excellent adhesion and dispersion. The particles probably initiated crazes. At high PPE content the number of crazes was multiplied, thus increasing the toughness (Fig. 3). At low PPE content the craze

*Dept. of Materials Science and Engineering, U. of Michigan, Ann Arbor, MI 48109. USA.
‡Dept. of Mechanical Engineering, U. of Sydney, Sydney, NSW 2006, Australia.

initiation actually reduced the toughness to well below that of pure PA-66. In the crack wake the PPE particles appear to have bridged the cracks. It is possible that had the PA-66 matrix been incapable of crazing, the mechanism in this system would have been the same as that observed in (A) above. These observations suggest that for particles to effectively nucleate as many crazes as possible they must be compliant in the sense of being able to elongate to accomodate the extended crazes.

C. PA-66/PPE/SEBS. The compositions of these alloys are identical to those in (B) except for the presence of SEBS block copolymers in the PPE. The toughening mechanisms of such alloys have been reported [2]. The main difference is that cavitation in the form of crazes in PPE occurs ahead of the crack tip due to the presence of SEBS. These crazes serve two functions: they increase the compliance of the PPE particles which allows them to support more crazes in the PA-66 matrix, which are nucleated by the crazes inside PPE in the first place. The crazes then relief the constraint caused by the sharp crack, allowing shear plasticity to occur over a larger volume of the material. We note that these crack tip mechanisms produce much greater toughness (Fig. 3) than the crack wake mechanisms described in (A).

D. PBT/PC. No stabilizer was used in producing these alloys, hence some exchange reaction probably occurred, producing good dispersion. The 40/60 and 50/50 alloys have bi-continuous structures [Fig. 4a] while in the remainder the minor phase forms particles. The alloys with high PC content has good interfacial adhesion but not those with high PBT content due to insufficient shear mixing in processing the latter. The 40/60 alloy has the highest toughness in terms of the essential work of fracture [3](Fig. 4c). The toughening mechanism in these alloys is also crack wake particle bridging and drawing [Fig. 4b]. The effective ness in bridging appears to be enhanced by the intermeshing domains. Previous work has shown that when a core/shell rubber is added to these compositions the toughening mechanism is cavitation of the rubber followed by extensive shear plasticity, all occurring in the crack tip region [4]. Moreover, these alloys are far tougher than those without the rubber, albeit at a sacrifice in the modulus.

MODEL

Except for the PA/PPE alloys the materials that do not contain a phase that can cavitate easily share a common toughening mechanism, i.e., ductile particles bridge the crack faces and plastically draw. When the particle concentration was high the stress transmitted to the surrounding matrix was apparently high enough to cause further plastic deformation. At first glance it might appear that good adhesion is required for particle bridging, and high ductility of the particles will increase energy dissipation. Particle size would seem to have little relevance. The importance of these material properties and geometric parameters are examined in the model described in the following.

With sufficient adhesion the advancing crack would bypass a particle in its path, causing this particle to bridge the crack faces. But for the particle to then yield and draw some particle debonding must take place, otherwise the particle is too constrained and will fracture cohesively in tri-axial tension. Obviously the debonding must not proceed all the way around the particle (Fig. 5). These apparently contradicting requirements on particle adhesion can be resolved if we recall that the interfacial stress is balanced during initial debonding by the resistance of the particle to cavitate in triaxial tension, while during the particle stretching stage it is balanced by first the uniaxial yield stress and then the drawing stress. For high molecular weight ductile polymers containing few flaws, as such small particles must be, the uniaxial yield and draw stresses must be substantiall lower than the cohesive strength. This has indeed been demonstrated by Narisawa even in bulk specimens [5]. Thus it is possible to reach a level of adhesion, probably by means of copolymers, that can satisfy these requirements. Once the particles have partially debonded, then the toughening effect can be estimated by suitably modifying a model proposed by Przystupa and Courtney for toughening of ceramics by ductile particles [6]. The model [7]gives:

$$K_C \geq AK_{crm} + E_m f W_p h / 2AK_{crm}$$

where K_C is the fracture toughness of the composite, K_{crm} is the intrinsic critical stress intensity of the matrix, A (>1) accounts for crack bowing, E_m is the matrix modulus, f is the volume fraction of particles, W_p is the plastic work of drawing a particle, and h is the gauge length of a particle. Using experimental parameters and reasonable values gleaned from the literature, the model gives excellent fit (solid line, Fig. 1) to the data for DGEBA epoxy/PA-12 described in (A) above, using reasonable parameters. We note that the fit is sensitive to the following factors comprising W_p: (a) The ultimate elongation assumed for the particles. Literature values of "ultimate elongation to break" are of little use in this computation since the true ultimate strain of materials in the form of micro-particles is required. We have estimated

this value from the extension observed in the micrographs. (b) The orientational hardening coefficient. Once again a true stress true strain curve is required. Since such data for PA-12 do not exist, we have estimated it from data on PA-66, PA-6 and high density PE [8], all with similar hardening coefficients. One final parameter that the fit is sensitive to is the gauge length, *h*. It must be estimated from careful microscopic observations. Clearly, all else being equal, the larger the particle size, the larger *h* is. This prediction is loosely consistent with observations we have made in our laboratories. Its validity awaits further confirmation.

We now return to the orientational hardening of the dispersed phase. Data from G'Sell and Jonas [8] show that for several crystalline polymers the ultimate true tensile strength can be several times the yield strength of many engineering plastics. Thus while these particles are being drawn they can in turn cause neighboring particles to deform by deforming the surrounding matrix, and sometimes giving rise to multiple secondary cracks or crazes.

In PBT/PC with 40/60 and 50/50 compositions the morphology consists of interpenetrating domains of irregular shapes [Fig. 4a]. Some such particles appeared to be especially efficient in bridging because they were deeply anchored into the surrounding matrix [Fig. 4b].

In summary, in all systems examined in this work, matrix shear plasticity did not appear to have significant contributions to the toughness (unless an easily cavitating phase is present), but the ductility of the particles and how they were attached to the matrix were of primary importance. Thus this toughening mechanism may be particularly effective for brittle matrices unable to deform by crazing or shear yield. In ductile matrices when rubber was added to the dispersed particles the fracture mechanism was completely transformed. Deformation processes occurred in advance of the crack tip and both crazing and shear plasticity could be observed in the matrix, depending on its nature While bridging still occurred, the toughness of such alloys was greatly enhanced by the matrix plasticity and/or crazing, and bridging was no longer the dominant toughening mechanism.

List of references

1. Pearson, RA, and Yee, AF, 1986, J. Mater. Sci. 21, 2475.
2. Sue, HJ, and Yee, AF, 1989, J. Mater. Sci. 24, 1447.
3. Wu, JS, Mai, YW, and Cotterell, B, 1993, J. Mater. Sci. In press.
4. Wu, JS, and Mai, YW, 1993, J. Mater. Sci. In press.
5. Narisawa, I, and Ishikawa, M, 1990, Adv. Poly. Sci 91/92, ed. Kausch, HH, Springer Verlag, Chap. 8.
6. Przystupa, MA, and Courtney, TH, 1982, Metal. Trans. A, 13, 881.
7. Cardwell, BJ, Yee, AF, to be published.
8. G'Sell, C, and Jonas, JJ, 1979, J. Mater. Sci. 14, 583.

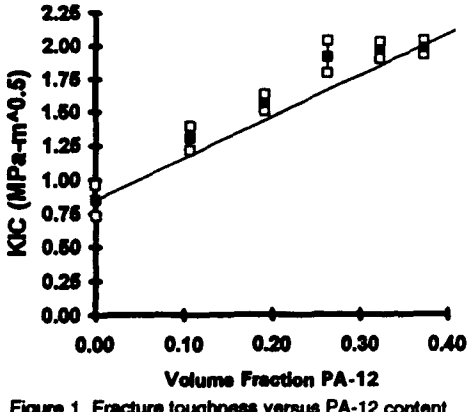

Figure 1 Fracture toughness versus PA-12 content of epoxy/pip system

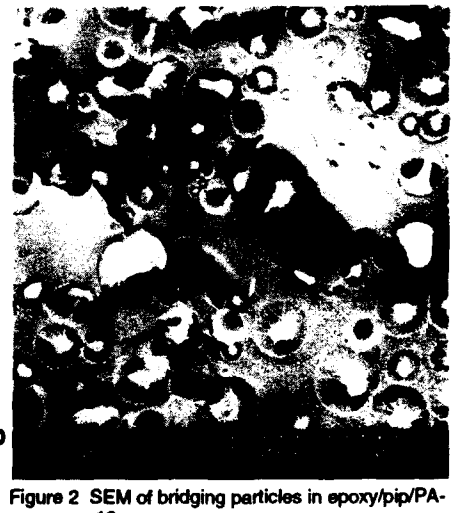

Figure 2 SEM of bridging particles in epoxy/pip/PA-12 process zone

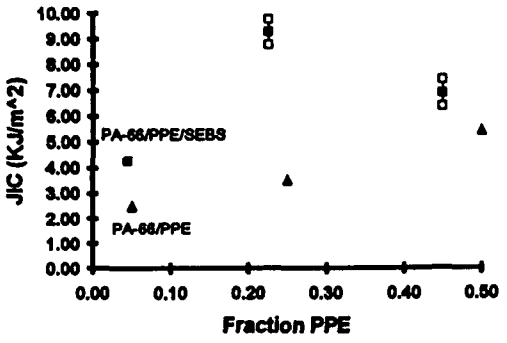

Figure 3 a.) Fracture toughness of PA-66/PPE/SEBS system

b.) TEM of process zone formed at crack tip of 50% PPE blend

Figure 4 a.) Bi-continuous structure of PBT/PC blend

b.) Drawn bridging particles in PBT/PC blend

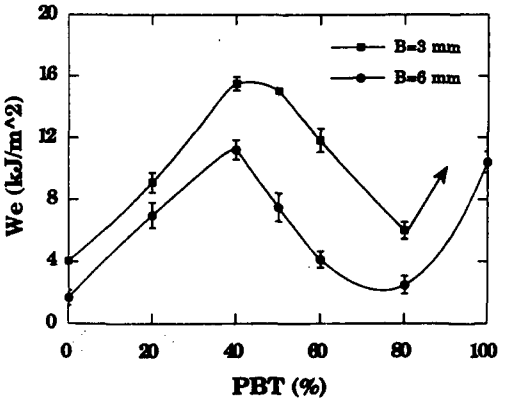

c.) Essential work of fracture of PBT/PC blends for two sample thicknesses

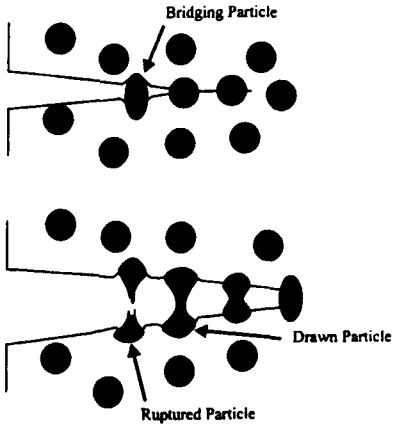

Figure 5 Schematic of crack bridging mechanism

A MODEL FOR PARTICLE CAVITATION AND DILATATION BAND FORMATION IN RUBBER TOUGHENED PLASTICS

A Lazzeri* and C B Bucknall**

A model is proposed for the deformation of plastics containing cavitated rubber particles. The basic principles are that cavitation occurs at a critical volume strain [1,2], and that yielding then follows through the formation of cavitated shear bands (dilatation bands). A theory of yielding in porous media, first advanced by Berg, and later developed by Gurson, is adapted to include the effects of mean stress, and applied to toughened plastics. The model predicts band angles that are determined by the current *effective* void content of the material. It accounts for observed changes in the kinetics of tensile deformation in toughened nylon following cavitation, and explains effects of particle size and rubber modulus on the brittle-tough transition temperature.

INTRODUCTION

Cavitation of rubber particles has been reported over the past 20 years in many toughened plastics, notably epoxy resins and nylons. In some cases, void formation shows no obvious pattern, while in others it is concentrated into well-defined bands. Polarized light microscopy studies by Yee and Pearson [3] on toughened epoxy resin show that the yield zone contains a high density of shear bands, which run from one cavitated particle to another; and recent work by Sue [4] has demonstrated the formation in toughened epoxy resins of 'croids' - craze-like planar regions of cavitated particles lying ahead of an advancing crack. There is an obvious relationship between 'croids' and the crazes reported by Argon et al [5] in styrene-butadiene block copolymers, where cavitation occurred quantitatively in small spheres or rods of polybutadiene, on planes normal to the applied tensile stress. Rubber-toughened plastics appear to form a continuous spectrum of deformation bands, ranging from 'ordinary' crazes through 'croids' and cavitated shear bands to void-free shear bands. Each type of band is characterised by its angle to the applied stress, its void content, and the degree of interconnection between voids. The present paper concentrates on 'dilatation bands', in which shear is combined with cavitation in various proportions.

THEORY

An earlier paper [1] proposes a new criterion for cavitation of the rubber phase in toughened plastics, according to which particles cavitate when the stored volumetric strain energy within the rubber phase exceeds a critical value. This principle is developed further in poster paper P62 [2]. Until they cavitate, particles are strongly resistant to volumetric expansion. However, a very small void, which can form without altering the volume V_p of a particle , turns it effectively into a void of volume V_p. A concentration of such voids, having a *local* volume

* University of Pisa, Via Diotisalvi 2, 56100, Pisa, Italy

** Advanced Materials Group, Cranfield University, Bedford MK43 OAL

fraction f within a planar band, is the starting point for the propagation of a dilatational band, which combines shear parallel to the plane with extension normal to it [6-8]. For a polymer, the criterion developed by Gurson [6-7] for this type of dilatational yielding can be modified by adding a further term in the mean stress σ_m to give the following expression for the effective stress σ_e at yield:

$$\sigma_e = \sigma_o \sqrt{\left(1 - \frac{\mu\sigma_m}{\sigma_o}\right)^2 - 2f\cosh\left(\frac{3\sigma_m}{2\sigma_o}\right) + f^2} \qquad (1)$$

where σ_o and μ are defined by the modified von Mises criterion for non-cavitating polymers:

$$\sigma_e = \sqrt{\frac{(\sigma_1-\sigma_2)^2+(\sigma_2-\sigma_3)^2+(\sigma_3-\sigma_1)^2}{2}} = \sigma_o - \mu\sigma_m \qquad (2)$$

When $\mu = 0$, Eqn 1 reduces to Gurson's equation. As shown in Fig. 1, the relationship predicted by Eqn 1 (solid line) between void content f and the yield stress in uniaxial tension is similar to that found by Gloagen *et al* between rubber particle volume fraction V_p and yield stress in uniaxial compression for a series of toughened PMMA blends (dotted line; data) [9]:

$$\sigma_{yc}(V_p) = (1 - 1.375V_p)\,\sigma_{yc}(0) \qquad (3)$$

Equation 1 predicts that dilatation bands are formed on planes with their normals at various angles ψ between 0° and 38° to the tensile stress direction. As shown in Fig. 2 for a typical polymer having $\mu = 0.39$, for the case of uniaxial tension ψ decreases from 38° in the absence of cavitation to 0° at $f = 0.52$, whereas under plane strain conditions at a crack tip, ψ decreases to zero at $f = 0.04$. Figure 3 compares the predicted relationship between f and yield stress under two conditions: uniaxial tension, which to a good approximation follows Eqn 3 (with f and σ_{yt} replacing V_p and σ_{yc}), and plane strain loading at a crack tip, with Poisson's ratio = 0.4. It is clear that the main effect of cavitation is to lower yield stress at the crack tip.

EVIDENCE FOR FORMATION OF DILATATION BANDS

Optical and electron microscopy studies do not always reveal an obvious spatial pattern of void formation in toughened plastics. In the work of Yee and Pearson [3], it was only the use of polarized light microscopy that drew attention to the presence of connecting shear bands between the cavitated particles. In the light of Fig. 3 in paper P62 [2], it is not surprising that cavitation is seen in isolated large particles when the distribution of particle sizes is broad, nor that dilatation bands initiate on planes in which large particles are relatively close together.

An example of such a cavitation band can be seen in Fig. 4, which shows an osmium-stained section from a broken Charpy impact specimen of toughened nylon 6. Figure 5 emphasises the main features of the band: a line of relatively large cavitated polybutadiene particles, sheared parallel to the void line, runs across the micrograph. This observation suggests that dilatation bands grow by repeated particle cavitation around their edges, where volume strains are relatively high. The main requirement is that there is a sufficient concentration of larger particles within the region of enhanced strain. The best examples of particle cavitation within well-defined bands, with little or no void formation visible outside the bands, are seen in materials containing a very narrow distribution of particle sizes [4,5]. This point can also be understood in the light of Fig. 3 in paper P62 [2]: when one or two particles begin to cavitate, there are always other particles of similar size nearby, which are already close to the critical cavitational strain, and need only a small increase in local volume strain to initiate void formation. Thus the band will propagate along the preferred angle ψ.

The most reliable data on band angles in toughened plastics are to be found in the light scattering patterns published by Breuer *et al* [10], who noted the formation of voids connected with shear bands. The advantage of light scattering is that it averages information from a large number of bands, whereas electron and optical microscopy provide detailed data on individual bands.

The relationship between particle cavitation and loading conditions can conveniently be analysed using a *cavitation diagram*, as illustrated schematically in Fig. 6. The upper bound is the locus of yielding when the effective void content $f = 0$, and the lower bound is drawn for $f = 0.2$. All toughened materials are initially void-free: they cavitate on reaching a critical volume strain, and therefore a critical σ_m. Where there is a range of particle sizes, cavitation occurs over a range of σ_m, which is marked by shading in the diagram. The heavy dotted line represents a transition from void-free to fully-cavitated state. The diagram is useful not only in comparing stress states, but also in analysing the effects of strain rate and temperature, which cause the two bounds on yield stress to shift relative to the range of σ_m at which cavitation occurs.

DISCUSSION

Evidence for the effects of particle size on cavitation can be seen in the work of Gaymans et al [11] on the impact behaviour of toughened nylon 6. Over the range 1.0 to 0.2 μm, reducing particle size results in a decrease in brittle-tough transition temperature, which is probably related to the decrease in interparticle spacing [12,13], while the maximum impact energy at higher temperatures remains constant. However, if the particle size is reduced further, the trend in the brittle-tough transition is reversed, and the maximum impact energy decreases linearly with R. This effect is explained by the cavitation criterion. Another of its predictions is that cavitation resistance increases with the shear modulus G_r of the rubber, which is also consistent with the impact data of Gaymans *et al* [13] for rubber-modified nylon 6. Finally, the formation and expansion of dilatation bands explains the observed acceleration in the tensile creep rate of toughened nylon 6.6 when cavitation begins at an applied stress of 30 MPa [14].

ACKNOWLEDGMENTS

The authors thank the Science and Engineering Research Council (GR/H06354) and the CNR of Italy for financial support of this project. They also thank Drs. R. J. Gaymans and K. Dijkstra for providing the toughened nylon sample shown in Fig. 4.

REFERENCES

1. A. Lazzeri and C.B. Bucknall, J. Mater. Sci. **28** (1983) 6799.
2. C.B. Bucknall, A.M. Karpodinis and X.C. Zhang, Paper P62, this conference.
3. A.F. Yee and R.A. Pearson, in A.C. Roulin-Moloney (ed.), "Fractography and Failure Mechanisms in Polymers and Composites", Elsevier, London 1989.
4. H.Y. Sue, J. Mater. Sci. **27** (1992) 3098.
5. A.S. Argon, R.E. Cohen, O.S. Gebizlioglu and C.E. Schwier, *in* Adv. Polym. Sci. **52/53** (H.H. Kausch, ed.), Springer, Heidelberg, 1983.
6. A.L. Gurson, Ph.D. Thesis, Brown University (1975).
7. A.L. Gurson, ICF4 Fracture 1977, Waterloo, Canada (D.M.R. Taplin, ed.), Vol. 2A, p. 357, Pergamon, Oxford, 1977.
8. P.F. Thomason, "Ductile Fracture of Metals", Pergamon, Oxford, 1991.
9. J.M. Gloaguen, P. Heim, P. Gaillard and J.M. Lefebvre, Polymer, **33** (1992) 4741.
10. H.Breuer, F.Haaf and J.Stabenow, J. Macromol. Sci.- Phys. **B14** (1977) 387.
11. R.J. Gaymans, R.J.M. Borggreve and A.J. Oostenbrink, Makromol. Chem, Macromol. Symp. **38** (1990) 125.
12. S. Wu, Polymer, **26** (1985) 1855.
13. R.J.M. Borggreve, R.J. Gaymans, J. Schuijer and J.F. Ingen-Housz, Polymer **28** (1987) 1489.
14. C.B. Bucknall, P.S. Heather and A. Lazzeri, J. Mater. Sci. **28** (1993) 6799.

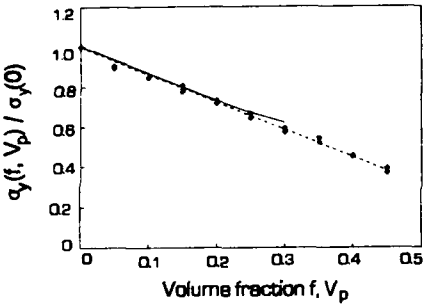

Fig.1. Comparison of Eqn. 1 for uniaxial tension with compressive yield data on RTPMMA [9].

Fig.4. A dilatation band in toughened PA6. Specimen courtesy of R.J. Gaymans and K. Dijkstra.

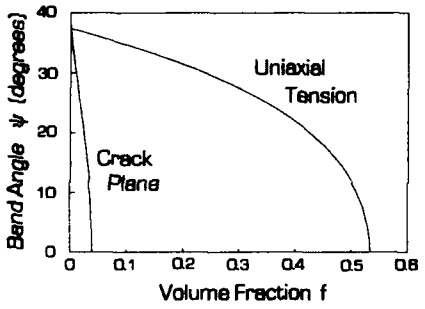

Fig.2. Band angles Ψ (see Fig. 5) as predicted by Eqn 1.

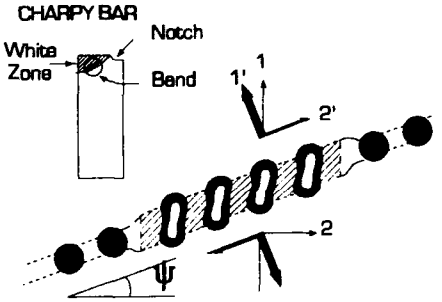

Fig.5. Schematic diagram of dilatation band, based on Fig. 4.

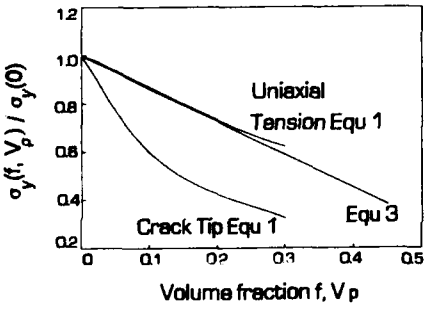

Fig.3. Predicted effect of void content on yield in uniaxial tension vs. at crack tip.

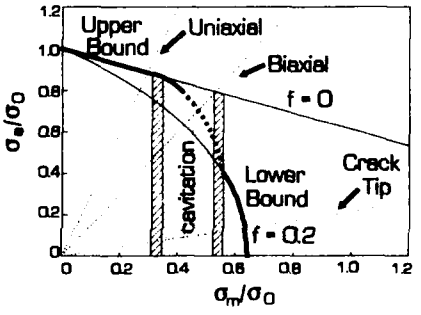

Fig.6. Schematic cavitation diagram for polymer containing 20 vol.% rubber.

DEFORMATION MICROMECHANICS IN RUBBER-TOUGHENED ACRYLIC POLYMERS

P.A. Lovell*, A.J. Ryan, M.N. Sherratt and R.J. Young

The paper describes the deformation micromechanics in rubber-toughened acrylic polymers studied using optical microscopy, transmission electron microscopy and real-time, small-angle X-ray scattering. The materials investigated contain refractive index-matched toughening particles with 2, 3 and 4 radially-alternating rubbery and glassy layers. For the 3-layer particles the following have been varied: (i) layer thickness, (ii) glassy core size and (iii) overall particle diameter (up to 0.3 μm). The results indicate that the mechanism(s) depend upon the mode and rate of deformation. There is strong evidence that the particles cavitate prior to shear yielding in tensile deformation. However, in the fracture of notched three-point bend specimens microcrazing is the most important mechanism.

INTRODUCTION

This paper presents results from studies of the deformation micromechanics of the range of novel rubber-toughened poly(methyl methacrylate) (RTPMMA) materials described herein [1].

EXPERIMENTAL

Materials

The preparation of the materials and the nomenclature used to define them is described separately [1].

Studies of Deformation Micromechanics

The matrix PMMA and each of the RTPMMA materials were compression-moulded into plaques of 3 mm thickness (for tensile specimens), 6 mm thickness (for impact fracture specimens) and 12 mm thickness (for low-rate fracture specimens). Polishing/sectioning techniques [2-4] for observing deformation zones have been used to elucidate toughening mechanisms. Tensile specimens were deformed to fracture before polishing. Single and double edge-notched fracture specimens were subjected to sub-critical crack growth in 3-point bend mode prior to polishing. The specimens were either (i) polished from two faces to obtain thin sections for optical microscopy, or (ii) polished from one face followed by ultramicrotoming and then staining with ruthenium tetroxide to obtain sections for examination by transmission electron microscopy (TEM). Fracture surfaces also were examined by scanning electron microscopy (SEM).

X-ray scattering experiments were performed using the synchrotron source at the Daresbury SERC Laboratory. Real-time, simultaneous small-angle X-ray scattering (SAXS) and tensile testing was carried out with 10 s time resolution employing an area detector on beamline 8.2 and a Polymer Laboratories Minimat tensile testing apparatus. Static ultra-small-angle X-ray scattering (USAXS) experiments were carried out on pre-deformed tensile samples employing a Bonse-Hart camera with a linear detector on beamline 2.1.

* Polymer Science and Technology Group, Manchester Materials Science Centre, University of Manchester & UMIST, Grosvenor Street, Manchester, M1 7HS, United Kingdom

RESULTS AND DISCUSSION

Optical microscopy of specimens from tensile tests show significant differences in deformation behaviour. The 2L, 3LA, 3LAI, 3LE and 4L materials develop diffuse shear bands and stress-whiten at, and beyond, the yield point. The 3LB and 3LD materials stress-whiten with shear bands emanating from diamond-shaped features which form just prior to yield, and also develop an undulating surface texture. The 3LC materials show similar shear bands emanating from diamond-shaped features and have surface texture, but do not significantly stress-whiten. Examples of the different types of shear banding are shown in *Figure 1*.

SEM of fracture surfaces from tensile specimens shows the presence of numerous holes and dome-like features with diameters similar to, and also smaller than, those of the toughening particles, suggesting that cavitation and/or debonding of the toughening particles contributes to stress-whitening. TEM of sections taken from just below fracture surfaces of tensile specimens confirms the presence of cavities inside toughening particles (see *Figure 2*).

Real-time simultaneous SAXS and tensile testing has shown that particle cavitation/debonding precedes yielding (see *Figure 3*) and gives no evidence of the characteristic scattering pattern of crazes [5]. Instead, the scattering pattern indicates the presence of voids which become increasingly elongated in the tensile direction as the strain increases. USAXS experiments on pre-deformed specimens have confirmed that the voids are elongated in shape and have their principal axis lying in the direction of the tensile axis.

Optical microscopy of deformation zones formed at the tips of sub-critically grown cracks in the RTPMMA materials shows flame-shaped plastic zones. The cores of the plastic zones are highly birefringent in samples obtained at low rates of deformation and are surrounded by fine dark bands. Stained TEM sections taken close to and around the the crack tip reveal that the particles are connected, through the matrix, by fine bands which have a craze-like structure and are considered to be microcrazes. The principal deformation mode, therefore, is microcrazing (*Figure 4a*). However, similar non-stained sections (*Figure 4b*) show clear evidence of particle cavitation and indicate that cavitation is associated with formation of the crazes.

The TEM micrographs shown in *Figure 5* are typical of the deformation around and ahead of cracks grown sub-critically under impact conditions. *Figure 5a* is a micrograph taken at relatively low magnification in the plane normal to the crack and shows the presence of microcrazes. At higher magnification (*Figure 5b*), the bands can be seen to have propagated between (and, in some cases, through) the particles, with no evidence of particle cavitation. Hence, fracture under impact conditions appears to be dominated by microcrazing.

ACKNOWLEDGEMENTS

The authors express their thanks to the Science and Engineering Research Council and ICI plc for funding this research programme. The assistance of Mike Chisholm and Bill Jung of ICI plc is gratefully acknowledged.

REFERENCES

1. A.C. Archer, P.A. Lovell, J. McDonald, M.N. Sherratt and R.J. Young, *Mechanical Properties of Rubber-Toughened Acrylic Polymers*, paper P104.
2. R.A. Pearson and A.F. Yee, *J. Mat. Sci.*, **21**, 2475 (1986)
3. H-J. Sue and A.F. Yee, *J. Mat. Sci.*, **24**, 1447 (1989)
4. R.A. Pearson and A.F. Yee, *J. Mat. Sci.*, **26**, 3828 (1991)
5. R.A. Bubeck, D.J. Buckley, E.J. Kramer and H.R. Brown, *J. Mat. Sci.*, **26**, 6249 (1991)

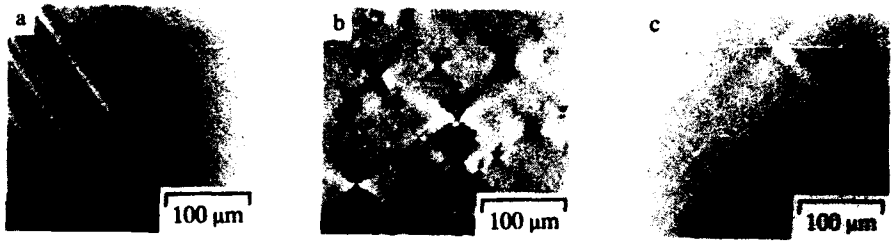

Figure 1. Optical micrographs from fractured tensile specimens showing shear deformation bands viewed between crossed, polarising filters to enhance contrast between the birefringent bands and the undeformed matrix: (a) bands typical of those observed in 2L, 3LA, 3LAI, 3LE and 4L materials, (b) bands typical of those observed in 3LB and 3LD materials, and (c) bands observed in 3LC materials.

Figure 2. TEM micrograph of a non-stained section taken from just below fracture surface in the stress-whitened region of a 3LA34 tensile specimen. The presence of cavities inside the toughening particles is clearly evident.

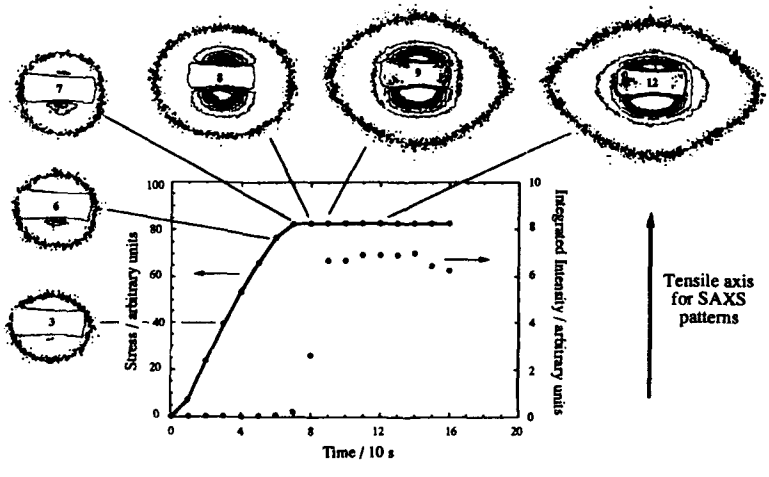

Figure 3. Results from simultaneous SAXS–tensile testing of 3LE31 showing that the onset of voiding occurs just prior to the yield point and that the extent of voiding increases dramatically during the early stages of plastic flow.

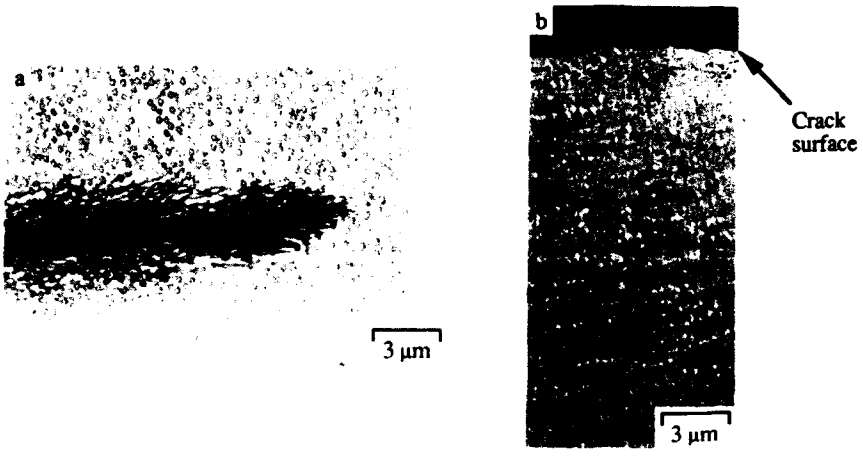

Figure 4. Micrographs of the deformation at the tips of cracks grown sub-critically at low rate in single edge-notched, 3-point bend specimens. (a) TEM micrograph of a stained section near the crack tip in 3LAI35. (b) TEM micrograph of a non-stained section adjacent to the crack in 3LB21.

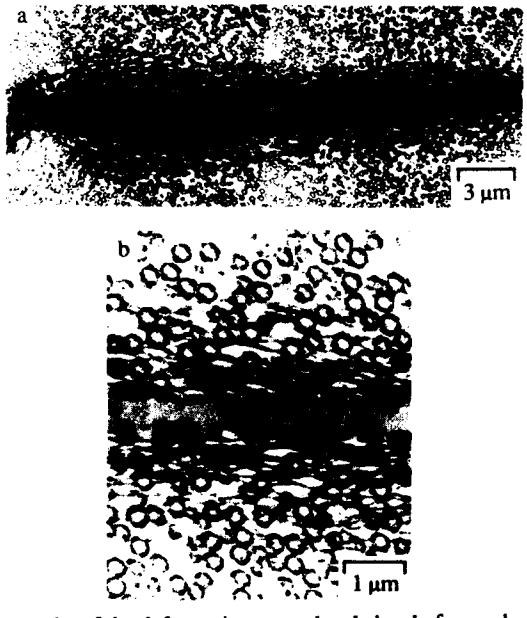

Figure 5. TEM micrographs of the deformation around and ahead of a crack sub-critically grown under impact in a double edge-notched, 3-point bend specimen of 3LE31. (a) Low magnification micrograph showing fine deformation bands in the plane normal to the crack. (b) The bands in (a) shown at higher magnification.

POLYAMIDE-RUBBER BLENDS: INFLUENCE OF DEFORMATION SPEED ON CRACK PROPAGATION PROCESS

R.J. Gaymans, K. Dijkstra* and H. Janik**
University of Twente, P O Box 217, 7500 AE Enschede, The Netherlands

The fracture propagation of PA-blends is studied with a notched tensile test as function of test speed. For the blends two transitions are observed one at low speeds and one at high speeds. At low speeds a minimal amount of rubber is sufficient to give a high propagation energy. On increasing the rate the propagation energy is lowered. At even higher speeds the energy increases again. At very high speeds most samples are once more brittle. The high speed transition seem te be corrolated with a melt blunting process.

INTRODUCTION

Polymers fracture under notched impact conditions nearly always brittle but become tough at elevated temperatures. On blending in rubber the temperature of the sharp brittle to tough (BT) transitions is lowered. At the BT transition the crack propagation changes from an unstable to a stable crack growth (1-3). The BT-temperature decreases with rubber concentration (1-3) and decreasing particle size (3). These two parameters can be combined to an interparticle distance parameter (ID) (3-4). This ID has however no correlation with the impact levels (1,2,5). The meaning of the ID is still a point of discussion.
We studied the influence of deformation speed on PA 6/EPR blends with a notched tensile test method and analyzed the fractured samples. The blends on PA 6 (Akulon K124) and Ethylene-Propylene Rubber (EPR) (Exxelor VA 1801) were made on a Berstorff ZE 25 twin screw extruder. The particle sizes of the blends were 0.3 - 0.4 μm. Notched tensile impact (NTI) tests were carried out on a Schenck VHS servo-hydraulic tensile tester (1,2). A clamp speed of 1m/s in the NTI is comparable to the speeds in the notched Izod test.

RESULTS AND DISCUSSION

We are interested in the BT transition, the transition of an unstable to stable crack propagation. The crack propagation energies are determined from the area in the stress displacement curves. PA 6 (injection moulding type) has in the 10^{-6} - 10 m/s piston speed range a very low crack propagation energy (fig 1). Thus the PA is brittle over the whole speed region.

* presently at DSM Research, P O Box 18, 6160 MD Geleen, NL
** on leave from Technical University of Gdansk, Poland

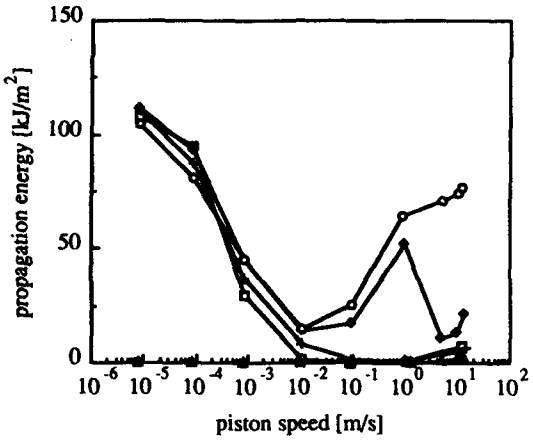

Figure 1 Propagation energy versus piston speed on PA 6/EPR with varying rubber content (wt %): ▲ 0%, ▫ 5%, + 10%, ◆ 15%, o 20%

The blends give a complex picture. They all start high at low piston speeds, fall to near zero at 10-2 m/s and some increase again at higher rates. At low speeds with small amounts of rubber the material is at RT already tough. The propagation energy at low speeds (in the tough region) is little dependent on the rubber concentration. Surprisingly above 1m/s the 15 and 20 % blends, the crack propagation energy increases again, but at 5m/s the 15 % blend is nearly brittle again. The 15 and 20% blends show clearly a discontinuous behavior. The 15% blend shows a low speed BT at 10-2 m/s and a high speed BT at 5 m/s. The small increase in propagation energy at the highest test speeds is still puzzling.

The maximum stress in these samples is complex too. In the PA 6 the stress first rises a bit with

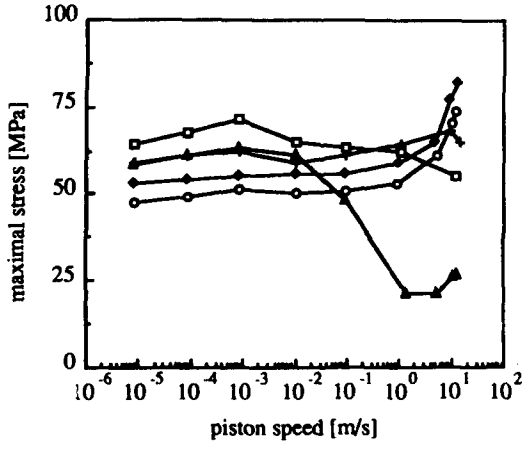

Figure 2 Maximum stress versus piston speed on PA 6/EPR with varying rubber content (wt %): ▲ 0%, ▫ 5%, + 10%, ◆ 15%, o 20%

speed, a behavior which is expected for a sample which still can reach its yield point. At higher speeds the maximum stress falls off and the material becomes more brittle. Surprisingly at the highest speeds 10 and 13 m/s the maximum stress increases a bit again. As the propagation energy is zero the initiation energies show the same trend. In the blends the maximum stress at low rates decreases as expected with the rubber concentration. At high rates the 15 and 20% blends show an unexpected strong upswing in the maximum stress. The maximum stress before fracture can increase if the stress concentration factor ahead of the notch is lowered.

All these results indicate that the high speed data cannot be obtained by extrapolating the low speed data. The extrapolated low speed data should just give brittle fracture for all the samples. So the fracture process at the high speeds must be different from the process at low speeds. This indicates that there is an extra deformation mechanism operative in the high speed regime which enables the crack propagation to become stabilized under these conditions. The highest speed data even suggest that this mechanism becomes operative before a crack is initiated which results in a sudden increase in the maximum stress. These findings suggest that there are two BT transitions one at low test speeds and one at high test speeds. Similar behavior have been observed with PP/EPDM blends (6).

The structure of the deformed material perpendicular to the fracture surface is studied with SEM and TEM. Of a tough broken sample at 1 m/s in the deformed layer next to the fracture surface a 3-5 μm zone can be seen with only a few round cavities, a zone (50-100 μm thick) with strongly deformed cavities and a zone 1-2 mm thick of round cavities (fig 5). A similar structure has been observed by Oostenbrink et al (7) on fractured notched Izod sample

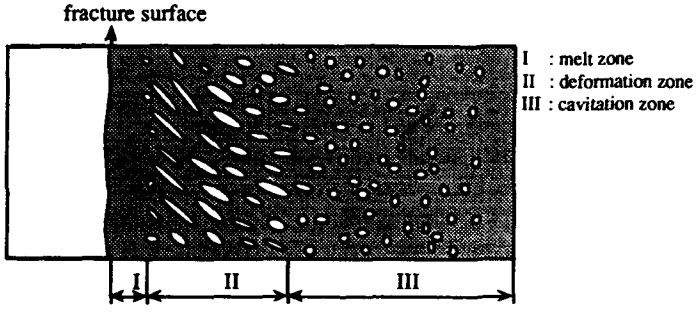

Figure 3 Cartoon structure deformed layer perpendicular the fracture surface, fractured tough at a high test speed

On samples which have been deformed at low speeds (10^{-2} m/s) a cavitated structure which is strongly deformed (50-100 μm thick) and further away a cavitated structure with round cavities can be seen, but not the noncavitated structure next to the fracture surface. A Similar structure development was also observed on PP/EPDM blends (6). With polarized light microscopy an isotropic layer could be observed next to the fracture surface of the high speed tested sample.

At high speeds the zone next to the fracture surface is clearly relaxed and relaxation of highly deformed PA can only take place in the melt.

The relaxation of cavitated structure was tested by suspending a cavitated sample in a oil bath for 5 minutes (8). This test was carried out at several temperatures and it was observed that the cavitated

structure disappeared at 230°C, just above the melting temperature of PA 6.
Temperature measurements with an IR camera during drawing a sample at high deformation rates (but much lower than in the rates in the fracture surface) and gave an overall temperature increases of 140°C (7).
The oil bath experiments and the temperature measurements with the IR-camera strongly indicate that the relaxed layer next to the fracture surface only visible in the high speed fractured samples is due to melting. If a melt layer is formed in the fracture zone then crack tip blunting takes place. The occurrence of crack blunting might be concluded too from the upswing in maximum force in the NTI at the high test speeds.
The difference between the low and the high speed data is that at high speeds the process becomes adiabatic and apparently melt blunting can then take place.

CONCLUSIONS

The PA (injection moulding grade) at RT is brittle over the broad test speed range 10^{-5} - 10 m/s.
The PA-EPR blends are tough at RT and at low speeds. A few % rubber is for this region sufficient for excellent impact behavior. In the 10^{-2}m/s region all PA-EPR blends are nearly brittle. Surprisingly at high deformation speeds the crack propagation energy increases again and almost all samples are brittle again at 10 m/s.
The results show that there are two fracture propagation processes one at low piston speeds and one at high piston speeds. Thus also two tough to brittle transitions one at low speeds and one at high speeds. The high speed transition is in agreement with the izod data and is dependent on the rubber concentration and particle size and show a good correlation with the ligament thickness. Of the low speed transition we still know little.
In the high speed transition melt blunting takes place and this melt blunting decrease the stress concentration factor ahead of the crack or notch and higher stresses are necessary to initiate or propagate a crack. The melt blunting might be correlated with the ID parameter.
The function of the rubber in PA-rubber blends is to create stable cavities on loading. Due to cavitation the von Mises stress in the matrix is strongly increased and plastic deformation is possible (1,5). The von Mises stress in a cavitated system is a function of the cavity concentration. The cavity size does not play a role in this mechanism. The rubber particle size or ligament thickness have no effect on the onset of plastic deformation, but may have an effect on the extend of plastic deformation (maximum draw ratio). A small change in draw ratio has under isothermal conditions little effect but under adiabatic conditions it may result in local melting and with that of melt blunting.

REFERENCES

1 K. Dijkstra, PhD Thesis, University of Twente, The Netherlands, February 1993
2 K. Dijkstra, J. ter Laak and R.J. Gaymans, PA 6 Rubber blends, Part 6, Polymer in press
3 R.J.M. Borggreve, R.J. Gaymans, J. Schuijer and J.F. Ingen Housz, Polymer, 28, 1489 (1987)
4 S. Wu, Polymer , 26, 1855 (1985)
5 K. Dijkstra, H.H. Wevers and R.J.Gaymans, PA 6 Rubber blends, Part 7, Polymer in press
6 A. van der Wal and R.J. Gaymans, PRI, Churchill Conf., April 1994, Poster P60
7 A.J. Oostenbrink, K. Dijkstra, A. van der Wal and R.J. Gaymans, PRI Conference; Deformation and Fracture of Polymers, Cambridge April 1991, preprints 50
8 K. Dijkstra, and R.J. Gaymans, PA 6 Rubber blends, Part 2, J. Mat. Sci., submitted

REAL-TIME CRYO-DEFORMATION OF POLYPROPYLENE AND IMPACT MODIFIED POLYPROPYLENE IN THE TRANSMISSION ELECTRON MICROSCOPE.

Robert C. Cieslinski*

Dynamic plane stress failure has been observed directly in the transmission electron microscope as a function of temperature using a commercially available *cooling/straining holder in conjunction with a copper deformation cartridge*. The low temperature cooling stage permits studies of the ductile-brittle transition when the transition is between +23 and -170°C and the events occurring during the deformation can be recorded in real time using a CCD video camera. A change in deformation mode was observed on the sub-micron level for polypropylene and impact modified polypropylene. At room temperature, polypropylene and impact modified polypropylene deform by shear yielding. Below the ductile-brittle transition the polymer chains become rigid and crazing dominates.

INTRODUCTION

A previously described technique (1) allows the real-time observation of dynamic plane stress polymer failure in the transmission electron microscope. After bonding a thin section of polymer to an annealed copper cartridge, it is plastically deformed in tension in the TEM using a screw-driven tensile stage while a low light CCD video camera records the deformation and fracture processes. Recently, a low temperature cryo-tensile stage has become commercially available. The stage can be used from room temperature down to of -170°C. Thus, the failure of a polymer can be studied below its ductile-brittle transition temperature.

This paper demonstrates the use of this stage to study failure and toughening in polypropylene and impact modified polypropylene.

The deformation of polypropylene has been extensively reviewed by Friedrick (2). Jang, Uhlmann, and Vander Sande have conducted tensile experiments on PP and rubber modified PP's over a wide range of temperatures and strain rates (3). These investigators have shown that the ductile-brittle transition is strongly affected by both temperature and strain rate. For a given temperature, there is a critical strain rate above which crazing dominates and below which shear yielding is dominant. The ductile-brittle transition was explained as being due to the alteration in deformation mode (4). The experiments conducted herein allows visualization of the change in deformation mode with temperature.

EXPERIMENTAL

The single tilt cold strain holder and CCD camera were manufactured by Gatan**. The key to performing these experiments directly in the transmission electron microscope was the development of a specimen cartridge which could support the thin section of bulk polymer and still deform plastically under load. The cartridge manufactured by PCM Products† was designed at Dow. Several cartridge configurations now exist. Details on the design and applications of the grids are described in reference (1).

* The Dow Chemical Company, 1897F Bldg., Midland, MI 48667
** Gatan Inc., 6678 Owens Drive, Pleasanton, CA 94588-334.
† PCM Products, P.O. Box 5399 Tittusville, FL. 32783-5399.

RESULTS

The unique capability to do tensile deformation directly in the transmission electron microscope allows one to examine the details of the deformation in real time as a video camera records the deformation. The two limiting conditions, plane strain and plane stress are often used to describe the deformation of a thermoplastic subjected to a tensile loading; for a thin microtomed polypropylene film, plane stress dominates. In this case the deformation usually continues by a semi-homogenous yielding process. Figure 1. shows a thin section of polypropylene deformed at 23°C to an elongation of 66%. During the deformation, shearing in the surrounding matrix material was observed on the video display. The void produced during the deformation was associated with an unidentified nucleating aid. The nucleating aid concentrates stress and initiates the deformation. Because the nucleating aid is not well bonded to the polypropylene matrix, a void forms with continuing deformation. A whitened area resembling crazing is seen emanating from the equators of the void. However, this is not a craze because the white area is homogeneously thinned (i.e. yielding) during deformation without the voids that are typical of crazing. This type of deformation has recently been termed fibrillated shear in crystalline polymers (5). The fibrillated shear zones crossed PP spherulite boundaries and were increased in number as the amount of nucleating aid increased. Voids always formed around the nucleating aid and at extensions exceeding 200% the void would become a crack which upon further extension would propagate through the fibrillated shear zones until the film failed.

Temperature effects are illustrated in Figure 2. As the temperature decreased the elongation of the specimen is reduced and shear yielding gradually gives way to crazing. The first appearance of crazing in the shear zones occurred at -5°C just above the ductile-brittle transition; voiding occurred in the deformation zone and the boundaries between this zone and the matrix material became sharp. As the temperature was further lowered, the boundaries became sharper and increased voiding resulted in fibrils in the deformed region. The shape and aspect ratio of the crazes also changed as the temperature was lowered. Low aspect ratio crazes formed near the ductile-brittle transition and high aspect ratio crazes formed below the transition. Donald (6) observed similar results in her studies on polystyrene films as a function of temperature and molecular weight.

Rubber Modified Polypropylene

The addition of a low modulus elastomer to polypropylene greatly increases the low temperature impact toughness (11-13), reduces the yield stress and shifts the ductile-brittle transition to lower temperatures. Ethylene-propylene-diene elastomer (EPDM) is used to modify isotactic polypropylene for use in automotive applications. The in-situ cryogenic deformation of polypropylene was compared for two modifiers, EPDM and a new class of ethylene-octene copolymers. The new polyolefin elastomers are prepared using Dow's constrained geometry catalyst technology (CGCT) and have recently become commercially available under the Insite™ trademark. The main advantage of the Insite technology elastomers, other than their relatively low cost, is their ability to impart ductile failure in PP blends with high melt flow (MF≥20) at low temperature (-20°F). The PP/Insite blends have higher net melt flows than their EPDM analogs resulting in easier processing.

Commercial specifications require ductile failure at -20°F (-29°C). The materials were deformed in the transmission electron microscope down to a temperature of -31°C. The effects of room temperature deformation for the Insite elastomer modified materials are shown in Figure 3. Similar results were observed for the PP/EPDM blends. The rubber functions as a stress concentrator and nucleates shearing (rubber assisted shear deformation). The stress concentration is strongly affected by the number of elastomer particles. At the high loadings used in commercial applications, local yielding is caused by overlap of particle stress fields. Wu (14) has shown that there is a critical interparticle distance which reduces the critical stress for matrix yielding to about half of that required without rubber. The particle size of the Insite elastomer is smaller than the EPDM, resulting in a smaller interparticle distance for the same loading and thus providing a higher extent of yielding. The addition of the Insite elastomer reduced the average spherulite size of the PP from 4.6 to 3 μm which has been shown previously to increase the fracture resistance (2,3.) While there is poor adhesion between ethylene-propylene rubber (EPR) (15) and PP, good adhesion was observed between the

matrix and the EPDM and Insite elastomers. During deformation the rubber can be observed to expand by several hundred percent before the elastomer eventually cavitates. Even then, the rubber fibrils bounded to the PP stabilize the cracks which form during cavitation.

As the temperature was decreased shear yielding gave way to crazing. The change in the mode of deformation occurred at approximately -5°C, the same temperature at which crazing started in the unmodified PP and not at the transition temperature shown in the Dynatup impact studies. The differences between the Dynatup impact data and the TEM tensile results arise because of the strain rate difference. The impact tests were conducted at a rate of approximately 2.4×10^6 µm/sec whereas the material was deformed in the TEM between 0.1 and 1 µm/sec. Jang, et al, conducted extensive tensile testing over a wide range of temperatures and strain rates (3). When they plotted the normalized yield stress (defined as the maximum engineering stress in the stress-strain curve divided by the test temperature) vs. the log strain rate, they noted a transition zone in which crazes and shear bands coexist. For a given test temperature there is a strain rate which is dominated by crazing and for a given test strain rate there exists a temperature which restricts crazing from shear yielding. In this investigation, deformation mechanisms were studied as a function of temperature only because of the limited strain rate range capability with the present stage. Within this range (0.1 - 1µm/sec.), the onset of crazing was the same for PP and rubber modified PP. The deformation volume is considerably higher in the presence of rubber.

At -31°C, rubber particles nucleated crazing in the polypropylene matrix. As the material deforms, the rubber bridges the crazes, maintaining the craze integrity. EPDM rubber will expand by a factor of two before cavitation occurs. Some particles undergo greater elongation depending on the amount of shear and critical stress around the particles. During this elongation the EPDM is thinning and at 200%, the EPDM particles have broken down into rubber fibrils. The rubber fibrils are still well bounded to the PP matrix and will span and maintain the stability of the cracks generated through matrix crazing. Further elongation results in breaking the rubber fibrils and cracks propagate to failure. Insite™elastomers were found to expand by as much as 400% before cavitation and fibrillation. The greater elongation of Insite elastomers is due to higher their elasticity at these temperatures. This may be due to differences in entanglement density.

REFERENCES

1. Cieslinski, R. C J. Mater. Sci. Letters 1992, 11, 813.
2. Friedrich, K. Advances in Polymer Science 52/53, "Crazing in Polymers" (Springer-Verlag), Ed. H. H. Kausch (1983) 226-274.
3. Jang, B. Z., Uhlmann, D.R. and Vander Sande, J.B. J. Appl. Polym. Sci.. 1984, 29, 3409.
4. Matsushige, K., Radcliffe, S. V. and Baer, E. J. Appl. Polym. Sci. 1976, 20, 1853.
5. More, A. P. and Donald, A. M. Polymer 1992, 33, 4081.
6 Donald, A. M. J. Mater. Sci. 1985, 20, 2630.
7. Donald, A. M. J. Polym. Sci. Phys. Ed. 1982, 20, 899.
8. Idem, Polymer 1984, 23, 461.
9. Henkee, C.and Kramer, E. J. J. Polym. Sci. Phys. 1984, 22, 721.
10. Lauterwasser, B.D.and Kramer, E.J. Phil. Mag. 1979, 39A, 469.
11. Ramsteiner, F., Kanig, G. Hechmann, W. and Guber, W. Polymer 1983, 24, 365.
12 Jang, B. Z., Uhlmann, D. R. and Vander Sande, J. B. J. Appl. Polym. Sci. 1980, 30, 2485.
13. Lovinger, A. J. and Williams, M. L. J. Appl. Polym. Sci. 1980, 25, 1703.
14. Wu, S. J. Appl. Polym. Sci. 1988, 35, 549.
15. Jancar, J., DiAnselmo, A and DiBenedetto, A. T. Polym. Comm. 1991, 32, 367.

Figure 1. Polypropylene deformed at room temperature (-23°C). Arrow indicates nucleating aid.

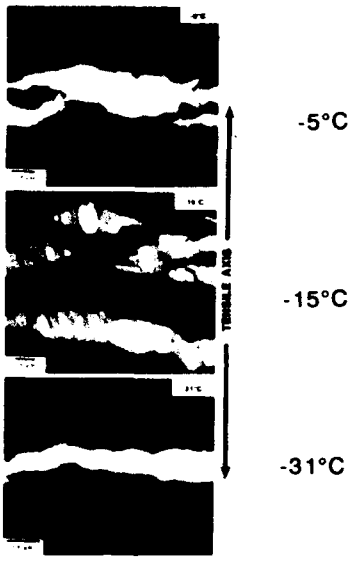

Figure 2. Polypropylene deformed at -5°C, -15°C and-31°C showing a transition from fibrillated shear to crazing.

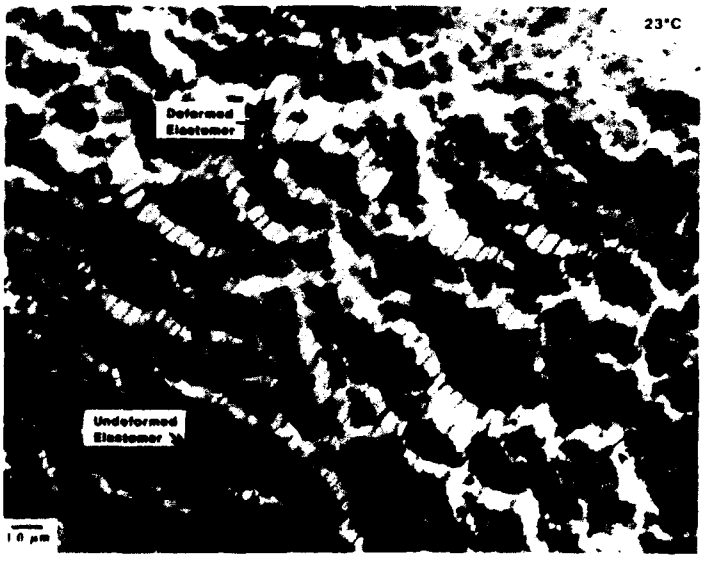

Figure 3. Room temperature deformation for 30% elastomer loading in polypropylene.

PREDICTIVE MODELS FOR THE DEFORMATION AND YIELD OF TOUGHENED POLYMERS

F J Guild* and A J Kinloch†

The mechanical properties and failure mechanisms of toughened polymers have been investigated using the finite element analysis method. The materials investigated include rubber-toughened epoxy resin and multi-stage particulate reinforced PMMA. Results from the predictive models are compared with experimental observations leading to significant elucidations of their mechanical properties and failure mechanisms.

INTRODUCTION

Technological developments are allowing the manufacture of an increasing range of toughened polymeric materials. Comprehensive experimental evaluation of all possible materials is unrealistic, so predictive modelling is an economical tool for the design and selection of potentially new materials. This paper presents result from predictive models of toughened polymers using the method of finite element analysis.

Two important toughening mechanisms have been identified for two-phase materials consisting of a rubbery phase dispersed in a matrix of crosslinked polymer, such as epoxy resin (eg 1). The first is localised shear yielding, or shear banding, which occurs in the matrix between rubber particles. The second mechanism is the internal cavitation of the rubbery particles, and the subsequent growth of these voids by plastic deformation of the epoxy matrix. A further important mechanism for toughened, thermoplastic, acrylics may be craze growth in the matrix (2). The aim of any model must be to predict the initiation and growth of these various micromechanisms.

* Department of Materials Science & Engineering, University of Surrey, Guildford, Surrey GU2 5XH
† Department of Mechanical Engineering, Imperial College of Science, Technology and Medicine, Exhibition Road, London SW7 2BX

MATERIALS

Results presented in this paper are for polymeric materials toughened with either single-stage or multi-stage particles. The single-stage particles are composed of rubber and are in a matrix of crosslinked epoxy resin. The modelling is carried out assuming fixed properties for the epoxy matrix (E = 3 GPa, ν = 0.35) and for the rubber spheres (E = 1 MPa, ν = 0.49992). These rubber properties were chosen since they imply a value of bulk modulus of about 2 GPa, which is the expected value.

The results for the multi-stage material presented here are for thermoplastic PMMA matrix toughened by the addition of two different 3-stage particles, 3LB and 3LD (2). Both these particles have an inner glassy core of 100 nm diameter, surrounded by a rubber annulus leading to values of diameter of 202 nm for the 3LB particles and 255 nm for the 3LD particles. The outer stage is a further glassy layer; the values of total diameter of the particles is 240 nm for the 3LB particles and 301 nm for the 3LD particles. The material properties used for the PMMA were the measured values (E = 2.96 GPa, ν = 0.39). The properties for the rubbery phase were identical to those described above. The properties of the glassy layer are hard to define; analyses were carried out assuming the glassy layers to be identical to the matrix PMMA. However, values of volume fraction were calculated with respect to the whole particle, using the values of total particle diameter.

FINITE ELEMENT MODELLING

The finite element modelling is carried out for a representative cell of the material. Constraints are applied to the shape of the deformed cell; the application of these constraints models the interactions between neighbouring rubber spheres. Predictive modelling of particulate-filled composite materials is frequently based on the assumption that the material consists of a collection of cylinders. Such analysis is relatively straightforward, since the constraints required may be simply applied by forcing the sides of the cylinder to remain straight. This material model was used for some analyses of the rubber-toughened epoxy and the analyses of the multi-stage particulate reinforced PMMA. A more accurate material model has been developed; this model assumes that the shape of the representative cell is a sphere, reflecting the overall isotropy of the material. The development of this model is described elsewhere (3); an iterative procedure is required to deduce the overall elastic properties of the material. The use of this more accurate model may be essential for the proper modelling of the growth of a shear band.

The bonding between the particle and the matrix is generally considered perfect until cavitation. However, the modulus matching for the multi-stage material indicates that bonding may be imperfect. Analyses were carried out assuming the particles to be present but totally debonded. The values of Young's modulus derived from these analyses were identical to the values derived assuming voids.

RESULTS

Predicted values of Young's modulus for the rubber-toughened epoxy derived from the two material models are shown in figure 1. The values predicted by the more accurate spherical model are all higher, and show a smaller change with volume fraction than values predicted by the cylindrical model. The variation of the maximum Von Mises stress with volume fraction for "crack-tip" triaxial loading for the different conditions is shown in figure 2. The results indicate that shear band growth will be promoted by cavitation. At higher volume fractions, results from the two material models are significantly different. The growth of a shear band has been investigated using the cylindrical model. Some initial results, for unidirectional loading, are shown in figure 3; the elements exceeding the plastic limit are shown for different levels of applied strain. These results illustrate the importance of using the more accurate spherical model; at level 4 failure has started at the corner, separate from the original shear band.

Predicted values of Young's modulus for the multi-stage thermoplastic PMMA toughened with the 3LD particles are compared with experimental values in figure 4; similar results are found for the 3LB particles. The experimental values are closer to the predicted values assuming voids, or debonded particles. This unexpected result is the subject of present investigation. Failure mechanisms in these materials include cavitation of the rubbery phase and craze growth in the PMMA matrix (2). The stress concentration leading to the initiation of these mechanisms were compared for the two particles. For both materials, the values of stress concentration factor for the range of volume fraction are similar. The values of stress concentration factor of direct stress, leading to craze growth, are almost identical for the two materials, with a value of 2.1 at 35% volume fraction. Similarly, the values of stress concentration factor for the hydrostatic tensile stress in the rubbery annulus are almost identical, with a value of 0.30 at 35% volume fraction. These results indicate that the change in particle morphology has no influence on the failure mechanisms.

CONCLUDING REMARKS

Predictive modelling is a powerful tool for the investigation of toughened polymers. The failure processes for rubber-toughened epoxy may be examined using the improved material model. The influence of bonding and particle morphology on the properties of toughened PMMA may also be investigated.

ACKNOWLEDGEMENTS

The authors gratefully acknowledge valuable discussions and provision of experimental data from Professor R J Young, Dr P A Lovell and M N Sherratt (Manchester Materials Science Centre). The computer time used is supported by a grant from SERC.

REFERENCES

1 Kinloch,AJ,1989, in Advances in Chemistry Series 222.
2 Lovell,PA,Ryan,AJ,Sherratt,MN & Young,RJ,1993,pap.3,this conf
3 Guild,FJ,and Kinloch,AJ,1993,*J Mater Sci Lett* (in press)

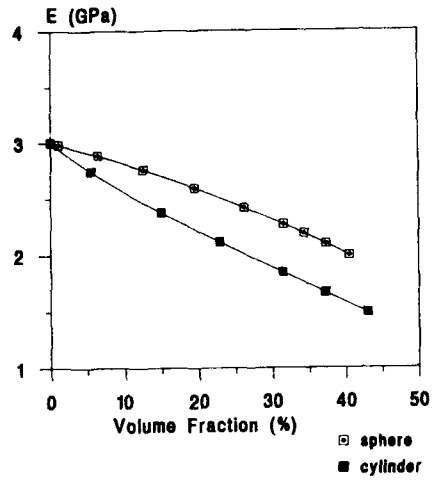

Figure 1 Predicted values of Young's modulus for the rubber-toughened epoxy

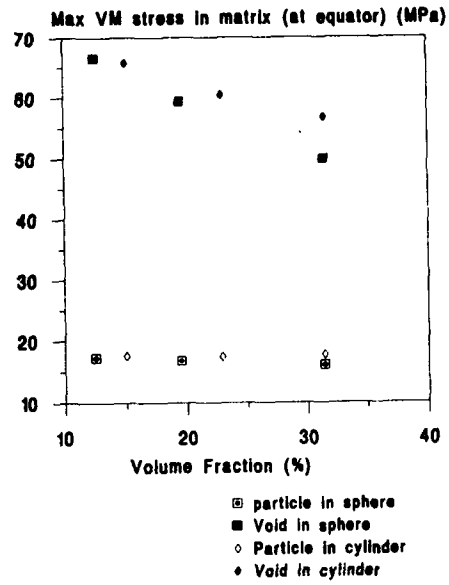

Figure 2 Maximum Von Mises stress in rubber-toughened epoxy (applied uni strain = 1%)

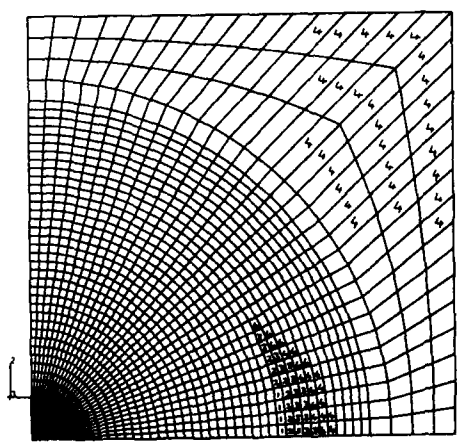

level	1	2	3	4
strain (%)	1.8	2.0	2.2	2.4

Figure 3 Predicted development of a shear band in rubber-toughened epoxy

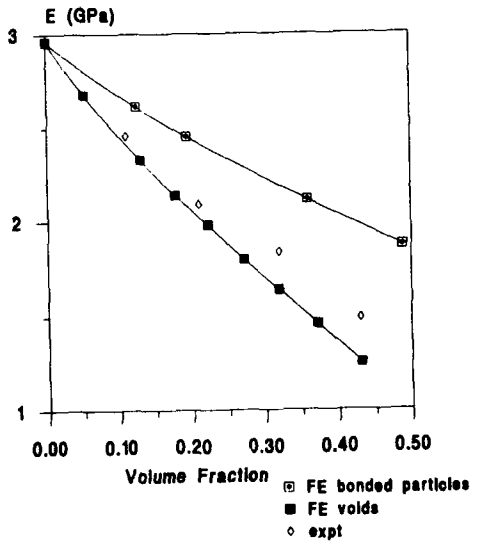

Figure 4 Predicted and experimental values of Youngs modulus for PMMA with 3LD particles

ULTIMATE TOUGNESS OF AMORPHOUS POLYMERS

H.E.H. Meijer and M.C.M. van der Sanden
Centre for Polymers and Composites, Eindhoven University of Technology
P.O.Box 513, 5600 MB Eindhoven, The Netherlands

As shown by Kramer et al. (1-6), the maximum attainable strain of amorphous polymers can be understood from a molecular (network density) point of view at least on a microscopic level such as the craze extension ratio and the draw ratio in shear deformation zones. In this study it is demonstrated that the maximum network strain can also be reached on a macroscopic level, provided that the material locally is made thin enough e.g. by the incorporation of sub-micron "holes". For the most frequently used thermoplastic polymers, the typical critical material length scale ("the inter hole distance") ranges from 20 to 200 nm. This concept is valid in slow speed and high speed notched tensile testing and also applies on thermosets. Thus, the ultimate toughness of amorphous polymers is reached.

Introduction

Ultimate properties of polymeric materials (stiffness, strenght and toughness) are major topics of research. Nowadays, ultimate stiffness and strength can be directly related to the structure and arrangement of molecular chains and are experimentally confirmed for a selected range of polymers. A thorough understanding of the parameters governing the ultimate macroscopic toughness of amorphous glassy polymers, however, was still lacking.

Toughness is, in a first approximation, proportional to the total energy involved in deformation up to fracture, i.e. the area under the stress-strain curve. Since the stress at which amorphous glassy polymers deform is within the limited range of 50-80 MPa and the strain to break varies in a much wider range (1-150%), the strain to break can be used as a discriminating parameter. On a microscopic level (i.e. inside deformation areas) a satisfying correlation has been established between the local strain and the strain to break based on stretching the molecular network to its full extension (1). The molecular network is characterized by the molecular weight between nodes of enhanced friction, i.e. entanglements for thermoplastic polymers and crosslinks for thermosetting polymers. On a macroscopic scale the strain to break is often two decades below the expected strain to break. This paradox was the issue for our research.

Experimental results

In this study (7-9), the concept of a *critical thickness* is introduced below which amorphous glassy polymers deform up to their maximum draw ratio (read: toughness) given by their equilibrium polymer-specific molecular network density. A decrease of the sample dimensions in one (thin films) or two (thin ligaments) dimensions results in a sharp increase of the macroscopic strain to break up to a value comparable with the draw ratio (λ_{max}) of the molecular network, see Figure 1. For example, the strain to break of polystyrene (PS) can be increased from 1% up to 200% by decreasing the (local) specimen size below 50 nm. The (local) specimen dimensions can be easily controlled via the use of thin films (separated by non-adhering spacers) or by the introduction of (preferably) non-adhering rubbery particles. The average distance between the rubbery particles determines the local thickness in the latter case. Below the critical thickness, all amorphous glassy polymers deform via shear yielding, as demonstrated with tensile dilatometry.

An explanation for the phenomenon of a critical thickness is postulated based on an energy criterion for brittle fracture. If deformation is initiated locally, deformation will continue throughout the complete sample only if catastrophic fracture of fibrillated ligaments is prohibited anywhere in the sample. Decreasing the size of the sample finally results in an equilibrium between the stored elastic energy in the sample (locally around the ligament) and the (brittle fracture) surface energy of the fibrillated sample (the stretched ligament) which is deformed up to λ_{max}. A further decrease of the ligament thickness prohibits brittle fracture of the fibrillated ligament for the testing conditions applied. Hence, macroscopically ductile deformation behaviour prevails and ultimate toughness is obtained.

The critical thickness (ID_c) has been experimentally determined for a wide range of thermoplastic and thermosetting polymers and proves to be highly dependent on the molecular network density showing no differences between the two type of networks, which can be understood from the typical time-scale of the experiments, see Figure 2. ID_c varies from 0.05 μm for polystyrene (low network density) up to a few micron for relatively densely crosslinked thermosets. This material-dependent critical thickness can be quantitatively understood from the energy-based criterion via the network density dependence of (i) most important: the natural draw ratio (λ_{max}) and (ii) the secondary influence of the brittle fracture surface energy.

The influence of extrinsic variables on the absolute value of the critical thickness can be predicted relatively easy via a strain rate and temperature dependence of the yield stress and Young's modulus of the pure polymer.

Any adhesion between the matrix and the dispersed elastomer added to create the desired local thickness in most practical (melt-mixed) systems (lowering of interfacial adhesion), and any subsequent increase in the elastomer cavitation stress, influence the value of the critical thickness in an unfavourable manner: the critical thickness deceases with an increasing degree of adhesion and/or cavitation stress of the elastomer or, alternatively, the brittle-to-tough transition temperature shifts to higher temperatures at a constant ligament thickness, see Figure 3.

Conclusions

Based on the above findings one of the most ductile amorphous glassy polymers proves to be polystyrene that reveals its ultimate ductility in a non-adhering holey morphology only if the local thickness is below the critical value of 50 nm. Hence, the development of sub-micron foam-like structures based on PS offer a challenging prospect in confirming the findings in this research, see Figure 4. An onset towards the development of these nano-sized structures has been made in our laboratory.

References

1. Donald, A.M., Kramer, E.J., Polymer, 1982, 23, 461
2. Donald, A.M., Kramer, E.J., J. Mat. Sci., 1982, 17, 1765
3. Donald, A.M., Kramer, E.J., J. Mat. Sci., 1982, 17, 2351
4. Kramer, E.J., Adv. Polym. Sci. 1983, 52/53, 1
5. Donald, A.M., Kramer, E.J., J. Mat. Sci., 1985, 20, 2630
6. Kramer, E.J., Berger, L.L., Adv. Polym. Sci. 1990, 91/92, 1
7. Van der Sanden, M.C.M., Meijer, H.E.H., Lemstra, P.J. Polymer, 1993, 34, 2148
8. Van der Sanden, M.C.M., Meijer, H.E.H., Tervoort, T.A. Polymer, 1993, 34, 2961
9. Van der Sanden, M.C.M., Meijer, H.E.H., Polymer, 1993, 34, 5063

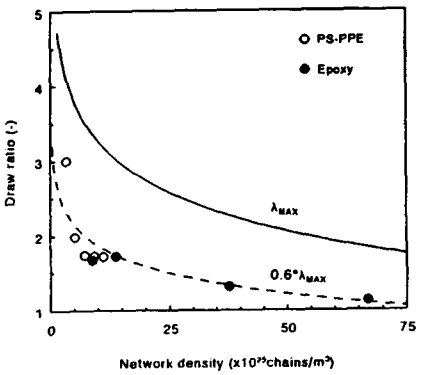

Figure 1. Draw ratio versus network density (entanglement and/or crosslink density).

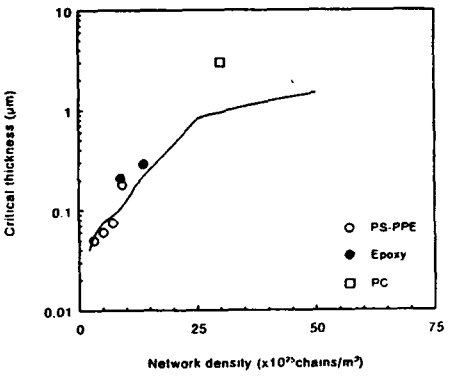

Figure 2. Critical thickness versus network density (entanglement and/or crosslink density).

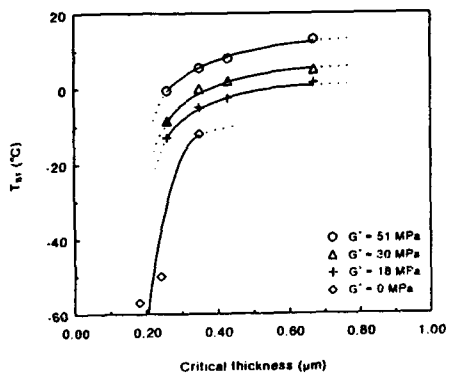

Figure 3. Brittle-to-tough transition temperature (T_{BT}) of PC/rubber blends versus the critical thickness of PC (parameter: the dynamic shear modulus of the dipersed rubbery phase)

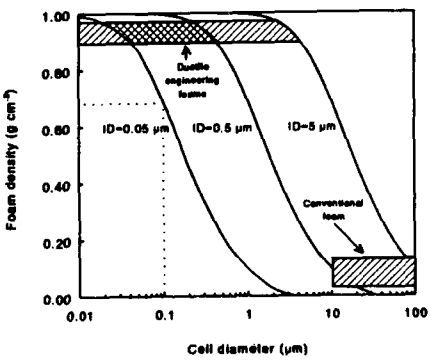

Figure 4. Foam density as a function of the cell diameter for different values of the critical intercellular distance

THE EFFECT OF RUBBER PROPERTIES ON THE MODE OF DEFORMATION IN RUBBER MODIFIED POLYSTYRENE

Arminda Magalhães da Silva* and Rein Borggreve**

The fibrillar craze microstructure in blends of polystyrene with a second, rubbery phase based on polystyrene-triblockcopolymers, was studied using small angle X-ray scattering (SAXS) and transmission electron microscopy (TEM). The observed coarsening of the craze microstructure with the increase of rubber content was attributed to a change in stress state in the ligaments in between the rubber particles due to rubber particle cavitation. Plasticization effects due to low molecular weight components were believed to be insignificant in these systems.

INTRODUCTION

For many years it has been accepted that the role of rubber particles in toughening a crazing matrix like polystyrene (PS) is to generate stress concentrations so that a large number of crazes can be initiated (1). However, Bubeck et al. (2) found from real time small angle X-ray scattering experiments that cavitation of rubber particles is preceding matrix crazing and could be an essential part of the deformation mechanism. On the contrary, Okamoto et al. (3) recently concluded from post mortem TEM studies that crazing is inducing cavitation of the rubber particles.

It is known that coarsening of craze microstructure (craze fibril diameter) in glassy polymers occurs in the presence of low molecular weight components (4,5). More recently Argon et al. (6) proposed a new toughening mechanism (local plasticization) in which finely dispersed low molecular weight polybutadiene locally dissolves in a PS matrix (in front of the craze tip) causing an enhancement in craze growth rate and a coarsening of the craze fibril diameter. Also, the increase of the fibril diameter in HIPS was attributed to the plasticization by the low molecular weight tail of the rubber particles (7) or the presence of mineral oil (8).

The aim of this study is to investigate the relation between eventual rubber particle cavitation and the craze microstructure in a PS matrix. In order to exclude the effects of plasticizers in the polymer matrix or low molecular weight tails in the impact modifier we have prepared blends of a pure PS and a rubbery blockcopolymer with a narrow molecular weight distribution by melt blending in an extruder. Injection moulded tensile bars of blends of different compositions have been deformed up to different strains. Blend morphology and craze microstructure were examined with TEM and SAXS.

*Universidade do Minho, Portugal
**DSM Research, The Netherlands

EXPERIMENTAL

All polymers used for this study are commercial products. Polystyrene (PS) (M_w=340000 g/mole, M_w/M_n=2.6, $T_{g,DSC}$=101°C) was obtained from Shell. The triblock copolymers (TBC) are sold under the trade name Kraton™ G1651 and Kraton™ G1652 (Shell). They consist of two PS-end blocks and a middle block of hydrogenated polybutadiene. GPC was used to determine the molecular weight of the components. The M_w values for respectively Kr1651 and Kr1652 are 24-100-24 kg/mole, M_w/M_n=1.15 and 7-35-7 kg/mole, M_w/M_n=1.20. The PS content is approximately 30 wt% for both blockcopolymers. There is less than 1% low molecular weight material (below 5000g/mole) present.

The blending was conducted in a range of compositions on a twin screw extruder at 240°C. Tensile tests were performed on a Zwick Tensile Machine Mode 1445 using standard injection moulded specimens (ASTM D638) at a strain rate of $1.7*10^{-4}$ s^{-1} at room temperature.

The morphology of the blends was examined with a transmission electron microscope (Philips CM 200), operated at an accelerating voltage of 120 kV. The samples were cryosectioned and the microtomed sections were hardened and stained by exposure to ruthenium tetroxide (RuO_4) vapours. Also, the microstructure of deformed samples was observed on thin sections. The sectioning direction was at an angle of approximately 90 degrees to the principal tensile axis to minimize damage of the craze microstructure.

In order to perform the small-angle X-ray scattering experiments, crazes were initiated by drawing tensile specimens to a certain strain level at a strain rate of $1.7*10^{-4}$ s^{-1}. After drawing, the samples were held extended, using a special device, and the fibrillar craze microstructure was characterized using a Kratky camera, equipped with a position sensitive detector. The undeformed sample was used as background and the data were scaled to an absolute intensity scale using a Lupolen standard. Mean fibril diameter ($\bar{D}$) of the craze matter was obtained by performing a standard Porod analysis (9,10) on the smeared data. A fibril volume fraction of 0.25 for the craze was assumed for all samples, based on previous data (6).

RESULTS

The stress-strain experiments showed the expected behaviour of increasing toughness (as measured from strain to fracture) as the blockcopolymer fraction increased (Figure 1). It is readily seen that the blend PS/Kr1651 is substantially more ductile than the blend PS/Kr1652. There is also an expected decline in tensile modulus, yield stress and flow stress (Figure 2) as the rubber content increases. Both types of blends show the typical behaviour of reduced strain to fracture at higher strain rates.

The morphology of undeformed PS/Kr1651 (25%) blend shows elongated rubber particles with a broad distribution in particle size (1-2 μm), whereas the PS/Kr1652 (25%) has very irregular shaped particles, although with the same average particle size (1-2 μm).

Figure 3 shows a micrograph of a deformed sample. It demonstrates that the plastic deformation of the sample was the result of crazing. Also there is evidence that the crazes were initiated by rubber particles. The micrograph shows crazes interacting with particles. Some crazes appear white, at least far from the rubber particles. With this technique no extensive cavitation within the rubber particles could be detected.

The mean fibril diameter, displayed in Figure 4, is strongly dependent on rubber fraction, being about three times the value of the pure PS for the material with 25 wt% blockcopolymer.

DISCUSSION and CONCLUSIONS

In our opinion the increase in craze fibril diameter with the increase of rubber content can not be attributed to the low molecular weight tail of the rubber, since the total amount of low molecular weight material present in the blend which can act as a plasticizer is well below the required concentration (7).
A possible explanation could be that (cavitated) rubber particles are changing the stress state of the ligaments between the particles. The increase of craze fibril diameter with a decrease of plastic constraint in thin films was already reported by Donald et al. (11,12).

ACKNOWLEDGEMENTS

The financial support of this work by the JNICT (Portugal) is gratefully acknowledged. This research also benefited from the use of the facilities of DSM Research (The Netherlands). Thanks to M. Walet for performing the TEM work and Dr. R. Scherrenberg for the assistance in interpreting the SAXS data.

REFERENCES

1. Bucknall, C.B., "Toughened Plastics", Applied Science Publishers, London, 1977
2. Bubeck, R.A., Buckley, D.J. Jr., Kramer, E.J., Brown, H.R., J. Mat. Sci., 1991, **26**, 6249
3. Okamoto, Y., Miyagi, H., Mitsui, S., Macromolecules, 1993, **26**, 6547
4. Kramer, E.J., "Developments in Polymer Fracture", ed. E.H.Andrews, Applied Science, London, Chap.3, p.55, 1979
5. Brown, H.R., Njoku, N.G., J. Pol. Sci. Pol. Phys. Ed., 1986, **24**, 11
6. Gebizlioglu, O.S., Beckham, H.W., Argon, A.S., Cohen, R.E., Brown, H.R., Macromolecules, 1990, **26**, 3968
7. Buckley, D.J.Jr., PhD Thesis, Cornell University, 1992
8. Brown, H.R., Mat. Sci. Reports, 1987, **2**, 315
9. Paredes, E., Fischer, E.W., Makromol. Chem., 1979, **180**, 2707
10. Brown, H.R., Kramer, E.J., J. Macromol. Sci. Phys., 1981, **B19**(3), 487
11. Donald, A.M., Chan, T., Kramer, E.J., J. Mat. Sci., 1981, **16**, 669
12. Chan, T., Donald, A.M., Kramer, E.J., J. Mat. Sci., 1981, **16**, 676

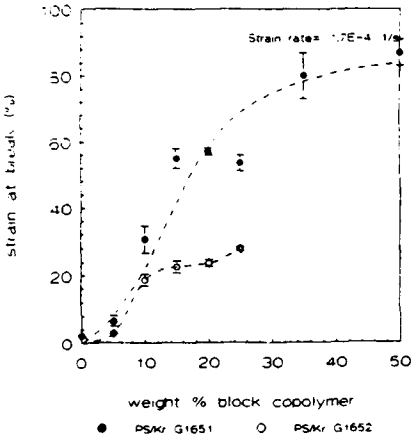

Figure 1. Dependence of the strain to break of blends on the concentration of block copolymer.

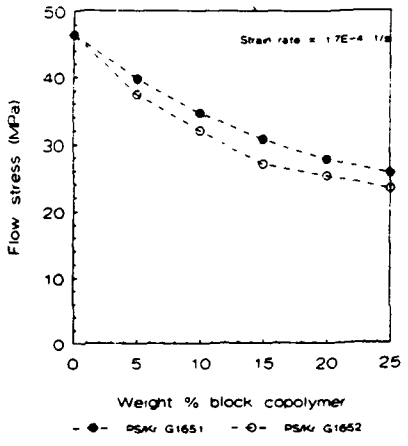

Figure 2. Dependence of the flow stress of blends on the concentration of block copolymer.

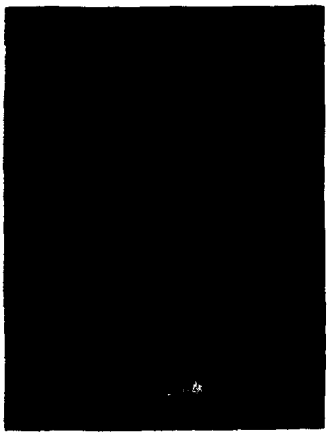

Figure 3. TEM micrograph of deformed blend PS/Kr 1651: blend containing 5 wt% block copolymer.

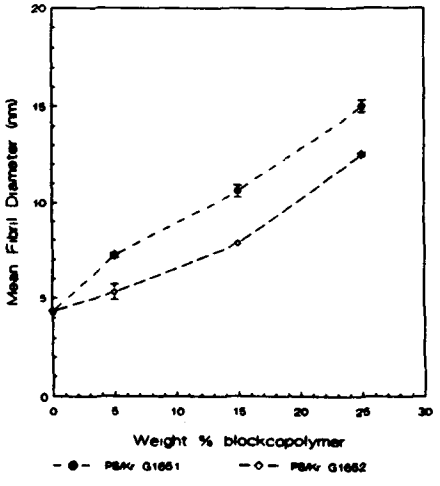

Figure 4. Dependence of mean fibril diameter on the concentration of block copolymer.

ROLE OF THE RUBBER PARTICLE IN TOUGHENED POLYSTYRENE

C B Bucknall, C A Correa, V L P Soares and X C Zhang*

A new model is proposed to explain the stress-strain behaviour of HIPS. The rubber particles first cavitate in accordance with a critical energy criterion, forming load-bearing elastomeric fibrils between polystyrene sub-inclusions. The cavities then act as nuclei for craze initiation. As the crazes extend and thicken, their growth is restrained by the fibrillated rubber, which takes an increasing share of the applied stress as the strain increases. This strain-hardening effect is enhanced when the rubber is cross-linked. The model is supported by experiments on HIPS blends in which the cross-linking, size, and volume fraction of the rubber particles are varied. The use of γ-irradiation to increase cross-linking while leaving the polystyrene relatively unaffected is shown to be particularly effective in the study of toughening behaviour.

INTRODUCTION

Numerous optical and electron microscopy studies have shown that rubber particles cavitate at an early stage in the tensile deformation of toughened plastics. In the case of HIPS and ABS, these observations are supported by real-time SAXS measurements on tensile impact bars, which show extensive non-craze voiding beginning a little before the yield point and continuing until final failure [1]. The accumulated evidence has led some observers to conclude that rubber particles act essentially like voids, relaxing the constraints inherent at a crack tip, and inducing a plane-strain to plane-stress transition. However, this explanation does not account for a number of well-established facts, including the need for good adhesion between particles and matrix (especially in relatively brittle matrices such as PS), and the importance of particle size. The present paper addresses these problems by identifying three stages in the deformation behaviour of the rubber particle: (a) before cavitation, when it is resistant to volume changes (typical bulk moduli are 2 GPa); (b) immediately after cavitation, when its resistance to extension and dilatation are at a minimum; and (c) after large-strain deformation in the neighbouring matrix, when the fibrillated membranes of rubber are highly stretched, and capable of supporting nominal stresses in the order of 5 to 10 MPa.

EXPERIMENTAL

Experiments consisted mainly of tensile tests on compression-moulded HIPS specimens. Charpy tests were also carried out on sharply-notched specimens. The composition and morphology of the materials are described in an earlier paper [2]. They include conventional HIPS polymers containing 'salami' particles up to 6 μm in diameter, and grades containing monodisperse core-shell particles with diameters of 0.2 μm. The maximum (polybutadiene) rubber content was 8.5 wt%, but the presence of polystyrene sub-inclusions raised the volume fraction of rubber particles, ϕ, to higher levels, ranging from 0.12 to 0.44, depending upon method of manufacture. Compositions were also varied by melt-blending with polystyrene.

* Advanced Materials Group, Cranfield University, Bedford MK43 OAL

In order to vary the properties of the rubber without altering composition or morphology, HIPS samples were subjected to γ-irradiation in air at a dose rate of 3 Mrad/hour, to a maximum of 80 Mrad. This resulted in a linear increase in the T_g of the rubber, from –69.5° to –57.3°C. At the same time, the swelling index in toluene fell from 11.2 to 5.7, and the gel content increased from 29 to 35%. The Mn of the polystyrene phase remained constant at about 70,000, but Mw increased from 191,000 to 305,000.

RESULTS AND DISCUSSION

The tensile test data presented in Figs. 1 and 2 show the effects of irradiating HIPS containing 44 vol% of 6 μm salami particles. The yield stress σ_y (initial load maximum) and the flow stress σ_f (subsequent load minimum) rise continuously with increasing dose, whereas the breaking stress σ_b remains almost constant for doses up to 20 Mrad. Beyond this point, σ_y, σ_f and σ_b converge. In order to determine whether the increasing Mw of the PS plays a significant part in these changes, a sample of the same HIPS was subjected to a radiation dose of 20 Mrads, and blended with PS to give a final $\phi = 0.17$. Conversely, PS was irradiated in the same way, and mixed with unirradiated HIPS. Both materials were compared in tensile tests at 23°C with an unirradiated blend of the same composition. Irradiation of the HIPS raised σ_y by 3%, and σ_f by 12%, whereas irradiation of PS alone lowered σ_y by 3% and σ_f by 5%. On the basis of this evidence, it is reasonable to conclude that the changes in behaviour recorded in Fig. 1 are due mainly to the increase in cross-linking of the rubber phase with irradiation, and that the increase in Mw of the PS matrix is of minor importance.

Cross-linking the rubber raises its shear modulus G_r, thereby making it more resistant to cavitation, the criteria for which are discussed in detail in Poster P62 [3]. This accounts in part for the rise in σ_y with radiation dose. However, cavitation of the rubber particles does not in itself contribute significantly to total extension. In HIPS, yielding is due to multiple craze formation, accompanied by stretching of adjacent rubber particles. A feature of the new model is that the cavitated particles provide free surfaces from which crazes can extend by the meniscus instability mechanism [4], and that the kinetics of craze initiation therefore depend upon the elastic volume strain, which governs particle cavitation.

Immediately after yield, the area of active crazes increases rapidly, and smaller stresses are required to maintain a fixed strain rate. Consequently, the yield maximum is followed by a load minimum. At this stage, not only is the area of active crazes increasing, but also individual crazes are thickening by drawing PS from the walls. This process causes the fibrils of rubber within the cavitated particles to become highly stretched, as illustrated in Fig. 3, so that the nominal stress on the cavitated rubber particle increases, and the applied stress on the HIPS therefore rises with increasing strain. The process can be modelled as illustrated in Fig. 4, using a 5-element modified Takayanagi model, in which the craze is an Eyring flow element. If σ_{appl} eventually exceeds σ_y, independent cavitation of rubber particles can recommence, involving smaller particles. Otherwise, new cavitation during drawing occurs only when particles are engulfed in advancing craze fronts.

The stress required to draw fibrils from the walls of a PS craze at 23°C is ~30 MPa [5]. Since σ_f for the unirradiated HIPS in Figs. 1 and 2 is only 10 MPa, it follows that about a third of the area in the actively deforming zone is occupied by PS craze, the remaining two thirds being fibrillated rubber. Furthermore, if the rise of 5 MPa in σ_{appl} between the load minimum and break in that HIPS is due entirely to the rubber, the nominal stress on the fibrillated rubber immediately before break must be $5x(3/2) = 7.5$ MPa, in reasonable agreement with experimental observations on uniaxial failure stresses in rubbers. This would suggest that the HIPS eventually fails when the rubber fibrils begin to rupture. At very high levels of irradiation, the critical volume strain for cavitation is also high. Under these conditions, there is no period of stable flow, and the HIPS fails almost immediately after reaching σ_y.

Further insight into cavitation effects was gained by stretching a HIPS specimen at 23°C to a tensile strain of 1.4% (just beyond yield), and annealing at 105°C for 3 hours in vacuum to heal the crazes formed. In a repeat tensile test under identical conditions, the pre-strained sample showed a reduction in σ_y from 15 to 14 MPa, but no change in σ_f. By contrast, when a pre-strained, annealed HIPS bar was subjected to a 20 Mrad dose of radiation, σ_y remained unchanged to 14 MPa, but σ_f rose from 11 to 13 MPa. These observations are consistent with the model outlined in the Introduction. Cavitation or fibrillation of the rubber involve irreversible tearing of the rubber phase around the growing void. Pre-straining eliminates the need to tear the rubber during cavitation, and therefore reduces the critical volume strain at which fibrillation begins. Irradiation has little effect upon this part of the deformation, but increases the modulus of the rubber phase, thus raising the flow stress.

The failure stress of polystyrene in uniaxial tension is about 40 MPa. It follows that rubber particles must cavitate at lower stresses if they are to toughen HIPS effectively. This places limits on the shear modulus of the rubber and the diameters of the particles that can cavitate, as explained in Poster P62 [3]. All other factors being equal, particles with diameters of 0.2 μm will cavitate at higher stresses than those with diameters above 1.0 μm. Furthermore, the absolute length to which each rubber particle can stretch will be determined by its diameter and rubber content. Consequently, HIPS materials containing small core-shell particles tend to have high yield stresses, and to form very thin crazes. These conclusions are supported by experimental observations on HIPS materials with differing morphologies.

Charpy impact tests between −100° and 23°C on sharply-notched bars showed a large, progressive decrease in fracture energy with radiation dose, but relatively small changes in the transition temperatures: the first increase in toughness occurred at about −60°C, with a second transition at −15°C. Room temperature impact energies fell from 47 J m^{-1} in the unirradiated HIPS to 14 J m^{-1} at 60 Mrads. This pattern of behaviour correlates well with that seen in the tensile tests.

CONCLUSIONS

It is clear from this work that cavitated rubber particles in HIPS cannot be treated simply as having void-like properties. After the particles have cavitated, there is a yield drop. The fibrillated rubber then causes strain-hardening, taking an increasing share of the applied stress, until it eventually fails. The model outlined in the Introduction accounts for a number of key features in the deformation behaviour of HIPS, including the initiation of crazes preferentially from larger rubber particles, the relative inefficiency of small rubber particles as toughening agents, the yield drop and subsequent strain hardening seen in tensile tests, and the adverse effects of cross-linking in the rubber phase upon fracture resistance. It also requires a new approach to the kinetics of craze initiation, which resolves earlier difficulties [6]. The model is capable of further development to place it on a fully quantitative basis.

ACKNOWLEDGMENTS

The authors thank the Brazilian Research Council (CNPq) and the SERC (GR/H06354 and H71130) for financial support of this work.

REFERENCES

1. Bubeck, R A, Buckley, D J, Kramer, E.J. and Brown, H, *J Mater Sci.* **26** (1991) 6249.
2. Bucknall, C B, Davies, P, and Partridge, I K, *J Mater Sci.* **22** (1987) 1341.
3. Bucknall C B, Karpodinis A M and Zhang X C, Paper P62, this conference.
4. Argon, A S and Salama, M M, *Phil Mag.* **43** (1977) 1217.
5. Fellers J F and Kee, B F, *J Appl Polym Sci* **18** (1974) 2355.
6. Bucknall, C B, Davies, P, and Partridge, I K, *J Mater Sci.* **21** (1986) 307.

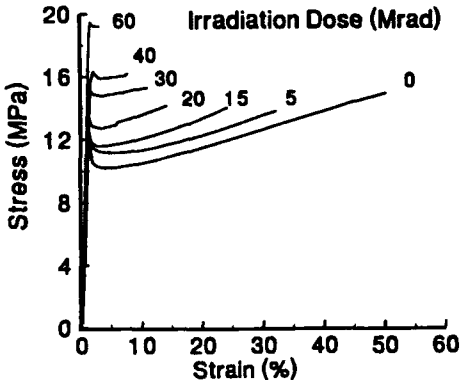

Fig.1. Effects of γ-irradiation on tensile behaviour of HIPS with 8.5 wt% rubber, $\phi = 0.44$.

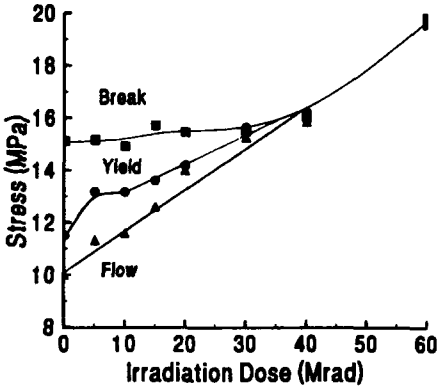

Fig.2. Average values of σ_y, σ_f and σ_b from experiment shown in Fig. 1. Strain rate 6.6×10^{-4} s^{-1}; 23°C.

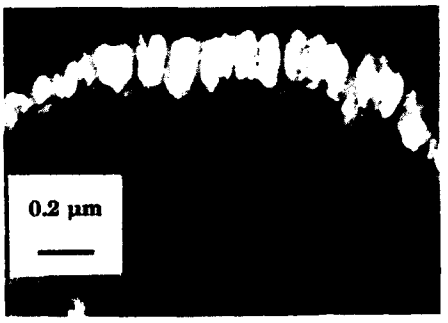

Fig.3. Detail from cavitated 'salami' particle showing strained rubber fibrils.

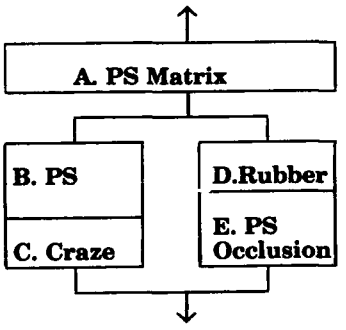

Fig.4. Modified Takayanagi model for craze growing in parallel with fibrillated rubber particle.

MOLECULAR DEFORMATION PROCESSES IN POLYMERS

R.J. Young*

It is demonstrated that Raman spectroscopy can be used to follow molecular deformation in a wide range of polymer fibres including aramids, polyesters and polyethylene fibres. It is found that the wavenumbers of the Raman bands of the fibres shift generally to lower frequency under the action of tensile stress due the mechanical deformation resulting in direct stressing of the polymer backbones. The behaviour can be interpreted in terms of chain stretching and it is found that for a given type of polymer fibre the amount of chain stretching increases with fibre modulus. It is shown that there is a remarkable similarity between the behaviour of the different types of fibres.

INTRODUCTION

In recent years Raman spectroscopy has been used to study the deformation of a wide variety of high-performance fibres such as aramids [1,2], rigid-rod polymer fibres [3,4], carbon fibres [5,6], and ceramic fibres [7,8]. The use of Raman spectroscopy to study fibre deformation is based upon the finding that for such high-performance fibres the bands in the Raman spectra shift in wavenumber upon the application of macroscopic stress or strain. This enables the fundamental micromechanics of the deformation of the molecules within the fibres to be studied in detail [2]. It also allows an accurate determination of the deformation of the fibres within a composite matrix [9-11] where the stress and strain distribution can be mapped along individual fibres in the matrix and from which the interfacial shear stress may be derived. This present paper is concerned with a comparison of the behaviour of a number of different types of polymer fibres and it is demonstrated that the phenomenon is of widespread importance in obtaining a full understanding of the effect of fibre microstructure upon the deformation behaviour of polymer fibres.

AROMATIC POLYAMIDE FIBRES

A typical Raman spectrum for a single filament of a Kevlar 49 aramid fibre is shown in Figure 1 and it is found that the wavenumbers of the different Raman bands shift on the application of stress or strain [1]. This type of behaviour has been reported for both aramid fibres [1,2] and a wide range of other high-performance fibres [3-8]. It is shown in Figure 2 that there is an approximately linear shift in peak position of the 1610 cm^{-1} phenylene group stretching aramid Raman band, $\Delta\upsilon$, with tensile strain, e, for three fibres tested with different values of Young's modulus, Kevlar 29, 49 and 149. In contrast, it is found that when the fibres are embedded in an epoxy resin bar and

*Manchester Materials Science Centre, University of Manchester and UMIST, Grosvenor Street, Manchester, M1 7HS, UK.

subjected to compressive deformation the Raman bands shift to higher wavenumber as shown in Figure 3. In addition it is found that the increase in wavenumber is not linear and for some fibres at a certain strain, the increase in wavenumber tends to a plateau value [12] due to fibre yielding. It is also found from direct observation of the fibres in an optical microscope that at a critical strain, kink bands are found to form along the fibres [12]. The strains at which the kink bands are observed are indicated by an arrow for each of the fibres in Figure 3 and it can be seen that they are close to, but do not exactly match, the strains at which the curves plateau. It should also be noted that the initial slopes of the curves in Figure 3 are higher for fibres of lower modulus which is the opposite of the behaviour of the fibres in tension (Figure 2) and this may give a clue as to why the fibres with higher tensile modulus tend to have inferior compressive properties [12].

GEL-SPUN POLYETHYLENE FIBRES

Well-defined Raman spectra can also be obtained from high-performance gel-spun polyethylene fibres [13,14] and it is found that the Raman bands tend to shift to lower wavenumber on the application of tensile strain as shown in Figure 4 for Spectra 1000. For this material, however, there is unusual behaviour in that the 1128 cm^{-1} C-C symmetrical stretching Raman band tends to split into two well-defined peaks as shown in Figure 4. It has been demonstrated that this is due to the unique highly-oriented chain-extended microstructure of the material and a successful model based on this microstructure has been developed [14] to explain the deformation behaviour.

POLYESTER FIBRES

Although in the past there has been considerable attention paid to the molecular deformation processes in high-performance fibres, recent work has demonstrated that Raman spectroscopy can also be used to follow deformation of conventional materials such as poly(ethylene terephthalate) (PET) fibres [15,16]. This is demonstrated in Figure 5 where it can be seen that the wavenumber of the 1616 cm^{-1} Raman band shifts to lower frequency on the application of tensile strain. This behaviour is similar to that of the aramid fibres shown in Figure 2 but in the case of PET the rate of shift per unit strain is much lower than for the aramids. The non-linear shape of the curve in Figure 5 has been shown to be related directly to the stress/strain curve of the fibre.

MOLECULAR DEFORMATION PROCESSES

It is clear that the Raman technique offers a unique method of following chain deformation processes in a wide range of polymer fibres. The general picture that emerges is that when a series of fibres is prepared from the same base polymer the rate of shift *per unit strain* of a particular Raman band is proportional to the fibre modulus [2,14]. This is shown in Figure 6 where all the data for the phenylene-group stretching (aramids and PET) fall on the same line and those for the C-C deformation (polyethylene) lie on a different line. The implication of this is that the rate of shift *per unit stress* is constant and therefore independent of the fibre modulus [2]. Moreover, it can be seen that the slopes of the two lines are similar for Raman bands in different types of fibres.

ACKNOWLEDGEMENTS

This research is part of a large programme of work supported by the SERC through a research grant. The work upon the aramid fibres was performed by D. Lu and M.C. Andrews and the fibres were supplied by Du Pont. The research on the polyethylene fibres was undertaken by W.F. Wong and the fibres were supplied by DSM. The work on the PET fibres was performed by W.-Y. Yeh and the fibres were supplied by Dr. R. Huijts of Akzo Research. The author is grateful to the

Royal Society for support in the form of the Wolfson Research Professorship in Materials Science.

REFERENCES

1. C. Galiotis, I.M. Robinson, R.J.Young, B.J.E. Smith and D.N. Batchelder, *Polymer Comm.*, **26** (1985) 354.
2. R.J. Young, D. Lu, R.J. Day, W.F. Knoff and H.A. Davies, *J. Mater. Sci.*, **27** (1992) 5431.
3. R.J. Day, I.M. Robinson, M. Zakikhani and R.J. Young, *Polymer*, **28** (1987) 1833.
4. R.J. Young, R.J. Day and M. Zakikhani, *J. Mater. Sci.*, **25** (1990) 127.
5. I.M. Robinson, M. Zakikhani, R.J. Day and R.J. Young, *J. Mater. Sci. Lett.*, **6** (1987) 1212.
6. Y.Huang and R.J. Young, *J. Mater. Sci.*, in press.
7. X. Yang and R.J. Young, *J. Mater. Sci.*, **28** (1993) 2536.
8. X. Yang, X. Hu, R.J. Day and R.J. Young, *J. Mater. Sci.*, **27** (1992) 1409.
9. M.C. Andrews, R.J. Day and R.J. Young, *Comp. Sci. and Tech.*, **48** (1993) 255.
10. M.C. Andrews and R.J. Young, *Journal of Raman Spectroscopy*, **24** (1993) 539.
11. M.C. Andrews, R.J. Day, X. Hu and R.J. Young, *J. Mater Sci. Lett.*, **11** (1992) 1344.
12. D.Lu, Ph.D. Thesis, Victoria University of Manchester, 1992.
13. B.J. Kip, M.C.P. van Eijk and R.J. Meier, *J. Polym. Sci., Polym. Phys. Edn.*, **29** (1991) 99.
14. W.F.Wong and R.J. Young, *J. Mater. Sci.*, in press.
15. L.J. Fina, D.I. Bower and I.M. Ward, *Polymer*, **29** (1988) 2146.
16. R.J. Young and W.-Y. Yeh, *Polymer*, in press.

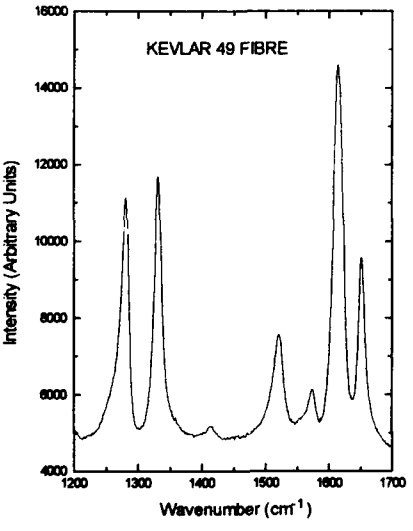

Figure 1 Raman spectrum obtained from a single filament of Kevlar 49.

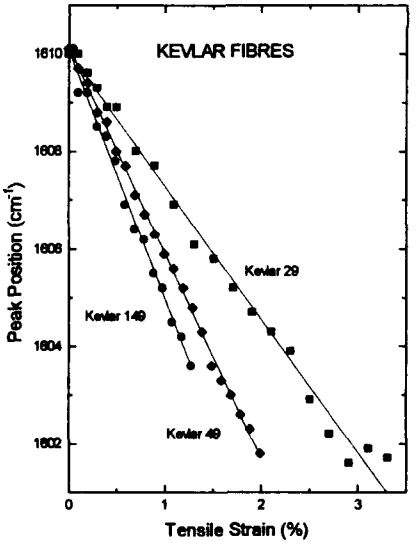

Figure 2 Shift of the position of the aramid 1610 cm^{-1} Raman band with tensile strain.

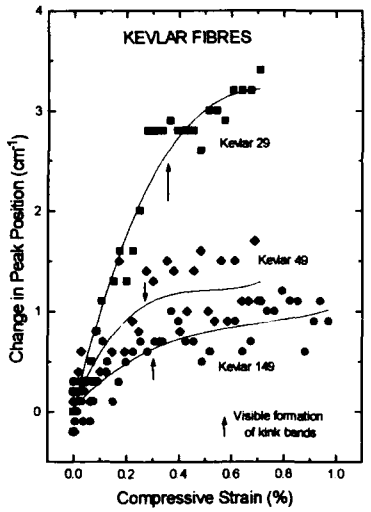

Figure 3 Shift in the position of the aramid 1610 cm^{-1} Raman band with compressive strain.

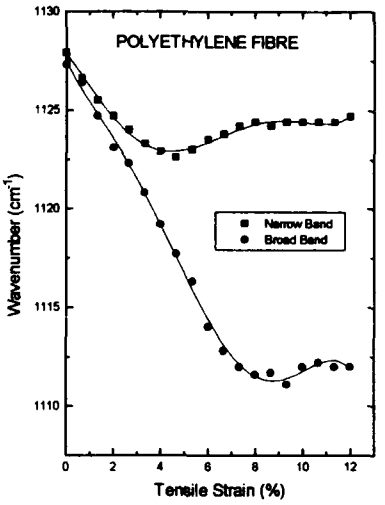

Figure 4 Dependence of the wavenumber of the 1128 cm^{-1} Raman band with strain for a Spectra 1000 gel-spun polyethylene fibre.

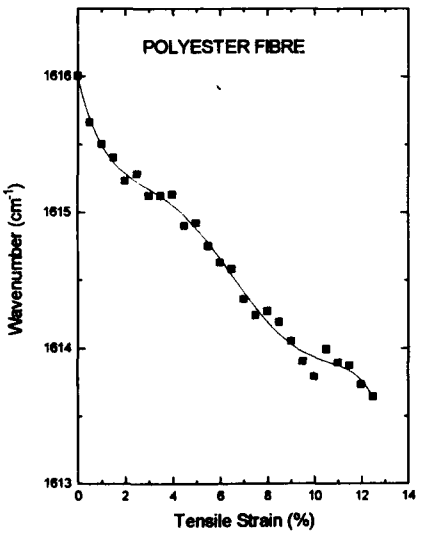

Figure 5 Dependence of the position of the 1616 cm^{-1} Raman band upon strain for a PET polyester fibre.

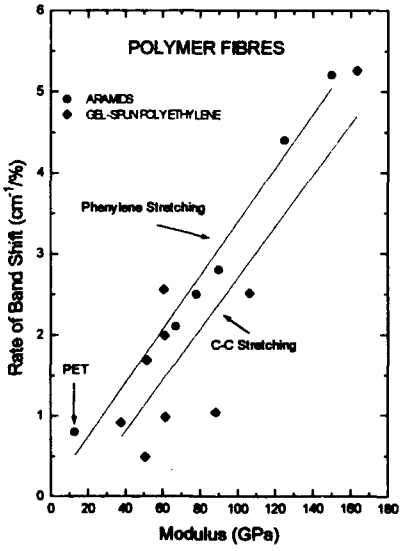

Figure 6 Dependence of the rate of Raman band shift per unit strain upon fibre modulus for a variety of polymer fibres.

PREDICTION OF THE MOLECULAR MECHANICAL RESPONSE OF POLYMERS AND BIOPOLYMERS

R. Pachter*, P. D. Haaland*, R.J. Young§, R.L. Crane* and W. W. Adams*

In our continuing effort towards the understanding of the molecular and microscopic bases of polymer mechanical properties, a computational study of single chain polymer and biopolymer moduli is presented. A different response to strain is demonstrated for synthetic PPTA compared to biopolymer chains containing an amide bond. These results help to explain the experimental observation that while all extended chain synthetic high performance polymers fail in compression, silk fibers that contain helical structures do not 'kink'. Moreover, for a better understanding of the molecular deformation, the strain dependencies of PPTA's normal mode frequencies were determined, indicating a negative linear dependence on strain, as has also been observed experimentally.

INTRODUCTION

Computational chemistry has become a valuable tool for analyzing the dynamics, structure and elasticity of polymers, especially the theoretical prediction of the ultimate mechanical properties, as recently reported, for example, by Klunzinger and Eby (1). Previous calculations focus mainly on the use of empirical potential energy functions, described by Rutledge and Suter (2), Sorensen et al (3), and Tashiro et al (4), while the evaluation of chain moduli and electronic properties of polymers by a molecular orbital approach constitutes a continuing effort of our laboratory. The study of rigid-rod polymers by Adams et al (5), Wierschke et al (6), and Shoemaker et al (7,8), PE by Horn et al (9), PPP and C_{60} by Haaland et al (10, 11), and biopolymers by Pachter at al (12, 13), offered insight into deformation processes at the molecular level and their strain-dependent stiffness behavior. Although the predicted stiffness compared well with macroscopic stress-strain curves for rigid-rod fibers, the theoretical moduli were shown to be higher than those determined experimentally, resulting from the imperfections and morphology in real materials, while these calculations are performed on models of idealized single polymer chains. The semi-empirical method also systematically overpredicts bond stiffness as compared to ab initio calculations carried out for polyethylene (7). This theoretical approach is most advantageous for comparisons of related polymers, and for properties prediction of polymers not yet synthesized. Indeed, it is the purpose of this study to report a comparison between the predicted mechanical response of single chain polymers and biopolymers. The calculations also offer an insight into the strain dependency of the polymer's normal mode frequencies, and are compared with experiment.

*Materials Directorate, Wright Laboratory, Wright-Patterson AFB, Ohio, U.S.A.
§Manchester Materials Science Centre, University of Manchester and UMIST, U.K.

Polymer Structure Calculations

The modulus and strain-dependent frequency calculations for a polymer cluster model follow a two-stage protocol: after an equilibrium geometry of the cluster is calculated, a translation vector that defines the polymer chain is incrementally increased or decreased, representing molecular tensile or compressive strain, and the geometry of the cluster under this constraint is optimized. The dependence of the heat of formation on molecular strain can thus be established. The stiffness of the polymer chain is given by the second derivative of the heat of formation vs. strain relationship, thereafter used to evaluate a single polymer chain modulus. For each of these strained geometries a normal mode analysis may also be carried out in order to determine the strain-dependence of the system's characteristic frequencies. Details of this approach have been previously described in reference 5.

PPTA

The ΔH_{ff} vs. ΔL dependence (Figure 1) for PPTA (14) results in a modulus of 330 GPa, overestimating the experimental range of 120-200 GPa as described in reference 15. This can be partially corrected by biasing the Hessian with experimental vibrational frequencies by a method derived by Karasawa et al (16), yielding a value of approximately 290 GPa, that is comparable to values obtained by recently reported atomistic simulations of PPTA reported by Rutledge et al (17). The dashed line in Figure 1 is the force curve (10^{-10} N), indicating that 'kinking' occurs at approximately 2.5% compressive strain (the force curve is the molecular equivalent of a strain-stress curve). The overall response is similar to that of other rigid-rod polymers reported in reference 5. The equilibrium geometry and heat of formation for a two-repeat unit was also determined, resulting in a difference in $\{\Delta H_{ff}$/repeat unit$\}$ of approximately 5 kcal/mol.

Strain dependency of the PPTA normal mode frequencies. The PPTA modes that represent torsional vibrations between the phenyl groups or in the ring (e.g. 922.2 cm^{-1}, 1553.5cm^{-1}, 1692cm^{-1}, 1694cm^{-1}, 1734cm^{-1}), exhibit frequencies with a linear dependence on the percentage strain applied dE (cf. Figure 2). Notably, a negative slope for strain-induced frequency changes in PPTA single fibers has also been observed experimentally by Young (18), with a slope of ca. -2 $d\Delta\upsilon/dE$, while the average slope shown in Figure 2 yields a value of -13 $d\Delta\upsilon/dE$. However, Young has shown (17) that $d\Delta\upsilon/dE$ is proportional to Young's modulus, that may explain in part our overestimation of these slopes, since the predicted modulus is also overestimated.

Comparison of Biopolymer Chains and PPTA

A distinctly different response of an α-helical chain of poly(L-Ala) to the application of strain has been predicted by Pachter et al (12, 13), where no buckling was shown in compression to a strain of 15%, with a predicted modulus of 60 GPa. The force (10^{-10} N) curve indicates that in distinct contrast to PPTA, there is no evidence for 'kinking'. Only small energy variations were calculated in tension, with a similar response for poly(L-Glu). Even at ca. 40% tensile strain there was incomplete extension of the chain with breaking of the hydrogen bonds, and thus no large increase in the heat of formation. At higher extensions a structure approaching more β-sheet type may result. These results demonstrate a 'spring-like' behavior of α-helical biopolymer chains in contrast to the extended biopolymer systems. Interestingly, although synthetic high performance polymers fail by 'kinking' as shown, for example, by Greenwood and Rose (19), and Robertson (20), Mahoney et al (21) report that spider silk fibers containing α-helical structures on the surface do not 'kink', which is consistent with our calculations. Our analysis helps explain the molecular elasticity of biopolymers that consist of α-helical strands and hence the apparent prevalence in Nature for coiled coils.

REFERENCES

1. Klunzinger, P.E., and Eby, R.K., 1993, Polymer 34, 2431.
2. Rutledge, G.C., and Suter, U.W., 1991, Polymer 32, 179.
3. Sorensen, R.A., Liau, W.B., and Boyd, R.H., 1988, Macromolecules 21, 194.
4. Tashiro, K., Kobayashi, M., and Tadokoro, H., 1978, Macromolecules 11, 908.
5. Adams, W.W., Doudis, S.D., Wierschke, S.G., Haaland, P.D., and Shoemaker, J.R., 1991, Preprints of the 8th International Conference on Deformation, Yield and Fracture of Polymers.
6. Wierschke, S.G., Shoemaker, J.R., Pachter, R., Haaland, P.D., and Adams, W.W., 1992, Polymer 33, 357.
7. Shoemaker, J.R., Horn, T.R., Haaland, P.D., Pachter, R., Adams, W.W., 1992, Polymer 33, 351.
8. Shoemaker, J.R., 1991, M.Sc. Thesis, Air Force Institute of Technology.
9. Horn, T.R., Haaland, P.D., Pachter, R., Adams, W.W., 1993, Polymer 34, 2481.
10. Haaland, P.D., Pachter, R. and Adams, W.W., Polymer, in press.
11. Haaland, P.D., Pachter, R., Pachter, M., and Adams, W.W., 1992, Chemical Phys. Lett. 199, 379.
12. Pachter, R., Haaland, P.D., Crane, R.L. and Adams, W.W., 1993, Biological Materials, Material Research Society Symposium Proceedings 292, 199.
13. Pachter, R., Crane, R.L. and Adams, W.W., 1993, Silk Polymers: Materials Science and Biotechnology, (Kaplan, D., Adams, W.W., Farmer, B.L., Viney, C., eds.) 44, 283.
14. The invention by duPont of the spinning of liquid crystalline acid solutions of the stiff-chain of PPTA opened the field of extremely high performance organic fibers (S. Kwolek, U. S. Patent No. 3 600 356, 1971)
15. Allen, S.R., 1988, Polymer 29, 1091; Tashiro, K., Kobayashi, M., and Tadokoro, H., 1977, Macromolecules 10, 413; Gaymans, R.J., Tijssen, J., Harkema, S., and Bantjes, A., 1976, Polymer 17, 517.
16. Karasawa, N., Dasgupta, S., and Goddard, W.A., 1991, J. Phys. Chem. 5, 2260.
17. Rutledge, G.C., Suter, U.W., and Papaspyrides, C.D., Macromolecules 24, 1934.
18. Young, R.J., 1993, Advances and Characterization of Solid Polymers (Ed. Spells, S.J.), Chapter 8.
19. Greenwood, J.H. and Rose, P.G., 1974, J. Mater. Sci. 9, 1809.
20. Roberstson, R.E., 1969, J. Polym. Sci. A-2 7, 1315.
21. Mahoney, D.V., Vezie, D.L., Eby, R.K., Adams, W.W., and Kaplan, D., 1993, Silk Polymers: Materials Science and Biotechnology, (Kaplan, D., Farmer, B.L., Viney, C., Adams, W.W. eds.) 44, 196.

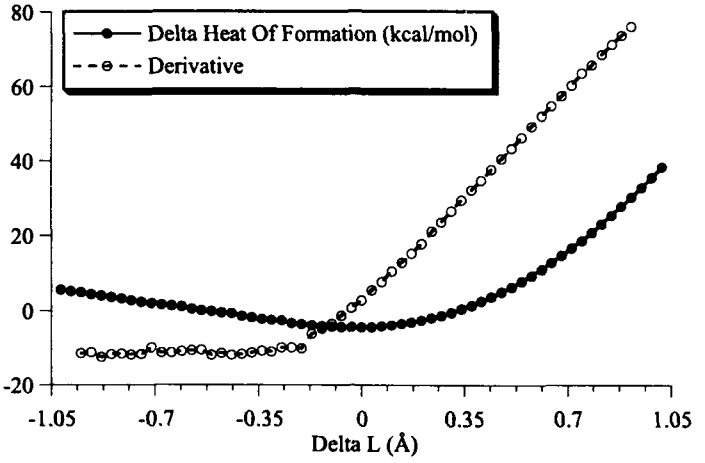

Figure1 Energy difference (ΔH_{ff}) vs. change in Tv length (ΔL) in PPTA

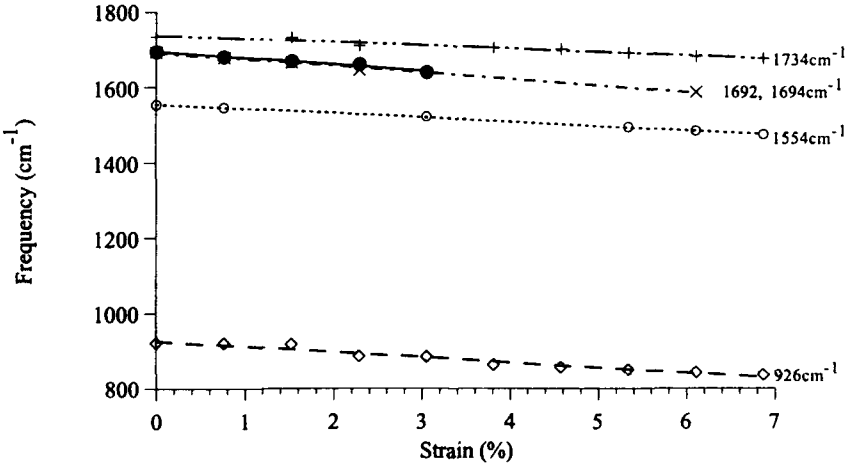

Figure 2 Changes in mode frequencies of PPTA as a function of the percentage strain applied

STUDYING THE DEFORMATION BEHAVIOUR OF HIGH-PERFORMANCE FIBRES IN TENSION AND COMPRESSION BY SPECTROSCOPIC-MECHANICAL METHODS

C Galiotis and C Vlattas*

A modified version of the Cantilever Bending Beam (CBB) method is employed to subject a number of high-performance Liquid Crystal Polymer (LCP) fibres to a gradient of axial tensile and compressive stresses. The molecular deformation of the filaments in tension and compression is monitored by scanning along the length of the filaments with a Laser Raman Microprobe. Strain hardening phenomena in tension and strain softening phenomena in compression are studied. Finally, a method of deriving stress-strain curves from the Raman spectroscopic data is demonstrated. The compressive strength of these fibres is consequently predicted.

INTRODUCTION.

LCP fibres represent an alternative to carbon fibres for composite applications. However, it is well established that these fibres are an order of magnitude weaker in compression in spite of their superior tensile behaviour. Small amount of work has been done towards the understanding of the compressive deformation of these fibres. Techniques of measuring the compressive stress or strain to failure have been developed and the mode of failure has been investigated.

In this study, a modified CBB method (1) is employed to subject a number of LCP fibres (Table 1) to an axial compressive stress gradient. Single filaments are glued onto the top surface of PMMA bars. By deflecting the beam up or down, the filaments are subjected to a gradient of compressive or tensile strain. The molecular deformation of the embedded fibres is monitored by scanning along their length with a Laser Raman Micropobe (2). Past work has shown that Raman vibrational frequencies related to the skeletal backbone shift to lower values under tension and higher values under compression. An improved methodology is presented allowing us to derive relationships between Raman frequency and applied stress or strain. Good estimates of the strain dependence of fibre modulus and the compressive strength are obtained.

*Dept. of Materials, Queen Mary and Westfield College, University of London

EXPERIMENTAL

The specimen preparation, the CBB assembly and the Laser Raman Spectroscopy setup for data aquisition have been demonstrated elsewhere (2). Single filaments were also tested in tension according to the ASTM procedure with a strain rate of 0.04 min^{-1} (Table 1).

RESULTS / DISCUSSION

A typical plot with the y-axis representing the Raman frequency shift between the embedded fibre and the values of the corresponding stress-free fibre in air, and with the x-axis representing the applied mechanical strain is given in Figure 1 for Kevlar® 49 fibre. In order to derive mathematical expressions for the Raman frequency shift vs strain relationships, cubic spline interpolations are fitted to the raw data. The shift of the Raman frequency for a given backbone vibrational mode, is due to the deformation of covalent bonds along the chain. For LCP fibres which can be considered as aggregates of crystallites connected in series, $\Delta\nu$ is proportional to stress, σ:

$$\Delta\nu(\varepsilon) = k\sigma(\varepsilon) = f(\varepsilon) \qquad (1)$$

where **k** represents the stress sensitivity of the Raman frequency and $f(\varepsilon)$ the spline function. It has been found that **k**=4.0cm-1/GPa for all Kevlar fibres (3). By differentiation, an estimation off the tangent Young's modulus can be obtained along with a stress-strain relation:

$$E(\varepsilon) = \frac{1}{k}\frac{d\Delta\nu(\varepsilon)}{d\varepsilon} \quad , \quad \sigma(\varepsilon) = \frac{1}{k}f(\varepsilon) \qquad (2)$$

The derived stress-strain curves for all commercial Kevlar® fibres are shown in Figure 2. The initial compressive Young's modulus follows the trend K149>K49>K29 but all fibres fail by kinking when a compressive stress of approximately 300 MPa is reached. The strain hardening in tension and the strain-softening in compression can be attributed to axial-shear coupling and associated "misorientation" of the crystallites/pleats in Kevlars and fibrills in PBZT. The results for all fibres are summarized in Table 2.

CONCLUSIONS

Various types of LCP fibres have been subjected to tension and compression. A conversion based on the scaling of $\Delta\nu$ with applied stress derived stress-strain curves from the optomechanical data. The inherent weakness of LCP fibres in compression is a consequence of their plastic instability in shear as manifested by their inherently low values of shear modulus and strength.

Fibre	d / μm	E / GPa	ε_f / %	σ_{ult} / MPa
Kevlar® 29	12.0	80±15	3.0±0.2	2400±250
Kevlar® 49	12.0	120±10	2.5±0.2	3250±200
Kevlar® 149	12.5	160±20	1.2±0.3	1920±250
Kevlar® 49 HT1420d	11.9	125±10	2.5±0.2	3400±250
Kevlar® 49 HT2160d	14.6	120±10	2.6±0.3	3600±300
PBZT	16.5	260±20	1.4±0.3	3920±300

Table 1. Tensile properties of LCP fibres.

Fibre	E_0 / GPa	ε_f / %	σ_{ult} / MPa
Kevlar® 29	70	0.75±0.05	304±45
Kevlar® 49	110	0.55±0.05	362±40
Kevlar® 149	140	0.30±0.10	260±60
Kevlar® 49 HT1420d	110	0.60±0.05	373±30
Kevlar® 49 HT2160d	110	0.60±0.05	469±30
PBZT	260	0.35±0.05	620±40

Table 2. Compressive properties of LCP fibres.

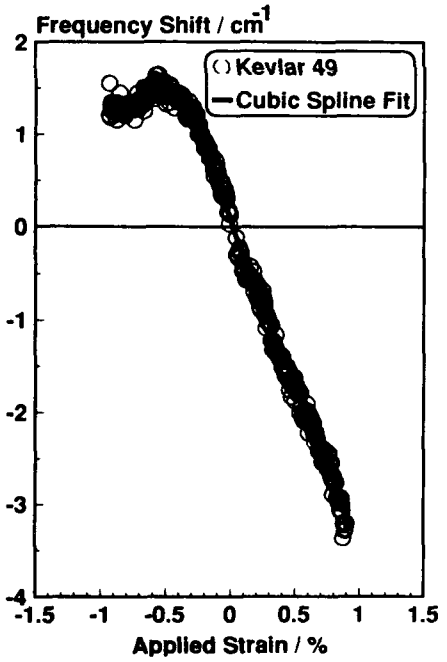

Figure 1. Δν - ε data for Kevlar® 49.

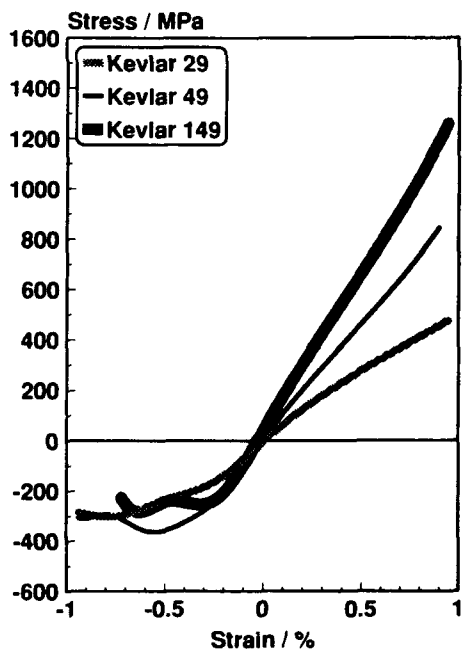

Figure 2. σ-ε curves for all Kevlar® fibres.

SYMBOLS USED

Dn = Raman Frequency Shift , cm^{-1}
ε = Applied Strain , %
σ = Applied Stress , GPa
k = Raman Frequency Stress Sensitivity , cm^{-1}/GPa
E = Young's Modulus / GPa
ε_f = Failure Strain / %
σ_{ult} = Strength / MPa

REFERENCES

1. Melanitis, N. and Galiotis, C., *J. Mater. Sci.*, **25** (1990), p.5081
2. Vlattas, C. and Galiotis, C., *Polymer*, **32**, No.10 (1991), p. 1788
3. Vlattas, C. and Galiotis, C., Submitted to *Polymer* (1993).

ASPECTS OF THE MECHANICAL PROPERTIES OF SPIDER DRAGLINE SILK

D.V. Mahoney* and R.K. Eby**

Wide-angle and small-angle X-ray data are presented together with the results of birefringence measurements. The crystals belong to Warwicker's Group 3b with cell dimensions of 10.6, 9.44 and 6.95 Å for a, b, and c, respectively. The minimum crystal dimensions in the corresponding directions are 23, 16 and 38 Å. There is a meridional peak corresponding to 79 Å. The crystals reorient up to a strain of 0.1, but the birefringence increases linearly up to a strain of 0.3. These results are discussed in terms of the question of uniform stress in the fibers.

INTRODUCTION

Fibers of dragline silk from Nephila clavipes have been shown by Mahoney et al (1) and Cuniff et al (2) to undergo deformations up to about 40% in compression without evidence of kinking and in tension without failure by Butterworth and Lenz (3). The X-ray moduli have been determined for N. clavipes and the domesticated silkworm Bombyx mori by Becker et al (4). The values of 17 and 29 GPa, respectively, are much less than the values of 150 GPa determined by computational modeling for β-poly-L-alanine with the Tripos force field (1) and 200 GPa with the protein-based Kollman force field (2). They are also much less than the of 147 GPa determined from the slope of the longitudinal acoustic dispersion curve calculated for β-poly-L glycine with a modified Urey-Bradley force field by Fanconi (5) and 155 GPa from Treloar's method for B. mori by Iizuka (6). These results raise a question about the validity of the assumption of uniform stress in the analysis of the X-ray data by (1) and Nakame et al (7). We present data obtained to provide further insight to this question.

RESULTS

The fiber pattern shown in Figure 1 was obtained with a bundle of filaments which had been obtained by silking the spiders at a rate of approximately 1.1 cms^{-1}. Nickel-filtered Cu radiation was used in conjunction with a 0.3 mm pinhole collimator and an area detector. After subtraction of air scatter, the digitized data were analyzed to obtain scans in 2θ such as the equatorial one shown in Figure 2. Fitting these showed the unit cell

*3M, 6801 River Place Blvd., Austin, Texas 78726
**Morton Institute of Polymer Science, The University of Akron, Akron, OH 44325-3909

dimensions to be consistent with Warwicker's (8) Group 3. Further, the crystals are in Group 3b since the peak at larger angles in Figure 2 is the more intense one (8). The unit cell dimensions are 10.6, 9.44 and 6.95 Å for a, b and c, respectively. Using the Scherrer equation and correcting for instrumental broadening with a silicon standard , yielded minimum crystal dimensions of 16 Å in the b (hydrogen bond) direction, 23 Å in the a (side group) direction and 38 Å in the c (covalent) direction. These are similar to values obtained for B. mori and other silks by Gopal et al (9), Samashekar et al (10) and (7). The longitudinal extent of the present crystals is less. Fiber patterns were obtained as a function of stress on the bundle of filaments. After correcting for instrumental broadening, the intensity distribution in χ yielded the half-widths at half of the maximum intensity as shown in Figure 3. The value at zero strain is about twice the value reported for B. mori.(7) As reported for other fibers, there is a decrease of the change of half-width with increasing strain. Small angle patterns were obtained with a bundle of filaments, 0.38 mm pinhole collimators and a 71.5 cm evacuated camera. The pattern shown in Figure 4 exhibits a meridional reflection corresponding to approximately 79 Å in the c direction. This can be seen in Figure 5 which was obtained by integrating over the 1.1 mm wide band in Figure 4. Artificially produced silk gut has been shown by Fraser et al (11) to exhibit a diffuse meridional reflection corresponding to 80 Å, but it was not observed in fibers of B. mori. Birefringence measurements were made with a tilting compensator and single filaments mounted in clamps that could be moved with respect to one another. A plot of birefringence as a function of tensile strain is shown in Figure 6. The increase of birefringence is nearly linear to a strain of 0.3.

DISCUSSION

The minimum crystal dimension, 38 Å and the long period, 79 Å, in the c direction are consistent with a possible periodic sequence of crystals and lower density domains along the fiber. If this is correct, the maximum extent of the latter would be 41 Å. These dimensions are qualitatively consistent with the sequencing of alanine rich crystalline and other domains in a protein of the silk as discussed by Xu et al (12) and Mello et al (13). However, they are not consistent with the low crystallinity discussed by Gosline et al (14). This suggests that there are other low density domains in addition to those in the periodic structure. Since these are probably occupied by a different protein-molecule (12), they would most likely be in parallel with the periodic structure mentioned above and would complicate the stress distribution within the fiber. Another question could arise from the observed increase of birefringence to a strain of 0.3 and the discontinued reorientation of the crystals at a strain of 0.1. It seems likely that this results from a relatively greater reorientation of the disordered components of the fiber in comparison to the crystals. This coupled with the discussion just above is consistent with a non-uniform distribution of stress in the fiber.

REFERENCES

1. D.V. Mahoney, D.L. Vezie, R.K. Eby, W.W. Adams and D.L. Kaplan, 1993 "Silk Polymers: Materials Science and Biotechnology", D.L. Kaplan, W.W. Adams, B. Farmer, C. Viney, editors, ACS Symp. Series 544.

2. Philip M. Cunniff, Stephen A. Fossey, Margaret A. Auerbach, John W. Song, David L. Kaplan, W. Wade Adams, Ronald K. Eby, Dave Mahoney, Deborah L. Vezie, 1994, Polymers for Advanced Technologies, in press.

3. G.A.M. Butterworth and R.W. Lenz, 1966, Report C65593 to U.S. Army Natick Laboratories; Fabric Research Laboratories, Inc., Dedham, MA.

4. M.A. Becker, D.V. Mahoney, P.G. Lenhert, R.K. Eby, D.L. Kaplan and W.W. Adams, 1993, "Silk Polymers: Materials Science and Biotechnology", D.L. Kaplan, W. W. Adams, B. Farmer, C. Viney, editors, ACS Symp. Series 544.

5. B.M. Franconi, 1972, Chem. Phys, 57, 2109, .

6. E. Iizuka, 1965 Biorheology 3, 1.

7. K. Nakamae, T. Nishino and H. Ohkubo, 1989, Polymer, 30, 1243.

8. J.O. Warwicker, 1960, J. Mol. Biol. 2, 350.

9. Gopal Krishne Urs, R.; Subramanya, G.; Somashekar, R., 1993, Text. Res. J. , 63, 610.

10. Somashekar, R.; Gopalkrishne Urs, R. 1993, Polymer , 34, 2711.

11. Fraser, R.D. B.; MacRae, T.P. 1973, "Conformation in Fibrous Proteins and Related Synthetic Polypeptides"; Academic Press, New York, 314.

12. Xu, M., Lewis, R.V., *Proc.*1990 Natl. Acad. Sci., U.S.A. , 87. 7120.

13. C.M. Mello, K. Senecal, B. Yeung, P. Vouros, and David Kaplan, 1993, "Silk Polymers: Materials Science and Biotechnology", D.L. Kaplan, W. W. Adams, B. Farmer, C. Viney, editors, ACS Symp. Series 544,67.

14. J.M. Gosline, M.W. Denny, M.E. DeMont, 1984 Nature, 309, 551.

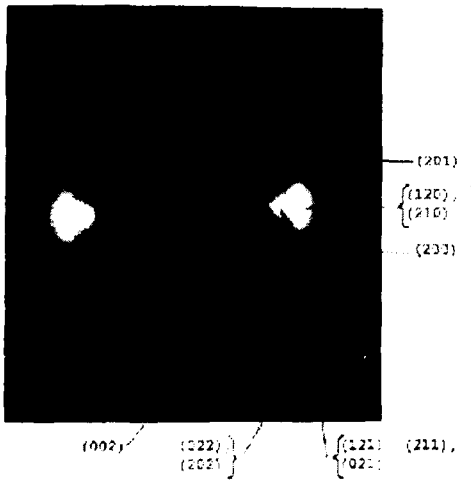

Figure 1 X-ray fiber pattern

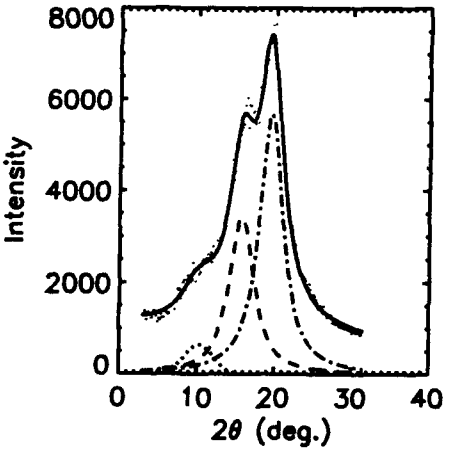

Figure 2 Equatorial scan of Figure 1

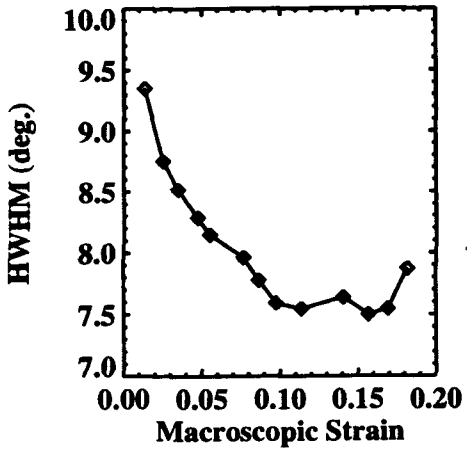

Figure 3 Half-width vs strain

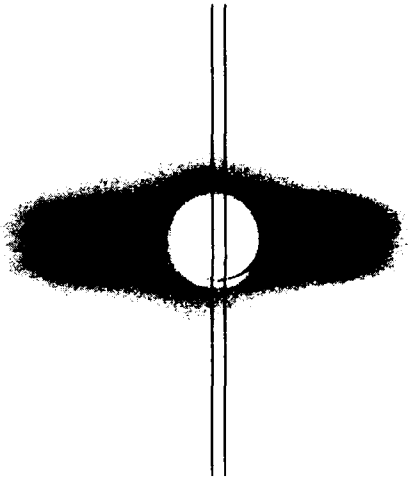

Figure 4 X-ray small-angle pattern

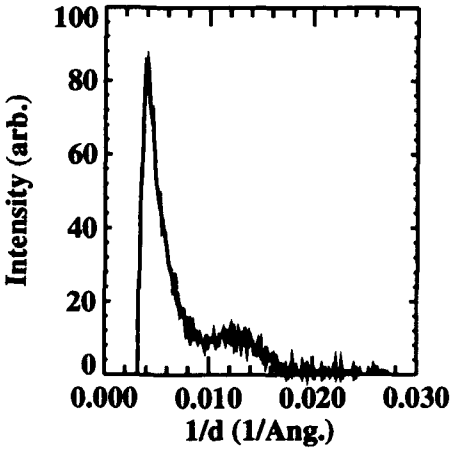

Figure 5 Meridional profile of Figure 4

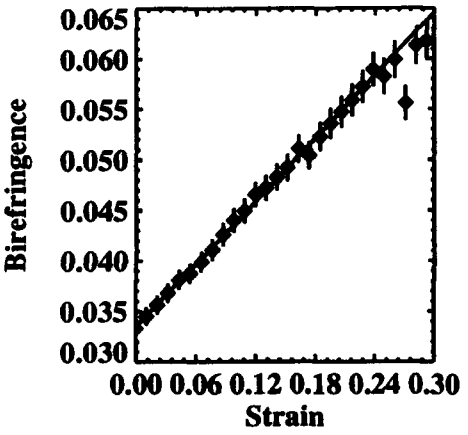

Figure 6 Birefringence vs strain

ULTRASTRUCTURAL STUDIES OF THE MECHANISM GOVERNING COMPRESSIVE DEFORMATION IN HIGH PERFORMANCE POLYMERS

Deborah L. Vezie* and Edwin L. Thomas*

To gain insight into the relationship between mechanical properties, microstructure, and kinking in high performance polymers, a detailed investigation into the nature, types, and interactions of kinks in rigid-rod polymers was performed. Previous publications have cited characteristic kink angles and kink widths. Our work demonstrates that there are no unique kink angles in PBO, as the values for kink angles are dependent upon strain and there are no unique axial kink widths, as kink boundaries translate and grow axially with increasing strain. As with other systems that kink, including hcp metals and foliated rock, it is likely that a shear instability, rather than Euler buckling, initiates kink formation when resolved shear stresses on misoriented crystallites exceed the shear strength of the material.

INTRODUCTION

The PBX-type rigid-rod polymer fibers have among the highest mechanical tensile properties ever measured in polymeric systems, but are not yet viable for general structural applications because of poor compressive strengths. As with other high performance fibers, rigid-rod polymer fibers compressively deform by kink band formation. A *kink is a localized region of axial shear* deformation where the deformed region is rotated with respect to the undeformed region. Kinking is a process of strain energy dissipation via a localized rather than homogeneous deformation; this process and the resulting length scale of the kinked region are strongly dependent upon the structure and mechanical properties of the material undergoing deformation. Kinks can be formed in uniaxial compression, shear, torsion, and bending, and are found in a wide variety of materials including hexagonally close-packed metals, foliated rock, uniaxial fiber composites, minerals, card decks and oriented, semi-crystalline polymers. The common features to all materials that kink is their highly anisotropic mechanical nature and easy planes of slip. Many attempts have been made to improve the compressive properties of rigid-rod fibers, with limited success, partially because the micromechanisms of kink formation are not well understood. This study focuses on compressive deformation in the rigid-rod fibers, polyparaphenylene benzobisthiazole (PBZT) and polyparaphenylenebenzobisoxazole (PBO), with an emphasis on PBO. Geometrical models on the interactions between multiple kinks will be discussed as well as whether a shear or buckling instability initiates kink formation and at what level of structure kink initiation occurs.

EXPERIMENTAL PROCEDURE

The morphology of the PBO fiber used in this study, designated PBO 8A 600°C HT (tension heat treated) has been well characterized by Martin and Thomas (1,2). In the present study, kinks were generated by the nylon matrix shrinkage technique described by DeTeresa (3) and by a second method we will call the "twist and peel" method in which individual fibers are twisted a given number of times (in this case 50 twists/inch), allowed to untwist, and then peeled apart with tape, revealing kinks in the interior of the fiber. After coating with 1nm of tungsten, kinks were imaged using a Hitachi S-900 field emission, immersion lens high resolution SEM (HRSEM) at 1.0 keV.

*Dept. of Materials Science and Engineering, MIT, Cambridge, MA, 02139 USA

RESULTS AND DISCUSSION

Single Kink Geometries

Many studies of high performance polymers have attempted to correlate kink boundary angles to material properties. However, two angles are required to describe a planar-like defect; we choose α, the change in molecular orientation across the kink boundary, and β, the angle between the normal to the kink boundary and the molecular or fiber axis (kink boundary angle). To properly measure the two kink angles, the kink must be in the in-plane orientation as described by Evans and Adler (4). A standardized method for measuring kink angles is proposed in Figure 1. When $\beta = \alpha/2$ the kinked region is isovolumetric and at a minimum strain energy. The volume within the kinked region increases and the strain energy increases when $\beta > \alpha/2$. HRSEM images of kinks produced by both methods described above show that $\beta > \alpha/2$ for single kinks, which indicates that there is lateral expansion within the kink. Figure 2 is a HRSEM image of a single kink produced by the twist and peel method. This particular kink has two sharp, well defined boundaries and an axial width of 50nm, with $\alpha = 34.5°$ and $\beta = 21.5°$.

Two types of kink boundaries are observed in PBO. Sharp, well defined boundaries were observed in the smallest of kinks (< 50 nm axial width), whereas in the larger kinks had diffuse, poorly defined boundaries. Kinks were sometimes observed to have one sharp and one diffuse boundary, which would explain the "sharp" and "smooth" boundaries observed by Martin and Thomas (7). Most often, however, two diffuse boundaries were observed within a kink band.

As a kink forms, α must increase, but for the minimum energy condition to be maintained, β must also increase. An increase in β means that the kink boundary rotates through the material (it may also axially translate as it rotates). If β were to remain fixed as α increased, then $\beta < \alpha/2$, which would result in lateral compression within the kink band. In PBO, we find β is always greater than $\alpha/2$, indicating that the kink boundary rotates past the minimum energy condition. In contrast, the kink boundary cannot rotate in continuous fiber composites because the fibers break as the kink is formed. When the kink boundary is not free to rotate, an irregular boundary, as well as axial splitting results, as shown by Argon (5). In a material such as PBO where the kink boundary does rotate, the kink can also widen axially (boundary translates). Axial widening of kinks explains the range of single kink widths observed in this study (40nm - 0.4μm). Axial widening also demonstrates the fallacy of correlating kink widths to "buckling lengths" in those models of compressive strength based on Euler buckling. It should be noted that β is a function of strain and therefore has an indeterminant value. In summary, there are no characteristic values of α and β, nor are there characteristic axial kink widths for any of the high performance polymer fibers.

Multiple Kink Geometries

Multiple kinks that form in bundles are more common than single kinks (e.g. see Vezie (6)). Kinks often form in parallel arrays when thin sections of fiber are peeled from the fiber. Kinks may also intersect, forming a void and/or axial split at their intersection. Sometimes kinks are also found to terminate at the point of intersection. The intersection of many kinks is the origin the surface bulges commonly observed in rigid-rod fibers deformed by uniaxial compression.

Kink Initiation: Buckling Instability vs. Shear Instability

Compression tests as a function of orientational misalignment by Gilman and Read (8) and Gilman (9) in zinc single crystals and by Gay and Weiss (10) and Paterson and Weiss (11) in foliated rock have shown that kink initiation is caused by a shear mechanism in which the resolved shear stress on a misaligned region exceeds the shear strength of the material, producing a local plastic shear deformation and subsequent kink formation. Although a PBO fiber is a highly

oriented system, large local misorientations have been documented (2). Since our fiber microstructure is much more complex than zinc, and just as complex as foliated rock, with large, locally inherent misorientations, a resolved shear stress-induced localized plastic deformation is highly probable for our system. Moreover, the lateral interactions at all length scales in the rigid-rod polymers are weak, resulting in poor shear properties. Therefore it can be inferred that shear must be the initiation mechanism for kinking in the rigid-rod fibers if we assume that kinking is a universal compressive deformation mechanism in highly aligned anisotropic systems with easy planes of shear. In PBO, the highest shear stresses are resolved on the most misoriented *crystallites*, which are localized regions along microfibrils. Therefore, the shear instability is at the *microfibrillar* level rather than at the *chain* level. When the microfibrils slip during the kinking process, the chains within the crystallites must also slip. An Euler buckling instability is not a reasonable model for kink initiation because first mode buckling, which gives the lowest critical load, cannot produce the proper kink form. Second mode buckling would be required to produce two kink boundaries. Also, resolved shear stresses are active at far lower loads than a critical buckling load.

Deformation by kinking is a combination of slip in the axial direction and bend plane formation which defines the kink boundaries. The process of axial slip is dependent upon the shear strength, k, and shear modulus, G, of the material, which in highly oriented high performance polymers, is dependent upon both the lateral interactions between chains and the lateral interactions between any other units of microstructure, such as the microfibrils. Bend plane formation is dependent upon the bending stiffness, EI, which is a function of the elastic modulus and the geometry of the unit undergoing bending as it influences the first moment of inertia. If the tensile modulus, E_t, and compressive modulus, E_c, for a given microstructural unit or whole fiber are not equal, as is the case for many high performance polymers, the neutral axis in a bent fiber will shift from the centerline of the unit undergoing bending, resulting in a different moment of inertia for each of the tensile and compressive regions, as shown by Fahey (12). The bending stiffness is then a function of both the elastic tensile and compressive moduli of the fiber. Therefore, a reasonable model for the maximum compressive load in a system deforming by kinking should contain the following material properties: shear strength, shear modulus, tensile modulus, and compressive modulus, as well as the geometry of the system. Presumably, in the different stages of kinking (nucleation, propagation, and kink broadening) different material properties may dominate the process at different times.

At kink initiation, the shear strength is the primary property of interest (5). Plastic deformation in the form of slip is dependent upon the shear strength of the material. At a later stage when the dislocations within the kink glide to form the boundaries (6), the shear modulus becomes an increasingly important parameter in determining the deformation (the energy of a dislocation is directly proportional to the shear modulus of the material). As the boundaries travel and α increases, the bending stiffness and elastic moduli become critical. Therefore, depending on the stage of kinking, any of the above material properties, k, G, E_t, and E_c, will have a direct relationship with the measured compressive strength of the material. To acurately correlate compressive strength to other material properties, it is important to determine the stage of kinking (i.e. initiation, propagation, axial widening) and the number of pre-existing kinks in the material.

SYMBOLS USED

α = change in molecular orientation across the kink boundary

β = kink boundary angle

k = shear strength

G = shear modulus

E_t = elastic tensile modulus

E_c = elastic compressive modulus

REFERENCES

1. Martin, D.C., and Thomas, E.L., 1991, Macromolecules, 24, 2450

2. Martin, D.C., and Thomas, E.L., 1991, Phil. Mag., 63, 903

3. DeTeresa, S.J., 1984, Ph.D. Thesis, University of Massachusetts

4. Evans, A.G., and Adler, W.F., 1978, Acta Metal., 26,725

5. Argon, A.S., 1972, "Fracture in Composites", in "Treatise on Materials Science and Technology", Academic Press, New York, 79

6. Vezie, D.L., 1993, Ph.D. Thesis, Massachusetts Institute of Technology

7. Martin, D.C., and Thomas, E.L., 1991, J. Mater. Sci., 26, 5171

8. Gilman, J.J., and Read, T.A., 1953 (January), Trans. AIME, J. Metals,49

9. Gilman, J.J., 1954 (May), J. Metals, 49

10 Gay, N.C., and Weiss, L.E., 1974, Tectonophysics, 21, 287

11. Paterson, M.S., and Weiss, L.E., 1966, Geol. Soc. America Bull.,77, 343

12 Fahey, M.T., 1993, Ph.D Thesis,Massachusetts Institute of Technology

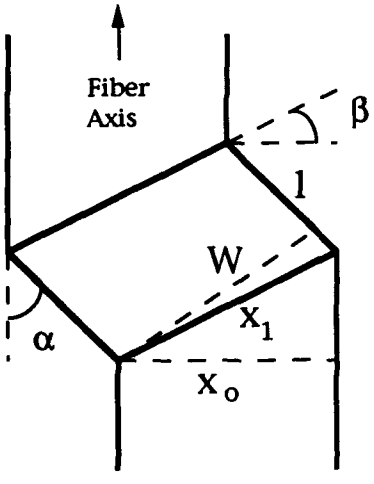

$$W = x_o \frac{(\cos \alpha - \beta)}{\cos \beta}$$

Figure 1. Standardized model for measurement of kink angles α and β in the in-plane orientation.

Figure 2. HRSEM image of a 50 nm single kink with two sharp, well defined boundaries. α = 34.5°, β = 21.5°

YIELDING AND HYSTERESIS OF POLYMER FIBERS

M.G.Northolt and J.J.M.Baltussen *

Yielding of polymer fibers is explained by the onset of a sequential plastic orientation process of chains brought about by the resolved shear stress. An equation for the yield strain, ε_y, is derived, showing that ε_y is mainly dependent on the degree of orientation. This yielding mechanism also explains the difference between the first loading tensile curve and the hysteresis curves.

INTRODUCTION

At temperatures below the glass transition fibers made of aliphatic polyamides, poly(ethylene terephthalate) (PET), cellulose II and poly(p-phenylene terephthalamide) (PpPTA) have essentially the same kind of tensile curve. As shown in Fig. 1, these curves consist of a nearly straight initial part up to the yield strain near 1 %, a short yield range, characterized by a decrease of the slope, and a more or less concave section almost up to fracture. These three stages are more pronounced in medium and low oriented fibers like PA 66, PET and cellulose II Cordenka than in highly oriented fibers, such as Twaron PpPTA and cellulose II EHM. This similarity in shape extending over a considerable part of the tensile curve indicates that the same deformation mechanism governs the tensile behaviour of these various kinds of polymer fibers.

Yielding in oriented fibers is observed near a strain ε_y = 1 %, in isotropic samples near 2 % and is independent of the strain rate. Unloading of the fiber after the first extension up to a strain larger than ε_y results in a small but permanent extension of the fiber. As shown in Fig. 1 and 2 it is remarkable that ε_y varies little for fibers made from different polymers and for fibers from the same polymer but with very different moduli. On the other hand the yield stress, σ_y, varies over a wide range. It is this particular phenomenon that is explained by the simple theory presented in this paper. The theory can also be applied to derive the compressive yield strain and stress of a fiber.

A modified series model has been proposed for the extension of oriented and (semi)crystalline fibers [1][2][3]. A consequence of this model is the sequential plastic orientation of chains during yielding. This mechanism and the assumption of a shear yield stress, τ_y, accounts not only for the yield near 1 %, but also explain the difference between the first loading curve and the repeated loading or hysteresis curves of semi-crystalline and wholly paracrystalline polymer fibers.

* Akzo Research Laboratories, P.O.Box 9300, 6800 SB Arnhem, The Netherlands

THEORY

The fiber is considered to be built up of a parallel array of identical fibrils and subjected to a uniform stress along the fiber axis [1][2][3]. A fibril consists of a series of oblong shaped domains arranged end to end. In a domain the chains run parallel to the symmetry axis having an angle ϕ with the fiber axis. All domains in a fibril are isotropic transverse to the symmetry axis and have identical mechanical properties. The orientation function of the axes measured along the meridian is $\rho(\phi)$ and the fraction of domains at angle ϕ is given by the function $N(\phi) = \rho(\phi)\sin\phi$. In the modified series model the domain properties pertaining to the elastic extension of of the fibril are the chain modulus e_c and the modulus for shear between the chains g. According to this model the fiber modulus is given by

$$\frac{1}{E} = \frac{1}{e_c} + \frac{\langle \sin^2\phi_o \rangle_E}{2g} \qquad (1)$$

where $\langle \sin^2\phi_o \rangle_E = \langle \sin^2\phi_o \cos\phi_o \rangle / \langle \cos\phi_o \rangle$ is the strain orientation parameter before loading the fiber. For an isotropic sample this orientation parameter equals 0.5. Equation (1) is based on the strain definition used in the modified series model [1]. The single shear modulus is an approximation since in many polymer fibers there is no isotropy in a plane transverse to the chain axis owing to the different kinds of intermolecular interactions.

The stresses acting on the domain are the normal stresses $\sigma\cos^2\phi$ and $\sigma\sin^2\phi$, directed parallel and perpendicular to the symmetry axis, and the four shear stresses $\tau = \sigma\sin\phi\cos\phi$. The stress $\sigma\cos^2\phi$ causes extension of the domain along the chain direction, while the shear stresses bring about the rotation of the chains through shear deformation of the domain. The effect of the relatively small stress $\sigma\sin^2\phi$ on the tensile deformation is not taken into consideration. Because in linear polymers $e_c \gg g$, the tensile deformation of a fiber is largely governed by the resolved shear stress τ. A shear yield stress, τ_y, is proposed, above which the resolved shear stress causes a plastic rotation of the chains in addition to the elastic and viscoelastic rotational contributions to the fiber strain. It is assumed that the shear yield stress is equal to a small but constant fraction f of the shear modulus $\tau_y = fg$. The onset of yielding for a particular domain occurs when $\sigma\sin\phi\cos\phi = \tau_y$. In this way plastic rotation is initiated in domains with angles (up to 45°) in the tail of the distribution $N(\phi)$. So, for increasing stress a sequential plastic orientation process of chains occurs, as shown in Fig. 3. The largest rotational plastic contribution to the fiber extension originates from the most disoriented chains. For a broad distribution $\sigma = 2\tau_y$ is the minimum fiber stress at which the plastic rotation starts. A visible effect of the plastic rotation manifested by a decrease of the slope in the tensile curve will be observed when at least a considerable fraction of chains is subjected to a shear stress $\tau \geq \tau_y$. In order to simplify the analysis without losing the typical features of the proposed theory, a fibril is now regarded as consisting of a bundle of parallel aligned zig-zag chains with an angle ϕ_a, being the average over $0 < \phi < \pi/2$ of the distribution $N(\phi)$ and given by $\phi_a = \arcsin\sqrt{\langle \sin^2\phi_o \rangle_E}$. It is assumed that up to the yield strain, ε_y, the fiber extension is almost purely elastic $\sigma = E\varepsilon$. This leads to the following equation for the yield strain

$$e_y = \left(\frac{1}{e_c} + \frac{\langle \sin^2\phi_o \rangle_E}{2g} \right) \frac{fg}{\sin\phi_a \cos\phi_a} \qquad (2)$$

It can be shown from this equation that ε_y is practically independent of e_c and depends little on g. For medium oriented fibers $\varepsilon_y \approx \frac{1}{2} f \tan\phi_a$ and for isotropic fibers $\varepsilon_y = \frac{1}{2} f$. Because the interchain forces in the linear polymers considered here consist only of secondary

interactions, it is assumed that f has approximately the same value in these polymers, which implies that the yield strain is nearly the same for these polymers and depends only on the orientation distribution.

RESULTS AND DISCUSSION

The parameter f is determined from the observed yield strain of isotropic samples. Isotropic sheets and fibers of PA 66, PET and PpPTA show that yielding occurs in the strain range of 1.5 to 2.0 %, and is independent of the strain rate, which means that $0.03 < f < 0.04$. Using equation (2) the yield strain ε_y has been computed as a function of $<\sin^2\phi_o>_E$ for different kinds of polymer fibers, taking $f = 0.035$. The e_c values are: PA 66 196, PET 125, cellulose II 89 and PpPTA 220 GPa. Shear moduli g have been derived from initial moduli E_o using equation (1). The orientation parameters have been measured either by X-ray diffraction or by birefringence measurements, the resulting g values being 1.9 GPa for PpPTA, 1.7 for cellulose II, 1.0 for PET and 0.8 for PA 66. Fig. 4 shows that the calculated yield strain depends practically only on $<\sin^2\phi>_E$. Comparison of the observed ε_y values, as shown e.g. for PET in Fig. 2, with the calculated curves shows a good agreement. The precise course of the yielding in the tensile curve is controlled by the distribution $N(\phi)$ and the sequential orientation mechanism.

Now the difference between the first loading curve and the repeated loading or hysteresis curves, which is observed for all polymer fibers considered here, can be explained. In Fig. 5 the observed first loading curve of a cellulose fiber is represented by curve (1). During unloading of the fiber, after having been subjected to a stress σ_p well above the yield stress σ_y, curve (2) is followed. Next repeated loading up to a stress σ_p results in the hysteresis curves (3)-(2)-(3)-(2)..... If the load is subsequently increased for the first time to a stress $\sigma > \sigma_p$, then from P onwards the so-called first loading curve (1) is followed again, involving a considerable change of the slope at P. The sequential orientation process during yielding provides the most likely interpretation for this behaviour. Yielding is caused by the onset of plastic rotation of chains, presumably by the temporarily loosening or disrupting interchain secondary bonds. During first loading of the fiber up to a stress σ_p (curve (1)) the most disoriented chains are the first ones whose rotation towards the fiber axis involves a plastic contribution, say, down to angle ϕ_2 in Fig. 3 and given by $\phi_2 = \frac{1}{2}\arcsin(2\tau_y/\sigma_p)$. If now cyclic loading is applied up to a maximum stress σ_p no plastic rotation can occur, because chains with angles large enough to cause a shear stress $\tau \geq \tau_y$ are absent. Due to the permanent contraction of the orientation distribution caused by the first loading and the absence of plastic rotation, the slope of the upward branch of the hysteresis curve (3) is steeper than that of the first loading curve up to P. However, when after a loading cycle σ is increased well above σ_p, domains with $\phi < \phi_2$ will be subjected to the shear yield stress. Accordingly, the chain rotation due to shear again contains a plastic contribution and as a result the tensile curve beyond P will resume the course of the first loading curve (1).

In conclusion, this theory has provided an equation for the yield strain which is experimentally confirmed. Moreover, it demonstrates that the shear stress governs the tensile deformation of the fiber and that the orientation distribution of chains is the dominant structural characteristic determining the tensile extension of polymer fibers, irrespective of the kind of morphology, i.e. whether the fiber is semi-crystalline like PA 66 and PET, or wholly paracrystalline like cellulose II and PpPTA.

REFERENCES

[1] Northolt, M.G. and van der Hout, R., 1985 Polymer 26, 230.
[2] Northolt, M.G. et al., 1989, J. Polym. Sci. Phys. Ed. 27, 1107.
[3] Northolt, M.G. and Sikkema, D.J., 1989, Advances in Polymer Sci. 98, 115.

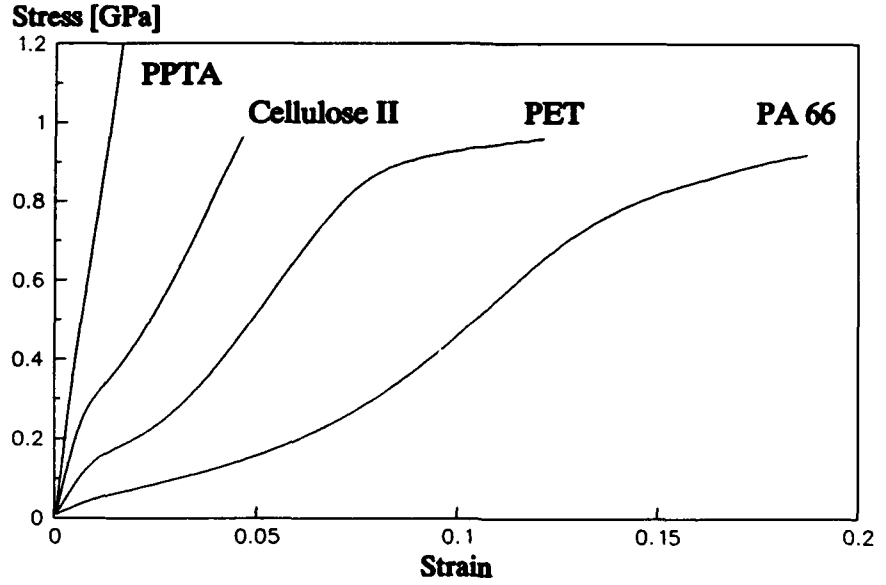

Fig. 1 Tensile curves of PpPTA, Cellulose II, PET, and PA 66.

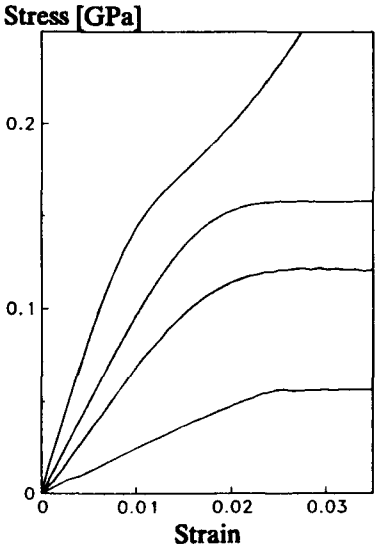

Fig. 2 The yield range of PET fibers with different degrees of orientation.

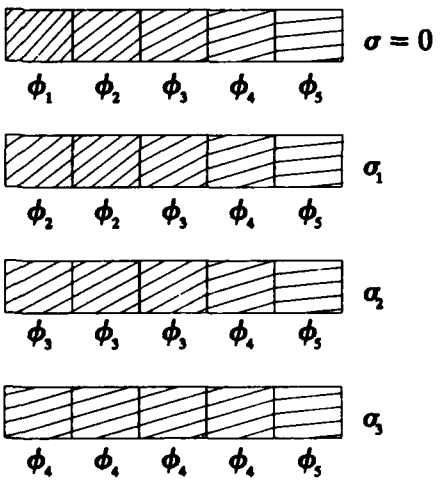

Fig. 3 The schematic presentation of the sequential plastic orientation mechanism during yielding.

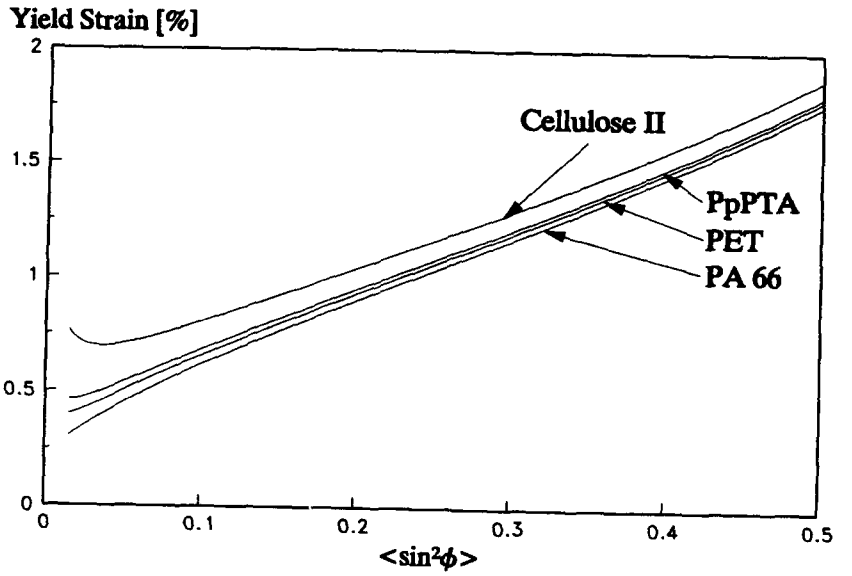

Fig. 4 Calculated yield strain as function of the orientation for PpPTA, cellulose II, PET and PA 66 fibers.

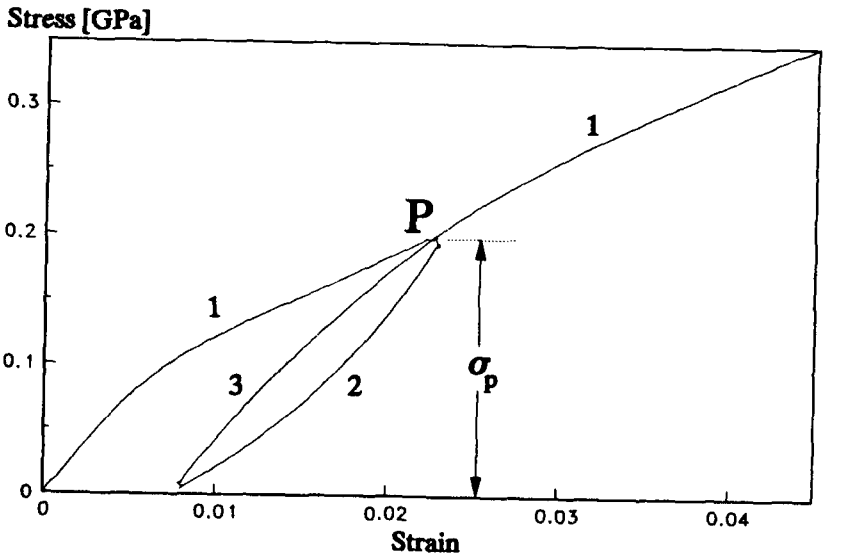

Fig. 5 First loading curve (1), hysteresis curves (2) and (3) for a maximum stress σ_p and subsequently continued loading above σ_p of a cellulose fiber.

MEASURING THE ELASTIC PROPERTIES OF HIGH MODULUS FIBRES

P.J.Hine* and I.M.Ward*

This paper describes the measurement of the elastic constants of several highly oriented polymers. The method makes use of the hot compaction process, developed and patented in this laboratory, which enables a solid section of highly oriented polymer to be produced from an aggregate of highly oriented fibres. As only a small percentage of the original fibre is lost during the process, the compacted materials offer an opportunity for measuring fibre properties in the bulk. An ultrasonic immersion technique has been used to measure the compacted materials elastic properties

INTRODUCTION

A complete description of the elastic properties of a drawn high modulus fibre is seldom available, because although it is relatively simple to measure the longitudinal and torsional moduli, it is often extremely difficult to measure the transverse modulus and Poisson's ratios of a fibre that is sometimes only tens of microns in diameter. Methods do exist for measuring transverse properties of fibres, for instance the transverse compression test, and a number of authors have used this method to determine the transverse properties of for instance polyethylene fibres. This is, however, a difficult measurement to make, especially when the fibres have a small diameter.

The advantage of the compaction technique is that it provides a sample of substantial size on which a set of consistent measurements can easily be made, giving a full set of elastic constants all determined under the same conditions of temperature and frequency.

This paper describes the measurement of the elastic properties of five different fibre types: melt spun polyethylene, gel spun polyethylene, polypropylene, polyethylene terephthalate and a thermotropic liquid crystalline polymer.

* *IRC in Polymer Science and Technology, University of Leeds, Leeds, LS2 9JT*

EXPERIMENTAL

The experimental details for the fibres used in this study are shown below in Table 1.

FIBRE	GRADE	COMPACTION TEMPERATURE
Melt Spun Polyethylene	TENFOR	138
Gel spun Polyethylene	DYNEEMA	145
PET	(38035 T800)	256
Polypropylene		173
LCP	VECTRAN	280

In the hot compaction process (British Patent No GB2253420) high modulus fibres are made into thick section homogeneous products by the process of 'selective melting' under low compressive forces. By choosing a suitable temperature, usually just inside the melting range of the fibre, it is possible to melt a given proportion of the fibres' surface. On cooling, this molten fraction reforms to bind the structure together. For a close packed hexagonal arrangement of fibres, only 9% of the melted and reformed material is needed to fill all the gaps in the structure, resulting in the compacted material being predominantly composed of the original fibre. Figure 1 below shows a typical transverse section taken through a compacted melt spun polyethylene fibre material, etched to give contrast between the different morphologies. This micrograph was taken by Professor Bassett and his colleagues at The University of Reading. Further details of the compaction process can be found in [1,2].

Figure 1: A typical transverse section through a compacted sample.

The technique used for measuring the elastic properties of the compacted materials was the ultrasonic velocity method, originally developed by NPL [3] and further explored by Lord [4] in this laboratory. The sample to be measured is placed in a water bath (25°C) between two ultrasonic transducers (2.25 MHz), one acting as a transmitter and one as a receiver. The basic measurement is the time of flight for a sound pulse to travel between the transducers. Measurements are taken with and without the sample in place and over a range of incidence angles, allowing both longitudinal and shear waves to be propagated through the sample. The variation of the longitudinal and shear wave velocities with incidence angle depends on the elastic properties of the material in the plane of sound propagation and computer fitting procedures allow these elastic properties to be determined.

THEORY

The anisotropic behaviour of an oriented material is described by the generalised Hooke's law.

$$\varepsilon_i = S_{ij}\sigma_j \qquad \text{where } i, j = 1,.....6$$
$$\sigma_i = C_{ij}\varepsilon_j$$

These two equations relate applied stresses (σ_j) and strains (ε_j) to measured strains (ε_i) and stresses (σ_i).through the compliance constants S_{ij} and the stiffness constants C_{ij}. Knowledge of these constants therefore completely specifies the elastic behaviour of the material under any conditions of stress or strain. The compliance constants can be further related to the more commonly used engineering constants: for example

$$\text{Longitudinal Young's Modulus } E_{33} = \frac{1}{S_{33}} \qquad \text{Transverse Young's Modulus } E_{11} = \frac{1}{S_{11}}$$

$$\text{Shear Modulus } G_{44} = \frac{1}{S_{44}}$$

$$\text{Poisson's Ratios } \nu_{12} = -\frac{S_{12}}{S_{11}} \quad \text{and} \quad \nu_{13} = -\frac{S_{13}}{S_{33}}$$

Using the ultrasonic immersion technique it is possible to calculate the stiffness constants (C_{ij}) for each compacted sample. As the compacted samples were transversely isotropic this gave five independent stiffness constants: C_{33}, C_{11}, C_{13}, C_{12} and C_{44} where the 3 axis is defined as the fibre axis direction. The compliance constants, and hence the engineering constants, were then obtained by matrix inversion.

RESULTS

The results for five fibre types are shown below in Table 2.

Fibre	E_{33}	E_{11}	ν_{13}	ν_{12}	G_{44}
TENFOR	57.7	4.68	0.45	0.55	1.63
DYNEEMA	74.2	4.19	0.47	0.58	1.36
PET	14.0	3.70	0.39	0.65	1.62
PP	14.0	3.30	0.38	0.49	1.67
LCP	97.2	3.24	0.48	0.73	1.30

For the TENFOR fibre we can compare the above results with those from a previous study carried out by Leung et al [5], where they measured the elastic constants of die-drawn Rigidex 50 polyethylene (draw ratio=20), also using ultrasonics but at the slightly lower frequency of 10 MHz. The results are shown below in Table 3.

Process	E_{33}	E_{11}	ν_{13}	ν_{12}	G_{13}
Compacted	57.7	4.68	0.45	0.55	1.63
Die-Drawn	62.5	4.76	0.44	0.52	1.60

The agreement is excellent and so gives confidence in the current technique.

There are two points worth noting when trying to extract the fibre properties from the measured compacted elastic constants. Firstly there will be an effect of misorientation of the fibres, for it is not possible to get perfect alignment in the compacted materials. This only affects the value of E_{33}, for while a 5° misalignment causes a drop of 20% in E_{33}, a similar misalignment only affects the other four constants (E_{11}, G_{13} υ_{13} υ_{12}) by less than 1%. It is likely, therefore, that the values of E_{33} shown in Table 2 are a lower bound. The second point is the effect of the melted and reformed phase. Although it only forms a small percentage of the total material, it could have a potentially large effect on the transverse properties. This is currently under further investigation.

REFERENCES

. P.J.Hine, I.M.Ward, R.Olley and D.C.Bassett, J.Mat.Sci, **28** (1993) 316.

:. R.Olley, D.C.Bassett, P.J.Hine and I.M.Ward, J.Mat.Sci, **28** (1993) 1107.

3. B.E.Read and G.D.Dean, The determination of the dynamic properties of polymers and composites, Adam Hilger Ltd, Boston, 1991, 31.

4. D.Lord, PhD thesis, University of Leeds, 1989.

5. W.P.Leung et al, Polymer, **25** (1984) 447.

"MOLECULAR VELCRO" - DYNAMICS OF A CONSTRAINED CHAIN INTO AN ELASTOMER NETWORK

K.P.O'Connor* and T.C.B. McLeish+

We discuss the dynamics of the healing process when contact is made between a cross-linked elastomer network and polymers that are end-tethered on to a solid surface. We find that there are generally three stages to the approach to the equilibrium, "mushroom" conformation. Entanglements in the network have a major affect on the time-scale of the healing process. We compare our findings with adhesion experiments on PI/PS interfaces and qualitatively predict both the time-scales and the change in toughness over the process. We introduce the modifications required at high coverage - the "brush" regime.

INTRODUCTION

In recent years there has been a great amount of activity, both theoretically and experimentally, in the study of polymer interfaces involving both polymer statics and dynamics. The static properties influence the depth and strength of the interface, and knowledge of polymer dynamics tells us how quickly the interface forms.

There are a number of practical systems which have physical similarities including a polymer/polymer weld [1,2], a diblock polymer at the boundary between incompatible homopolymers [3-5] and solid/polymer interfaces where the solid has polymer chains chemically attached [6-8]. In this note we focus on the interface formed between a cross-linked elastomer matrix and chemically identical N-mer chains[1] that are end-tethered onto a solid surface.

Model

We consider here, for simplicity, the low coverage regime, $\sigma<1/b^2N$. On initial formation of the interface, we assume the grafted chains reside in an unentangled layer of network material of width $d=a/2$, where a is the characteristic distance between network topological constraints. Unless the cross-link density is very high, the value of a is approximately that for the entangled elastomer melt. We approach the problem by considering a grafted chain which has partially entered the network at a distance R from the anchor site, via the motion of its free end. The section of the chain which penetrates the network is confined to a tube of diameter a, and consists of N_t monomers, while the remainder is now topologically confined to a slab of thickness d, and consists of $N-N_t$ monomers (Figure 1). The curvilinear distance from the tube entrance to the chain free end (the N_tth tube monomer) defines the tube length, L.

*Department of Physics, University of Sheffield, UK
+ Polymer IRC, University of Leeds, UK

We can calculate the entropic part of the confined chain's free energy using the Green function method [9].. A surface energy term is included to allow for dissimilar solid/polymer chemistry. An expression for the free energy, F, is given in equation (1), to a good approximation, by neglecting logarithmic terms and is strictly valid when $b(N\text{-}N_t)^{1/2} \gg d$ and $b(N_t)^{1/2} \gg a$ (the confining dimensions are a lot smaller than the Gaussian dimensions of the relevant chain sections):

$$\frac{F}{k_B T} \approx \frac{\pi^2 b^2}{6}\left[\frac{(N-N_t)}{d^2}+\frac{2N_t}{a^2}\right]-\frac{\alpha L}{a}+\frac{3}{2b^2}\left[\frac{R^2}{(N-N)_t}+\frac{L^2}{N_t}\right]+\phi_{eff}\chi \qquad (1)$$

The dimensionless constant α (of order unity) is network-model dependant, ϕ_{eff} is the effective grafted chain surface density and χ is a Flory parameter describing direct interactions with the surface.

By independently minimising the free energy with respect to the dynamical variables, N_t and L, for a fixed value of R, we find the free energy has the potential minima,

$$N_t^{min.} = N - \frac{3}{\pi b^2}\frac{R}{\gamma}; \qquad L^{min.} = \frac{\alpha b^2 N_t^{min.}}{3a}, \quad where \quad \gamma = \sqrt{\frac{1}{d^2}-\frac{(2-\alpha^2/\pi^2)}{a^2}+\frac{6\phi_{eff}\chi}{\pi^2 b^2}} \qquad (2)$$

The existence of a minimum confirms our guess that under certain conditions a grafted chain may enter the network, at a distance from its grafting point to find a metastable equilibrium. The equilibrium must be metastable because over long time scales the classical "mushroom" configuration [10] of untangled end-grafted chains must be achieved with R=0. The metastable states with R temporarily fixed we call "runners" in analogy with plants having trailing surface roots. The trailing sections of chain are stretched in the sense that $R \sim (N - N_t)$.

Dynamics

We will now consider the dynamics of the healing process. In general there are three stages to the approach to the equilibrium mushroom configuration:

i) Rapid Network Penetration. The relaxation of a Gaussian chain, from a perturbed state to its equilibrium state, is well described by the Rouse model [9]. In this model the equation of motion for a Rouse chain is solved in terms of eigenmodes. The mode amplitudes are such that the motion of chain segments of ΔN has a Rouse relaxation time, $\tau_{\Delta N} \approx \tau_1 \Delta N^2$, where τ_1 is the characteristic relaxation time of a Kuhn segment.

The first dynamical occurrence on making the interface is the diffusion of the grafted chain (initially completely flattened) into the unentangled surface layer of the cross-linked network. This has a characteristic time $\tau_d \approx \tau_1(d/b)$. Once embedded in this layer the chain free end will do one of two things. If there is a tunnelling solution at the chain end-to-end distance R, the chain end will bury itself in to the network to the extent dictated by the minima equations (2), in a time $\tau N_t \approx \tau_1 N t^2$. Otherwise, the chain free end diffuses in the slab only, until it reaches R<R*. As this process involves the whole chain its characteristic time scale is $\tau N_t \sim \tau_1 N^2$.

(ii) "Breathing" Mode Relaxation. Once buried in the network, the chain may renew its conformation by back-tracking down its current tube and tunnelling out into a new tube. This process is completed when the chain free end has founts its way back to the tube entrance and is similar to the "breathing" mode relaxation of star polymers (Figure 2). To calculate the characteristic occupation time of a particular tube, τ_T, we use the

simple theory of the activated process, following the simple treatment of entangled star polymers [11]. The result is

$$\tau_T = \tau_{N_t} \exp\left[\frac{\alpha^2 b^2 N}{6a^2} - \pi(\gamma - \gamma_0)R\right], \qquad \gamma_0 = \sqrt{\frac{1}{d^2} - \frac{2}{a^2} + \frac{6\phi_{eff}\chi}{\pi^2 b^2}}, \tag{3}$$

where γ_0 is found by minimising F when L=0. The first term in the exponent gives the longest tube occupation time (when R=0), this is when the grafted chain becomes essentially a star arm in a fixed network [9,11]. It is known that these time scales can be very long (days). The value of τ_T is less than for a star arm with $N = N_t^{min}$ due to the absence of a fixed monomer constraint at the entrance of the tube.

(iii) R Co-ordinate Hopping. On time scales greater than τ_T, the appropriate free energy on this time scale is the R paramaterised potential of equation (1), given by the substitution of the minimum values of N_t and L;

$$F(R) = \frac{\pi^2 b^2 N}{3a^2} + \pi\gamma R \tag{4}$$

As γ cannot be negative the chain end's equilibrium position is always in the tube above its graft point. In the case where γ is positive the chain end moves there by hopping in and out of tube entrances, for $R<R^*$.

The time taken for the chain end to tube-hop from its initial starting position, R_0, to the graft point is calculated by integrating over the intervening tube occupation times,

$$\tau_R \approx \tau_{N_t} \exp\left(\frac{\alpha^2 b^2 N}{6a^2}\right)\left[1 - \exp\left(-\pi(\gamma - \gamma_0)R_0\right)\right] \tag{5}$$

Interface Toughness.

We will now consider how the R-distribution relaxes during the healing process and see what bearing this might have on the interface toughness. The interface toughness, G, can be estimated by models which consider the energy dissipation of a chain being pulled out of a polymer matrix [7,12]. As both the chains friction constant and pull-out path distance (tube length) are proportional to N_t we generally have the relationship $G \sim N_t^2$. By substituting the average R values into the expression for N_t^{min} we can estimate the increases in G over the healing process, $t > \tau N_\tau$,

$$\frac{G_{\tau_R}}{G_{\tau_0}} \approx \left[\frac{1 - 3\left(\pi^2 b^2 \gamma^2 N\right)^{-1}}{1 - 3\left(\pi b \gamma N^{1/2}\right)^{-1}}\right]^2 \tag{6}$$

For a chemically neutral interface, with the typical parameter values $N=10^3$, a=10b, d=0.6a the toughness ratio is, $G_{\tau R}/G_{\tau 0} \sim 2$.

Experimental Comparison.

Our work here is strictly applicable to surface coverages somewhat less than those considered by Reichert & Brown. However, the estimates in this short work bear favourable comparison, at least

qualitatively, with their experimental results. On initial formation of the PS/PI interface they experienced a rapid partial recovery of the equilibrium toughness. This corresponds to the short time scale Rouse dynamics in our work. The remaining toughness deficit was recovered over an exponentially long time (days) as would be expected from the "star-like" relaxation of the R-distribution in our work.

The case of high surface coverages corresponds to the "brush" regime, and may be treated in a self-consistent-field approximation. Similar regimes of dynamics exist, which will be treated in detail elsewhere. In the meantime await experiments properly appilcable to this work.

ACKNOWLEDGEMENTS

K. P. O'Connor wishes to thank ICI and the S.E.R.C. for financial support, and the D46 Committee for some useful comments.

REFERENCES

1. Wool, R.P., O'Connor, K.M., 1981, J.Appl.Phys., 52(10), 5953
2. Adolf, D., Tirrell, M., 1985, J. Polym. Sci: Polym. Phys. 23, 413
3. Reichert, W.F., Brown, H.R., Preprint (IBM Almaden Research Centre).
4. Semenov, A.N., 1985, Sov. Phys. JETP, 61, 733
5. Shull, K., Winey, K.I., Thomas, E.L. and Kramer, E.J., 1991, Macromolecules, 24, 2748.
6. de Gennes, P.G., 1989, J. Phys. Fr., 2551
7. O'Connor, K.P., McLeish, T.C.B., 1992, Macromolecules, 33, 4314
8. Milner, S.T., Witten, T.A., Cates, M.E.,1988, Macromolecules, 21, 2610
9. Doi, M., and Edwards, S.F., 1986, "The Theory of Polymer Dynamics", Clarendon Press, Oxford
10. Field, J.B., Toprakcioglu, C., Dai, L., Hadziioannou, G., Smith, G., Hamilton, W., 1992, J. Phys. II France, 2, 2221
11. Pearson, D.S., Helfand, E., 1984, Macromolecules, 17, 888
12. Evans, K.W., 1987, J. Polym. Sci: Polym. Phys. 25, 353

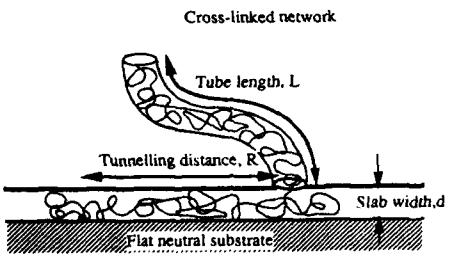

Figure 1

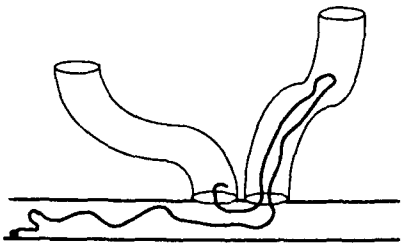

Figure 2

RANDOM COPOLYMERS VS. BLOCK COPOLYMERS TO REINFORCE POLYMER INTERFACES

Chi-An Dai*, Kevin H. Dai*, Christopher K. Ober*, Chung-Yuen Hui†, Edward J. Kramer*

The fracture toughness G_c of the interface between polystyrene (PS) and poly (2-vinylpyridine) (PVP) sharply increases as the areal chain density, Σ, of random copolymer is increased. Our evidence shows that the random copolymer weaves back and forth across the interface and that the loops so formed are long enough to entangle with the homopolymers. Just as for long diblock copolymers, there is a transition from pure chain scission for $\Sigma<\Sigma^*$ to craze fracture for $\Sigma>\Sigma^*$ for the interface reinforced by the random copolymer. However, Σ^* is decreased drastically from its value for the diblock copolymer, showing that about 8 such entangled loops are formed per random copolymer chain.

INTRODUCTION

It is well known that block copolymers can be used as polymeric surfactants to decrease the interfacial tension between two homopolymer phases and to promote adhesion at the interface between them. However, block copolymers are costly to make and may form micelles in the bulk polymer, rather than segregating to the interfaces. While extensive segregation[1] and mechanical testing experiments[2,3] have been done on block copolymer systems, only one paper has examined the effect of random copolymers[4]. In this study, we show that random copolymers are an attractive alternative to block copolymers for reinforcing polymer interfaces.

EXPERIMENTAL SECTION

1. Characterization of random and diblock copolymers:

Free radical polymerization was used to synthesize the random copolymer $(dPS_{0.48}\text{-}r\text{-}PVP_{0.52})_{N=7000}$ where N is the polymerization index of the random copolymer chain. The molecular weight of the random copolymer was measured using gel permeation chromatography and is listed in Table I. Forward recoil spectrometry (FRES), an ion beam technique which is sensitive to hydrogen and deuterium, was used to determine the composition ratio of deuterated styrene and hydrogenated 2-vinylpyridine in the copolymer chain. The diblock copolymer dPS-*b*-PVP was synthesized using anionic polymerization[1]. The polymerization indices of the dPS and the PVP blocks were respectively 800 and 870. Both random and diblock copolymers contain nearly 50% dPS.

2. Sample preparation and fracture toughness measurement:

Plates of PS and PVP were made by compression molding at 160°C. A thin film of the random or diblock copolymer was spun cast from a toluene solution

* Department of Materials Science and Engineering
† Department of Theoretical and Applied Mechanics
Cornell University, Ithaca, New York, 14853, USA

onto the PVP plate. The PS plate was then welded to the copolymer coated PVP plate by annealing at 160°C for 2 hours. The resulting sandwich was cut into several strips for fracture measurements. The interfacial fracture toughness, G_c was measured using the asymmetric double cantilever beam method. A razor blade was inserted into the PS/PVP bimaterial plate and initiated a crack ahead of the razor blade. A steady state crack propagation was achieved by driving the razor blade at constant speed. G_c could then be extracted from the sample geometry and the crack length[5,6].

3. Areal chain density measurement:

Since random and diblock copolymers were labeled with deuterium on the styrene component, FRES could be used to measure the areal chain density of copolymer at the interface. By analyzing the ratios of deuterium on each side of the fracture surface to the total deuterium (Σ_{PS}/Σ and Σ_{PVP}/Σ), we also gain important information about the fracture mechanism.

RESULTS AND DISCUSSION

We compare the fracture toughness, G_c of the PS/PVP interface as a function of the areal chain density Σ for the random copolymer to that for the block copolymer in Figure 1. At small values of Σ, G_c increases hardly at all with increasing Σ for both random copolymer and block copolymer additions. Above $\Sigma = 0.004$ chains/nm^2, the G_c of the interface reinforced by the random copolymer increases rapidly, eventually attaining a value close to 150 J/m^2. The G_c of the interface reinforced by the block copolymer also shows an increase but only above a $\Sigma = 0.03$ chains/nm^2 and this increase occurs over a wider Σ regime than for the random copolymer. The value of G_c attained by adding the optimum amount of copolymer is also less for the block copolymer than for the random copolymer.

To understand these surprising results we investigated the fracture mechanism for both the diblock and random copolymer reinforced interfaces by measuring the amount of dPS on each side of the fracture surface. In Figure 2a, the fraction of the dPS block of the diblock copolymers found on PS side is plotted as a function of total areal chain density. Almost all the deuterium is found on PS side up to $\Sigma^* = 0.03$ chains/nm^2 at which point a transition occurs and beyond which almost all the deuterium is found on PVP side. For $\Sigma < 0.03$ chains/nm^2, fracture occurs along the PS/PVP interface and the diblock copolymers were broken near the joint of each block. For $\Sigma > 0.03$ chains/nm^2, crazing occurred on the PS side followed by failure of the craze fibrils where the dPS block and homopolymer PS meet. The change in the locus of fracture indicates that above Σ^* the stress to break the diblock copolymer chains at the PS/PVP interface is higher than the crazing stress of PS resulting in crazing of the PS and subsequent craze failure. A similar transition from chain scission to crazing is also observed for the interface reinforced with the random copolymer. However, Σ^* is decreased from 0.03 to around 0.004 chains/nm^2 and about equal amounts of deuterium are found on both surfaces below Σ^* as the interface is fractured by chain scission.

Rather than forming a polymer "brush" at the interface like the diblock copolymer, we believe the random copolymer weaves back and forth across the PS/PVP interface forming loops in both phases. Such a morphology is suggested both by our result that half of the dPS is found on each side of the fracture for $\Sigma < \Sigma^*$ and by a recent theory of the segregation of random copolymer to a liquid/liquid interface[7]. At the transition, the stress to break the random copolymer "stitches" crossing the PS/PVP interface is equal to the crazing stress of PS. For the random copolymer the number of chains broken at the interface is just equal to $n_{loop}\Sigma^*$

where n_{loop} is the number of loops per chain that are effectively entangled across the interface. At the transition therefore,

$$n_{loop}\,\Sigma^{*}\,f_b = \sigma_{craze}$$

where f_b denotes the force required to break a single C-C bond (~2×10^{-9} N) [3] and σ_{craze} is the crazing stress of PS (~55 MPa) [3]. The number of effectively entangled loops per random copolymer chain is thus estimated to be ~ 8.

We have shown that long random copolymers can be remarkably effective in reinforcing immiscible polymer interfaces. This effectiveness apparently comes about because the random copolymer loops back and forth across the interface. Loops so formed are long enough to entangle with the homopolymers, allowing stresses larger than the crazing stress to be transferred across the interface. At first glance these results appear to run counter to our intuition about how random copolymers should behave. After all PS and PVP are highly immiscible polymers, with a Flory parameter $\chi \sim 0.11$ at the annealing temperature[1]. One might expect that the random copolymer would form a condensed thin film at the interface, penetrating only a little into either homopolymer, leading to a very weak interface. But our intuition fails because we ignore the entropy of segregated random copolymer chains; forming such a confined film would require that the random copolymer chains be flattened into thin pancakes along the interface producing a large loss in entropy. As shown by Yeung et al.[7], the minimum free energy is achieved by a compromise structure in which the random copolymer is confined to the vicinity of the interface and forms relatively large loops into either phase. Our results can thus be viewed as a confirmation, albeit indirect, of the theory of Yeung et al.[7] .

ACKNOWLEDGMENTS

We acknowledge the support of the Cornell Materials Science Center which is funded by NSF-DMR-MRL and fellowship support from the Dow Chemical Co. through the Polymer Outreach Program at Cornell.

REFERENCES

1. Shull, K. R.; Kramer, E. J.; Hadziioannou, G.; Tang, W., *Macromolecules* **23**, (1990) 4780.
2. Brown, H. R., *Macromolecules* **22**, (1989) 2859.
3. Creton, C.; Kramer, E. J.; Hui, C.-Y.; Brown, H. R., *Macromolecules* **25**, (1992) 3075.
4. Brown, H. R.; Char, K.; Deline, V. R.; Green, P. F., *Macromolecules* **26**, (1993) 4155.
5. Kanninen, K. F., *Int. J. of Fracture* **9**, (1973) 83.
6. Creton, C.; Kramer, E. J.; Hadziioannou, G., *Macromolecules* **24**, (1991) 1846.
7. Yeung, C.; Balazs, A. C; Jasnow, D., *Macromolecules* **25**, (1992) 1357.

TABLE I: Molecular weight of random and diblock copolymers

	dPS-*r*-PVP	dPS-*b*-PVP
Polymerization indices	3360-*r*-3640	800-*b*-870
Polydispersity index	~2.5	<1.1

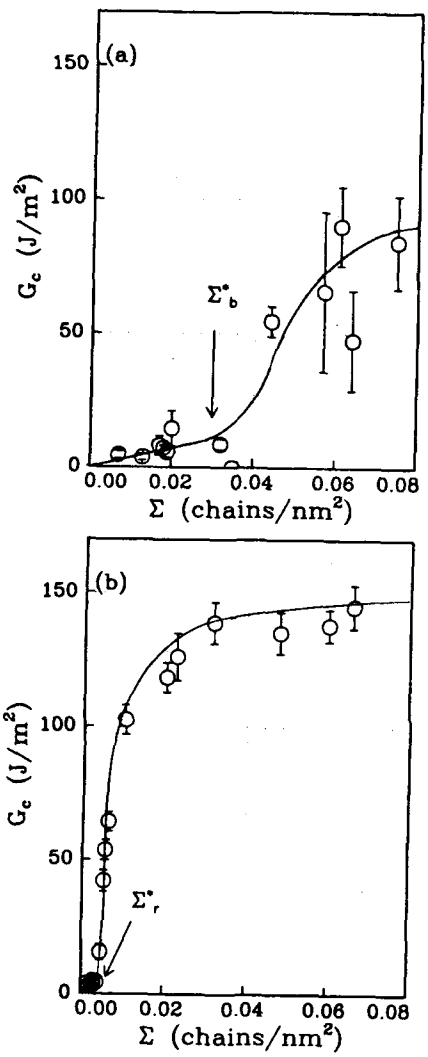

Figure 1. The fracture toughness G_c for block (a) and random copolymers (b) as a function of the areal chain density Σ of copolymers at the interface. Σ^*_r and Σ^*_b are the values of Σ at which a transition from chain scission to crazing followed by craze failure occur.

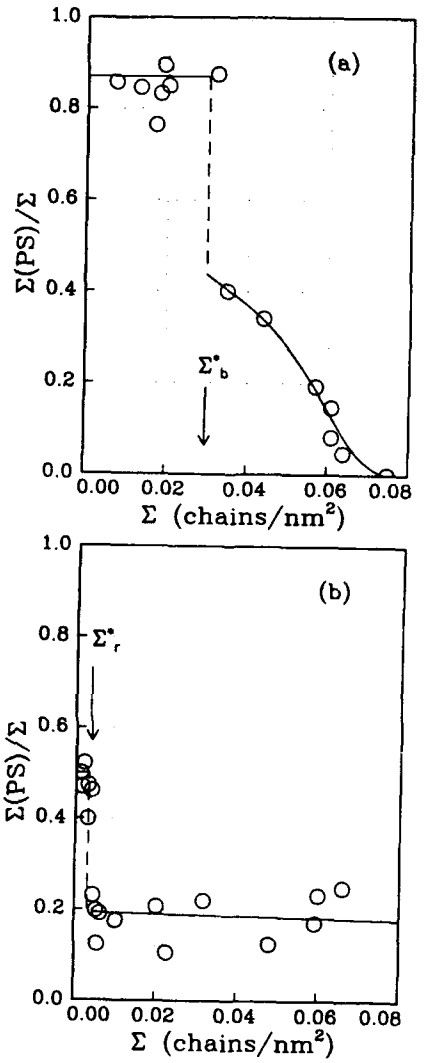

Figure 2. The fraction of the dPS component of the copolymer found on the PS side of the interface as a function of the areal chain density, Σ. (a) block copolymer, (b) random coplymer.

FRACTURE BEHAVIOUR OF POLYMER INTERFACES BY AN ASYMMETRIC DUAL CANTILEVER TEST AND DEFORMATION IN AN ENVIRONMENTAL SCANNING ELECTRON MICROSCOPE (ESEM)

C.D. Breach, A.M. Donald and R.A.L. Jones*

An asymmetric dual cantilever beam test is used to determine the strength of the adhesive bond formed between dissimilar polymer interfaces and homopolymer interfaces which are welded together above T_g. The same technique is used to study autoadhesion just below T_g. A tensile test rig mounted inside an ESEM (Environmental Scanning Electron Microscope) is used for studying propagation of cracks along interfaces.

INTRODUCTION

The asymmetric dual cantilever beam test is a means of obtaining critical strain energy release rates G_{1C} for bimaterial interfaces whilst taking into account the different elastic moduli and/or craze stresses of each polymer. Ordinary dual cantilever beam testing of dissimilar polymer interfaces overestimates the G_{1C} because crazes at the crack tip deviate into the polymer of lower modulus before returning to the interface. This overestimates toughness. Increasing the thickness of the lower modulus polymer introduces a mode II component which tends to keep the crack at the interface and gives more realistic values of G_{1C} (1).

The purpose of this work was to examine variations with thermodynamic incompatibility of the toughness of dissimilar polymer interfaces and to examine the crack tip motion using an ESEM. Unlike a conventional SEM, an ESEM does not require samples to be coated with a conducting material and produces images capable of resolving relatively fine detail even as the samples crack or change dynamically during imaging.

EXPERIMENTAL

Materials

A series of random SMMA copolymers of varying composition were selected for adhesion studies with PMMA and PS because it is possible to maintain the T_g of the copolymer constant and the same as the homopolymer. Random copolymers of MMA/EA of varying compositions (80/20, 70/30, 60/40) were also studied for adhesion with PMMA only and in this case the T_g varies with composition. Once

*Cavendish Laboratory, University of Cambridge.

synthesised, the random copolymers were fractionated twice to remove as large an amount of low molecular weight material as possible. Monodisperse PMMA of molecular weight 685,000, polydisperse PMMA and polydisperse PS were also used in these studies. The adhesion of polydisperse SMMA and sheets of polydisperse PC to commercial sheet PMMA was also studied for comparison.

Moulding

The polymers used were moulded in a hot press. The conditions used were 160°C for PMMA, PS and SMMA. Interfaces were formed by bringing the faces of each half into contact and applying a light pressure to ensure good interfacial contact. Interfaces between PMMA/SMMA, PMMA/PS, MMA-EA/PMMA and PS/SMMA were formed at 125°C and the interface between PMMA/PC at 160°C. Autoadhesion studies on PMMA and PS were carried out at 125°C and for PC at 160°C. Sub-T_g autoadhesion studies on monodisperse PMMA and polydisperse PMMA and PS were carried out at 95°C.

Fracture Testing

The razor test described by Brown (1) was used to follow the path of the crack ahead of a razor blade inserted slowly (~1μm/s) into the interface (1). For autoadhesion studies a symmetric dual cantilever specimen was used. The crack length ahead of the razor blade edge was photographed from above at regular intervals as the razor blade was inserted.

RESULTS AND DISCUSSION

The kinetics of G_{1C} for autoadhesion of PMMA and PC is shown in figure (1), and conforms as expected to a $t^{0.5}$ form (2). For the dissimilar polymer interfaces, the correct geometry was determined by calculating G_{1C} for several different asymmetries and taking as correct, the geometry which resulted in a minimum G_{1C}. Variation of G_{1C} with geometry of the dissimilar polymer interfaces is shown in figure (2).

Similar tests were performed in an ESEM by using the same kinds of samples mounted in a tensile test rig and using tension to propagate the crack along the interface instead of a razor blade. Using this system cracks were propagated at various crosshead velocities ranging from 1μm/s to 100μm/s corresponding to crack velocities with a lower bound of approximately 0.9μm/s. The various combinations of dissimilar polymers were studied using this method and as an example, figure (3) shows a micrograph of a PC/PMMA interface prepared with the incorrect geometry (PC thickness>PMMA) where it can be seen that the crack tip deviates into the thinner PMMA side.

G_{1C} was also determined for samples of homopolymers 'cold' welded at sub-T_g temperatures. Table 1 shows some results for sub-T_g autoadhesion of PMMA at 95°C (T_g is 105°C). Clearly there is a significant effect.

Autoadhesion of PMMA may be due to a liquid like surface structure. It has been found by Keddie, Jones and Cory (3) that in thin films of polystyrene, T_g is less than the value for the bulk. At high temperatures close to T_g whilst the bulk remains glassy, the surface may be locally mobile. If two like surfaces are brought into contact near to the T_g adhesion may take place because the surface chains entangle. This is a possible explanation for the results of table 1. The fact that sub-T_g autoadhesion also occurs in monodisperse PMMA suggests that the interfacial strength is not simply derived from low molecular weight chains which diffuse to the interface in the polydisperse PMMA. The low molecular weight chains may however be the cause of the decrease in G_{IC} of the polydisperse PMMA with time.

TABLE 1: G_{IC} of PMMA junctions cold welded at 95°C

Polymer	Molecular Weight	Time (weeks)	G_{IC} (J/m²)
Polydisperse PMMA	200,000	3	13±3.5
Polydisperse PMMA	200,000	5	10±-1
Monodisperse PMMA	685,000	3	8±1.5

REFERENCES

(1) Brown, H.R., J. Materials Science, 25 2791 (1990)
(2) Brochard-Wyart, F., 'Fundamen ' s of Adhesion', Ed. Lieng Huang Lee Plenum Press (1991)
(3) Keddie, J.L., Jones, R.A.L. and Cory, R.A. To be published.

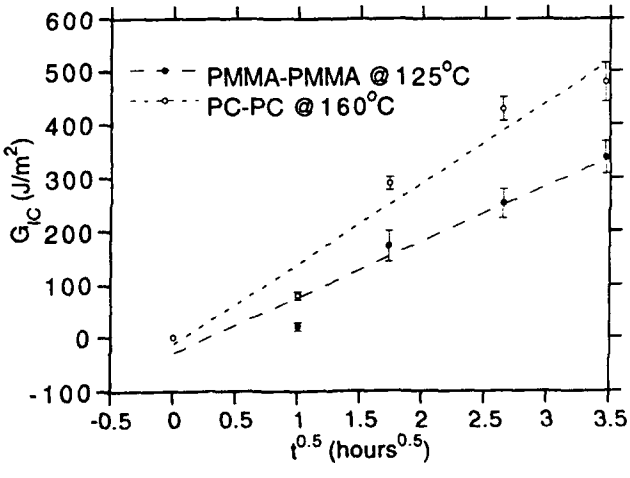

FIGURE 1: Kinetics of Autoadhesion

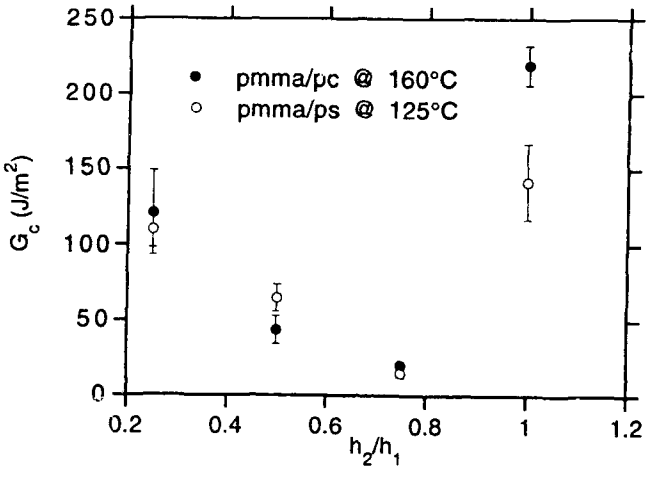

FIGURE 2: G_{1C} vs thickness ratio h_2 (PMMA)/h_1

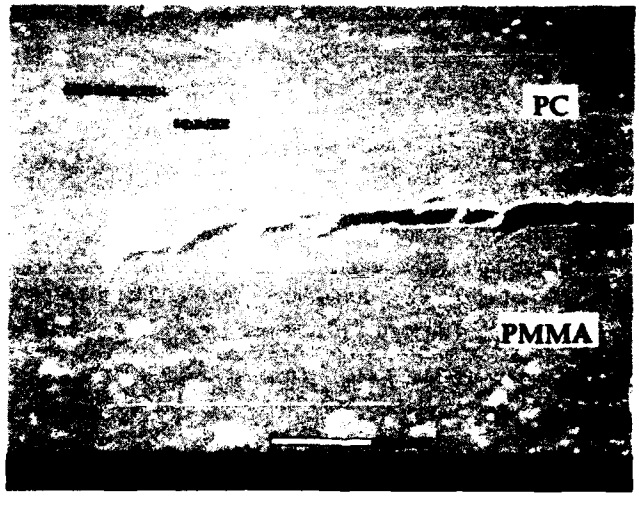

FIGURE 3: ESEM micrograph of crack in PC (1.0mm)/PMMA (0.75mm) interface

THE ANALYSIS OF ELASTIC-PLASTIC BENDING EFFECTS IN THE PEEL TEST

A.J. Kinloch, C.C. Lau and J.G. Williams*

The peel testing of flexible laminates is described and the results have been analysed using an energy-balance approach. From considering the external work done, the stored energy and energy dissipated in the peeling arm and the energy dissipated during bending of the peeling arm near the peel front the values of the adhesive fracture energy, G_a, may be ascertained. It is shown that elastic-plastic loading and unloading during the bending of the peeling arm must be taken into account and, in addition, the fact that the peel arm does not act as a built-in beam must be considered.

INTRODUCTION

The peel test is widely used for evaluating adhesives and laminated structures used in packaging. It has the great advantage of simplicity of execution and, at first sight, of analysis. In many cases the peeled strip can be regarded as inextensible, but infinitely flexible strip, which is peeled by a force P at an angle θ, as shown in fig. 1. The energy release rate, G, for the peeling process may be carried out in the usual way using,

$$G = \frac{1}{b}\left(\frac{dU_{ext}}{da} - \frac{dU_s}{da} - \frac{dU_k}{da} - \frac{dU_d}{da}\right)$$

where b is the strip width, a the length and,
U_{ext} is the external work
U_s is the strain energy
U_k is the kinetic energy
and U_d is the dissipated energy.

For steady-state slow peeling considered here $U_k = 0$ and for the inextensible but flexible strip $U_s = U_d = 0$. The load P moves $a(1 - \cos\theta)$ for a peeled length a (see fig. 1) so we have,

$$G = \frac{dU_{ext}}{bda} = \frac{P}{b}(1-\cos\theta) \qquad \ldots\ldots\ldots\ldots\ldots\ldots\ldots\ldots\ldots\ldots (1)$$

the simple result. For an extensible, but flexible strip, refinements to allow for elastic stretching can be included via U_s and also for dissipation via U_d but the changes are usually minor [1].

* Imperial College of Science, Technology & Medicine, London, UK.

When the analysis is applied in practice it often works well but sometimes a pronounced dependence of G on θ and on the thickness h is reported [2]. It has long been recognised [2] that these effects arise from local bending at the point of peeling (0 in fig. 1) which is shown in fig. 2. At the contact point the strip has a root angle θ_0 and a radius of curvature R_0. If $\theta_0 = \theta$ then the strip is behaving in a completely flexible manner and there is no bending and hence no dissipation. If $\theta_0 = 0$ all the energy goes via bending and if the strip is elastic the local moment M_0 may be found by equating G values,

$$G = \frac{P}{b}(1-\cos\theta) = \frac{6M_0^2}{b^2h^3E} \qquad \ldots\ldots (2)$$

where E is the Young's Modulus and we may find R_0 via,

$$\frac{1}{R_0} = \frac{12M_0}{Ebh^3} \qquad \ldots\ldots (3)$$

A recent analysis [1] has noted that in fact $0<\theta_0<\theta$ and θ_0 can be approximated by considering the deformation of a length 2/3h beyond the contact point as shown in fig. 2. Thus

$$\theta_0 = \frac{2h}{3R_0} \qquad \ldots\ldots (4)$$

and only part of G is now transmitted by bending and is given by [1]

$$G_B = \frac{P}{b}[1-\cos(\theta-\theta_0)] \qquad \ldots\ldots (5)$$

and the remainder goes by direct external work. For elastic deformation $U_d = 0$ so this does not solve the problem and we must consider the elastic-plastic bending of the root region so that U_d may be computed.

Elastic-Plastic Bending Analysis

The most useful model is that of elastic behaviour for $\varepsilon<\varepsilon_y$ of $\sigma = E\varepsilon$ and for $\varepsilon>\varepsilon_y$, $\sigma = E\varepsilon_y(1-\alpha) + E\varepsilon\alpha$, i.e. linear work hardening of αE. The deformation of the beam is controlled by the elastic core region and we may describe the deformation process via the diagram of the moment M versus 1/R, the radius of curvature as shown in fig. 3(a). The peeling strip is shown in fig. 3(b) and the initial elastic and the elastic-plastic bending OAB occurs immediately on loading and the strip unloads elastically until at C there is zero moment. The strip is then further straightened by reverse bending in CDE until it is straight under load at E. On removing the load the strip recovers to F giving a residual curl which is characteristic of plastically deformed peeling strips. The energy absorbed plastically, U_d, is given by the area OABCDE

and after much tedius algebra, we arrive at the result [3,4],

$$\frac{G}{\hat{G}}.\frac{1-\cos(\theta-\theta_0)}{1-\cos\theta} = f_2(k_0)$$

..... (6)

and $\frac{G_d}{\hat{G}}.= f_1(k_0)$

..... (7)

where $\hat{G} = \frac{Ehe_y^{\ 2}}{2}$

..... (8)

$$f_1(k_o) = \frac{4}{3}\alpha(1-\alpha)^2k_0^2 + 2(1-\alpha)^2(1-2\alpha)k_0 + \frac{2(1-\alpha)}{3(1-2\alpha)k_0}[1+4(1-\alpha)^3]$$

$$-(1-\alpha)[1+4(1-\alpha)^2]$$

and

$$f_2(k_0) = \frac{\alpha}{3}[1+4(1-\alpha)^2]k_0^2 + 2(1-\alpha)^2(1-2\alpha)k_0 + \frac{8}{3}\frac{(1-\alpha)^4}{(1-2\alpha)k_0}$$

$(\alpha < 1/2)$ $\qquad -4(1-\alpha)^3$

and $k_0 = \frac{h}{2\varepsilon_y R_0}$

The root rotation is the same expression as in the elastic case, equation 4, and may be rewritten as,

$$\theta_0 = \frac{4}{3}\varepsilon_y k_0$$

..... (9)

G_d is the energy absorbtion rate so the true adhesive value is $G_a = G - G_d$. In any test P is determined for a given θ, b and h so that G may be found. From a supplementary tensile test E, ε_y and α are found and hence $\hat{G}$ can be determined. For each value of G a value of θ_0 is determined from equations (6) and (9) by iteration via k_0 and hence G_d is found from equation (6) and hence G_a. Thus θ_0 is computed in each test and provides a useful cross check on the validity of the scheme if it is measured during the experiment.

Experiments

A series of experiments were conducted [4, 5] on PE-Aluminium foil and PET-PE laminates in which θ was varied and by performing the tests on a small peeling rig in an optical microscope θ_0 could also be measured. Tables 1 and 2 give typical sets of results. In table 1 the PE was peeled from the foil and G increased markedly with θ as expected. θ_0 could only be measured to an accuracy of about ± 5% and the range is given. The computed θ_o values are slightly low but follow the

same trend and G_a is sensibly constant. In table 2 the data is for peeling 12 μm PET from PE. The PET is a much stiffer material and θ_o is smaller but a similar degree of agreement is achieved and G_a is again reasonably constant. In table 3 PE of various thicknesses was used in a 180^0 test. There is the commonly observed maximum in G, here at about 100 μm, and again there is good agreement in θ_o and G_a is constant.

Conclusion

The two well-known observations, i.e. that G varies with θ and h, have been explained in terms of elastic-plastic energy dissipation and constant adhesive energies computed. The essential factor is the root rotation θ_o and the observations confirm the model used.

REFERENCES

1. Williams, J.G. J. Adhesion, 41, 225 - 239, 1993.
2. Gent, A.N. and Hamed, G.R. J. App. Pol. Sci., 21, 2817, 1977.
3. Aravas, N., Kim, K.-S. and Loukis, M. J. Mater. Sci. Eng., A107, 159-168, 1989.
4. Lau, C.C., Kinloch, A.J. and Williams, J.G. Accpt. for pub. in Int. J. Fracture, 1994.
5. Lau, C.C. PhD thesis, Univ. London, 1993.

TABLE 1 PE-Al laminate, h = 35μm,
ε_y = 0.078, E = 140 MPa, α = 0.1, $\hat{G}$ = 14.9 J/m²

			calculations	
θ^0	G J/m²	θ_o(exp)(°)	θ_0(°)	G_a J/m²
45	183	24 - 30	20.4	236
90	333	40 - 47	34.5	228
120	375	48 - 58	41.7	218
135	412	50 - 60	46.1	223
150	467	55 - 62	51.7	236

TABLE 2 PET-PE Laminate, h = 12 μm
ε_y = 0.024, E = 3.8 GPa, α = 0.03, $\hat{G}$ = 11.0 J/m²

			calculations	
θ^0	G J/m²	θ_o(exp)(°)	θ_0(°)	G_a J/m²
30	100	5 - 8	7.6	61.6
60	108	7 - 12	9.4	42.0
90	125	9 - 13	11.1	37.8
120	184	13 - 19	14.8	46.5
150	232	15 - 20	19.6	45.7

TABLE 3 PE-Al laminate, $\theta = 180^0$
ε_y = 0.094, E = 70 MPa, α = 0.055, $\hat{G}$ = 0.31 J/m² per micron

			calculations	
h(μ m)	G J/m²	θ_o(exp)(°)	θ_0(°)	G_a J/m²
30	195	54 - 66	59.5	69.8
45	205	41 - 49	50.0	62.3
60	240	38 - 46	46.0	69.3
75	260	38 - 45	43.4	71.5
105	260	24 - 32	36.1	67.3
135	225	22 - 28	29.1	59.5
165	240	22 - 28	27.1	65.4
215	220	17 - 21	21.9	68.2

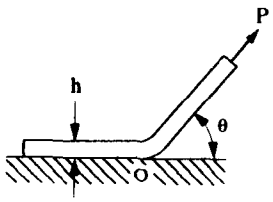

Fig.1 The Peel Test

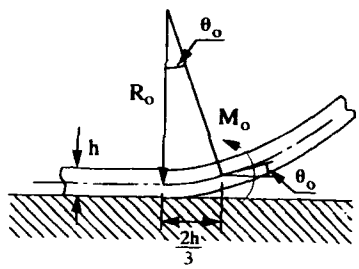

Fig.2 Root Rotation

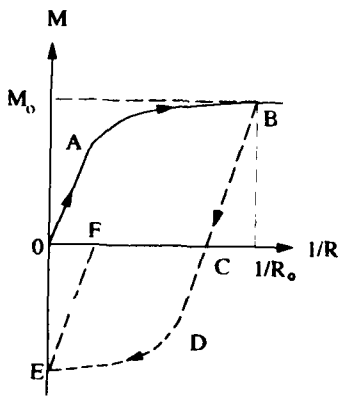

(a)

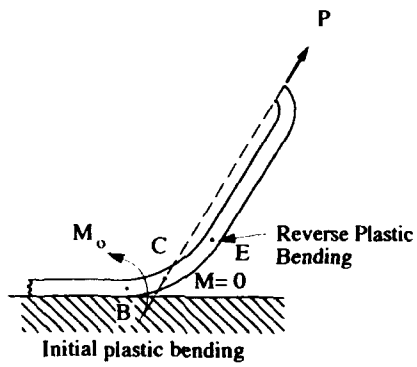

(b)

Fig.3 Elastic - Plastic Bending

THE RATE MECHANISM OF PLASTIC FLOW BY CHAIN SLIP IN HIGHLY TEXTURED QUASI-SINGLE CRYSTALLINE HDPE AND NYLON 6

A.S. Argon*,[1] L. Lin* and G.J. Vancso**[2]

Highly oriented samples of HDPE and Nylon 6 with quasi-single crystalline texture have been used in simple shear experiments to study the kinetics of plastic flow by chain slip. The activation parameters determined from strain rate change experiments have been interpreted in the context of thermally activated motion of screw dislocations in these quasi-single crystalline materials with long range coherence. The latter has been established through recent WAXS, SAXS and atomic force microscopy studies having molecular level resolution.

INTRODUCTION

While the mechanisms of plastic deformation in glassy polymers have been explored both experimentally and theoretically with considerable intensity by many investigators over the past several decades, comparatively little attention has been given to clarify the mechanisms of plasticity in the crystalline component of semi-crystalline polymers. Clearly, the principal reason for this neglect is the complexity of the structure in its usual spherulitic form and the exceedingly small dimensions of lamellar crystalites. Young and Bowden (1) noted that high density polyethylene (HDPE) deformed in plane strain to very large strains in a channel die acquires a quasi-single crystalline (QSC) texture of high perfection, and that such material can be used for definitive deformation experiments to probe crystallographic slip resistances. Such large strain plane strain compression experiments producing highly textured material have recently been carried out again by Argon and co-workers on both HDPE (2) and Nylon 6 (3). The resulting material was then used to measure the plastic resistances of the most prominent chain slip mechanisms in both HDPE (4) and Nylon 6 (5) at room temperature. Additional new studies of Bartzcak, et al. (6) based on deconvolution of X-ray scattering from the amorphous component in HDPE strained in plane strain to $\epsilon_e = 1.86$, and atomic force microscopy (AFM) results carried out by Schönherr, et al. (7) on the same material, demonstrated that the amorphous component is nearly as highly oriented as the crystalline material in the flow direction, and is much more diffusely distributed than previously realized, with a remarkable level of long range coherence in the chain direction.

Here we discuss the use of such QSC HDPE and Nylon 6 in simple shear experiments, probing the kinetics of chain slip. Because of space restrictions, and because of its much stronger anisotropy of chain slip, we present only the results on Nylon 6.

[1]*Department of Mechanical Engineering, Massachusetts Institute of Technology, Cambridge, MA, USA
[2]**Department of Chemistry, University of Toronto, Toronto, Ontario, Canada

EXPERIMENTAL DETAILS

Structure of QSC HDPE and Nylon 6

The preparation of the QSC material by channel die compression, probing their structure by WAXS, SAXS, AFM and determination of their anisotropic plastic shear resistances with micro-shear experiments have been discussed in great detail elsewhere (2-7). Of these results we present only Fig. 1, showing a montage of AFM nanographs of molecular resolution obtained from the (100) surface of a HDPE sample, strained to $\epsilon_e = 1.86$, in plane strain compression, covering a total length of 40 nm. The quasi-straight traces are individual molecules. The absence of an identifiable, well separated amorphous component is striking. In Nylon 6, nanographs with equally harp definition could not be obtained for reasons that are most likely of operational nature, but could also be due to the partitioning of the morphology into two symmetrically arranged domains, as discussed below.

Figure 2 shows the geometry of the QSC Nylon 6 and its orientation relative to the flow (FD), loading (LD) and constraint (CD) directions of plane strain compression. As it is depicted in the upper right hand corner of the figure, the plane strain compression results in an equally partitioned density of two sets of monoclinic domains, resulting not in a macroscopic monoclinic quasi-crystal, but in a material with orthotropic symmetry, with the chain axes of both sets being parallel to the FD. The coherence lengths of the two separate domains remain undetermined.

While the properties of the best chain slip system (001)[010], containing hydrogen bonds in the plane, are easily probed in micro-shear experiments, those of the second best chain slip system, (100)[010], with their planes making angles of 69° with the LD are not. A compromise, then, is to probe the principal orthotropic system (100)[010] which bisects the planes of the two monoclinic domains. Thus, in what follows the latter symbolism will refer to this orthotropic system. The critical resolved shear stresses τ_o and shear moduli s_{66}^{-1} of the (001)[010] system measured by Lin and Argon (5,8) in micro-shear experiments at 294 K, on slabs strained to $\epsilon_e = 1.39$ are given in Table I. Results on the (100)[010] system are presented elsewhere (8).

TABLE 1 - Results of Simple Shear Experiments on the (001)[010] System of a QSC Nylon

T (°K)	$\dot{\gamma}_1$ (10^{-3}sec^{-1})	$\dot{\gamma}_2/\dot{\gamma}_1$	s_{66}^{-1} (MPa)	τ_0 (MPa)	τ_f (MPa)	$\Delta\tau_f$ (MPa)	v^* (Å^3)	a^* (Å^2)
295	2.36	1	576	16.7	33.1	-	-	-
295	23.6	1	586	20.1	34.9	-	-	-
295	2.36	2	588	16.8	32.8	0.54	5207	2117
295	2.36	5	580	16.3	32.4	1.17	5580	2268
255	2.36	10	594	28.5	42.5	3.45	2386	970
274	2.36	10	580	24.1	34.4	2.70	3225	1311
295	2.36	10	584	17.0	32.3	1.86	5023	2042
306	2.36	10	502	15.1	28.5	1.58	6154	2502
311	2.36	10	147	13.1	27.6	1.47	6723	2733
327	2.36	10	100	8.2	22.7	1.40	7422	3017
344	2.36	10	54	8.2	14.6	1.40	7808	3174
366	2.36	10	40	7.9	11.5	1.54	7552	3070

Simple shear experiments. Stress strain experiments in simple shear, probing the principal chain slip system (001)[010] in a QSC Nylon at 8 temperatures ranging from 255 K to 366 K at the base shear strain rate of 2.36×10^{-3}sec^{-1} are shown in Fig. 3. The curves also show the stress jumps that result from a sudden 10 fold increase in the shear strain rate, including typical yield overshoots and effects of returning to the base strain rate. Similar experiments were conducted also on the

orthotropic (100)[010] system, and on untextured material for reference. The details of these additional experiments can be found elsewhere (8). Curves of the type shown in Fig. 3 were used to determine the s_{66}^{-1} shear moduli, the CRSS, τ_0 to the flow stress τ_f, and the magnitudes of the stress jumps $\Delta\tau_f$ used to determine the activation parameters.

Figure 4 shows the temperature dependence of the s_{66}^{-1}, s_{55}^{-1}, shear moduli of the QSC material and the shear modulus of the untextured material. The very different levels of the moduli are a result of the characteristic orthotropic symmetry of the textured material. The figure shows clear evidence of a glass transition between 305-310 K, that is attributable to the amorphous component. Figure 5 shows the temperature dependence of τ_0 and τ_f for the two prominent chain slip systems, determined from Fig. 3, (and its counterpart for (100)[010]). The temperature dependence of the stress jumps (from base to the peak of the yield rise) are also given in Table I.

DISCUSSION AND CONCLUSIONS

The shear activation volume v_f^* which can be determined from the jumps in the flow stress $\Delta\tau_f$, using the well known relation:

$$v_f^* = KTd\ell n\dot{\gamma}/d\tau_f$$

gives important information on the size of the region involved in a strain producing single activation event. These have been calculated from the information in Fig. 3 for the (001)[010] system, and are listed in Table I, for the 8 different temperatures. Similar information on the (100)[010] system and the untextured material also exists (8), but is not presented here. A complementary activation volume v_o^*, obtained from the strain rate dependence of τ_o, obtained at 295 K has also been calculated from the information in Table I, and is 2888 $\mathring{A}^3$.

We note that while there is a clear glass transition in the shear moduli there is no corresponding transition in τ_o and τ_f, as can be seen in Fig. 4. This indicates that the resistances τ_o and τ_f are a property of the crystalline component alone, and that inelastic shear strain is derived only from the crystalline component.

We now interpret the observations as being related to the mobility of screw dislocations in the QSC, which should be controlling the kinetics of chain slip. We base this conclusion on the observation that substantial bending and straightening in individual molecules should be present in the cores of edge dislocations, making these cores rather extended and therefore subject to little resistance from the lattice to displacement. Proceeding further, we interpret τ_o to be the CRSS for short range motion of screw dislocations for which the activation area $a_o^* = v_o^*/b$ is quite large at 1174$\mathring{A}^2$ at 295 K (for a Burgers vector of 2.46$\mathring{A}$). Considering the activation configuration to be a double kink with a kink height of 23.95 $\mathring{A}$ (the intermolecular spacing on the 001 plane), we obtain a kink spacing of 49$\mathring{A}$ at 295 K. While this is quite large, it is not unreasonable.

We interpret τ_f to be the overall resistance to long range motion of screw dislocations, with the differential of $\tau_f - \tau_o$ arising from the internal misfit stresses due to distributed amorphous pockets, acting as a field of solute, in analogy with solid solution strengthening in metals. From the activation volume v_f^* we determine a set of activation areas a_f^* (listed in Table I) ranging from 970$\mathring{A}^2$ at 255 K to 3070$\mathring{A}^2$ at 366 K (exhibiting a definite stress dependence). Taking 2000$\mathring{A}^2$ as an average for this activation area, we calculate a mean spacing of roughly 45$\mathring{A}$ for the amorphous pockets in the 001 plane. While these results are quite reasonable for the QSC with its long range coherence, the question of their applicability to material with spherulitic morphology remains unanswered – in view of the relatively large activation dimensions that were obtained.

ACKNOWLEDGEMENT

This research has been supported by a DARPA/ONR program on simulation of polymer prop-

erties under Contract N00014-86-K-0768.

REFERENCES

1. Young, R. J., and Bowden, P. B., 1973, *J. Mater. Sci.*, **8**, 1177.
2. Galeski, A., Bartczak, Z., Argon, A.S. and Cohen, R.E., 1992, **Macromolecules**, **25**, 5705.
3. Galeski, A., Argon, A.S., and Cohen, R. E., 1991 **Macromolecules**, **24**, 3953.
4. Bartczak, Z., Argon, A. S. and Cohen, R.E., 1992, **Macromolecules**, **25**, 5036.
5. Lin, L., and Argon, A. S., 1992, **Macromolecules**, **25**, 4011.
6. Bartczak, Z., Galeski, A., Argon, A. S. and Cohen, R. E, 1994, **Polymer**, submitted for publication.
7. Schönherr, H., Vancso, G. J., and Argon, A.S., 1994, **Polymer**, submitted for publication.
8. Lin, L., and Argon, A.S., 1994, **Macromolecules**, submitted for publication.

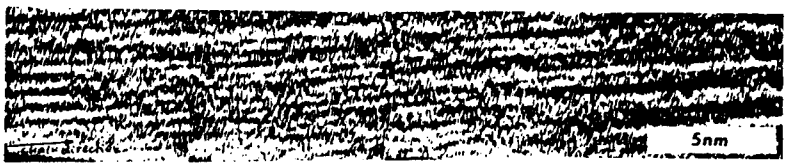

Figure 1 A montage of nanographs of the (100)(LD) surface of a highly textured HDPE.

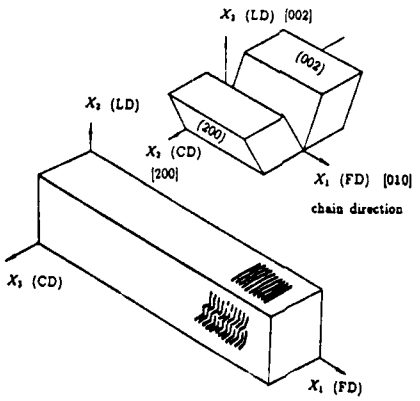

Figure 2 Symmetry axes of the textured quasi-single crystalline Nylon

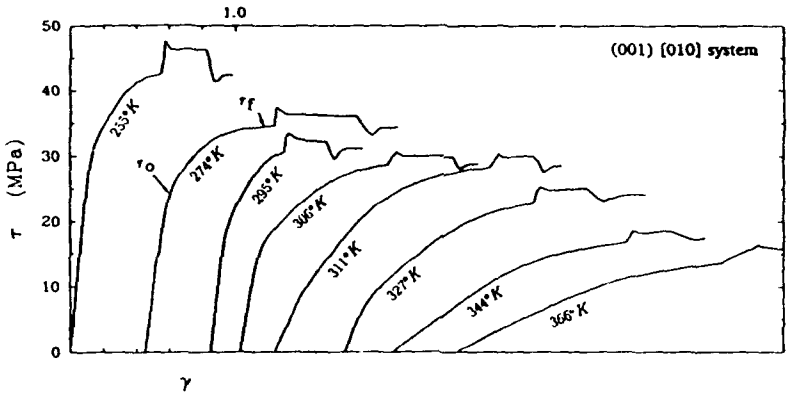

Figure 3 Simple shear stress strain curves of the (001)[010] system in Nylon

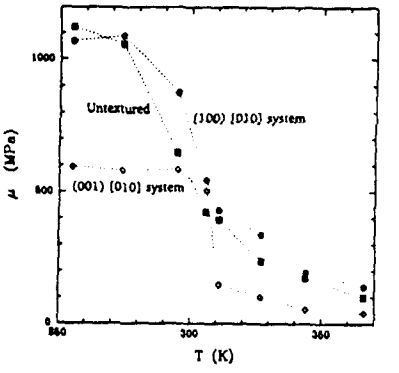

Figure 4 Temperature dependence of the shear moduli of the textured Nylon

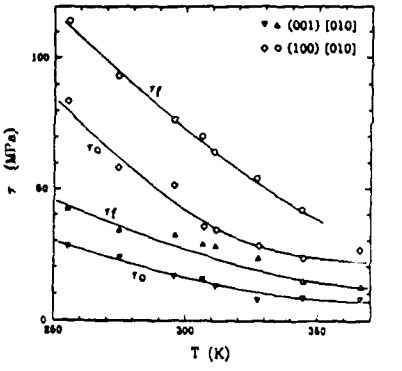

Figure 5 Temperature dependence of τ_0 and τ_f for the (001)[010] and (100)[010] systems

THE TENSILE PROPERTIES OF SEMI-CRYSTALLINE POLYMERS: THE POLYETHYLENES

L Mandelkern*

The tensile properties of molecular weight fractions of linear polyethylene and samples having most probable molecular weight distributions have been studied within the framework of the phase structure of such systems. Attention is given to the influence on the deformation process of molecular constitution and the independent structural variables that define the crystalline state. Of particular concern has been the changes that occur in the general features of the force-length curves, the yield stress and the ultimate properties.

INTRODUCTION

The tensile properties of linear polyethylenes have been investigated within the framework of our current understanding of the phase structure of crystalline polymers (1)(2)(3). Particular attention is given to the influence of molecular constitution and the independent structural variables that govern the crystalline state (1)(4). The objective has been to study the influence of these variables on the general features of the force-length curve and on the key tensile parameters such as yield stress and ultimate properties. The main focus has been on an extended range of molecular weight fractions of linear polyethylene and samples with narrow and defined molecular weight distributions (most probable). Some specific results with more polydisperse samples and random ethylene copolymers will also be presented and discussed. The main results are limited to a draw rate of 1"/min (strain rate 6.35 min^{-1}) and ambient temperature. As will be indicated, a few specific studies deviate from these conditions for particular purposes.

General Characteristics: At room temperature, samples equal to or less than about 4×10^4 are brittle. They became ductile at molecular weights above 1.5×10^5 at the deformation rates used. An intermediate molecular weight range thus exists where, depending on structural factors, one or the other type of deformation is observed (*cf seq.*). The ductile or plastic deformation of the polyethylenes have been extensively studied (5)(6)(7). The general character of the force-length curves obtained in this deformation region, for the well-defined samples studied here, are qualitatively similar to those previously reported (7). As the molecular weight increases (crystallinity level decreases) the yield stress decreases, the extent of the invariant

*Department of Chemistry and Institute of Molecular Biophysics, Florida State University, Tallahassee, FL 32306-3015

force-length region also decreases and the strain hardening process predominates. The deformation becomes homogeneous at the higher molecular weights.

Brittle-Ductile Transition: The type of deformation that occurs can be characterized by the draw ratio after break, λ_B. A brittle sample is defined when $\lambda_B \simeq 1$. Higher values describe the ductile type deformation. The brittle-ductile transition has been studied in detail and analyzed in terms of crystallinity level, interlamellar thickness and molecular weight. A very important observation in this connection is that as either of these parameters are varied the transition from one type of deformation to the other is very sharp and independent of the draw-rate (8). There are thus structural factors built into the system that determine the type of deformation. As an example for a most probable sample $M_w = 7.1 \times 10^4$ the deformation is brittle, $\lambda_B = 1$, for a core crystallinity level, α_c, of 0.67. However, for $\alpha_c = 0.64$ the same polymer becomes brittle with $\lambda_B = 12.5$. A similar sharp transition is observed when the interlamellar thickness, L_A is considered as the independent variable. When L_A is greater than about 65 Å it is found, for all the polymers studied, that the samples are ductile. Below this value of L_A the samples are brittle.

The interlamellar region is composed of chain units in disordered conformations. The concentration, trajectory, and elastic properties of disordered sequences that transverse the space from one lamellae to another are crucial to the deformation characteristics of the system (9). At low molecular weights, a plausible reason for embrittlement is that a sufficient number of connecting, disordered sequences are not present. In the modest molecular weight range, where the transition occurs, the decrease in the number of chain units within a disordered sequence can occur by further crystallization. Irrespective of the mechanism(s) that may be operating the major consideration is the sharpness of the transition.

Yield Stress: It is well known that the yield stress of the polyethylenes depends on the crystallinity level at room temperature. There is a linear relation between the yield stress and crystallinity level at low and moderate levels. However, at the higher crystallinity levels a plateau develops at a yield stress of about 32 MPa. The plateau region is comprised of specimens that are either in the brittle or transition region. Such specimens, however, are also found in the linear region, along with the ductile ones. No direct influence is found of either molecular weight, distribution, or supermolecular structure on the yield stress. The specific linear relation that is observed depends on the method used to determine the crystallinity level. The yield stress is directly proportional to the core crystallinity level. The yield stress is also linear with the density determined crystallinity level. However, in this case the straight line does not pass through the origin. These results suggest that the crystallites, and related regions undergo some kind of structural change during the yielding process. Several different types of mechanisms have been proposed for yielding.

Young (10) and Crist (11) have independently proposed that the yielding involve the thermal activation of screw dislocations with Burgers vector parallel to the chain direction. A specific dependence of the shear yield stress on the crystallite thickness is deduced from this theory. It is found from this new data for linear polyethylene, which covers a wide range of crystallite thickness, that the expected

dependence is not fulfilled. Despite the lack of quantitative agreement the theory does predict the correct order of magnitude of the yield stress. Alternatively, Flory and Yoon (12) have proposed that a partial melting-recrystallization process is involved in the complete deformation process including yield. Small-angle neutron scattering studies have confirmed this hypotheses (13)(14).

Complex yielding behavior, including double yields, has been reported for ethylene copolymers and a linear polyethylene (7)(15)(16)(17). We have now established the conditions under which complex yielding is observed in terms of the crystallinity level of the sample, the molecular weight, and the temperature and rate of deformation (17). Six distinctly different yielding patterns are observed and are shown to vary systematically with these quantities. A qualitative explanation, based on partial melting-recrystallization processes, is invoked to explain all of the results.

Ultimate Properties: The ultimate properties will be discussed in terms of λ_B, the draw rate after break. It is demonstrated that for a ductile deformation λ_B depends only on the weight average molecular weight, M_w, of the system and is independent of other key structural variables including crystallinity level, crystallite thickness and supermolecular structure. A continuous decrease of λ_B with M_w is observed. The functional form is very similar to that reported previously (5)(6)(18) but has now been extended to higher and lower molecular weights. It is also demonstrated that for the temperature and deformation rate studied here, there is no effect of polydispersity on the nature of the molecular weight dependence of λ_B.

Co-Workers: The work presented is the results of the efforts of Drs. R. Popli, A. J. Peacock, M. A. Kennedy, M. D. Failla, J. C. Lucas and Ms. F. L. Smith. Their contributions are gratefully acknowledged.

Acknowledgement: Support of this work by the Office of Naval Research and the National Science Foundation Polymer Program Grant DMR 89-14167 is gratefully acknowledged.

References:

1 Mandelkern L, Accounts of Chemical Research 23 (1990) 380.

2 Mandelkern, L.: in 'Crystallization of Polymers, NATO ASI Series' Dosière, M. (Ed.), Kluwer Academic Publishers, The Netherlands, 1993, pp.25.

3 Mandelkern L, Chemtracts-Macromolecular Chemistry 3 (1992) 347.

4 Mandelkern L, Polym J 17 (1985) 337.

5 Ward I M, 'Mechanical Properties of Solid Polymers', John Wiley New York, (1971).

6 Ward I M, 'Mechanical Properties of Solid Polymers', John Wiley New York, 2nd. Ed. 2, (1983).

7 Popli R and Mandelkern L, J Polym Sci ,Polym Phys Ed 25 (1987) 441.

8 Mandelkern L, Smith F L, Failla M, Kennedy M A and Peacock A J, J Polym Sci, Polym Phys Ed 31 (1993) 491.

9 Brown N and Ward I M, J Mater Sci 18 (1983) 405.

10 Young R J, Materials Forum 11 (1988) 210.

11 Crist B, Fischer C J and Howard P R, Macromolecules 22 (1989) 1709.

12 Flory P J and Yoon D Y, Nature 272 (1978) 226.

13 Wignall G D and Wu W, Polym Comm 24 (1983) 354.

14 Wu W, Wignall G D and Mandelkern L, Polymer 33 (1992) 4137.

15 Seguela R and Rietsch F, J Mater Sci Ltrs 9 (1990) 46.

16 Brooks N W, Duckett R A and Ward I M, Polymer 33 (1992) 1872.

17 Lucas J C, Failla M D, Smith F L, Mandelkern L and Peacock A J, (1993), submitted for publication.

18 Andrews J M and Ward I M, J Mater Sci 5 (1970) 411.

REAL-TIME IN-SITU X-RAY DIFFRACTION STUDY OF POLYETHYLENE DEFORMATION

M. E. Vickers * and H. Fischer #

A range of polyethylenes has been studied by X-ray diffraction during deformation. Changes in the crystalline orientation have been related to the load/extension curve. This was altered by changing the molecular weight, number of side-chains and strain rate. At the first yield point crystalline orientation was only just observable. Beyond this point the (110) reflection oriented to give four maxima which imply tilted polymer chains and lamellae. Subsequently the chains oriented parallel to the draw direction. Relaxation of the crystalline orientation has also been studied.

INTRODUCTION

Recently there has been renewed interest in the deformation behaviour of polyethylene, in particular the observation of double yield points (1-3). Some morphological models have been proposed, mostly based on older ex-situ work (4,5). However, real-time in-situ data from several different techniques are required to clarify and confirm the morphological changes that are occurring during the deformation of polyethylene.

EXPERIMENTAL

Small dumbbells (Table 1) were cut from pressed plaques of the materials described in Table 2. The specimens were deformed in a Minimat small scale tensile tester with software control. It was observed that most of the specimens yielded at a similar position (about 4 mm from the fixed end) and the neck propagated towards the moving end. The rig was positioned so that the X-ray beam (1 mm^2) illuminated this position and specimens were observed during deformation to check that they did yield at the expected position. Most runs were carried out at a crosshead speed of 1mm min^{-1} (2.78 x 10^{-3} s^{-1}) but some fast runs, 10 mm min^{-1}, and a few slow ones, 0.1mm min^{-1}, were also performed.

* BP Research and Engineering, Chertsey Rd, Sunbury-on-Thames, TW16 7LN, UK
# University of Bristol, H H Wills Physics Laboratory, Tyndall Av, Bristol, BS8 1TL, UK

The X-ray data were collected in transmission with CuKα radiation, a Siemens 2-dimensional electronic detector and a sample to detector distance of 35 or 17.5 mm. Most of the data were collected in 10 s frames with 17 s between frames. The fastest data collections were 3 s frames with 3.5 s for data dumping and a few longer data collections were carried out to obtain information on the weaker reflections. In addition, to confirm and extend the in-situ work, some ex-situ studies were carried out using standard WAXS and SAXS photographic techniques, a 4-circle diffractometer and TEM.

TABLE 1 - Dumbbell dimensions (mm)

Gauge length	6
Gauge width	3
Thickness (thin)	0.2-0.3
and (thick)	0.4-0.5
Total length	25
Radius	2
Maximum width	8

TABLE 2 - Description of materials

Material	Mw	No of side-chains/1000 C atoms
A	131,000	<0.5
B	206,000	6.2
C	126,000	21
D	385,000	<0.5
E	~1.5M	<0.5

RESULTS AND DISCUSSION

The shape of the deformation curve was observed to be sensitive to changes in the molecular structure of polyethylene and to the rate of deformation (Figures 1 and 2), as reported in the literature. (For ease of comparison, all the data shown here relate to thin samples.)

At the position of maximum load no local strain nor whitening were observed. The X-ray data, see Figure 3, showed small variations in intensity around the diffraction ring. It is possible that small amounts of material are just beginning to orient. For all the samples, the (110) reflection clearly split to give a four point pattern characteristic of tilted lamellae and polymer chains before whitening, necking or inhomgeneous strain were observed. Materials subjected to a higher load gave an additional diffraction peak which is usually assigned to the monoclinic phase of PE. As deformation continued, the (110) maxima moved closer together and the intensity on the equator increased and sharpened to give fibre orientation (the polymer chains in the draw direction). Some data showed that the tilted and fibre morphology coexisted for a while.

The transition from tilted to fibre orientation can be related to the deformation curve. Materials with a higher molecular weight and more side-chains maintained the tilted morphology for longer (figure 1). For these materials the deformation was spread over a

larger region of the sample. They are expected to have more tie-molecules which inhibit both inter and intra lamellar shear. The transition also occurred at a lower extension for faster deformation rates, consistent with the changes in the deformation curve (figure 2). No relaxation in the crystalline orientation was observed after 5 minutes with or without load near the first and second yield points. However, relaxation was noted after more than 15 minutes.

REFERENCES

1. Brooke, N. W., Duckett, R. A., and Ward, I. M., 1992 Polymer 33 1872
2. Seguela, R. and Rietsch, F., 1990 J. Mat. Sci. Letters 9 46
3. Springer, H., Hengse, A., and Hinrichsen, G., 1993 Colloid and Polym. Sci. 271 523
4. Peterlin, A., 1971 J. Mat. Sci. 6 490
5. Kasai, N. and Kakudo, M. 1964 J. Polym. Sci. A 2 1955

ACKNOWLEDGEMENTS

We would like to thank BP Chemicals for permission to publish this paper. Numerous BP Chemicals colleagues at both Sunbury and Grangemouth made contributions to this work for which we are grateful. In particular, Val Rose has allowed us to use her TEM micrographs. Finally BP would like to thank Professor E Atkins (University of Bristol) for allowing us to use the in-situ X-ray facility.

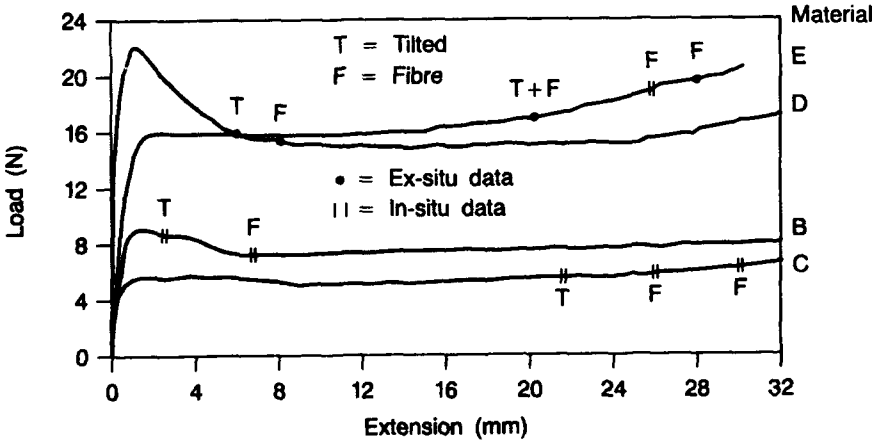

Figure 1 Load v Extension for polymers B, C, D and E (standard strain rate) showing transition from tilted to fibre morphology

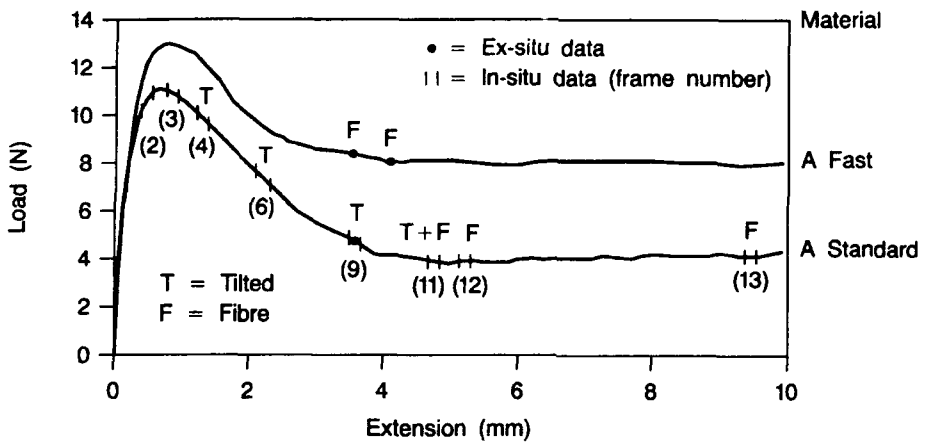

Figure 2 Load v Extension for polymer A (standard and fast strain rates) showing transition from tilted to fibre morphology

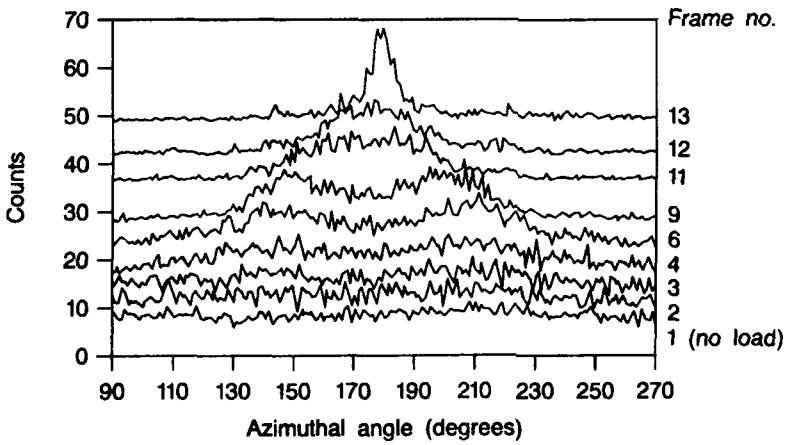

Figure 3 X-ray data collected on polymer A (standard strain rate) Azimuthal scan on (110) reflection

MICROSTRUCTURE INVESTIGATION OF PLASTICALLY DEFORMED PMMA BY LOW FREQUENCY RAMAN SCATTERING

T. Achibat*, E.Duval*, A.Mermet* and M. Aboulfaraj+, S. Etienne+ and C. G'Sell+

Plastically shear deformed polymethylmethacrylate (PMMA) samples were studied by Low Frequency Raman Scattering. The spectra were seen to be anisotropic. The observed increase of Raman scattering at low frequency, after deformation, is interpreted, assuming a non continuous nanostructure, by a softening of bonding and an increase of the volume of less cohesive regions.

INTRODUCTION

The structure of glassy polymers at the nanometric scale is still not clearly established, and so is, a fortiori, the deformation effect on this microstructure. It is why Low Frequency Raman Scattering (LFRS) measurements were carried out to obtain more information on how this structure evolves after various treatments.

In disordered systems like glassy polymers, the acoustic vibrational modes are non propagating and can therefore be observed by LFRS. The LFRS intensity $I(\omega)$, as a function of the frequency $\omega/2\pi$, is expressed as follows for Stokes scattering:

$$I(\omega) = C(\omega)g(\omega)[n(\omega)+1]/\omega$$

where $C(\omega)$ is the coefficient of light-vibration coupling, $g(\omega)$ the Vibrational Density Of States (VDOS) and $n(\omega)$ the Bose factor. It was shown (Achibat et al (1)) that for $\omega<70$ cm^{-1} in wave-number, $C(\omega)$ is proportional to ω in amorphous polymers, so that the reduced LFRS intensity, $I(\omega)/[(n(\omega)+1)]$ is proportional to $g(\omega)$.

This reduced intensity appears as a broad band which exhibits, for most of the polymers, a shoulder on its low frequency wing. This shoulder is responsible for the presence of a peak in $I(\omega)$ at room temperature (see the experimental results part). This peak, situated between 10 and 20 cm^{-1} in polymers, is characteristic of the glass structure and is called the "boson peak". It is a consequence of the low

* L.P.C.M.L. URA CNRS 442, Université Lyon I, 69622 Villeurbanne Cedex, France.
+ Laboratoire de Métallurgie Physique et Science des Matériaux URA. CNRS 155
Ecole des Mines, Parc de Saurupt, 54042 Nancy Cedex, France.

energy VDOS excess, in comparison with the Debye regime. As this excess appears at very low energy, it is expected to come from a softening of the physical bonding between molecular chains at different points in the network. The low energy VDOS excess was interpreted (Duval et al. (2), Achibat et al. (3), Sokolov et al. (4)) by a non continuous random network at the nanometric scale: there would exist domains, of about 5 nm in size, inside of which cohesion is stronger than in the relatively narrow spacings between them. This simple description is in agreement with the existence of density fluctuations. Obviously, the density is larger inside the cohesive domains and lower in the spacings. This described nanostructure is expected to change after plastic deformation.

EXPERIMENTAL TECHNIQUE

The PMMA used for this work is appproximately 54% syndiotactic and 37% isotactic and its number average molecular weight is 58 000 g/mol. The geometry of the sheared samples is shown in figure 1. The shear deformation was carried out with a servo-hydraulic material testing machine MTS 810 equipped with a system for videometric measurements of deformation (G'Sell et al (5)). The deformation was carried out at 80°C, with a deformation rate of 5.10^{-4} s^{-1}. Two kinds of samples were studied: (1) samples which were deformed up to $\gamma=1$ then frozen down to room temperature while still under stress and then unloaded, (2) samples which were first plastically deformed up to $\gamma=1$, then sheared in the opposite direction and then unloaded when both the final macroscopic strain ($\gamma_f=0$) and stress were equal to zero. These latter samples are thereafter called cycled samples.

The PMMA deformed sample was illuminated with the 514.5 nm line of an Argon laser. The laser beam was parallel to the torque momentum of the shear deformation (see fig. 1). The backscattered light was analyzed with a 4 m focal length quintuple Dilor monochromator equipped with a photon counting system. This spectrometer analyzed the vertically polarized component of the scattered light. Therefore, with either a vertical or horizontal polarization of the laser beam, we could measure respectively the polarized or depolarized Raman scattering. By rotating the sample around the laser beam direction, the LFRS was measured for various angles θ between the laser polarization and the shear stress direction. This θ angle was chosen positive for a rotation vector in the same direction as the shear torque momentum and the laser beam (fig. 1).

EXPERIMENTAL RESULTS

The polarized LFRS intensity $I(\omega)$ and the reduced one $I_R(\omega)=I(\omega)/[(n(\omega)+1)]$ of non deformed PMMA are shown in figure 2. The "boson peak" appears at 16 cm^{-1} in $I(\omega)$. The broad band which is observed in $I_R(\omega)$ exhibits a maximum at 83 cm^{-1}, and a shoulder at 13 cm^{-1}.

LFRS from deformed PMMA ($\gamma=1$)

The LFRS is anisotropic and depends on the angle θ between the laser polarization and the shear stress direction. In comparison with the LFRS of non deformed PMMA, a shift of the broad band and an increase of scattering at lower frequencies were observed. From the symmetry properties of the effect, it was found that the long axis of the macroscopic strain ellipsoïd was oriented at $\theta=+35°$, in agreement with birefringence measurements. The effect was maximum when the laser polarization was perpendicular to the long axis ($\theta=-55°$) (fig. 3) and minimum when the polarization was parallel to the long axis.

The deformation effect was quantitatively estimated by subtracting LFRS reduced intensities of non deformed samples from those of the deformed samples, after they were normalized with respect to the maximum at 83 cm^{-1}. The resulting subtractions reflect an increase of scattering at low energy and a slight shift of the band towards higher energies (fig. 4).

LFRS from cycled PMMA (γ_f=0)

The LFRS of cycled PMMA is less anisotropic. We observed for the different angles θ an increase of the intensity at low frequency. The effect was maximum for $0° \leq \theta \leq 20°$ (fig. 5).

Effect of ageing and annealing

The increase of Raman scattering at low frequency of a deformed sample (γ=1) which was kept at room temperature during one year was weaker than that of the same sample when recorded only 15 days after it was deformed. On the other hand, the LFRS change induced by the deformation disappeared after an annealing at 140°C during 2 hours (fig.6).

DISCUSSION

The major effects observed on LFRS, as resulting from the shear deformation are the anisotropy and the increase of scattering over the lower-frequency (40 cm^{-1}) wing of the broad-band. This anisotropy reflects the orientation of polymer chains under shear stress. The increase of Raman scattering at low frequency reveals an additionnal softening of vibrational modes. The fact that the deformation effect is maximum when the laser and scattering polarizations are perpendicular to the molecular chain orientation, and nearly zero when they are parallel, shows that the increase of low-frequency scattering is related to the local orientation. It also shows that the vibrational motion, which is responsible for the deformation induced LFRS excess, is perpendicular to the orientation. This behaviour is interpreted by an increase in volume of the spacings where the less interacting molecular chains are oriented by the shear stress. The alignement of the chains in those spacings is followed by a partial disentanglement and orientation of the more cohesive domains.

The change of LFRS which is also observed after plastic cycling shows that a modification of the nanostructure still remains even if the final macroscopic deformation is zero. This is in agreement with the disappearance of the shear overshoot after cycling. The modifications induced by plastic deformation are metastable and vanish by ageing and after annealing close to the glass transition temperature. Finally our results are in agreement with the results of Hasan et al (6) obtained from positron annihilation lifetime spectroscopy.

REFERENCES

1. Achibat, T., Boukenter, A. and Duval, E., 1993, J. Chem. Phys.,99, 2046.

2. Duval, E., Boukenter and Achibat, T., 1990, J. Phys. Condens. Matter, 2, 10227

3. Achibat, T. , Boukenter, A., Duval, E. , Lorentz, G. and Etienne, S. , 1991, J. Chem. Phys , 95, 2949.

4. Sokolov, A. P., Kisliuk, A., Soltwisch, M., and Quitmann, D. , 1992, Phys. Rev. Lett., 69, 1540.

5. G'Sell, C., Hiver, J. M., Dahoun, A., and Souahi, A., 1992, J. Mater. Sci., 27, 5031.

6. Hasan, O. A., Boyce, M. C.,Li, X. S., and Berko, S., 1993, J. Polymer Science B, 31, 185.

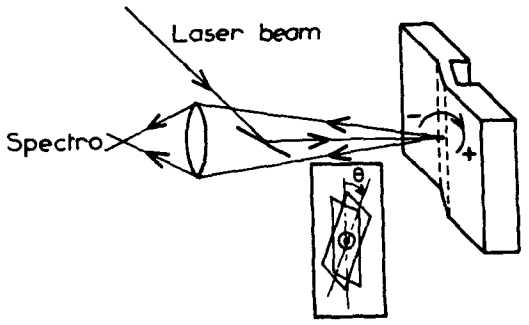

Fig.1- Geometry of the sample, laser excitation and scattering
The inset shows the rotation angle θ

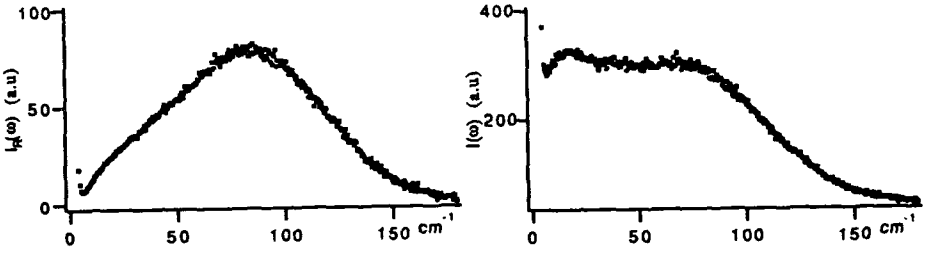

Fig.2- LFRS of non-deformed PMMA

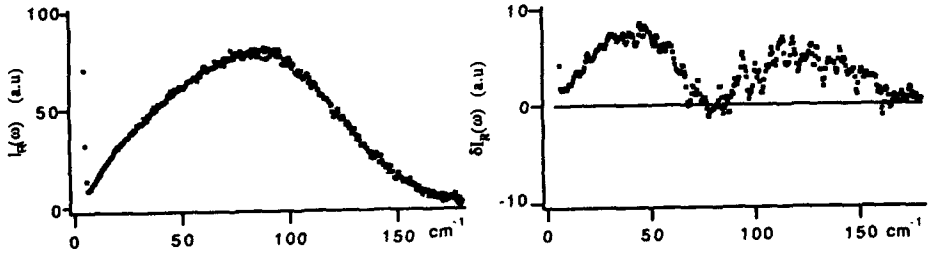

Fig.3- LFRS of deformed PMMA (γ=1) for θ=-55°

Fig.4- $I_R(\gamma=1, \theta=-55°)$-$I_R$(non-deformed)

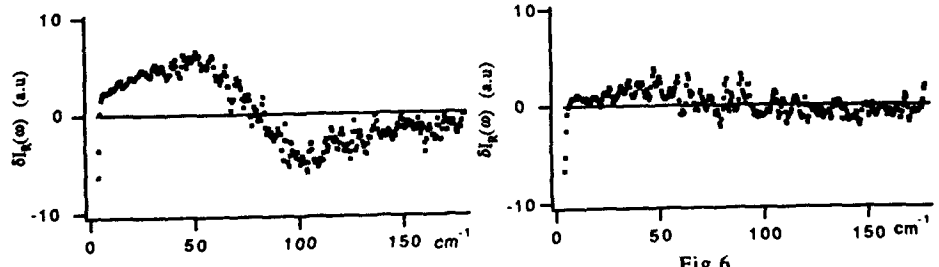

Fig.5
I_R(cycled, θ=0°)-I_R(non-deformed)

Fig.6
$I_R(\gamma=1$, annealed, θ=-55°)-I_R(non-deformed)

NON-LINEAR RESPONSE OF AMORPHOUS POLYMERS : PLASTIC DEFORMATION, CREEP TEST, STRESS RELAXATION AND α+β MECHANICAL RELAXATIONS

Perez J*, Ladouce L*, Quinson R*

The results of both dynamic mechanical and large stress plastic deformation performed on amorphous polymers below and through their glass transition temperature were interpreted in a common theoretical frame. Nevertheless, some secondary features remain rather poorly undersood. The theory mentioned above is then extended by taking into account of both the details of the dislocation dynamics (nucleation and propagation of shear microdomains) and molecular mobility described in terms of hierarchically constrained conformational changes.

INTRODUCTION

The dynamic mechanical response of various polymers below and through their glass transition temperature Tg have been successfully described on the basis of two assumptions:
(i) the existence of quasi-point defects (QDP) corresponding to positive or negative nanofluctuations of specific volume (1) (concentration Cd).
(ii) the hierarchically constrained nature of molecular dynamics (2,3).
Under the application of a stress, some QPD are accordingly activated into shear mirodomains (SMD), which, in turn, reversibly expand (anelastic strain) until they ultimately merge irreversibly with one another (viscoplastic strain).
On the basis of these simple arguments the time dependent shear compliance was expressed as:

$$J(t) = \frac{1}{G_u} + A\left[1 - \exp -\left(\frac{t}{\tau_{mol}}\right)^{\chi}\right] + A\left(\frac{t}{\tau_{mol}}\right)^{\chi'} \qquad (1)$$

A is a constant increasing with C_d, τ_{mol} is the time for a translational molecular motion and is given by

$$\tau_{mol} = t_0\left(\frac{\tau_\beta}{t_0}\right)^{1/\chi} \qquad (2)$$

with τ_β: the time characterizing the elementary molecular motion (conformational change) assumed to be responsible for the secondary or β relaxation .t_0 is a scaling parameter and χ is a measure of the degree of hierarchical constraint of the correlated molecular motions; χ increases with C_d between 0 (fully constrained situation) and 1 (constraint free situation).The corresponding complex shear modulus was then obtained by taking the Fourier transform of $J(t)^{-1}$ such that

* Lab GEMPPM - U.A. CNRS 341 - INSA Villeurbanne 69621 Cédex (FRANCE)

$$G^*(i\omega) = G_r + \frac{G_u - G_r}{1 + (i\omega\tau_{mol})^{-\chi} + Q(i\omega\tau_{mol})^{-\chi'}} \qquad (3)$$

where G_r is the relaxed modulus for the primary relaxation which corresponds to the value of the modulus at the rubbery plateau; the parameter χ' ($0<\chi<\chi'<1$) decreases with the length of chain segments between entanglements or crosslinking nodes; Q is a constant of the order of unity.

At high stress, the response of amorphous polymers is non linear: a molecular theory for the sub-Tg plastic mechanical behaviour of those materials was presented (4,5) considering:
-a thermomechanical activation of β process yielding:

$$\tau_\beta = \tau_0 \exp\left(\frac{U_\beta\left(1 - \frac{\sigma}{\sigma_0}\right)^{3/2}}{kT}\right) \qquad (4)$$

with σ_0: stress involving jumps over barriers at 0 K.
- a non conservative movement of dislocation bordering SMD, thus provoking an increase of desorder i.e. of C_d. Inversely, when C_d increases, the molecular mobility increases allowing for structural relaxation and subsequent decrease of C_d. In short, the plastic flow could be viewed as a stationary regime resulting from a balance between QPD produced by mechanically forced displacement of dislocations and QPD annihilated through structural relaxation.

The whole theory was shown to successfully describe both low (mechanical spectroscopy) and high (plasticity) stress mechanical tests (6). Nevertheless, secondary features have to be noticed suh as
(i) the occurrence of a large anelastic component with the plastic response of amorphous polymers,
(ii) the amplitude of stress relaxation is higher than that modeled with the theory here above recalled (7),
(iii) the non linear creep behaviour and the rate of strain recovery which is more rapid than the rate of creep (or the so called Turner's effect (8)).
Then the theory needs for further developpements.

DISLOCATION DYNAMICS

We propose to represent the energy profile corresponding to the energy state of a local region in which a SMD is nucleated and expands. For that purpose, the usual calculation (9) of the energy of a dislocation loop (radius R, shear vector b) is shown considering:
(i) the elastic energy of the strain field of the dislocation

$$2\pi R \frac{Gb^2}{4\pi} \ln\left(\frac{2}{\sqrt{3}}\frac{R}{b}\right) \qquad (5)$$

(ii) the work done by the applied stress $\pi R^2 \sigma_{shear} b$ (with σ_{shear}: shear component of the applied stress)
Let us apply both results on the Somigliana dislocation loop bordering a SMD: the energy profile obtained for several stresses is shown in figure 1a. Up to this point, such size dependence of the energy of a SMD could be compared to that calculated by Bowden and Raha (10). But in addition we must take into account further considerations:
(i) for SMD with a radius smaller than a certain value of about $\sqrt{3}b/2$ corresponding to the core of the associated dislocation, there is no elastic energy.
(ii) the average size of SMD just before their coalescence is equivalent to the distance between two activated QPD, so that it can be estimated to lie between 2 and 3 nm i.e. R close to 4b; beyond this

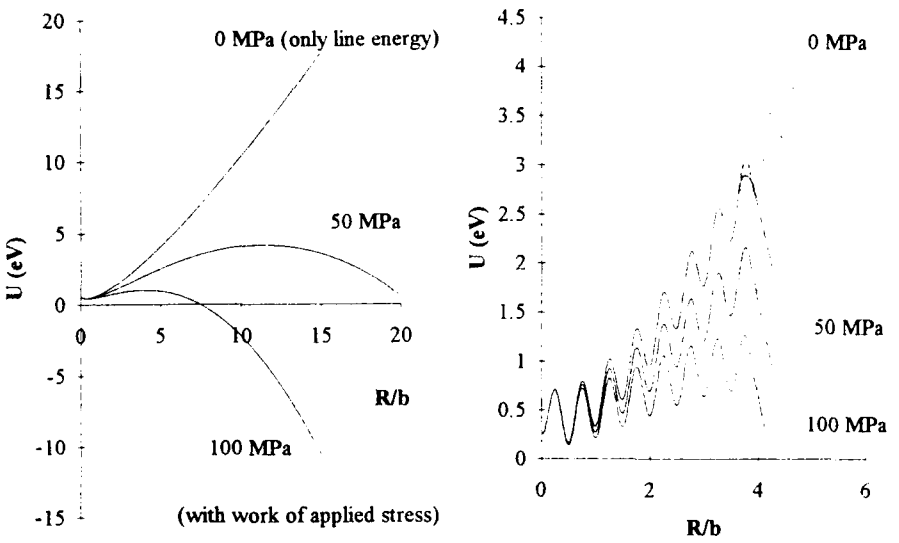

Figure 1: (a) Energy of a SMD vs its radius; (b) same as (a) but with (i) limitation of line energy due to SMD coalescence and (ii) barriers for conformational changes.

critical size, the annihilation of the dislocation elastic energy ought to occur over a distance more or less comparable to the core of this disloc ..ion.

(iii) superposed on this energy profile, we must add a succession of barriers corresponding to conformational changes in agreement with the assumption of growth of SMD thanks to hierarchically correlated molecular movements; the height of elementary barriers is taken equal to Uβ.

Then, the curves presented in figure 1b have to be considered. Such a representation is semi-quantitative since realistic values of the different parameters have been used. However, the distance between two successive barriers and their number are arbitrary; besides, with only one spatial coordinate, this simplified view does not take into account that molecular motions leading to the SMD growth in the stress direction can only be obtained with hierarchically correlated processes.

STRAIN RESPONSE: DISCUSSION AND CONCLUSIONS

In any case, with the preceeding representation, the energy state of an unactivated defect corresponds to the first well. Each other well corresponds to a possible energy state for activated SMD. Moreover, the height of the barriers determines the amount of thermal energy necessary for the passage from one state to another, i.e. the kinetics of such a change.

In figure 1b, it is pointed out that the whole energy profile falls down with increasing applied stress. The resulting consequences are:

-The equilibrium population of each well is modified; then, to obey to the new equilibrium, several defects must be activated and some of the preexisting SMD must grow.

- The passage from an energy state to a more activated one (growth of SMD) will be faster, the applied stress is high since the height of barriers is decreased

Consequently, increasing the stress results in non linear behaviour corresponding to both increase of the response amplitude and a faster kinetics for occupying new states.

Such a picture could justify common description (7) of (i) the main or α mechanical relaxation (low stress thermally activated jumps over the highest barrier) and (ii) plasticity (thermally activated jumps over barriers which have become lower when the stress has been increased). Moreover, it could explain:

-the increase of the anelastic component of the response with stress, since more numerous activated states are occupied: this results in higher amplitude of relaxation or antirelaxation stress (11) and increasing anelastic creep compliance (12).

-Turner's observations (8): the energy barriers to cross for a SMD growth are higher than that after stress removal, to come back (figure 1b); consequently, the rate of recovery of anelastic strain is higher than the rate of anelastic deformation.

- the low temperature shift of α relaxation when the stress is increased until α and β relaxation merge together (11) since, for high stress, the main barrier is completly smeared out while elementary barrier only decreases a bit.

The improvement of such analysis is now going on in our group for a quantitative description of experimental data related to the non linear behaviour of amorphous polymers submitted to high stress.

REFERENCES

1 Perez J, Rev Phys Appl 21 (1986) 93
2 Perez J, Cavaillé J Y, Etienne S and Jourdan C, Rev Phys Appl 23 (1988) 125
3 Cavaillé J Y, Perez J and Johari G P, Phys Rev B39 (1989) 2411
4 Cavaillé J Y, Perez J and Mangion M B, Proc 8th Int Cong on Def Yield and Fract Pol Cambridge (1991)5/1
5 Mangion M B, Cavaillé J Y and Perez J, Phil Mag 66 (1992) 73
6 Ouali N, Mangion M B and Perez J, Phil Mag 77 (1993) 827
7 Ouali N, thesis INSA Lyon (1992)
8 Turner S,' The physics of Glassy Polymers', Ed Haward R N, Appl Sci Pub, London, 1973
9 Hirth J P and Lothe J, 'Theory of Dislocations', Mc Graw Hill New York, 1968
10 Bowden P B and Raha S, Phil Mat 29 (1974) 149
11 Quinson R and Perez J, Polymer, submitted
12 Ladouce L, Perez J, Vassoille R, Vigier G, J Mat Sci, accepted for publication

NEW APPROACH TO PLASTIC DEFORMATION OF GLASSY POLYMERS

E Oleinik*

Extensive measurements of the stored energy of cold work (using a deformation calorimetry method), the recovery of residual strain and the release of the stored energy upon heating were performed with linear and cross-linked glassy polymers, several semi-crystalline polymers and immiscible blends based on PC. The results of these experiments could not be explained and understood in the framework of current models of polymer deformation, and the necessity for a new model for the inelastic deformation of glassy polymers was evident.

The main features of the process are the storage by a sample during its cold working of a high amount of internal energy, which starts at the very beginning of straining. The level of stored energy reaches 70-95% of the mechanical work expended in deformation at low strains (below ϵ_y) and 30-45% at higher strains. The stored energy shows the tendency to level off at compressive strains of 25-35% (at room temperature) for most of the cases. The fraction of the expended work stored in polymeric glasses is much higher compared to metals, where it is normally less than 5-10%, and seldom is as high as 15%.

We were able to show that the energy storage in polymer glasses appears to be due to the stress biased formation of special shear "defects"-Plastic Shear Transformations (PST)-which are small, local-scale structural rearrangements. Each PST carries a small strain (shear displacement) and is surrounded by an elastic field. All these fields are the microscopic carriers for the macroscopic stored energy of cold work, in the sample.

The nucleation of PSTs is not connected with the free volume changes in a sample, but with the conformational rearrangements in macromolecules. The formation of PSTs brings the glass into a new excited metastable thermodynamic state. All the following processes which happen in polymers upon loading (such as yielding, steady plastic flow, deformation hardening and softening, formation of cracks, crazes or shear bands) are occurring in the new, but not native, state of the glass. Macroscopic yielding happens only when the PST's concentration reaches some critical level which is characteristic for a given polymer and strain conditions.

The second important stage of the deformation process is the termination of the PST (ie death). The termination is the process responsible for the dissipation of the stored energy excess. If the dissipation is not occurring effectively the

* Institute of Chemical Physics Russian Academy of Sciences, Moscow

energy excess may dissipate through the nucleation and development of cracks or crazes, and the material may show brittle behaviour. The necessary feature of the PST termination process is the conformational rearrangements in the macrochains. Since, the major part of macrostrain is collected in the PST's nucleation, but not in its termination, the whole inelastic deformation of glassy polymers is close to pure anelasticity. A comparison of the deformation behaviour of crystals and glasses is also considered in the presentation.

THE EFFECT OF LIMITING CHAIN MOBILITY ON THE YIELDING AND CRAZING BEHAVIOUR OF BPA-PC DERIVATIVES

C.J.G. Plummer, H.-H. Kausch (EPF de Lausanne, CH-1015, Switzerland).
C.L. Soles, A.F. Yee, C. Xiao, J. Wu (University of Michigan, Ann Arbor, MI, USA).

TEM studies of the phenomenology of deformation in thin films of bisphenol-A polycarbonate (BPA-PC) and alternating block copolymers of the form $(B_xtT_xt\text{-})_n$, $(B_xT_x\text{-})_n$ and $(B_xt\text{-})_n$, where B is a BPA block, T a rigid tetramethyl-BPA-carbonate and t, a flexible terephthaloyl linkage have highlighted the importance of the range of co-operative motions between B units, and the coupling between the T and B units, for yield and disentanglement.

INTRODUCTION

Studies of alternating block copolymers (ABC) have suggested that γ relaxation in bisphenol-A polycarbonate (BPA-PC) involves in-chain co-operative motion of 7 repeat units [1], and that such motion facilitates shear yielding. Insertion of terephthaloyl linkages (t) decouples co-operative motions in ABC's of rigid tetramethyl-BPA-carbonate (T) and more mobile BPA-carbonate (B) units of the form $(B_xtT_xt\text{-})_n$ [2], leading to a rise in yield stress, σ_y, when $x < 7$, but little change when $x \geq 7$. This is of practical significance; the ductility can be manipulated without significantly altering the T content, and the high temperature performance (T_g remains 50 K greater than in BPA-PC). The object of the present study is to further this investigation, using transmission electron microscopy (TEM) to examine deformation in thin films of BPA-PC and $(B_xtT_xt\text{-})_n$, $(B_xT_x\text{-})_n$ and $(B_xt\text{-})_n$ at different temperatures. We consider first the basic phenomenology of deformation in BPA-PC thin films, followed by a discussion of the decoupling effect of the t units on the range of co-operative motion in $(B_xt\text{-})_n$, and finally, the combined effects of decoupling and T unit addition in $(B_xtT_xt\text{-})_n$ and $(B_xT_x\text{-})_n$. The synthesis of the polymers and the film preparation method are described in [3] and [4] respectively. The solvent was dichloromethane, and care was taken to avoid unintended physical ageing and crystallization during preparation. Unless stated otherwise, the films were strained at $d\varepsilon/dt \sim 5 \times 10^{-4}\ s^{-1}$, using the Polymer Laboratory Minimat™ tensile test machine, and examined using a Phillips EM 300 TEM.

RESULTS AND DISCUSSION

BPA-PC homopolymer. In unaged BPA-PC films, diffuse shear is seen at room temperature. When the temperature is raised to a critical value T_{sc} there is a transition to localized deformation. T_{sc} coincides with the transition from localized shear (DZs) to disentanglement crazing in aged films (for similar $d\varepsilon/dt$ and M) [5]. In unaged films, the transition is also marked by the onset of crazing, but is less well defined, shear and crazing coexisting above T_{sc}. Clearly σ_y and the crazing stress, S_c, are similar in this temperature range, whereas in aged films σ_y is higher than S_c. S_c is written [6]

$$S_c \sim \sigma_f^{1/2}(\gamma + \nu_e d_e f_d/2)^{1/2} \qquad \ldots (1)$$

(σ_f = flow stress, γ = Van der Waals surface energy, ν_e = entanglement density, d_e = entanglement spacing, f_d = force to break/disentangle a chain). In BPA-PC, $\nu_e d_e f_d/2$ is large at room temperature since ν_e is large, and the chains break. The transition from shear to crazing as the temperature increases is due to f_d dropping towards zero at the onset of disentanglement. However since S_c depends on $\sigma_f^{1/2}$ rather than σ_f it is possible that there will be a transition back to crazing at low temperature, where σ_f is relatively large. What we observed was a transition from diffuse to localized shear at -100 °C, coinciding with the γ transition. Crazes such as shown in Figure 1a did not occur until -120 °C. Note that the craze in Figure 1a has the well developed fibrils seen in scission crazes in other polymers, and that the deformation modes seen above T_{sc} are absent.

x	M_e	M_w	T_g
3	2219 2334	55090	171 °C
5	3565 2949	70990	164 °C
7	2902 7615	96110	164 °C
9	2547 3514	93320	160 °C
BPA-PC	1810 2309	116810	154 °C

Table I: Materials parameters for $(B_xt\text{-})_n$; the M_e values in the left and right hand columns are from measurements made independently using different apparatuses.

$(B_xt\text{-})_n$ alternating block copolymers. The deformation behaviour of $(B_xt\text{-})_n$ is compared with that of BPA-PC in Figure 3. At low T the behaviour for all the polymers is as for BPA-PC. T_{sc} also varies little with x, the main variation being in the range of mixed deformation above T_{sc}, its being relatively narrow in both BPA-PC and for small x. This is explicable in terms of changes in σ_y. If crazing represents the onset of disentanglement as is suggested for BPA-PC, the criterion for crazing is that the force to disentangle a chain, f_d, falls below the chain scission force of about 2×10^{-9} N. Here $f_d \sim (M/M_o)^{\alpha} \nu \zeta_o$, where ζ_o is a monomeric friction coefficient, v is the disentanglement rate and $\alpha \sim 1$. Berger and Kramer suggested the temperature dependence of ζ_o to be that of disentangling melts well above T_g [6]. The values of ζ_o in this regime were estimated using empirical additive rules [7], and change little with x at a given T. Extrapolation to below T_g gives ζ_o consistent with the observed shear to craze transition temperatures, though it is not clear if this is justified. The implication however is that the relatively minor changes in T_g, M, M_e and t content as x is increased, make little difference to the crazing behaviour (materials parameters for BPA-PC and the $(B_xt\text{-})_n$ polymers are given in Table I). On the other hand, at room temperature, σ_y is considerably lower in $(B9t\text{-})_n$ than in BPA-PC, but then rises for $x < 7$ in accordance with the notion that yielding is facilitated as the range of co-operative motion increases, and that the t linkages decouple this motion, limiting its range. It is noteworthy that M_e for BPA-PC is equivalent to 7 repeat units, so entanglement should restrict the maximum range of the γ relaxation to 7 repeat units, consistent with these observations and those cited in the introduction. As long as the range of the γ relaxation is unchanged, the effect of adding t linkages is to increase chain flexibility. For $x = 7$ however, chain flexibility begins to decrease on further t addition, owing to restriction of the range of main chain motions. M_e should be an *increasing* function of chain flexibility [8], so that the peak in M_e at $x = 7$ (Table I) is consistent with the above qualitative picture. This interpretation differs from that of Prevorsek and De Bona [9] who argued that addition of t units results in a monotonic increase in stiffness with x. However these authors did not consider $9 > x > 3$, which is precisely the range in which the peak in M_e is observed.

The relatively low σ_y explains the extensive mixed deformation for large x (given $\sigma_f \sim \sigma_y$, and the weak dependence of the crazing stress on σ_f).That T_{sc} remains approximately constant in spite of rises in T_g also means that in $(B3t\text{-})_n$, there is an extended regime of disentanglement crazing. However, as T rises, and as $d\varepsilon/dt$ is decreased, the character of the crazes changes; they take on the 'flame' shape usually associated with DZs and the craze body resembles a perforated sheet (Figure 1b). This is a gradual transition. Figure 1b is for 150 °C and $d\varepsilon/dt \sim 5 \times 10^{-7}$ s^{-1}, and is an extreme case. The voiding appears to be a post-drawing phenomenon similar to the Type II crazing observed in bulk BPA-PC close to T_g [10]. That the voids nucleate in rows perpendicular to the principal stress axis is expected from the form of the biaxial stress field around an isolated void.

It is less clear why material separating the rows of voids is relatively undeformed, whereas the deformation ratio of the the material separating voids within the rows is large at these temperatures (because of disentanglement). A possible explanation for this is highly accelerated physical ageing, which has also been seen during step-straining of crazes [11].

$(B_xtT_xt\text{-})_n$ and $(B_xT_x\text{-})_n$ alternating block copolymers. The behaviour of bulk $(B_xtT_xt\text{-})_n$ and $(B_xT_x\text{-})_n$ as reported in [2,3] was briefly alluded to in the introduction. Here we summarize some of the salient observations. The T homopolymer has a T_g of approximately 200 °C, a γ relaxation peak near room temperature, and is brittle. Increasing x in $(B_xT_x\text{-})_n$ improves ductility because of co-operative motion between the B and T units at low x (broadening the γ relaxation peak of the T homopolymer and moving it to lower temperature) and re-establishment of long-range co-operative motion among the B units for $x \geq 7$ (reappearance of the BPA-PC γ relaxation). The inclusion of a t linkage between the B and T blocks decouples their motion so that for low x, instead of a single broad relaxation peak, two well separated peaks are observed. Thus $(B3tT3t\text{-})_n$ yields less readily than $(B3T3\text{-})_n$, the mobilizing effect of the B units on the T units being absent in the former case. Deformation maps for thin films of $(B_xtT_xt\text{-})_n$ and $(B_xT_x\text{-})_n$ are given in Figure 2b. Note that M and T_g are similar for all the copolymers (T_g ~200 °C). For $x \geq 7$ we observe transitions from diffuse shear to localized mixed shear and crazing in $(B_xT_x\text{-})_n$ at a similar temperature to those in BPA-PC and the $(B_xt\text{-})_n$ polymers. For lower x, T_{SC} rises with decreasing x. In $(B_xtT_xt\text{-})_n$, T_{SC} also rises with x but is much higher than in the other polymers. Finally, in aged films of both $(B_xtT_xt\text{-})_n$ and $(B_xT_x\text{-})_n$ (held overnight at T_g - 30 K), shear deformation is no longer diffuse and there is a transition from localized DZs to crazing which coincides with T_{SC} in the unaged films.

These results show that by changing x one can influence σ_y without greatly changing the composition of the chains. Further, in the presence of T units, varying x also influences T_{SC}, and by implication, the temperature of the onset of disentanglement. Since t units alone have a relatively minor effect on T_{SC}, if the effective monomeric friction coefficient is a truly additive property, the conventional picture suggests disentanglement ought to remain substantially independent of x. This is clearly not the case however; coupling of B and T units, and the lubricating effect of long range B motions, which facilitate mobilization of the T blocks, also appear to promote disentanglement. It might be tempting to account for the transition to crazing as being a consequence of the onset of localized deformation. However, the predominance of localized DZs in aged films deformed at ambient temperature shows that whilst localized deformation may be a necessary condition for crazing, it is not a sufficient one. In regimes where crazing is able to occur by disentanglement, we suggest that co-operative motion is needed to 'lubricate' the chains and facilitate the disentanglement process. In other words we suggest that disentanglement may also be available as a relaxation mechanism for material undergoing plastic drawing, reducing work hardening, and hence provoking the transition to localized deformation. The onset of disentanglement crazing and the diffuse to localized shear transition are both manifestations of the same phenomenon.

REFERENCES

1. Jae Young Jho, A.F. Yee, Macromolecules **24** 1905 (1991).
2. C. Xiao, A.F. Yee, Macromolecules **25** 6800 (1992).
3. C. Xiao, J.Y. Jho, A.F. Yee, submitted to Macromolecules.
4. B.D. Lauterwasser, E.J., Kramer, Phil. Mag. **A39**, 469 (1979).
5. C.J.G. Plummer, A.M. Donald, J. Poly. Sci. - Poly. Phys. Ed. **27**, 235 (1989).
6. E.J. Kramer, L.L., Berger, Adv. Poly. Sci. **91/92**, Ch. 1, Ed. H.-H. Kausch (1990).
7. D.W. Van Krevelen, "Properties of Polymers", 3rd Ed., Elsevier, 1990.
8. W.W. Graessley, S.F. Edwards, Polymer **22**, 1329 (1981).
9. D.C. Prevorsek, B.T. De Bona, J. Macromol. Sci.-Phys. **B19(4)**, 605 (1981).
10. M. Dettenmaier, Adv. Poly. Sci. **52/53**, Ch. 3, Ed. Kausch, H.-H. (1983).
11. C.J.G. Plummer, A.M. Donald, Polymer **32**, 3323 (1991).

ACKNOWLEDGEMENTS

The authors wish to acknowledge the help of Marsha A. Samus of the Ford Polymer Science Department and Dr. Dongming Li of the Exxon Chemical Company Polymers Group.

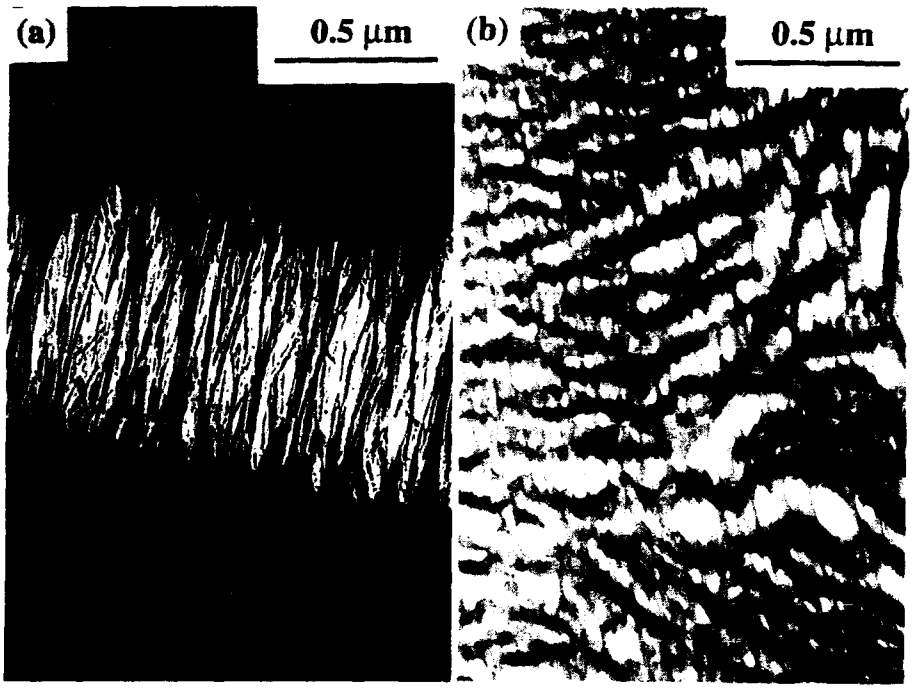

Figure 1. (a) Deformation in BPA-PC at -120 °C ($d\varepsilon/dt \sim 5 \times 10^{-4} s^{-1}$); (b) deformation at 150 °C in $(B3t\text{-})_n$ ($d\varepsilon/dt \sim 5 \times 10^{-7} s^{-1}$, tensile axis vertical).

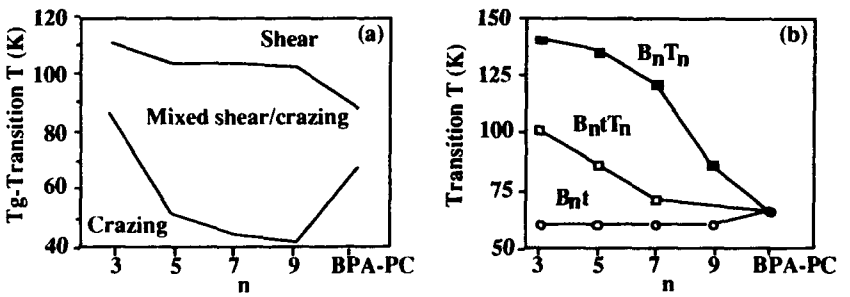

Figure 2. Deformation maps: (a) $(B_Xt\text{-})_n$, regimes of crazing, mixed crazing and shear, and diffuse shear are shown as a function of T_g - T; (b) $(B_XtT_Xt\text{-})_n$ and $(B_XT_X\text{-})_n$, the temperature of the transition from diffuse shear to localized deformation is shown in each case ($d\varepsilon/dt \sim 5 \times 10^{-4} s^{-1}$).

MODELLING THE NONLINEAR STRESS-STRAIN BEHAVIOR OF GLASSY POLYMERS AND COMPOSITES

T. S. Chow
Xerox Webster Research Center, 800 Phillips Road, 114-39D, Webster, NY 14580

A unified account of the structural relaxation and nonlinear deformation in glassy polymers and composites is presented. Using our statistical dynamic theory of glassy state relaxation, we predict the nonlinear stress-strain relationships as a function of physical aging, strain rate, temperature, external stress fields, and the filler concentration in composites.

INTRODUCTION

It has been recognized that volume relaxation, viscoelastic response, and plastic yielding share the same structural relaxation in the glassy state [1]. Existing constitutive equations have their limitations [2]. On the basis of our statistical dynamic theory of glasses [1], the deformation kinetics in the glassy state are considered as a result of the local configurational rearrangements of molecular segments, and the dynamics of holes (free volumes) provide a quantitative description of the segmental mobility. This new concept will be utilized to discuss the important effect of the glassy state relaxation on the nonlinear stress-strain behavior of glassy polymers.

GLASSY STATE RELAXATION

Consider a lattice consisting of n holes and n_x polymer molecules of x monomer segments each. The total number of lattice sites (N) and volume (V) are written as: $N(t) = n(t) + xn_x$, and $V = vN$ where t is time, and v is the volume of a single lattice cell. The hole number n(t) consists of both equilibrium and nonequilibrium contributions in the glassy state. Minimizing the excess Gibbs free energy due to hole introduction with respect to the hole number, we obtain the equilibrium hole fraction

$$\bar{f}(T) = \frac{\bar{n}}{\bar{N}} = f_r \exp\left[-\frac{\varepsilon}{R}\left(\frac{1}{T} - \frac{1}{T_r}\right)\right] \tag{1}$$

where ε is the mean energy of hole formation, R is the gas constant, and the subscript r refers to the reference condition at $T = T_r$, which is near T_g. We have analyzed the hole dynamics and fluctuations on a fractal lattice [1], and have obtained the nonequilibrium hole fraction for a system started from equilibrium

$$\delta(T,t) = \frac{n(t)-\bar{n}}{\bar{N}} = -\frac{\varepsilon}{R}\int_0^t \frac{q\bar{f}}{T^2}\Psi(t-t')dt' \qquad (2)$$

where $q = dT/dt < 0$ is the cooling rate, and Ψ is the relaxation function. Different paths of time integration in Eq.(2) describe different thermal history behavior of the glassy state relaxation and recovery kinetics -- the memory effect. When further analysis is carried our, the relaxation function is derived

$$\Psi(t) = exp\left[-\left(\frac{t}{\tau_o}\right)^{\beta}\right], \qquad 0<\beta\leq 1 \qquad (3)$$

where β defines the relaxation spectrum, $\tau_0 = \tau_r a$ is the relaxation time, and the shift factor

$$a(T,\delta) = \left(\frac{\bar{f}+\delta}{f_r}\right)^{-\frac{1}{\beta(\bar{f}+\delta)}} \qquad (4)$$

At $T = T_r$, we have $\delta = 0$, $\bar{f} = f_r$, and $\tau_0 = \tau_r$ which requires $a = 1$. In the vicinity of T_g, Eq. (4) reduces to the form of Doolittle's equation. We have determined [1] the hole parameters for polystyrene (PS): $\varepsilon = 3.58$ kcal/mol, $\beta = 0.48$, $\tau_r = 30$ min and $f_r = 0.032$. These parameters will be used to calculate the effect of physical aging later.

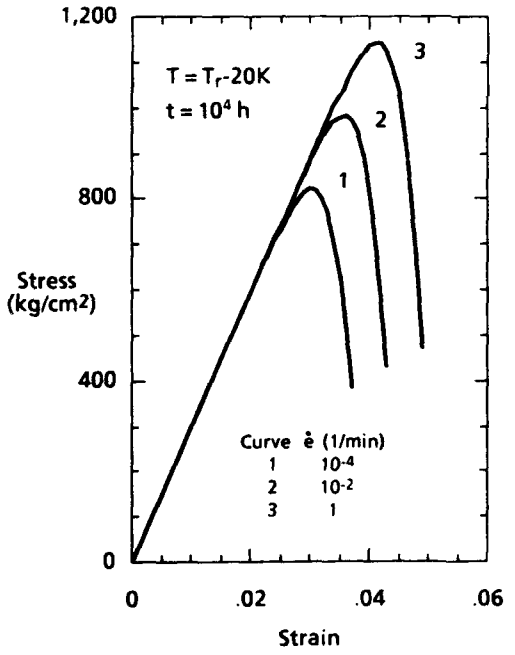

Figure 1. Effect of strain rate [3] on the compressive stress-strain curves of PS.

STRESS-STRAIN BEHAVIOR

Consider the uniaxial compression except in the case of differing stress fields. At high stress levels, the contribution from the external work done on a lattice cell has to be included in the structural relaxation. By taking into account the long range cooperative interaction, the external work done by a compressive stress (σ) acting on a hole cell during yielding is $\Delta w = -\sigma\Omega N/n = -\sigma\Omega/f$, where Ω is the compressive activation volume. The nonlinear relaxation time takes the form [1]

$$\tau(T,\delta;\sigma) = \tau_o(T,\delta)\exp\left(-\frac{\sigma\Omega}{2f\beta kT}\right) \tag{5}$$

The stress-dependent relaxation modulus of physically aging polymers can be written in the form: $E(t,\sigma) = E_o\Psi[t/\tau(\sigma)]$ where E_o is the Young's modulus and Ψ is given by Eq. (3). Integrating E, we get

$$\sigma(e) = E_o(T,\delta)\int_0^e \exp\left\{-\left|\frac{e'\exp(2.303\,\sigma(e')/K)}{\dot{e}\,\tau_o(T,\delta)}\right|^\beta\right\}de' \tag{6}$$

where $K \sim 1/\Omega$ is a constant, e is the compressive strain, and $\dot{e}$ is the strain rate. Eq. (6) together with Eqs. (1-4) will be applied to calculate many different effects on the nonlinear stress-strain behavior of PS with a single set of parameters.

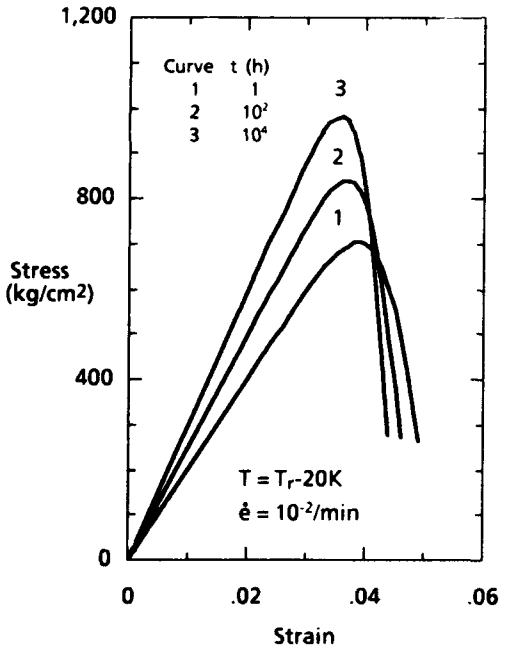

Figure 2. Effect of physical aging [3] on the compressive stress-strain curves of PS.

By using $K = 90\ kg/cm^2$, $E_o = 29.6 \times 10^3\ kg/cm^2$ and $\tau_o = 2 \times 10^{14}$ min at 23°C for a well aged PS, the calculated strain rate effect is shown in Figure 1. When the polymer is quenched isobarically from liquid to glass for annealing before it is quenched again to room temperature, the effect of physical aging is calculated in Figure 2. In order to discuss the influence of external stresses, Δw has to be generalized in the form: $\Delta w = -\sigma_{ij}\Omega_{ij}/f$ where σ_{ij} and Ω_{ij} are the stress and activation volume tensors, respectively. For PS, we have determined the activation volumes in uniaxial tension $\Omega(+)$, in compression $\Omega(-)$, in shear Ω_{12} and in hydrostatic compression v [4]

$$\left| \Omega_{11}(+), \Omega_{11}(-), \Omega_{12}, v \right| = \left| 111.7, 98.8, 158.6, 19.2 \right| \mathring{A}^3 \tag{7}$$

which is used to calculate the effect of stress fields in Figure 3. Eq. (6) can also be extended to predict the nonlinear deformation in polymer composites [5].

REFERENCES

1. Chow, T. S., 1992, Adv. Polym. Sci. 103, 149; 1992, Macromolecules 24, 440.
2. Landel R. F., and Peng, S. T. J., 1986, J. Rheology 30, 741.
3. Chow, T. S.,1993, Polymer 34, 541.
4. Chow, T. S.,1992, J. Rheology 36, 1707.
5. Chow, T. S.,1991, Polymer 32, 29.

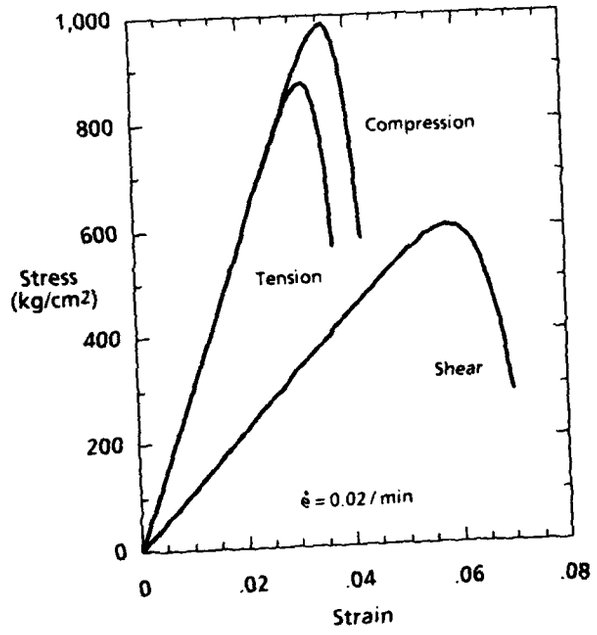

Figure 3. Effect of stress fields [4] on the nonlinear stress-strain curves of PS at 23°C.

CONSTITUTIVE BEHAVIOUR UNDER LARGE STRAINS OF CROSSLINKED POLYMETHYL METHACRYLATE BELOW AND ABOVE THE GLASS TRANSITION

C G'Sell, A Souahi *

The mechanical properties of a crosslinked grade of PMMA were investigated up to large strains under tension, compression and simple shear. The tests were performed in the glassy state and in the rubber-like state at temperatures between 95°C and 150°C. Along each of the selected loading paths, the constitutive stress-strain curves were determined as a function of the strain-rate and temperature. Above T_g, a well defined rubber-like response is observed. Below T_g, a marked yield transient is recorded, followed by a steady state plastic regime whose strain-hardening shows a remarkable continuity at T_g with the rubber-like behaviour. The results are discussed in terms of enthalpy barriers at yield and reduction of configuration entropy at large strains.

INTRODUCTION

Although the yield behaviour of polymethyl methacrylate (PMMA for short) has been the object of numerous papers (*e.g.* 1-3) most of them were focused on the onset of the plastic regime and only a few studies were devoted to the response of the material at large strains. This is because the standard tensile tests (which constitute the most common source of information) are generally affected by various artefacts : i) brittleness at room temperature, ii) early necking in the ductile regime close to the glass-transition temperature, iii) grip slippage in the rubber-like state above T_g. Apart pioneer workers (4) who tediously corrected the above artefacts in view of assessing the intrinsic tensile stress-strain relations, the information available on the constitutive equations of PMMA in the plastic range is still lacking of precision or completeness. Thanks to a new generation of video-controlled tests developed in this laboratory (5,6), the true stress-strain behaviour of materials can now readily be assessed at any temperature and at constant true strain rate under uniaxial tension or compression and under simple shear. It was the object of this work to co-operatively apply these techniques to the model case of a crosslinked polymer in the vicinity of the glass-transition temperature. Furthermore, we aim to discuss the origin of the stress consolidation which is observed at large strains, either in the glassy state and in the rubberlike state.

MATERIAL AND METHODS

The PMMA utilised in this work has been provided under the form of thick plates (15 mm) by the Orkem company. It is an industrial grade polymerised with a small amount of trimethylol-1,1,1-propane trimethacrylate (TRIM) which causes the polymeric chains to form crosslinks at fourfold junctions. The network thus obtained, which swells by a factor of 4.0 in chloroform at 25 °C, is rather loose, with an average molecular weight between crosslinks, M_c, equal to 2840 ± 230 g/mole (7). The fraction of soluble chains is very low (1.5 %) and the glass-transition is observed at 118 °C.

* Laboratoire de Métallurgie Physique & Science des Matériaux (URA CNRS 155), Ecole des Mines (INPL), Parc de Saurupt, 54042 Nancy, France.

In order to start from a reproducible structural state, the plates were carefully dehydrated at 138 °C for 24 hours under vacuum and then cooled very slowly to room temperature. Also, after the sample were machined, they were stress-relieved at 70 °C for 12 hours and subsequently kept under vacuum. Consequently, the specimens tested can be considered as dry and over-aged.

The testing system applied in this work was detailed elsewhere for the cases of uniaxial tension and simple shear (5, 6). It is described here for the first time in the case of compression. In each of the three loading modes, the local true strain is measured by a video-controlled extensometer which analyses in real time the distortion of the specimen profile (for tension and compression) or of an ink marker printed on the specimen (for shear). In the new case of compression, the testpieces have an axisymmetric hourglass shape which ensures the correct axiality of the load and reduces the risks of buckling, oblique kinking, grip slippage etc. As illustrated in Fig. 1, the deformation begins at the weakest cross section of the sample where it induces a certain barrelling. The true strain is assessed locally through the reduction of diameter by the relation $\varepsilon = 2\ \mathrm{Log}\,(D_o / D)$ which applies for incompressible materials. As for the true stress, it is determined at the same cross-section by the relation $\sigma = (4F/\pi D^2) \times F_T(D, R_c)$, where F_T is a correction factor taking into account the effect of stress triaxiality (here, the Bridgman factor is used). In this system, the test is entirely controlled by a microcomputer which captures and analyses the image of the specimen, records the load, determines ε and σ, and readjusts the speed of the servo-hydraulic actuator in real time in order to keep constant the local compression strain-rate $\dot{\varepsilon}$.

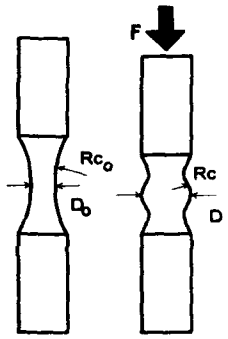

Figure 1
Axisymmetric geometry (before and after deformation) utilised for the compression tests

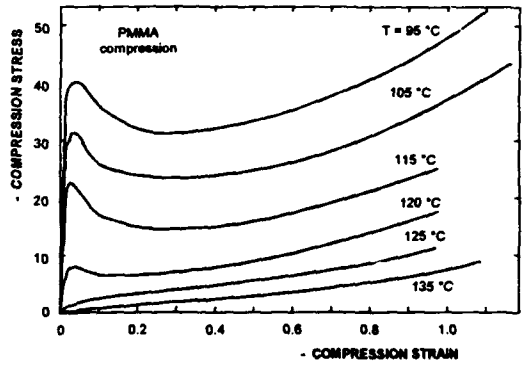

Figure 2
Stress-strain behaviour of the crosslinked PMMA under compression at a true strain-rate of $\dot{\varepsilon} = -5 \times 10^{-4}\ s^{-1}$.

EXPERIMENTAL RESULTS

Considering the very large quantity of data accumulated in this work (10 temperatures x 3 loading modes x 3 strain-rates x 3 tests), we can only give in this short paper a few examples of the stress-strain records. The curves displayed in Fig. 2 illustrate the compression behaviour for six typical temperatures from 95 °C to 135 °C. It is visible that the glass-transition temperature represents a limit between two distinct regimes. At $T < T_g$, in the glassy state, the material exhibits a sharp yield point followed by a true stress drop. After this marked transient, a long steady-state plastic regime is observed with a gradual strain hardening. In oder the avoid ultimate instabilities, tests were interrupted at $\varepsilon \approx -1$, that is for a local compression ratio $\lambda \approx 0.36$. By contrast at $T > T_g$, that is in the rubberlike state, the yield peak vanishes and the stress increases monotonously. It is one interesting feature of the testing methods employed here to be capable of investigating the

behaviour of the material in the intermediate temperature region around T_g at precisely the same true strain-rate. Thus, one can note that the transition from the glass to the rubber is very progressive, in particular to what is concerned with the plastic strain hardening which rejoins the slope of rubberlike curve without any discontinuity. Only the strain-rate sensitivity coefficient, $m = |\partial \ln \sigma / \partial \ln \dot{\varepsilon}|_g$ at yield shows a maximum at T_g, passing from 0.1 at 95 °C to nearly zero at 140 °C through a broad peak of 0.2 at 12 °C. It is interesting to note that the negligible strain-rate sensitivity above T_g is coherent with the notion of hyper-elasticity for a crosslinked polymeric network. Also, it is corroborated by relaxation experiments which show that the stress remains nearly constant if the strain is held at a fixed value during a compression test at 140 °C. The influence of the loading mode on the mechanical response was reported elsewhere in detail (8). It was found that the yield stress is correctly represented by the equation $[(\sigma_1 - \sigma_2)^2 + (\sigma_2 - \sigma_3)^2 + (\sigma_1 - \sigma_3)^2] = 6[\tau_c - \eta \sigma_H]^2$ of the pressure-modified von Mises criterion (9). In this expression, the σ_i's are the principal stresses, $\sigma_H = (\sigma_1+\sigma_2+\sigma_3)/3$ is the hydrostatic pressure. For the crosslinked PMMA, the pressure sensitivity coefficient η is equal to 0.27 ± 0.3 in the temperature range investigated, while the critical shear stress τ_c decreases from 20.2 MPa to zero as T increases from 95 to 140 °C.

DISCUSSION AND CONCLUSIONS

The curves displayed in Fig. 2 for compression, together with those presented elsewhere (8) for tension and shear, show unambiguously the progressive evolution from the plastic strain-hardening to the rubber-like consolidation through the glass-transition temperature. This characteristic property of amorphous polymers has been remarked a long time ago by authors (*e.g.* 10) who proposed the simple interpretation that the large-strain behaviour is mostly controlled by the entropic force developed by the chain sections between crosslinks when they become oriented. In other terms, the recorded stress would be the sum of three components : two components relative with the activation and propagation of plasticity at the mesoscopic scale (namely the yield transient stress σ_{yt} and the steady-state stress σ_{ss}) and one component, σ_{or}, corresponding to the back-stress from the polymeric network orientation. Since the plastic components vanish above T_g, the orientational component becomes the hyper-elastic stress in the rubber-like state. The problem is now to give a quantitative prediction for σ_{or} on structural bases.

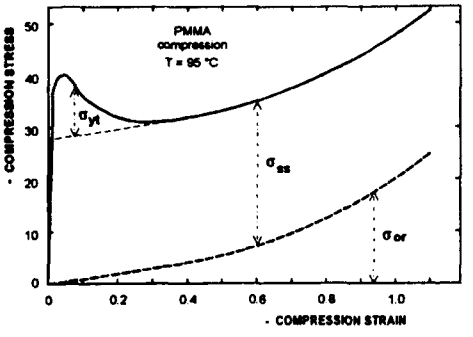

Figure 3
Decomposition of the compression stress into plastic components (steady-state σ_{ss} and yield transient σ_{yt}) and orientation component σ_{or}.

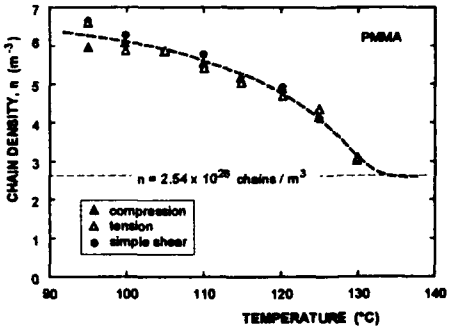

Figure 4
Variation of the chain density, n, with temperature and loading mode for the crosslinked PMMA network

Numerous models have been proposed to date for the interpretation of rubber-like elasticity. Most of them simplify the problem by considering a collection of chains constituted of freely jointed segments and crosslinked in an ideal network (11). The hyper-elastic stress is thus of entropic origin, the initial modulus of the equivalent (von Mises) stress-strain curve being equal to $3nkT$, where n is

the density of chain sections per unit volume, k the Boltzmann constant and T the absolute temperature. In the example of Fig. 3, the orientation stress curve (σ_{or}) corresponds to $3\,n\,k\,T = 9$ MPa, that is to $n = 5.9 \times 10^{26}$ chains/m^3 . Variations of n with the temperature for the three loading modes is represented in Fig. 4. It is interesting to note that above T_g the parameter n coincides quite correctly with the theoretical value, $n = 2.54 \times 10^{26}$ chains/m^3, deduced from the molecular weight between crosslinks. This proves at least the coherency of the mechanical data *vs.* the swelling data based on the same type of rubber-like elasticity models (7). At $T < T_g$, the chain density increases significantly, which indicates the development of new types of junctions between the macromolecules, presumably entanglements which play the role of physical crosslinks.

As for the large strain behaviour, a renewed interest is currently devoted to the modelling of the hyperelastic behaviour for polymeric networks under multiaxial loading modes. They are based on the notion of limited extensibility for chain sections of finite length (the average number of freely-jointed segments per chain being noted N). In particular, two approaches were recently proposed (12, 13), which differ by the organisation of the chains in the representative network cell : 8 chains per cell (12) or a random number of chains (13). In this work, we have tentatively applied the latter model to the case of the $\sigma_{or}(\varepsilon)$ curves deduced from experiments through the construction of Fig. 3. This fit provides a theoretical estimate of N which is found to vary with temperature (from $N \approx 3.5$ at 95 °C to 6 at 140 °C in compression) and loading mode (*e.g.* at 110 °C : $N_T = 5.8$, $N_C = 3.9$ and $N_S = 2.8$). Although the modelled curves thus obtained coincide quite nicely with the experimental data, they can be criticised in many aspects. On the experimental side, one should realise that the values of N rely entirely on the curvature of the $\sigma_{or}(\varepsilon)$ plots and their precision could be enhanced only if much larger strains were attained. However, even more important are the basic model ingredients. It is evident that the value $N \approx 6$ deduced from the stress-strain curves in the rubber-like regime is about 10 times too small in comparison with the value $N \approx 57$ obtained from the average molecular weight between crosslinks (or from the measured density of effective chains n). This discrepancy indicates that in the entropic model utilised, Wu & van der Giessen (13), overestimates the compliance of the network at large strains. Furthermore, the alternative model of Arruda & Boyce (12) could not do better since it predicts even more compliance. Although the modelling summarised in the present paper helps understanding the influence of temperature, crosslinking and loading mode on the mechanical behaviour of a PMMA network, the need for more realistic mechanisms in the prediction of entropic hyper-elasticity remains an open question whose study is in progress in this laboratory.

Acknowledgements
The authors are indebted to Drs. J-Cl Robinet and C Wrotecki, formerly at the Orkem Co., for kindly providing the material and for valuable microstructural information

REFERENCES

1 Bauwens-Crowet C, J Mater Sci 8 (1973) 968
2 Argon A S, Bessonov M I, Phil Mag 35 (1977) 917
3 Ouali N, Mangion M B M, Perez J, Phil Mag A67 (1993) 827
4 Hope P S, Ward I M, Gibson A G, Polymer 19 (1978) 136
5 G'Sell C, Hiver J-M, Dahoun A, Souahi A, J Mater Sci 27 (1992) 5031
6 G'Sell C, *in* 'Strength of metals and alloys', ed. McQueen et al., Pergamon, Oxford (1986) 1946
7 Flory P J, 'Principles of polymer chemistry', Cornell Univ. Press (Ithaca, NY), 1953
8 Souahi A, Thèse de Doctorat, INPL, Nancy, France (1992)
9 Haward R N, 'The physics of glassy polymers', Applied Science Publishers, London (1973)
10 Argon A S, Phil Mag 28 (1973) 839
11 Treloar L R G, 'The physics of rubber elasticity', 3rd ed., Clarendon Press, Oxford, UK (1975)
12 Arruda E M, Boyce M C, J Mech Phys Solids 41 (1993) 389
13 Wu P D, van der Giessen E, J Mech Phys Solids 41 (1993) 427

BIAXIAL HOT-DRAWING OF AMORPHOUS POLY(ETHYLENE TEREPHTHALATE)

A.M.Adams*, C.P.Buckley* and D.P.Jones**

A study has been made of biaxial drawing of amorphous, isotropic poly(ethylene terephthalate) (PET) film in the temperature region immediately above the glass transition. Results were used to examine the validity of the hybrid glass-rubber constitutive model for PET. It was found that data supported the proposed structure of the model, where glass-like and rubber-like stresses are coupled in parallel. Having isolated the rubber-like component of stress-strain curves, they were found to be fitted reasonably by the Edwards-Vilgis theory of rubber elasticity. To accommodate data for higher temperatures it was necessary for the model to include entanglement slippage which was arrested by the onset of crystallisation.

INTRODUCTION

Although there is substantial literature on the drawing of PET, there remains only limited understanding of how it should be modelled, for example in the important industrial context of manufacture of high performance films. There are a number of difficulties. *Firstly*, film manufacture primarily involves biaxial stressing at strain-rates beyond the range of commercial test equipment. *Secondly*, because film-grade PET has a molecular weight within only one order of magnitude of what is believed to be the entanglement-spacing molecular weight, in the time/temperature region of interest there are overlapping effects on the constitutive behaviour arising from several physical processes: bond-stretching, conformational entropy and entanglement slippage. *Thirdly*, it is known that during drawing molecular orientation causes crystallisation to occur and it is not known how to incorporate this correctly in a constitutive model.

In the light of this, our research on PET has the following objectives: (a) to exploit the recently developed Flexible Biaxial Film Tester (FBFT) (1) to study the hot-drawing of PET under biaxial stress and at strain-rates approaching those of practical importance; (b) to separate out systematically the contributions to constitutive response arising from the various physical mechanisms, determine how they should be separately described and then combine them together within a single constitutive model; (c) to determine the role of crystallisation and how it should be introduced into the constitutive model. Buckley *et al* described a hybrid glass-rubber constitutive model for PET near the glass transition, and demonstrated how it could be fitted to uniaxial and constant width (CW) stress-strain data obtained at constant elongation-rate (2). The present study extends the work further, by exploiting equal biaxial (EB) and other biaxial tests to test more searchingly the validity of the constitutive model, and including measurements of density change to investigate the role of stress crystallisation in modifying the mechanical response.

*Department of Engineering Science, University of Oxford, Parks Road, Oxford OX1 3PJ.
**"Melinex" Research Group, ICI Films, PO Box 90, Wilton Centre, Middlesbrough, Cleveland, TS90 8JE.

EXPERIMENTAL DETAILS

The FBFT biaxial testing machine was described at the previous conference in this series (1). The machine achieves flexibility in biaxial testing by means of computer-control of the three drive units, two controlling biaxial stretch on two perpendicular axes of a square test specimen, and the third controlling temperature through a rotary mixing valve which supplies the specimen chamber with a mix of air at different initial temperatures.

The material studied was amorphous PET film of nominal thickness 250 μm. It was produced by melt extrusion onto a water-cooled casting drum at 15°C. Number average molecular weight $M_n = 1.9 \times 10^3$ and birefringence $\Delta n = 2 \times 10^{-4}$, indicating a high degree of isotropy. Specimen edges were cut parallel to the machine and transverse directions (MD and TD respectively). They were mounted in the 24 pneumatic grips of the test machine, brought rapidly to the test temperature and maintained there for five minutes prior to testing.

All tests consisted of isothermal extension at constant elongation rates to pre-determined stretches on each axis, followed immediately by quenching to room temperature. Nominal elongation-rates used in the present work lay in the range 1 to 8 s^{-1}, and results were expressed in terms of the biaxiality ratio (θ) of the test, i.e. the ratio of elongation-rates on the two axes. The stress applied to each axis was measured by a load cell connected in series with one of the two central grips.

RESULTS AND DISCUSSION

Typical curves of true stress versus nominal strain, for constant width (CW, $\theta = 0$) and equal biaxial (EB, $\theta = 1$) straining, are shown in Figure 1 for a test temperature of 90°C, where it can be seen that the biaxiality ratio influences two major features of the curves. Yield occurs at a lower stress in EB straining than in the CW case, and strain-hardening intervenes sooner in the EB case than in the CW case. Both observations are consistent with the predictions of the hybrid glass-rubber constitutive model used in this work.

The central assumption of this model is that the free energies associated with bond-stretching and conformational change are additive, and hence their stress contributions to the total stress are also additive. The two stresses relax on different time and temperature scales through the processes of self-diffusion of backbone chain segments and of entanglement slippage respectively. However, as mentioned above, there is not a wide separation between them because of the low molecular weight of the polymer. They are resolved most readily by examining the results of drawing experiments as isometric plots of true stress versus temperature. Such a graph is shown for a nominal strain of 0.3 during EB drawing in Figure 2. Similar results have been already shown for CW drawing of PET (2). What is clearly apparent from all such data is that there exists a stress plateau in the region of 95 - 100°C. We interpret this feature as being the "rubber" plateau for the particular strain and biaxiality ratio shown. It corresponds to the region where the deviatoric bond-stretching contribution to stress is fully relaxed but the conformational stress has not commenced relaxation. Within this narrow range of temperatures the PET is deforming as a rubber network, in the manner proposed by Ward (3), with entanglements acting as physical crosslinks.

Following a procedure described previously (2), we have used the plateau stress together with experimental stress - strain curves obtained at lower temperatures where they are believed to be unaffected by entanglement slippage (at least up to nominal strains of 2.8), to estimate the underlying relation between rubber-like stress and network stretch λ^N. The resulting graphs, obtained from several CW drawing tests at a nominal elongation rate of 1/s are shown in Figure 3. They were least-squares fitted to the Edwards-Vilgis (EV) "sliplink" model of rubber elasticity. Superimposed on the experimental curves in Figure 3 is a stress - strain curve calculated for CW drawing with the EV theory, employing mean values of the fitted parameters: entanglement density $N_e = 3.6 \times 10^{26}$ m^{-3}, sliplink freedom factor $\eta = 0$, inextensibility factor $\alpha = 0.167$. The same values were then used to calculate the corresponding curve for EB drawing: this is compared with a curve deduced from

experimental EB data in a similar manner in Figure 4, where predicted and experimental CW curves for the same temperature are also shown. This Figure shows clearly how the experimental CW and EB curves differ, with EB drawing producing the more rapid strain-hardening, and it shows that the difference is accounted for approximately by the EV theory.

At higher temperatures, entanglement slippage intervenes during drawing. Its magnitude was calculated in two steps. First the procedure described above was repeated for higher temperatures, to estimate the relation between rubber-like stress and stretch. Then, treating Hencky strains due to network stretch and entanglement slippage as additive ($\ln\lambda = \ln\lambda^N + \ln\lambda^S$), for each stress the network strain $\ln\lambda^N$ was subtracted from the total strain to yield the "entanglement slippage" stretch λ^S for the corresponding rubber stress. Results obtained for CW drawing are shown in Figure 5 as plots of λ^S versus rubber stress. Two features are noteworthy. The degree of entanglement slippage increases with temperature, at given stress, as expected. At each temperature, however, the slippage does not continue indefinitely: at a certain point it is arrested - a process that appears to occur at a level of stress that decreases slightly with increasing temperature. This is believed to reflect the development of crystallinity that is known to occur during hot drawing of PET.

This crystallinity was estimated by measurement of density of specimens after the quench to room temperature, and an attempt was made to determine the criterion controlling the crystallinity level attained. Results for three biaxiality ratios (θ = 0,1,2) are shown in Figure 6, where density is plotted versus the maximum principal nominal strain at 90°C. Within the envelope of experimental scatter, the data appear to lie on a single line. Further work is required, however, to determine more precisely whether maximum strain is in fact the correct criterion for tests at a given temperature.

REFERENCES

1. Buckley, C.P., Jones, D.C. and Jones, D.P., 1991, 8th International Conference on Deformation Yield and Fracture of Polymers, Cambridge.
2. Buckley, C.P., Jones, D.C. and Jones, D.P., 1993, 9th Annual Meeting of the Polymer Processing Society, Manchester.
3. Ward, I.M., 1984, Polymer Eng. Sci, 24,724.

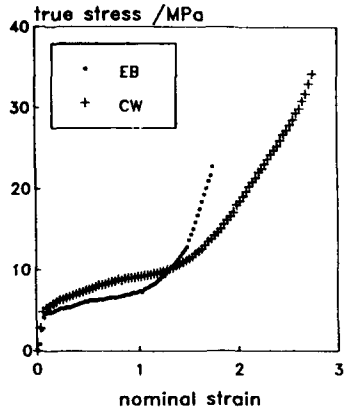

Figure 1: Stress-strain data for T=90°C and nominal strain-rate=1/s.

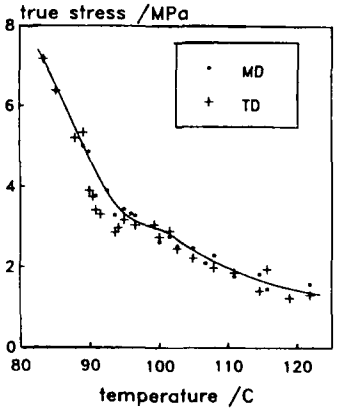

Figure 2: Isometric stress (at strain=0.3) for equal biaxial drawing at strain-rate=1/s.

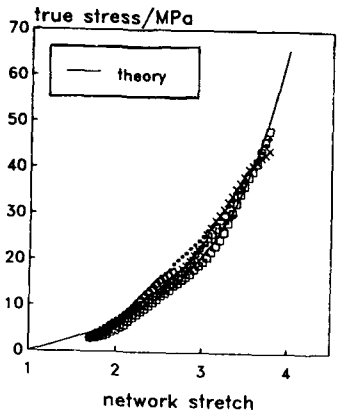

Figure 3: Network stress-strain curves estimated from CW experiments at 80-84°C, compared with fitted Edwards-Vilgis (EV) theoretical curve.

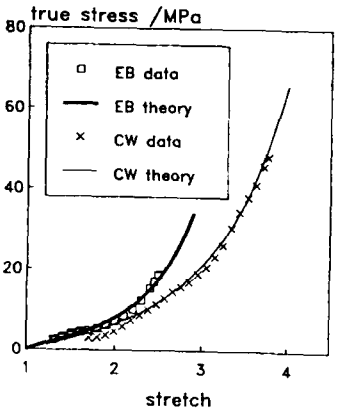

Figure 4: Network stress-strain curves for equal biaxial (EB) and constant width (CW) drawing at 83°C, from experiment and from EV theory.

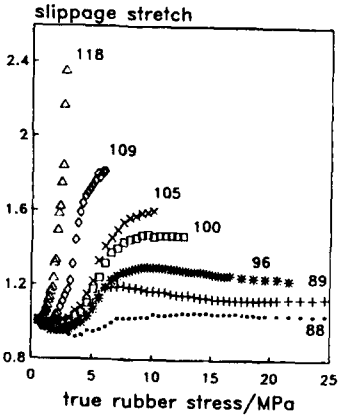

Figure 5: Entanglement slippage extension λ^s deduced from "rubber" component of CW stress-strain curves at nominal strain-rate = 1/s: various temperatures (°C).

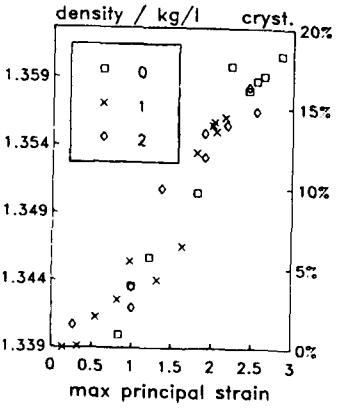

Figure 6: Density and deduced crystallinity for PET biaxially drawn at T=90°C and nominal MD strain-rate = 1/s (θ=0,1 and 2).

VOLUME RECOVERY AND PHYSICAL AGING: DILATOMETRIC EVIDENCE FOR DIFFERENT KINETICS

G B McKenna[1], C R Schultheisz[1] and Y Leterrier[2]

Torsional dilatometric experiments have been performed to study the volume recovery and physical aging responses of an epoxy glass subjected to up and down temperature jumps. The experiments show that the volume recovery kinetics are unaffected by large mechanical (torsional) deformations. Results from experiments performed at different temperatures indicate that the temperature dependence of the volume recovery kinetics and the kinetics of the evolution of the mechanical properties are different. These results are considered in light of material clock models of nonlinear viscoelasticity.

INTRODUCTION

A variety of mathematical models have been proposed to describe the nonlinear viscoelastic behavior of glassy materials, using constitutive relations in which the material time or clock is affected by an applied stress (1), strain (2) or volume change (3,4). Free volume concepts have been successfully applied to explain the volumetric recovery to equilibrium after temperature jumps (5), and Struik (6) hypothesized that the volumetric recovery after a quench from above to below the glass transition temperature would be slowed (rejuvenated) by mechanically induced changes in glassy structure, with the retardation of the volume evolution increasing as the applied stress increases. The further development of material clock models requires a full understanding of the relationships between volume recovery and the applied stresses or deformations. To this end, experiments are being performed using the NIST torsional dilatometer (7), in which the volume recovery and torsional modulus are monitored simultaneously in both up-jump and down-jump temperature histories. The torsional geometry was chosen because it results in second-order volume changes of similar magnitude to those caused by the temperature jump. Tension or compression dilatometry would result in first-order (Poisson's effect) volume changes that are significantly larger than those caused by the temperature change.

EXPERIMENT

The torsional dilatometer (7) allows simultaneous real-time measurements of temperature, volume change, torque and normal force in the cylindrical sample for arbitrary torsional

[1] NIST Polymers Division, Gaithersburg, MD, USA

[2] Ecole Polytechnique Fédérale de Lausanne, Lausanne, Switzerland

deformation histories. The single sample used in this study was 115 mm in length and 15.3 mm in diameter, and composed of a model epoxy (DGEBA/polypropylene oxide) that is fully described elsewhere (8). The glass transition temperature of the epoxy is 42.4°C as measured by differential scanning calorimetry at 20°C/min immediately following cooling at the same rate.

The temperature in the dilatometer is controlled by fluid from a constant-temperature bath circulating through a jacket surrounding the dilatometer chamber, and the dilatometer temperature is measured using a platinum resistance thermometer embedded in the wall of the dilatometer chamber. Temperature jumps are accomplished by changing from an initial bath (at temperature T_1) to a final bath (at T_0) using quick disconnects. The high precision ($\pm$ 1 mK) final bath, coupled with an enclosure that maintains the dilatometer surroundings at 27.0 $\pm$ 0.1°C, controls the temperature inside the dilatometer chamber to within $\pm$ 10 mK. The temperature of the initial bath is controlled to $\pm$ 0.1 K, and the magnitude of the temperature jump is controlled by adjusting the temperature of the initial bath. The sample was first annealed at 45°C, and the sample was then equilibrated at each initial temperature before applying the jump. In earlier experiments (9), the final temperature was T_0 = 35.5°C, with initial temperatures of T_1 = 34.8, 33.8 and 32.8°C for up-jumps and T_1 = 38.8, 39.8 and 40.8°C for down-jumps. A further set of experiments has used a final temperature of T_0 = 32.8°C with initial temperatures of T_1 = 30.8, 31.8, 33.8 and 34.8°C, in order to provide better resolution in both the time and the torque measurements. These lower temperature experiments require approximately 2×10^6 s (23 days) for the material to achieve equilibrium after a temperature jump. The origin of the aging time (t_e) is taken at 450 s after the jump to correct for the time required for the dilatometer to achieve the final temperature.

Sequential torsional strains were applied following Struik's (6) protocol. The torque was first applied for a time t_1 and then removed for $10t_1$; each successive torque application was for twice as long as the previous torque, and the post-torque relaxation time was always ten times as long as the torque itself. This protocol ensures that at each torque application the material has no memory of the previous deformation, and that the material does not change significantly during each deformation step, so that the torsion response provides a snapshot of the material at each aging time. Experiments with a final temperature of 35.5°C were performed at torsional strains of γ = 0.03 and γ = 0.05; the first torque was applied at an aging time of t_e = 450 s with t_1 = 45 s. Experiments with a final temperature of 32.8°C were performed with γ = 0.03; the first torque was applied at t_e = 910 s with t_1 = 90 s.

RESULTS

The volume evolution is shown in Figure 1 for an experiment with T_1 = 32.8°C, T_0 = 35.5°C, and γ = 0.05. Note that the solid line in the figure is the underlying volume recovery from an experiment with T_1 = 32.8°C, T_0 = 35.5°C, and γ = 0.03, which indicates that the magnitude of the applied strain and associated volume change has little effect on the underlying volume evolution, even at these relatively large strain levels. This result is consistent with prior work (10,11), in which it was argued that the underlying nonequilibrium thermodynamic state of the glass (as indicated by the changing volume) is decoupled from the mechanical stimuli.

At each torque application, the torsional stress relaxation was recorded and fit to a stretched exponential or Kohlrausch-Williams-Watts function (12,13) as

$$\sigma = \sigma_0 \exp\left(-(t_e/\tau)^{0.3}\right)$$

where t_e is the time after the application of the torque. The values of τ and t_e at each step were used to calculate aging time shift factors (a_{te}) using horizontal shifts of the stress data. The changing shift factors reflect the evolution of the mechanical response of the glass as a function of aging.

Figures 2 and 3 depict the aging time shift factor as $\log(a_{te})$ versus the volume departure from equilibrium for experiments with $T_0 = 35.5°C$ and $\gamma = 0.03$, indicating the relative rates of evolution of the volume and the mechanical response. It can be seen that in the down-jump experiments, the mechanical response achieves its equilibrium before the volumetric response, while in the up-jump experiments, it appears that the opposite is true. However, Figure 4 shows similar data from experiments with $T_0 = 32.8°C$ and $\gamma = 0.03$, and it appears that for both down and up-jumps, the evolution of the volume and the mechanical properties occur at similar rates. While experiments at $T_0 = 35.5°C$ (9) and previous work at $T_0 = 33.5°C$ (11) show differences in the time scale of evolution for the mechanical and volumetric responses, those at $T_0 = 32.8°C$ do not. This result suggests that the temperature dependence of the volume recovery kinetics and the mechanical evolution kinetics (physical aging) are different. Further work is required to explore these differences.

CONCLUSION

Results from up and down temperature jump experiments on an epoxy glass using the NIST torsional dilatometer have been presented, showing that the volume recovery kinetics are unchanged by the application of large mechanical deformations. Furthermore, it appears that the temperature dependence of the volume recovery response differs from that of the mechanical evolution (physical aging) response. Experiments comparing the evolution of the mechanical response with the enthalpy recovery have also shown that these properties evolve at different rates during physical aging (14). Such results suggest that the structural state of the glass is decoupled from the mechanical stress field and that different mechanisms are responsible for the structural recovery and the physical aging of the viscoelastic response. The decoupling of the volume (structure) from the mechanical stress field suggests that volume clock constitutive models will be inadequate for the description of the mechanical behavior of polymer glasses.

REFERENCES

1. Bernstein B and Shokooh A, J. Rheology 24 (1980) 189.
2. McKenna G B and Zapas L J, J. Rheology 23 (1979) 151.
3. Shay Jr. R M and Caruthers J M, J. Rheology 30 (1986) 781.
4. Knauss W G and Emri I, Polymer Eng. Sci. 27 (1987) 86.
5. Kovacs A J, Aklonis J J, Hutchinson J M, Ramos A R, J. Polymer Sci. Polym. Phys. Ed. 17 1097.
6. Struik L C E, Physical Aging in Amorphous Polymers and Other Materials Elsevier Amsterdam 1978.
7. Duran R S and McKenna G B, J. Rheology 34 (1990) 813.
8. Lee A and McKenna G B, Polymer 31 (1990) 423.
9. McKenna G B, Leterrier Y, Schultheisz C R, Polymer Eng. Sci. (1994) in press.
10. Lee A and McKenna G B, Polymer 31 (1990) 423.
11. Santore M M, Duran R S, McKenna G B, Polymer 32 (1991) 2377.
12. Kohlrausch F, Pogg. Ann. Phys. 12 (1847) 393.
13. Williams G and Watts D C, Trans. Faraday Soc. 66 (1970) 80.
14. Roe R-K and Millman G M, Polymer Eng. Sci. 23 (1983) 318.

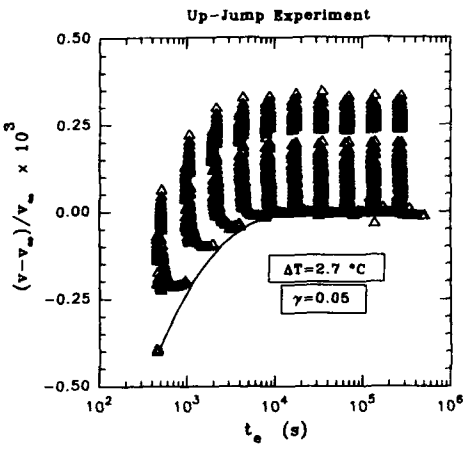

1. Volumetric response to an up-jump temperature history and sequential torque application. $T_1 = 32.8°C$, $T_0 = 35.5°C$ and $\gamma = 0.05$. Baseline volume evolution fit from experiment with $T_1 = 32.8°C$, $T_0 = 35.5°C$ and $\gamma = 0.03$.

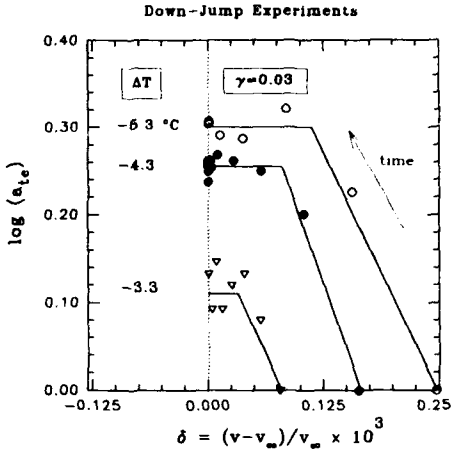

2. Aging time shift factor (a_{te}) versus deviation from equilibrium volume (δ) for down-jump temperature histories. $T_0 = 35.5°C$ and $\gamma = 0.03$.

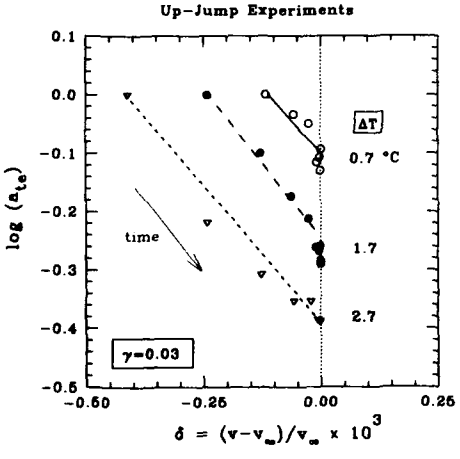

3. Aging time shift factor (a_{te}) versus deviation from equilibrium volume (δ) for up-jump temperature histories. $T_0 = 35.5°C$ and $\gamma = 0.03$.

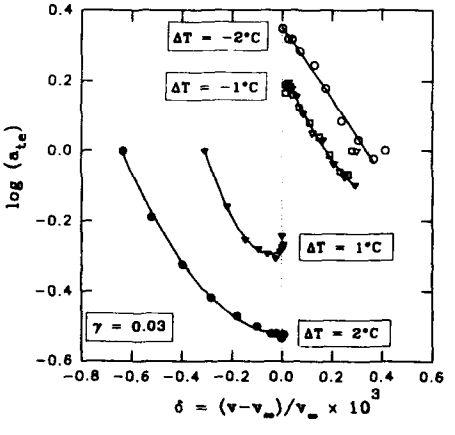

4. Aging time shift factor (a_{te}) versus deviation from equilibrium volume (δ) for up and down-jump temperature histories. $T_0 = 32.8°C$ and $\gamma = 0.03$.

THE EVOLUTION OF CRACKS IN BRITTLE SOLIDS

Derek Hull*

The geometrical conditions for the evolution of cracks on smoothly curving surfaces are outlined with particular reference to the no-twist condition. Crack growth round fibres and particles is used to illustrate the implications of the no-twist condition.

INTRODUCTION

Fracture mechanics is concerned largely with the critical conditions for the growth of a pre-formed (static) crack although, in reality, a new crack is usually nucleated at the tip of the preformed crack.

Fractography, on the other hand, involves primarily the description and interpretation of a fracture surface produced by a moving crack. The topology of a fracture surface is dependent on many microstructural and testing variables so that fractography offers the possibility of understanding the influence of these variables on the mechanics of crack growth.

The path of fracture is controlled mainly by the shape and position of the growing crack and the influence of applied loads on the static and dynamic stress fields. In isotropic, homogeneous, amorphous, brittle solids, such as inorganic glasses and brittle thermosetting resins, crack growth occurs with a minimum of deformation at the crack tip and the influence of microstructure only becomes important close to atomic dimensions. In brittle materials there is an important geometrical constraint (the no-twist condition) on crack growth which has a profound influence on the fracture surface topology. This is most readily demonstrated in glassy solids and in this paper we give an outline of the no-twist condition and relate this to observations typical of the fracture surface morphology in a brittle epoxy resin such as Ciba Geigy Araldite LY1927 epoxy resin mixed with hardener Araldite HY1927 in proportions 100:36 by weight.

* Department of Materials Science & Engineering, University of Liverpool, U.K.

NO-TWIST CONDITION

The conventional definitions of tilt and twist are illustrated in figure 1. The orientation of a crack tip AB at any point P, with reference to the plane of fracture ABCD, is described by three orthogonal vectors f_1 normal to the crack plane, f_2 parallel to the direction of crack propagation and f_3 tangential to the crack tip. In practice, for a continuously growing crack in a brittle solid, the type of crack twisting illustrated in figure 1b cannot occur ; this is the no-twist condition (1). To propagate on a new plane, as shown in figure 1b, the crack must renucleate. The no-twist condition requires that during evolution of the crack there is no rotation of the crack tip about f_2. In contrast, there is no restriction on tilting of the crack which can occurs by rotation of the crack plane about f_3.

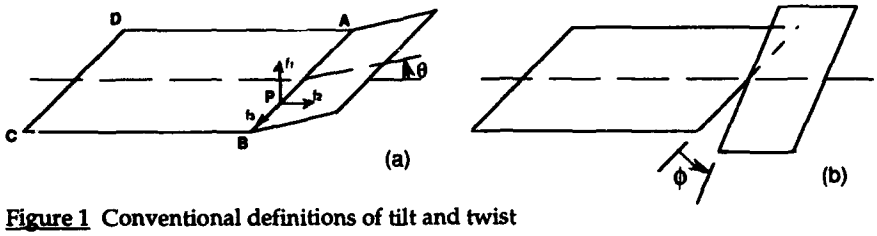

Figure 1 Conventional definitions of tilt and twist

In reality, the crack front is rarely, if ever, straight and the surface of the crack is rarely, if ever, planar. A more realistic representation of a crack, forming a smoothly curving surface, is illustrated in figure 2. The vectors f_1, f_2, and f_3 change continuously and the no-twist condition applies to each elementary length of the crack tip. In principle, any smoothly curving surface can be formed by the growth of a non-twisting crack but the path and orientation of the crack tip are strictly limited. Mapping of the evolution of the crack is achieved by determining the principal directions of curvature on the surface and then plotting the *lines of curvature*. Two orthogonal sets of lines result as shown in figure 3. The no-twist condition requires that the crack must grow such that the crack tip is always parallel to one set of lines of curvature.

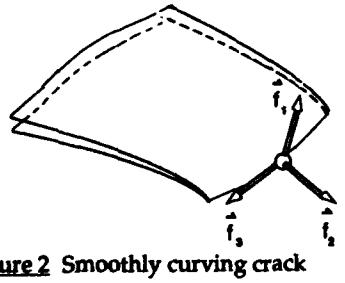

Figure 2 Smoothly curving crack

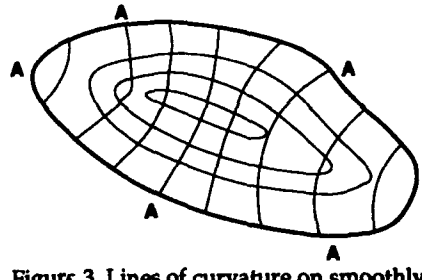

Figure 3 Lines of curvature on smoothly curving crack A-A-A

These ideas have been applied to a number of continuously curving surfaces including prismatic surfaces and surfaces of revolution, of which the Hertz cone is a particular example (1,2). For the purposes of this paper we consider the problem of the growth of a crack in the presence of either a fibre or a spherical particle, making the assumption, for

convenience, that there is a strong bond at the interface so that crack growth occurs through the matrix.

CRACKS GROWING ROUND FIBRES AND PARTICLES

For a planar crack growing normal to a fibre (figure 4a) there are no geometrical restrictions to the position of the crack since there is no rotation about f_2. The crack can expand round the fibre and join up on the other side. When a planar crack intersects a fibre lying parallel to the plane (figure 4b) the situation is much more complex. If the crack front is straight and parallel to the fibre the crack can grow round the fibre purely by tilting (rotation about f_3). This is achieved, in mechanics terms, by the influence of Mode II stresses and is an example of crack growth on a prismatic surface. However, for a curved crack front, even if it is lying in a planar surface, there is no 'no-twist surface' for the crack to pass the fibre. The only way the crack can avoid the fibre without generating twist forces at the crack tip is for the crack tip to straighten and form parallel to the fibre. Otherwise, if the curved crack is forced to move out of the original plane, twist forces are created, i.e. Mode III stresses act at the crack tip, and the crack will split up onto a number of fracture surfaces divided by river lines (figure 4c).

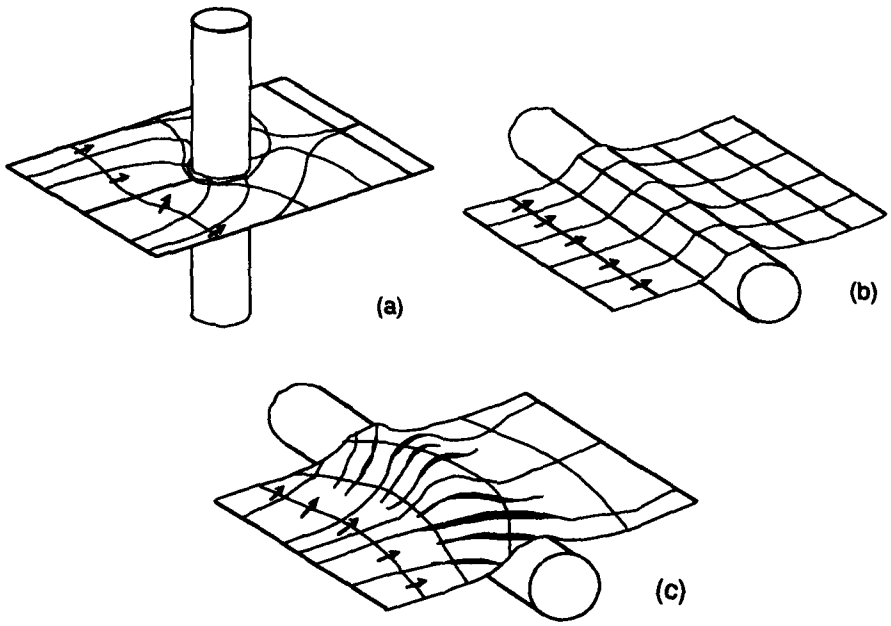

Figure 4 Cracks around fibres

An example of a surface which has formed with a predominantly Mode I loading but with a small amount of Mode III, generated using the type of approach described by Sommer (3), is illustrated in figure 5 (nb the geometry of the river lines involves additional complexity associated with the no-twist condition).

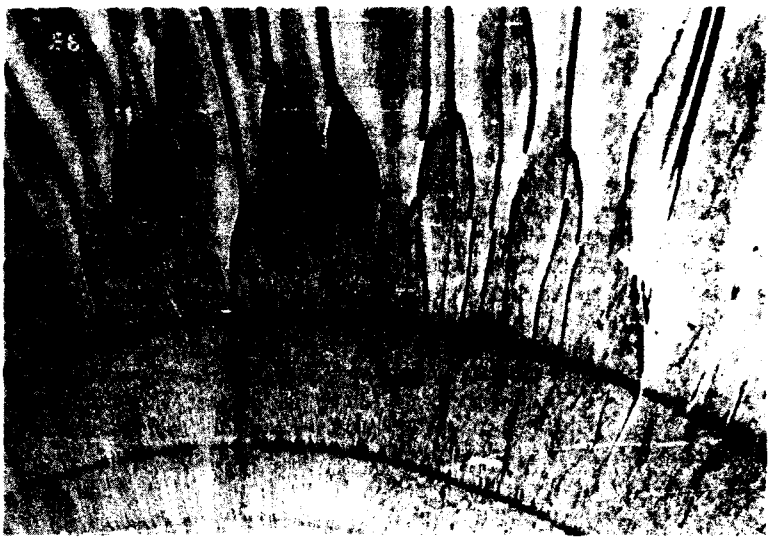

Figure 5 River lines on the fracture surface of a brittle epoxy resin formed in mixed Mode I/Mode III loading conditions.

The same approach can be used for particulate barriers to crack growth. In geometrical terms the crack can pass the particle in the way illustrated in figure 4a. However, any movement of the crack out of the plane leads to strict geometrical constraints if the no-twist condition is to be satisfied. It is possible to envisage a smooth continuous surface around a particle such that an initially planar crack can grow round the particle and form a planar crack on the other side. To determine the successive positions of the crack front to achieve this without twist requires determining the lines of curvature on this surface (a complex mathematical problem). In practice it seems likely that the elastic energy driving the crack will result in a crack path involving twist forces which then lead to the formation of river lines.

One can envisage many situations, particularly in the context of crack nucleation, where forces driving crack growth are not compatible with evolution of the crack satisfying the no-twist condition. This has important consequences for the interpretation of fracture mechanics experiments.

REFERENCES

1 Hull D, Int J Fracture 62 (1993) 119
2 Hull D, Int J Fracture (submitted)
3 Sommer E, Eng Fract Mechanics 1 (1969) 539

FRACTURE SURFACE ENERGY AND CRAZE FIBRIL STRESS IN PMMA IN WATER.

by R. Schirrer, L. Josserand *and P. Davies **

The fracture properties of Polymethylmethacrylate (PMMA) in water are of great importance in submarine applications. Compact tension specimens immersed in water have been loaded on a tensile machine and crack tips have been observed by means of optical interferometry during propagation. Fracture stress intensity factors, and plastic zone size have been measured as a function of loading time and crack speed in water. The results have been rationalized in terms of craze stress and craze life time at the crack tip, and in terms of a stress activated process of craze fibril growth and rupture. Water increases the fracture toughness, in spite of the fact that the microscopic craze stress and craze fibril life time decrease at the crack tip.

INTRODUCTION:

Crazing and fracture properties of polymers are strongly influenced by the environment: stress cracking and crazing due to chemical effects, crack-tip plasticizing by liquids or solvent gases, surface energy lowering by tensio- active liquids, molecular mobility modification by hydrostatic liquid pressure, etc...Environmental rupture has been widely studied, particularly from the experimental point of view, and general rules are known concerning chemical and physical effects of gases and liquids on polymer fracture. Nevertheless, most of these studies use very simple fracture tests to quantify the environmental effects, and although rather coarse values of environmental assisted fracture toughness are known, real time microscopic crack-tip behaviour under harsh environmental conditions has been much less studied. This is because special experimental equipment is required to investigate the material in this case. References 1 to 7 give an overview on the subject. In the present study, the single craze at a crack-tip propagating in PMMA in air and water has been investigated on a microscopic scale. Local material properties like craze fibril stress and craze fibril life-time have been investigated by means of optical interferometry. The material used was Altuglas PMMA (cast sheets). The advantage of this material is that there are already a great number of general mechanical property measurements available from many authors. It was measured that water decreases the mechanical properties of PMMA by means of a plasticizing mechanism, but the changes are rather small. As shown below, the fracture properties are much more affected than the small deformation mechanical properties.

* ICS(CRM-EAHP) 4, rue Boussingault F-67000 STRASBOURG,
** IFREMER, BP 70, 29280 PLOUZANE

FRACTURE PROPERTIES IN WATER

All the results shown below concern crack and/or craze propagation in PMMA immersed in water during the propagation. Fracture toughness has been measured with 30 mm width standard Compact Tension Specimens. The crack and craze velocity were measured with a telescope fitted onto a camera. The sample was illuminated with white light between two crossed polarizers to vizualise the birefringence due to the stress fields. Smaller samples (10 mm width) were observed by means of real time optical microscopic interferometry [8]. The samples were immersed in water by means of a small transparent tank fitted to the grips. Figure 1 shows one experimental setup. The samples were pre-cracked with a milled saw cut, and subsequently the crack was sharpened (in air) with a 100 Hz fatigue loading. Figure 2 shows by means of birefringence the crack and craze tips. Both tips can be separated and individually followed during the process if the craze (or plastic zone) is long enough to be resolved by the optical telescope.

Standardized fracture toughness measurements do not need the monitoring of the crack speed or length in a real time experiment. Nevertheless, the results of such simplified measurements are rather dispersed, one of the major reasons being the unknown crack-tip starting point on the load-deflection curve. Moreover, it is well kown that the fracture toughness depends strongly on the crack velocity, which may vary over several decades at the propagation starting point. More accurate results are obtained when considering the fracture energy as a function of crack speed for brittle material, or as a function of crack length for ductile materials. In the case of brittle materials like PMMA, the crack-tip velocity must be kept constant until quasi-stationary propagation is reached. The K_1 or G_1 value obtained for the particular velocity is then an intrinsic material property.

Figure 3 shows the values of K_1 versus velocity for a crack-tip propagating in air compared to that propagating in water. The toughness in water is about twice that in air, especially at low propagation speed. Careful examination of the experimental procedure showed that the loading history (i.e. loading rate) influences strongly the K_1 value achieved as a function of crack speed. This is in contradiction with the behavior in air. Surprisingly, a one decade change in loading rate doubles the toughness in the 0.001 mm/s velocity range. Consequently the K_1 versus velocity is no longer an intrinsic material property. There exists a knee in the K_1 curve, which corresponds to the velocity above which the crack-tip propagates steadily without increasing the plastic zone size at its tip.

The toughness varying with loading rate indicates that the plastic zone at the crack tip depends probably also on loading rate. Figure 4 shows the length of the plastic zone as measured with both techniques. The size increases with decreasing loading rate: at low rates, the crack tip yields and crack-tip blunting decreases the local stress intensity. Consequently, a higher external stress is needed to propagate the crack. Finally, the plastic zone size stabilizes and the crack+plastic zone system propagates steadily. Interferometric experiments showed that the plastic zone is a craze, as it is in air, where its size is loading rate independent.

CRACK TIP MODEL, CRAZE MICROMECHANICS

The material near the loaded crack tip is subjected to a stress field which is divergent at the tip. Due to that field, the material is damaged near the tip, and produces either a

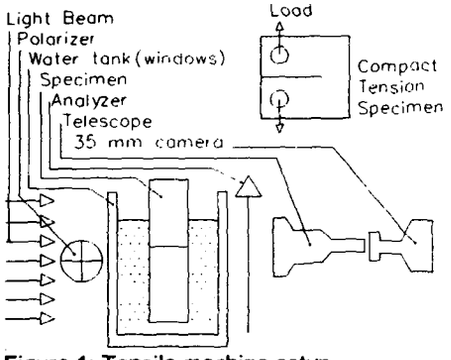

Figure 1: Tensile machine setup

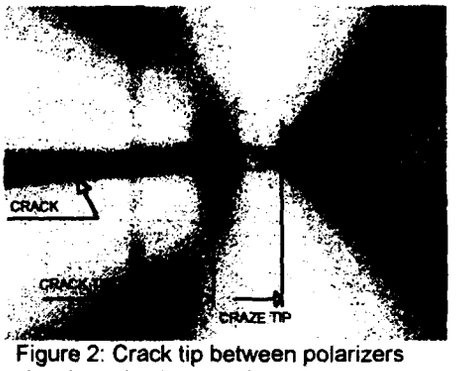

Figure 2: Crack tip between polarizers showing plastic zone tip.

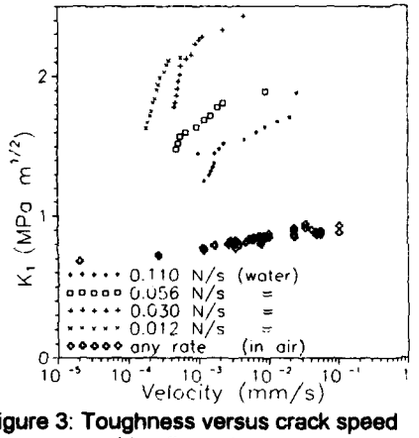

Figure 3: Toughness versus crack speed and loading rate.

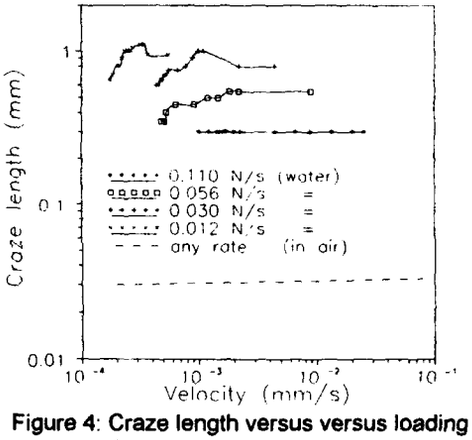

Figure 4: Craze length versus versus loading rate.

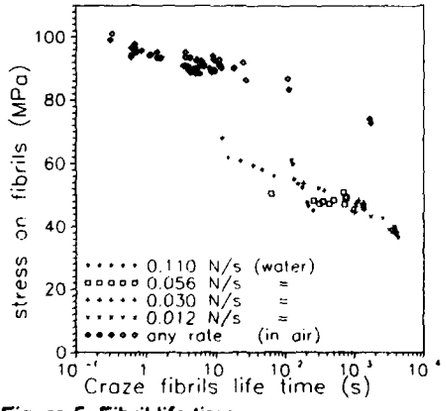

Figure 5: Fibril life time (all loading rates are plotted)

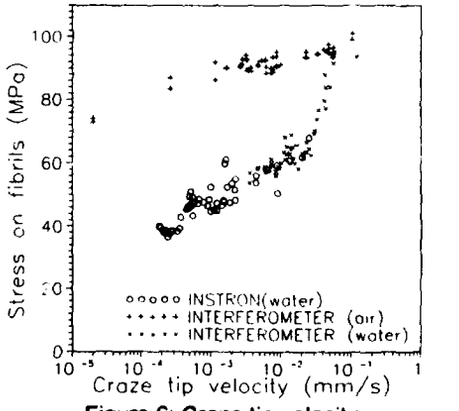

Figure 6: Craze tip velocity (all loading rates are plotted)

craze, or shear lips, or a complex structure of damaged material. In the case of the craze, which corresponds to the case of PMMA in water, stresses and strains in the vicinity are known [9]. In particular, it has been shown that the stress applied to the craze fibrils is rather constant (with a small peak at craze tip and end), and that its mean value σ_c is a function of the stress intensity factor K_1 and craze length S:

$$\sigma_c^2 = \pi K_1^2/8S.$$

Craze fibrils originate from bulk by cavitational mechanisms at the craze tip, and subsequently they grow mainly by extracting fresh material from the bulk. To some extent, they also grow by an extension mechanism. As they are subjected to a stress they break after a while. Each fibril is subjected to the stress during the time it takes for the craze to move over one craze length [9]. In a stationary propagation this time τ_c, which depend on the stress σ_c, is a function of the crack-craze velocity v_c:

$$\tau_c(\sigma_c) = S/v_c \text{ and hence } K_1(v_c) = (8\tau_c v_c/\pi)\sigma_c^{1/2}$$

Craze length, propagation velocity, and K_1 values are recorded during the experiments. Hence, the local, intrinsic material properties governing fibril extraction at the craze tip, σ_c and those governing fibril rupture, $\tau_c(\sigma_c)$ can be inferred. Figure 5 shows the craze fibril life time as a function of the stress applied to the fibrils. It appears that the loading rate is no longer a relevant parameter, as it was in the K_1 or S plot. This proves that the fibril life time is an intrinsic material property, as it is geometry independent. The influence of the loading rate on K_1 and S values is due to the fact that during the measurement macroscopic stationary rupture conditions are not reached. Therefore, the transient conditions under which K_1 and S were measured are variable and unknown. Locally, at the fibrils level, even under these macroscopic transient conditions, real intrinsic material properties govern the rupture. The plot shows also that the fibrils life time in water is 3 orders of magnitude lower than that in air at a given stress on the fibrils.

Figure 6 shows the craze tip velocity as a function of the stress on the fibrils. This is the second relevant intrinsic material property, governing the cavitation of the bulk leading to fibrils. Again, the loading rate is no longer a relevant parameter for the same reasons. The velocity in water is also about 3 orders of magnitude faster than in air, and the tensile machine measurement overlap very well the interference measurements. There is an interesting zone at 10^{-1} mm/s, where the values in water rejoin these in air. This corresponds to the velocity above which water cannot flow fast enough around the fibrils to reach the craze tip, or diffuse fast enough into the fibrils to soften them.

[1] Y.M. MAI, J. Mater. Sci. 10(1975)943-954
[2] D. PUTZ and G. MENGES, The British Polymer Journal, 10(1978)69-73
[3] P.J. BURCHILL and R.H. STACEWICZ, J. Mater. Sci. Letters 1(1982)446-450
[4] R.G. HILL et.al. J. Mater. Sci. 19(1984)1904-1916
[5] J. SHEN et.al. Polymer, 26(1985)511-518
[6] L.S. SMITH and J.A. SAUER, Plastics and Rubber Processing 6(1986)57-65
[7] V.A. KEFALAS and A.S. ARGON, J. Mater. Sci. 23(1988)253-258
[8] R. SCHIRRER and G. GALLERON, Polymer, 29(1988)634-640
[9] P. TRASSAERT and R. SCHIRRER J. Mater. Sci. 18(1983)3004

THE RELATIONSHIP BETWEEN SLOW CRACK PROPAGATION AND TENSILE CREEP BEHAVIOUR IN POLYETHYLENE

P.A. O'Connell*, M.J. Bonner*, R.A. Duckett* & I.M. Ward*
L.J. Rose+, A. Channell+

The velocity of propagation of the neck in samples of polyethylene film during cold drawing has been studied for a range of applied stresses. In all cases it was found that the neck velocity decreased with decreasing stress, becoming negligible below an apparent critical stress which depended on the grade of polyethylene. The neck propagation data, together with true stress : strain : strain rate data from a parallel investigation into the creep behaviour, have been used to test a new computer based model for the mechanism for craze growth during the initiation of slow crack propagation in polyethylene.

INTRODUCTION

The time scale for the growth of a craze at the tip of a crack or flaw can be a significant fraction of the total failure time of a sample of polyethylene subjected to a small constant stress. It is therefore important to understand the mechanisms involved in the growth of such a craze. It has shown that the crack velocity is constant until fibril failure occurs in those fibrils at the base of the craze, after which the crack accelerates to ultimate failure (Bhattacharya et al (1)). These fibrils grow by drawing-in of new material at the bulk/fibril interface and the subsequent creep of this drawn material (Cawood et al (2)).

The work to be described in this paper concentrates on measuring both the creep response and drawing behaviour of a range of materials and then linking these with crack growth data to model more quantitatively the processes involved in craze growth up to crack initiation.

For the purpose of this paper it is helpful to define the stresses which occur at or near the craze. Samples are loaded to an applied *bulk* stress. Due to the stress concentration effect of the crack a higher *effective* stress acts along the bulk/fibril interface. Finally the *true* stress acting on any element of the fibril is given by the product of the effective stress and the draw ratio of that element.

EXPERIMENTAL

Materials. Data from two grades of polyethylene are presented here.; a linear

* IRC in Polymer Science and Technology, University of Leeds, Leeds LS2 9JT
+ BP Chemicals, Grangemouth, Stirlingshire

high density homopolymer (HP) quenched cooled at >80C/min and a moderately branched copolymer (CP) cooled at 2C/min.

Yield neck propagation (YNP). Dumbbell samples are pre-necked at one end of the gauge length and this end attached to a fixed support with the free end loaded to the required nominal stress. The movement of the neck is then followed as a function of time. From this, the rate at which the neck moves through the isotropic section i.e. the rate of conversion of isotropic to drawn material, may be calculated.

Creep behaviour. Creep tests have been carried out on the drawn material using samples drawn to a number of different draw ratios and loaded over a range of stresses. By means of a displacement transducer attached to the lower end of the sample, the incremental strain and strain rate were followed. The true stress, total strain and strain rate were then determined and followed throughout the course of a run.

Crack growth data. Crack growth data have been supplied by BP Chemicals, Grangemouth using the single edge notch (SEN) testing geometry over a range of bulk stresses (Table 1). Measurements were taken of the crack opening displacement (COD) as a function of time, where the COD is the length of the base fibrils.

RESULTS

Yield neck propagation. It was found that the neck accelerates with time, which is associated with an increase in true stress due to creep in the undrawn section. The data were extrapolated to zero time to give the velocity, or conversion rate, at zero isotropic creep strain.

Data for the variation in the $\log_e$ (conversion rate) with stress for the HP are shown in Fig 1. All samples showed a linear region at high stresses with similar gradients; in general the higher crystallinity materials show a lower conversion rate at any given stress. Each material shows an apparent critical stress below which the conversion rate becomes very sensitive to the applied stress; i.e. this critical stress is essentially a threshold stress for YNP.

Creep behaviour. As the strain in the sample increased, the true stress was calculated assuming constant volume. The whole test was then represented graphically by a series of points in stress : strain :strain rate space. By using a wide range of initial conditions it was found that the data from each creep test described reproducible trajectories across a unique stress : strain : strain rate surface. The creep data also showed that in this region of the surface there is a maximum achievable draw ratio at which the sample fails.

Given that the surface is unique, then for a sample subjected to any given initial conditions its subsequent route over the surface is unique and moreover the time to reach the maximum draw ratio and hence failure is uniquely determined.

Crack growth data. The crack growth data show an initially linear region followed by an accelerating rate. The gradient of the linear region gives a COD rate, while the upturn is associated with the first signs of fibril failure and thus gives a failure time. Extrapolation to zero time gives a positive y-intercept and this is associated with an initial damage zone formed during notching.

MODEL FOR BEHAVIOUR

Computer routines have been written which model the formation and growth of a craze fibril. The computer model is recursive, i.e. growth is calculated in successive time intervals. In each time increment an element of material is drawn in at a user defined rate from both interfaces to its natural draw ratio. Using the strain in this element and the effective stress (another user defined variable), the true stress acting on this element can be found and the associated strain rate calculated from interpolation of the creep data. The element is allowed to creep at this rate for an increment of time. The new strain can then be calculated for this element, leading to a new true stress and hence strain rate, the values of which are used on the next recursion. This process is carried out for each element in the fibril, with each recursion adding a new element. We thus end up with a series of elements of differing draw ratio, with the draw ratio increasing towards the centre (mid-rib) of the fibril. It should be noted that the initial mid-rib element is set to be equal to the size of the initial damage zone as measured from the crack growth data. The crack opening displacement (COD) is simply the sum of all the individual elements.

We then calculate the COD rate at a given effective stress by following the COD (fibril length) as a function of time and determining the resulting gradient. The mid-rib element, which has been creeping for the greatest length of time naturally has the largest draw ratio. The time for the mid-rib element to reach the limiting draw ratio at a given stress determines the failure time of the fibril at that stress.

Application to experimental data. The computer model was run using a range of effective stresses, and at each stress, the time for the mid-rib element to reach the limiting draw ratio for that material (i.e. fibril failure) was found. The variation of failure time with effective stress was then determined. By comparing the experimental failure time from the SEN tests with this modelled failure time - stress relation the effective stress acting on the fibril via the bulk/fibril interface for any given bulk loading was inferred. The results for the quench-cooled HP and slow cooled CP are given in Table 1.

At this stage we could use the creep, YNP and effective stress data to calculate the COD rate data for comparison with experiment. Alternatively, we have chosen to use the creep and COD rate data and the effective stress to calculate the conversion rate at the fibril/bulk polymer interface. The computer model was run at the inferred effective stress for a given bulk loading using a range of conversion rates. For each conversion rate the model predicts a corresponding COD rate. Comparison of this with the experimental COD rate identifies the 'inferred conversion rate' corresponding to that particular effective

stress (Table 1). These calculated conversion rates are then compared with the experimental stress : conversion rate data found for quenched HP from the YNP work, Fig 1.

Although both curves show the same form of variation, with a reasonably linear region at high stress and an apparent threshold stress at lower stresses, the conversion rates inferred from the model are significantly below those measured in the neck propagation studies. This has been attributed to a plane strain constraint effect in the thicker sections of the SEN samples, increasing the effective yield stress of the material and thereby reducing the conversion rate.

REFERENCES

1. Bhattacharya S.K. and Brown N. J. Mat. Sci. 19 (1984) 2519
2. Cawood M.J., Channell A.D. and Capaccio G. Polymer. 34 (1993) 423

ACKNOWLEDGEMENTS

P. O'Connell was supported by a research contract with BP Chemicals Ltd, Research and Development, Grangemouth, Stirlingshire, Scotland FK3 9XH and M. Bonner is an SERC CASE student sponsored by the same organisation.

Material	Bulk stress (MPa)	Inferred effective stress (MPa)	Inferred conversion rate (μm/sec)
HP : Q	2	5.15	0
HP : Q	3	7.3	3.17×10^{-5}
CP : S	3	7.98	2.46×10^{-5}
HP : Q	4	15.47	4.14×10^{-4}
CP : S	4	14.83	1.37×10^{-4}
HP : Q	4.5	18.38	8.21×10^{-4}
CP : S	4.5	19.26	5.59×10^{-4}

Table 1 : Experimental and inferred data

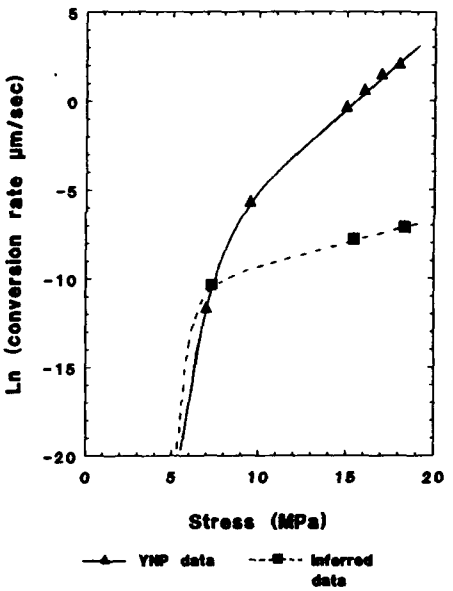

Fig 1 : Ln (conversion rate) : stress relation for HP : experimental and inferred

STATISTICS OF ATOMIC VIBRATIONS AND FRACTURE KINETICS

V I Vettegren and I I Ibrogimov*

We studied the nature of the inclinations from Zhurkov's fracture kinetics formula at the specific temperatures T_t and T_b. These inclinations were explained by the changes in the statistics of the fundamental atomic vibrations' modes from quantum to classic one.

About 40 years ago it was found the formula connecting the life time τ of mechanically loaded by stress σ solid states with their temperature T see (1-3):

$$\sigma = \frac{U_0}{\gamma} - \frac{kT}{\gamma} \ln \frac{\tau}{\tau_0} \qquad (1)$$

Zhurkov's formula (1) is valid for metals, alloys, crystals, polymers, glasses, composites and other materials.

According to modern hypothesis see references (1-3) the life time τ is determined by the probability of the interatomic bonds dissociation by the thermal fracture fluctuations. These fluctuations take the energy from the atomic vibrations' modes. In view of this hypothesis the formula (1) reflects the connection between the mean time τ needed to create fracture fluctuations. mechanical stress and material temperature.

It follows from form. (1) that mechanical strength changes proportionally to temperature when τ =const. However last years' investigations shown that there are certain inclinations from form. (1) at the characteristic temperatures T_t and T_b.

In fig. 1 are shown examples of the mechanical strength dependencies of high oriented polyethylene (PE) and polycaproamide (PA-6) filaments on temperature.

One can see that the strength and temperature are connected by nonlinear dependence at $T < T_t$, while at $T > T_t$ the strength is proportional to temperature although proportional coefficient grows at $T = T_b$.

* A.F. Ioffe Physical-Technical Institute of the Russian Academy of Sciences, Saint Petersburg, Russia.

In order to clarify the nature of these deflections we compare the strength-temperature dependencies with the same dependencies of thermal expansion coefficient (t.e.c.) for the lengths of regularity sequences of trans-isomers in polymer molecules. This expansion is caused by the changes in the valence angles of the carbon-carbon bonds in the main chain of macromolecules caused by atomic vibrations. The value of t.e.c. could be found by means of IR and Raman spectroscopy using the frequency shift of the regularity bands with growing temperature see ref. (4).

From fig. 1 one can see that t.e.c. grows at $T < T_t$, remains constant at $T_t < T < T_b$; its value grows rapidly at $T \cong T_b$ and again remains const at $T_b < T < T_{melt}$.

It is important to notice that the strength - temperature dependence is nonlinear when the t.e.c. change and is linear when the t.e.c. remains const.

It is a well known fact that the t.e.c. value significantly changes near the characteristic temperatures, which cause the changes in the statistics of one of the atomic vibrations' mode from quantum (Bose) to classic (Boltzman) see refference (5).

For the linear polymers PE and PA-6 the temperature T_t causes the changes of the twisting vibration modes' statistics, while T_b corresponds to the bending mode.

Zhurkov's formula (1) is based on the classic statistics which means that each atomic vibration mode has the energy kT. When the modes' statistics become quantum the energy of the mode E becomes lower than kT. In order to take into account the inequality of different modes' energy distribution Gilmann, Salganik and others (6-9) suggested to replace the temperature in form. (1) by the function $F(\theta/T)$. Thus form. (1) can be written as:

$$\sigma = \frac{U_0}{\gamma} - \frac{k \cdot \ln(\tau/\tau_0)}{\gamma} \cdot F(\theta/T) \quad \ldots\ldots\ldots\ldots\ldots (2)$$

The function $F(\theta/T)$ is not analytic. That is why one must have a method to determine it from independent experiments. We propose to determine this function for polymers using the frequency shift of regularity bands with temperature in IR and Raman spectra.

We have shown that $F(\theta/T)$ can be found from the equation:

$$F(\theta/T) = \frac{\Delta\nu(T)}{(\partial\nu/\partial T)_b} \quad \ldots\ldots\ldots\ldots\ldots\ldots\ldots (3)$$

It follows from (2) and (3) that

$$\sigma = \frac{U_0}{\gamma} - \frac{k \cdot \ln(\tau/\tau_0)}{\gamma (\partial\nu/\partial T)_b} \cdot \Delta\nu(T) \quad \ldots\ldots\ldots\ldots\ldots\ldots (4)$$

In fig. 2 we compare the experimental mechanical strength and this frequency shift for PE and PA-6. One can see that experimental data are well approximated by linear function according to formula (4).

The tangent of its slope angle coincides with calculated from formula (4).

These results prove the statement that the inclinations from

Zhurkov's formula at T_t and T_b are caused by the change of atomic vibrations' statistics from quantum to classic one.

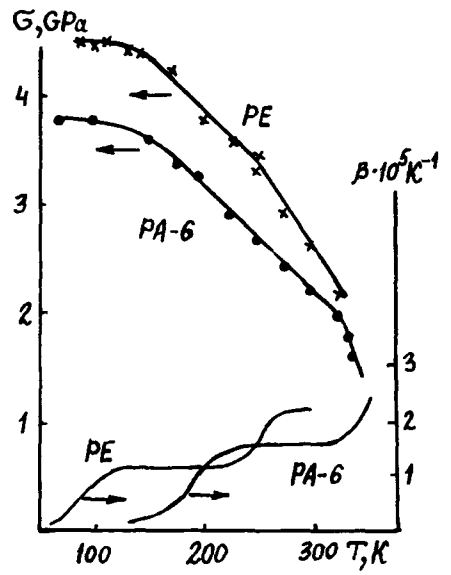

Figure 1 Mechanical strength and t.e.c. dependence on temperature

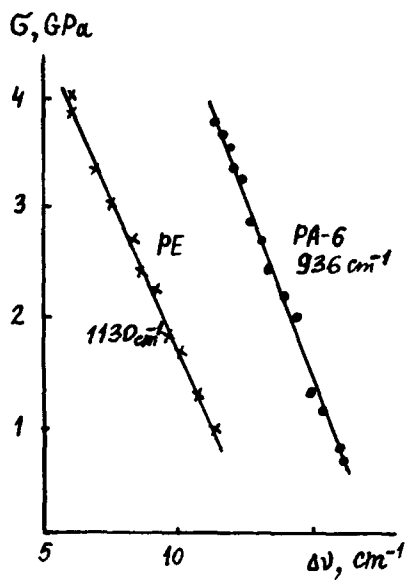

Figure 2 Comparison of strength and frequency shift of the regularity bands

SYMBOLS USED

σ = mechanical strength (Pa)

U_0 = fracture activation energy (kJ/mol)

γ = fracture activation volume (m^3)

k = Boltzman's constant (J/mol·K)

τ_0 = preexponential multiplier (sec)

T = absolute temperature (K)

T_b, T_t = characteristic temperatures (K)

T_{melt} = melting temperature (K)

$\Delta\nu$ = frequency shift of the regularity band (cm^{-1})

$(\partial\nu/\partial T)_b$ = frequency derivative with respect to temperature at $T > T_b$ ($cm^{-1}K^{-1}$)

REFERENCES

1 Zhurkov S N, Int J Fracture Mech *I* (1965) 311

2 Regel V R, Slutsker A I and Tomashevskii E E, Kinetic Nature of Strength of Solids, Moskow, USSR, 1974 (in Russian).

3 Kausch H H, Polymer Fracture, Berlin, Heidelberg, N Y, 1978.

4 Vettegren V I, Titenkov L S, Bronnikov S V, J Therm Anal *38* (1992) 1031

5 Girifalco L A, Statistical Physics of Materials, N Y, USA, 1973.

6 Gilman J J and Tong H S, J Appl Phys, *42* (1971) 3479

7 Salganik R L, Sov Phys Solid State, *12* (1970) 1051

8 Slutsker A I, Macromol Chem, Macromol Symp, *27* (1989) 207

9 Bronnikov S V, Vettegren V I and Frenkel S Ja, Polymer Eng & Sci, *32* (1992) 1204

PLANE-STRAIN DYNAMIC FRACTURE RESISTANCE of POLYETHYLENE from TESTS on WATER PRESSURISED PIPE.

C J Greenshields, S J K Ritchie and P S Leevers*

A standard test method for fracture of polyethylene (PE) pressure pipe has been used to investigate the effect of an axial score along the bore. Using water and/or air as the pressurising fluid, the plane strain dynamic fracture resistance of two PE resins was evaluated using a modified 'Irwin-Corten' analysis and compared with High Speed Double Torsion (HSDT) test data. Without an internal score, RCP cannot be sustained for water filled pipe, but a small included volume of air restores sufficient crack driving force for failure to occur. The variation in RCP performance with air volume has been studied to provide guidelines for safe operation of pipelines for the water industry.

INTRODUCTION

Full-scale tests on buried pipelines show that, above a critical pressure p_c, Rapid Crack Propagation (RCP) along an air pressurised pipeline can be sustained indefinitely (Greig, Yayla and Leevers [1]). The S4 (small scale steady state) test, aims to reproduce the steady state condition, observed in full scale tests, in specimens which are 7 diameters long (Yayla and Leevers [2]). It does so by suppressing axial backflow of gas which, in a long pipe, allows decompression ahead of the advancing crack. This prior reduction of crack tip pressure in a full scale failure results in the S4 critical pressure p_{cS4} being lower by a factor, supported by theory and limited experimental data, of 3.5.

The fractured surfaces of failed pipe specimens are generally brittle in appearance, except for a thin, plane-stress ductile tear zone at the pipe bore. Previous S4 tests on pipes have shown that the removal of this tough ductile layer by the introduction of an axial internal score (or notch), significantly decreases the critical pressure. Thus it is believed that this tough layer provides most of the resistance to RCP failure.

In 1969, Irwin and Corten first applied linear elastic fracture mechanics (LEFM) to the problem of predicting critical pressures in pipelines. The analysis was based on the assumption that all, and only, the strain energy stored in the pipe wall drives the crack. This is now known to be unrealistic since the pressure of the escaping gas on the pipe walls behind the crack tip generates almost all the driving force. The analysis may be used, however, to estimate plane-strain fracture resistance, using water pressurised, deeply notched pipe specimens.

Results from full-scale tests show that the fracture resistance of pipe grade polyethylenes is so high that RCP cannot be sustained in unnotched water pressurised pipe. The inclusion of a small volume of air enables failures to occur at slightly higher critical pressures than for air pressurised pipe (Greig [3]), but a good correlation between air volume and critical pressure has not previously been established.

* Department of Mechanical Engineering, Imperial College of Science, Technology and Medicine, London, England.

EXPERIMENTAL WORK

The S4 test rig, used in all tests reported here, complies with the international (ISO) standard for gas pipes [4] with one notable change: a rubber baffle was used to form a close seal with the pipe wall, almost eliminating axial flow of small air volumes to which normal S4 baffles would provide little resistance. The rubber allows any inward bending of the pipe wall which may occur during fracture.

The pipes used in the tests were extruded to 125 mm outer diameter from 'second generation' MDPE (MDPE-2) and modified HDPE (PE-100) resins.

Internally notched, air pressurised pipe tests Axial internal notches of various depths were introduced along the bores of several pipe specimens, including PE-100 (SDR 11 and 17.6), and MDPE-2 (SDR 11). The scores were cut using a Stanley knife blade mounted on a 'vehicle' which travelled down the pipe bore along a steel channel attached to a support frame. RCP fracture occurred along the notch and the mean notch depth was estimated after each test. The consistency of notch depth along the pipe length was within ±10%. The variation of critical pressure with notch depth was established initially for PE-100 SDR 11 at 20°C. Two further series of tests were completed, varying one parameter in each case — wall thickness (to SDR 17.6) and material (to MDPE-2).

Measurement of dynamic fracture toughness from the 'Irwin-Corten' analysis A set of tests, similar to those described above, was undertaken using internally notched water pressurised MDPE-2 SDR 11 pipe specimens at 0°C. Care was taken to remove all air from the system through a bleed valve in the end cap and the water was mixed with acetone to prevent freezing.

The presence of the pressurising medium undermines the assumptions on which the Irwin-Corten model is based. Since water has a high bulk modulus M, the strain energy stored is small, and if all of it were recovered during fracture, the crack driving force would become :

$$G = \frac{\pi p_0^2}{8E} D(SDR-2)^2\left[1+\left(\frac{E}{M}-1\right)\frac{1}{SDR}\right] \qquad (1)$$

G was calculated for each test by substituting the test pressure in equation (1) and multiplying by a factor $t/(t\text{-}a)$ account for the reduced crack path width. The dividing line between crack propagations and arrests defines the dynamic fracture resistance.

Water and air pressurised tests Critical pressures were established for a range of air/water volume ratios: 2.0, 3.8, 8.6, 17, 35, 50 and 75% (the maximum possible, due to 25% baffles, core and spacers) for MDPE-2 SDR 11 pipe at 3°C. The air volume was determined by viewing the water level through a polycarbonate window in the end cap.

RESULTS and DISCUSSION

Test results in Figures 1, 2 and 3 are plotted as crack propagations or arrests, according to the criterion defined in the S4 test specification [4].

The RCP performance of internally notched, air pressurised pipe is extremely poor (Figures 1 & 2). PE-100 pipe which cannot normally sustain RCP at 0°C, can do so at pressures of less than 2 bar at 20°C with a sufficiently deep notch, further lending support to the idea that pipe grade polyethylenes have very high ratios of plane-stress to plane-strain fracture resistance. The apparently abrupt transition to plane strain conditions occurs at a *critical notch depth* of 0.35 - 0.50 mm.

Performance of PE-100 and MDPE-2 are compared in Figure 1. For deeper notches, the critical pressures for the two materials at similar pipe dimensions and crack speeds, differ approximately by the ratio of the square root of their crack resistance, according to data from the High Speed Double Torsion (HSDT) test (Wheel and Leevers [5,6]).

In Figure 2, the results are plotted as a critical hoop stress σ_c instead of critical pressure to show the effect of wall thickness on RCP resistance. Previous tests on unnotched pipe have shown a 15 - 40% higher critical hoop stress for thinner walled SDR 17.6 over SDR 11 pipe [1,2]. In the notched pipe tests, the critical hoop stress is slightly less for SDR 17.6 pipe and critical notch depths for both materials are approximately equal. This implies that the depth of the tough ductile zone at the pipe bore is independent of wall thickness. Thus, decreasing the wall thickness should increase the overall fracture resistance of the pipe, which may contribute to the increased critical hoop stress in thinner walled unnotched pipes.

RCP could be sustained in sufficiently deeply notched, water pressurised pipe at pressures of 11 - 15 bar. Values for crack driving force were computed from test pressure using equation (1) (see Figure 3) giving a plane-strain fracture resistance G_D = 2.5 - 3.0 kJ m^{-2}. This compares well to HSDT test data for MDPE-1 [6]. The Irwin-Corten approach offers a simple alternative to the HSDT test. It has the advantage that, since the original morphology and internal stresses are preserved, the value of fracture resistance is more applicable to numerical modelling of RCP in pipes. The drawback, however, is that, unlike the HSDT test, the pipe test can only measure fracture resistance at one crack speed, determined by the system.

The inclusion of a 2% volume of air in water pressurised unnotched pipe restores sufficient crack driving force to sustain RCP (Figure 4). The critical pressure decreases linearly with increasing air volume until at 23%, the critical pressure reaches that of an air pressurised pipe. This may imply that during fracture, the air below a certain level in the pipe does not contribute to the opening of the pipe walls behind the crack tip, and thus provides no additional crack driving force.

SYMBOLS USED

G = Crack driving force (kJ m^{-2})
G_D = Dynamic fracture resistance (kJ m^{-2})
σ = Hoop stress (MPa)
E = Dynamic tensile modulus (MPa)
M = Bulk modulus (MPa)
D = External diameter of pipe (m)
a = Depth of notch (mm)
t = Pipe wall thickness (mm)
SDR (Standard Dimensional Ratio) = D/t
p_0 = Internal pipe pressure (bar)

ACKNOWLEDGEMENTS

This work was funded by WRc plc and SERC under a Postgraduate Training Partnership Scheme grant. The authors wish to thank Giles Pettit for the work on internally notched, air pressurised pipe.

REFERENCES

1 Greig J M, Leevers P S and Yayla P, Engineering Fracture Mechanics 42 No. 4 (1992) 663

2 Yayla P and Leevers P S, Engineering Fracture Mechanics 42 No. 4 (1992) 675

3 Greig J M, 'Rapid Crack Propagation in Hydrostatically Pressurised 250 mm Polyethylene Pipe', Proc Int Conf Plastic Pipes, Bath, England, 1988.

4 International Standards Organisation, International Standards ISO 4437, (Forthcoming Revision) 'Buried polyethylene (PE) pipes for the supply of gaseous fuels - Metric series - specification.'

5 Wheel M A and Leevers P S, Int J Fracture 61 (1993) 331

6 Wheel M A and Leevers P S, Int J Fracture 61 (1993) 349

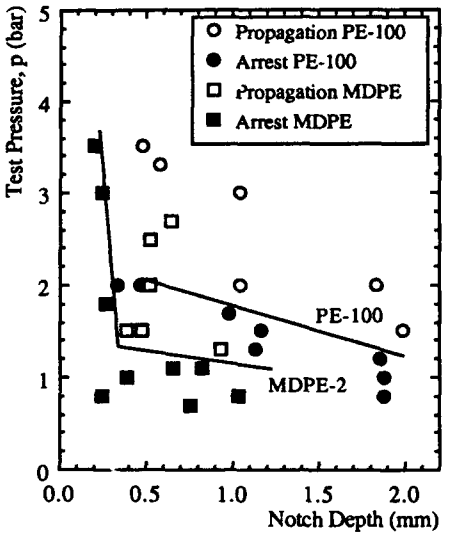

Figure 1 Notch depth v critical pressure in PE-100 and MDPE-2 SDR 11 125mm diameter pipe at 20°C

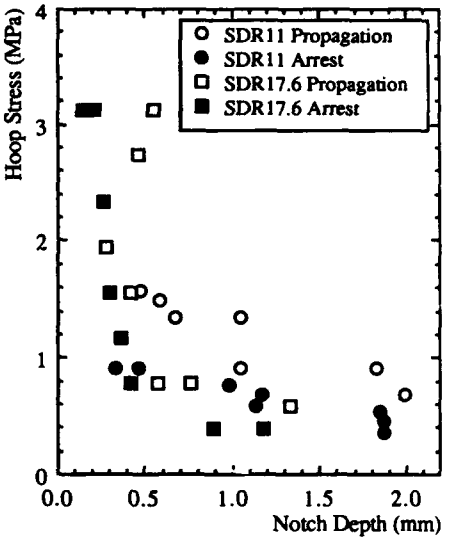

Figure 2 Notch depth v critical pressure in PE-100 SDRs 11 and 17.6 125mm diameter pipe at 20°C

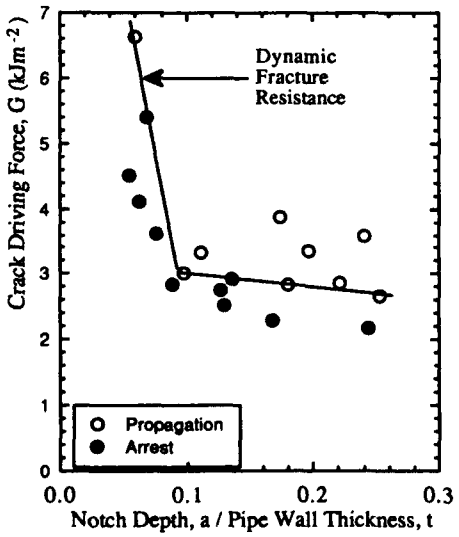

Figure 3 Response of the crack at various driving and notch depths in water pressurised notched MDPE-2 125mm SDR 11 pipe at 0°C (+2°C, -0°C)

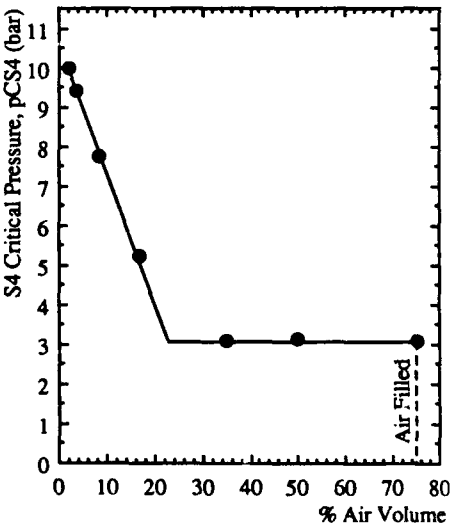

Figure 4 Effect of air volume on critical pressure in MDPE-2 125mm SDR 11 at 3°C (+0°C, -3°C)

THE EFFECT OF WATER ON THE MECHANICAL PROPERTIES OF POLYSTYRENE BEAD FOAM

N J Mills and P Kang
School of Metallurgy and Materials, The University of Birmingham, Birmingham B15 2TT

Water is rapidly absorbed into polystyrene packaging foam through open channels at the bead boundaries. However, the water penetration distance is only a few mm in 24 hours for the helmet mouldings examined because the channels are restricted near the surface of the moulding. The bending strength of polystyrene foam hardly changes after 24 hour water immersion, for the density range 20 to 56 kg m^{-3}, implying no change in the tensile strength of the surface bead boundaries. The fracture toughness of dry polystyrene foam that has been properly moulded is 80 to 110 kN $m^{-1.5}$, for densities in the range 20 to 70 kg m^{-3}. The effect of 24 hours water immersion on the fracture toughness is negligible.

1 Introduction.

Polystyrene foam is used for the shock-absorbing liners of many types of helmets. In 'soft shell' cycle helmets the polystyrene foam is the main structural element. Australian research(1) showed that cycle helmets exhibited 'full thickness cracking' in 86% of the 28 accident cases examined, and some soft shell helmets had broken into several pieces. We investigated whether there is an inherent weakness in polystyrene foam when wet, and if so, the material or processing causes of this weakness.

2 Foams and their penetration by ink

Foams were cut from a set of BS 6863 white-marked soft shell cycle helmets with a hot wire cutter. The other foams used were from the flat lids of a box.

Table 1 Polystyrene foams examined

No.	Source	Form	Thickness mm	Density kg m^{-3}	Mean bead diameter mm
1	BS 6863 helmet	curved	< 30	50.4	4.15 ± 1.26
2	BS 6863 failure	curved	< 30	70.4	2.56 ± 0.78
3	BS 6863 failure	curved	< 30	67.0	
4	Box lid	flat	20	56.5	2.35 ± 0.63
5	Box lid	flat	20	21.7	3.34 ± 0.78
6	Packaging	box	30	20.0	2.78 ± 0.85

SEM of the foam fracture surfaces showed that there are small three-sided channels at the bead boundaries of the moulded foam. These occur where three beads meet. The reason for their existence is that the bead moulding process must be carried out rapidly, so steam must be able to escape.

We studied the advance of water through the foam by immersing blocks of foam in black fountain pen ink to make the liquid front visible. The 0.10 Poise viscosity of the ink was the same as that measured for distilled water. Cube samples of side 25 mm were cut from helmet liners and mouldings with a hot wire cutter, taking care to preserve the inner and outer surface of the moulding. The initial ink penetration is along the channels that occur between three touching beads, although the complete bead face can be penetrated with time.

The moulding microstructure affects the ink penetration. For the 56 kg m^{-3} density box-lid moulding, the ink penetrated 4.5 m into the 25 mm cube after 6 hours, whereas for the BS 6863 cycle helmet moulding, the ink penetration is low. With the failed BS 6863 helmet the ink penetration of the outer surface of the moulding was limited to 0.5 mm, due to the inter-bead

channels being completely closed off in the moulding process. The cut surfaces of the same cube were penetrated by ink, showing that the moulded surface differed from the bulk of the foam.

The initial process of water advance is that of bead channel flow. Immediately after the water is present in the bead channels, it can start to diffuse across the bead faces. On some fracture surfaces ink had spread some distance across the polygonal bead faces. There was no evidence of ink accumulation in the closed foam cells below the bead faces, so it is deduced that diffusion of water into the cells is a slow process.

3 Mass increase in water immersion tests

Blocks of dimension 100 x 25 x 25 mm were hot-wire cut from the 56 kg m^{-3} density box lid foam, and the surfaces were trimmed with a new razor blade to remove any fused material. Two faces were the moulded surfaces. After immersion for the required period, the cubes were dried on each face with a tissue then weighed.
There are three stages in the water uptake process. The first is the filling of cut foam cells with water. The second stage, the penetration of the water to the midplane of the foam via the bead boundary channels, ends after approximately 20 hours. The third stage, possibly the penetration of water from the bead channels across the bead faces, continues to about 240 hours(fig 4b) where a second mass plateau appears. For samples from soft shell cycle helmets water ingress is effectively from the moulded surfaces only. The mass gain on water immersion is far less than for the box lid foams. The maximum relative gain lies between 3% for the helmet which passed BS 6863 to 8% for a liner which had broken up in BS impacts. These values are lower than the 40% for the 56 kg m^{-3} density box lids. We conclude that it is possible for water to penetrate through a 25 mm thick polystyrene moulding in 24 hours if there are open channels at the boundaries of the surface beads, but for most helmet liners water would only penetrate a few mm in that time.

4 Effect of 24 hours water immersion on bending strength

Only the surface layers of helmet liner foams are affected by 24 hours water immersion. In a soft shell cycle helmet local bending of the liner is possible, especially in regions surrounding the impact site. This bending places the outer surface of the foam in tension in the direction parallel to the surface. To see whether 24 hour water immersion reduces the tensile strength of the bead boundaries, bars were cut from the mouldings and loaded in 3 point bending. The analysis assumes that the material remains elastic and has a uniform Young's modulus, and calculates the maximum tensile stress on the surface of the bar at the point where fracture occurs. If the maximum load is F, the span of the bar is L and its width and depth are w and d, respectively, then the maximum stress is

$$\sigma_{max} = 1.5 \frac{F L}{w d^2} \qquad (1)$$

The tests were carried out with a 10 mm/min loading rate. Failure occurs when a crack appeared with a loud cracking noise in the centre of the tensile face of the bar. Table 2 shows that the fracture stresses are significantly higher than the compressive yield stresses. The value is particularly high for the helmet foam.

Table 2 Flexural strengths as a function of water immersion time

density kg m^{-3}	source	flexural strength MPa dry	1 day	dry flexural strength / compressive yield stress
22	box lid	0.38	0.38	3.0
50	helmet liner	1.75	1.35	4.0
56	box lid	1.27	1.12	2.3

When the bar fails, cracks initiate at the boundaries of the surface beads and propagate into the bar. Examination of the rest of the fracture surfaces showed that these were mainly trans-bead with fractured cell walls visible. Since the initiation of the fracture surface is along bead boundaries, it is possible to interpret the flexural strength data in table 2 as the tensile strength of the bead boundaries in the surface layers.

5. Effect of 24 hours water immersion on fracture toughness

The test rig is an adaptation of one used for fracture toughness measurements on solid thermoplastics(3). A falling mass impact loads the compact tension foam specimen, and a quartz crystal piezoelectric load cell and transient recorder record the load-time trace. The striker has a velocity of 1.85 m/s and a kinetic energy of 5.5 J just prior to impact, and after the inelastic collision with the lower grip and catcher plate the velocity is 1.63 m/s. The specimen size is 50 by 50 by 20 mm; the crack is cut with a hot-wire then sharpened with a new razor blade. For the helmet mouldings, a 20 mm section of the helmet liner, including the inner surface in the crack tip region, was used. After the peak in the force-time trace, the force declines to zero in 3 ms as the crack advances. As the crack travels 20 mm in 3 ms, the average crack velocity is 7 m/s. The fracture toughness values of the dry helmet foams are in the range 80 to 110 kN $m^{-1.5}$, and these are independent of the foam density for the limited range of densities examined(table 3). The energy absorbed by the sample during the whole of the crack propagation process was calculated from the area under the force distance curves, and this is given in table 3.

Five measurements of fracture toughness K_{IC} were carried out for helmet foams, to see the variability of the results. There was no significant change in the toughness after water immersion for 24 hours. There are no differences between the K_{IC} values for the helmet foams that pass the BSI wet impact test and those that fail, so the cause of the failure must be elsewhere. If the failure energies are divided by the crack area of 40 mm by 20 mm, the results for the helmets are in the range 125 to 250 J m^{-2}, showing that all these foams are in the category described by Stupak(1) as high toughness. For the box lid foams, the number of measurements is insufficient to prove that the effects of 24 hours of water immersion are significant.

Table 3 Fracture toughness of the polystyrene foams as a function of conditioning

Foam density kg m^{-3}	Source	conditioning	Force F N	K_{IC} kN $m^{-1.5}$	Energy mJ
50	helmet	dry	42 to 49	85 ± 10	99 ± 17
		wet	36 to 47	81 ± 3	102 ± 20
70	helmet	dry	72, 55	109, 89	191, 228
		wet	60	112	130
67	helmet	dry	44, 49	84, 90	108, 110
56	box lid	dry	42, 40	99, 78	115
		wet	30	65	62
22	box lid	dry	49, 36	110, 87	56, 20
		wet	8	19	22

6 Relating the fracture toughness to the fracture mechanism

Crack growth from the razor cut is initially across beads, hence the fracture surface will be trans-bead. After a few mm of growth, the crack diverts to be parallel to a bead surface. It runs either along the bead boundary, so that the bead skin is seen on the fracture surface(fig 1), or just below the boundary, so fractured cells are seen. A surfactant is used on the beads to prevent the pre-foamed beads from sticking together. Small islands of a foreign material can be seen on the bead skin. Energy dispersive X-ray microanalysis in a SEM showed the presence of calcium, but in a neighbouring area of fractured cells there was no calcium present. It is likely that the surfactant is calcium stearate. Fracture at the skin boundary is likely to be related to the weak surfactant layer.

The failure mechanism is similar to that proposed by Knott(2) for steel with a weak grain-boundary phase which fails at a critical tensile stress T(fig 2). If the grain(bead) diameter is D and there is a series of fractures at the grain boundaries just ahead of the advancing crack front, these must be caused by the elastic stress field of the crack, characterised by K_{IC}. The tensile stress σ, a distance r ahead of the crack, is related to the stress intensity factor K by

$$\sigma = \frac{K}{\sqrt{2\pi r}} \qquad (2)$$

Hence if the stress reaches the critical value T at a distance D/2 ahead of the crack tip and cracks initiate, then $K = K_{IC}$ and

$$K_{IC} \cong T\sqrt{\pi D} \qquad (3)$$

When values of T = 1.7 MPa from table 2, and D = 3.1 mm for the dry 50 kg m^{-3} density helmet liner are substituted into equation (3), $K_{IC} \cong 170$ kN $m^{-1.5}$. The predicted toughness for the dry 56 kg m^{-3} density box-lid moulding is $K_{IC} \cong 110$ kN $m^{-1.5}$. In using equation (3) the distance from the crack tip to the site where the bead boundary failure initiates is not exactly known, because the crack initiation site cannot be seen on the fracture surfaces. The bead boundary fractures must join up before the crack can propagate, so this may necessitate a higher value of K_{IC}. Nevertheless, the analysis confirms the link between the mechanism and the value of the fracture toughness.

References

1 P R Stupak, W O Frye & J A Donovan, 'The effect of bead fusion on the energy absoption of polystyrene foam', J Cellular Solids, **27**, 484 (1991)

2 J F Knott, *Fundamentals of fracture mechanics*, Butterworth, London, 1973, p 228.

3 A Gilchrist & N J Mills, 'Fast fracture of thermoplastics used for the shells of motorcycle helmets, J Mater Sci, **22** (1989) 2397

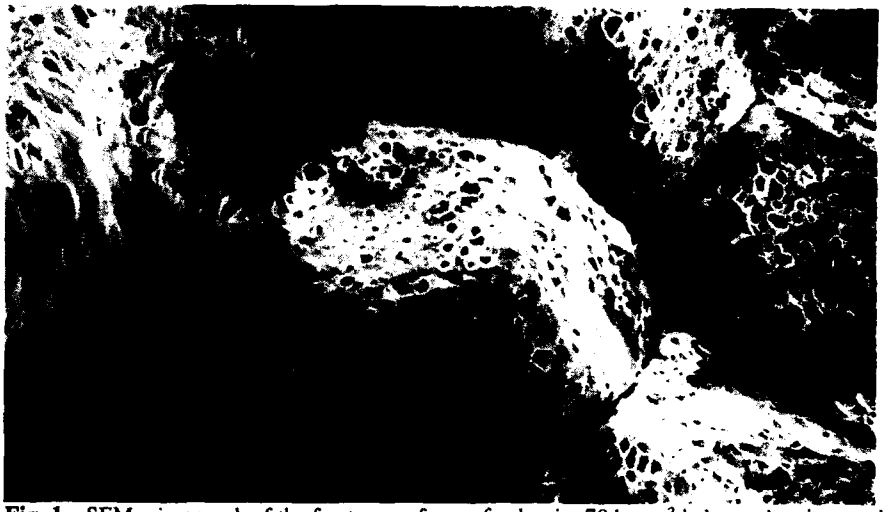

Fig 1 SEM micrograph of the fracture surfaces of a density 70 kg m^{-3} helmet, showing partially intact bead boundaries.

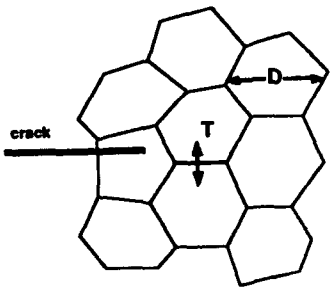

Fig 2 The fracture mechanism: the crack tip stress field initiates a bead boundary failure.

CYCLIC NEAR-TIP STRESSES FOR FATIGUE CRACKS IN POLYMERS: IN-SITU MEASUREMENTS, CRACK-TIP MICROSCOPY AND APPLICATIONS

L. Pruitt* and S. Suresh**

The evolution of cyclic near-tip stress fields ahead of fatigue cracks is known to have a pronounced effect on the fracture response of materials subjected to cyclic loading. Examples of such effects include the initiation of fatigue cracks from stress concentrations under fully compressive cyclic loads and crack growth retardation following tensile overloads. In this work, we have completed ***direct*** and ***in situ*** measurements of cyclic near-tip stresses ahead of fatigue cracks in polymers subjected to fully compressive and fully tensile cyclic loads, by recourse to photoelasticity and laser interferometry. The magnitudes of all stress components have been determined during both the loading and unloading phases of the fatigue cycle, in an attempt to establish a link between the evolution of near-tip stress fields and the advance of the fatigue crack.

INTRODUCTION

Cyclic near-tip fields which develop within the damage zone ahead of fatigue cracks have a significant effect on the fracture resistance. The zone of residual stresses is the result of permanent strains retained within the cyclic near-tip damage zone upon unloading from far-field stresses. Experimental evidence has demonstrated that near-tip residual stresses have important implications in a variety of fatigue situations. For example, residual tensile stresses are responsible for the inception and growth of mode I fatigue cracks in notched components under fully compressive cyclic loads in metals [1,2], ceramics [3,4] and polymers [5, 6] while residual compressive stresses are considered one of the governing factors in the retardation of fatigue crack growth following a tensile overload [7]. In this work, we present ***direct*** and ***in situ*** experimental measurements of cyclic stress fields ahead of fatigue cracks in model amorphous polymers subjected to far-field cyclic compression and cyclic tension loading. While the main focus of the work centers around fatigue of amorphous polymers, the results of this study have an equally general applicability to compression and tension fatigue of crystalline metals and ceramics, and semi-crystalline polymers.

MATERIALS AND EXPERIMENTAL METHODS

The experimental work reported in this paper focuses on amorphous materials: polycarbonate (PC), an allyl diglycol carbonate (CR 39), and a rubber-modified, high impact polystyrene (HIPS). PC and CR 39 were chosen for their photoelastic properties. The HIPS was chosen for its susceptibility to crazing and its amenability to detailed transmission electron microscopic analyses. The PC was obtained in plate form from GE, Schenectady, NY. It has a weight average molecular weight of 35,000. PC has the following mechanical properties at room temperature: tensile yield strength = 30 MPa, ultimate tensile strength = 32 MPa, and tensile modulus = 2.95 GPa. PC has the following stress-optical properties: fringe stress coefficient, f = 13.8 kN/m, and stress optic material constants, $A = -93.3 \times 10^{-12}$ m^2/N and $B = -100 \times 10^{-12}$ m^2/N. (f, A, and B are defined in the following sections.) The photoelastic resin CR39 was obtained from PPG Co., Pittsburgh, PA, in plate form. The CR 39 resin has the following room temperature properties: tensile

*Department of Mechanical Engineering, University of California, Berkeley, CA 94720, USA
**Department of Materials Science and Engineering, MIT, Cambridge, MA 02139, USA

strength, σ_t = 6.7 MPa, fringe stress coefficient, f = 14.62 kN/m, and stress optic material constants, $A = -116 \times 10^{-13}$ cm^2/dyne and $B = -164 \times 10^{-13}$ cm^2/dyne. (f, A, and B are defined in the following sections.) The HIPS was procured from Dow Chemical Co., Midland, MI in plate form. The polymer is fully amorphous; its weight average molecular weight, M_w, is 240,000 and number average molecular weight, M_n, is 86,000 (i.e., a polydispersity of 2.8). The polystyrene contains 7.5 weight percent butadiene rubber in the form of gel particles which have an average diameter of 1–2 μm. The high-impact polystyrene has the following mechanical properties at room temperature: tensile yield strength = 18 MPa, ultimate tensile strength = 16.6 MPa, and tensile Young's modulus = 1.65 GPa.

Experiments were conducted on single-edge-notched (SEN) plates for compression fatigue and compact tension specimens for tension fatigue. The SEN geometry is as follows: width, W = 25.4 mm, height, $2H$ = 25.4 mm, notch length, a_0 = 8.9 mm, thickness, T = 4.8 mm, and notch-root radius, ρ = 0.127 mm. The CT dimensions are: length L = 19 mm, width measured from the center of holes W = 15 mm, height $2H$ = 19 mm, notch length a_0 = 5.33 mm, notch-root radius ρ = 0.5 mm, notch-tip angle θ = 60°, thickness of PC, T = 2.54 mm and thickness of HIPS, T = 3.17 mm. The specimens were tested in a servohydraulic closed loop testing machine. All experiments were conducted in the laboratory air environment at a temperature of about 23°C and relative humidity of about 60%. The loading frequency ν was chosen to be 5 Hz, to avoid hysteretic heating effects, with a sinusoidal waveform and a load ratio, R = 30 for compression and 0.1 for tension (R is defined as the ratio of minimum load to the maximum load of the fatigue cycle).

Photoelasticity was used to obtain the loci of equal differences of principal stresses termed ***isochromatics*** and the principal stress directions termed ***isoclinics*** (see [6] for details). In the photoelasticity measurements, a polarized beam of light passes through a two-dimensional photoelastic material stressed in its plane, the light is split into two perpendicular components which coincide with the principal stress directions and whose velocities are proportional to the magnitude of the principal stresses. The principal stress difference is found using the stress-optic law: $(\sigma_1 - \sigma_2) = \frac{nf}{T}$, where the fringe order n is the number of wavelengths of interference, f is the fringe stress coefficient and T is the specimen thickness. The isoclinics are determined by rotating the crossed polars in the plane polariscope with a white light source at 10–15° intervals. The isoclinics provide the loci of points along which the principal stresses are parallel.

A Mach–Zehnder laser interferometer technique was employed in an attempt to measure the loci of equal sums of principal stresses, termed ***isopachics*** (see [6] for details). The laser interferometer splits the incident laser beam into two optical paths with one of the paths passing through the crack-tip region of the transparent photoelastic material. The beams are then recombined creating an interference pattern, due to displacements perpendicular to the plane of the model. The principal stress sum is given by the expression from [8]: $(\sigma_1 + \sigma_2) = \frac{2N_p\lambda}{T(A+B)}$, where N_p is the order of the isopachic fringe, and A and B are stress-optic material constants. Using the isochromatics, isoclinics and isopachics, the principal stresses were individually identified assuming plane stress deformation. The cyclic stress fields surrounding the notch tip and fatigue crack tip were determined explicitly for different levels of unloading and stages of the fatigue test. All the TEM observations reported here were made on a Phillips EM 420T electron microscope operating at a voltage of 120 kV.

RESULTS AND DISCUSSION

First we will discuss the results of cyclic compression in the resin and then cyclic tension. Figure 1a is a black and white optical micrograph of the isochromatic $(\sigma_1 - \sigma_2)$ fringe pattern and Figure 1b is the corresponding isopachic $(\sigma_1 + \sigma_2)$ fringe pattern as the specimen is unloaded to –0.55 MPa (the least compressive stress) of the first compression fatigue cycle. Using the overlay of isochromatics and isopachics in combination with isoclinics, all the stress components can be determined for that stage of unloading (for plane stress conditions). The σ_{yy} component of stress acting on the plane of the notch is of particular interest to mode I crack advance. Values of σ_{yy} were determined for a multitude of geometric points surrounding the notch tip. Figure 1c shows the contours of constant σ_{yy} so computed around the notch tip during the first compression cycle at the unloading stage of –0.55 MPa, respectively. Upon unloading to the least compressive stress of the compression fatigue cycle, a notch-tip residual tensile normal stress of +9.1 MPa is seen over a distance of nearly 0.1 mm.

An examination of Figure 1c shows that, during unloading, there develops a region of residual tensile stresses whose magnitude is in excess of the tensile strength of the material (6.7 MPa). The distance directly ahead of the crack tip, over which tensile residual stresses exceed the tensile strength of the resin is approximately 0.25 mm upon unloading from the first compression cycle. This distance is the saturation crack length observed for CR 39 at the imposed cyclic loading conditions in this specimen geometry. In addition, the development of a stable mode I fatigue crack ahead of the notch in the photoelastic CR39 when subjected to compression fatigue loading is qualitatively similar to that seen in other amorphous polymeric materials, semicrystalline polymers, as well as ceramics and metals.

Figure 2 is transmission electron micrographs of microscopic damage ahead of the compression fatigue crack emanating from the notch in HIPS. This micrograph indicates that the primary deformation mechanism ahead of the fatigue crack tip is craze formation. The crazes are readily identified as fine bands with fibrillar structure, where the fibrils are typically 20 nm in diameter. The occurrence of crazes oriented parallel to the plane of the compression fatigue crack and normal to the far-field compression axis suggests the existence of a zone of residual normal tensile stresses in the immediate vicinity of the crack tip (since crazes are oriented normal to the local principal tensile stress). The TEM observations also offer micromechanistic evidence of the role of tensile residual stresses in in uencing crack-tip damage under far-field cyclic compression loading. The TEM observations are consistent with the quantitative cyclic stress measurements.

Figure 3a shows the overlay of isochromatics and isopachics for the first tension fatigue cycle at $K = 0.057$ MPa$\sqrt{\text{m}}$ in PC. The contours of σ_{yy} are shown in Figure 3b, note that residual compressive stresses of -7.2 over 0.3 mm are generated as the specimen is unloaded from far-field tension to $K = 0.057$ MPa$\sqrt{\text{m}}$ (minimum in the tension fatigue cycle). The residual compressive stresses evolve during unloading from a far-field tensile stress. In addition, as the fatigue crack advances the zone of residual compression increases in size and magnitude. The total distance of residual compression is consistent with the calculated cyclic damage zone size using linear elastic fracture mechanics (see [9] for details).

CONCLUSIONS

Quantitative stress analysis using photoelasticity and laser interferometry directly demonstrates that ***tensile*** near-tip stresses evolve in notched specimens upon unloading from far-field compression, while ***compressive*** residual stresses develop upon unloading from far-field tension. The quantitative stress measurements provide a clear and unambiguous mechanistic justification for craze formation as well as the inception of a mode I fatigue crack ahead of the notch tip (in a direction parallel to the plane of the notch and normal to the far-field uniaxial compression axis) during cyclic compression loading. In addition, the results of our stress analysis provide justification of post-overload fatigue crack retardation due to residual compressive stresses ahead of tensile fatigue cracks.

ACKNOWLEDGMENTS

This work was supported by the Office of Naval Research under Grant N00014-89-J-3099 to Brown University and under N00014-93-1-1339 to MIT. The authors thank Drs. G. Yoder and A.K. Vasudevan for their support of the work and for helpful discussions.

REFERENCES

1. Reid, C.N., Williams, K. and Hermann, R., Fat. Engng. Mater. Struct. 1 (1979) 267.
2. Holm, D.K., Blom, A.F., and Suresh, S., Eng. Fract. Mech. 23 (1986) 1097.
3. Ewart, L. and Suresh, S., J. Mater. Sci. 22 (1987) 1173.
4. Suresh, S. and Brockenbrough, J.R., Acta Metall. 36 (1988) 1455.
5. Pruitt, L., Hermann, R., and Suresh, S., J. Mater. Sci. 27 (1992) 1608.
6. Pruitt, L. and Suresh, S., Phil. Mag. A 67 (1993) 1219.
7. Wheeler, O.E., J. Basic Eng. 94 (1972) 1181.
8. Nisida, M., and Saito, H., Experimental Mechanics 4 (1964) 366.
9. Pruitt, L. and Suresh, S., sent to Polymer for publication.

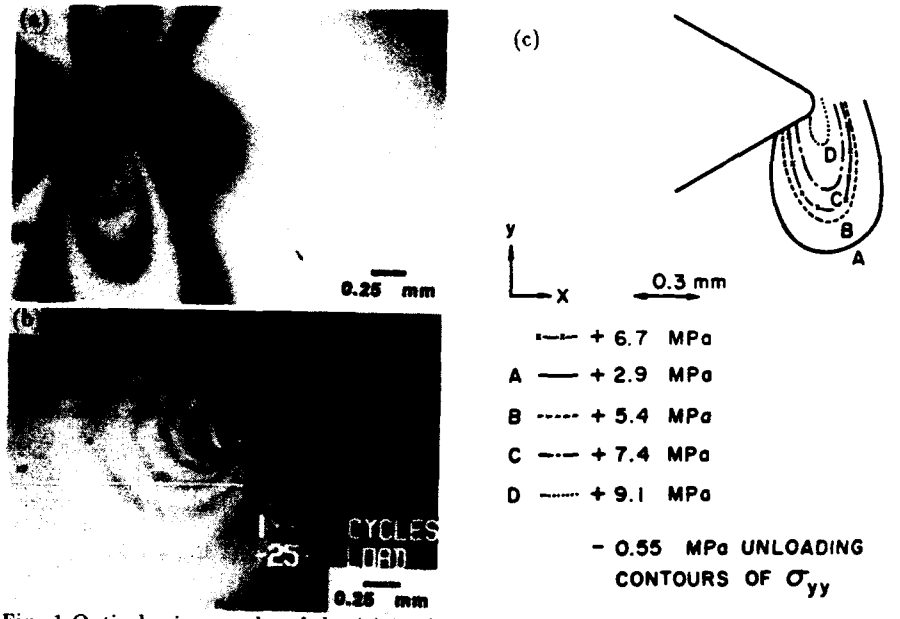

Fig. 1 Optical micrographs of the (a) isochromatic pattern, (b) isopachic patterns and (c) contours of constant σ_{yy} at the notch tip as the specimen is unloaded to -0.55MPa in the first compression fatigue cycle.

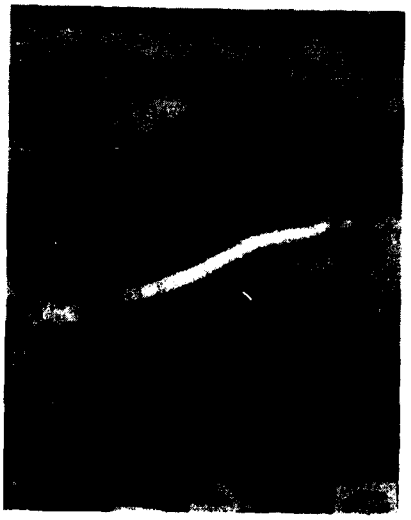

Fig. 2 TEM of damage zone ahead of a compression fatigue crack in HIPS, the craze is in the plane of the notch.

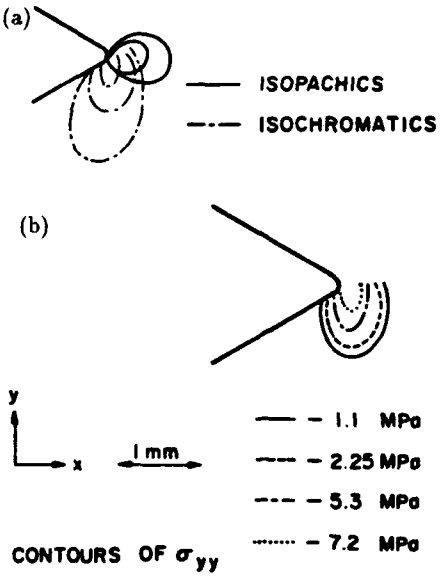

Fig. 3 (a) Overlay of isochromatics and isopachics (b) contours of σ_{yy} at $K = 0.571$ MPa$\sqrt{\text{m}}$.

DIRECT MEASUREMENT OF STRAIN ENERGY RELEASE RATES DURING FATIGUE FRACTURE OF REINFORCED NYLON 66

M. G. Wyzgoski and G. E. Novak*

Fatigue crack propagation rates are normally expressed in terms of the change in stress intensity factor, ΔK. For fiber reinforced nylon 66 we have shown that the use of a calculated ΔG in place of ΔK is preferred since crack growth rate data for different fiber orientations collapse onto a single ΔG relationship, where ΔG is the strain energy release rate. We have now measured ΔG directly during the fatigue experiment for comparison with the calculated value. For the parallel crack orientation similar ΔG values are observed, whereas for the perpendicular case, measured values are much larger than calculated. Implications of these findings for predicting fatigue crack growth rates are discussed.

INTRODUCTION

Earlier studies have demonstrated the value of a fracture mechanics approach to characterize the fatigue fracture behavior of both unfilled and glass fiber reinforced nylon plastics [1-5]. It was shown that the use of a strain energy release rate model provided a superior representation of the results since it lead to a generalized plot for different glass fiber orientation directions [2]. The use of the strain energy model also provided a basis for predicting the fatigue behavior of all reinforced nylons [5]. Strain energy release rate based upon an independent modulus measurements, however, we are now measuring ΔG directly during the growth of the fatigue crack. This report compares the calculated and directly measured values of strain energy release rate for glass or carbon fiber reinforced nylon 66.

EXPERIMENTAL

Both 33% glass filled and 40% carbon filled nylon 66 were injection molded into an end gated plaque which has dimensions of 50.8 mm by 203.2 mm by 3.2 mm. Following molding, the plaques were stored in desiccators to maintain their dry-as-molded condition and all testing was performed using only dry samples. Fatigue crack propagation measurements were performed using the previously developed procedures [1] in which a video recording and analysis system is employed to monitor cracks in compact tension samples. All measurements were conducted at a frequency of 0.5 Hz and a load ratio of 0.1. ΔG was first calculated from the modulus and the ΔK data using the relationship $G = K^2/E$ which under oscillating loading leads to $\Delta G = 1.22(\Delta K^2)/E$. Strictly speaking, under plane strain conditions, this expression should also be

*Polymers Department, General Motors NAO R&D Center, Warren, MI

multiplied by the term $(1-\nu^2)$, where ν is Poisson's ratio. Values for ν are not available for the different orientations for the glass filled nylon 66 and therefore this term was ignored. For the direct measurement of ΔG, two different procedures were adopted. First, the values of G at maximum and minimum loads were independently assessed from the area under the load-displacement curve by generally following the procedure outlined in the recent ASTM standard for G_{1c} determination [7]. This method utilizes the relationship $G = U/(BW\phi)$, where U is the energy (area under the curve), B is the thickness, W is the width, and ϕ is a calibration constant for the compact tension geometry. The second method for determining ΔG is based upon a compliance technique where $G = (P^2/2B)(dC/da)$ [8]. In this equation, which is valid for anisotropic materials, P is the load, B is the thickness, C is the sample compliance, and a is crack length. The ΔG values determined via the compliance method are considered the most fundamentally sound for the reinforced nylon material [8].

RESULTS

Figure 1 shows the fatigue crack propagation rates for cracking parallel or perpendicular to the preferred glass fiber orientation direction in the injection molded nylon 66 plaque. In Figure 2 these same data are replotted in terms of the calculated strain energy release rate using the independently measured tensile moduli for the glass reinforced nylon 66. The moduli are 6.5 GPa and 11.9 GPa for the parallel and perpendicular orientations. The results in Figure 1 confirm earlier results in showing a tremendous influence of fiber orientation on the rate of fatigue crack growth. However, it is also apparent that on a ΔG basis (Figure 2) the effect of orientation disappears as both data sets can be described by a single relationship. Again, these results are similar to what has been shown earlier.

Figure 3 compares the calculated ΔG results for the parallel orientation with the newly developed procedure whereby the ΔG values are determined directly during the fatigue experiment. The results from the three different methods are similar for the parallel orientation although consistently higher values are obtained from the calculation method.

However, in the case where the fatigue crack propagated perpendicular to the glass fiber axes, the direct measurements of ΔG show that a much higher strain energy release rate is associated with fatigue crack propagation. This is indicated by both the area method and the more fundamentally sound compliance approach which give comparable results. Figure 4 compares the directly measured ΔG values based upon compliance for the parallel and perpendicular orientations. In sharp contrast to Figure 2, these results do not suggest a general or universal strain energy release rate relationship but rather indicate a strong orientation dependence just as was seen for the original da/dN-ΔK plots (Figure 1). Data for carbon fiber reinforced nylon 66 showed similar results, namely, for the perpendicular case higher ΔG values were obtained. In the parallel orientation the directly measured ΔG was similar to the calculated value and, most significantly, was also equal to the measured value for glass fiber filled nylon 66.

DISCUSSION

The results presented here demonstrate a very good agreement between the calculated and measured ΔG in the case of the parallel sample orientation. In fact, the slightly higher ΔG values shown in Figure 3 for the calculated method are most likely due to our ignoring the Poisson's ratio term which would reduce the calculated ΔG values by an amount equal to $(1-\nu^2)$. For a typical value of $\nu = 0.35$ this would result in a 12% reduction in the calculated ΔG which

would make it indistinguishable from the directly measured values. These results indicate that the linear elastic fracture mechanics approach is viable for this type of material. This conclusion is further supported by the results for carbon fiber reinforced nylon 66. The coincidence of the compliance generated ΔG relationships for glass and carbon fibers in the parallel orientation is also a very significant result. It confirms the earlier findings using the calculated ΔG results and in so doing provides us with additional evidence that matrix fracture dominates the fatigue cracking process in reinforced nylons [2,5]. It is important to recognize the significance of these very positive findings. The ΔG relationship allows us to calculate fatigue crack growth rates for any fiber orientation and for any fiber type as well as for the unreinforced matrix. It therefore is the basis for a very general predictive model which hopefully can also be applied to other polymer types besides nylons.

Unfortunately the lack of agreement between calculated and directly measured ΔG values for the perpendicular orientation of fibers is not presently understood. Though it is not surprising that greater energy is needed to propagate a fatigue crack in a crack avoidance mode around the aligned fibers, it is not clear how to reconcile this result with the previous generalized calculated ΔG expression. Possible explanations for this will be described.

ACKNOWLEDGMENTS

The authors wish to thank Professor Gordon Williams of Imperial College for suggesting the compliance method for ΔG determination and for many helpful discussions.

REFERENCES

1) M. G. Wyzgoski and G. E. Novak, Research Report PO-814, Dec. 12, 1986.

2) M. G. Wyzgoski and G. E. Novak, Research Report PO-898, Mar., 1988.

3) M. G. Wyzgoski and G. E. Novak, Research Report PO-1006, Nov., 1990.

4) M. G. Wyzgoski and G. E. Novak, Research Report PO-1033, Nov., 1991.

5) M. G. Wyzgoski and G. E. Novak, Research Report PO-1061, May, 1993.

6) ASTM Standard D 5045-91a, Plane Strain Fracture Toughness and Strain Energy Release Rate of Plastic Materials, Sep., 1991.

7) Professor J. Gordon Williams, private communication.

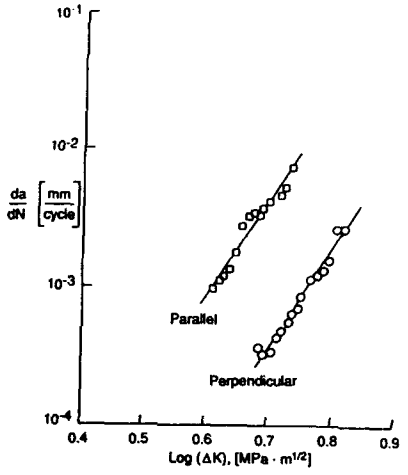

Figure 1. Fatigue Crack Growth Rates for Glass Fiber Filled Nylon 66.

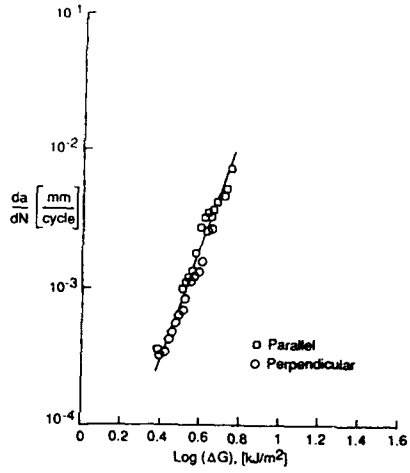

Figure 2. Fatigue Crack Growth Rates vs Calculated ΔG for Glass Filled Nylon 66.

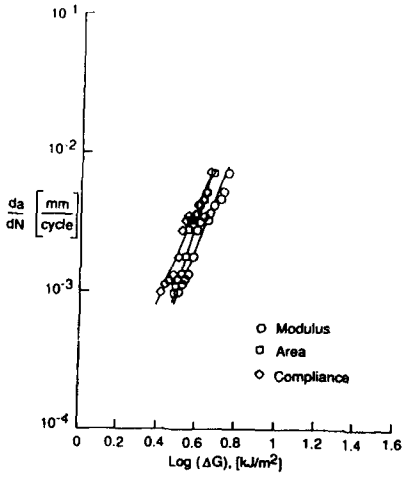

Figure 3. Calculated and Measured ΔG for Cracking Parallel to the Fibers.

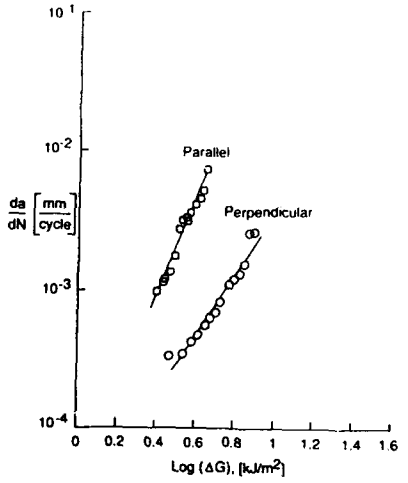

Figure 4. Results Using the Compliance Method for Cracking Parallel and Perpendicular to the Fibers.

THE DEFORMATION OF ELASTOMERIC O-RINGS COMPRESSED BETWEEN FLAT RIGID PLATES

W. E. Warren* and J. A. Weese*

Three dimensional effects of symmetrically compressing an o-ring between flat rigid plates is investigated. The o-ring is assumed to be an incompressible elastic material and the mixed boundary value problem is formulated within the framework of classical linear elasticity theory. The actual o-ring compression is strongly dependent on the conditions of contact between plate and o-ring. This transverse compression increases the toroidal radius and induces a reduction in the o-ring cross-sectional radius. The reduced contact pressure may threaten the integrity of the seal.

INTRODUCTION

Toroidal shaped o-rings are used extensively as environmental or pressure seals to prevent leakage of gas and moisture. O-rings are generally molded from relatively soft incompressible elastomeric materials and in application are compressed between relatively rigid flat plates. Effective sealing depends upon the contact pressure between o-ring and plate, and some interesting and significant effects of compression ratio, roughness, and surface flaws on this contact pressure have been determined through two-dimensional plane strain analysis (1,2). There are, however, three-dimensional effects related to sealing of o-rings which are not revealed through a two-dimensional analysis. For example, transverse compression of the o-ring changes its toroidal radius. Material incompressibility then induces a change in cross-sectional radius which may relax contact pressure and threaten the integrity of the seal.

In this work we provide a theoretical analysis of the three-dimensional effects of symmetrically compressing an o-ring between flat rigid plates. We assume the o-ring to be an incompressible elastic material and the problem is formulated within the framework of classical linear elasticity theory. We make use of our previous analysis (3) in which we obtain asymptotic approximations for the general axisymmetric solutions to the field equations of elasticity in terms of Boussinesq-Papkovich potentials defined in the orthogonal toroidal coordinate system. These asymptotic approximations provide solutions to the stress and displacement boundary value problems on the solid torus for a range of geometries typical of o-ring applications where (a/R)<<1 (see Fig. 1b).

* Texas A & M University, College Station, Texas 77843, USA.

ANALYSIS

The o-ring problem under consideration here represents a mixed boundary value problem in which the displacements due to the rigid flat plates are prescribed on a portion of the toroidal surface while the remaining portion of the surface is stress free. To formulate this problem, we first make use of the asymptotic potentials of (3) to obtain the singular solution to the problem of symmetrically located circular line forces acting on the o-ring surface of magnitude p per unit length in the z-direction and of magnitude q per unit length in the r-direction as shown in Fig.1. These singular solutions then provide the kernels for a distribution of tractions over the portion of the o-ring surface which is in

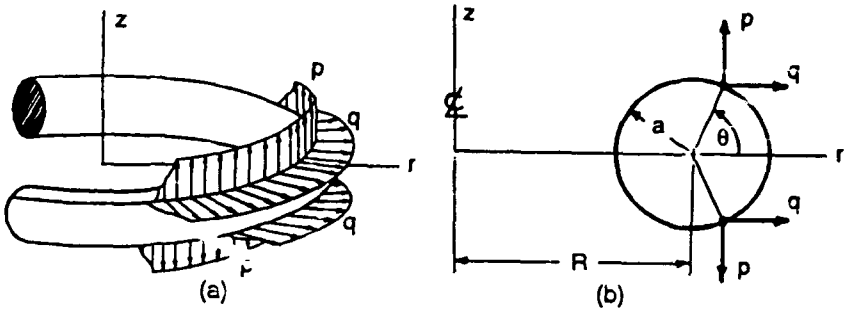

Figure 1. Torus with circular line load at angle θ : (a) schematic, and (b) in section.

contact with the rigid compressing plates. Integration of these kernels over the region of plate contact provides expressions for the boundary displacements as a function of the traction distribution functions $p(\theta)$ and $q(\theta)$. This formulation insures that the o-ring surface not in contact with the compressing plates is stress free. Invoking the displacement boundary conditions in the region of plate contact leads to singular integral equations of Hilbert type to evaluate the distribution functions $p(\theta)$ and $q(\theta)$.

The compressed o-ring is shown schematically in Fig. 2. The total angle of contact between o-ring and rigid plate is $2\alpha_0$, and the domain of contact is defined by $-\alpha_0 < \phi < \alpha_0$, where $\phi = \pi/2 - \theta$. We now consider the solution of two specific boundary value problems which are representative of typical o-ring installations.

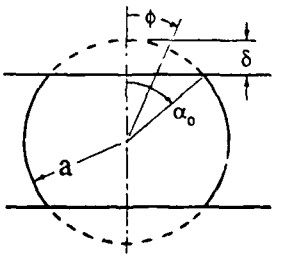

Figure 2. Compressed o-ring

Case 1- No Friction

For no friction, the boundary conditions at the o-ring surface of radius a are

$$\sigma_{\alpha\alpha} = 0 \ , \ \alpha_0 < |\phi| < \frac{\pi}{2}$$

$$u_z = -\delta + \frac{1}{2} a \phi^2 \ , \ -\alpha_0 < \phi < \alpha_0 \qquad (1)$$

$$\sigma_{\alpha\beta} = 0 \ , \ -\frac{\pi}{2} < |\phi| < \frac{\pi}{2}$$

where (α,β,γ) are toroidal coordinates as defined in (3,4), and u_z is the component of displacement in the z-direction. Invoking these boundary conditions on the integral representations of stress and displacements for an incompressible material requires that the distribution function $g(\phi) = 0$, and provides the singular integral equation

$$2G\phi = \frac{1}{\pi} \int_{-\alpha_0}^{\alpha_0} \frac{p(\xi)\, d\xi}{\phi - \xi} \ , \ -\alpha_0 < \phi < \alpha_0 \ , \qquad (2)$$

for determining the distribution function $p(\phi)$. Equation 2 has the bounded solution

$$p(\phi) = 2G\sqrt{\alpha_0^2 - \phi^2} \ , \qquad (3)$$

which represents the contact pressure between the flat rigid plate and the o-ring. The o-ring compression is then given by

$$\frac{\delta}{a} = \frac{1}{2}\alpha_0^2 \left[\ln\left(\frac{1}{\alpha_0}\right) + 2\ln 2 - \frac{1}{6} \right] \qquad (4)$$

and the radial displacement of the o-ring centerline u_r is given by

$$\frac{\bar{u}_r}{a} = \frac{1}{3}\left(\frac{R}{a}\right)\alpha_0^2 \ . \qquad (5)$$

Case 2 - No Slip

For the case of no slip at the contact surface, the boundary conditions at the o-ring surface are

$$u_r = 0 \ , \ -\alpha_0 < \phi < \alpha_0$$

$$u_z = -\delta + \frac{1}{2} a \phi^2 \ , \ -\alpha_0 < \phi < \alpha_o \qquad (6)$$

$$\sigma_{\alpha\alpha} = \sigma_{\alpha\beta} = 0 \ , \ \alpha_0 < |\phi| < \frac{\pi}{2} \ .$$

For this case, the radial displacement of the o-ring centerline is given by

$$\frac{\bar{u}_r}{a} = \frac{1}{4}\left(\frac{a}{R}\right)\alpha_0^2\left[\ln\left(\frac{1}{\alpha_0}\right) + 2\right]. \qquad (7)$$

RESULTS

Representative o-ring surface deformations for these two cases for an o-ring compression of 4 % ($\delta / a = 0.04$) are shown in Fig. 3. The difference between the two is significant. Compression of the o-ring enlarges the toroidal radius R and for the case

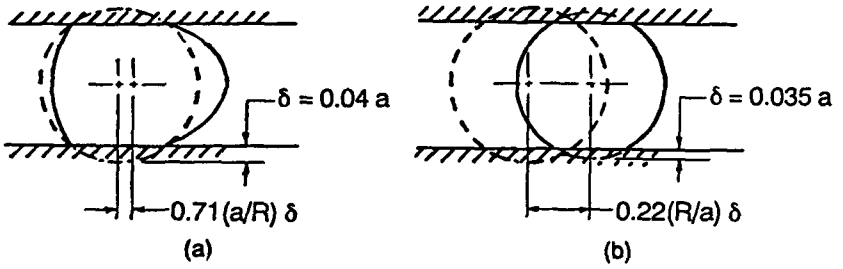

Figure 3. O-ring deformation at 4% compression for (a) no slip, and (b) no friction. Solid line is deformed and dashed line undeformed position.

of no slip, this change in R is small of order (a/R). For the case of no friction, the change in R is large of order (R/a). For ease of installation, o-rings are typically lubricated during assembly and this lubrication provides an essentially frictionless contact. In this situation for an incompressible elastomer, the large increase in R induces a reduction of the cross-sectional radius a and the compression is reduced from an initial 4% to an effective 3.5% as shown. If this change in o-ring geometry is not accounted for in the design of the o-ring seat, the resulting reduction in contact pressure may pose a threat to the integrity of the seal.

REFERENCES

1. Warren, W.E., Curro, J.G., and Amos, D.E., ASME J. Tribology , 110 , 4 (1988) 632.
2. Warren, W.E. and Amos, D.E., ASME J. Elec. Packaging , 113 , 1 (1991) 63.
3. Warren, W.E., Weese, J.A., and Mitchell, T.P., Proc. 17th Southeast Conf. on Theor. and Applied Mech. (1994) in press.
4. Morse, P. M. and Feshbach, H., 'Methods of Theoretical Physics', McGraw-Hill Book Co., (New York), 1953.

Poly-conformers Physics versus Macromolecular Physics:
Rubbery State Deformation.

J.P. Ibar,
Solomat Research Institute
p o Box 385
New Canaan CT 06840 USA

I. Introduction

Rubbers and rubberlike substances have fascinatingly unique mechanical properties They can be stretched to very high percentages of strain, e.g. 1000%, and can recover almost instantaneously their initial length upon the release of mechanical tension applied at both ends. The load-extension curves of rubberlike materials characterize in many respects the mechanical behavior of these substances. The Young's modulus (in the region of small extensions) is of the order of 107 dynes/cm2 for rubberlike materials compared to 10^{11}-10^{12} dynes/cm2 for glassy polymers, a loss of about four orders of magnitude. The force necessary to extend a rubber to a certain point is strongly a function of the temperature and the strain rate used. There is a great difference between "rubbers" on the one hand and "glassy" hard polymers on the other. Interpreting this difference is the main problem with which this paper will be concerned.

II. Potential Energy of a Free Conformer.

For simple macromolecules (polyvinyl chloride, Polyethylene, etc.) the macromolecule can be described with a succession of three-bond elements. For these simple systems the length of the bonds C1C2, C2C3, C3C4 corresponds to the length of covalent bonds of the repeating unit. The "conformation" of a three-bond element can be described energetically just like the conformation of a small molecule, say ethanol. For other systems the situation is slightly more complex and the length of the bonds of the repeating unit is not the length of C1C2, C2C3, C3C4 of the virtual three-bond elements, which we call "conformers".

Note: In my thesis work [1975], I called "bond-units" what I now call "conformers". Matsuoka used the word "conformer" in a publication of the North American Thermal Analysis Society (NATAS), at the San Diego meeting in 1989. Although Matsuoka used it in a rather similar context, presenting a theoretical model of the glassy state, I have taken the liberty of using the same word, without the same meaning, to describe the properties of the "bond-units". The interest in "conformers" to describe the rotational isomeric state of macromolecules has resonance in the work of Volkenstein, Lunn, Robertson, Miller, and more recently Matsuoka. The concept of "poly-conformers", and the possibility to conceive a poly-conformer physics, have already been coined by me under other names more than seventeen years ago. I find the new names more descriptive and appropriate.

The internal rotation barrier energy of a conformer, given a certain conformation, is the result of the electronic and steric interactions between adjacent atoms (or groups of atoms) of the same conformer. The Pauling sinusoidal function is often used for the internal rotation barriers.

$$V_t(\theta) = V_o(1 \pm \cos n\theta)$$

III. Potential Energy of a Bonded Conformer.

1) Van der Waals interactions.

The potential function for Van der Waals interactions between non-covalently bonded atoms can be approximated by a Buckingham or Lennard-Jones function.

2) Electrostatic Interactions.

This term takes into account the possible dipole-dipole interactions which appear when some pendant or backbone atoms of the chain are polar.

Consequently, the energy of a "bonded" conformer in a given conformation takes the theoretical form

$$V_b(\theta) = \sum V_O/2\ (1 \pm \cos n\theta) + \sum A*r^{-D}*\exp(-BR) - C*r^{-6} +$$

$$+ \sum \varepsilon^{-1} \left[\frac{\mu_i \mu_j}{a^3} - 3 * \frac{(\mu_i . a)(\mu_j . a)}{a^5} \right]$$

where h = summation over all non-covalently bonded pairs of atoms, k = summation over all adjacent pairs of atoms, l = summation over all pairs of dipoles.

The value of $V_b(\theta)$ can be theoretically computed from the above equation for any conformation of the conformer. This is practically done with the help of a computer and leads to the knowledge of the so-called "potential energy map" of a bonded conformer. The conformers are supposed to assume the conformations of lowest energy.

IV. A Statistical Unit for The Energetic Kinetic Network Theory: the "Conformer".

A bonded conformer has a different energy than a Free conformer, according to $V_b(\theta)$ and $V_f(\theta)$. A conformer can assume different "spatial conformations", correctly described in the value of the angle (θ) in the formulation of the potential wells. For each (θ) it is possible to compute the potential barriers $V_b(\theta)$ and $V_f(\theta)$, accordind to the equations above. The equation for $V_b(\theta)$ assumes that all bonds, from all other parts of the entire system, participate in the interactive stabilization of the conformer by inter molecular coupling. Computer simulations show that the energy of a few conformers acting cooperatively converge quickly to the same energy than millions of conformers coupling as a whole. In our new approach, conformers can interact with one another, according to the $V_b(\theta)$ equation, or they may be free of inter-molecular interactions and have a potential energy defined by $V_f(\theta)$. So, for a given spatial conformation given by (θ), there are two "energetic" states, depending on whether $V_b(\theta)$ or $V_f(\theta)$ is used. When conformers interact with one another, they do not necessarily require the whole set of bonds to interact with them, and, therefore, we conceived that nodules of bonded conformers, forming systems of coupled bonds, co-exist with free to move conformers, probably located between the conformer nodules (i.e. at their interface). Details are provided in [1].

We seem to need a statistical theory which can structure the conformers between those which couple up in systems and those at their interface (Fig. 1). All types of conformers should be part of a grand ensemble statistics, and, therefore, coupling between all types of conformers is expected, whether they belong to systems or not. For systems, the intrinsic energy, calculated from the conformational population of the conformers, should vary with temperature, thermal history, pressure etc. Their number and size should also vary. The free energy of the free conformers depends on their complexion, and their number. We speculate that the use of the EKNET statistics described in [1] to the potential barriers $V_b(\theta)$ and $V_f(\theta)$ permits to describe the effect of inter and intra molecular interactions between conformers. In the EKNET statistics, the kinetic units (here conformers) are divided between the b and the F type (Fig. 2), and further, the b conformers can gather into Ns systems. The conformation assumed by the conformer can be the same, either trans, cis, gauche, irrespective of its type, b or F, or the size of the system it belongs to. Any spatial and energetic conformation can be assumed by a conformer, but among the whole set of conformational states, only a certain number are stable, while others are "transients".

For our purpose here, we do not need to specify the real potential profile. What is important is to realize that flexed (cis-gauche) or unflexed (trans) conformations are more or less probable, as evidenced by the potential energy profile to characterize such a statistical distribution. The cis, gauche and trans conformation have different probability of existence for a given amount of thermal energy. Any change in the energy input modifies the distribution of conformers in the different levels. A mechanical and a purely thermal energy input will have different consequences on a system. A thermal energy input is isotropic, whereas a mechanical energy input can be highly anisotropic (e.g., stretching in one direction). It is expected that anisotropic mechanical energy will have a great influence on the structure of the EKNET, i.e. on the number of systems, sub-systems and their structure (the population of the conformers in the different conformation energy levels because alignment in the direction of stress will result in two mechanisms which modify the statistics: 1) an increase of the number of stretched systems in the direction of pull, and 2) an increase of the probability to have relaxing conformers of all types (flexed and trans) lining up in the direction of pull, at the expense of the other directions.

V. Macromolecular Physics or Poly-conformers Physics?

In summary a polymer can be viewed as a set of "conformers", i.e. a set of three-bond elements -real or virtual- belonging or not to the same macromolecule, submitted to intra-intermolecular forces described by the energy potential $V_b(\theta)$ and $V_f(\theta)$, and to which the equations of the EKNET theory apply. Conformers gather into statistical systems which might belong to several macromolecules, thus the macromolecules themselves have lost their individual entity in the definition of the perturbed or unperturbed Free Energy which must be minimized. The Energetic Kinetic Network theory (EKNET) does not require, in its hypotheses and derivations, a description of the changes which occur to the individual macromolecules. The dynamic systems dealt with here are not macromolecules. However, the fact that macromolecules are present is crucial, as explained in [1]. All past statistical theories concentrate on the macromolecular aspect of polymeric materials, and try to determine the macroscopic properties from the characteristics of the individual macromolecules. In the proposed theory an alternative view point is presented to describe the properties of polymeric materials. It is suggested that below a certain transition temperature, the Tg+ transition (which can be associated with Tl,l), the existence of the Energetic Kinetic Network dominates over the network of macromolecules, and in particular is responsible for visco-elastic effects, rubber elasticity and the glass transition temperature. Above the Tg+ transition, which is the temperature of the collapse of the structure of the Energetic Kinetic Network (EKNET), the properties are dominated by the presence of the macromolecules.

VI. Mechanical Deformation. A New Statistical Approach.

In the EKNET approach of mechanical deformation, one is concerned with the changes occurring to the conformers statistics by application of a stress field. Stretching imposes an addtional constraint to the statistics: the number of conformers with a given type of spatial conformation, say the trans conformation, must increase or decrease at a rate which directly relates to the external force. A polymer is formed of Co conformers (per unit volume) which are distributed in the different Energetic Kinetic levels of the systems and sub-systems, as described by the set of equations of the EKNET theory applied to the non-covalent inter-intra molecular energy potential. These Co conformers respond to an energy input (under the form of thermal, mechanical or electrical energy) in a cooperative manner: this creates the structure of the Free Energy. The deformation of an "amorphous" polymeric material consists of the creation, the growth (or shrinkage), and the "orientation" (i.e. the change in the partition function) of Energetic Kinetic Systems, among a set of conformers which can also relax, ie. re-organize their structure without force. The orientation of the stretched systems is achieved via a modification of the energy gap De with the applied stress.

In addition to the EKNET constants (Δm, vm and Δeo), the study of the mechanical properties of a polymer requires the knowledge of:

1) The kinetic behavior of a "stretched" system, which determines the number (variable) of stretched systems which respond in a cooperative manner to the external mechanical effort. This relates to the kinetic stretch rate (variable) for each system which, in turns, determines the force (Δe - Δeo).

2) The kinetic behavior of a "relaxed" system, which determines how much of the global kinetic stretch rate is contributed by the increase of the number of relaxing conformers in the direction of pull. This is made possible by kinetic isotropic structuring, which favors the allocation of conformers-without distortion of their statistics by a force-in the direction of pull. Let us briefly explain:

Systems can "kinetically stretch" (the rate of variation of all the trans conformers varies, i.e. Rs = ($dntF/dt$ + $dntb/dt$) is non zero, and this requires a change of Δe), or they can "relax" (there is no imposed variation of the kinetic rate and De remains constant). Some systems can stretch, which create both force and extension, while other conformers relax. The partition between the Bo,s conformers which are part of the stretched systems and those Bo,r which create the set of relaxing conformers is variable, as extension occurs, and is governed by minimization principles. In the rubbery region, especially at low strain rates, relaxation of the conformers keeps occuring with the overall effect to translate and rotate trans bonds into the direction of pull, at the expense of the other directions. This isotropicity of the relaxing conformers occurs without force, by increasing in the direction of pull the total number of conformers available for the statistics, while contracting that number in the other perpendicular directions. When the

total number of relaxing conformers increases in the direction of pull it provides more elongated (trans) conformers in this direction and, therefore, the requirement for the stretched systems to produce more trans conformers by changing Δe is reduced. Accordingly, the number of stretched systems and the kinetic stretch rate at which they stretch decreases. This favors the minimization of the disturbance of the potential well Δe, which requires the action of a stress.

In essence, the high extensibily of rubberlike material is due to its ability to re-organize the number of relaxing conformers from the perpendicular to the pulling directions, a phenomenon occuring at constant volume. The low modulus observed for rubbers is the consequence of that extensive relaxation and relative little stretching of the systems to accomodate the imposed deformation. The number of stretched systems and the number of conformers per system is a function of the temperature, the stretch rate and the time of elongation, i.e. the strain amplitude. This results in visco-elastic effects.

In the glassy state all the systems of the structure are strained in the same time, and at the same kinetic rate. In the rubbery state, systems may stretch and relax, which obviously results in very different results as far as orientation is concerned. For processing purposes, the mechanisms of inducing the maximum orientation by stretching the Energetic Kinetic Systems, and reducing relaxation, is important to elucidate. This results in Rheomolding considerations.

NOTES

1. J.P. Ibar, in "Fundamentals of Thermally Stimulated Current Analysis and Relaxation Map Analysis", Chapter 7, *SLP Press (1993).*

2. The equations for the Relaxing conformers and the Stretched systems will be given at the conference.Simulated Stress-Strain curves at various strain rates and temperatures are provided below and will be discussed at the meeting.

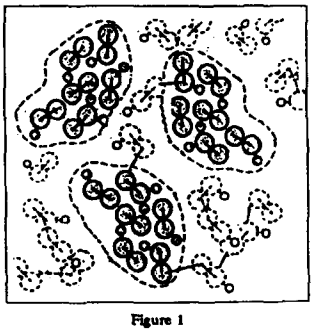

Figure 1

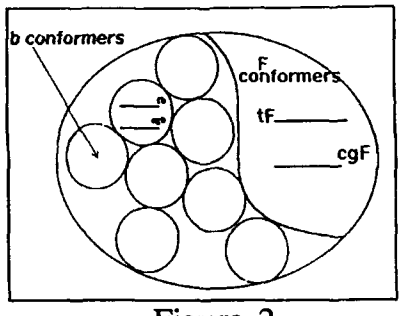

Figure 2

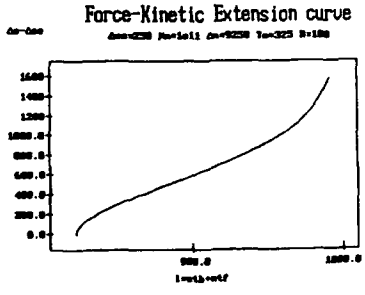

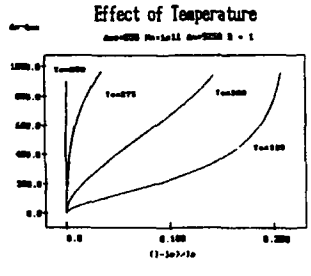

RUBBER-ELASTIC DEFORMATION OF PVC FATIGUE CRAZE

Y. Imai, T. Ohno and T. Takase
Department of Mechanical Systems Engineering
Nagasaki University

Deformation of crack-tip crazes was measured on PVC and changes of craze displacement and stress during a crack growth retarded period were analyzed. With load repetition, crazes grow and come to deform rubber-elastically. Employing the inverse Langevin approximation, the increase of extension was attributed to the increase of random links between tangled junctions of molecular chains in craze fibrils. The number of links was found to increase almost linearly with repetition. Using the density distribution of links, the fractured surface roughness variation was also explained.

INTRODUCTION

Fatigue cracks of some thermo-plastics grow discontinuously depending on the intensity of loading and arrest bands are observed on the fractured surface similar to the usual fatigue striations. Konczol et al (1) measured the deformation of crack-tip crazes of several polymers by interference optics and found the critical extension ratio of craze fibrils, which should be reached when the crack front jumping occurs. In this report, how the craze stress-extension relation changes in the course of crack growth retarded duration(GRD) will be discussed. With the inverse Langevin approximation (2) being employed, the increase of craze extension may be attributed to the increase of random links in a molecular chain of craze fibrils, that is, to the decrease of physical entanglement of molecular chains. The result is very suggestive for the mechanism of disentanglement process.

EXPERIMENTAL METHOD AND ANALYSIS

The same loading apparatus as before (3) was installed on the microscope stage and CT specimens of 12x12.5x5 mm were fatigued at the rate of 1/60 Hz. During the fatigue loading, the crack tip region was observed and the interference patterns like shown in Fig.1 were recorded continuously. Permanent strain of the craze is obtained to be 1.73 from the refractive index 1.30 of the relaxed craze. Assuming that the craze strain at the minimum load falls to this relaxed level, as Konczol et al did, the craze original width was estimated. With the applied stress intensity and the measured fringe orders as a function of the distance from the craze tip, the craze stresses and extension ratios were calculated.

RESULTS AND DISCUSSION

Craze growth and stress-extension relation

The interference patterns shown in Fig.1 were obtained under the loading, K_I=0.02–0.35 MPa$\sqrt{m}$, where the crack front jumped for 88 μm almost instantaneously after 1588 cycles GRD. Fig.2 shows the craze width variation at 10%, 48%, and 97% of the GRD. Near the crack tip, the growth of width almost ceased after 10%. At other location, however, new fibrilation widened the craze in associated with lengthening. Craze growth was intensive at the early stage of GRD.

Measured extension ratios were plotted against calculated stresses in Fig.3, where only the data near the crack tip were used because the craze width there changes very little with repetition, which simplifies the analysis. In the early stage of GRD, pathes of loading(open symbols) and unloading(closed ones) did not coincide. With the load repetition, however, the craze gradually came to deform non-linear elastically, that is, rubber-elastically with diminishing hysteresis.

Rubber-elastic extension

PVC is believed to form a bulky state by entanglement of molecular chains. Crazes are then formed through micro-void nucleation and fibril formation (4). Now, assume that the craze fibrils consist of physically tangled molecular chains (N per unit volume), each of which has n freely-jointed random links on an average between tangled junctions. When the above random link network is subjected to a simple extension in the ratio, λ, required tensile force per unit unstrained area, σ can be expressed from the inverse Langevin approximation (2) as,

$$\sigma = \frac{NkT}{3}\sqrt{n}\left\{L^{-1}\left(\frac{\lambda}{\sqrt{n}}\right) - \frac{1}{\lambda\sqrt{\lambda}}L^{-1}\left(\frac{1}{\sqrt{\lambda n}}\right)\right\} \qquad (1)$$

where $L^{-1}(\lambda/\sqrt{n})=\beta$ is the inverse Langevin function and $\lambda/\sqrt{n}=L(\beta)=\coth\beta-1/\beta$. k, T are Boltzmann's constant and the absolute temperature, respectively.

Larger number of random links gives larger extension for the same stress. Therefore, according to this approximation, the increase of craze extension due to load repetition can be attributed to the increase of random links in molecular chains of craze fibrils. Furthermore, the increase of random links may be brought about through the disentanglement of molecular chains. When employing Eq.1 for the craze extension, however, it is natural to use the restriction that the total number of links per unit volume of craze, nN, should be kept constant.

Solid lines in Fig.3 give the relation of Eq.1 for values of n labelled in the diagram and NnkT/3=16 MPa. Only by changing the n value, good approximations were achieved. The n value increases almost linearly with repetition at the rate depending on the craze size and applied stress intensity as shown in Fig.4.

Crack growth and roughness of fracture surface

Distribution of the true stresses acting on the extended craze fibrils at the maximum load are shown in Fig.5. The true stress gradually increases with load repetition over the whole length of craze, whereas the strength of craze fibrils may

decrease due to the decrease of tangled junctions. This situation is favored for the simultaneous breakdown of craze fibrils over substantial length, resulting in the crack front jumping.

Increasing of the density of li... causes more extension of fibrils and higher true stress, which will enhance the possibility of fibril breakdown. The tendencies of craze growth and increase of links may lead the following: Near the crack tip, the fibrils are old and the link density is evenly distributed along them. Hence, any position along the fibril may become a breaking site. Apart from the crack tip, on the other hand, most part along the fibril is young except the central portion where high density may be attained. Hence, only the central portion of the fibril may become the site.

The above consideration allows the computer simulation of length distribution of broken fibrils which remain on the fractured surface as shown in Fig.6, where the assumption was made that fibrils break at random at the location where the density of links exceeds 35. Actual fractured surfaces between adjacent arrest bands are well simulated: rough surface in front of the arrest band and gradual decrease of roughness toward the next band.

REFERENCES

1. Konczol,L., W.Doll,W., and Bevan,L., 1990, Colloid & Polymer Science 268-9, 814.
2. Treloar,L.R.G., 1975, "The physics of rubber elasticity", 3rd ed. Oxford Univ. Press, Oxford, p.113.
3. Imai,Y., Takase,T., and Nakano,K., 1989, J. Mater. Sci. 24, 3289.
4. Kausch,H.H., 1978, "Polymer Fracture", Springer-Verlag, Berlin, p.272.

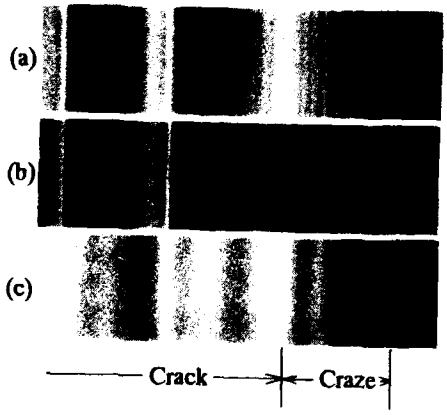

(a) K_I=0.35 MPa$\sqrt{m}$
(b) K_I=0.14 MPa$\sqrt{m}$
(c) K_I=0.02 MPa$\sqrt{m}$

Fig.1 Change of interference fringes observed near the PVC fatigue crack tip.

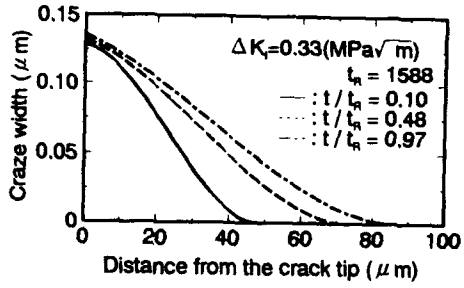

Fig.2 Growth of craze width during a retarded duration.

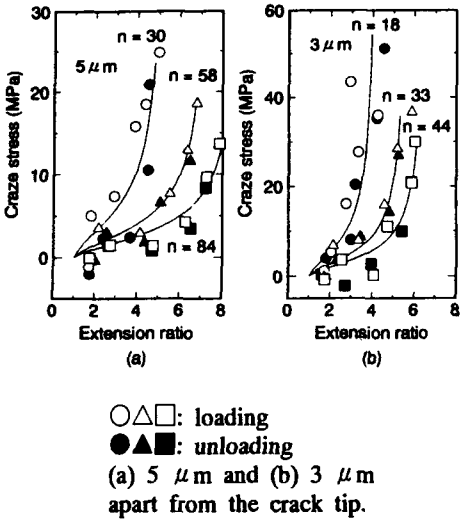

Fig.3 Stress vs. extension relation of craze fibrils

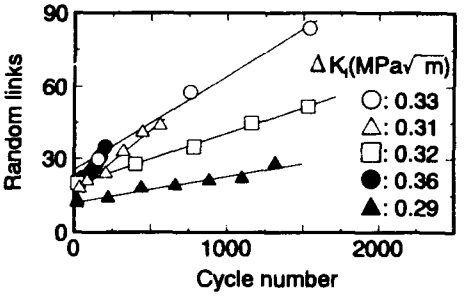

Fig.4 Increase of the number of random links in craze fibrils with load repetition.

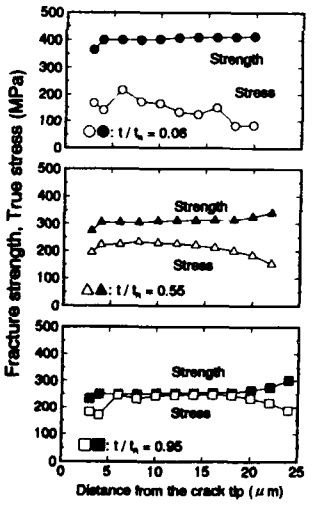

Fig.5 Distribution of true stress and fracture stress acting on the craze fibrils.

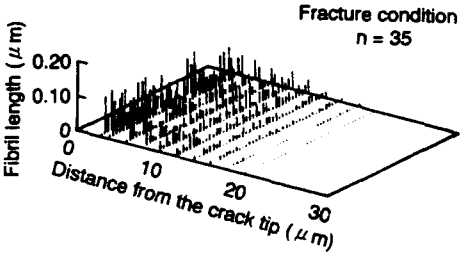

Fig.6 Computer simulation of fractured surface roughness.

CRACK-TIP DAMAGED ZONE, K1 VALUES AND PROPAGATION OF A CRACK IN RUBBER TOUGHENED PMMA

C. Fond, R. Berthet and R. Schirrer *

The fracture energy of Rubber Toughened Poly(Methyl MethAcrylate) (RT-PMMA) is measured by using Compact Tension specimens under medium rate of loading. Load and crack length are measured during the test. The size of the whitened damaged material at the crack tip is loading rate dependent and therefore the classical K_1 test in not valid for this material. The behaviour of the whitened damaged zone is recorded by means of photo elasticity. The stress-strain law of the material at a microscopic scale at the crack tip influences the rate of loading of the toughening rubber particles.

EXPERIMENTS

Instrumented Specimens

An experimental device has been developed to test pre-notched polymeric samples at medium loading rate. The samples are pre-cracked under fatigue cycling (50 Hz). The crack speed and length are important parameters for toughness measurements. Therefore, the position of the crack tip is followed by measuring the resistance of a metallic layer coated on one side of the sample. The post-mortem marks of crack arrests (when visible) on the crack surface show that the accuracy of the crack-tip position is ±2% of the length of the sample (±2% of 36 mm, fig. 1). As the fracture surface energy is primarily related to the size of the crack tip damaged zone ("process-zone"), the whitening (if any) related to the damage of an initially transparent material is recorded on a photograph at the initiation of the propagation. The flash light is triggered by the cut by the crack of an electric circuit (a metallic layer is also coated on the other side of the sample).

Validation with PolyCarbonate

In PolyCarbonate (PC), in plane strain state, the non linear behaviour is confined in a very small zone at the crack tip. Therefore it has been used to test the validity of the experiment. The linear elastic fracture mechanic (L.E.F.M.) can then be applied to quasi-static and dynamic propagation to analyse the fracture toughness (Freund [1]). However,

* ICS (CRM-EAHP) 4, rue Boussingault F-67000 STRASBOURG

a significant scatter of the energy release rate values is always expected, depending on the sharpness of the initial crack. Figure 2 shows that the viscoplasticity of PC leads to a decrease of the fracture energy when the crack velocity increases. As the energy release rate does not depend on the crack length, the L.E.F.M. may be used to calculate fracture toughness.

PROPAGATION OF A DAMAGED CRACK TIP IN RT-PMMA

Size of the damaged zone and fracture energy

K_1 testing using Compact Tension (C.T.) samples show that RT-PMMA is very sensitive to the loading rate: paradoxically, the size of the damaged zone decreases when the crack length increases at constant speed (the final size of the whitened material is up to the ten times smaller than the initial one). Similarly to this decrease of thickness, the J_1 values deduced from the stiffness measurement of the sample or the G_1 deduced from L.E.F.M. decrease with the crack length at quasi-constant crack velocity (fig. 2, Berthet [2]). It was pointed out that the initial size of the damaged zone it strongly dependent on the loading time (typically 10^{-3} s) and that it may be larger than the steady-state propagating zone size (typically 1 to 300 ms^{-1}). Therefore, a transient state takes place at the beginning of the propagation, leading to the observed damaged zone size decrease. Isoclines obtained by setting the sample between crossed polarizors at the beginning of the propagation (fig. 4) show that the level of the shear stresses at the damaged zone boundary is very low, and that hydrostatic pressures seems to be locally the most significant solicitation.

Propagation of the damage

The global behaviour described above is related to local micro-mechanics and micro-mechanisms around the rubber particles (Mauzac and Schirrer [3]) and to viscoplasticity and crazing. Therefore, an attempt will be made to quantify these mechanisms by means of finite element simulations (including local large scale yielding and dynamic effects) at the scale of the rubber particles. Such an approach needs first to describe the damaged material behaviour as a function of the loading rate around the particles in front (outside) of the damaged zone (fig. 3). One of the major difficulty in the finite element analysis will be to introduce a rupture criteria for the locally plasticised material.

REFERENCES

[1] L. B. Freund, (1972, J. of the Mech. and Ph. of Solids, 20, p. 129-140.
[2] R. Berthet, (1993), private communication
[3] O. Mauzac and R. Schirrer, (1992), J. of Mat. Sciences 25-12, 5125-33.

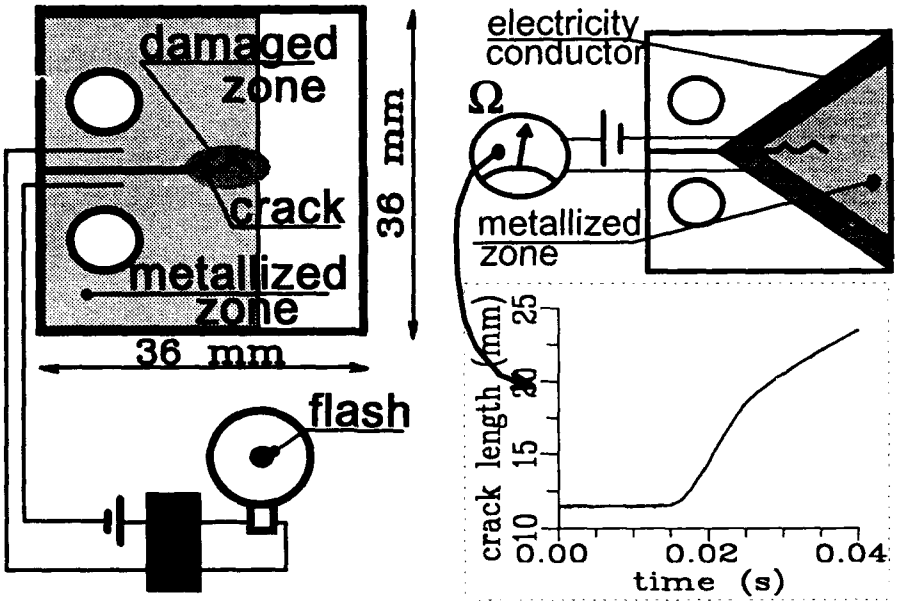

Figure 1 instrumentation of the sample to trigger a flash and measure the crack length

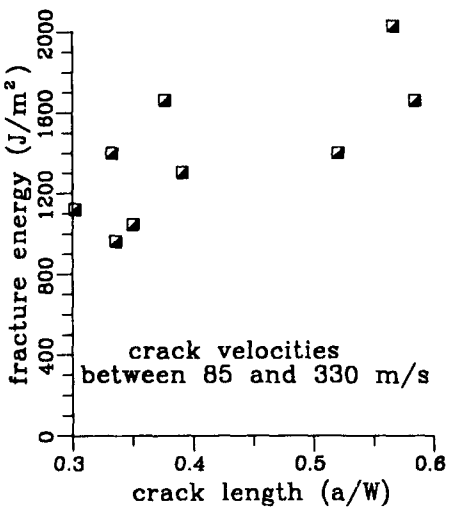

The material used for validation is a commercial grade of PolyCarbonate.

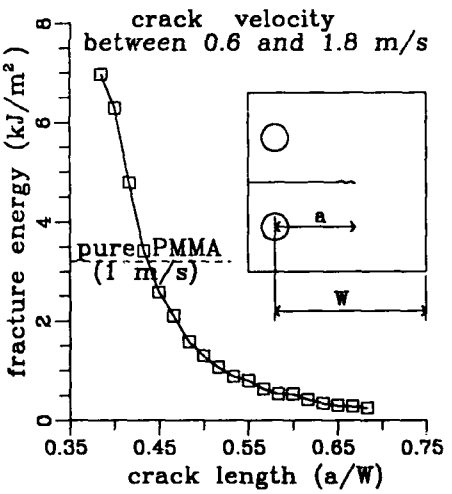

The material tested is a commercial grade of Rubber Toughened Poly(Methyl MethAcrylate)

Figure 2 Fracture energy versus crack length: the test is valid for PC and invalid for PMMA

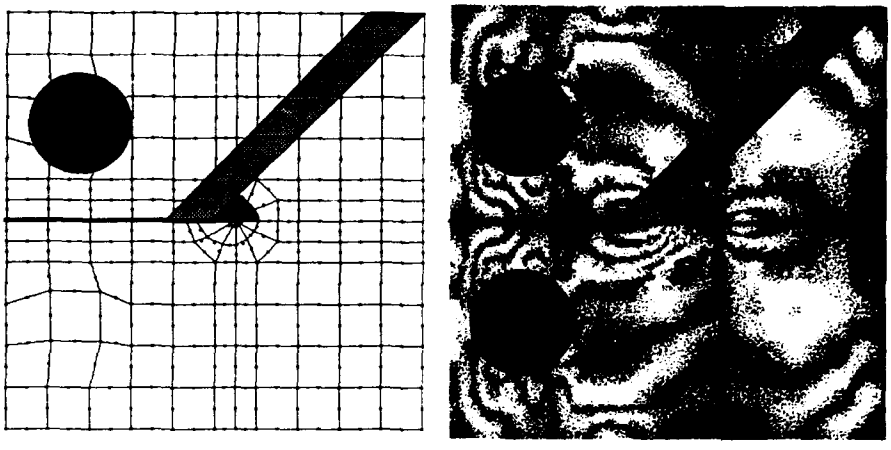

Figure 3 Finite element simulation of photo elasticity: mesh (symmetric) and fringe pattern for crossed polarizers.

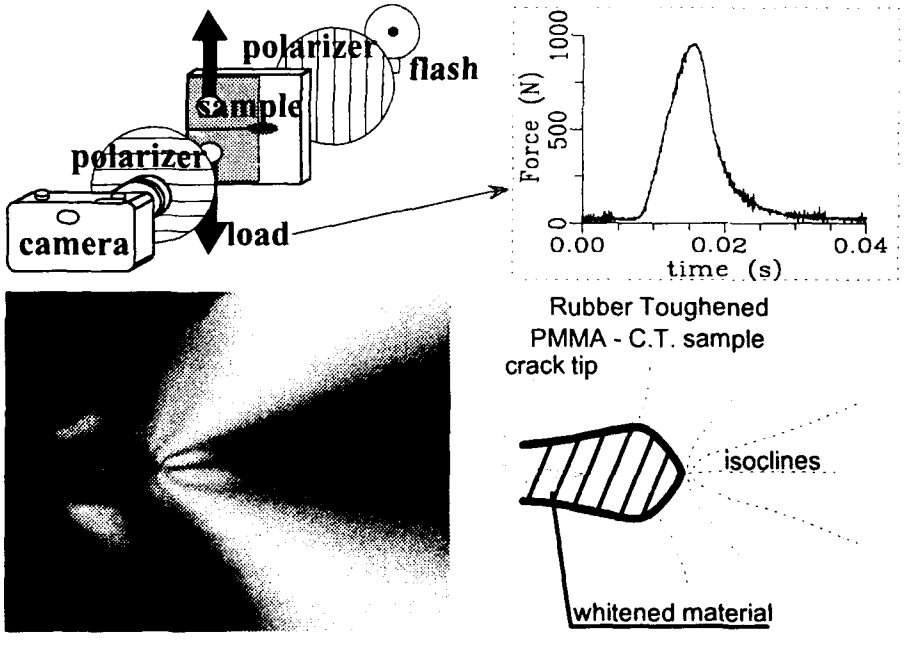

Figure 4 Photograph of a crack tip damaged zone in a RT PMMA under crossed polarizers

THE LONG-TERM AGING EFFECTS OF VISCOELASTIC POLYMERS AND ITS FINITE ELEMENT METHOD

Feng ZhiGang and Zhou Jianping
Department of astronautics,National University of Defence Technology,ChangSha,People's Republic of China

The solid propellant is a sort of nonlinear viscoelastic particulate composite polymers. During the storage time of the solid rocket motor,because of the thermal aging,moist aging and oxide aging,it may become weak,sometimes failure. The effect of the long-term aging should be derterminated in the analysis of the structural perfection of solid rocket motor. Some experimental datas related to aging effect are given in the paper and the finite element method is introduced to dertermine the deformation, stress and strain of the solid propellant grain in storage. Many numerial results about the aging effects of viscoelastic polymers beams are presented in this paper,also.

INTRODUCTION AND EXPERIMENT

HTPB composite solid propellant has been used popularly in the field of aviation and aerospace for its better property. During its storage time,because some protecting ways, such as filling-nitrogen and sealing hermetically, has been undertaken,the aging caused by light,radiation and moistness can be ignored and the thermal aging becomes the main cause for propellant aging. The relaxtion function which includes the aging factor can be presented as (in reference (1))

$$E(t) = E_0^0 + \triangle v E_0^1 + \sum_{i=1}^{n} (E_i^0 + \triangle v E_i^1) e^{-\alpha_i t} \tag{1}$$

where v is crosslinking density, and it can be expressed as:

$$v = \frac{0.1012 - 0.0961 e^{-0.0595t}}{1 - 0.837 e^{-0.0595t}} \quad (10^{-6} mol/mm^3) \tag{2}$$

$$\triangle v = v\ (t)\ - v\ (0) \tag{3}$$

Let $n = 4$, $\alpha_i = 10^{i-1}\alpha (i = 1,2,3,4)$, where α is a constant. By applying the least square method to the experimental results (1), the followings can be obtained

$E_0^0 = 2.3677$; $E_0^1 = 7.8135 \times 10^7$; $E_1^0 = 1.1548$
$E_1^1 = 1.8493 \times 10^7$ $E_2^0 = 4.0586$; $E_2^1 = -1.5526 \times 10^7$
$E_3^0 = 1.5320$; $E_3^1 = 1.7767 \times 10^7$ $E_4^0 = 6.4697$
$E_4^1 = 12.452 \times 10^7$; $\alpha = 0.0366$

THE INVERSE TRANSFORMING OF CREEP FUNCTION

For viscoelastic polymers:

$$\int_0^t E(t-\tau)J(\tau)d\tau = t \tag{4}$$

Equation (2) can be transformed into the following form for the convenient of numerial solution:

$$v(t) = A_0 + \sum_{i=1}^{K} A_i e^{-0.0595it} \tag{5}$$

Where A_i (i=0,1,...K) can be determined by

$$\min_{A_0,A_1,\ldots A_k} \int_0^{T_M} \left[\frac{0.1012 - 0.0961e^{-0.0595t}}{1 - 0.837e^{-0.0595t}} - \left(A_0 + \sum_{i=1}^{K} A_i e^{-0.0595it} \right) \right]^2 dt \tag{6}$$

The numerical results of this approaching with a various k are shown in figure 1. Applying (5) and (1) to (4),a proper form of creep function can be gived as

$$J(t) = J_0 + \sum_{i=1}^{N} J_i (1 - e^{-\frac{t}{\tau_i}}) \tag{7}$$

THE FINITE ELEMENT METHOD

The details of this technique can be found in reference (2)

A constitutional model of polymer materials considering mechanical damage has been given in reference (3) and it can be presented as

$$\varepsilon = \int_{-\infty}^{t} J(t-\tau)\frac{\partial\bar{\sigma}(\tau)}{\partial\tau} d\tau \tag{8}$$

Applying (7) to (8) leads to the viscoelastic incremental constitutional model

$$\{\triangle\sigma\}_{k+1} = (1-\omega_{k+1})[E](\{\triangle\varepsilon\}_{k+1} - \{\triangle\varepsilon^c\}_{k+1} - \{\triangle\varepsilon^T\}_{k+1}) - \frac{\triangle\omega_{k+1}}{1-\omega_k}\{\sigma\}_k \tag{9}$$

Hence using the idea of the finite element method we obtain

$$[K(\omega_k)]\{\triangle u_i\}_{k+1} = \{\triangle Q(\omega_k)\} + \{\triangle Q^c(\omega_k, \triangle\omega_{k+1})\} \tag{10}$$

where

$$[K(\omega_k)] = \int_V (1-\omega_k)[B]^T[E][B]dV \tag{11}$$

$$\{\triangle Q(\omega_k)\} = \int_V [N]^T\{\triangle p\}_{k+1}dV + \int_S [N]^T\{\triangle P\}_{k+1}dS + \int_V (1-\omega_k)[B]^T[E](\{\triangle\varepsilon^c\}_{k+1} + \{\triangle\varepsilon^T\}_{k+1})dV \tag{12}$$

$$\{\triangle Q^c(\omega_k,\ \triangle\omega_{k+1})\} = \int_V \triangle\omega_{k+1}[B]^T$$
$$\left[[E]\left(\{\triangle\varepsilon\}_{k+1} - \{\triangle\varepsilon^c\}_{k+1} - \{\triangle\varepsilon^T\}_{k+1}\right) + \frac{1}{1-\omega_k}\{\sigma\}_k\right] dV \quad (13)$$

NUMERICAL RESULTS

1. A beam with a fixed end and the another end subjected to monotonous tension loading is investigated. The numerical solution has been carried out up to initiation with the mesh given in Figure 2 and the numerical approach is given in Figure 3 when aging–time are 0,1,5,20 days.

2.The deformation of a beam under its own weight is shown in Figure 4.

SYMBOLS USEDE

B = strain matrix

D = physical matrix

E = relaxtion function

J = creep function

K = stifness matrix

P = force

u = displacement

ω = damage variable

ε = strain

σ = stress

REFERENCE

1. J.P. Zhou and Y.C. L, 1989,"Crosslink density of ageing particle–filled polymer materials and its influence on mechanical behavior", Second Inter. Conf. on Development and Design with Advanced Materials(ATMAM89), Montreal, Canada

2. Z.G. Feng, 1993,"The finite element method of composite prollant",Thesis,National Unvi. of Defense Tech., ChangSha,China

3. Y.C. L and J.P. Zhou,1989,"A constitutional model of polymer materials considering mechanical damage and chemical ageing interaction", Computational Mechanics'88, Vol.1, Springe–Verlag

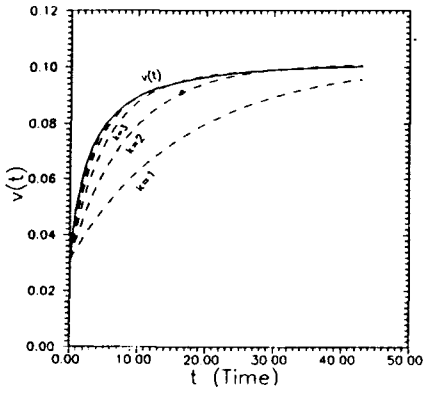

Figure 1 Approach to v,k = 1,2,3,...

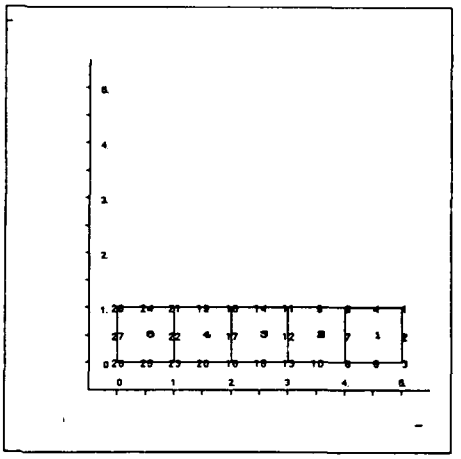

Figure 2 Finite Element Method Mesh

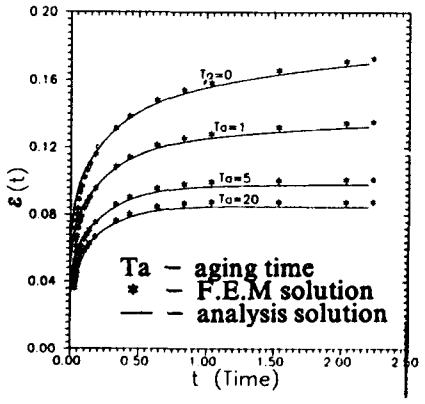

Figure 3 Deformation of a beam

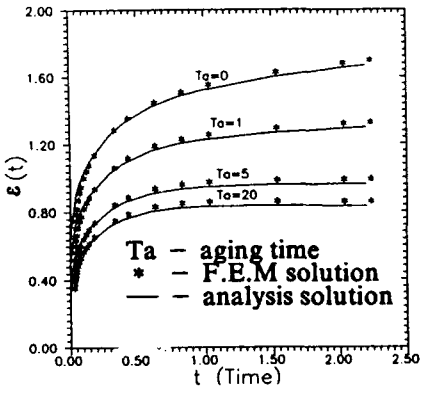

Figure 4 Deformation of a beam under its weight

A KINETIC APPROACH TO THE DESCRIPTION OF ELASTICITY IN A WIDE TEMPERATURE RANGE FOR ORIENTED POLYMERS

S V Bronnikov*

An equation adequately describing the temperature dependences of Young's modulus for oriented polymers in a wide temperature range (from cryogenic to the melting temperature) is proposed. It bases on kinetic principles and takes into account the change in the statistics of certain (twisting and deformation) atomic vibrations at the Debye mode temperatures. The statistics substitution "triggers" relaxational transitions and causes peculiarities on the temperature dependences of Young's modulus.

The elasisity relaxation is known to be caused by thermal fluctuations (1). Therefore, Young's modulus, E, of oriented polymers decreases with increasing both temperature, T, and loading rate, $\dot{\varepsilon}$, by an Arrhenius type equation presented in reference (1)

$$E = E_0\left(1-\frac{kT}{W_0}\ln\frac{\dot{\varepsilon}_0}{\dot{\varepsilon}}\right) \quad (1)$$

where E_0 is Young's modulus at $T \to 0$ K, W_0 is the activation energy of the Young's modulus relaxation, k is the Boltzmann constant, and $\dot{\varepsilon}_0 \cong 10^{13}$ Hz.

Equation (1) predicts the linear dependence of elasticity with temperature at $\dot{\varepsilon}$ = const. Nevertheless, experimental results show its validity only in certain temperature range.

Figure shows the temperature dependence of Young's modulus, E(T), for drawn polyethylene (PE) fiber over a wide temperature range at $\dot{\varepsilon}$ = 0.1 Hz. At moderate temperatures, $T_t < T < T_b$, the experimental points fall on straight line in accordance with Eq. (1). At both low, $T < T_t$, and high, $T > T_b$, temperatures, the experimental E values are lower than those predicted by Eq. (1). Such dependences are revealed to be typical for 30 oriented polymer fibers of different chemical structures.

*Institute of Macromolecular Compounds, Russian Academy of Sciences, St. Petersburg, Russia

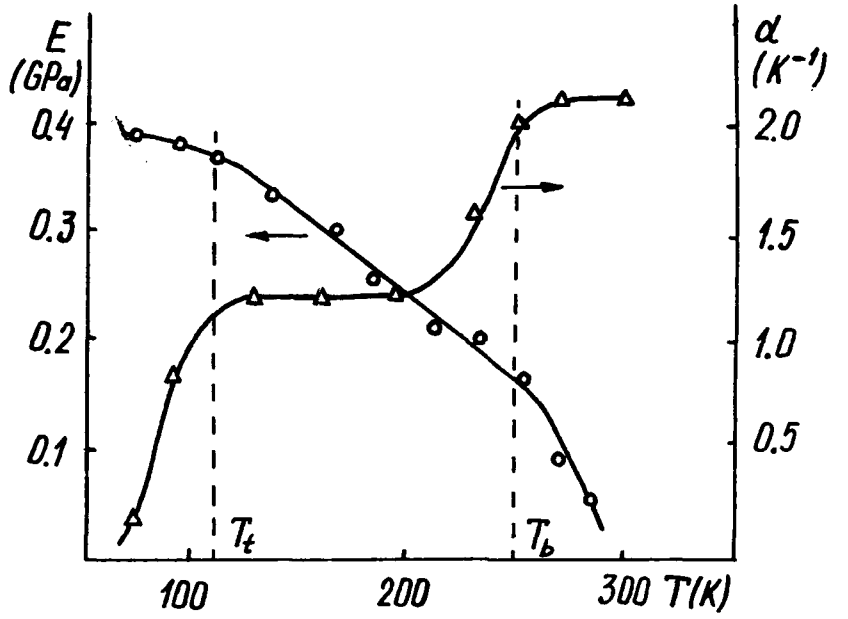

Figure Temperature dependence of Young's modulus (●) and thermal expansion coefficient (Δ) for oriented PE fiber

To clarify the reasons of mentioned deviations from linearity, the relation between activation energy, classic heat capacity, C, and thermal expansion coefficient, α, should be taken into account (2)

$$W_0 = \frac{\varepsilon_* C}{\alpha} \qquad (2)$$

where $\varepsilon_* \cong 0.1$ is the ultimate deformation of interatomic bonds. Thus, Eq. (1) becomes

$$E = E_0\left(1 - \frac{k\alpha T}{\varepsilon_* C} \ln\frac{\dot{\varepsilon}_0}{\dot{\varepsilon}}\right) \qquad (3)$$

Figure shows also temperature dependence of the thermal expansion coefficient, α(T), being determined by the shift of the the regularity bands in IR and Raman spectra (3). The α parameter is shown to change in a complicated manner. The E(T) dependence is suggested to be explained by the variability in α over the investigated temperature range.

Following the standart procedure (4), the thermodynamic Debye temperature, θ, should be introduced as $\theta = h\nu/k$ where h is the Plank constant and ν is the maximum frequency of acoustic vibrations. At $T \geqslant \theta$, they obey the classic (Maxwell-Boltzmann) statistics. At $T \leqslant \theta$, the vibrations obey the quantum (Bose-Einstein) statistics, and α is described as follows from reference (4)

$$\alpha = \sum_m \alpha_m = \frac{S}{V} \sum_m C_m G_m \qquad (4)$$

where α_m is the contribution of the m-th vibrational mode to thermal expansion, G_m is the mode Gruneisen parameter, and C_m is the contribution of the m-th vibrational mode to heat capacity, and S and V are constant. C_m was shown in reference (4) to be a quantum function

$$C_m = k \sum_m F(\theta_m/T) = k \sum_m \left[\frac{\theta_m}{4kT} + \frac{\exp(-\theta_m/T)}{[1 - \exp(-\theta_m/T)^2} \right] \qquad (5)$$

In Eq. (5), the Debye mode temperature, θ_m, characterizes the temperature at which the quantum statistics is substituted by the classic statistics. Therefore, Eq. (4) shows that complications in $\alpha(T)$ are caused by the change in the statistics of atomic vibrations. The substitution of Eqs. (4) and (5) into Eq. (3) results in

$$E = E_0 \left[1 - \frac{kS \sum_m G_m F(\theta_m/T)}{C\varepsilon_*} \ln \frac{\dot{\varepsilon}_0}{\dot{\varepsilon}} \right] \qquad (6)$$

Figure shows that Young's modulus in accordance with Eq. (6) varies slightly at $T < T_b$ because α is too small. At $T_t < T < T_b$, its slope becomes constant because $\alpha \cong$ const; and at $T < T_b$, it increases again because α attain a new constant value. Therefore, Eq. (6) shows that complications in E(T) dependence over a wide temperature range are caused by atomic statistics substitution.

Characteristic temperatures, T_t and T_b, being compared with the temperatures of the main relaxation transitions, T_β and T_α, result: $T_t \cong T_\beta$ and $T_b \cong T_\alpha$. Hence, the relaxation transitions are supposed to be caused by the statyistics substitution for atomic vibrations.

REFERENCES

1 Vettegren V I, Bronnikov S V, Korzhavin L N, Frenkel S Ya, J Macromol Sci-Phys 29 (1990) 285

2 Zhurkov S N, Fiz Tverd Tela 22 (1980) 3344

3 Vettegren V I, Titenkov L S, Bronnikov S V, J Therm Anal 38 (1992) 1031

4 Wunderlich B and Baur H, Adv Polym Sci 7 (1970) 151

MORPHOLOGY AND DEFORMATION/FRACTURE BEHAVIOR OF PMMA IONOMERS AND THEIR BLENDS

X. Ma, J.A. Sauer and M. Hara
Department of Mechanics and Materials Science, Rutgers University.

The morphology and deformation/fracture behavior of a new amorphous ionomer based on poly(methyl methacrylate)(PMMA) and its blends have been investigated, and the results are compared with those obtained for polystyrene (PS) ionomers and PS ionomer blends. The results indicate the general applicability of our conclusions.

INTRODUCTION

An incorporation of ionic groups into polymer chains (e.g., a formation of ionomers) leads to significant changes in physical properties, mainly arising from the formation of ionic aggregates, such as ionic clusters (1). We have elucidated the effect of ion incorporation on the deformation modes of ionomers, and have correlated them with bulk mechanical behavior, such as tensile and fatigue behavior (2). In addition, we have shown that mixing ionomers with their precursor polymers leads to microphase separated, rigid-rigid blends with enhanced mechanical properties, without losing the transparency of the original polymer (3).

Most ionomers investigated so far are made from PS-based polymers, such as partially sulfonated PS and poly(styrene-co-methacrylate). In this work, we extend our previous studies on PS ionomer system to the PMMA ionomer system, to prove the general applicability of our previous conclusions, and to develop more useful ionomers for engineering applications.

EXPERIMENTAL

The PMMA-based ionomers with low ion content (less than 1 mol%) were prepared by the hydrolysis of PMMA with NaOH in THF/H_2O (50/50). The ionomers with high ion content (more than 6 mol%) were prepared by neutralizing the random copolymers of MMA and methacrylic acid (MAA) with NaOH in benzene/methanol (90/10). The blends of PMMA and PMMA ionomers were made by solution blending in benzene/methanol. Both the ionomer and the ionomer blend specimens were obtained in a powder form by freeze-drying. TEM specimens were prepared by casting from proper solvents. The specimens for bulk mechanical testing were compression molded; e.g., rectangular test specimens with dimensions 12mm x 2.5 mm x 0.5 mm were made for dynamic mechanical measurements.

RESULTS AND DISCUSSION

PMMA Ionomers

The effect of an introduction of ionic groups into PMMA on the dynamic storage modulus is shown in Figure 1. With increasing ion content, a T_g increases, a rubbery plateau due to ionic crosslinking is developed, and at higher ion content (24.7 mol%) little softening is seen. This behavior is typical for amorphous ionomers, such as PS-based ionomers (1).

The deformation mode is changed from crazing only for PMMA to crazing plus shear deformation upon the introduction of ionic groups. It is well known that divalent salts form stronger ionic bonds than monovalent salts (1), and the addition of only 0.8 mol% of ionic groups into PMMA can induce shear deformation (see Figure 2), whereas the Na-salt ionomer of the same ion content shows only crazing. The overall deformation mode indicates that crazes are getting shorter and interact with shear deformation. The similar change in deformation modes is also seen for the PMMA ionomers with high ion content (e.g., 12.4 mol%). Such behavior is interpreted as arising from an increased "strand" density (4) due to ionic crosslinking effect of the ionic aggregates, as demonstrated for the PS ionomers (2).

PMMA Blends

The mixing of PMMA ionomers with PMMA leads to the formation of rigid-rigid blend materials. Because of the difference in the polarity between the component polymers, microphase separation occurs as seen in Figure 3. These blends are also transparent (see Figure 4), no loss of transparency is seen at all compositions studied even at high temperature. This is because the refractive indices of two polymers are very close (the difference is less than 0.01), due to the very similar chemical structures of the component polymers. The study of PS ionomer/PS blends indicate the similar characteristics (3), therefore, these characteristics are generally observed for ionomer/ionomer precursor blends.

ACKNOWLEDGMENT

Acknowledgment is made to the U.S. Army Research Office for support of this research.

REFERENCES

1. Eisenberg A. and King M., 1977, "Ion-Containing Polymers," Academic Press, New York.

2. Hara M. and Sauer J.A., J. Macromol. Sci., Rev. Macromol. Chem. Phys., in press.

3. Hara M., Bellinger M., and Sauer J.A., 1992, Colloid Polym. Sci 270, 652.

4. Kramer, E.J. and Berger, L.L., 1990, Adv. Polym. Sci. 91/92, 1.

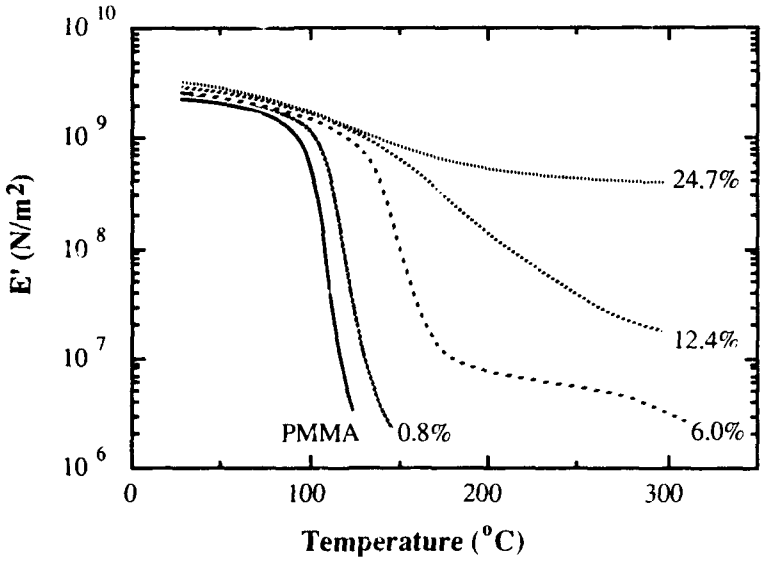

Figure 1 Storage modulus vs. temperature for PMMA ionomers with various ion content

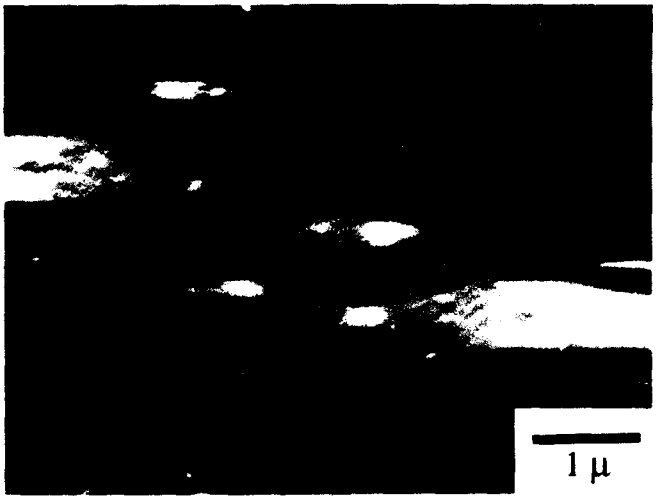

Figure 2 TEM micrograph of deformed PMMA ionomer (0.8 mol%; Ca salt) thin film

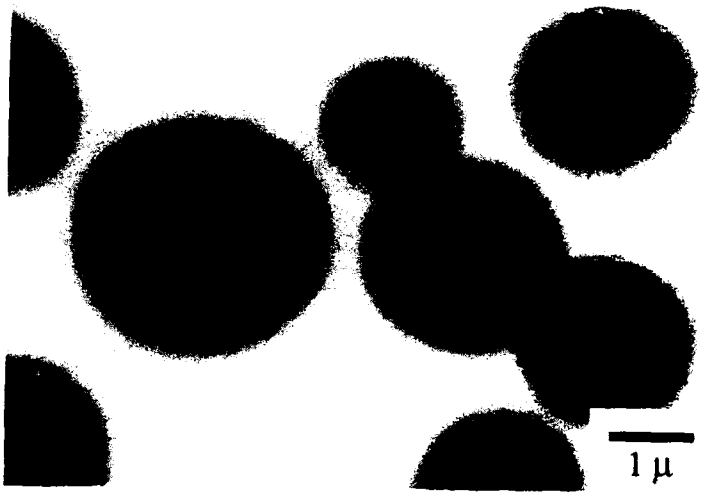

Figure 3 TEM micrograph of PMMA ionomer (12.4 mol%; Na salt)/PMMA (30/70) blend thin film

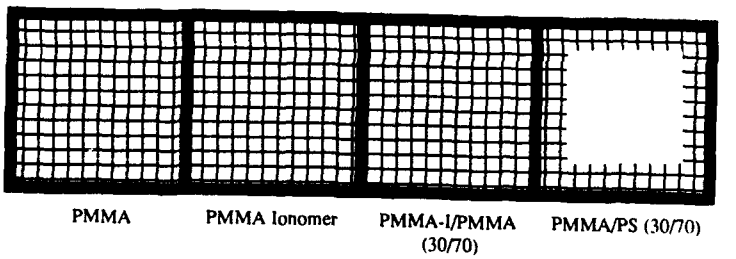

Figure 4 Table indicating the transparency of specimens: PMMA, PMMA ionomer, PMMA ionomer/PMMA (30/70), as well as PMMA/PS (30/70)(taken for comparison)

FATIGUE FAILURE IN THERMOPLASTIC COPOLYESTERS

E. J. Moskala*, T. J. Pecorini*, and L. T. Germinario*

The fatigue behavior of thermoplastic copolyesters of dimethyl terephthalate with ethylene glycol (EG) and 1,4-cyclohexanedimethanol (CHDM) was determined as a function of EG/CHDM ratio. Fatigue crack propagation (FCP) tests were performed on compact tension specimens using a load ratio o 0.1 and a sinusoidal waveform with a frequency of 10 Hz. Fatigue resistance, as measured by the crack growth rate at a arbitrary value of stress intensity factor range, decreased dramatically with increasing CHDM content. The mechanisms of fatigue crack propagation were identified using scanning electron microscopy (SEM) and atomic force microscopy (AFM), and were related to differences in the physical properties of the copolyesters. AFM provided novel information concerning the mechanisms of fatigue crack propagation which was not attainable through the more customary SEM.

INTRODUCTION

As plastics become more prevalent in engineering applications, an understanding of their resistance to failure under fatigue loading becomes critical. The ability of plastics to resist fatigue crack propagation (FCP) may be affected by material properties such as chemical composition, molecular weight, crystallinity, and crosslinking, as well as by experimental parameters such as mean stress level, test frequency, waveform, and temperature (1-5). The objective of this work was to determine the effect of copolymer composition on the FCP behavior of a series copolyesters of dimethyl terephthalate with ethylene glycol and 1,4-cyclohexanedimethanol.

EXPERIMENTAL

Sample Preparation Thermoplastic copolyesters of dimethyl terephthalate with ethylene glycol (EG) and 1,4-cyclohexanedimethanol (CHDM) were supplied by Eastman Chemical Company. The CHDM content, yield strength (σ_y), tensile modulus (E), and inherent viscosity (IV) of each copolyester are listed in Table I. Compact tension specimens were machined from 6.2-mm thick, amorphous, injection-molded plaques. The specimens were notched in the mold-flow direction with a band saw. A razor blade was then tapped into the root of the notch, and a fatigue precrack was grown from the razor-sharpened notch prior to any data acquisition.

Fatigue Tests Fatigue tests were performed at room temperature on a MTS closed-loop servohydraulic testing machine using a sinusoidal waveform with a frequency of 10 Hz. The tests were conducted in load-control using a minimum-to-maximum load ration of 0.1. Crack length was measured by computer using an elastic compliance technique. Fatigue crack propagation rate, da/dN, was determined by an incremental polynomial method described in ASTM Standard E647-88a (6) and plotted versus stress intensity factor range, ΔK, according to the Paris equation, $da/dN=A\Delta K^m$, where A and m are material parameters (7).

Fractography Scanning electron microscopy (SEM) experiments were performed on a Cambridge Instruments Stereoscan 200 scanning electron microscope. Fracture surfaces were coated with a thin layer of gold in a sputtering chamber before the SEM observations. Atomic force microscopy (AFM) experiments were conducted with a Digital Instruments Nanoscope III scanning probe microscope under ambient conditions, using the large area (J-head) piezoelectric element. Sample surfaces were scanned with triangular, 200 micron Nanoprobe cantilevers, supplied with integrated pyramidal Si_3N_4 tips. Topographic, 3-D profiles were obtained in constant force mode.

*Eastman Chemical Company, P.O. Box 1972, Kingsport, TN 37662.

RESULTS AND DISCUSSION

A log-log plot of da/dN versus ΔK for the series of copolyesters is shown in Figure 1. Low FCP rates at high values of ΔK are indicative of good fatigue resistance. Clearly, increasing the concentration of CHDM co-units in the copolyester has a deleterious effect on resistance to fatigue crack propagation; the value of da/dN, at any particular value of ΔK, increases dramatically with increasing CHDM concentration. For example, at a value of ΔK of 1.2 MPa$\sqrt{m}$ ($\log\Delta K \approx 0.09$), the value of da/dN increases almost seven hundred-fold as CHDM concentration increases from 4 to 68 mole percent. (See Table II.) Additionally, the value of ΔK at the onset of unstable crack propagation decreases with increasing CHDM content. (See Table II.)

Such large differences in fatigue resistance were reflected in fracture surface features. Not surprisingly, given the similarities in FCP behavior, the fracture surfaces of COP31 and COP68 were similar. The same was true for the fracture surfaces of COP4 and COP10. For the sake of brevity, micrographs of only COP31 and COP4 will be presented.

Fatigue crack propagation typically occurs either by discontinuous growth band (DGB) formation or by striation formation. A striation is a fracture surface marking which corresponds to the position of the crack tip as a result of an individual cycle or load excursion. A DGB, on the other hand, is a fracture surface marking which corresponds to an increment of crack growth caused by multiple cycles.

Fatigue crack propagation in COP31 occurs by DGB formation at low values of ΔK and by striation formation at high values of ΔK. A scanning electron micrograph of striations in COP31 (ΔK= 1.2 MPa$\sqrt{m}$) is shown in Figure 2a. The width of the striations agrees well with the macroscopic FCP rate recorded in Figure 1 (1.54 mm versus 1.12 mm). A scanning electron micrograph of DG bands in COP31 (ΔK= 0.8 MPa$\sqrt{m}$) is shown in Figure 2b. Each DGB corresponds to approximately 80-100 cycles. The morphology of the DG bands in COP31 is generally similar to what has been reported for other amorphous glassy polymers (1); relatively smooth dark regions alternate with fibrillated, light regions. The morphology of DG bands in COP4, shown in Figure 2c (ΔK= 1.3 MPa$\sqrt{m}$), however, is decidedly different; large strips of drawn material alternate with bands of porous, voided material. Each DGB corresponds to approximately 350-400 cycles. (It should be noted that the width of a striation or DGB will increase with increasing ΔK. The widths reported here correspond to the specified value of ΔK.) It is evident from the micrographs shown in Figure 2 that considerably more plastic deformation occurs during DGB formation in COP4 than in COP31, which may account for the superior fatigue resistance of COP4.

Depth profiles of these fracture surfaces were obtained by AFM. A profile of the striation region in COP31, Figure 3a, shows that maximum striation depth is approximately 50 nm. The average striation width-to-depth ratio is approximately 40:1. Depth profiles of DG bands in COP31 and COP4 are shown in Figures 3b and 3c, respectively. Note the distinct differences in the profiles for these two materials. The maximum peak-to-valley depth in COP4 is approximately 2 μm, compared to only 0.5 μm for COP31. The depths of both DG bands, however, are significantly greater than the striation depth shown in Figure 3a.

According to a model for discontinuous crack growth proposed by Döll and Könczöl (8), a large rounded peak attributed to melted craze fibrils identifies the beginning of a DGB (point X in Figure 3b). Several sharp spikes from fibrils which failed in a pseudo-brittle fashion follow. Finally, a relatively flat region marks the end of the DGB (point Y in Figure 3b). A three dimensional atomic force micrograph of DG bands in COP31 is shown in Figure 4. The fibrils which failed in a pseudo-brittle fashion, from A to C in Figure 4, form two distinct regions, from A to B and from B to C. The fibrils in region AB are randomly dispersed, whereas the fibrils in region BC tend to be aligned in 1-μm wide bands, parallel to the crack front. A modified version of the model proposed by Döll and Könczöl (8) for DGB formation is proposed in Figure 5. The craze preceding the crack tip lengthens after N cycles. Then, the most highly extended fibrils fail thermally on a per cycle basis creating increments of craze extension, Δc. Finally, the bulk of the craze fibrils fail in a pseudo-brittle fashion creating the profile shown in Figure 3b. The incremental craze extension that occurs during thermal failure of the craze fibrils gives rise to the banded fibril region on the fracture surface in Figure 4 (region BC).

In contrast, the mechanism for DGB formation in COP4 is not well understood. One possible scenario is outlined in Figure 6. High triaxiality ahead of the crack tip generates voiding. As the voids ripen and coalesce, the ligament between the voids and crack tip is elongated. The ligament eventually ruptures and the crack jumps through the voided region before becoming arrested.

CONCLUSIONS

The fatigue resistance of copolyesters of dimethyl terephthalate with EG and CHDM decreased with increasing CHDM content. Novel DG bands in EG-rich copolyesters contributed to superior fatigue resistance. Atomic force microscopy was shown to be a powerful technique for identifying and measuring fractographic features.

REFERENCES

1. R.W. Hertzberg and J.A. Manson, *Fatigue of Engineering Plastics*, Academic, New York, 1980.
2. E.J. Moskala, *J. Appl. Polym. Sci.*, **49**, 53, (1993).
3. M.G. Wyzgoski, G.E. Novak, and D.L. Simon, *Polym. Eng. Sci.*, **25**, 4501 (1990).
4. H. Kim, R.W. Truss, Y. Mai, and B. Cotterell, *Polymer*, **29**, 268 (1988).
5. T.R. Clark, R.W. Hertzberg, and J.A. Manson, *J. Test. Eval.*, **18**, 319 (1990).
6. ASTM Standard E647-88a, *Standard Test Method for Measurement of Fatigue Crack Growth Rates*, American Society for Testing Materials, Philadelphia, 1990, vol 3.01, p. 648.
7. P.C. Paris and F. Erdogan, *J. Bas. Eng. Trans. ASME Ser. D* **85(4)**, 528 (1963).
8. W. Döll and L. Könczöl, *Advances in Polymer Science*, **91/92**, 137 (1990).

Table I. Copolyesters Used in This Study

Material	Mole % CHDM	σ_y (MPa)	E (MPa)	IV* (dl/g)
COP4	4	56.3	2.32	0.666
COP10	10	56.8	2.29	0.652
COP31	31	49.5	1.99	0.718
COP68	68	43.5	1.70	0.719

*Measured at room temperature in a 60/40 phenol/tetrachloroethane mixture.

Table II. FCP Properties Versus % CHDM.

Material	da/dN at ΔK=1.2 MPa$\sqrt{m}$ (mm/cycle)	ΔK at Instability (MPa$\sqrt{m}$)
COP4	2.45×10^{-6} *	3.51
COP10	2.08×10^{-5}	2.64
COP31	1.11×10^{-3}	1.39
COP68	1.64×10^{-3}	1.23

*Extrapolated Value.

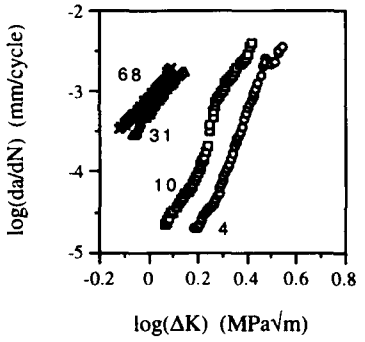

Figure 1. Log-log plot of da/dN versus ΔK. CHDM Content as Indicated.

Figure 2. Scanning Electron Micrographs of (a) Striations in COP31, (b) Discontinuous Growth Bands in COP31, and (c) Discontinuous Growth Bands in COP4. Size bar equals 10 μm. Crack growth is from left to right.

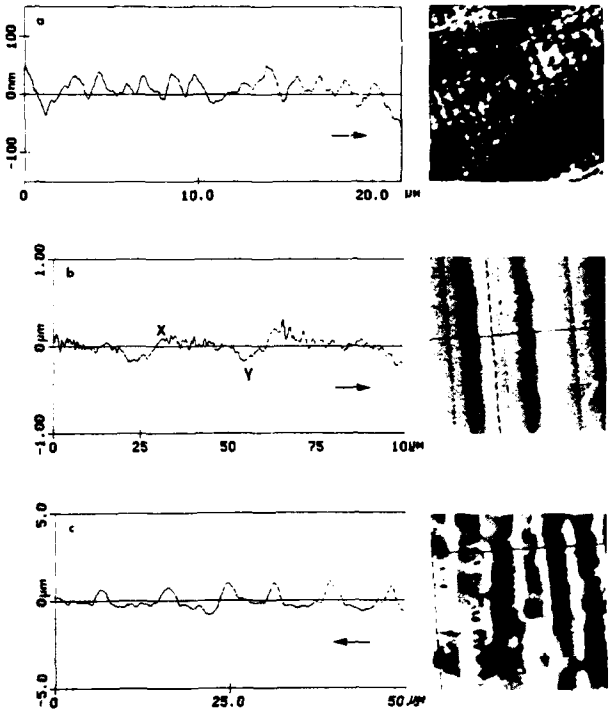

Figure 3. Atomic Force Micrographs and Line Scans for (a) Striations in COP31, (b) Discontinuous Growth Bands in COP31, and (c) Discontinuous Growth Bands in COP4. Arrows indicate direction of crack growth.

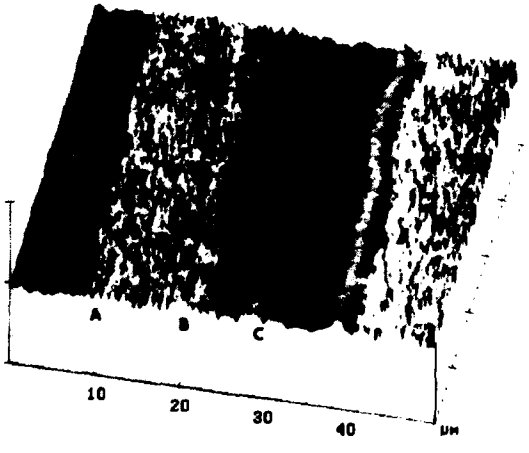

Figure 4. Three Dimensional Plot of Discontinuous Growth Bands in COP31. (X: 10 µm/division, Z: 1 µm/division)

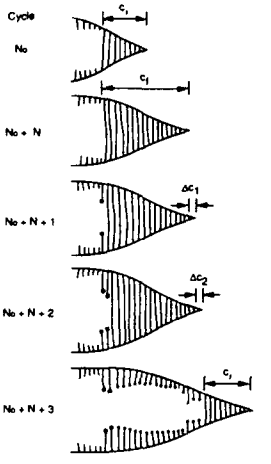

Figure 5 Model for the Formation of Discontinuous Growth Bands in COP31.

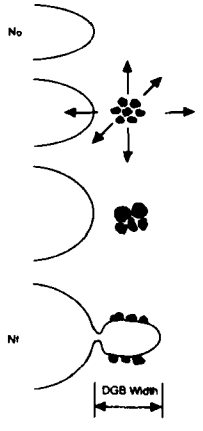

Figure 6 Model for the Formation of Discontinuous Growth Bands in COP4.

THE FATIGUE CRACK PROPAGATION BEHAVIOR OF CELLULOSE ESTERS

T.J. Pecorini* and E.J. Moskala*

Two mechanisms of fatigue crack propagation were identified in cellulose acetate propionate (CAP): a crazing mechanism which dominated at low values of stress intensity (ΔK), and a shear yielding mechanism which dominated at high values of ΔK. Increasing the concentration of plasticizer or increasing the temperature produced a decrease in both the yield strength and the value of ΔK at the onset of the transition between the two mechanisms. In addition, the transition in crack propagation mechanism created a V-shaped feature on the fracture surface; the width of the V-shaped feature can be used to weigh the relative contributions from the crazing and shear yielding mechanisms towards the overall FCP rate. Finally, the K-decreasing procedure retards the transition from plane-strain-shear yielding to crazing due to an "underloading" phenomenon, associated with the nucleation of a craze within a preexisting plane-strain-shear zone.

INTRODUCTION

Cellulose esters are commonly used in such diverse applications as toothbrush handles, tool handles and eyeglass frames, where resistance to fatigue can be of critical importance. In most commercial applications, a plasticizer, such as dioctyl adipate is often added to these esters to improve their moldability. Since plasticizer concentration can dramatically affect the mechanical properties of these materials, the purpose of this work is to determine the effect of plasticizer content on the fatigue crack propagation (FCP) response of a particular cellulose ester, cellulose acetate propionate.

EXPERIMENTAL

The cellulose acetate propionate (CAP) material used in this study was a product of Eastman Chemical Company, Kingsport, TN. The CAP was plasticized with dioctyl adipate. Resins containing 6%, 9%, 12% and 14% plasticizer content were examined (CAP6, CAP9, CAP12 and CAP14, respectively).

FCP testing was performed on compact tension specimens, machined from 6.2mm thick injection-molded plaques; the width equalled 50.8mm for all specimens. The specimens were notched with a band saw, sharpened by razor tapping, and subsequently fatigue precracked prior to data acquisition. All specimens were notched along the mold-flow direction. Fatigue tests were performed at ambient conditions using a sinusoidal waveform with a frequency of 1Hz and a minimum to maximum load ratio of 0.1. Tests were performed under computer control using both the constant-load-amplitude and K-decreasing test procedures described in ASTM 647-91 (1). With the constant load amplitude procedure, ΔP is held constant while ΔK continuously increases with increasing crack length. With the K-decreasing procedure, load is shed incrementally according to the equation,

$$C=(1/K)(\Delta K/da) \quad (1)$$

whereby ΔK decreases by steps. A standard K-gradient of -0.08/mm was used for K-decreasing testing. The crack length increment used to determine the step size was 0.127mm. At least two specimens were run at each test condition shown herein. Growth rates were modelled by Paris law equations (2).

Fracture surfaces were examined by optical microscopy using a Wild M400 light optical microscope.

* Eastman Chemical Company, P.O. Box 1972, Kingsport, TN 37662.

RESULTS AND DISCUSSION

Figures 1 and 2 show FCP data for CAP as a function of plasticizer content and temperature, respectively. For all conditions, the data corresponding to low ΔK values lie on one Paris-law line, while the data associated with higher ΔK values lie on a second, almost parallel Paris-law line, indicating that FCP is insensitive to these parameters within these growth regions. (The fracture toughness of CAP is also observed to be insensitive to plasticizer content (3).) Paris law equations which describe the FCP behavior are depicted in Figure 1.

It is also apparent that these two near-parallel Paris-law lines are linked by a curved transition region - at growth rates which are found to decrease with increasing plasticizer content and increasing temperature. The plasticizer concentration (Pz) and temperature (T) each produce linear correlations with yield strength (σ_y); $\sigma_y = 53.7 - 0.54T$; $\sigma_y = 58.2 - 1.92Pz$. If we select two unique combinations of plasticizer concentration and temperature which are known to produce identical yield strength values, the growth rates associated with this transition also become identical (see Figure 3). Thus, the FCP behavior of a plasticized CAP at any temperature can be predicted from the FCP behavior of a plasticized CAP containing an equivalent plasticizer concentration at room temperature. These results strongly suggest that yield strength dictates the value of ΔK at which the transition in FCP mechanism occurs.

In addition, a V-shaped feature is observed on the fracture surface of each specimen (see Figure 4). The value of the crack length, and consequently the ΔK, at the tip of the V-shaped feature decreases as plasticizer concentration increases. Thus, it is presumed that the transition regime coincides with the development of the V-shaped feature; the linear region of the FCP curve described by the low ΔK Paris-law line occurs to the left of the V-shaped feature, and the linear region described by the high ΔK Paris-law line occurs after the V-shaped feature has fully formed. By assuming that fatigue crack propagation in CAP is controlled by simple rule-of-mixtures from two distinct fatigue cracking mechanisms, we are able to predict the overall FCP response for each CAP by using the information from the fracture surface to weigh the relative contributions from each crack growth mechanism. A typical predictive curve is shown in Figure 5 for CAP12 at 23°C. Similar predictions are easily made for the other CAPs.

This transition region is believed to be associated with a transformation between crazing, which controls fatigue crack growth along the low-ΔK Paris-law line, and plane-strain-shear yielding which controls growth along the high-ΔK Paris-law line. Furthermore, the transition may be controlled by the degree of triaxiality within the specimen at the crack tip. Note that the yield strength, which controls the transition point, affects the degree of triaxiality (4). During a constant-load-amplitude test, a preexisting craze first transforms to plane-strain-shear at the surface, where increased biaxiality is found. As the ΔK increases, the center of the sample becomes less triaxial, whereby the transformation is driven deeper towards the center of the specimen, creating the V-shaped feature.

The transition is found to be reversible, as found by performing a K-decreasing test. (The K-decreasing procedure begins the test at its highest ΔK value and subsequently reduces ΔK by a series of incremental steps (5,6).) However, while the V-shaped feature points in the direction of crack growth in the constant-load-amplitude specimen, the feature now points in the opposite direction in the K-decreasing specimen (See Figure 6). In addition, use of the K-decreasing test method lowers the growth rate (and ΔK) required to produce the transition, often by as much as an order of magnitude, as shown in Figure 7. Nonetheless, at points along the FCP plot which are away from the transition regime, constant-load-amplitude and K-decreasing data still coincide.

Upon a K-decreasing test, transition to a craze growth mechanism requires nucleation of a craze within the center of the preexisting plane-strain-shear zone (i.e., in the center of the specimen where the triaxial stresses are greatest). By some combination of phenomenon, the ΔK required to produce an equivalent state of triaxiality is lower in a K-decreasing path than in a K-increasing path, whereby an "underloading" is observed on the FCP plots. Once nucleated, however, the craze formed during a K-decreasing test grows more rapidly at the existing ΔK level than the plane-strain-shear zone, since the craze requires less energy per unit crack length to propagate (4,7). Growth bands associated with individual load steps are observed in Figure 6. (These bands are not striations.) The lower portion of the figure is associated with plane-strain-shear growth; here the bands are parallel. However, once the craze has initiated, the craze bands increase in both width and length with each load reduction period, whereby the craze bows out ahead

of the current crack front. Due to the large degree of "underloading", the craze mechanism rapidly becomes dominant across the entire thickness of the sample.

ACKNOWLEDGEMENTS

The authors wish to thank Eastman Chemical Company for permission to publish this work.

REFERENCES

1. ASTM Standard E647-91, "Standard Test Method for Measurement of Fatigue Crack Growth Rates", 'Annual Book of ASTM Standards', Vol. 03.01, American Society for Testing and Materials, (Philadelphia), 1992, pp. 654-681

2. Paris P C and Erdogan F, J.Bas. Eng. Trans. ASME Ser D 85 (1963) 528

3. Moskala E J and Pecorini T J, unpublished research

4. Hertzberg R W and Manson J A, 'Fatigue of Engineering Plastics', Wiley (New York), 1976

5. Saxena A, Hudak S J, Donald J K, and Schmidt D W, J. Test. Eval. 6 (1978) 167

6. Clark T R, Hertzberg R W, and Manson J A, J. Test. Eval. 18 (1990) 319

7. Takemori M T, Morelli T A and McGuire J, J. Mater. Sci. 24 (1989) 2221

FIG. 4 - Optical micrograph of fracture surfaces for CAP6 (top), CAP9, CAP12, and CAP14 (bottom). Arrowheads locate the tips of V-shaped regions. Crack growth is from left to right.

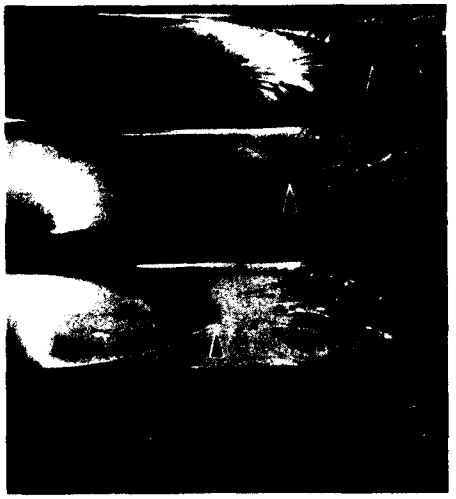

FIG. 6 - Optical micrograph of fracture surface for CAP12 obtained during a K-decreasing test. The lower portion of the figure shows plane-strain-shear growth, while the upper portion displays craze growth. Crack growth is from bottom to top.

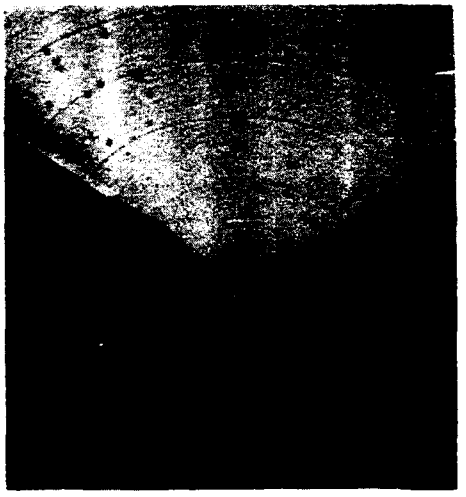

FIG. 1 - Log-log plot of da/dN versus ΔK for CAP as a function of plasticizer concentration. CAP 14 Δ ; CAP12 o ; CAP9 □; CAP6 ● .

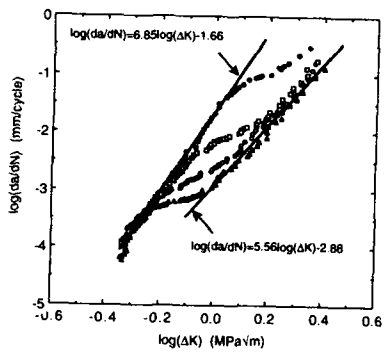

FIG. 2 - Log-log plot of da/dN versus ΔK for CAP9 at 13°C ● , 23°C ▲ , and 35°C ■ .

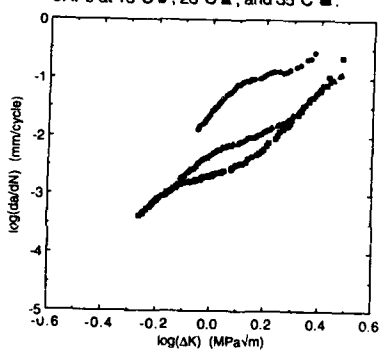

FIG. 3 - Log-log plot of da/dN versus ΔK for CAP12 at 23°C x and CAP9 at 35°C ■ .

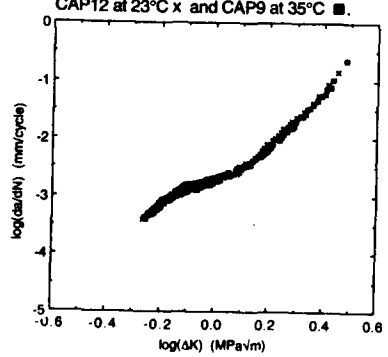

FIG. 5 - Predicted x and experiemntal o FCP curves for CAP12 at 23°C.

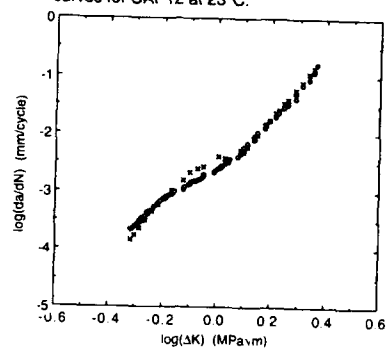

FIG. 7 - Log-log plot of da/dN versus ΔK for CAP12. Rising arrows indicate the constant-load amplitude procedure x, falling arrows indicate the K-decreasing procedure o.

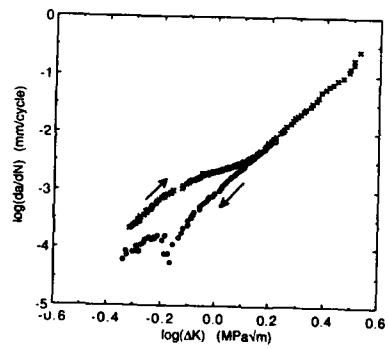

DEFORMATION AND FRACTURE OF POLYPROPYLENE EXPOSED TO ULTRAVIOLET IRRADIATION UNDER STRESS

Li Tong, B O'Donnell and J R White
Materials Division, Department of Mechanical, Materials and Manufacturing Engineering, University of Newcastle upon Tyne, Newcastle upon Tyne, NE1 7RU

Injection moulded bars made from polypropylene have been exposed to ultraviolet irradiation while loaded in uniaxial tension or in four point bending, then subjected to a uniaxial tensile test. The chemical degradation at various depths within the bars has been investigated using infrared analysis and gel permeation chromatography. The results show that photodegradation is accelerated by tensile stress and retarded by compressive stress. The fracture mechanisms have been investigated using scanning electron microscopy.

INTRODUCTION

Stress-assisted chemical reaction, such as *mechanico-oxidative* degradation in rubbers, has been long recognised. Davis and Sims (1) suggest that polymers fail more rapidly when weathered under load but do not refer to quantitative studies. DeVries *et al* (2,3) showed that ultraviolet (UV) degradation of polyethylene and nylon 6 is accelerated by stress. Baumhardt-Neto and De Paoli (4) loaded polypropylene (PP) films in tension during UV irradiation and assessed degradation by measuring the mechanical properties and the carbonyl index (using infrared analysis). Their results indicated that under some conditions stress accelerates photo-oxidation whereas under others it retards it. They list various ways in which stress may influence the reaction rate but note that it is difficult to deduce the controlling factors from their measurements (4). The experiments described here were conducted to compare the effects of tensile and compressive stresses on the photo-oxidation of PP.

EXPERIMENTAL

Specimen preparation

Tensile test bars measuring approximately 190mm x 12.7mm x 3.0mm were injection moulded from polypropylene (ICI GXM 43) using a tool with an end-gated cavity.

Exposure conditions

Exposures were conducted at 30°C. The UV was provided by fluorescent tubes with spectral output matching the spectrum of solar radiation at the Earth's surface fairly closely for wavelengths below 360nm down to the cut-off at approximately 290nm. For wavelengths below

320nm the intensity at the sample surface was in the range 1.7-4Wm^{-2}, similar to summer conditions in Jeddah, Saudi Arabia. Details of the Jeddah climate and of the weathering of polymers exposed there are given by *Qayyum and co-workers* (5-9). Some bars were loaded in uniaxial tension via a simple lev r at stresses up to 10MNm^{-2}; the UV illumination was applied to one face only. Other bars were placed in 4-point bending jigs; the UV illumination was applied to the tensile surface of some bars and to the compressive side of others.

Molecular weight and infrared measurements

Samples were prepared by milling the bars using a single point cutter and collecting the machine swarf or chips for gel permeation chromatography (GPC) or infrared (IR) analysis. GPC was carried out at Rapra Technology Ltd.. IR absorption measurements were made with a *Nicolet 20 PC-IR* Fourier transform spectrometer using 128 scans.

Mechanical testing

After chosen periods of conditioning, samples were tensile-tested to fracture using 20mm min^{-1} crosshead speed. Selected fracture surfaces were examined in the scanning electron microscope.

RESULTS

Observations during exposure and mechanical testing

Bars exposed to UV and stressed at 10, 9 and 8MNm^{-2} broke in this order during the sixth week. A bar stressed at 7MNm^{-2} survived to the end of the sixth week but contained a large crack similar to those seen just before failure in the bars exposed at higher stresses.

When bars exposed to UV in the unstressed state were tensile tested fine crazes developed in the exposed corners first then larger crazes formed near the exposed surface. Just prior to fracture coarse crazes formed in the unexposed surface. Bars exposed to UV for 6 weeks or more were very brittle and broke easily if not handled carefully. The tensile strength fell as UV exposure increased; the effect was greater in samples held in tension during exposure. Examination of the surfaces of samples that were tensile tested after irradiating in the laboratory often revealed the formation of a brittle layer. High magnification images of samples that were tensile tested after irradiating for short periods showed that the underlying material had a fibrillated appearance characteristic of cold drawn polypropylene whereas the discrete embrittled layer had fragmented, unable to take up a large deformation. The unexposed surface of bars that were bent during exposure showed less damage than equivalently exposed unstrained bars. Compression at the unexposed surface may have inhibited degradation here so that less damage occurred during the tensile test. Discussion of the failure of weathered polymers is given by *O'Donnell et al* (10).

Molecular weight and infrared measurements

Figure 1 shows the molecular size distributions for samples cut from the surfaces (0.35mm) of bars (i) as-moulded; (ii) exposed to UV for 6 weeks unstressed; and (iii) broken during the sixth week of exposure to UV while loaded in tension at 10MNm^{-2}. The unstressed

bar gave a strong shift to lower molecular weights and the stressed bar gave a larger shift. The large increase in the low molecular weight fraction (<1000) is of particular interest.

Plots of number average molecular weight, M_n, versus depth for an as-moulded bar and for bars exposed to UV radiation (i) for 6 weeks unstressed; and (ii) under uniaxial tensile stress of $10MNm^{-2}$ until failure in the sixth week respectively are given in figure 2. UV exposure caused a significant fall in M_n, particularly near to the surfaces, and the the stressed polymer suffered greater degradation than the unstressed material. Molecular degradation is most severe near the exposed surface but significant degradation is also present near to the unexposed surface. Near the back surface the UV intensity from direct transmission plus reflection from external surfaces in the exposure room amounted to no more than 5% of the radiation incident on the exposed surface. Oxygen depletion in the centre is the most likely cause of the low degradation recorded there, though the distribution of products of reaction may also be important.

Through-depth M_n values for a bar bent for 8 weeks with the tensile surface exposed to UV are given in figure 3. Results for an unstrained sample exposed at the same time are shown for comparison. Near the exposed surface, degradation appears to be more developed in the bent sample. Near the unexposed surface the degradation is greater in the unstrained sample, indicating that compressive stress (at the concave surface of the bent bar) may inhibit reaction. Although the protective influence of compressive stress is the most important deduction from figure 3 it is also notable that the extent of degradation near the unexposed surface of the unstressed bar is considerable, indicating that the lower UV intensity is sufficient to promote the degradation reaction(s) and that rate limitation must be attributed to something else. Samples taken from bars with which the compressive surface was exposed to UV showed less molecular weight reduction near the exposed surface.

Spectra obtained the top 0.1mm of bars exposed unstrained for periods up to 12 weeks are given in figure 4. There is no carbonyl resonance (in the range $1700-1800cm^{-1}$) for unexposed moulded material but a significant peak appeared after 4 weeks exposure. Also shown in figure 4 is the spectrum obtained from the surface of a bar exposed for 24 weeks while bent (tensile surface exposed). The strained sample gave the most prominent carbonyl peak but this cannot be attributed to the effect of stress with certainty because the unstressed samples with which it is compared were all exposed for shorter periods.

CONCLUSIONS

Tensile stress accelerates molecular degradation caused by photochemical reaction and this generally leads to diminished engineering properties. Compressive stress retards reaction. Photochemical degradation occurs preferentially near the surface.

ACKNOWLEDGEMENTS

We are grateful to S R Holding of Rapra Technology Ltd. for making the GPC measurements and assistance in interpreting the results.

REFERENCES

1. Davis, A and Sims, D., 1983, "Weathering of Polymers", Appl.Sci.Publs., Barking, England
2. DeVries, K.L., and Hornberger, L.E., 1989, Polym.Degrad.Stab. 24 213
3. Igarashi, M. and DeVries, K.L., 1983, Polymer 24 769, 1035
4. Baumhardt-Neto, R. and De Paoli, M.-A., 1993, Polym.Degrad.Stab. 40 53, 59
5. Qayyum, M.M. and Davis, A., 1984, Polym.Degrad.Stab. 6 201
6. Qayyum, M.M. and White, J.R., 1985, J.Mater.Sci. 20 2557
7. Qayyum, M.M. and White, J.R., 1986, J.Mater.Sci. 21 2391
8. Qayyum, M.M. and White, J.R., 1987, Polymer 28 469
9. Qayyum, M.M. and White, J.R., 1989, Plast.Rubb.Proc.Applics. 12 171
10. O'Donnell, B., Qayyum, M.M., Li Tong and White, J.R., Plast.Rubb.Compos.Proc.Applics. *in press*

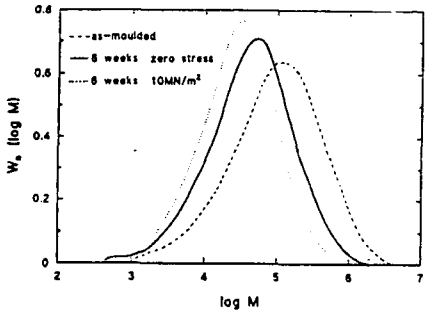

Fig.1 Molecular weight distributions

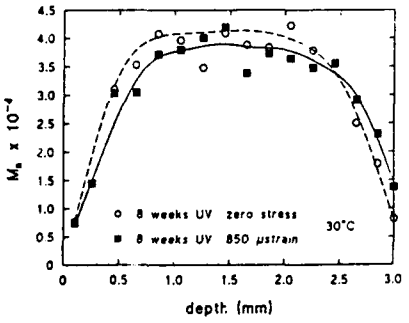

Fig.3 M_n versus depth for bars exposed while bent at 850 microstrain at the surface.

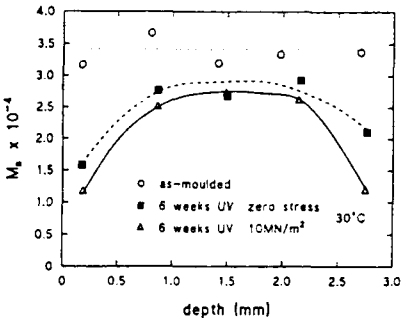

Fig.2 M_n versus depth for bars exposed for 6 weeks unstrained and while at $10MNm^{-2}$ tension

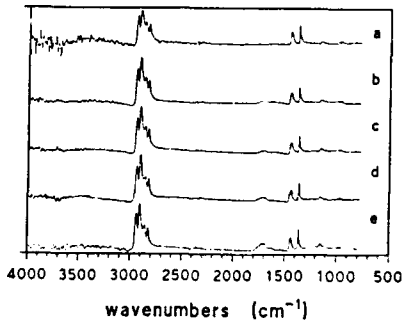

Fig.4 Infrared spectra for surfaces of (a) as-moulded bar; (b),(c),(d) unstrained bars exposed for 4,8,12 weeks; (e) is for bar exposed for 24 weeks while bent at 850 microstrain.

A UNIFIED MODEL OF INELASTIC BEHAVIOUR AND FRACTURE OF POLYMERS INCLUDING SECOND-ORDER-EFFECTS

H. Altenbach[1] & A.A. Zolochevsky[2]
[1]Otto-von-Guericke-Universität Magdeburg, Germany
[2]Kharkov Technical University, Ukraine

Many different amorphous and crystalline polymers show in tests several types of non-negligible second-order-effects, e.g. different behaviour in tension and compression, different normalized stress-strain-curves and the Poynting-Swift-effect. The constitutive equations for inelastic behaviour and the criteria of strength (limit state) of these isotropic materials can be developed by an unified approach, based on a potential formulation (creep potential, flow potential) or on the limit surface formulation including all three invariants of the stress tensor. In the paper a general theory is developed . Finally, a comparison of experimental and theoretical results for multiaxial stress states is given.

INTRODUCTION

In the classical material's behaviour models based on a potential formulation, the equivalent stress depends only on the second invariant of the stress tensor

$$\sigma_{eq} = \sigma_{eq}[I_2(\boldsymbol{\sigma})]$$

In this case the model, based on such an assumption, reflects the same behaviour of the material in tension and compression, without dependence on the hydrostatic stress state etc. For such models we can show a good agreement between theory and experimental data for steel, many alloys etc. On the other side for some light alloys, cast irons, polymers, ceramics, composites and porous materials we get a disagreement between experimental data of multiaxial strain or limit state behaviour and theoretical results predicted by the second invariant theory. The reason for that disagreement can be obtained by some simple experiments. Different amorphous and crystalline polymers show in tests several types of non-negligible so-called second-order-effects: different behaviour in tension and compression, different normalized stress-strain-curves, influence of hydrostatic pressure, the Poynting-Swift-effect etc. These second-order-effects are not connected with the material's anisotropy. Therefore it is necessery to modify the classical constitutive equations for this class of material's behaviour.

The constitutive equations for inelastic behaviour and the criteria of strength (limit state) of these isotropic materials can be developed by an unified approach. The constitutive assumption is the existence of a potential (creep potential, flow potential) or a limit surface. The potential or the equation of the limit surface can be introduced as a function of the equivalent stress, depending on all three invariants

$$\sigma_{eq} = \sigma_{eq}[I_1(\boldsymbol{\sigma}), I_2(\boldsymbol{\sigma}), I_3(\boldsymbol{\sigma})]$$

THEORETICAL BACKGROUND

The potential or the limit surface can be described by a function F in dependence of the equivalent stress. In classical theories F is only a function of the second invariant (von Mises-type theories). The first extension of von Mises-type theories can be given in the following form: the expression of the equivalent stress includes also the first or the third invariant. In general the function is more complex, we may assume a dependence on all three invariants: the linear, the quadratic and the cubic invariant. There are different expressions for these invariants. Introducing the invariants purly mathematically, we get the following formulae

$$\begin{aligned} I_1 &= \boldsymbol{\sigma} \cdot \cdot \mathbf{I} && \text{(linear invariant)} \\ I_2 &= \boldsymbol{\sigma} \cdot \cdot \boldsymbol{\sigma} && \text{(quadratic invariant)} \\ I_3 &= (\boldsymbol{\sigma} \cdot \boldsymbol{\sigma}) \cdot \cdot \boldsymbol{\sigma} && \text{(cubic invariant)} \end{aligned}$$

$\boldsymbol{\sigma}$ is the stress tensor, $\mathbf{I}$ is the second rank unity tensor. Let us suggest some new combinations of these invariants, e.g.

$$\sigma_1 = BI_1, \sigma_2^2 = CI_2 + AI_1^2, \sigma_3^3 = LI_3 + KI_1I_2 + DI_1^3,$$

and propose an equivalent stress formulation in the following way

$$\sigma_{eq} = \alpha\sigma_1 + \sigma_2 + \gamma\sigma_3$$

α and γ are numerical coefficients.

The material-dependent coefficients in the expressions of the invariants (in the general case they are 6: A, B, C, D, K, L) can be derived from so-called simple basic tests, realising homogeneous stress states. So the material-dependent coefficients are derived as functions of a set of material parameters.

A CREEP MODEL

In this case we assume the following constitutive equations

$$\dot{\boldsymbol{\epsilon}}^{creep} = \mu \frac{\partial F^{creep}(\sigma_{eq})}{\partial \boldsymbol{\sigma}},$$

where μ is a Lagrange multiplier. In the general case we introduce the following equivalent stress

$$\sigma_{eq} = \alpha BI_1 + \sqrt[2]{CI_2 + AI_1^2} + \gamma\sqrt[3]{LI_3 + KI_1I_2 + DI_1^3}$$

The material-dependent coefficients of the creep model can be determined by some simple basic creep tests

1. uniaxial tension

$$\begin{aligned} \dot{\epsilon}_{11}^{creep} &= L_+\sigma_{11}^n, \\ \dot{\epsilon}_{22}^{creep} &= Q\sigma_{11}^n \end{aligned}$$

2. uniaxial compression

$$\dot{\epsilon}_{11}^{creep} = -L_-|\sigma_{11}^n|$$

3. pure torsion

$$2\dot{\varepsilon}_{12}^{creep} = N\sigma_{12}^{n},$$
$$\dot{\varepsilon}_{11}^{creep} = M\sigma_{12}^{n}$$

4. hydrostatic pressure

$$\dot{\varepsilon}_{11}^{creep} = \dot{\varepsilon}_{22}^{creep} = \dot{\varepsilon}_{33}^{creep} = -P|\sigma_{11}^{n}|$$

The constants L_+, L_-, Q, M, N, P and the creep exponent n are known from tests.

In many practical situations the material's behaviour can be described by simplified expressions. Let us introduce only three material parameters. In this case we have different possibilities for the determination of equivalent stress and creep constitutive equations, e.g.

1. $\gamma = 0 \Longrightarrow \sigma_{eq} = \alpha B I_1 + \sqrt[2]{CI_2 + AI_1^2}$

$$\dot{\boldsymbol{\varepsilon}}^{creep} = 2\lambda\sigma_{eq}\left(\frac{AI_1\mathbf{I} + C\boldsymbol{\sigma}}{\sqrt[2]{CI_2 + AI_1^2}} + \alpha B\mathbf{I}\right) \tag{1}$$

2. $\alpha B = D = K = 0 \Longrightarrow \sigma_{eq} = \sqrt[2]{CI_2 + AI_1^2} + \gamma\sqrt[3]{LI_3}$

$$\dot{\boldsymbol{\varepsilon}}^{creep} = 2\lambda\sigma_{eq}\left(\frac{AI_1\mathbf{I} + C\boldsymbol{\sigma}}{\sqrt[2]{CI_2 + AI_1^2}} + \gamma\frac{LI_3\boldsymbol{\sigma}\cdot\boldsymbol{\sigma}}{3\sqrt[3]{LI_3}}\right) \tag{2}$$

3. $\alpha B = D = L = 0 \Longrightarrow \sigma_{eq} = \sqrt[2]{CI_2 + AI_1^2} + \gamma\sqrt[3]{KI_1I_2}$

$$\dot{\boldsymbol{\varepsilon}}^{creep} = 2\lambda\sigma_{eq}\left(\frac{AI_1\mathbf{I} + C\boldsymbol{\sigma}}{\sqrt[2]{CI_2 + AI_1^2}} + \gamma\frac{K(I_2\mathbf{I} + 2I_1\boldsymbol{\sigma})}{3\sqrt[3]{KI_1I_2}}\right) \tag{3}$$

COMPARISON WITH EXPERIMENTAL DATA

In the following table a comparison between the predicted data by different simplified creep deformation formulae and experimental data, described in the paper by Lewin & Lehmann, 1977 (1), is given for polyvenyl chlorid.

TABLE 1: Comparison of experimental and theoretically calculated data

σ_{11} MPa	σ_{22} MPa	ε_{11}^{creep} 10^3	ε_{11}^{creep} 10^3	ε_{11}^{creep} 10^3	ε_{11}^{creep} 10^3
		Experiment	Eq. (1)	Eq. (2)	Eq. (3)
-14.88	14.88	3.12	4.22	3.85	3.97
-17.10	17.10	4.99	6.76	6.17	6.37
9.93	9.93	0.18	0.15	0.16	0.16
22.05	22.05	2.10	2.29	2.43	2.43

DISCUSSION

Material's behaviour models including second-order-effects can be formulated by the assumption of the existence of potential. In the classical theory the potential depends only on the second invariant of the stress tensor. In the general case it is necessery to introduce a potential based on all three invariants. Numerical results (see table 1) demonstrate, that in special cases we can take into account the second and the first or the third invariant. In both situations we get a good agreement between the experimental creep strains and the theoretically calculated ones.

More details about the determination of the material dependent parameters in the general case are given by Altenbach, Schieße & Zolochevsky, 1991 (2). A limit state model is developed by Altenbach, Lauschke & Zolochevsky, 1993 (3). A creep model with isotropic damage is introduced by Altenbach & Zolochevsky, 1992 (4). Further investigations should be connected with an optimal choice of the simple basic tests for determination of material dependent parameters and anisotropy.

ACKNOLEDGEMENT

The research project on modelling of material behaviour including second-order-effects was promoted by a stay of the second author (A.Z.) at the universities of Magdeburg and Aachen with the financial support of the Alexander von Humboldt-Stiftung.

REFERENCES

1. Lewin, G., amd Lehmann, B., 1977, Wiss. Zeitschr. TH Magdeburg 21, 415
2. Altenbach, H., Schieße, P., and Zolochevsky, A.A., 1991, Rheologica Acta 30, 388
3. Altenbach, H., Lauschke, U., and Zolochevsky, A., 1993, ZAMM 73, T372
4. Altenbach, H., Zolochevsky, A.A., 1992, ZAMM 72, 375

YIELD AND FRACTURE BEHAVIOUR OF EPOXY NETWORKS MODIFIED WITH RUBBER OR/AND GLASS BEADS

A Maazouz, H Sautereau and J F Gérard*

L Mercante, R Frassine and A Pavan**

The yield and fracture behaviour of a neat epoxy resin and of two- or three-phase particulate composites made of the same epoxy matrix were studied. The dispersed phase(s) consisted of a soft elastomer or hard glass beads or both types of inclusions (hybrid system).
The stress-strain response was measured under various states of stress so as to determine the yield surface of each material. All materials obey a modified von Mises yield criterion, with the stress level dependent - but the pressure sensitivity factor independent - of inclusion type and content. For the hybrid composite the yield stress is mainly determined by the elastomer content.
The fracture behaviour was studied by three-point bending and double torsion tests, whereby both stable and unstable (stick-slip) crack propagation was observed. Both initiation and arrest values of the fracture energy are substantially larger for the hybrid composite.

INTRODUCTION

Different ways of toughening epoxy resins have been investigated. Mostly, either an elastomer or a rigid filler such as glass beads is introduced as a dispersed phase (1,2). In the former case the nature of the elastomer and the morphology and volume fraction of the dispersed rubbery phase are the most important parameters. In the latter case, the mechanical behaviour depends on volume fraction, particle size, and aspect ratio of the filler and also on the degree of adhesion between filler and matrix (3-5).

Numerous works have been done on these two approaches, but relatively few papers describe the behaviour of hybrid composites comprising a thermoset matrix and both types of inclusions, one softer (elastomer) and one harder (rigid filler) than the matrix. Kinloch, Maxwell and Young (6,7) showed that such a combination offers large possibilities of improving the fracture properties. Above all it is possible to improve toughness without impairing stiffness.

Aim of this paper is to report on the yield and fracture properties of a hybrid particulate composite based on a polyepoxy DGEBA-Dicyandiamide (DDA) modified with an elastomer (ETBN) and reinforced with glass beads.

* Laboratoire des Matériaux Macromoléculaires, URA CNRS n°507
Institut National des Sciences Appliquées de Lyon, F-69621 Villeurbanne Cedex, France
**Dipartimento di Chimica Industriale e Ingegneria Chimica,
Politecnico di Milano, Piazza L. da Vinci 32, I-20133 Milano, Italy

EXPERIMENTAL

The epoxy network used as the matrix was prepared from the diglycidyl ether of bisphenol-A (DGEBA) and dicyandiamide (DDA) catalyzed with BDMA (benzyldimethylamine) with a stoichiometric ratio aminohydrogen-to-epoxy equal to 0.6. The cure schedule was 60 minutes at 120°C followed by 60 minutes at 180°C (8).

The elastomer was introduced in the form of an ETBN copolymer synthetized from a carboxy-terminated acrylonitrile-butadiene copolymer (CTBN1300x8 Goodrich) and DGEBA (COOH-to-epoxy ratio = 0.065). The amount of CTBN introduced varied from 0 to 15 % by weight.

"A" type glass beads (Sovitec 040A) with an average diameter of about 40 μm were used without any surface treatment. Their volume fraction in the hybrid composite materials varied from 0 to 30%. The composition of the materials is here denoted C(x, ϕ_g), where x represents the initial amount (percent by weight) of CTBN and ϕ_g the percent volume fraction of glass.

RESULTS AND DISCUSSION

Determination of the transition temperatures of the materials provides some indications of their phase structure. T_g values obtained by DSC. The decrease in T_g observed with the introduction of the elastomer is to be attributed to the plasticizing effect of some CTBN dissolved in the epoxy network (about 3% of CTBN)(9). Such an evaluation cannot be extended to the epoxy/elastomer/glass materials, because of the epoxy/glass interaction which leads to a reduction of the chains mobility (10).

Scanning electron microscopy (SEM) of the fracture surfaces of the materials containing ETBN (with or without glass beads) shows that the elastomer formed particles with an average diameter of about 2 μm, irrespective of the presence of the glass filler (Fig.1).

From the above results we conclude that phase structure and morphology are substantially the same for all materials. This set of preparations is therefore ideally suitable to study the influence of the volume fraction of glass beads and/or elastomer on the mechanical behaviour of these composites.

The experimental results obtained on the pure epoxy resin (matrix), on the 15 wt-% elastomer-modified epoxy [C(15,0)], on the 20 vol-% glass bead filled epoxy [C(0,20)], and on the hybrid composite comprising the same epoxy matrix and 15 wt-% elastomer and 20 vol-% glass beads [C(15,20)] are summarized in Table II.

The effect of soft/hard inclusions on the Young modulus is well documented and does not need commenting. The yield stresses measured under three different states of stress are plotted in Fig.2 as τ_{oct}, the octahedral shear stress, versus σ_m, the mean normal stress or hydrostatic tension. It appears that the data can be well described by a modified von Mises criterion (11,12) of the form:

$$\tau_{oct} = \tau_o - \mu \sigma_m$$

in which τ_o, the shear yield stress, and μ, the pressure sensitivity factor, are material constants. Their values for the four materials examined are reported in Table II. (It is to be noted that all materials tested fractured before yielding in uniaxial tension. The measured stresses at break, which are also reported in Fig.2 for comparison, were not included in the calculations).

Table II *Young modulus and constants of the modified von Mises yield criterion.*

	Material			
	Matrix	C(15,0)	C(0,20)	C(15,20)
E (GPa)	2.9	1.8	4.8	2.9
τ_o (MPa)	40.6	32.8	46.1	32.2
μ	0.25	0.22	0.23	0.22

The value of μ is nearly the same for all materials tested, i.e. the pressure sensitivity of the

yielding matrix is unaffected by the presence of extraneous inclusions. By contrast the value of τ_o depends on inclusion type and content.

It is worth observing that the yield stress dependence on inclusion type and content does not parallel the Young modulus dependence. For example, the addition of 20 vol-% glass beads counterbalances the reduction in modulus brought about by the introduction of 15 wt-% CTBN (compare matrix and C(15,20) in Table II) whereas it leaves the values of the yield stresses (e.g. τ_o) nearly unchanged (compare C(15,0) and C(15,20) in Table II or Fig.2). Thus it appears that the onset of yielding is mainly controlled by the soft inclusions in these hybrid composites. These results clearly point to the possibility of obtaining - by a suitable combination of soft and hard inclusions - enhanced yieldability without sacrificing the material stiffness.

Table III shows the fracture results obtained from DT and SE(B) tests at 1 mm/min displacement rate. In DT tests, crack propagation was unstable, showing the typical "stick-slip" behaviour in all materials examined. Therefore, the values of the critical strain energy release rate at both crack initiation (G_{Ici}) and crack arrest (G_{Ica}) are reported. In SE(B) tests, crack propagation was also unstable, but no evidence of "stick-slip" behaviour was noticed. The values of the critical strain energy release rate at crack initiation obtained on the modified materials in SE(B) were substantially larger than the ones obtained in DT. This inconsistency is likely to be attributed to the different notch severity in the two cases.

Table III *Critical strain energy release rate values (obtained at 1 mm/min).*

		Material			
		Matrix	C (15,0)	C (0,20)	C (15,20)
G_{Ici} (DT, initiation)	(kJ m^{-2})	0.21	0.25	0.18	0.45
G_{Ica} (DT, arrest)	(kJ m^{-2})	0.14	0.12	0.14	0.26
G_{Ic} (SE(B), initiation)	(kJ m^{-2})	0.14	0.87	0.40	1.92

Results obtained on the neat epoxy (matrix) in DT tests at varying displacement rates are shown in Fig.3: the "stick-slip" behaviour is observed up to rates of 10 mm/min, while at the higher rate of 100 mm/min stable crack propagation is observed. The material C(0,20) behaved essentially the same, while with the materials C(15,0) and C(15,20) the transition from unstable to stable behaviour appears shifted to a much higher rate (out of the range explored).

The fracture energy values measured on composite materials appear quite less rate dependent than those of the pure matrix, at both crack initiation and arrest (Fig.4).

Finally, both initiation and arrest values of the fracture energy in the hybrid composite are substantially larger than in the other three materials here considered.

It may be concluded that rubber modification may be effective in reducing the rate sensitivity of the epoxy matrix. Furthermore, by combining elastomer and glass inclusions the fracture resistance is improved while maintaining the beneficial attenuation of the rate dependence observed with the rubber modification.

An investigation of the fracture surfaces by scanning electron microscopy (SEM) also showed some evidence of the toughening mechanisms acting in the different materials: while the presence of the elastomeric particles leads to localized shear yielding of the matrix, the presence of the glass beads seems to promote a crack pinning process.

REFERENCES

1 Sultan, J N and McGarry, F T Polym.Eng.Sci. 13 (1973) 29.
2 Drake, R and Siebert, A R SAMPE Quarter. 6 (1975) 11.
3 Young, R G in "Structural Adhesives", A J Kinloch Ed., Elsevier, London (1986) 163.
4 Moloney, A C , Kausch, H H and Steiger, H R J.Mater.Sci. 18 (1983) 208.
5 Moloney, A C , Kausch, H H , Kaiser, T and Beer, H R J.Mater.Sci. 22 (1987) 381.
6 Kinloch, A J , Maxwell, D L and Young, R J J.Mater.Sci. 20 (1985) 4169.

7 Young, R J , Maxwell, D L and Kinloch, A J J.Mater.Sci. 21 (1986) 380.
8 Amdouni, N , Sautereau, H , Gérard, J F and Pascault, J P Polymer 31 (1990) 1245.
9 Maazouz, A , Sautereau, H and Gérard, J F Polym.Networks and Blends 2(2) (1993) 65.
10 Amdouni, N , Sautereau, H and Gérard, J F J.Appl.Polym.Sci. 45 (1992) 1799.
11 Bauwens, J C J.Appl.Polym.Sci. A2.5 (1967) 1145.
12 Sternstein, S S and Ongchin, L Polym.Preprints 10(2) (1969) 1117.

Fig.1 SEM micrograph of the C(15,20) hybrid material

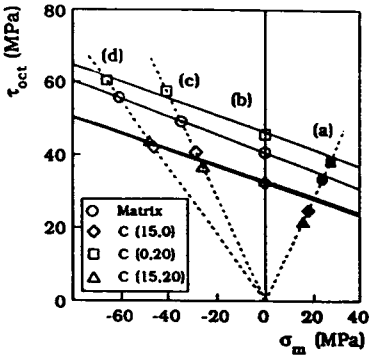

Fig.2 Variation of the octahedral shear stress with mean normal stress at yield: a)uniaxial tension; b)simple shear; c)uniaxial compression; d)plane-strain compression. Filled points: break).

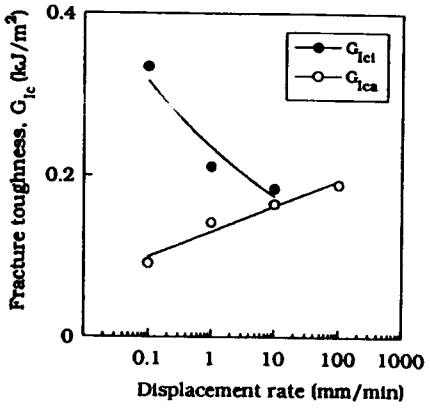

Fig.3 Fracture toughness at crack initiation (filled points) and crack arrest (empty points) vs. displacement rate, measured in DT, for the neat epoxy.

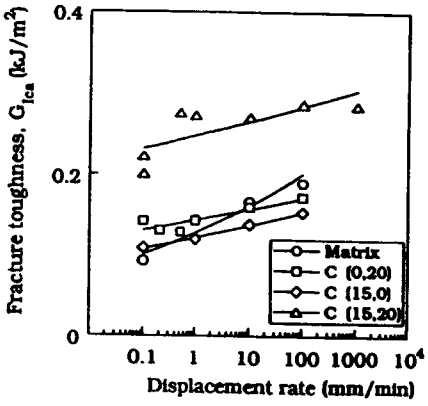

Fig.4 Fracture toughness at crack arrest vs. displacement rate, measured in D.T., for all the materials examined

FRACTURE BEHAVIOUR OF POLYSTYRENE AND RUBBER TOUGHENED POLYSTYRENE

D.G. Cook*, A. Rudin** and A. Plumtree
Institute for Polymer Research * Department of Chemical Engineering,
** Department of Chemistry, *** Department of Mechanical Engineering,
University of Waterloo, Waterloo, Ontario, Canada, N2L 3G1

The impact behaviour of polystyrene and rubber toughened polystyrene has been investigated. Emulsion polymerization permitted mono-dispersed latex particles to be made, which were then used to toughen polystyrene. This allowed the effect of particle size, interparticle spacing, volume fraction of rubber, the extent of core-shell bonding, shell crosslinking and amount of rubber crosslinking to be assessed.

MOLECULAR WEIGHT

The fracture of polystyrene and rubber toughened polystyrene has been examined under impact conditions using an instrumented testing machine. It was found that because of a greater number of molecular entanglements the general fracture properties of both types of polystyrene were improved when the molecular weight was increased. Fig. 1 represents an inverse relationship between molecular weight for the polystyrene resin and K_c and G_c. Molecular weight effects crazing due to changes in entanglement density. Strength and extensibility are determined by the entanglement network within the fibril (1). Hence, changes in the fibril strength and extension result in changes to the failure stress and ultimately to G_c and K_c. The entanglement of molecules also explains why the fracture parameters correlate to melt index, since melt properties such as viscosity (2) or melt index are dependent on entanglements in the melt.

TOUGHENED POLYSTYRENE

By incorporating monodispersed emulsion polymerized PBA rubber core/polystyrene shell particles into the polystyrene matrix, it was possible to investigate, in a controlled manner, the effect of the particle character, size and volume fraction on the fracture behaviour. Results of the impact tests for the latex/polystyrene composite and for the matrix polystyrene alone showed that there was a substantial increase in the unnotched impact energy of the composite over the matrix resin, whereas the notched impact energy improved slightly.

Particle Size and Interparticle Spacing

The fracture resistance increased with particle diameter to an optimal toughness in the 2-3 μm region. There was no significant toughness increase over that of the matrix for smaller particle diameters, whereas after the optimum, the impact energy decreased slowly with increasing particle size.

The effect of particle size and interparticle spacing is shown in Figure 2. A change in particle size results in plots of different slopes, with the larger diameter particles being more effective than the smaller particles for a given interparticle spacing. A possible reason for this behaviour is the ability not only to initiate more crazes at the surface of the largest particles, but also to be more effective craze barriers. For a given interparticle spacing, large diameter particles are more effective than small particles. On the other hand, for a given particle size, the impact energy increases with a decrease in interparticle spacing in the matrix. Since the particle spacing is closer for smaller particles for a given rubber content, these two trends combine to give an optimum impact energy.

Incompatible Shell

A polymethyl methacrylate shell was exchanged for the polystyrene shell and no impact improvement was observed over the unmodified matrix polystyrene. Examination of the fracture surface showed that the toughening particles had completely debonded from the matrix and were strewn about the fracture surface. The diameter of these corresponded to the outside shell diameter of the latex particles (2-6 μm) suggesting that the incompatibility between the shell and matrix resulted in fracture at the matrix/shell interface rather than at the shell/core interface.

Core/Shell Strength

Adhesion between the rubber core and polystyrene shell was controlled by the degree of interpenetration into the core. The unnotched impact energy increased with the degree of interpenetration, whereas the notched impact energy remained relatively constant. When the unnotched impact energy was plotted against the area under the tan δ peak, a linear relationship was seen (Fig 3). A linear dependence of tan δ on the amount of rubber in toughened materials has been observed previously (3), but in the present case the rubber content was constant and only the rubber/matrix interface changed.

Shell Crosslinking

Crosslinking affects the ability of the shell polystyrene to incorporate into the matrix polystyrene, as the polymer chains must have sufficient mobility to entangle between the two

phases. To investigate this effect, the degree of crosslinking was changed by varying the amount of divinyl benzene in the polystyrene shell from 0 to 2·5 wt%. In general the results indicated that as the shell crosslink level increased both unnotched and notched energies were lowered, presumably because of a weaker PS shell/matrix interface. However, the uncrosslinked shell will not form a full IPN with the rubber core and may have a weaker core/shell interface. Apparently, some shell crosslinking is desirable, but too much is detrimental.

Polystyrene Shell Thickness

The effect of shell thickness was examined by varying the polystyrene shell thickness from 0·3 μm on the poly(n-butyl acrylate) core. The results from impact measurements for 8 wt% rubber blends indicate that the polystyrene layer thickness, within the range considered, has little effect on impact toughness.

Rubber Core Crosslinking

An important variable in rubber toughening is the degree of crosslinking in the rubber phase. For the latexes synthesized, the rubber crosslinking was varied by changing the amount of allyl methacrylate from 0·3 to 3·0% by weight in the poly(n-butyl acrylate) rubber phase. The unnotched and notched impact energies increased as the crosslinking was reduced, particularly for the notched impact energy. The major effect of crosslinking is an increase in the glass transition temperature.

REFERENCES

1. Donald, A.M. and Kramer, E.J., 1982, J. Polym Sci: Polym Phys. 20, 899.

2. deGernes, P.G. 1979, "Scaling Concepts in Polymer Physics", Cornell Univ. Press, Ithaca, NY.

3. Krause, S. and Broutman, L.J., 1974, J. App Polym Sci. 18,2945.

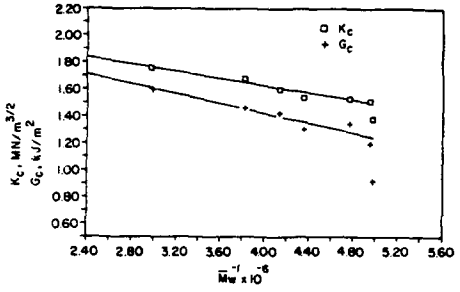

Fig. 1. Fracture toughness K_c and critical strain energy release rate G_c versus $1/M_w$

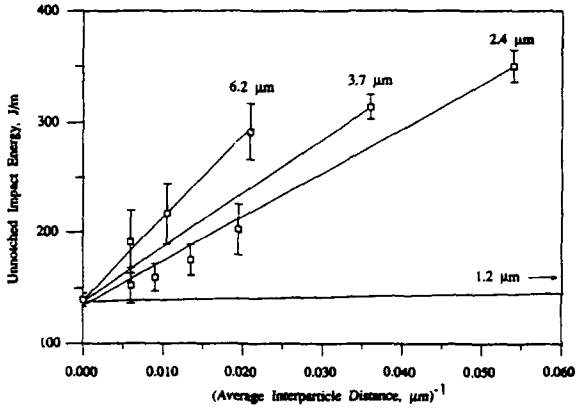

Fig. 2. Impact energy (J/m) vs. (average interparticle distance, μm)$^{-1}$

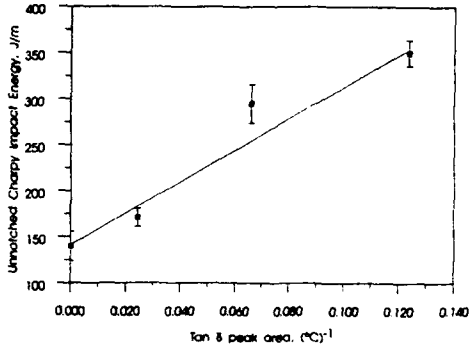

Fig. 3. Unnotched Charpy impact energy (J/m) versus tan δ area (°C)$^{-1}$ for latex/polystyrene composites. The intercept value is that of the matrix polystyrene.

USING THE ESSENTIAL WORK OF FRACTURE METHOD FOR STUDYING PHYSICAL AGING IN THIN DUCTILE POLYMERIC FILMS

J. A. Nairn
Material Science and Engineering, University of Utah
Salt Lake City, Utah 84112 USA

Water-filled drop impact tests on full-scale, blow-molded polyester bottles showed that the impact properties change dramatically after about 30 days of aging at realistic storage temperatures. We used the essential work of fracture technique to study the effect of physical aging on the fracture toughness of thin specimens cut from the sides of blow-molded bottles. Significant drops in toughness were found to occur after relatively short amounts of aging. Additional experiments confirmed that the drop in toughness was due to physical aging and not to chemical degradation.

INTRODUCTION

Many types of blow-molded, plastic bottles are manufactured from polyester resins. Regardless of whether the resin has the potential for crystallization or not, the rapid cooling of the blow-molding process leads to an amorphous solid. The glass transition of typical polyester resins is in the range of 70 to 80°C. Because bottles are commonly stored in ware houses that might reach 50°C, there is a concern about the effects of physical aging on the mechanical properties of blow-molded bottles.

Some recent water-filled, drop impact tests on bottles from a series of polyester resins show that impact properties can degrade significantly after only 30 days of aging at 50°C (Smilie (1)). Because these impact tests were on full-scale specimens, there is no question that aging is an important factor. Two problems with the impact tests are that they require much material (more than 25 bottles for each data point) and that they rely on break/no break observations. This paper describes use of the essential work of fracture method (EWFM) (Cotterell and Reddell (2), Mai *et al.* (3), and Saleemi and Nairn (4)) as an alternative method for monitoring aging. Our first goal was to get quantitative and more extensive results with far less material. These results could then potentially be used to screen and develop new resins. In the long range, more extensive results could be used to make predictions about bottle durability as a function of storage temperature.

MATERIALS AND METHODS

The DuPont company provided us with cylindrical, blow-molded bottles manufactured from four different polyester resins. The resins are labeled here as resins A, B, C, and D. All resins are copolyester resins polymerized from some mixture of glycols and some mixture of diacids. Resin A uses a glycol mixture that is 92 mole % ethylene glycol and 8 mole % cyclohexane dimethanol. Its acid is 100% terepthalic acid. Resin B uses 100% ethylene glycol . Its acid is 97 mole % terepthalic acid and 3 mole % isothalic acid. Resin C uses a glycol mixture that is 70 mole % ethylene glycol and 30 mole % cyclohexane dimethanol. Its acid is 100% terepthalic acid. Resin D uses 100% ethylene glycol. Its acid is 100% terepthalic acid. When cooled slowly, resins B and D are semicrystalline while resins A and C are amorphous.

The fracture characterization was done using EWFM (2-4) which is a method specifically designed for measuring plane-stress fracture toughness in thin ductile materials. In brief, a series of deeply, double edge notched specimens were loaded until failure and the total work of fracture was recorded. The series of specimens varied only in ligament length. To insure plane-stress conditions in all specimens, the ligament was restricted to being longer then four times the thickness and shorter than the plastic zone size or 1/3 the width, whichever was shorter (2-4). By EWFM, a plot of work of fracture per unit ligament area as a function of ligament length should be a straight line. The intercept defines the essential work of fracture, w_e, and the intercept defines the nonessential or plastic work of fracture, w_p. w_e is associated with plane stress fracture toughness; we looked for changes in w_e with aging. w_p is associated with yielded around the crack tip that does not lead to fracture.

Our EWFM specimens were cut from the sides of the cylindrical bottles. The long axis of the specimens were nominally 150 mm long and were parallel with the axis of the bottle. The samples were 25 mm wide. The notches were cut perpendicular to the long axis of the specimens and thus perpendicular to the axis of the bottles. The specimen thicknesses varied from bottle to bottle but were in the range of 0.3 to 0.6 mm. We were able to cut ten specimens from each 80 mm diameter bottle. A single EWFM experiment required 15 to 20 specimens and thus needed only two bottles.

RESULTS AND DISCUSSION

A series of specimens were placed in ovens at 50°C. After 0, 30, 45, and 60 days of aging, we measured the essential work of fracture (w_e), the glass-transition temperature (T_g), the yield strength (σ_y), and the density (ρ). Figure 1 shows all w_e results as a function of aging time. All resins showed a significant drop in toughness after only 30 days of aging. Between 30 and 60 days of aging there was little change in toughness or perhaps a small increase. Resins B and D, the semicrystalline resins, showed the highest toughnesses before aging, but decreased the most (about 50%) after 30 days of aging. We suggest that semicrystalline resins quenched to an amorphous state are farther from the equilibrium state than an amorphous resin and thus more susceptible to physical aging. Resins A and C, the amorphous resins, started with a lower toughness, but decreased only 15 to 20% after aging for 30 days. We also aged samples at 65°C for 0, 1, 14, and 28 days. At this higher temperature, the effects of aging are similar, but most changes occur within one day of aging.

Besides changes in toughness, aging also caused T_g to increase 5-10°C, σ_y to increase 15-20%, and ρ to increase slightly. The changes in ρ were consistently increases, but they were almost unresolvable. The changes in T_g, σ_y, and ρ were similar for all resins and thus not suitable for differentiating among the resins. The changes in ρ were too small to be a useful tool for monitoring aging.

We claim that all the changes were due to physical aging and that there were no chemical degradation effects. The direct evidence to support this claim was that there was no change in solution viscosity (with phenol as the solvent) as a function of aging time. A decrease in molecular weight due to chemical degradation should have led to a decrease in solution viscosity. Some indirect results supporting physical aging were the increase in T_g, the increase in σ_y, and peaks in the DSC curve near the glass transition region (see Fig. 2). A loss in molecular weight due to chemical degradation should cause either no change or a decrease in T_g and σ_y, contrary to the observed increase. Peaks in the DSC curve near the glass transition region are a kinetic effect associated with aging before heating. The longer the aging before heating, the larger should be peaks; this prediction agrees with our observations (see Fig. 2).

Figure 3 is a cross-plot of the w_e results as a function of the water-filled, drop impact results. The data include both unaged and aged specimens. The aged specimens were all aged at 50°C for 60 days. The numbers for the impact results are the statistically predicted drop height for which 50% of the bottles break upon impact. The lines indicate that there is a reasonable correlation between w_e and impact height for each class of resins (amorphous or semicrystalline), but that the correlation is resin dependent. Among all resins groups, we find that w_e is not necessarily a good predictor of impact height. For example, the semicrystalline resins have a higher w_e than the amorphous resins, but a

lower impact height before aging and a comparable impact height after aging. More work is needed before we can relate w_e results for real-world bottle performance.

CONCLUSIONS

The essential work of fracture technique is capable of monitoring changes in mechanical properties caused by physical aging. EWFM is a very sensitive technique. The percentage changes in w_e were larger than the percentage changes in T_g, σ_y, and ρ. Furthermore, changes in w_e reveal differences between resins that were not apparent from other properties. If those differences can be related to real-world performance, EWFM will be a valuable tool for selecting bottle resins. Another benefit of EWFM is that we can get results with much less material. There is thus the potential for larger scale testing that could lead to methods for predicting the temperature dependence of the aging process. Perhaps time-temperature superposition can be applied to fracture toughness and limits can be placed on acceptable bottle storage conditions.

SYMBOLS

EWFM = essential work of fracture method
w_e = essential work of fracture (J/m^2)
w_p = nonessential or plastic work of fracture (J/m^3)
T_g = glass transitions temperature (°C)
σ_y = yield strength (MPa)
ρ = density (g/cm^3)

REFERENCES

1. Smilie, A., DuPont Canada, Inc., unpublished results, 1993.
2. Cotterell, B., and Reddell, J. K., 1977, Int. J. Fract. Mech. 13, 267.
3. Mai, Y. W., Cotterell, B., Horlyck, R., and Vigna, G., 1987, Polym. Eng. and Sci. 27, 804.
4. Saleemi, A. S., and Nairn, J. A., 1990, Polym. Eng. and Sci. 30, 211.

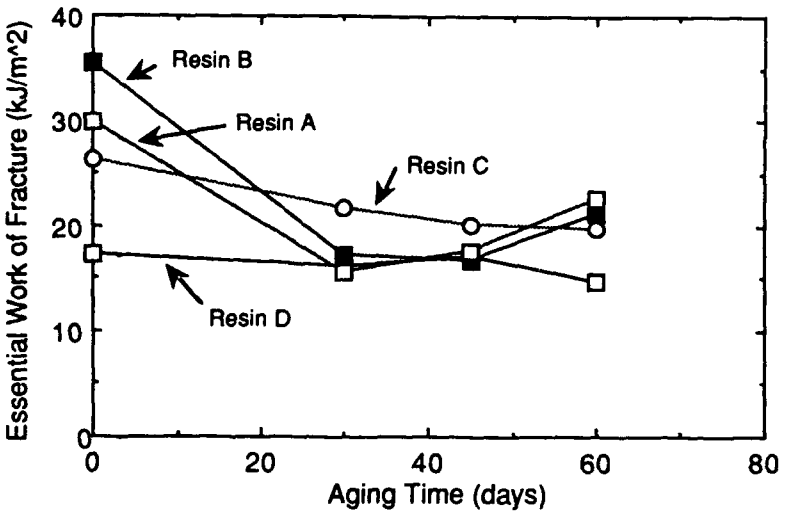

Figure 1: The essential work of fracture for a series of polyester resins as a function of aging time at 50°C. The filled symbols are for semicrystalline resins and the open symbols are for amorphous resins.

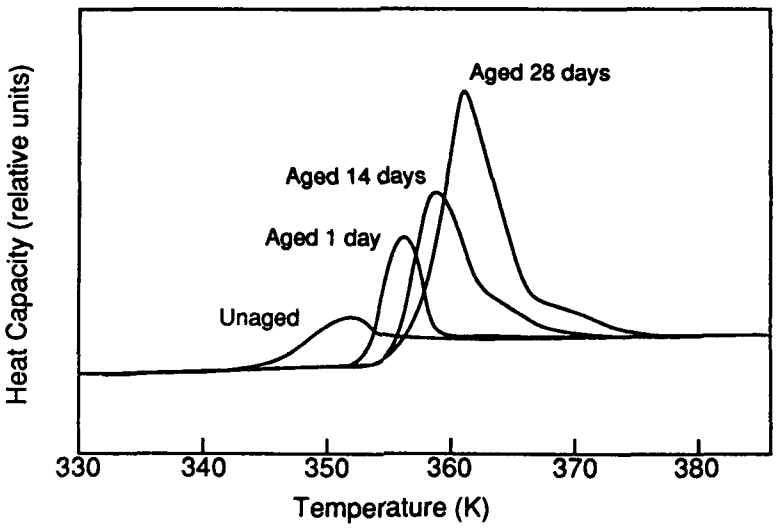

Figure 2: The glass transition region from the DSC of resin A as a function of aging time at 65°C. The peaks are a kinetic effect caused by aging before doing the DSC experiment.

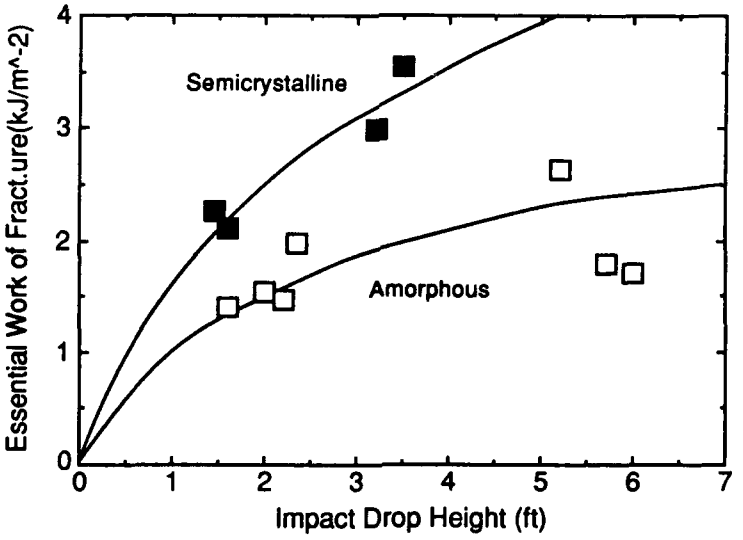

Figure 3: Cross-plot of the essential work of fracture as a function of the impact drop height. The data points are for all resins and include both unaged and aged specimens. The filled symbols are for semicrystalline resins and the open symbols are for amorphous resins

MECHANICAL PROPERTIES OF THERMOPLASTIC POLYMER FOAMS: INFLUENCE OF FOAM DENSITY AND CELL MORPHOLOGY.

J.M. Steuten[+], H.L.Bos[+‡], H. Beukers[*], M. Wessling[*].

Microcellular foams of SMA (Styrene Maleic Anhydride) and PC (Polycarbonate) were prepared with foam densities in the range of twenty to eighty percent of the bulk polymer density. Cells with average diameters of 1-10 μm could be obtained. From the experimental crushing strength data the modulus E and yield strength σ of the foam can be calculated. The theory proposed by Gibson and Ashby (1) to express the relative modulus E/E_0 and yield stress σ/σ_0 (the subscript 0 refers to the bulk property) as a function of relative foam density had to be modified to fit the data obtained .
The parameters describing the contributions of the cell edges and faces correlate with the cell morphologies observed. Depending on foaming conditions significantly different cell-geometries and average cell wall thicknesses were found. Foam density has a larger effect on mechanical properties than variations in foam morphology.

INTRODUCTION

Recently much research has been directed towards preparation and characterization of microcellular foams with cell diameters of 1-10 μm and cell densities of 10^9-10^{12} cm^{-3}. Interesting properties, such as relatively high impact strength and low thermal conduction have been anticipated. Collias et al. (2) find a brittle to ductile transition in sharply notched PC induced by the presence of microbubbles. Seeler and Kumar (3) demonstrate improved fatigue life of microcellular PC compared to unfoamed PC at relative densities $\rho/\rho_0>0.83$, where ρ and ρ_0 are the foam and the bulk density respectively. Improved ductility for PS microcellular foams in uniaxial tension has been demonstrated by Waldman (see (4)).
We prepared microcellular PC and SMA over a wide range of relative densities to systematically investigate their mechanical properties.

EXPERIMENTAL

Microcellular foams were prepared from injection moulded and subsequently annealed samples of SMA and PC by expansion at elevated temperatures of the CO_2-saturated polymer (Figure 1). Before foaming the samples had a size of 3.2*6.4*30 mm^3. By systematic variation of processing conditions, i.e. saturation pressures of 10-50 bar and foaming temperatures of 80-180°C, different foam densities and cell morphologies could be obtained. The resulting foams were characterized by foam density, cell size, cell size distribution and where possible by cell

+ DSM, P.O. Box 18, 6160 MD Geleen, The Netherlands.
* Twente University, Dept. Chemical Engineering, P.O. Box 217, 7500 AE Enschede, The Netherlands.
‡ present address: ATO-DLO, P.O. Box 17, 6700 AA Wageningen, The Netherlands.

shape measurements. Foam density was determined by weighing and immersion of the samples in water. Cell size, cell size distribution and cell shape were determined from SEM photographs. Crushing strength measurements were used for the mechanical characterization. From the resulting crushing strength curve the modulus and yield stress of the foams were calculated.

RESULTS AND DISCUSSION

SEM micrographs in Figure 2 show the cell size distributions of some of the microcellular PC and SMA foams. Foam densities were in the range $(0.2\text{-}0.8)\rho_0$. Cells with an average diameter of 1-10 μm and average cell wall thicknesses of 0.2-0.9 μm were obtained. An increase in saturation pressure at constant foaming temperature leads to a decrease in cell size distribution due to a higer nucleation rate.

Typical crushing strength curves showing the influence of foam morphology are given in Figure 3. Following Gibson and Ashby (1) the relative modulus E/E_0 and yield stress σ/σ_0 are expressed as a function of relative foam density (Figure 4). The relative modulus can be expressed as (1):

$$\frac{E}{E_0} = C_1*\left(\frac{t_e}{l}\right)^4 + C_2*\left(\frac{t_f}{l}\right) \qquad (1)$$

with:

$$\frac{t_e}{l} \sim \left(\phi\frac{\rho}{\rho_0}\right)^{1/2} \qquad \frac{t_f}{l} \sim (1-\phi)\frac{\rho}{\rho_0} \qquad (2)$$

where E and E_0 are the foam and polymer modulus respectively, t_e is the cell edge thickness, t_f the cell face thickness, l the cell edge length and ϕ is the fraction of polymer in the cell edges. Constants C_1 and C_2 have been shown to equal approximately unity (1). A similar expression holds for the yield stress. Eqs. (2) are valid for relative foam densities $\rho/\rho_0<0.2$ (1). The foams of this study have relative densities of $0.2<\rho/\rho_0<0.8$ and visual observation of SEM micrographs of the foamed samples shows that the cell walls have thicknesses very similar to those of the cell edges implying that $t_e \approx t_f$. We therefore modified Gibson & Ashby's equation:

$$\frac{\rho}{\rho_0} \sim \left(\frac{t_e}{l}\right)^2 + C_3*\frac{t_f}{l} \quad \text{to obtain by first order approximation } (t<<l) \qquad \frac{\rho}{\rho_0} \sim \frac{t}{l} \qquad (3)$$

and subsequently, using eq. (1):

$$\frac{E}{E_0} = \alpha*\left(\frac{\rho}{\rho_0}\right)^4 + \beta*\left(\frac{\rho}{\rho_0}\right) \qquad (4)$$

α and β represent the contributions of cell edges and cell walls respectively in a qualitative fashion (see fig. 2). Figure 4 shows the comparison of the experimental data to the theoretical prediction using eq. (4). In the same figure the prediction based on an equation proposed by Kumar & Vander Wel (5) is shown. In the range of foam densities studied equation (4) describes the data better than the equation proposed by Kumar and Vander Wel. Extrapolation of the yield stress and the modulus of the foams to the value at $\rho/\rho_0=1$ gives a value comparable to the yield stress and modulus measured in compression and tension on bulk samples of PC and SMA.

REFERENCES

1. Gibson, L.J., and Ashby, M.F., 1989, "Cellular Solids, Structure and Properties", Pergamon Press.
2. Collias, D.I., Baird, D.G., and Borggreve, R.J.M., J Mater Sci, submitted.
3. Seeler, K.A., and Kumar, V., 1993, J Reinforced Plast & Comp 12, 359.
4. Kumar, V., 1992, "Microcellular Polymers: novel materials for the 21-th century. In: Cellular Polymers", Rapra conference papers.
5. Kumar, V., and Vander Wel, M., 1991, Proc. SPE ANTEC '91, 1406.
6. Wessling, M., Borneman, Z., Boomgaard, v.d. Th., and Smolders, C.A., 1994. J. Appl. Polym. Sci., accepted for publication.

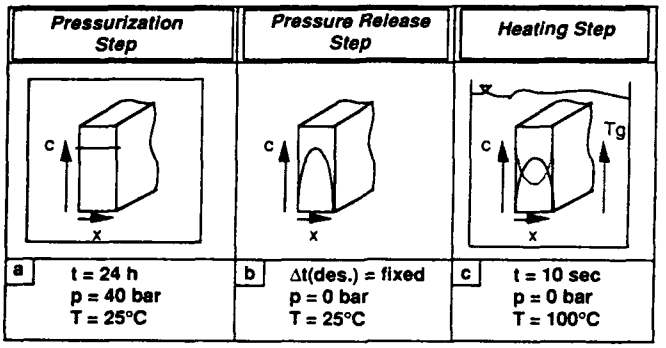

Figure 1. Basic foaming principle showing the individual preparation steps (6).

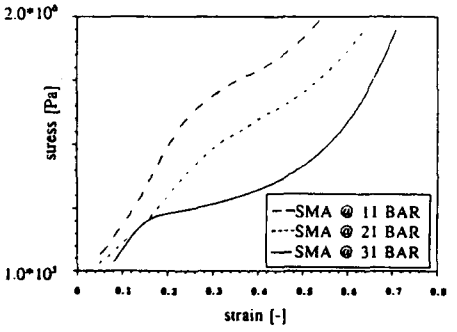

Figure 3. Crushing strength curves for SMA showing the influence of foam morphology. The saturation pressures are 11, 21 and 31 bar, and the foaming temperature is 443 K.

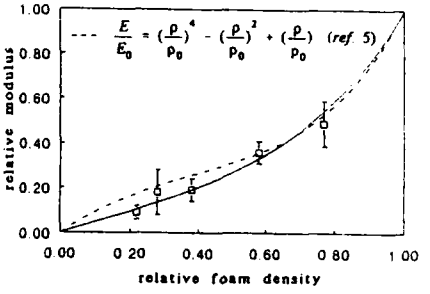

Figure 4. Relative modulus E/E_0 as a function of relative foam density ρ/ρ_0 for SMA (saturation pressure is 31 bar). The solid line represents the prediction using eq. (4).

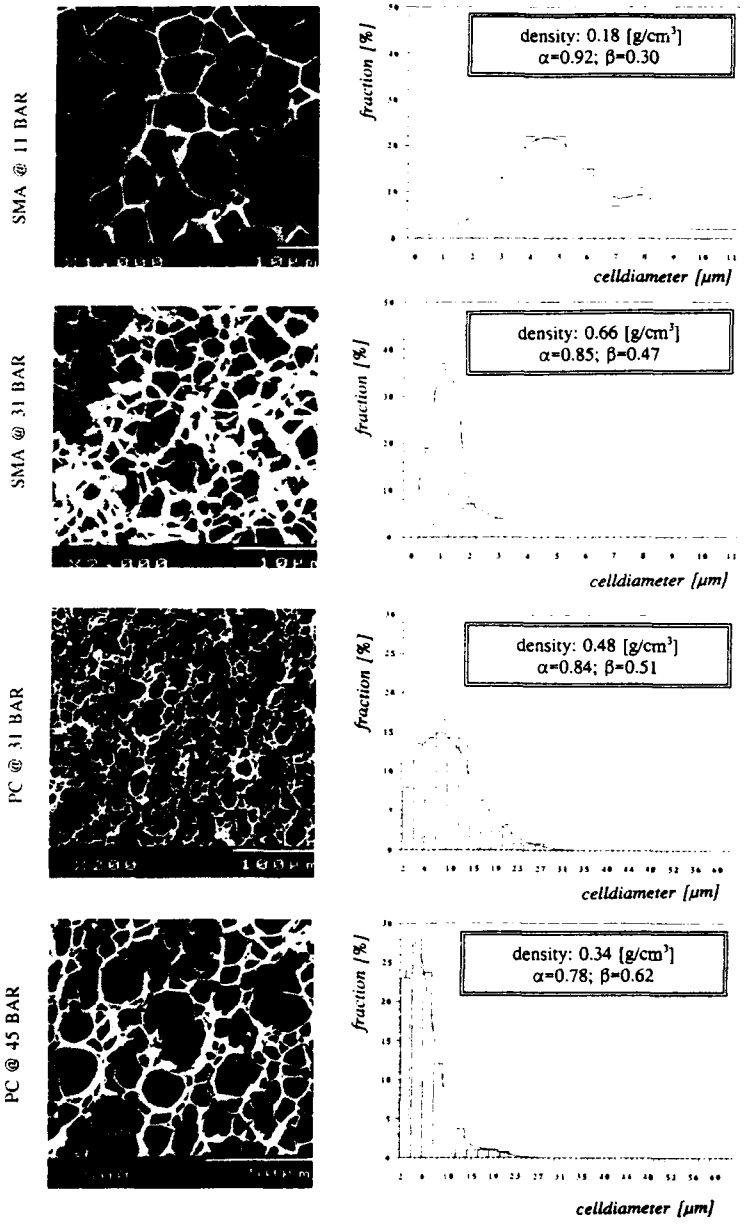

Figure 2. Cell size and cell size distributions of microcellular PC and SMA foams. Saturation pressure, foam density and cell structure parameters α,β are indicated. Foaming temperature is 443 K for SMA and 423 K for PC.

HEALING OF MICROPORES IN SEMICRYSTALLINE POLYMERS

Petrov A.I., Razuvaeva M.V., Betehktin V.I.

The influence of annealing and high hydrostatic pressure on the kinetics of healing of pores which arise during orientation of PTFE and high density PE at 293 K have been studied by small angle X-ray scattering (SAXS), measurements of density, isometrical heating and differential scanning calorimetry (DSC). The activation energy and volume have been estimated. The correlation between porosity healing and internal compressive stresses that arise on heating of prestrained polymers have been found and the analysis of energetics of the process of annealing of the prestrained samples have been carried out. The analysis of the obtained data lead to a conclusion that healing of pores is connected with the process of viscous flow of macromolecules into the pore due to segmental motion. On annealing the healing of pores is due to the action of internal compressive stresses σ_{int} which have the energetical nature. The pressure is accelerated the flow of macromolecules into the pores, until the segmental motion do not put on the breaks by decreasing the free volume.

It has been shown [1,2] that healing of pores on annealing of prestrained polymers lead to restoration of their mechanical characteristics. This work is a continuation of the study [3,4] of specific features of pore healing on annealing in a free and loaded states or under high hydrostatic pressures in the samples of PTFE and high density PE prestrained at 293 K.

METHOD

The initial porosity in samples of PTFE with $M = 2 \cdot 10^6$ and high density PE with $M = 10^7$ was induced by drawing under atmospheric conditions and the draw ratio was 1,9 for PTFE and 6 for high density PE. Then the samples were unloaded in order to relax the elastic strains at room temperature for about 24 h. The porosity, sizes, shapes and concentration of micropores in the prestrained samples and after different pressures and annealing temperatures was controlled by measurements of density (the accuracy was $1 \cdot 10^{-4}$) and SAXS. A Kratky small angle X-ray camera was employed which formed a narrow Xray beam (3 x 0,005mm). For the case of Mo K_α- emission it is possible to obtain the scattering curve for angles ranging from 0,6 min to several degrees. The size (L) and concentration (N) of micropores in the Guinier approximation can be calculated from the slope of the plot of scattering intensity (I) versus angle of scattering (φ) according to expression:

$$I \sim I_0 \cdot A \cdot N \, (V^2/L) \exp(-\pi^2 L^2 \varphi^2 / 3\lambda^2)$$

where V is the scattering volume, A is a constont and λ is the

wavelength of radiation. For determination of sizes in direction of stretch axis $L_{\parallel}$ or in perpendicular direction $L_{\perp}$ the plane of primary beam was parallel or perpendicular to the axis of orientation. To study the internal compressive strains that are responsible for contraction of the drawn samples on annealing the technique of isometrical heating was used [6] . The temperature dependences of strains were recorded on the equipment with rigidity 50 $N \cdot mm^{-1}$ and for heating rate 0,5 $deg \cdot min^{-1}$. DSC was used for estimation of difference entalpy ΔH for different states of polymer. The investigated samples have been heated at the rate of 10 $deg \cdot min^{-1}$ and the DSC curves were recorded. The value ΔH was estimated from the difference areas under the DSC curves of prestrained samples and unstrained polymer. We assume that the entalpy of unstrained samples was zero. The annealing of prestrained samples was carried out in the interval of temperatures from 293 to 578 K and from 293 to 413 K for PTFE and high density PE, respectively. A high hydrostatic pressure camera with silicon oil was employed, which formed pressure up to 1000 MPa.

RESULTS AND DISCUSSION

It has been found that the beginning (333 K) and behaviour of the curve of porosity healing (W) on annealing of PTFE in the free state correlates with changing of entalpy ΔH and with the internal compressive stresses σ_{int} which revel on isometrical heating of prestrained samples (Figure 1). In this case the annealing of drawn samples is accompanied by heat evolution that evidences the energetical nature of the internal stresses. On annealing the hydrostatic pressures of rather small values (6MPa) accelerate healing of porosity very much (Figure 1, curve 4).

The annealing under external compression load or in streching of samples accelerates the process of porosity healing when $\sigma < \sigma_{int}$ (Figure 2). On drawing the process of porosity healing does not take place when $\sigma = \sigma_{int}$ and the porosity in the samples increases when $\sigma > \sigma_{int}$.

Analysis SAXS curves have shown that on annealing of PTFE the size $L_{\parallel}$ decreases and the size $L_{\perp}$ remains nearly constant (Table 1). The ratio $L_{\perp}/L_{\parallel}$ increases by a factor of 2. This means that the shape of micropores changes strongly with an increase of the temperature.

It has also been established that in the interval of pressures from 0,1 to 80 MPa the degree of pore healing in PTFE is the highest. A further increase of pressure up to 1000 MPa very slightly influences a value of porosity (Figure 3). With increasing of temperature under pressure the porosity healing becomes very intensive. The sizes $L_{\parallel}$ and $L_{\perp}$ decrease, but the ratio $L_{\perp}/L_{\parallel}$ remains constant (Table 2). This means that the shape of pores under pressure remains unchanged.

The concentration of pores under pressure and on annealing remains unchanged and the observed decreasing of pores volume very correlates with changing of a value of W, as was shown by SAXS.

From the analysis the kinetic of porosity healing the following values of activation parameters were obtained. In the region low temperatures from 373 to 448 K the energy for activation of the process of porosity healing is $E = (57 \pm 6)$ $kJ \cdot mol^{-1}$ and the activation volume is $\Delta V = (800 \pm 70)$ $sm^3 \cdot mol^{-1}$, and at high temperatures from 533 to 563 K $E = (160 \pm 20)$ $kJ \cdot mol^{-1}$,

$\Delta V = (11,5 \pm 0,5) \cdot 10^3\ sm^3\ mol^{-1}$.

The process of pore healing was also studied in the prestrained and unstrained samples of high density PE. In the prestrained samples of high density PE the beginning of pore healing was at T > 293 K, when σ_{int} arise.(Figure 4). The greatest degree of pore

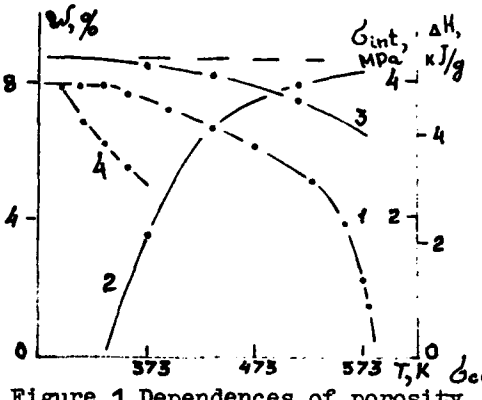

Figure 1 Dependences of porosity (1,4), internal compressive stresses (2) and entalpy (3) on annealing temperature for PTFE.

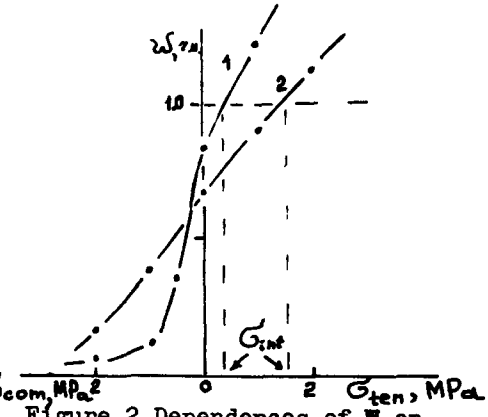

Figure 2 Dependences of W on stresses at constant temperature. PTFE (473 K) - 1, PE (353 K) - 2.

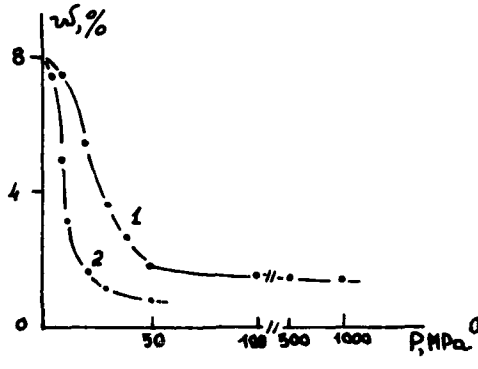

Figure 3 Dependences of porosity on pressure for PTFE at different temperatures: 1 - 293, 2 - 333 K.

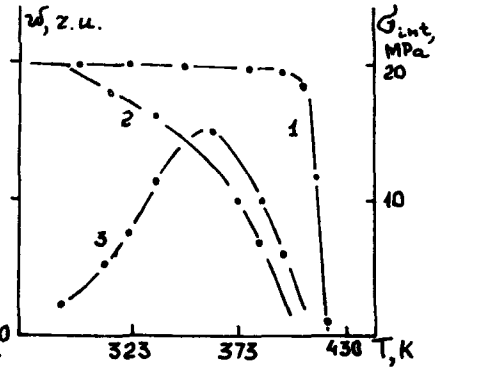

Figure 4 Dependences of W (1,2), σ_{int} (3) on annealing temperature for high density PE: 1 - unstrained; 2,3 - drawn samples.

healing was observed at T> 363 K, when the amorphous part of a polymer transforms from rubberlike to viscous state.

In the unstrained porous samples of PE the healing takes place only near the melting temperature. The isometrical stresses haven't been found in all interval of temperatures.

The obtained data show that healing of pores in the prestrained

polymers at rather low temperatures is connected with viscous flow of macromolecules into the pores [8] , for instance, due to segmental motion. The increasing the energy of activation and activation volume at high temperatures gave evidence that the degree of cooperation motion increases. The driving force of pore healing in the drawn polymers is a internal compressive stresses, which arise during orientation and connected with distortion of polymer structure. In the unstrained porous PE σ_{int} haven't been found and driving force of pore healing will be able a Laplases pressure. The viscous flow of material into the pore under hydrostatic pressure is very sensitive to a value of pressure, until the segmental motion do not put on the breaks by decreasing the free volume at P > 80 MPa [9].

Table 1

P, MPa	0,01	5	15	30	40	100
$L_{\perp}$, nm	92±9	86 ± 9	79 ± 8	69 ± 7	65 ± 6	64 ± 6
$L_{\parallel}$, nm	130 ± 10	120 ± 10	110 ± 10	100 ± 10	93 ± 9	85 ± 9
$L_{\perp}/L_{\parallel}$	0,71	0,72	0,72	0,69	0,70	0,75

Table 2

T, K	293	403	453	489	526	543	563	579
$L_{\perp}$, nm	100±10	100±10	100±10	98±9	98±9	100±10	100±10	110±10
$L_{\parallel}$, nm	120±10	120±10	110±10	100±10	87±9	80±8	70±7	62±6
$L_{\perp}/L_{\parallel}$	0,83	0,83	0,91	0,98	1,13	1,25	1,43	1,77

REFERENCES

1 Wendorff J.H, Polymer 21 (1980) 553
2 Garbella R.W, Wachter J, Wendorff J.H, Progr Colloid & Polymer Sci 71 (1985) 164
3 Petrov A, Razuvaeva M, Sinani A, Egorov V, Betekhtin V, Mechan compzit Mater 2 (1990) 273
4 Petrov A, Razuvaeva M, Sinani A, Betekhtin V, Mechan Compozit Mater 6 (1989) 1121
5 Slutzker A, Kuksenko V, Mechanica polymerov 1 (1975) 84
6 Laiius L, Kuvshinskii J, Fizika tverdova tela 5 (1963) 3113
7 Godovskii U, Teplofizicheskie metodi issledovaniy polymerov, Moscow, Chimiy (1976) 216 p.
8 Bershtain V, Egorov V. Vysokomolek Soed A27 (1985) 2440
9 Olkhovik O. Vysokomolek Soed A18 (1976) 1012

SCRUTINIZING THE TENSILE NECKING OF POLYETHYLENE BY MEANS OF VIDEO-CONTROLLED EXTENSOMETRY

Valérie Gaucher, Philippe François and Roland Séguéla,*

The plastic necking of polyethylene under uniaxial extension at constant cross-head speed is investigated by means of a new method of analysis of the longitudinal and transverse strains at a very local scale in the neck, using computer-assisted video-controlled extensometry. The nominal stress-time and true strain-time curves disclose several distinct deformation régimes that are discussed in conjunction with the fine features of the neck profiles. Neck formation is studied from the comparison of the true stress-strain curve recorded as a function of time, at a given locus, with the true stress-strain curves recorded along the neck, at various times. Also reported is the measurement of volume changes larger than purely elastic effects as a function of strain.

INTRODUCTION

Measuring in real time the local true strain of heterogeneously deformed plastic materials has been a matter of preoccupation for a long time. Indeed, this is a necessary path for establishing the constitutive equations of the plastic flow which requires constant true strain rate experiments as well as for studying the thermal activation of the elementary processes of plasticity. G'Sell and coworkers[1,2] have developped several equipments in this aim. A computed-assisted video-monitored extensometer provided with two cameras has been recently elaborated in our laboratory[3], on the basis of the device contrived by G'Sell et al.[2], for investigating longitudinal and transverse strains on flat hour-glass-shaped samples under tensile testing. This paper deals with a new method of analysis that allows longitudinal strain measurements at a very local scale in strongly necking-prone materials.

EXPERIMENTAL METHOD

The two CDD video cameras equipped with zoom lenses allow digitizing the front and side views of the sample into 512 x 512 pixel images. The present method of investigation involves the use a linear target, about 5 mm long in the z tensile axis, aslent with respect to this axis in the region of the minimum width of flat hour-glass shaped samples. The principle of the analysis of the local deformation in the neck is shown in Figure 1, in projection in the (x,z) plane. From the discrete front image of the sample are recorded the coordinates of the distorted target and sample edges for the calculation of the various ingredients of the relation that gives the local longitudinal strain, ε_z (as defined according to the usual convention dL/L)

$$\frac{\tan \beta_o}{\tan \beta} - \frac{\tan \beta_o}{\tan \alpha} \times \frac{x}{x_e} = \frac{1+\varepsilon_x}{1+\varepsilon_z} \qquad (1)$$

* Laboratoire Structure et Propriétés de l'Etat Solide, URA CNRS 234, Université des Sciences et Technologies de Lille, Villeneuve d'Ascq , France.

The second term of the left-hand member of relation (1) accounts for the incidence of the gradient of transverse displacement of matter along the neck that contributes to the target distortion but does not represent true plastic deformation. It has been assumed that, in any cross-section of z coordinate, necking involves no gradient of longitudinal displacement (i.e. horizontal lines remain horizontal) and affine displacements in the x axis (i.e. homogeneous transverse strain). The slopes of the distorted target and the neck width profile, $\tan\beta$ and $\tan\alpha$ respectively, are determined from a fitting procedure based on the propagation of a second order polynomial over 10 experimental points and taking the computed value of the polynomial derivate at mid-distance of the fitted segment ($\tan\beta_0$ is the slope of the target prior to deformation). The transverse strain, ε_x, is determined from the change in width of the sample all along the target range. The gauge profile prior to deformation is assumed linear in this range, the error being less than 2%. The transverse strain, ε_y, is only determined at the minimum width of the neck in order to check the deformation isotropy.

The drawing experiments have been conducted on a screw-driven Instron testing machine at the constant cross-head speed of 0.5 mm/min.

MATERIAL

The material under investigation is an ethylene-butene random copolymer with the following characteristics: density = 0.950 gcm^{-3}, crystal weight fraction = 0.70, M_n = 30000 and M_w = 157000. Sheets about 3 mm thick were compression-molded at 180°C and slowly cooled at about 20°C/min. The hour-glass-shaped test pieces were cut out from the sheets thanks to a cutting punch. The curvature radius and the minimum width of the gauge were respectively 58 mm and 6 mm.

RESULTS AND DISCUSSION

Figure 2 shows that the strong changes of shape with temperature of the yield point of the nominal stress-time curve can be readily assigned to radical changes of the true strain variation with time. Several domains can be identified according to the true strain rate. This supports the previous conclusion that two mechanisms may operate in the course of the plastic deformation of polyethylene.[4,5,6]

The true stress-strain curve at 80°C (Figure 3) discloses a change of plastic deformation régime which suggests that two processes having different parameters of thermal activation and different strain-hardening rates operate successively. It is suspected that, for energetics reasons, only one of them is operative at 20°C .

The evolution with time of the neck width profiles (Figure 4) shows that deformation gradually slows down and eventually stops in the less strained parts of the neck, i.e. at the nascence of the neck shoulders having convex curvature, and concentrates in the more strained concave parts of the neck.

The mechanism of neck formation can be further analyzed from the comparison of the true stress-strain curve $\sigma=f[\varepsilon(t)]_{z_0}$ recorded as a function of time at the very locus z_0 where the neck was initiated with the true stress-strain curves $\sigma=f[\varepsilon(z)]_{t=cste}$ recorded along the neck, at various times (Figure 5). At the yield point labelled (1), the neck is just being initiated, and the data recorded along the target fall on the true σ-ε curve. The data from the stages (2) and (3) depart significantly from the true σ-ε curve. Stress triaxiality effects can be suspected,[7] the effective stress being higher than the measured σ_z in the low strain range, and lower in the high strain range, because of the change of curvature of the neck profile from convex to concave. However, it cannot account for the drop of stress below the σ-ε

curve in the low strain range for the two cases (2) and (3) which, in another connection, is consistent with the previous observation (Figure 4) that deformation gradually stops in the less strained regions of the neck as it forms. This is *a priori* contradictory with the statement that stress triaxiality is the driving force of neck propagation[7] since deformation stops in the very region (convex) where stress triaxiality involves an additional compressive contribution.

Volume changes larger than purely elastic effects have been measured as a function of strain (Figure 6). At 20°C, a strong voiding effect occurs beyond the yield point. This obviously results from the fibrillar transformation which involves interfibrillar cracks. However, the volume expansion reaches a value of 20% under stress that has never been suspected previously. It is moreover worth noticing that it decreases to about nil after unloading, indicating that the voids can resorb themselves. This is in good agreement with the void content of a few % usually reported from *postmortem* density measurements of necked polyethylenes.

CONCLUSION

The present method of analysis of heterogeneous plastic deformations allows scrutinizing fine details of the process that could not be suspected otherwise. The measurement of the true values of stress, strain, strain rate and volume change will help understanding the tensile double yield phenomenon by allowing notably a correct characterization of the thermal activation of the elementary processes.

REFERENCES

1 G'Sell C. and Jonas, J.J. *J. Mater. Sci.* 1979, **14**, 583.
2 G'Sell C., Hiver J.-M., Dahoun A. and Souahi A. *J. Mater. Sci.* 1992, **27**,5031.
3 François P., Gloaguen J.M., Hue B. and Lefebvre J.M. *J. Phys. III* 1993, to appear.
4 Séguéla R. and Rietsch F. *J. Mater. Sci., Lett.* 1990, **9**, 46.
5 Séguéla R. and Darras O. *J. Mater. Sci.* submitted for publication.
6 Brooks N. W., Duckett R. A. and Ward I. M. *Polymer* 1992, **33**, 1872.
7 G'Sell C., Aly-Helal N. A. and Jonas J.J. *J. Mater. Sci.* 1983, **18**, 1731.

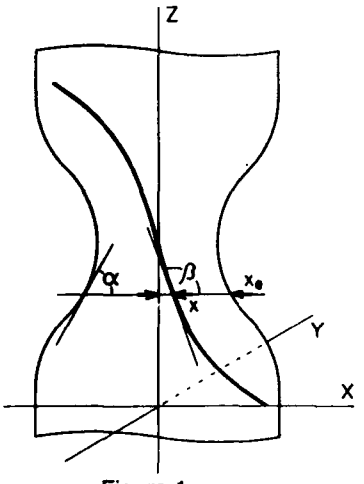

Figure 1
Principle of analysis of the local deformation in the neck from an originally linear target.

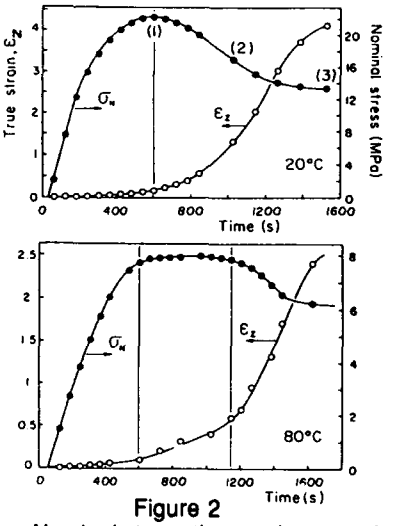

Figure 2
Nominal stress-time and true strain-time curves at 20 and 80°C.

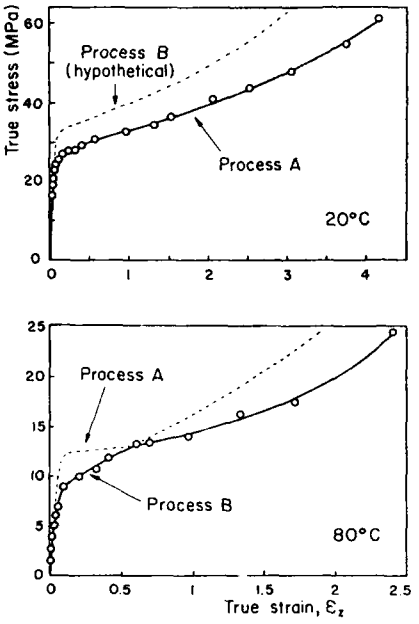

Figure 3
True stress-strain curves at 20 and 80°C.

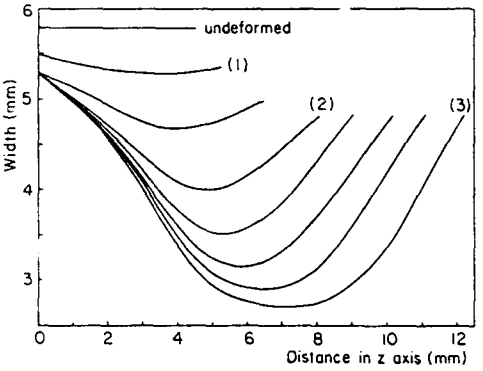

Figure 4
Neck width profiles in the target range at various times of the drawing, at 20°C.

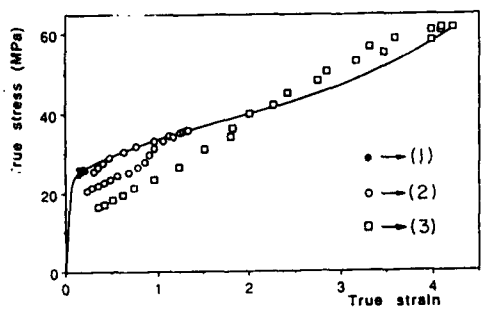

Figure 5
True stress-strain curves as a function of time in the centre of the neck (---) and along the neck at various times (1),(2),(3), see Fig. 2.

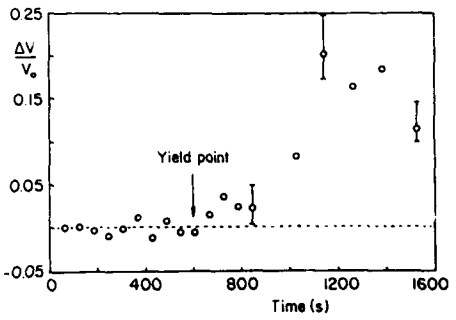

Figure 6
Relative volume variation with strain at 20°C.

DUCTILE-BRITTLE TRANSITIONS IN PIPE GRADE POLYETHYLENE

R.E. Morgan and P.S. Leevers*

The instrumented sharp-notched Charpy impact test has been used to characterise the temperature-thickness sensitivity of the ductile-brittle transition of a pipe grade of modified high density polyethylene. The impact data successfully discriminate between different batches of the resin, ranking them in the same order of performance as that observed in the standard 'S4' pipe fracture test.

Current testing techniques are both expensive and time consuming for large diameter pipes, which are at greatest danger of brittle failure. This method offers an alternative small scale test technique.

INTRODUCTION

Modified High Density Polyethylenes, categorised as 'PE-100' have shown remarkable resistance to Rapid Crack Propagation (RCP). RCP has proved to be unsustainable at any pressure in PE-100 pipelines at 0°C in both the S4 [1] and British Gas full scale tests [2]. Research has shown that this is due to a low ductile-brittle transition temperature (DBTT) rather than a high dynamic fracture toughness. The plain strain toughness is, in fact, little better than that of conventional MDPE resins.

The geometry and processing sensitivity of the DBTT makes the exploitation of PE-100 in pressurised gas pipelines hazardous without knowledge of the DBTT of the specified pipe batch. The gas distribution industry recognises the danger of RCP failure and currently *every batch* of PE-100 produced is tested for RCP resistance at 0°C, the minimum operating temperature in the UK.

The geometry and temperature sensitivity of the ductile-brittle transition of a number of pipe grade PE resins has been studied using the S4 pipe test and the Instrumented Charpy test [3]. By keeping the test temperature constant, and varying the specimen thickness a nil ductility thickness can be found that characterises the resin.

EXPERIMENTAL

The Instrumented Charpy test has already been described extensively [3]. Charpy specimens were cut from the wall of 180 mm diameter SDR11 pipe, of wall thickness 16.4 mm. The specimen depth, D was kept constant at 10 mm, the length, L at 55 mm and span at 40 mm. Specimens thicknesses (B) of 5, 6, 7, 8, 10, 12 and 14 mm were tested at a temperature of -25 °C at an impact speed of 1.5 m/s.

*Department of Mechanical Engineering, Imperial College, London.

This temperature was selected to ensure the transition occurred in the range of thicknesses tested. The samples were oriented as shown in Fig.1. This was done to ensure the morphology of the samples was consistent in the thickness (B) direction, as the pipes morphology is known to vary significantly through the wall thickness of the pipe due to variations in cooling rate during the extrusion process.

A load-displacement curve was recorded for each test. The curve was then integrated to produce an energy-displacement curve, and the peak load and total energy absorbed recorded. These values were then converted to a fracture toughness using the BDø analysis [4], ø being the LEFM correction for the notch. The peak load toughness, G_p has conventionally been interpreted as a crack initiation toughness. The total toughness G_t, (which strictly speaking is determined illegally using the LEFM assumptions) characterises resistance to crack propagation. When $G_p=G_t$, the specimen has no resistance to fast fracture after initiation and will fail in a purely brittle manner.

The transition temperature of the pipe was determined using the Small Scale Steady State ('S4') pipe test. This test has shown good correlation with the British Gas full scale test, which simulates RCP directly in a 20 m pressurised pipeline. Tests were carried out at various temperatures and pressures to locate the transition-temperature locus. A sharply defined transition is found using this technique.

RESULTS

Fig. 2 shows a plot of test pressure against temperature for three batches of PE-100. The batch-to-batch variation of the DBTT can be seen clearly, as can the worrying proximity of the transition temperature to 0 °C.

Figure 3 shows a plot of G_p and G_t against 1/B. Notice that batch A has the highest nil ductility thickness, and a more rapidly increasing toughness with decreasing thickness than batches B and C. This suggests that batch A will remain tough for greater thickness *or* lower temperatures. The S4 test also ranks batch A as having the lowest transition temperature. The Charpy test successfully ranks batches B and C in the same order as the S4 test.

The initiation toughness, G_p does not differ between the three batches. The initiation toughness does not, therefore, characterise the ductile-brittle transition of a PE pipeline.

DISCUSSION

The two tests described do not correlate directly with each other, but provide a qualitative solution to the problem. The ductile-brittle transition is thought to be caused by a transition from plane stress to plane strain. Ductile tear lips develop on the bore of the pipe in the S4 test and on the surface of the Charpy specimens as the test temperature is raised, or the sample thickness decreased. Side-grooving the Charpy specimen and notching the bore of a pipe in the S4 test removes the transition, causing brittle failure under all test conditions and demonstrating the importance of the tear lips. The similarity of the processes acting in the two tests and the fact that they rank materials in the same order of performance is, therefore not surprising.

Direct correlation between the two tests is inappropriate for a number of reasons. Firstly, the strain rates are different, the S4 test being significantly higher. The high strain rate sensitivity of PE will therefore result in different material properties and therefore transition temperatures for the two tests. The crack tip stress field and constraining effect of the two tests is different again making direct correlation inappropriate.

CONCLUSION

The high RCP resistance observed in PE-100 pipelines is due to a low ductile-brittle transition temperature rather than to a high dynamic fracture toughness of the resin.

Charpy impact tests on material machined from the wall of pipe discriminates clearly between different batches of PE-100.

The ranking observed in the Charpy data is the same as that observed in the S4 pipe test.

Impact data can therefore be used to discriminate between different batches of PE-100 and could be used as the basis for a quality control test.

ACKNOWLEDGEMENTS

The authors wish to express their appreciation of a Special Research Grant for this project from the UK Science and Engineering Research Council. Robert Morgan wishes to acknowledge additional support from Uponor Aldyl (UK) and from Neste Polyeten (Sweden).

REFERENCES

1. Greig J M, Leevers P S and Yayla P, Engineering Fracture Mechanics Vol. 42 No. 4 (1992) 663
2. Greig J M and Ewing L, Proc. 5th Intl. Conf. Plastic Pipes, York England (1982)
3. Harry P G and Marshall G P Plastics and Rubber International Vol.16 (1991) 13
4. Plati E. and Williams J G Polymer Engineering and Science Vol.15 No.6 June (1975) 470

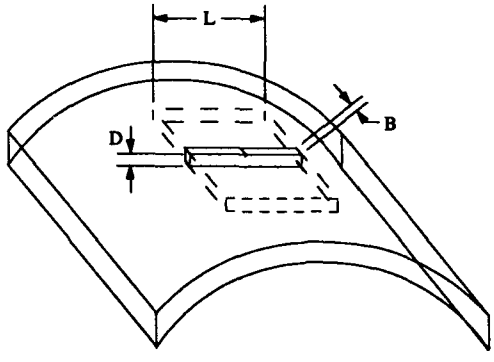

Figure 1 Schematic of Charpy specimen.

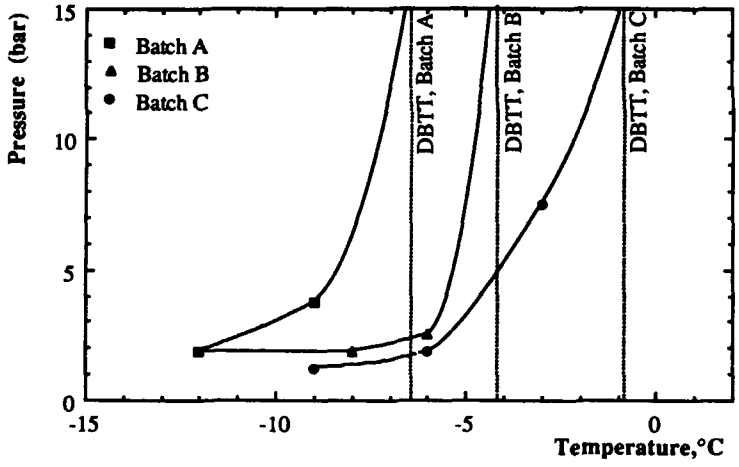

Figure 2 DBTT for three batches of PE-100 measured using the S4 pipe test.

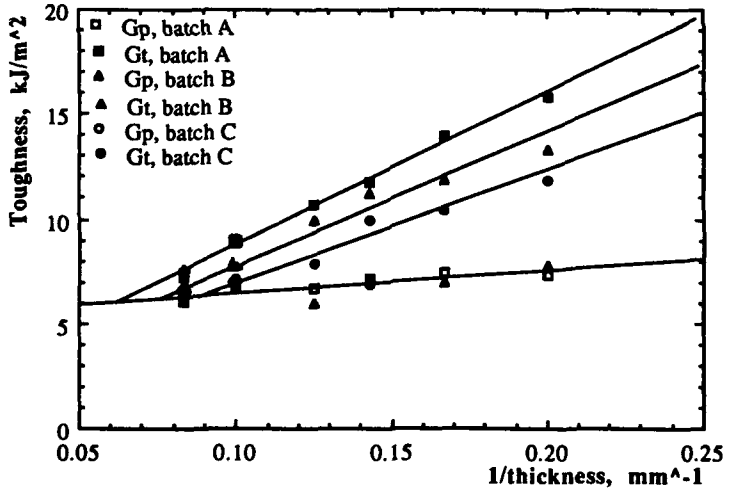

Figure 3 Plot of total (G_t), and initiation (G_p), toughness against reciprocal thickness for three batches of PE-100.

TOUGHENING MECHANISM OF FLAME-RETARDED PLASTICS

L.Utevskii*, I.Finberg*, E.Reznik*, M.Muskatel*
E.Gutman**, S.Lach**

The following methods of toughening flame-retarded (FR) plastics by improving Izod notched impact value are discussed:
- amorphisation of crystalline flame retardant during processing of FR-plastic;
- combining toughening and FR-enhancement;
- proper selection of surface treatment of filler-like FR.

Often the addition of a flame-retardant (FR) to plastic decreases the impact of the FR-plastic. However, decbromodiphenyl oxide (DBDPO) in high impact polystyrene (HIPS) has practically no detrimental effect. X-ray data suggests a possible connection with the amorphization of DBDPO during plastic processing as a result of the combined action of temperature and shear stress (Figure 1).

A combination of toughening and FR-enhancement, i.e. improved FR efficiency, was observed for acrylonitrile butadiene styrene terpolymer (ABS), HIPS and styrene-maleic anhydride (SMA) copolymer, flame-retarded with octabromodipyhenyloxide (OBDPO) or with tribromostyrene (TBS), when ethylene-propylene diene (EPDM) (1) copolymer or styrene-ethylene-butylene (SEBS) copolymer was used as a toughener (Figures 2 and 3).

The introduction of the FR via a master batch (MB) in the toughener may be crucial to the combination of toughening and of FR-enhancing (Figures 4 and 5).

The special effect of impact improvement with the proper selection of the surface treatment of filler-like FR is demonstrated on the application of magnesium hydroxide in polypropylene (Figure 6).

*Dead Sea Bromine Group, P.O.Box 180, Beer Sheva, Israel 841001
**Ben Gurion University of the Negev, Beer Sheva, Israel

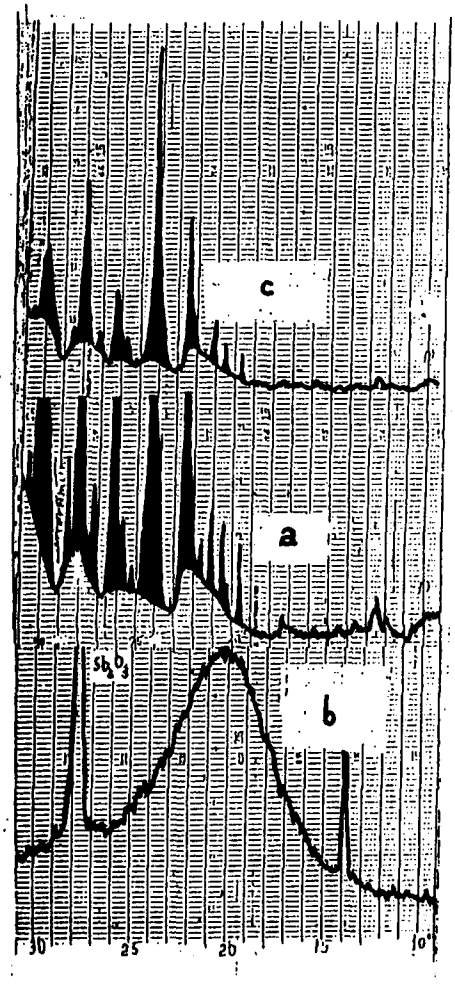

Figure 1. X-ray diffractograms of DBDPO (a), HIPS/DBDPO+SB_2O_3 (b), and hand ground DBDPO (c): typical DBDPO peaks are blackened.

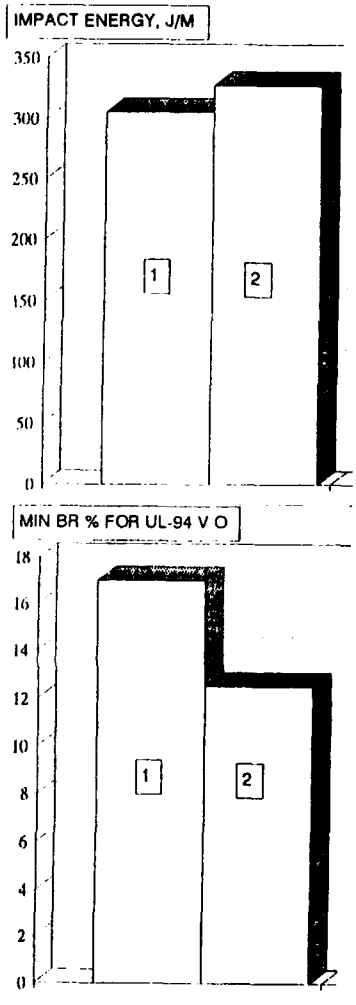

Figure 2. Toughening and FR-enhancement of ABS flame-retarded with octabromodiphenyl oxide (OBDPO):
[1] without EPDM
[2] with 5% EPDM

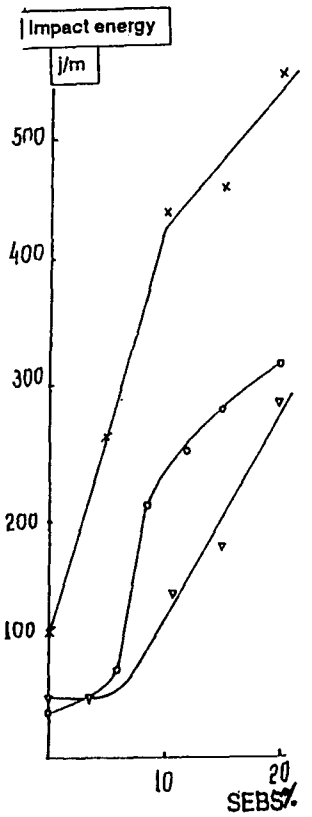

Figure 3. Toughening and FR-enhancing of ABS(x), SMA(o) and HIPS(v) with SEBS/TBS

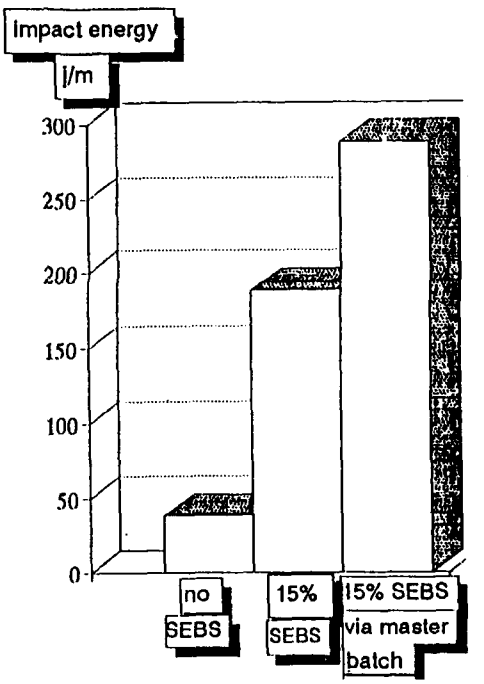

Figure 4. Toughening and FR-enhancing of ABS/TBS with SEBS

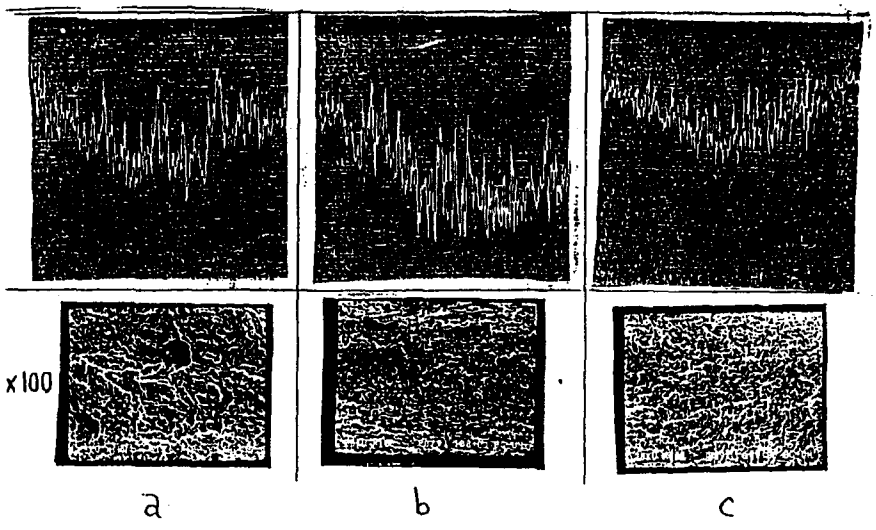

Figure 5. Image analysis (line-profile) and SEM microphotographs of impact break for ABS/TBS (a), ABS/SEBS/TBS MB (b) and ABS/(TBS+SEBS) (c)

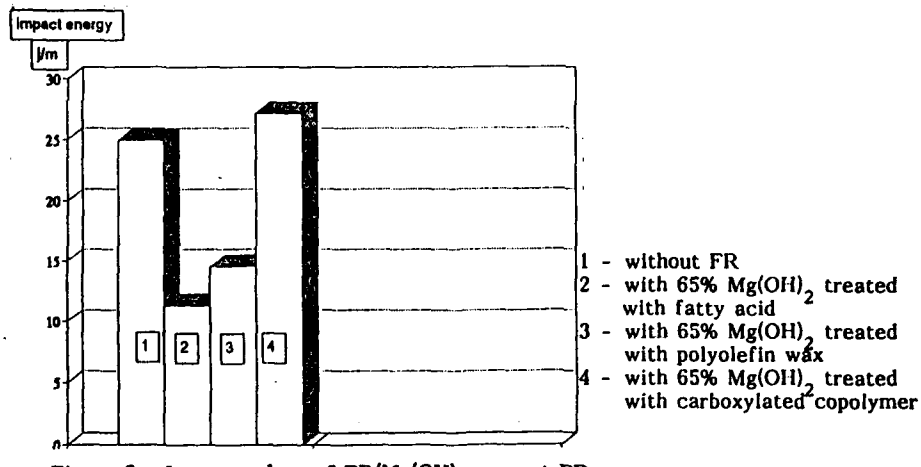

Figure 6. Impact values of PP/$Mg(OH)_2$ vs neat PP

REFERENCE

1 Utevski E, Reznik-Vaks E, Peled M, EP 391,275 (1990)

IMPACT FRACTURE OF TOUGHENED, FLAME-RETARDED ABS PLASTICS CONTAINING MINERAL FILLER

A.Bobovitch, E.Gutman*
M.Scheinker, L.Utevski and M.Muskatel**

The impact fracture of flame-retarded acrilonitrile-butadiene-styrene (ABS) based on thermally polymerized polypentabromobenzyl acrylate (PBB-PA) was compared with that of ABS based on thermally polymerized PBB-PA in the presence of inorganic filler.

It was shown that polymerization on the inorganic filler of the flame retardant (FR) improves the heat stability of the FR and the thermomechanical properties of the plastic.

INTRODUCTION

One of the better known methods of achieving flame retardancy of the polymeric matrix is to introduce bromine-containing FRs. Actimer (Tradename) FRs is an innovative family of bromine containing monomers which can be polymerized with or without a polymer matrix.

Flame retardancy can create a number of problems, one of which is a possible decrease in impact energy.

Mineral fillers enhance properties of plastics and lower their price (1) but can also decrease impact energy(2). Theoretically, impact resistance of a filler polymer should improve if stress concentration points are spread more evenly throughout the plastic matrix because this should encourage crazing and retard cracking (3).

Often the surface of mineral fillers is specially treated with a coupling agent to improve the performance of fillers in plastics (4), and sometimes toxic materials such as silanes (5) are used for this purpose. Other methods of improving matrix filler adhesion are plasma discharge (6), chemical reaction (7) and the grafting of the polymer onto the filler particle surface (8).

This report suggests an additional method for matrix filler adhesion by the thermal polymerization of active FR monomers on the surface of filler particles followed by the application of the polymerizate into the polymer matrix.

*Ben Gurion University of the Negev, Beer Sheva, Israel
**Dead Sea Bromine Group, Beer Sheva, Israel

EXPERIMENTAL DETAILS

Pentabromobenzyl monoacrylate (PBB–MA) was polymerized with an inorganic filler in a twin-screw extruder at 240°C. The PBB-PA produced was analyzed thermogravi- metrically. Flame retardancy was achieved by compounding ABS pellets with the PBB-PA in the extruder followed by injection molding. All the formulations were prepared with 4.6% inorganic filler.

Molded specimens were subjected to UL-94 testing (9). Notched Izod impact energy was evaluated according to ASTM D256-81 and heat deflection temperature (HDT) was measured according to ASTM D648.

RESULTS AND DISCUSSION

It was shown that polymerization on the filler improves the heat stability of the FR (Figure 1). Heat stability of the polymerizate increases dramatically when the filler load is increased from 5% to 20%. Although heat stability of the polymerizate decreases in the 20-50% filler load range, it is nevertheless higher than with no filler.

The HDT (1.6 MPa) of ABS flame-retarded with the different additives gave the following values:

Additives	HDT (°C)
PBB-PA	62.8
PBB-PA + 50% PBB-PA / 50% filler polymerizate	72.4
PBB-PA + 50% PBB-PA / 50% filler polymerizate + 10% Chlorinated polyethylene (CPE)	71.1
Mixture of PBB-PA with filler + 10% CPE	67.6

From the above, it can be seen that the HDT of ABS with PBB-PA polymerized on filler is higher by comparison to ABS with a mixture of PBB-PA and filler. Toughening with 10% CPE does not decrease the HDT value of FR ABS.

When ABS was flame retarded with various additives the following impact energy values were obtained:

Additives	Impact energy value (J/m)
PBB-PA	20.3
PBB-PA + 50% PBB-PA / 50% filler polymerizate	35.3
Mixture of PBB-PA with filler	28.4
75% PBB-PA / 25% filler polymerizate	28.7

The same materials toughened with 10% CPE produced the following impact energy values: 58.3 J/m, 60.6 J/m, 59.6 J/m, and 67.2 J/m.

After substitution of PBB-PA by PBB-PA/filler polymerizate or alternatively PBB-PA+filler mixture, the flame retardancy level decreased from UL-94 V-O to UL-94 V-2. Toughening of the filled ABS with 10% CPE restored the flame retardancy level the UL 94 value to V-O.

The impact energy and flame retardancy results demonstrate that:
- the addition of inorganic filler to ABS/PBB-PA increases impact energy;.
- the increase in impact energy is higher when the mixture of PBB-PA and PBB-PA/filler polymerizate is added;

- toughening of ABS/PBB-PA with 10% CPE was effective for all the formulations and gave an impact energy of 60-70 J/m.
- toughening of ABS/PBB-PA with CPE enhanced flame retardancy, i.e. from UL-94 V-2 to UL-94 V-O.

The difference between the surface and line profile of the fracture of a toughened and non-toughened ABS plastic are shown in Figure 2.

REFERENCES

1. Hirshler M.M., Polymer 25 (1984) 405
2. Han C.D., Sandford C. and Yoo H.I. Polym. Eng. Sci. 19 (1978) 849
3. Nakagawa H. and Sano H., Polymer Prepr. 26(2) (1985) 249
4. Sohn J.E. J.Adhesion 19 (1985) 15
5. Abate F. and Heihens D., Polymer Commun. 24 (1983) 137
6. Shreiber H.P., Werthrimer M.R and Lambla M., J. Appl. Pol. Sci. 27 (1982) 2269
7. Takayanagi M., Kajajama T. and Katagose T., Ibid. 3903
8. Jiang M, Wang S and Jin X., J. Mater. Science Letters 9 (1990) 1239
9. Test for Flammability of Plastics Materials for Parts in Devices and Appliances, 4th ed., June 10, 1991.

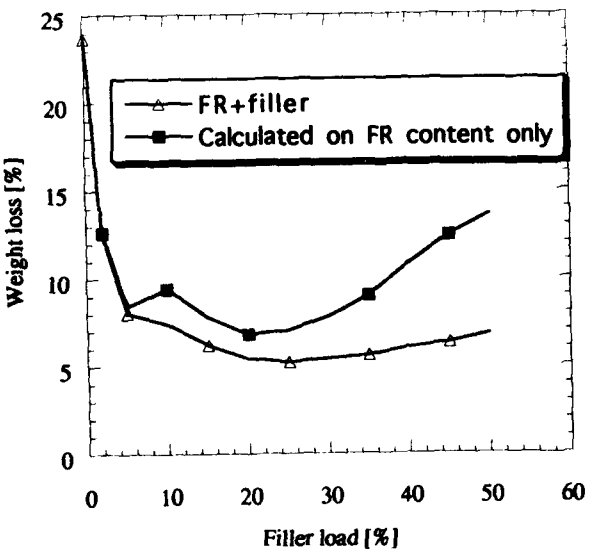

Figure 1 Weight loss of FR polymerized on filler and of FR only in this composition as a function of filler load

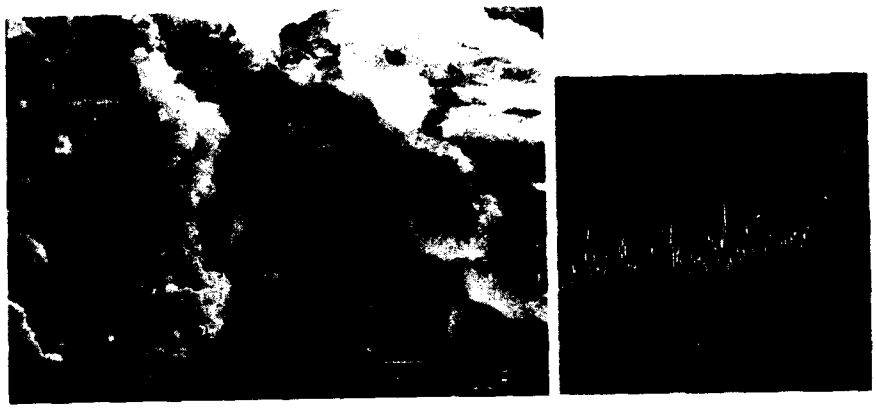

a

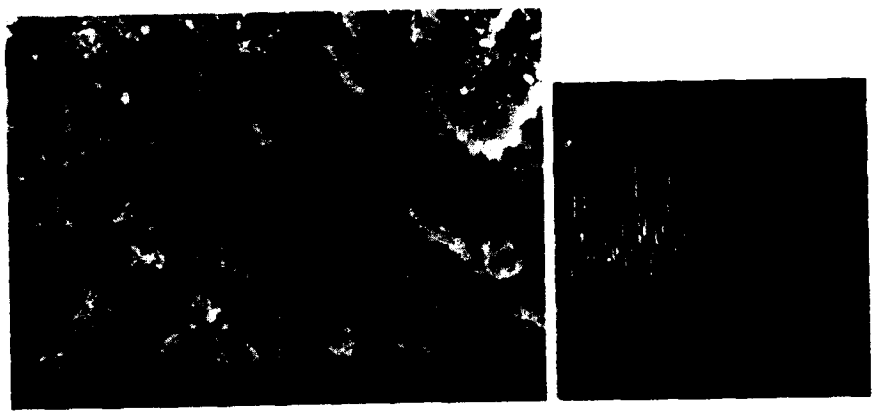

b

Figure 2 Fracture surface and line profile of the fracture of non-toughened FR-ABS (a) and of flame-retarded ABS toughened with 10% CPE (b)

STRESS-RELAXATION DUE TO ENVIRONMENTAL EFFECTS ON POLYPROPYLENE AND FIBER REINFORCED POLYESTER

E. Gutman and R. Soncino*

Stress-relaxation tests were carried out on two types of Fiber Reinforced Polyester (FRP)[530 (Isophtalic) and 660 PA (Bisphenol A)] and on Polypropylene (PP). The FRP and PP were exposed to different environments such as NaOH, KOH, H_2SO_4, HNO_3 (at various concentrations),boiling water, and hot air (100 °C). The changes that occurred in the parameters of relaxation, especially in τ (relaxation time) indicate that FRP type 530's most effective environments are 6M KOH and 2M H_2SO_4, FRP type 660 PA's most effective environments are HNO_3 (at all concentrations), 6M H_2SO_4 and boiling water. PP is effected by all of the environments. The mathematical treatment of stress-relaxation is based on the three-element model. This model correlates well (97-98%) with the experimental data and therefore gives a reliable calculation of τ.

INTRODUCTION

There is an extended use of polymers as structural material, especially in chemical industry. Polymer degradation under severe conditions such as environments, active work media, and etc.(1) must be ascertained in order to determine its performance under those conditions.

It is well known that unsaturated three dimensional polyesters such as 530 and 660 PA have good thermoset characteristics to resist the corrosion attack by weak alkalis and strong acids (2). We used in our study bases and acids such as NaOH and HNO_3, respectively, in order to observe a corrosion attack. PP is also known for its chemical resistance but it is slowly attacked by concentrated strong acids such as H_2SO_4, especially in the range of temperatures 100-125 °C.

Stress-relaxation is one of the useful methods of evaluating the influence of active media on the mechanical behavior of polymeric materials (3). Stress-relaxation is an effective tool in studying the chemical reactions which may occur in polymers because of the interconnection between kinetics of the chemical bond rupture and of mechanical relaxation processes.

There are several models which describe the stress-relaxation process. All of these models are based on various combinations of springs and dashpots in series and/or in parallel. This report is based on the three-element model of the standard linear solid: a spring and a dashpot in series, and a single spring parallel to the series (Figure 1). The three-element model is represented by the following equation:

$$\sigma(t) = \sigma_2 + \sigma_1 \exp(-t/\tau) \quad \text{.....(1)}$$

*Department of Materials Engineering, Ben Gurion University, Beer Sheva 84105, Israel

EXPERIMENTAL DETAILS

Specimens with dimensions of 2.0 x 9.2 x 60 mm were exposed to the following environments:
1) air (25 °C)
2) hot air (100 °C)
3) boiling water
4) bases- NaOH and KOH (concentrations of 1M and 6M)
5) acids- H_2SO_4 and HNO_3 (concentrations of 0.5 M, 2M and 6M)
For no. 2-5 above, the specimens were exposed at 100 °C for 3 hrs.

After the exposure process, the specimens underwent stress-relaxation tests in an Instron machine at room temperature.

Scanning Electron Microscopy was used both after the exposure of the specimens to the different environments and the proceeding stress relaxation tests.

Examples of SEM fractography and stress-relaxation curves are shown in Figures 2 and 3, respectively.

RESULTS AND DISCUSSION

The analysis of environmental effects on the behavior of polymeric materials was based on the stress-relaxation tests. The changes that occurred in τ due to the exposure to the different environments are presented in Table I. The mathematical analysis of the values of τ shows that the error range of τ is not more than 10%. Therefore, only changes of τ over 10% were taken into account in order to define the effective environments.

It can be seen that FRP types 530 and 660 PA are effected by the following environments (Table I): 1M NaOH, KOH (1M and 6M), 6M H_2SO_4, HNO_3 (0.5M, 2M and 6M). In addition, FRP type 530 is also effected by 2M H_2SO_4 and FRP type 660 PA is also effected by boiling water. FRP type 530's most effective environments are 6M KOH and 2M H_2SO_4, while FRP type 660 PA's most effective environments are 6M H_2SO_4, HNO_3 (at all concentrations) and boiling water. Both of FRP types are not effected by 6M NaOH, although they are effected by 1M NaOH.

PP is effected by all environments, especially by hot air (100 °C), boiling water, NaOH (at all concentrations), 6M KOH, 6M H_2SO_4 and 6M HNO_3.

The results demonstrate the following phenomena:
1) Both of the two investigated types of FRP are effected by the same environments. The resulting changes of τ show that the mechanical behavior demonstrates corrosion effects.
2) FRP 530 and 660 PA are not effected by higher concentrations of NaOH.
3) PP is effected by all environments, apparently because of the exposure temperature (100 °C).
4) SEM results indicate that both FRP types are attacked by active media (bases and acids) causing microstructure changes (cracks in the matrix and in the fiber-glass, and also fiber pull-out). PP do not show any apparent change in its microstructure.

REFERENCES

1) Nicholson J. W., 'The Chemistry of Polymers', Royal Society of Chemistry Paperbacks, Cambridge, 1985
2) Encyclopedia of Polymer Science and Engineering, vol. 4 and 12, John Wiley & Sons, USA, 1986
3) Eyring H. and Krausz A. S., 'Deformation Kinetics', John Wiley & Sons, USA, 1975

SYMBOLS USED

$\sigma(t)$ - stress as a function of time (Kg/mm^2)

$\sigma_{1,2}$ - stresses developed on springs 1 and 2, respectively (Kg/mm^2)

t - time of testing (min.)

τ - relaxation time (min.)

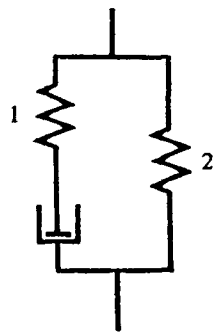

Figure 1 Three-element model

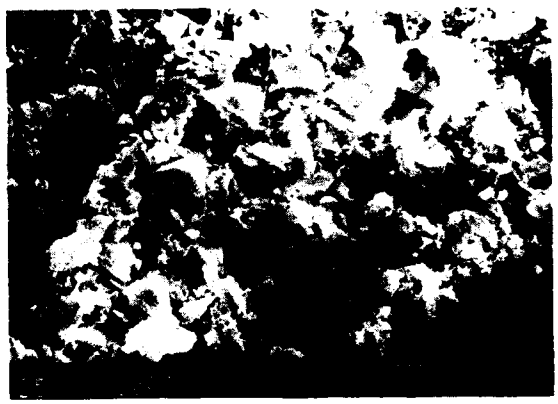

Figure 2 SEM Fractography of FRP 530 exposed to 1M NaOH

Environments	Relaxation Time (min.)			Effected by Environment		
	PP	FRP 530	FRP 660 PA	PP	FRP 530	FRP 660 PA
air (25 °C)	0.756	0.755	0.774	(control)	(control)	(control)
air (100 °C)	1.149	0.712	0.846	yes*	no**	no
water (100°C)	1.168	0 807	0.503	yes	no	yes
1M NaOH	1.177	0.626	0.679	yes	yes	yes
6M NaOH	1.174	0.777	0.765	yes	no	no
1M KOH	1.068	0.890	0.871	yes	yes	yes
6M KOH	1.150	0.536	0.539	yes	yes	yes
0.5M H_2SO_4	1.093	0.698	0.781	yes	no	no
2M H_2SO_4	1.032	0.986	0.705	yes	yes	no
6M H_2SO_4	1.178	0.962	0.565	yes	yes	yes
0.5M HNO_3	1.071	0.648	0.442	yes	yes	yes
2M HNO_3	0.941	0.557	0.415	yes	yes	yes
6M HNO_3	1.162	0.654	0.418	yes	yes	yes

*yes: values of τ that changed more than 10% (compared to air at 25 °C)

**no: values of τ that changed less than 10% (compared to air at 25 °C)

Table I The effect of the environments on τ

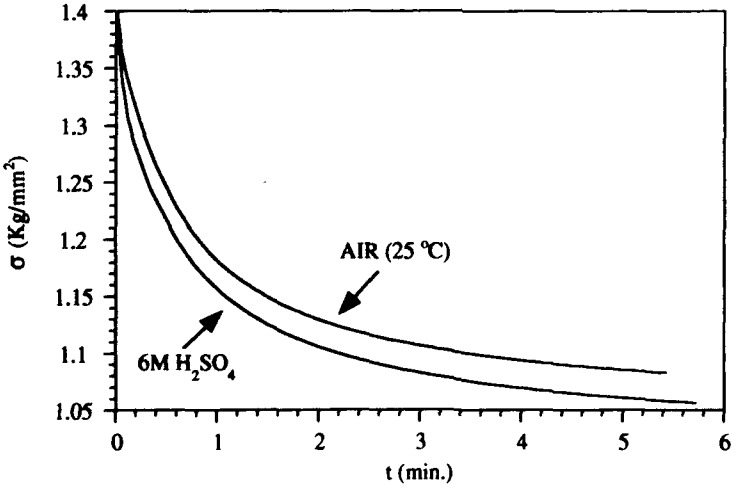

Figure 3 Stress-relaxation curves for PP (air 25 °C and 6M H_2SO_4)

A Three Dimensional Nonlinear Viscoelastic Model

L. Zhang* and L. J. Ernst*

A 3D model has been developed for nonlinear viscoelastic time-dependent behaviour including the aging effects. Various tests have been done such as uniaxial cyclic loading, long-term creep, short-term biaxial creep and a creep loading for a plate specimen with a circular hole for a thermoset material, polyester. The comparison between theory and experiment shows a very good agreement.

1. Introduction

A nonlinear viscoelastic model has been developed with a numerical algorithm for the finite element method. A creep Poisson's ratio has been adopted in order to set up a 3D theory. The model has a potential to deal with nonlinear time-dependent behavior and takes into account the aging influence for the long-term behaviour of polymer materials.

Compared with experiments, the theory has been found to perform very good for both short-term and long-term creep behaviour, and the cyclic loading response, for uniaxial as well as for biaxial loading situations. The calculated creep deformation and the stress redistribution in a plate with a circular hole also agrees quite well with experimental results.

2. Theory

A three dimensional nonlinear viscoelastic model has been developed in Zhang & Ernst 1993[1]. It is an extension of Schapery's uniaxial theory (Schapery 1969[2]) with the use of a creep Poisson's ratio, ν_c, which is generally different from the instantaneous elastic Poisson's ratio, ν (Zhang 1993a[3]).

$$\varepsilon_i = g_0 A_0 S_{ij}\sigma_j + g_1 \int_0^t \Delta A \frac{d}{d\tau}(g_2 S^c_{ij}\sigma_j)\, d\tau \ . \tag{1}$$

The kernel function in Equation (1) is

$$\Delta A(\psi-\psi') = \sum_p A_p [1 - e^{-\lambda_p(\psi-\psi')}] \text{, and } \psi = \int_0^t \frac{dt'}{a_\sigma} \ , \quad \psi' = \int_0^\tau \frac{dt'}{a_\sigma} \tag{2}$$

where ψ and ψ' are the shifted times; A_0 the initial value of compliance; the nonlinear functions g_0, g_1, g_2 and a_σ in Equation (1) depend on an invariant, the octahedral shear stress.

The expressions of stresses and strains are $(\varepsilon_1, \varepsilon_2, \varepsilon_3, \varepsilon_4, \varepsilon_5, \varepsilon_6) = (\varepsilon_{11}, \varepsilon_{22}, \varepsilon_{33}, \varepsilon_{12}, \varepsilon_{23}, \varepsilon_{13})$ and $(\sigma_1, \sigma_2, \sigma_3, \sigma_4, \sigma_5, \sigma_6) = (\sigma_{11}, \sigma_{22}, \sigma_{33}, \sigma_{12}, \sigma_{23}, \sigma_{13})$. The tensors in Equation (1) are

*Laboratory for Engineering Mechanics, Delft University of Technology, The Netherlands

$$S_{ij} = \begin{bmatrix} 1 & -\nu & -\nu & 0 & 0 & 0 \\ -\nu & 1 & -\nu & 0 & 0 & 0 \\ -\nu & -\nu & 1 & 0 & 0 & 0 \\ 0 & 0 & 0 & 1+\nu & 0 & 0 \\ 0 & 0 & 0 & 0 & 1+\nu & 0 \\ 0 & 0 & 0 & 0 & 0 & 1+\nu \end{bmatrix} \quad \text{and} \quad S^c_{ij} = \begin{bmatrix} 1 & -\nu_c & -\nu_c & 0 & 0 & 0 \\ -\nu_c & 1 & -\nu_c & 0 & 0 & 0 \\ -\nu_c & -\nu_c & 1 & 0 & 0 & 0 \\ 0 & 0 & 0 & 1+\nu_c & 0 & 0 \\ 0 & 0 & 0 & 0 & 1+\nu_c & 0 \\ 0 & 0 & 0 & 0 & 0 & 1+\nu_c \end{bmatrix}. \tag{3}$$

The physical aging effects can be implemented into the model by shifting the kernel function, ΔA, horizontally on the logarithmic scale (Struik 1978[4] and Zhang 1993b[5]). We replace ψ by a long-term shifted time (or the so-called effective-time) $\bar{\psi}$ in Equation (2)

$$\bar{\psi} = \int_0^t \frac{dt'}{\bar{a}_\sigma} \text{ and } \bar{\psi}' = \int_0^\tau \frac{dt'}{\bar{a}_\sigma}. \tag{4}$$

If there is no coupling effect between the stress-induced shifting and the aging-induced shifting, $\bar{a}_\sigma$ can be written as

$$\bar{a}_\sigma = a_\sigma \left(\frac{t_e + \tau}{t_e} \right)^\alpha, \tag{5}$$

where a_σ is purely the stress-induced shifting factor as previously defined in Equation (2); the aging-induced shifting rate α can be measured by tests; t_e is the initial aging time.

A numerical scheme has been constructed and implemented into the finite element package, DIANA (Zhang 1993c[6]).

3. Comparisons between Experiment and Theory

The model parameters were determined by a dog-bone sample having a rectangular cross-section (11 mm^2) (Zhang 1993d[7]). Although these tests concerned simply a uniaxial tensile creep-recovery loading state, the established model is expected to be able to describe 3D stress-strain behavior of a polymer material under complicated loading situations.

Some different tests were carried out with various specimens in order to evaluate the quality of the theory. Rectangular cross-section (45 mm^2) dog-bone specimens were used for cyclic loading tests; tube specimens for biaxial creep tests; and the specimens of a plate with a circular hole for a distributed 2D stress field creep situation.

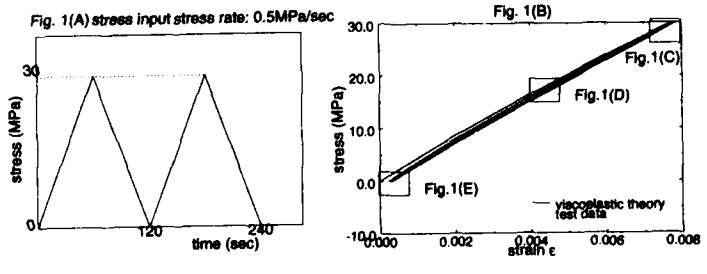

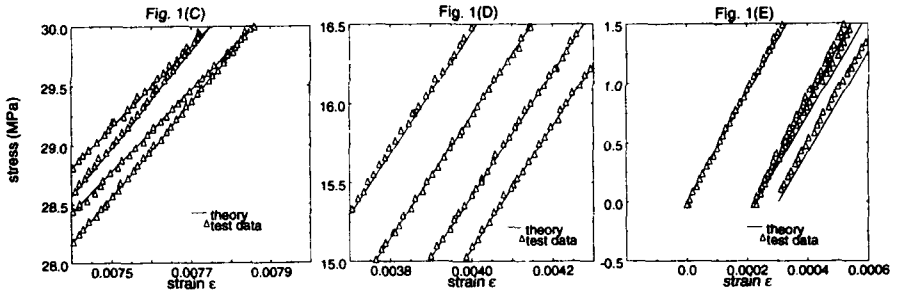

Figure 1. A two-cycle uniaxial stress-input test shows a satisfactory coincidence between the experiment and the theory: (A) stress input; (B)~(E) strain output

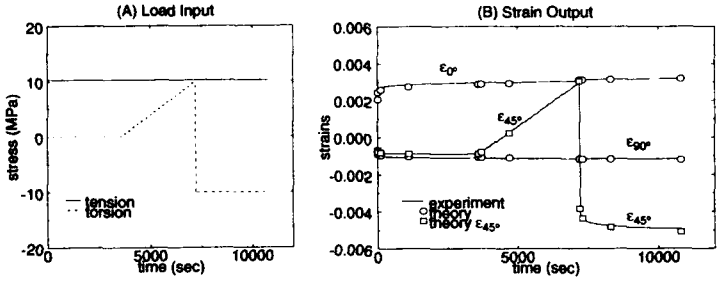

Figure 2. Biaxial creep test, one of the results from various combinations of loading

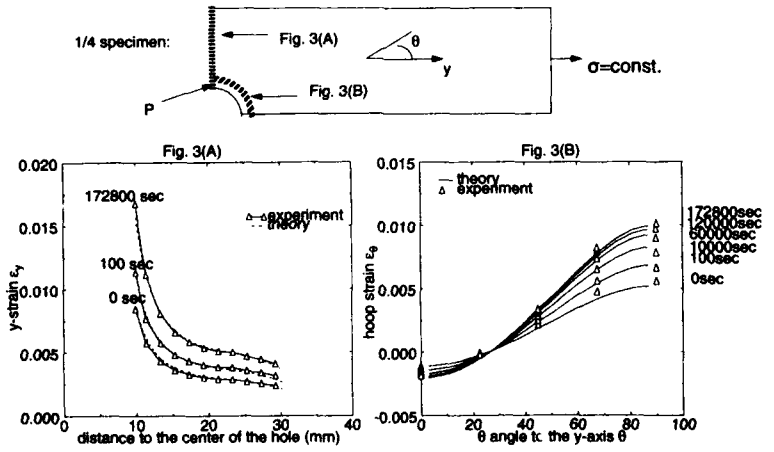

Figure 3. Short-term creep test with 2D stress distribution

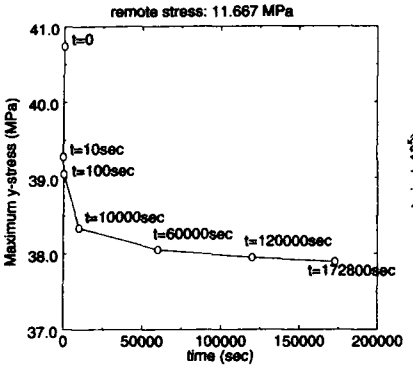

Figure 3(C) Stress redistribution, the stress concentration change at point P

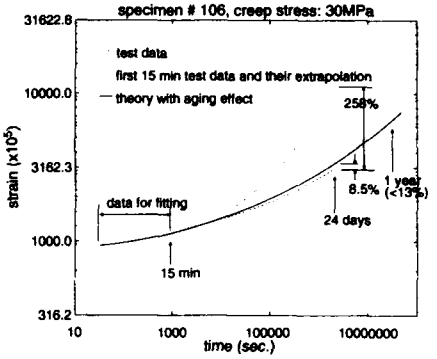

Figure 4. Physical aging influence in long-term creep deformation

4. Discussion

The model given here can describe 3D nonlinear time-dependent behaviour and physical aging affected long-term creep successfully. The experimental results also revealed that the chemical aging (additional cross-linking) gives no influence in the shifting rule of physical aging, but does change the creep rule by modifying the exponent of the exponential law in Equation (2) (Zhang 1993b[5]). The instantaneous Poisson's ratio of our material (DSM Synolite 593-A-2) is 0.353. While the experimentally measured creep Poisson's ratio however is 0.417 and slightly depends on the creep stress level. The tests were carried out under a moderate nonlinear stress range which was about half of the maximum tensile stress. Under this stress level, the theory performs extremely well. For most cases, the error is smaller than 3% in cyclic loading calculations. The accuracy is also satisfactory in the biaxial loading situation, see e. g. Fig. 2. Other tests with combinations between shear-first and tension-next and vice versa have also shown an excellent agreement with the results of the theory.

5. References

1. Zhang, L. and L. J. Ernst, 1993, 'A Three Dimensional Model for Nonlinear Viscoelasticity', *Topics in Applied Mechanics*, eds. J. F. Dijksman and F. T. M. Nieuwstadt, Kluwer Academic Publisher 1993, pp. 253-260
2. Schapery, R. A., 1969, 'On the Characterization of Nonlinear Viscoelastic Materials', *Polymer Eng. & Sci.*, Vol. 9, No. 4, pp. 295-310
3. Zhang, L., 1993a, 'Poisson's Ratios in Viscoelasticity', Report LTM-999, Delft University of Technology, The Netherlands
4. Struik, L. C. E., 1978, *Physical Aging in Amorphous Polymers and other Materials*, Elsevier Science Publication, Amsterdam
5. Zhang, L., 1993b, 'Aging Phenomena of Polyester', Report LTM-996, Delft University of Technology, The Netherlands
6. Zhang, L., 1993c, 'Implementation of Nonlinear Viscoelasticity in DIANA', Report LTM-1006, Delft University of Technology, The Netherlands
7. Zhang, L., 1993d, 'An Application of a Simplified Nonlinear Viscoelastic Model', Report LTM-1001, Delft University of Technology, The Netherlands

LENGTH CHANGES IN GLASSY POLYMERS UNDER LARGE STRAIN INELASTIC FREE-END TORSION

Wu Pei-Dong and Erik van der Giessen

Laboratory for Engineering Mechanics, Delft University of Technology, The Netherlands.

Amorphous glassy polymers become progressively anisotropic during large inelastic deformations. Large strain elastic-viscoplastic torsion of cylindrical tubes of glassy polymers is investigated numerically under free-end conditions. The influence of the wall thickness on length changes in twisted polymeric tubes is emphasized.

INTRODUCTION

A torsion test seems to be ideally suited for the experimental determination of material parameters in the range of large strains, whether elastic or inelastic. The major advantage for this purpose over tensile tests is that deformations during torsion remain homogeneous in axial direction until fracture, without showing strain localization in necks etc. In addition, the torsion test is attractive because it may reveal aspects of the deformation-induced anisotropy of the material under consideration.

Amorphous polymers below their glass transition temperature and beyond yield are observed to become progressively anisotropic with continued plastic deformation. Although the physical origins are completely different, metals also exhibit anisotropic hardening during plastic deformations. As a result of such induced anisotropy, at room temperature, specimens of most (initially isotropic) metals tend to elongate during torsion when the specimen's ends are axially free, as observed first by Swift (1). The magnitude of the elongation varies between metals but is typically of the order of 10% for a shear strain of 3. Swift (1) also noted that tests done using tubes showed as much as 50% more extension compared to similar tests on solid bars [see also Ref. (2)]. In the metals plasticity community it is now well-known that the prediction of this axial elongation depends strongly on the constitutive modelling. In the case of plastically deforming amorphous polymers, where these issues have not yet been firmly established, this pertains in particular to the description of anisotropic hardening or orientation hardening. Thus, the torsion test seems to provide a simple yet effective measuring technique for assessing the adequacy of constitutive models for amorphous glassy polymers.

Very recently, Wu and Van der Giessen (3) developed a numerical method, which is capable of simulating large strain torsion of tubes with any wall thickness, based on a recent elastic-viscoplastic constitutive model for amorphous polymers [Refs. (5), (7)]. Here, we apply this technique to investigate length changes in twisted tubes of a typical amorphous polymer such as PC under free-end torsion. In particular we focus on the influence of the tube thickness on the length changes.

CONSTITUTIVE MODEL

It is assumed that a glassy polymer must overcome two physically distinct sources of resistance before large strain inelastic flow may occur. Below the glass transition temperature, prior to initial yield, the material must be stressed to exceed its intermolecular resistance to segment rotation. Once inelastic flow occurs, molecular alignment takes place with ongoing inelastic deformations, resulting

in an anisotropic internal resistance. Argon (4) developed the following expression for the plastic shear strain rate $\dot{\gamma}^p$, which ensues once chain segment rotation becomes possible:

$$\dot{\gamma}^p = \dot{\gamma}_0 \exp\left[-\frac{As_0}{T}\left(1-\left(\frac{\tau}{s_0}\right)^{5/6}\right)\right], \tag{1}$$

as a function of the applied shear stress τ. Boyce *et al.* (5) extended this expression to include the effect of pressure and strain softening. They used $s + \beta p$ instead of the athermal shear strength s_0, where p is the pressure and β is a pressure dependence coefficient. Further, s is assumed to evolve with plastic straining via $\dot{s} = h\,(1 - s/s_{ss})\,\dot{\gamma}^p$, where h is the rate of resistance drop with respect to the plastic strain and s_{ss} is the assumed saturation value of s.

Once the material is stressed to the point of overcoming intermolecular barriers to chain motion, the molecular chains will tend to align along the direction of principal plastic stretch. This action decreases the configurational entropy of the system which, in turn, is responsible for the internal resistance to continued flow. This process of network distortion is very similar to that of a rubber network. To describe this so-called entropic hardening, Boyce *et al.* (5) introduced a back stress tensor **B** which is taken to be coaxial with the plastic stretch tensor, while its principal values B_i ($i = 1, \ldots 3$) are taken to be related to the plastic stretches λ_i^p according to a non-Gaussian network model for rubber elasticity. Originally, they adopted the classical so-called three-chain model. However, Arruda and Boyce (6) found that this model was not capable of picking up the strain hardening observed experimentally in PC and PMMA, and they proposed a so-called eight-chain model. Very recently, Wu and Van der Giessen (7) developed a so-called full network model in which full account is taken of the 3-D orientation distribution of the individual chains in the network. According to that model, the principal back stress components are given by the following integral

$$B_i = \frac{1}{4\pi} C^R \sqrt{N} \int_0^{\pi} \int_0^{2\pi} \mathcal{L}^{-1}\left(\frac{\lambda^p}{\sqrt{N}}\right) \frac{\lambda_i^{p\,2} m_i^{0\,2} - \lambda^{p\,2}/3}{\lambda^p} \sin\theta_0 \, d\theta_0 \, d\varphi_0; \tag{2}$$

$$\lambda^{p\,2} = \sum_{j=1}^{3} \lambda_j^{p\,2} m_j^{0\,2}; \quad m_1^0 = \sin\theta_0 \cos\varphi_0, \quad m_2^0 = \sin\theta_0 \sin\varphi_0, \quad m_3^0 = \cos\theta_0,$$

where $\mathcal{L}$ is the Langevin function, $\mathcal{L}(x) = \coth x - 1/x$, N is the number of links per chain and C^R is the rubber modulus. For detailed discussion of these network models we refer to Refs. (5), (6), (7).

PROBLEM FORMULATION AND RESULTS

We consider a homogeneous, circular tube with an initial outer radius R_{o0}, inner radius R_{i0} and initial length L_0 which is subjected to a twist Φ produced by an applied torque M. The lateral surfaces of the bar are stress-free and all properties are assumed to be axisymmetric and homogeneous along the axial direction. Although anisotropy will be induced during the deformation process, the behaviour remains axisymmetric and the bar remains circular cylindrical with a current outer radius R_o, inner radius R_i and current length L. The end faces of the bar are constrained to the extent that they remain plane and perpendicular to the axial direction, so that we may assume that any cross-section of the bar remains plane. In the free-end condition, the end faces are fully stress-free, but allowing for the development of an axial displacement U uniform over the end face. A numerical approach is adopted to solve the governing equations using a special purpose finite elements (3). In the formula-

tion of the finite element equations, full geometrical nonlinearity is taken into account.

The torsion problem described above involves a number of nondimensional groups, and therefore we introduce the following quantities:

$$\Gamma = \Phi \frac{R_{o0}}{L_0}, \bar{\tau} = \frac{3M}{2\pi R_{o0}^3 (1-\alpha^3) s_0}, e = \frac{L}{L_0}. \tag{3}$$

These quantities can be used to efficiently present the overall response of the specimen irrespective of its exact geometry. Calculations have been carried out for tubes which initially have a outer radius R_{o0} = 3.175 mm, a length L_0 = 6.35 mm (i.e. R_{o0}/L_0 = 0.5) and various inner radii (α = 0, 0.25, 0.50, 0.75). In reference (3), a set of material parameters have been used to simulate the large strain fixed-end torsion of a circular cylindrical tube having the same length L_0 and outer radius R_{o0} with α = 0.50 at room temperature (T = 294 K). It was found that the predicted torque response was in good agreement with the experimental results for PC found in reference (8). We proceed by employing the same parameters, bearing in mind that the major purpose of this paper is to examine in some detail the influence of the wall thickness on length changes in twisted tubes under free-end torsion. All numerical calculations were carried out at a constant twist rate $\dot{\Phi} = 0.02 \text{rad s}^{-1}$ corresponding to a shear rate at the outer surface of the bar of 0.01s^{-1}.

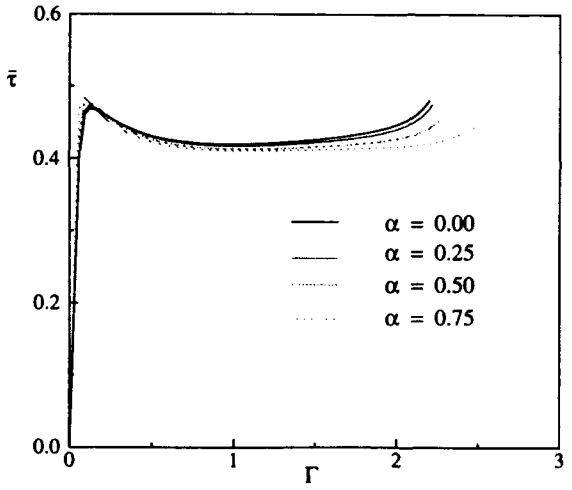

$\dot{\gamma}_0 = 2 \times 10^{15} \text{s}^{-1}$
A = 240K/MPa
C^R = 3.7MPa
N = 6
h = 500MPa
β = 0.08
E = 2623MPa
ν = 0.3
s_0 = 111MPa
s_{ss}/s_0 = 0.92

Figure 1 Torque responses of tubes with different inner radii.

In Figure 1 the torque responses are plotted in terms of the nondimensional torque $\bar{\tau}$ and the shear strain Γ defined in (2). As has been demonstrated by Wu and Van der Giessen (3), the stress distributions in tube are quite nonuniform. Figure 2 shows the axial elongation development in tubes. The axial elongation is found to increase almost linearly up to $\Gamma \approx 1$ while growing increasingly fast for larger twists. Also shown in Figure 2 is that a significant difference in axial elongation between the tubes with different α. At $\Gamma \approx 2.2$, the elongation in a tube with α = 0.75 is as much as 50% more compared to that in a solid bar (α = 0).

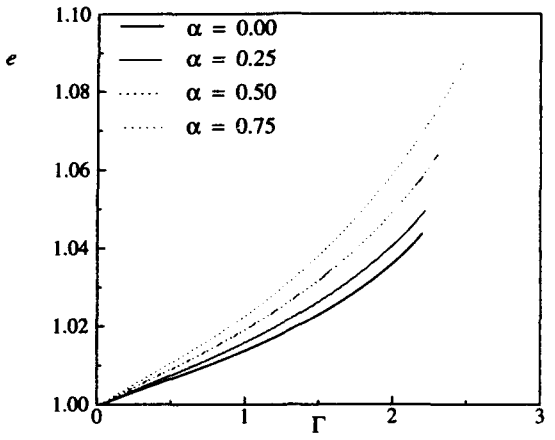

Figure 2 Influence of wall thickness on axial elongations.

SYMBOLS USED

B, B_i = back stress tensor and its principal components
U, e = axial displacement and axial extension
L_0, L = initial and current length of the specimen
M, $\bar{\tau}$ = applied torque and normalized torque
p = hydrostatic pressure
R_{i0}, R_i = initial and current inner radius of the specimen
R_{o0}, R_o = initial and current outer radius of the specimen
s, τ = shear strength and effective shear stress
s_0, s_{ss}, h, $\dot{\gamma}_0$, β, C^R, N, A, E, ν = material parameters
T = absolute temperature
α = the ratio of inner radius to outer radius of the specimen in initial configuration
Φ, Γ = torsion angle and shear strain at outer surface of the specimen
$\dot{\gamma}^p$ = plastic shear strain rate
λ_i^p = principal plastic stretches
m_i^0; θ_0, φ_0 = unit vector components and coordinates in orientation space

REFERENCES

1 Swift H M Engng 4 (1947) 253
2 Billington E W J Phys D: Appl Phys 10 (1977) 533
3 Wu P D and Van der Giessen E Int J Mech Sci 35 (1993) 935
4 Argon A S Phil Mag 28 (1973) 839
5 Boyce M C, Parks D M and Argon A S Mech Mater 7 (1988) 15
6 Arruda E M and Boyce M C J Mech Phys Solids 41 (1993) 389
7 Wu P D and Van der Giessen E J Mech Phys Solids 41 (1993) 427
8 Wu W and Turner A P L J Polym Sci.: Polym Phys Edition 11 (1973) 2199

TOUGHENING OF PMMA BY ABSORPTION AND DESORPTION OF AN ACETONITRILE AQUEOUS SOLUTION

M. Kawagoe*, M. Morita*, and S. Nunomoto**

The tension tests of PMMA were performed in air at room temperature using the sheet specimens which were previously soaked in a 40 % acetonitrile aqueous solution and then dried. For the specimen pre-soaked for 24h and dried for 480h, in which the penetrant of 5.5% remained, shear yielding clearly takes place at 42MPa without any crazes, and the fracture strain reaches about 148%. Such enhanced ductility may be related to higher peak of β-relaxation at room temperature in the treated specimen.

INTRODUCTION

Poly(methyl methacrylate) (PMMA), as well known, behaves as a brittle material under tension in usual environments, e.g. in air at room temperature. In order to enhance the toughness of PMMA various methods to mix or blend PMMA with rubber or ductile polymer like polycarbonate (PC) are extensively investigated.

In this paper we describe a quite different and more convenient way to obtain toughened PMMA by applying absorption and desorption phenomena of an acetonitrile aqueous solution.

EXPERIMENTAL

The material used is a commercially available PMMA sheet of 1 mm thickness (Mitsubishi Rayon Co., M_w=6.16 x 10^5 , M_w/M_n=4.60). The rectangular speciemens 82 mm long by 17 mm wide were prepared for the absorption and desorption tests. Their cut sides were polished with No.1000 abrasive paper. The dumbbell-shaped specimens with a gauge length of 40 mm and width of 17 mm were machined from the sheet. All the specimens were annealed at 90 °C for 2h and slowly cooled to room temperature in a forced-air oven.

* Department of Mechanical Systems Engineering, Faculty of Enginering, Toyama Prefectural University, Toyama, Japan
** Department of Industrial Chemistry, Toyama National College of Technology, Toyama, Japan

The rectangular specimens were immersed in a 40 % acetonitrile aqueous solution at 20°C for 72h and then dried in air at room temperature. The weight of specimen were measured at an appropriate time interval using an electronic balance.

The dumbbell-shaped specimens were also immersed in the solution at 20°C for 6h, 12h, and 24h, and dried in air at room temperature for 480h. They then were offered to the tension tests made in the same environment by use of an Instron-type testing machine (Schimazu Co., AGE-50KN). The nominal strain rate were 12.5 %/min.

The dynamic viscoelastic measurements were also conducted using the rectangular specimens which were treated by the same way as that for the tensile specimens. The storage modulus and loss tangent were meaured at 1Hz at a constant heating rate of 5.0°C/min by means of a dynamic viscoelastic testing machine (Oritentec Co., VFA-1KNA).

RESULTS AND DISCUSSION

The absorption and the desorption behaviours of the reagent are shown in Figures 1(a) and (b), respectively. The equilibrium solubility of about 32% was achieved for about 48h immersion. It is unclear wheather the type of diffusion is the usual Fickian or not (the case II), because of rough data points. The weight reduction during drying very rapidly takes place in contrast with the absorption process. It is noted that the weight reduction is no longer observed for drying time over 200h and the penetrant of about 5.5 % stably remains in the specimen.

Figure 2 shows the results of tension tests of the specimens which were pre-soaked in the reagent for different periods and then dried. For both the specimens pre-soaked for 6h and 12h, brittle farcture behaviour is commonly observed, although the slight plastic deformation may be seen for the 12h-treated specimen. In contrast with these specimens and the untreated one, which was fractured at the stress of 84MPa and the strain of 9%, shear yielding clearly takes place at 42MPa and the fracture strain is achieved to about 148% for the specimen which was pre-soaked for 24h and dried. Observing the surface of this specimen could never find any crazes. Therefore this treatment may change PMMA to a completely ductile polymer without crazing mechanism.

The results of the dynamic viscoelastic measurements are indicated in Figure 3. Comparing with the untreated specimen reveales that the glass transition temperature was lowered to about 80°C (about 110°C for the untreated specimen), and the β-relaxation becomes much clearer to indicate a higher peak value at 20°C (a broad curve with a lower peak at 50°C for the untreated one). The β-relaxation, probably due to side chain mobility, is related to toughness and high impact resistance.

Thus it may be concluded that the clear β-relaxation at room temperature contribute to shear yielding and large plastic elongation of the 24h-treated specimen.

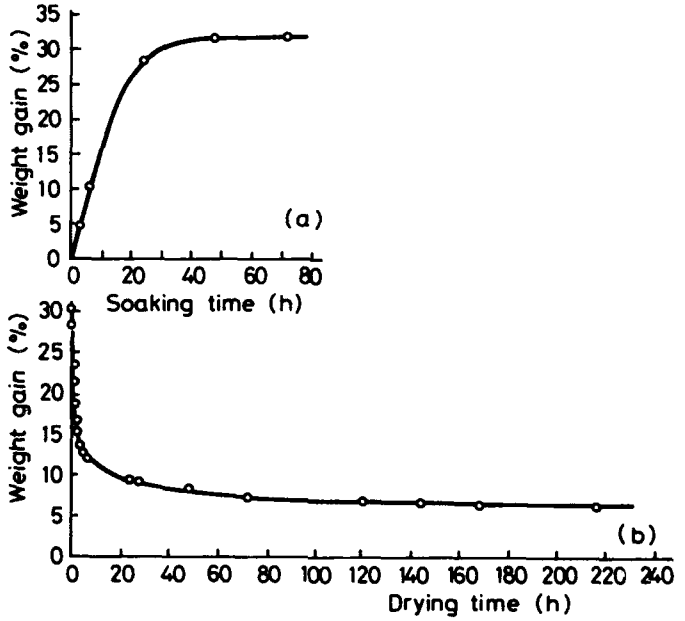

Figure 1 (a) Absorption of 40% CH_3CN aqueous solution by PMMA sheet 1mm thick at RT. (b) Desorption curve in air at RT.

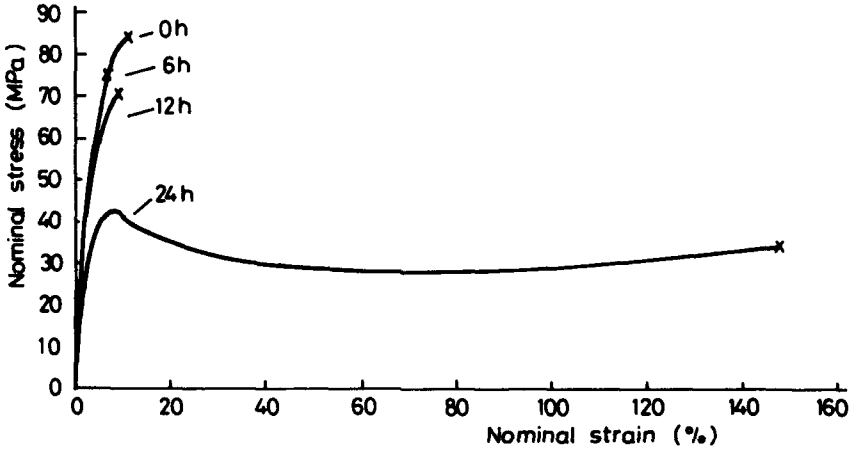

Figure 2 Tensile stress-strain curves for the specimens soaked in 40% CH_3CN solution for different periods and then dried.

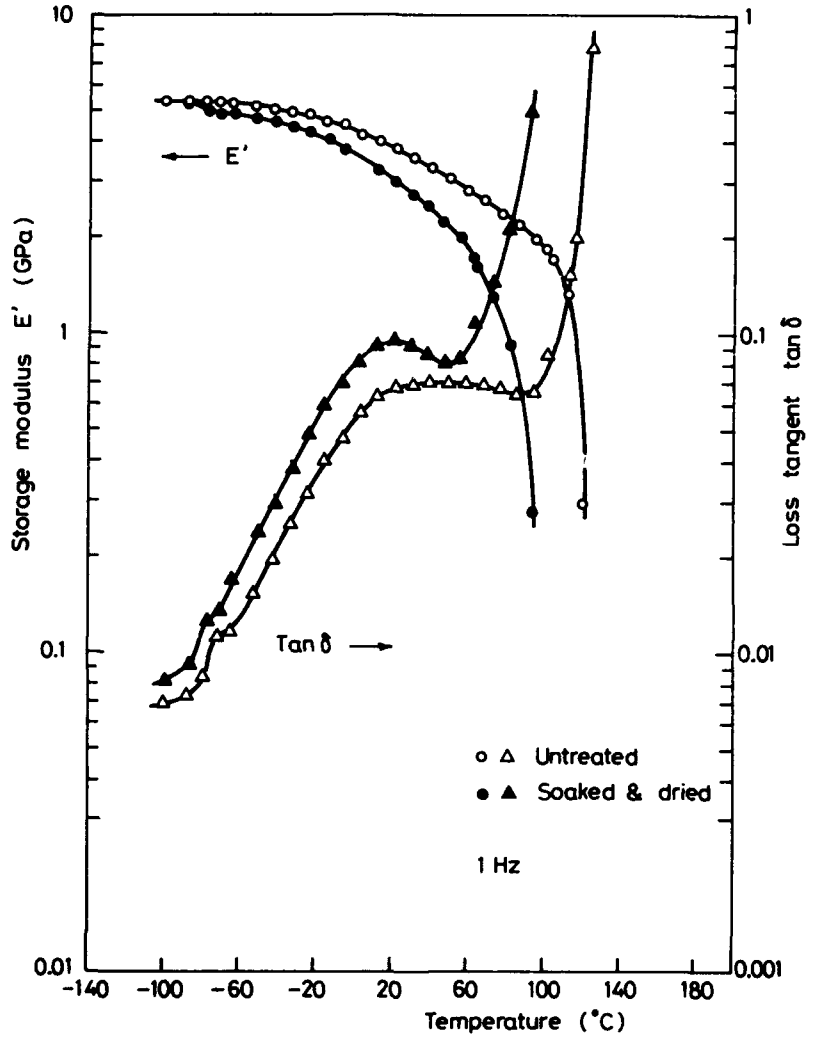

Figure 3 The dynamic viscoelastic properties of the untreated and the treated specimens

Fatigue Crack Growth of Solid Polymers under High Pressures

Masayoshi KITAGAWA and Takashi YOSHIOKA

In order to investigate the effect of hydrostatic pressure on the fatigue crack growth behaviour of solid polymers. An apparatus was designed for maximum pressure 3000kgf/cm^2. It was shown that (1) the fatigue crack growth rate at pressures higher than 500kgf/cm^2 were newrly insensitive hydrostatic pressure, (2) the slope on a log(dc/dN) vs Δ K diagram was higher at the high pressures than at 1kgf/cm^2 and (3) the shear lips and the tear lines was rarely observed at the high pressures.

1. INTRODUCTION

Hydrostatic pressure is one of the important factores influencing the mechanical properties of solid polymers. Therefore, the pressure dependent behaviour of solid polymers such as elastic modulous, yield stress, fracture stress etc. has been widely studied by many reseachers since the pioneering work of Rabinowitz ,Ward and Parry. But less attension has been paid to the fatigue crack growth behaviour. Fatigue crack growth data under high pressures have not been measured up to date. This is probably due to a reason that it is difficult tc produce a testing machine which can apply cyclic loading to a test specimen keeping a high pressure nearly constant during the test. In this paper, fatigue crack growth behaviour of polycarbonate(PC),poly(methylmethacrylate)(PMMA)and polyvinylchrolide(PVC) was investigated using a newly deviced high-pressure apparatus.

2. TESTING APPARATUS

A home-made high-pressure torsion apparatus used here is schematically illustrated in Fig. 1. The pressure vessel ⑫ is designed for a pressure of 3000 kgf/cm^2. A compact tension specimen ② held between the grips ③ is subjected to cyclic tensile load. The rotary motion of the axis ⑧ driven by

Department of Mechanical Systems Engineering, KANAZAWA UNIVERSITY,
2-40-20, Kodatsuno, Kanazawa, JAPAN

the servo-motor is converted to the longitudinal displacement by means of the screw ④. The cyclic load is measured through a load cell ① in the chamber. The load is controlled between the predetermined maximum and the minimum(= 0) loads by a micro-computer. The parts ⑤ -A and ⑤ -B are supported by two rigid side-plates. These plates prevent the roatation of the grips ③. The shaft ⑧ is suported by two miniature ball bearings put in the block ⑤ -B . A needle bearing ⑥ and a ball bearing ⑦, which are placed in the cover ⑪ to relieve the affect of the eccentricity of the shaft ⑧, make smooth the revolution of the shaft ⑧. The cover ⑪ is designed so that the shaft ⑧ may be easily inserted into the cover ⑪ after the specimen is set at the grips. Since the rotary shaft ⑧ and the axis ⑨ do not move in the longitudinal direction when the specimen is pulled, the applied pressure is nearly kept constant during the test. The leakage of a pressure memedium (turbine oil) is stopped by 4 O-rings and back-up rings ⑩. Therefore, fatigue crack growth test is performed under a constant hydrostatic pressure without its considerable fluctuation. The pressure medium is turbin oil.

3. EXPERIMENTAL

The materials used was commercial PC, PMMA and PVC plates with thickness 3mm. Compact tension(CT) specimens 30mm x 28mm were machined from these plates. After the notch was machined by a fret saw, the natural crack at the notch root was introduced by a home-made machine at a cyclic frequency of about 5Hz at an applied load less than that for the fatigue test mentioned below. The crack growth rates was less than $1x10^{-4}$mm/cycle.

The cyclic tests were conducted at a triangular wave form between zero and a predetermined maximum load. Since the angular velocity of the shaft ⑥ is kept constant, the cyclic frequency decreases with increasing crack length. The test frequency is within the range 0.5 to 0.2 Hz. The tests were executed at room temperature (25 ° C) under predetermined pressures of 1, 500, 1000, 1500 and 1900kgf/cm^2. In order to investigate the effect of environmental fluid on the crack growth, tests were also conducted both in air and in turbine oil at an atmospheric pressure using large CT spevcimens 100mmx96mm.

Since the fatigue striations of PC and PMMA were known to form each load repetition in the stress intensity factor ranges ΔK tested here, the crack growth rates (dc/dN) were measured from their spacings on the fractographs taken from the broken specimen surfaces.

4. RESULTS and DISCUSSIONS

4.1 dc/dN vs. ΔK

The pressure medium may affect the crack tip for two reasons that (1) the environmental agent used may chemically attack the polymer and

accelerate crazing near the crack tip and (2) the viscos liquid penetrated into the narrow crack planes may hydrodynamically alter the pressure distribution along the crack planes due to their opening and closing motion and hence, may change the stress intensity factor. For PC, the effect of the environmental fluid on the crack growth rate was found to be very small at an atmospheric pressure.

The pressure dependence of the fatigue crack growth rate in the pressure ranges up to 2000 kgf/cm^2 is shown in Fig. 2, where the band denotes the range of the dispersion of the growth rate data at 1kgf/cm^2. Although the data are considerably dispersed from specimen to specimen they may nearly fall within a band width and constitute linear lines parallel to each other, the slopes of which are steeper than those at 1kgf/cm^2. It is found that the crack growth rates at pressures higher than 500kgf/cm^2 are nearly insensitive to hydrostatic pressure.

4.2 Fracture surfaces

When a crack in a relatively thin plate of polycarbonate(PC) propagates in an atmospheric pressure, shear lips may form at the free surfaces. The crack plane is inclined at about 45° to the loading axis as schematically shown in Fig. 3a. But the shear lips were not observed on the faracture surfaces even at a relatively low pressure of 500 kgf/cm^2 and the fracture surfaces tested at pressures higher than 500kgf/cm^2 were flat as shown in Fig. 3b. Since an increase in the yield stress by applying hydrostatic pressure may depree the formation of shear yielding in PC and the crack advances in a plane strain state, the crack planes may become flat.

There exist many fatigue striations which correspond to the successive positions of the advancing crack front as a result of individual load repetitions. Besides the striations, in an atmospheric pressure, the surface is covered with many tear lines along the crack growth direction. On the other hand, on the surfaces tested at the high pressures, the tear lines abruptly dissapeared ahead of the initial crack introduced in air. In spite of the presence of the tear lines, the shape of the striation seems to be not so affected by hydrostatic pressure.

The authors wish to thank Mr. Kitayama and Mr. Takagi for their technical assistance.

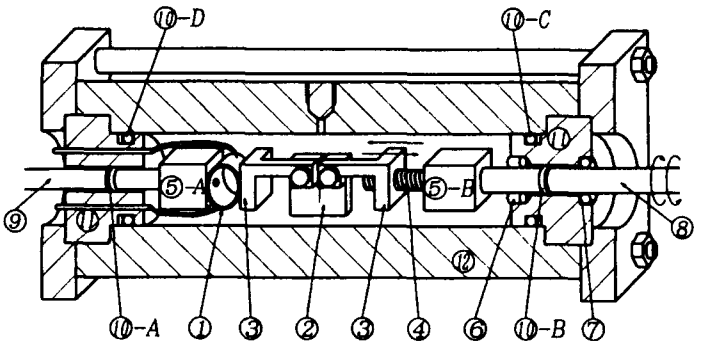

Fig. 1 Schematic illustration of fatigue machine under high pressure.

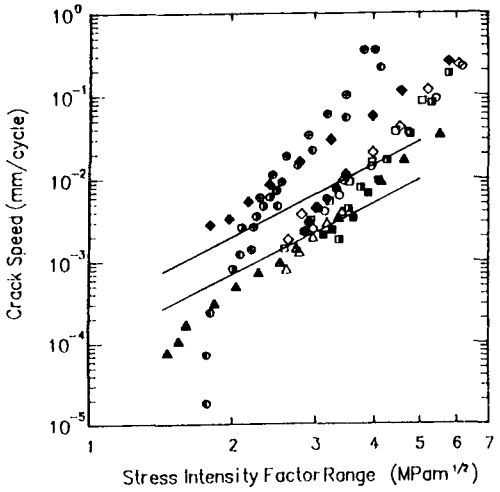

Fig. 2 Fatigue crack growth rates as a function of stress intensity factor ranges under □ □ ■ ; 500 kgf/mm², △ △ ▲ ; 1000 kgf/mm² ○ ○ ○ ○ ● ; 1500 kgf/mm² and ◇ ◆ ; 1900 kgf/mm².

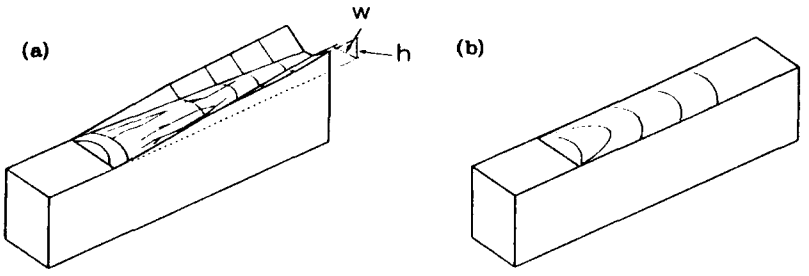

Fig. 3 Schematic illustration of fracture surfaces under (a) 1kgf/mm² and (b) high pressure.

Structure and Strength of Spider Silk

Masayoshi KITAGAWA and Hiroshi SASAGAWA

Since the spider silk is used to attack and capture insects, its strength may be expected to be higher than that of the cocoon silk. In this paper, the structure and mechanical properties of the drag lines, one of the silks produced by different glands located on the abdomen of spider, were investigated. It was shown that the spider silk has the high strength comparable with that of an aramid fibre Kevlar.

1. Introduction

The silks produced by the silkworms are not the only ones made in nature. They are produced by a wide variety of insects. But much attension has not been paid to the structure and the strength of their silks compared with those of the cocoon silks. Since the spider silk is used to attack and capture insects, its strength may be expected to be higher than that of the cocoon silk. But early attempts to determine their strengths have not been made successfully.

Most spiders produce at least 6 different silks by different silk glands located on their abdomen to use them in order to make the webs, catch and wrap the preys, protect a cluster of eggs and so on. The drag line among them is produced by the major ampullate glands to constitutes the frame and radial lines of the orb web. In this report, the mechanical properties of the drag lines produced by Nephila Clavata spider (called "Jorougumo" in Japan) which inhabits all over Japan are summarized.

2. Experimental

The spiders were collected at a small park in the suburbs of Kanazwa city (Japan) and were breeded in a small chamber (2mx1mx1m) made by our laboratory. After some samples were taken from them, they were set free at the park where they lived before.

Department of Mechanical Systems Engineering, KANAZAWA UNIVERSITY,
2-40-20, Kodatsuno, Kanazawa, JAPAN

2.1 Observation of drag line

A number of drag lines taken directly from spiders were glued on a paper with a single edge notch at its center. The paper was quickly separated by a pair of tweezers in a chamber filled with liquid nitrogen. Some drag lines fractured in a brittle manner. They were coated with gold to investigate the shape of their cross sections through a scanning electron microscope (SEM).

In order to examine the structure of the drag lines, they were treated with ion etching. Ion etcing was carried out at an electric power of 25 w and a gas pressure of $2x10^{-5}$ Torr during 3 and 20 minites. Argon gas was used as an etching gas. Their surfaces were observed by SEM.

2.2 Mechanical properties

When a spider hold by one hand was swung lightly, she lowers herself producing a pair of continuous drag lines. The drag line produced in this way pushed carefully against a framed thin paper coated with a binding agent at its both ends. About 10 to 20 specimens for every spider were obtained. A considerable portion of these samples were rejected due to their irregularity. These samples were taken from spiders collected at different dates. The specimens were put in a decicator for about one month up to the date of the experiment.

The dynamic properties of the temprature dependence and the frequency dependence of dynamic storage modulus E' and dynamic loss tangent tan δ were measured by a viscoelastic testing instrument Reovibron(Orienteck Co. Japan). Samples were heated at 5 ° C/min in air under relaxed conditions. The properties were measured at a constant frequency of 1 Hz.

Tensile tests were performed in a strain rate of 10^{-3}/sec at room temperature(20 ± 2 ° C) by a home-made testing machine with a load cell of 10gf. The test data were recorded on a microcomputer. After a specimen was set between the grips and the paper frames parallel to the specimen fibre were cut off and then the tensile test started.

3. Results and discussions

The observation on the drag lines and their fracture surfaces broken in liquid nitrogen showed that (1) the skin surface of the drag line is featureless with no distinctive markings, (2) the structure of the skin layer is not so different from that of the interior and (3) the cross section is round. These observations indicate that the structure of the drag line is distingushed from that of cocoon silk consisting of two protein layers of fibroin and sericin and the cross sectional area is calculated exactly by measuring the diameter.

Fig.1 denotes the SEM photographs of the ion etched surfaces of the drag lines at a time of ion etching 3 and 20 minites. Many protrusions like a match head with a dimension of about 20-50 nm, which become deep with an increase in time of etching, lie in a row along its long axis. It is supposed from this etching mode that the spider drag line consists of the crystalline and amorphous regions as schematically illustrated in Fig. 2.

The dynamic mechanical properties of E' and tan δ for the samples taken at July and October are plotted as a function of temperature in Fig. 3 where the values of E' are normalized by the reference value at room temperature. The values of tan δ considerably scatters due to the irregularities of the samples forming when they were picked from spiders. It is shown that the glass transition temperature is higher for the samples taken at October than for those at July. This may be caused by the difference in the degree of crystallinity between the drag line fibres at July and at September.

Fig. 4 denotes the load(P)-strain(ε) curves of the drag line fibres for spiders with various lengths (or collected at different dates). In Fig. 5, they are rewritten into the stress(σ)-strain(ε) curves. Their curves are considerably scatters spider to spider probably due to the irregularity of the samples made and are not always linear even in the region at small strain. They may be caused by a somewhat lack of carefulness for the specimen preparation, but not by yielding. It is shown that (1) the rigidity of the bibre is higher for a spider of September than for one at July probably due to the difference of degree of crystallinity, (2) the fracture strain ε_T is about 0.3, which is fairy large compared with that of cocoon silk, (3)the fracture load P_T(perhaps corresponding to the ability for catching prey) increases with an increase in the spider length and (4) the fracture stress σ_T of about 150-200MPa is comparable with the strength of aramid fibre.

The spider silks have many interesting features. When immersed in acid liquid, the surface layer of the fibre is etched chemically, swells and its rigidity decreases considerably. This characteristics may be available for the environmental assessment on acid rain, exhaust gas by car, etc..

The authours wish to thank Dr. Kinari (Kanazawa Univ.) for his technical assistance and Dr. Ohsaki(Japan paper making Co.), Dr. Yoshida (Ritsumeikan Univ.) and Mr. Tokumoto (Kanazawa City) for their available discussions of chemical and ecological aspects of spiders.

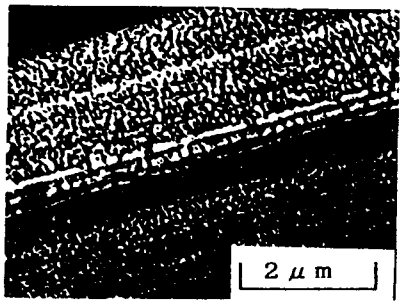

Fig. 1 SEM observation of ion etched drag lines.

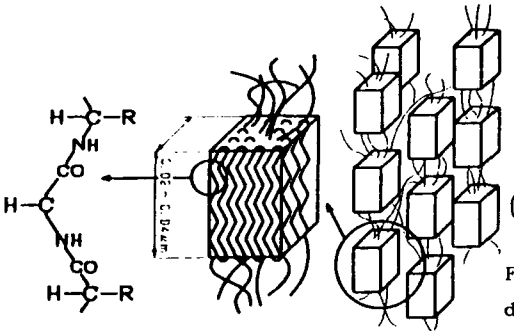

Fig. 2 Schematic illustration of structure of drag line

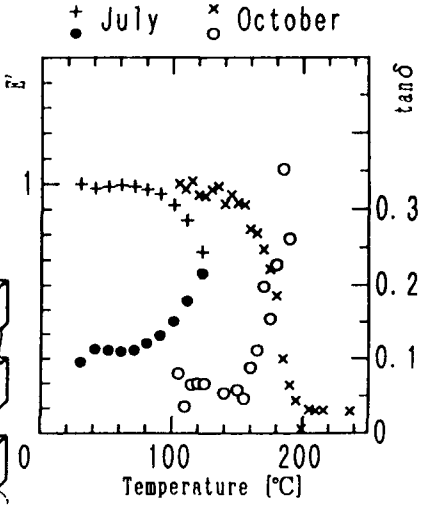

Fig. 3 Dynamic properties of drag lines.

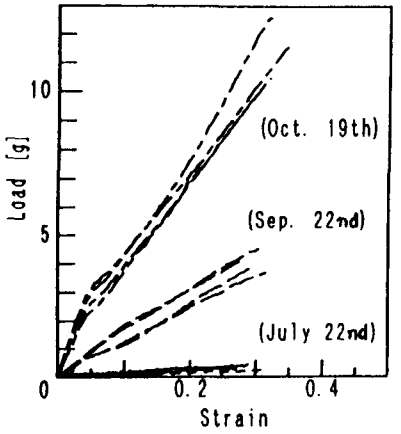

Fig. 4 Load-strain curves of drag lines collected at different dates.

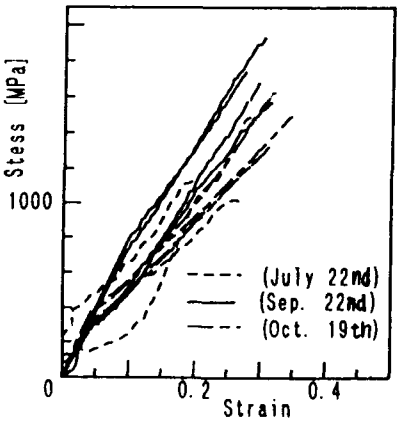

Fig. 5 Stress-strain curves of drag lines.

FRACTURE BEHAVIOURS OF POLYCARBONATE AND CELLULOSE-ACETATE EXPOSED UNDER HIGH HUMIDITY

Mitsuo NOTOMI*, Kikuo KISHIMOTO* and Takashi KOIZUMI*

Effects of high humidity and temperature exposure on the mechanical property of polycarbonate(PC) and cellulose acetate(CA) are investigated. The specimens are exposed under 85 ℃ 40% or 85 ℃ 85% for 8 days. Tension and fracture toughness tests are carried out at room temperature using dumbbell-shaped and single edge notched bend (SENB) specimens respectively. Since the crack propagation occurs in a stable manner, the crack resistance curves are measured by means of the multiple specimen method and the fracture toughness is determined. The results are summarized as the tensile strength failure strain diagram and the fracture toughness crack extension resistance diagram. The differences in fracture behaviours of two materials are clearly characterized by these two diagrams.

INTRODUCTION

Variations of tensile strength, bending strength, density and/or oxygen absorbed are usually measured to assess the degradation of polymers due to environmental agents, such as organic solvent, high humidity and ultraviolet light. Evaluation of the fracture toughness becomes important with increase in the use of polymers as structural materials, and several studies have been published on the degradation of polymers concerned about fracture toughness [1, 2, 3]. In this study, effects of high humidity and temperature exposure on mechanical properties are investigated by using two kinds of thermoplastic polymers, that is polycarbonate (PC) and cellulose-acetate (CA). The experimental results are plotted on the tensile strength failure strain diagram and the fracture toughness crack extension resistance diagram to represent the effects of environment. The differences in the change of fracture resistance of PC and CA are discussed by using the analytical results for the crack propagation in the elastic perfectly plastic body [4].

EXPERIMENTAL

Specimens

Polycarbonate used in this study is an amorphous thermoplastic processed from bisphenol A and has the number average molecular weight $M_w = 28,500$ and the glass transition temperature $T_g = 150$ ℃. Cellulose-acetate used is an induced cellulose produced by a natural cellulose treated with acetic anhydride and contains diethyl phthalate as a plasticizer. The two types of specimen are machined as shown in Figure 1. The first specimen is a normal tensile dumbbell type for the determination of stress and strain relation, and the second the single-edge-notched bend (SENB) type with 0.1mm width notch for fracture toughness test.

Experimental Procedures

The specimens are exposed in a chamber at 85 ℃ 85% or 85 ℃ 40% for 8 days. After exposure, the specimens are cooled down in air for several hours to the room temperature (22 ℃) and the tensile tests are carried out with a crosshead speed of 2.4 mm/min. Fracture tests

*Department of Mechanical and Intelligent Systems Engineering, Tokyo Institute of Technology

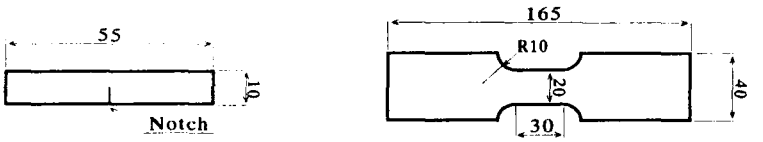

Figure 1 Dimension of specimens (right : tensile specimen, left : SENB specimen).

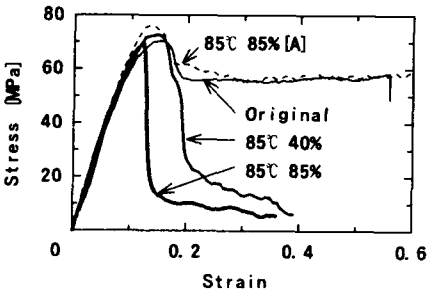

Figure 2 Stress-strain curves of PC

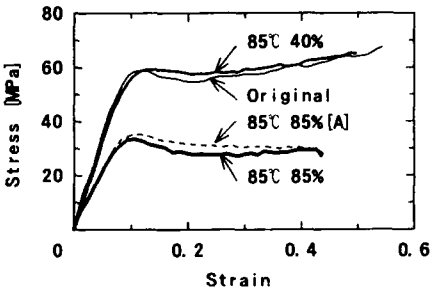

Figure 3 Stress-strain curves of CA

are also conducted using the SENB specimens with a span of 40 mm. A precrack is introduced after exposure by the tapping method [5]. Since the crack propagation occurs in a stable manner, the multiple specimen method [6] is applied to obtain the fracture toughness. After mechanical tests the fracture surfaces of the specimens are observed by a video-microscope.

RESULTS

Stress-strain relation

Typical stress strain curves of PC specimens are shown in Figure 2 in which the results of the specimen as received without exposure is also presented and denoted by "original". A almost constant region of the stress of the original specimen corresponds to the neck propagation. The specimen exposed at 85 ℃ 40% breaks just after the initiation of neck propagation while the specimen exposed at 85 ℃ 85% fails at the maximum stress. According to the observation of the broken specimens by the video-microscope, the failures of exposed specimens originate from the flaws at the side corner of the specimens. These flaws were considered to be produced at the time of milling and grown during the exposure. To confirm this speculation, some specimens were machined after the exposure. The result are also shown in Figure 2 and are denoted by 85 ℃ 85% [A]. The stress strain relationship of such specimen is restored to that of original one. Thus, we may conclude that the decrease of failure strain is caused by the growth of the flaws at the surface.

Figure 3 shows the stress-strain curves of CA specimens. As contrast to PC specimens, the stress gradually increases with the strain during neck propagation. Although the stress strain relation of the specimens exposed at 85 ℃ 40% is almost same as that of original ones, that of 85 ℃ 85% specimens is quite different -- less elastic modulus and tensile strength. The stress strain relation of the specimens machined after exposure is denoted by 85 ℃ 85% [A] and is similar to that machined before exposure for this case. The change of the material properties due to the exposure is more significant for CA than for PC.

Fracture toughness

Figure 4 shows the variation of the K_I against Δa for PC specimens. The lines in this figure are obtained by means of a least-squares fit. It is found that the slop of these lines dK/da increases and the value of the stress intensity factor at fracture initiation K_{in} decreases with an increase in the humidity of the exposure conditions. It was found from fractographic

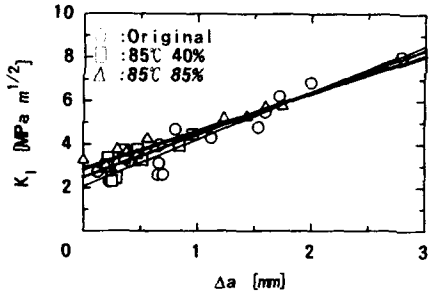

Figure 4 Variations of the K_I of PC specimens against Δa.

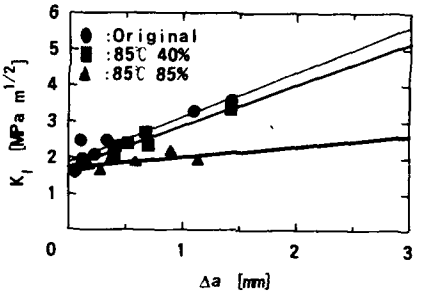

Figure 5 Variations of the K_I of CA specimens against Δa.

observation that the microvoids growth underneath the fracture surface was more extensive for 85 ℃ 85% exposure than for original. This would cause the increase in dK/da for exposed specimens.

Figure 5 shows the variation of the K_I of CA specimens against Δa. Although K_{in} and dK/da for the specimens of 85 ℃ 40% exposure is little different from those of original ones. dK/da for those of 85 ℃ 85% exposure drastically decreases than for the others.

DISCUSSION

Failure strain ϵ_f and tensile strength σ_B

The results of the tensile properties obtained by the experiments are summarized on the tensile strength (σ_B) and failure strain (ϵ_f) diagram as shown in Figure 6. The arrows in this figure denote that the failure of the specimen did not achieved due to the limitation of stroke length of the testing machine. By this diagram, differences of the exposure effects on each material can be seen distinctly. The tensile strength σ_B of PC is almost constant irrespective of the exposure conditions. The failure strain ϵ_f of the exposed specimens is as same as or slightly lager than that of original ones, if the surface flaws induced by the exposure are removed (compare the results denoted by × with those by △).

On the other hand, tensile strength σ_B of CA decreases when the specimens are exposed under high temperature and humidity. The failure strain ϵ_f for 85 ℃ 85% exposure is recovered by removing the surface flaws, and is almost the same as for original and 85 ℃ 40% exposure.

Fracture toughness K_{IC} and crack extension resistance dK/da

Figure 7 shows the diagram of K_{in} and dK/da. It is seen from the figure that the exposure of high humidity causes the enlargement of K_{in} and the reduction of dK/da for PC while the reduction of dK/da for CA without significant change in K_{in}. A slight increase in K_{in} for PC would be attributable to the increase of ϵ_f in the specimens without the influence of surface flaws, since σ_B is almost unchanged. On the other hand, the negligible change of K_{in} in CA is not necessarily interpreted from the variations of ϵ_f since the elastic modulus are decreased. The reduction of K_{in} due to decrease in elastic modulus would be compensated by the decrease of yield stress since the materials with less yield stress σ_y generally have a higher fracture toughness [7].

Based on the analytical model of the stable crack extension in an elastic-perfectly plastic body, the variation of dK/da will be discussed. By assuming the stress field at the tip of a crack as the Prandtl field, the increment of J-integral against the crack extension length Δa has been obtained by [4]

$$\frac{dJ}{da} = \frac{\beta}{\alpha}\frac{\sigma_y^2}{E}\ln\left(\frac{\rho}{\epsilon R}\right) \tag{1}$$

where $R = \lambda EJ/\sigma_y^2$. α, ρ and λ are parameters for the shape of a crack tip and are constant

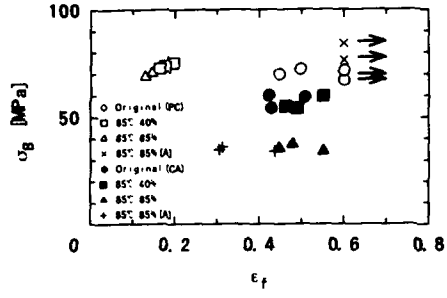

Figure 6 Failure strain and tensile strength diagram.

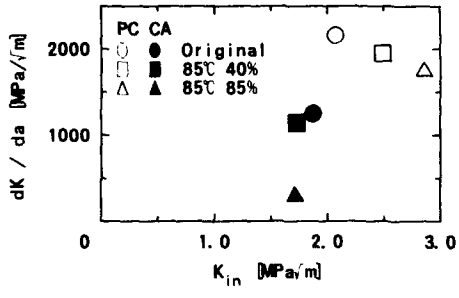

Figure 7 Fracture toughness and crack extension resistance diagram.

until the geometry of crack tip is invariable. β is a constant for a Poisson's ratio ν and ϵ is a logarithm to the base. Since the relation $J = (1-\nu)K^2/E$ holds for small scale yielding condition, Equation (1) reduces to

$$\left.\frac{dK}{da}\right|_{\Delta a=0} = \frac{\beta\sigma_y^2}{2\alpha(1-\nu^2)K_{in}} \ln\left(\frac{\rho\sigma_y^2}{\epsilon\lambda(1-\nu^2)K_{in}^2}\right) \tag{2}$$

for $\Delta a \simeq 0$. The above equation indicates that dK/da decreases with increase in K_{in}, which corresponds to the results of PC. Furthermore, equation (2) also indicates that dK/da decreases with decrease in σ_y as the results of CA.

CONCLUSIONS

The present paper presents experimental results of the effects of high humidity and temperature on mechanical properties of PC and CA. The following conclusions are drawn :
(1) Effects of exposure on mechanical properties of polymers can be represented by the tensile strength–failure strain diagram and the fracture toughness–crack extension resistance diagram.
(2) The surface flaws produced by milling the surface in preparing the test piece grow during exposure and affects the value of the failure strain. This influence can be removed by milling after exposure.
(3) The effects of the exposure on fracture toughness and crack extension resistance are different between PC and CA. This difference may be explained by the analytical results for the stable crack growth in the elastic–perfectly plastic body.

The authors wish to thank Daicel Chemical Industries, Ltd. for offering the CA; Teijin Kasei Co. Ltd. for offering the PC and K. Tonohara and M. Nakajima for their assistance with the experiments.

REFERENCES

[1] Laverty J J, Poly. Eng. and Sci. **28** 6 (1988) 360.
[2] Hill A J, Heater K J and Agrawal C M, Jour. of Poly. Sci. **28** 3 (1990) 387.
[3] Cheng T W, Keskkula H, Paul D R, Jour. of Appl. Poly. Sci. **45** 3 (1992) 531.
[4] Kanninen M F and Popelar C H, Advanced Fracture Mechanics, (1985) **378** Oxford Science Publications.
[5] ASTM D5046-91a *Standard Test Methods for Plane-Strain* Fracture Toughness and Strain Energy Release Rate of Plastic Materials, Annual Book of ASTM standards, ASTM Philadelphia (1991) 752.
[6] Huang D D and Williams J G, Jour of Mater Sci **22** (1987) 2503.
[7] Broek D, Elementary Engineering Fracture Mechanics, Martinus Nijhoff Publisshers (1986) 312.

FRACTURE MODELLING APPLIED TO POLYETHYLENE GAS PIPES

K.BOYTARD* , K.DANG VAN** , J.KICHENIN*** , J.LE COGUIC*

The polyethylene material presents a complex combination of typical behavial features (elasticity + viscosity + instantaneous plasticity). An original study has been undertaken based on the mutual inter-dependence between experimental testing and modelling to derive constitutive equations in direct connection with numerical schemes.
First, a simple model is suggested to describe satisfactorily the constitutive equations of the material. A local approach is then described to model the polyethylene fracture mechanism.

INTRODUCTION

The modelling of the behaviour and fracturing of materials was and still is widely based on the modelling of metals. The effects on metals are clear depending on the operating range : linear elastic within the reversible field, elastoplastic within a large field of low and average temperatures , viscoplastic. Numerous modelling schemes have been published, suggesting a separation of these effects; the suggested laws (and the associated numerical algorithms for structures) are given for elastoviscoplastic behaviour. To our knowledge, there has been no identified model that simultaneously combines these effects.

The PE material presents a complex combination of typical behavial features : elasticity, viscosity, instantaneous plasticity. These non-linear time dependent deformation properties are often illustrated by simple traction-relaxation-geometrical recovery tests (1). And, numerous authors have tried to apply elastoplastic laws to extrapolate the behaviour of polyethylene . Nevertheless, a number of complications occur :

- geometrical recovery, which is the aptitude of a PE structure to partially recover its initial shape when free from any load, cannot be extrapolated;
- even for small strains, instantaneous plasticity is present;
- the presence of residual stress even after years of service indicates that a threshold mechanism should exist and this is not the case of viscoelasticity,
- moreover with significant deformation, non linear features are prominent and instantaneous plasticity is still present,
- the very great sensitivity to temperature is also a major difficulty for conventional modelling.

* Gaz de France, Direction des Etudes et Techniques Nouvelles, France.
** Laboratoire de Mécanique des Solides, Ecole Polytechnique, France.
*** Commissariat à l'Energie Atomique, L.E.V., France

THE BEHAVIOUR OF POLYETHYLENE

The key problems are :
- on the one hand, to describe satisfactorily the constitutive equations of the material, which implies taking account of stress relaxation, geometrical recovery and strain rate effects;
-on the other hand, to study of real structures, and not only one dimensional tensile specimens, requiring the availability of numerical tools, such as finite element codes, providing an easy access to the predictions of the constitutive equations.

As an alternative to the Leed's one (2), a two mechanism model is chosen to analyze the behaviour of PE samples. Ward et al. put in evidence that a model, based on a pair of thermally activated Maxwell modes, accurately represents creep and stress relaxation phenomena for high-modulus PE fibres. Moreover, Sweeny and Ward demonstrated the superiority of this approach, based on a unique thermally activated Maxwell model as opposed to that of Escaig et al. (3) .

We propose a model associating a simple Maxwell model and an elastoplastic model with kinematic hardening. Our model comprises 5 parameters : modulus E_v and viscosity η for the Maxwell mechanism, modulus E_p, threshold σ_{pc} and a coefficient for kinematic hardening α for the elastoplastic mechanism, as explained elsewhere (1) (4) (5).

Thus, the first difference with respect to the Leed's theory is that an elastoplastic mechanism is replaced by a Maxwell mechanism, and the second difference is that thermal activation processes are disregarded for the sake of simplicity. Our theory is inspired by the study of bulk medium density PE samples obtained from extruded gas pipes (6).

FRACTURE MODELLING

For this purpose, we have adopted here a damaged model proposed by Bui and adapted for creep fracture by de Langre et al. (7). In this approach, the crack is surrounded by a totally damaged zone Ω_1 limited by a surface Γon which $\sigma.n = 0$. The changes taking place in this region govern crack growth. The resolution method of the local damaged model seeks for the variation of σ, ε, Γ knowing :
- the rheological behaviour within Ω_1
- the constitutive equations in Ω_1
- boundaries conditions for $\delta\Omega$
- the condition $\sigma.n = 0$ on Γ . The variation of Γ is controlled by a criterion on the internal parameters introduced in the constitutive laws
- $\sigma.n = 0$ in Ω_2.

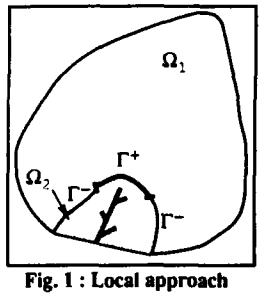

Fig. 1 : Local approach

Crack growth criteria correspond to the internal parameters of the rheological model: global anelastic deformation ε_{an}, anelastic deformation of the plastic mechanism ε_p.We postulate first that the fracture will occur when the damage, measured by the value of anelastic deformations, becomes too high. Nevertheless the numerical values of these parameters are not proportional to the level of the displacement at the boundaries if the approach is really local.

We decide to apply the Von Mises norm : $\| \varepsilon^{an} \| = \left(\frac{1}{2} \sum_{ij} \varepsilon^{an}_{ij} \varepsilon^{an}_{ji}\right)^{1/2}$

The critical value ε_R which controls crack propagation will be 0.2; this value characterizes ε^{ane} for a tensile test at 10 mm/min with a displacement level equal to 20%. We present two cases here :

(i) a tensile test :

Figure 2a shows the variation of the force during the test . Figure 2b shows the crack growth which goes schematically through a certain number of knots for a set displacement. Curves n°1 and 3 simulate a tensile test for a loading rate of 10mm/min and curves n°2 and 4 a tensile test for a loading rate of 1mm/min.

The criterion is naturally fulfilled at the tip of the crack first. Moreover, for a given criterion, the lower the tensile rate , the faster the crack initiates propagation for the same strain rate. The level of force is less significant at a lower loading rate. We can see on the figure 2a the discontinuities corresponding to different steps in crack growth.

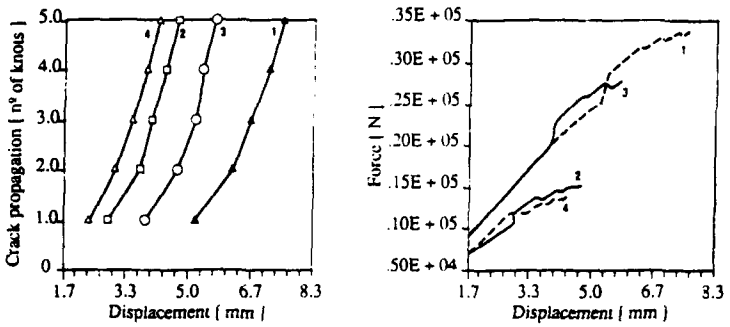

Fig. 2a & 2b : Comparison of the crack propagation with a " norm " criterion (2 loading speeds : tests 1, 2, 3, 4)

(ii) a relaxation test :

We used the previous results to evaluate the strain limit below which the crack does not progress. The figures 3a and 3b represent a numerical simulation ot the three following tests :
n°1, 2, 3: tensile test for a set displacement level at 3.82, 3.16, 2.16mm. Loading rate: 10mm/min

Crack initiation and propagation may take place within the relaxation phase, without loading. This is drawn in accordance with the set displacement level (Fig.3a). In the same way, force variation in time is shown on figure 3b.

The criterion chosen allows crack initatiation and propagation even below the displacement level in the above experiment.

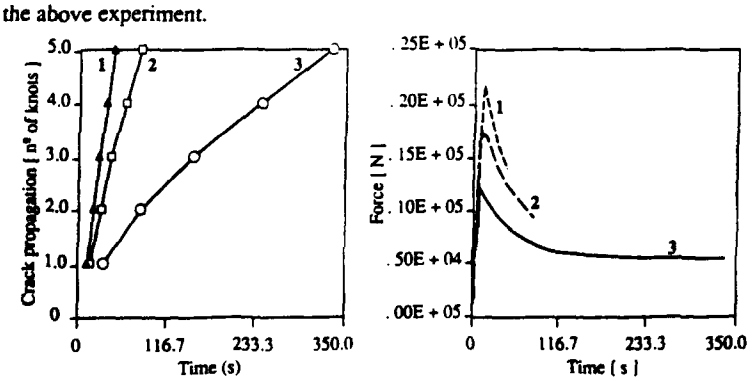

Fig. 3a & 3b : Comparison of the crack propagation. Relaxation test

EXPERIMENTAL AND MODELLING DATA

The Full Notch Creep Test method was proposed by Iimura and Nishio as a kind of accelerated test in which failure is accelerated by the "full-notch" effect as well as the effect of high temperature(8). For easy modelling, we used axisymmetrical samples .

Simulation was carried out on a half axisymmetrical specimen (length :2cm, diameter :3cm, notch : .5mm high and 1cm deep). A tensile test was performed with a loading rate of 10 mm/min. We studied a crack propagation criterion corresponding to an internal parameter associated with plastic deformation : ε^p

More precisely, let us assume that 921 is the number of the mesh initially adjacent to the crack tip and 922,923,924... the numbers of the meshes adjacent to the crack tip during propagation.

We define ε^p_{eq} the propagation parameter $\varepsilon^p_{eq} = \int \left[\sum_{ij} (\Delta \varepsilon_{ij})^2 \right]^{1/2} dt$

We decide that the crack may propagate when ε^p_{eq} reaches an arbitrary value (here, 5%) up to the element that is adjacent to the crack tip (first 921 then, 922, 923, and so on).

Figure 5a shows the distribution of the isovalues of the internal parameter ε^{anc}_{yy} for the first step of crack propagation. Figure 5b corresponds to the second step in the propagation process.

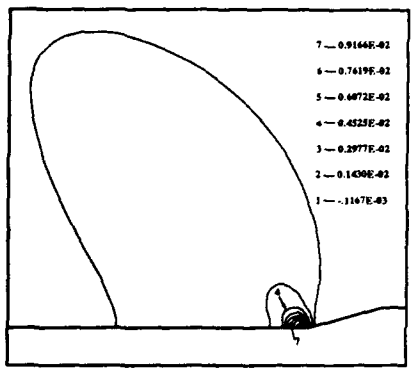

Fig. 5a : Isovalues of the parameter ε^{anc}_{yy} (1st step of propagation)

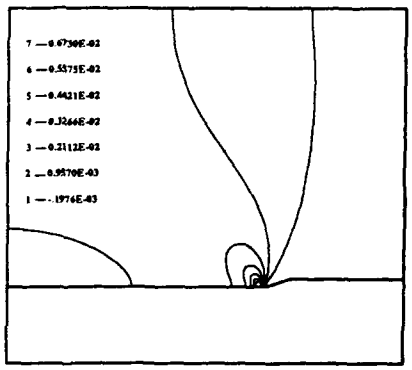

Fig. 5b :Isovalues of the parameter ε^{anc}_{yy} (2nd step of propagation)

CONCLUSION

In order to analyze the risk of fracture in PE pipe structures and to control the lifetime of the gas distribution network, GDF has undertaken a broad research program . The development of a tool to predict resistance to crack growth under different service conditions is based on realistic modelling of the behaviour of the material taking into account the three effects observed simultaneously (elasticity+viscosity+instantaneous plasticity). The resulting computation code is ed to simulate the initiation and the propagation of cracks in PE, using a local criterion. Qualitatively, the main features of crack propagation in PE have been determined, in particular the influence of the loading rate which is very different for PE cracks as compared with defects in metals. The next step of our research is focused on quantitative description of fracture mechanics in PE.

REFERENCES

1 J.KICHENIN,Comportement Thermomécanique du Polyéthylène. Thèse Ecole Polytechnique, 1992.

2 J.SWEENY, Proceedings of IUTAM, Creep in Structures, Leicester,1980,p.592.

3 J.M.LEFEBVRE, B.ESCAIG, J.Mat.Sci.,20,438(1985).

4 J.KICHENIN, K.DANG VAN; K.BOYTARD, paper submitted to European Journal of Mechanics.

5 J.KICHENIN, K.DANG VAN; K.BOYTARD, paper submitted to Journal of Materials Science.

6 J.KICHENIN, Rapport DEA, Ecole Polytechnique,1989.

7 E.DE LANGRE, Analyse de la Fissuration des Milieux Viscoplastiques. Application de la Théorie de l'Endommagement Brutal. Thèse Paris VI,1984.

8 S.IIMURA and N.NISHIO, Study of Service Life Prediction of Polyethylene, Proceedings of the 8th Plastic Fuel Gas Pipe Symposium,pp.34-39,1983.

INVESTIGATION INTO THE DEFORMATION BEHAVIOUR OF POLYMETHYLMETHACRYLATE

R J Levett* and A M Donald*

The strain at onset of crazing has been measured as a function of temperature at a known strain rate to investigate the different mechanisms of crazing in thin films of PMMA. The temperature dependence of the strain to craze of PMMA shows the transition from scission dominated crazing to disentanglement crazing at higher temperatures.

INTRODUCTION

Amorphous glassy polymers, such as PMMA, are a very important class of engineering materials. Such materials can exhibit a localised deformation process called crazing as well as conventional yielding processes. Crazing involves the formation of voided surfaces between polymer fibrils. The applied strain required to form crazes is dependent on the surface energy required to form fibrils, which in turn depends on the temperature of the polymer. The strain at onset of crazing can be measured as a function of temperature at a known strain rate to investigate the different mechanisms of crazing.

A basic theory for describing the mechanisms of crazing has been developed[1]. The basic approach of this theory is first to relate the crazing stress S_C to the surface energy Γ required to form the voids that separate the craze fibrils. Then the required Γ to form these voids is calculated by considering the necessary entanglement loss that must occur. The entanglement loss can occur due to either chain scission or disentanglement or both, and the type of crazing mechanism will be determined by strain rate, temperature and the molecular weight of the polymer.

The theoretical predictions of the crazing theory based on this surface energy Γ can be summarised by considering the general changes of the strain to craze as a function of temperature. At low temperature disentanglement will be inhibited and the entanglement loss

* Cavendish Laboratory, Cambridge University, UK

neccessary for fibrillation will occur by scission of the polymer. At higher temperatures disentanglement will become increasingly possible above a particular temperature determined by strain rate and molecular weight.

Crazing theory usually assumes that the polymer is monodisperse and experiments on crazing mechanisms in various polymer have preferentially been biased to monodisperse samples. A strategy used in this paper to investigate the effect of polydispersity is to modify the surface energy required to form fibrils by mixing low and high molecular weight samples of monodisperse PMMA.

EXPERIMENTAL

The monodisperse PMMA samples were supplied by Polymer Laboratories. Films ~ 0.5 μm thick were produced by drawing a microscope slide from a solution of PMMA in a suitable solvent (MEK or chloroform). The films were floated off onto a water bath and then picked up onto annealed copper grids that had been precoated with the same polymer. The films were bonded to the copper grids by annealing at a temperature above T_g in vacuo. The samples were then strained at various temperatures until deformation appeared in an optical microscope.

RESULTS AND DISCUSSION

The strain to craze as a function of temperature is shown in figures 1 and 2 for two different molecular weight samples of monodisperse PMMA. The graphs are approximately the same from 30 to 70°C. The lack of molecular weight dependence would indicate that the mechanism of crazing in these samples is scission since the craze surface tension, is independent of molecular weight. From 70°C upwards there is a marked molecular weight dependence, indicating the onset of disentanglement. Also apparent in the graph of strain to craze as a function of temperature for the lower molecular weight samples in fig 1 is a local maximum at the transition from scission to disentanglement. The higher molecular weight PMMA does show this behaviour for a low strain rate (fig 2) but not in the case of a high strain rate.

This additional transition has been explained[2] as the effect of the subsequent disentanglement of chains originally broken by scission reducing Γ in what is otherwise the scission regime. The force of disentanglement of a polymer chain is inversely proportional to its molecular weight squared. Thus fragments of a chain that have undergone scission but remained in the active zone (i.e. just outside the void tips separating fibrils) can disentangle and reduce the craze surface tension. This has been seen for polydisperse PES and

monodisperse PS. The local minimum in the strain to craze as a function of temperature, due to this effect, will only be apparent over a range of a few degrees because of the exponential dependence of the critical chain length for disentanglement on temperature. This consideration could explain the lack of a local minimum and maximum for the high strain rate and high molecular weight sample as a problem of the sampling frequency of the data.

The theory further states that if the molecular weight is increased the scission-disentanglement transition should increase in temperature, an effect clearly seen in figure 2. Another prediction of the crazing theory is that if the strain rate is increased so is the temperature of the scission-disentanglement transition. The temperature at which the peak occurs in the lower molecular weight sample is 70°C for the lower strain rate and 75°C for the higher strain rate, in accord with the prediction. The totality of these results confirm that scission is the dominant mechanism for crazing near room temperature,

Figures 3 and 4 show a comparison of pure PMMA of molecular weight 100,250 and the same with the addition of 5 % of PMMA with molecular weight below M_e. Above about 40°C the strain to craze in the blend seems somewhat less than for the monodisperse material, and the sharpness of the peak (marking the onset of disentanglement) is also reduced. The observation of the drop in the strain in the blend is consistent with earlier observations[3] of a reduction in the craze tip stress (related to the stress for craze propagation) for similiar PS blends compared with monodisperse material. The origin of this effect lies in the reduction in the density of entangled chains when a component below the entanglement molecular weight is added, thus reducing the necessary crazing stress. The onset of disentanglement will also be less well defined in this case, as seen in fig 4.

REFERENCES

1. Kramer, E.J. & Berger, L.L. in *Crazing in Polymers* (eds. Kausch, H.H.) 1 1990).
2. Plummer, C.J.G. & Donald, A.M. *Macromolecules* **23**, 3929 (1990).
3. Donald, A.M. & Kramer E.J., *Polymer* **24**, 1063 (1983).

ACKNOWLEDGEMENTS

The financial support of the SERC and ICI plc are gratefully acknowledged.

Figure 1. The strain to craze in PMMA as a function of temperature for monodisperse samples strained at a rate of 10^{-3} s^{-1} with molecular weights of A 480,000; B 1,400,000.

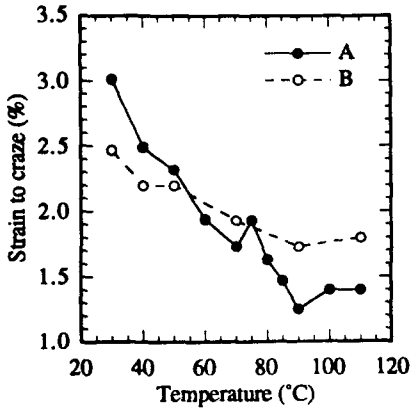

Figure 2. The strain to craze in PMMA as a function of temperature for monodisperse samples strained at a rate of 2.10^{-5} s-1 with molecular weights of A 480,000; B 1,400,000.

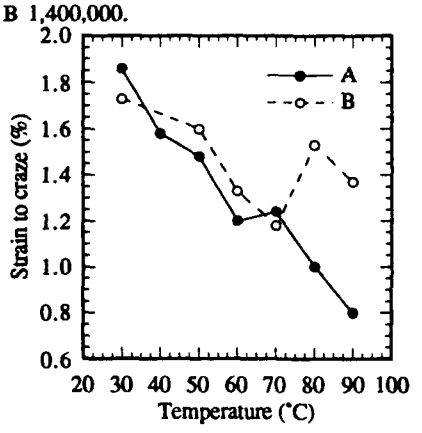

Figure 3. The strain to craze, at a strain rate of 10^{-4}, as a function of temperature for; A PMMA (M=100,250); B 95% PMMA (M=100,250) and PMMA (M=3000) 5%.

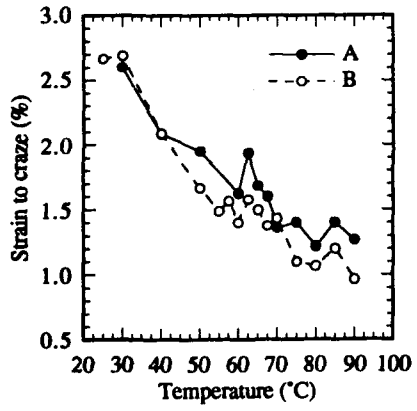

Figure 4. The strain to craze, at a strain rate of 10^{-5}, as a function of temperature for; A PMMA (M=100,250); B 95% PMMA (M=100,250) and PMMA (M=3000) 5%.

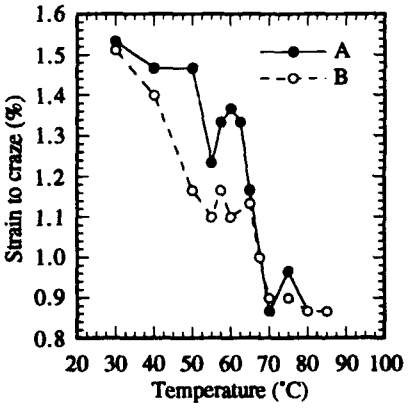

INFLUENCE OF TEMPERATURE AND PRESSURE ON THE STRUCTURE AND STRENGTH OF POLYPROPYLENE WELD JOINTS.

M. ABOULFARAJ*, M. COQUEBERT DE NEUVILLE* and C. G'SELL*

The hot-plate technique was investigated for welding polypropylene (PP) rods containing coarse α- and β-spherulites in nearly equal proportions. The effects of pressure and temperature on the joint quality were analysed by tensile tests with hourglass shaped specimens, microscopic observations and X-ray micro-diffraction spectra. The tensile tests do not reveal major differences between the welded and unwelded samples except a somewhat lower rupture strain in the welded specimens However, it is noticed that the necking occurred always at some distance from the weld joint. The structural analysis showed that he amount of β-spherulites in the weld joint is dramatically lower compared to the original material. This causes the yield stress to be higher than the original material and consequently the deformation to localise apart from the weld joint.

INTRODUCTION

The hot-plate technique is widely used to weld polymers. This process causes deep modifications in the structure. Those changes are enhanced in the case of PP with high amount of β-phase since the recrystallisation process changes the proportion of the β-structure and then the mechanical properties of the polymer.

In this paper, the structure and the properties of welded samples are systematically analysed as a function of welding temperature and pressure. The structure is investigated by microscopy of etched samples and by X-ray micro-diffraction. As for the mechanical properties, they are assessed by special tensile tests.

MATERIAL AND PROCEDURE

Intruded plates of PP were provided by ATOCHEM. The slow cooling phase in this process allows a high amount of β-phase in the material (≈ 50 %). PP cylindrical rods (∅ = 12 mm, L = 60 mm) were machined and welded by means of a specific set-up developed in this laboratory which allows the welding temperature and pressure to be controlled in a wide range (T = 200, 220 and 240 °C, P = 0.065, 0.13, 0.26 MPa).

The microscopic observations were performed on the welded specimens after they were truncated along the cylinder axis, finely polished and immersed during 18 hours in an appropriate etching solution to reveal their structure (1,2). The mechanical tests were performed on hourglass samples machined from the welded rods. The samples have their joint located at the minimum diameter in such a way that the stress is concentrated at the joint in order to characterise the process quality (3).

* Laboratoire de Metallurgie Physique et Science des Matériaux
Ecole de Mines, Parc de Saurupt, 54042 Nancy cedex

EXPERIMENTAL RESULTS AND DISCUSSION

Microstructure Analysis The etched samples were analysed by means of a metallographic microscope in the reflection mode. The α-structure appears bright and the β-phase dark (2). Figure 1 shows an overall view of the welded zone. Four different structures are distinguished :

- the original non-affected material with a high amount of β-phase and large spherulites (more than 100 μm diameter) ;
- the annealed zone composed of α-phase only. The β-phase melting temperature T_f being about 155°C, at temperature close to T_f, the β-structure is converted to α-phase (4). The thickness of this zone depends on the welding conditions as follow :

welding pressure = 0.13 MPa

welding temperature	200 °C	220 °C	240 °C
averaged annealed zone thickness	435 μm	300 μm	275 μm

welding temperature = 200 °C

welding pressure	0.065 MPa	0.13 MPa	0.26 MPa
averaged annealed zone thickness	450 μm	435 μm	275 μm

On these tables one can notice that the higher the temperature or the pressure, the thinner the annealed zone. The temperature effect could be modelled by considering the thermal equations and taking the melting enthalpy of the polymer into account (5). The results presented above can be explained as follows : the temperature gradient in the material increases with the welding temperature, increasing the welding pressure leads to a larger bead and then allows a higher temperature gradient in the material located in the vicinity of the melted material.

- the thin layer (60 μm wide) where the polymer was subjected to high shearing. The spherulitic structure is not visible. The spherulites are deformed under a shearing flow in the very viscous material (6) (figure 2) ;
- the central zone where the polymer melted and recrystallised. Close to the sheared zone, the spherulites have a columnar structure (figure 2). During the melt period, the temperature in this zone remains close to T_f. Therefore the motion of the macromolecules is hindered and they act as nuclei for the crystallisation. The columnar structure borders a spherulitic zone which contains mainly α-phase. The thickness of this zone depends on the welding conditions. The higher the temperature, the thinner the recrystallised zone. The same trend is observed by varying the pressure. It is also important to notice that in the recrystallised zone, the spherulites have a smaller size than in the unaffected material. During the weld process, the shearing of the melted material induces an increase in the number of nuclei and enhances the growth rate of the spherulites (7). These processes lead to a larger number of spherulites with a smaller size.

The X-ray micro-diffraction analysis allows the measurement of the proportion of the β-phase f_β, through the welding zone, and confirms the microscopic observations (see table I). The annealed zone is completely depleted in β-spherulites and the amount of β-phase in the recrystallised zone is decreased by 80%.

Table I

	Position	f_β (%)
Welded zone	0	8,5
	0,1	5
Annealed zone	0,2	0
	0,3	7
	0,4	21,4
Unaffected material	0,5	41,8
	0,6	52,9
	0,9	58,0

Tensile loading experiments on welded samples All the tensile loading tests were performed at the same strain-rate $\dot{\gamma} = 5.10^{-4}\ s^{-1}$. Figures 3 and 4 show that there is no major differences between the samples welded under various conditions. They also show that there is little difference between welded and unwelded specimens except the rupture strain is lower in the former case. It should be remarked that, in welded samples, necking always nucleates at some distance from the minimum diameter as it is seen on figure 5. This is the consequence of the difference in the polymer properties through the thermally affected material.

In view of interpreting the results obtained obove, the mechanical behaviour of an annealed unwelded sample was investigated in tensile experiment. Figure 6 shows that the annealed sample of the same polymer exhibited a higher yield stress and a lower rupture strain. The welded samples have a composite structure with a stiffer phase containing a high amount of α-spherulites boarded by the annealed zone and the unaffected polymer. During the load tests, although the minimum diameter is located at the joint to further the necking, the higher yield stress of the α-phase leads to plastic deformation in the unaffected material. The presence of this composite structure induces the appearence of a radial stress which leads to triaxial stresses promoting the necking in the unaffected polymer.

CONCLUSION

Welding PP containing a high amount of β-structure, brings a new structure to the joint. The annealed zone and the lower amount of the β-phase at the joint give the structure a higher yield stress and then the deformation localizes apart the weld joint when it is tested in tension.

REFERENCES

1 Olley R H, Basset D C, Polymer 23 (1982) 1707
2 Aboulfaraj M, Ulrich B, Dahoun A, G'Sell C, Polymer 23 (1993) 4817
3 G'Sell C, Hiver J M, Dahoun A, Souahi A, J Mater Sci 27 (1992) 5031
4. Varga J, J Mater Sci 27 (1992) 2557
5. Carslaw HS, Jaeger JC, Conduction of heat in solids, Second Edition, Clarendon Press, Oxford
6. Egen U, Ehrenstein GW, PLASTverarbeiter 37 (1986) 61
7. Tribout C., Monasse B, Haudin JM, Lory P, proc PPS 7 (1993) 442

Figure 1 : Overall view of the welded zone at the specimen centre

Figure 2 : Magnified view of part of the joint. three different structures are distinguished from the top
1. the columnar structure
2. the sheared zone
3. the annealed part.

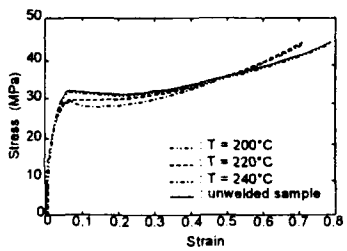

Figure 3 : Effect of welding temperature on the effective stress-strain curves.
$\dot{\varepsilon} = 5.10^{-4}\ s^{-1}$

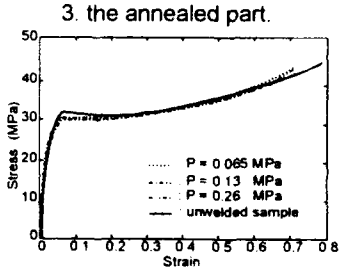

Figure 4 : Effect of welding pressure on the effective stress-strain curves.
$\dot{\varepsilon} = 5.10^{-4}\ s^{-1}$

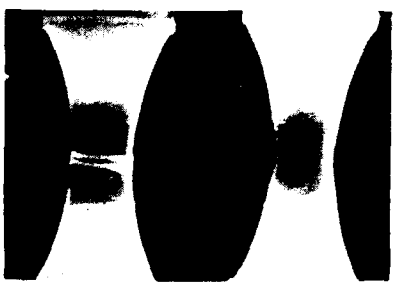

Figure 4 : welded and unwelded samples deformed at $\varepsilon = 0.6$

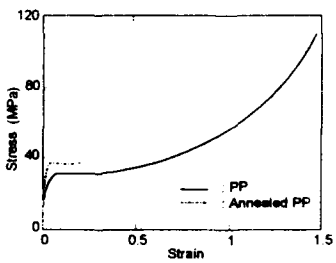

Figure 6 : effective stress-strain curves of PP and the same polymer annealed

IN-SITU S.E.M CHARACTERISATION OF α- AND β-SPHERULITES IN POLYPROPYLENE UNDER UNIAXIAL TENSION AND SIMPLE SHEAR

M. ABOULFARAJ*, C. G'SELL* and B. ULRICH*

Samples for tensile and shear experiments were prepared, and in-situ experiments were carried out in the SEM to study the mechanical properties of a single α- and β-spherulites under each loading mode. During the tensile tests, the β-spherulites exhibit an early plastic deformation while the α-spherulites remain nearly undeformed but later show the development of large cracks which appear at the equatorial region and at the boundaries perpendicular to the loading direction. During shear experiments, no cracking in any phase is observed and both types of spherulites deform plastically up to high strain. However, local analysis shows that the α-phase deforms less than the overall sample while the β-structure has a higher deformation than the applied strain. This difference in the behaviour is explained by considering the lamellae separation and the plastc slip mechanisms in both phases.

INTRODUCTION

The two phases α and β of isotactic polypropylene (PP), respectively monoclinic and hexagonal, were identified by direct observation in the scanning electron microscope (SEM) after an appropriate etching (1). The α-spherulites appear dark while the β- have a bright contrast (fig.1). This contrast difference is due to the etching. The sulfochromic solution attacks preferentially the β-phase since this structure contains only radial lamellae. In the α-spherulites case, the presence of tangential and radial lamellae make the surface more resistant to the acid attack (2).

This difference in the contrast allows direct observation of the mechanical behaviour of each phase. Results concerning the behaviour of single α- and β-spherulites under tensile and shear loading are reported.

MATERIAL

Intruded plates of PP were kindly provided by ATOCHEM. The slow cooling rate during this processing allows development of large spherulites. Two kinds of samples were machined out of the plates as it is shown in figure 2. A miniaturised testing machine was developed in our laboratory which can be introduced in the SEM chamber (fig. 3). Tensile and shear samples were finely polished and subsequently immersed during 18 hours in a sulfochromic acid, in order to reveal the spherulitic structure. The tensile strain is measured through the diameter contraction as follows (3) :

$$\varepsilon = 2 \ln(D_0/D)$$

* Laboratoire de Metallurgie Physique et Science des Matériaux
Ecole de Mines, Parc de Saurupt, 54042 Nancy cedex

The shear samples were engraved with a fine network of originally orthogonal markers. The local shear strain is obtained by measuring the angle θ of the distorted network :

$$\gamma = \tan(\theta)$$

EXPERIMENTAL RESULTS

The tensile experiments show that, at low deformation, crazes appear first at the equatorial region of the β-spherulites while the α-phase does not suffer any damage. At higher deformation, the plastic deformation propagates in the β-structure towards zones oriented ± 45° with respect to the loading direction. By contrast, the α-phase exhibits a very brittle behaviour. Cracks form at the centre of the spherulites or at boundaries and propagate perpendicularly to the loading direction (fig. 4).

By contrast to tensile loading, shear experiments do not show any cracking of the α-structure. Both spherulites deform plastically up to high deformations thanks to the negligible hydrostatic pressure. However, the local analysis of spherulite deformation shows that the α-structure deforms less than the sample while the β-phase has a higher deformation than the applied strain (fig. 5).

DISCUSSION

The difference in the behaviours of the α- and β-spherulites is related to their structure. The α-phase, which crystallises in the monoclinic cell, forms spherulites which contain radial and tangential lamellae. By contrast, the β-phase is made up only of radial lamellae separated by rubber-like chains structure since the glass transition temperature is about -20°C.

The plastic deformation of semi-crystalline polymers occurs by plastic slip mechanisms through the nucleation of dislocations which move on a selection of glide planes containing the **c** axis since the macromolecules are parallel to this direction. The critical resolved shear stress (CRSS) necessary to activate the nucleation and glide of dislocations is lower for "chain slip" than for "transverse slip". In the β-phase, it can be deduced from the symmetry of the lattice that the CRSS should increase in the following order $\{10\bar{1}0\}\langle 0001\rangle$, $\{10\bar{1}0\}\langle 1\bar{2}10\rangle$. In the α-phase, the easiest glide system is (010) <001>.

After previous studies (4,5), β-spherulites subjected to tensile loading should deform earlier at the equatorial region which is submitted to significant stress concentrations. For higher deformations, the process propagates toward zones inclined at ± 45° with respect to the loading direction. In these regions the lamellae are subjected to the highest shear stress along the active glide system, since they are radially oriented. In the α-phase, the presence of the tangential lamellae makes the deformation of the amorphous chains much more difficult. The interlocking structure limits the lamellar separation in the equatorial region of the spherulites. Plastic slip in the region oriented at 45° with respect to the loading direction is also considerably hindered. All those effects bring a higher yield stress to the α-structure but make this phase to be more brittle than β-spherulites.

In shear experiments, the hydrostatic stress is negligible. The cavitation observed in the α-phase is no longer observed and the spherulites can reach very high strains. However, a local analysis of the deformation of both phases showed that the β-spherulites deform more than the applied strain and the α-structure has a lower deformation than the sample. Once again the microstructure is responsible for such a behaviour. In the α-spherulites, the presence of daughter lamellae brings a higher stiffness to the structure and hinder the plastic deformation mechanisms (fig. 6).

CONCLUSION

The local deformation of α- and β-phases in coarse spherulitic PP, shows that the β-structure contributes to the plastic deformation of the material while the α-spherulites increase the stiffness and the yield stress of the material. This is because the presence of tengential lamellae in the α-phase makes "chain slip" mechanisms more difficult.

REFERENCES

1 Olley R H, Basset D C, Polymer 23 (1982) 1707
2 Aboulfaraj M, Ulrich B, Dahoun A, G'Sell C, Polymer 23 (1993) 4817
3 G'Sell C, Hiver J M, Dahoun A, Souahi A, J Mater Sci 27 (1992) 5031
4 Weynant E, Haudin J M, G'Sell C, J Mater Sci 15 (1980) 2677
5 Wang T T, J Pol Sci Pol Phys Ed 12 (1974) 145

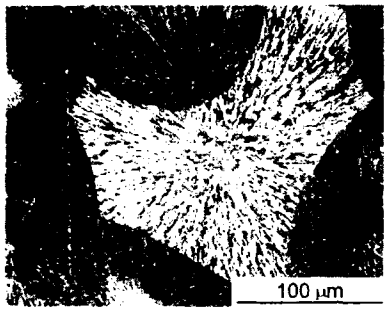

Fig.1 : Morphology of the α and β-spherulites observed in the S.E.M.

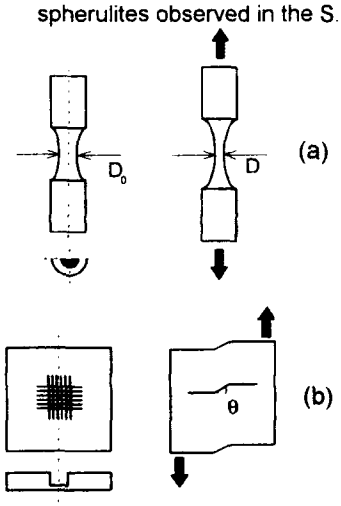

Fig.2 : Geometry of the samples used for tension and shear tests performed in the S.E.M.

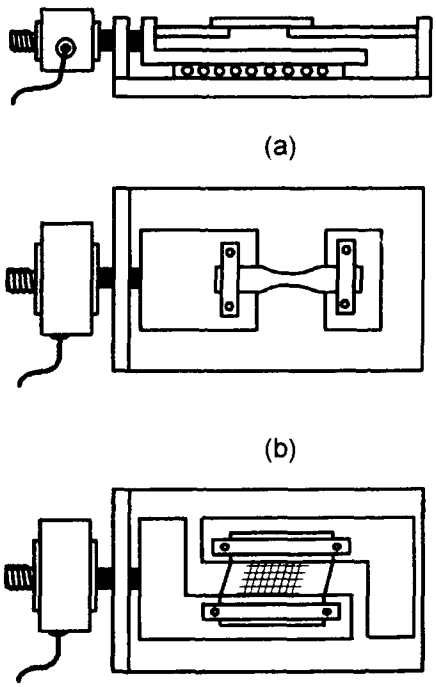

Fig.3. : Schematic diagram of the deformation apparatus
a) in the tensile loading configuration
b) in the shear loading configuration

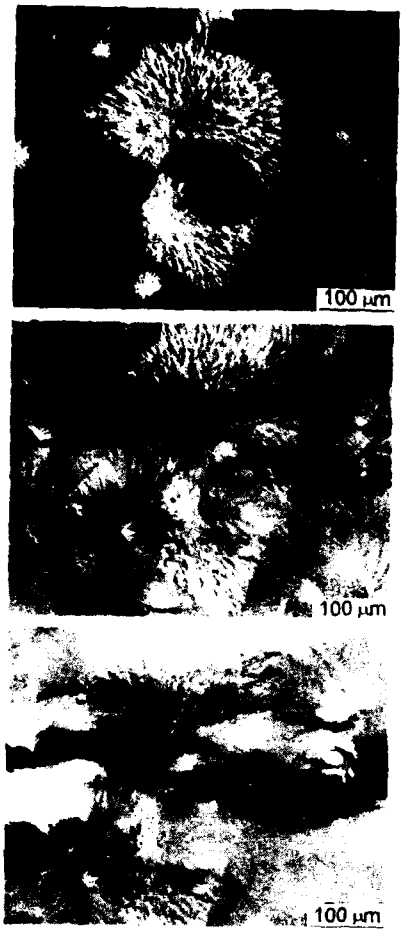

(a)

(b)

(c)

Fig.4. : Evolution of the structure during tensile loading (a) $\varepsilon = 0$ (b) $\varepsilon = 0.12$ (c) $\varepsilon = 0.32$

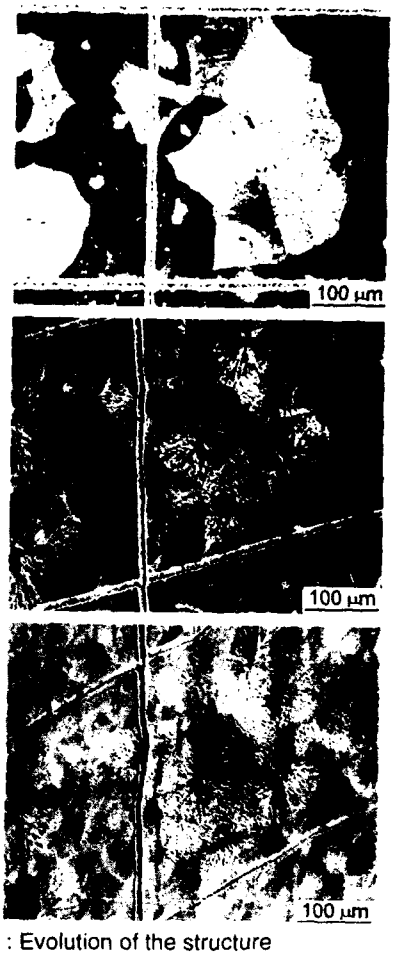

Fig.5. : Evolution of the structure during shear loading (a) $\gamma = 0$ (b) $\gamma = 0.23$ (c) $\gamma = 0.55$

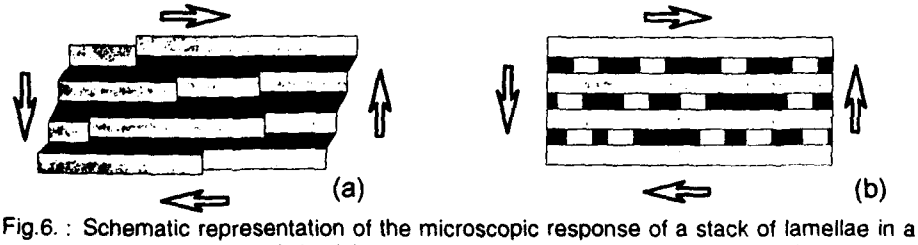

Fig.6. : Schematic representation of the microscopic response of a stack of lamellae in a generalised shear field. (a) random glide accompanied by the amorphous phase in the β-phase (b) interlocking effect of the tangential crystallites in the α-phase

DEFORMATION AND FRACTURE OF SURFACE EMBRITTLED POLYETHYLENE

Sunwoong Choi* and Lawrence J. Broutman**

The effect of thin brittle surface layer thickness ranging from 40μm to 160μm, produced as a result of UV aging, on long-term behavior of medium density polyethylene was examined. The deformation mechanism and molecular response to cause creep-crack initiation during stress-rupture testing of surface embrittled specimen is described using the activated rate process analysis. Based on the values of activation energies and activation volumes, it was concluded that the shorter failure times (surface embrittlement) for UV aged specimens was due to creep-crack initiation through progressive intercrystalline tie chain scission. For non-aged specimens, progressive and incremental pull out of tie molecules through polyethylene crystallites was proposed as the crack initiating mechanism.

INTRODUCTION

The presence of a thin brittle surface layer on polymers often causes an adverse effect on the mechanical behavior of polymeric materials. This phenomenon is known as surface embrittlement (1, 2, 3). The thin brittle surface layer can be produced by improper processing, weathering, environmental and chemical attack, and in some cases with the application of brittle coatings on the polymer surfaces. For the UV aged specimens for example, from the chemical and physical changes observed, the major cause of surface layer embrittlement was due to intercrystalline chain scission, crosslinking and modification in the chemical nature of macromolecules. In many cases the thin brittle surface layer can produce brittle failure in otherwise ductile polymers.

The long-term behavior of polyethylene subjected to a constant stress has been of interest to applications involving polyethylene pipes. The surface degradation during processing and sunlight exposure during storage are known to produce a brittle surface layer thickness in the order of few hundred microns thick. As a result, a large reduction in the lifetime of polyethylene pipe has been observed. The long-term performance of the polyethylene under stress is dependent on the crack initiation followed by the slow crack growth. Hence, the performance reduction is thought to be caused by the ease of crack initiation in the thin brittle surface layer.

This paper is concerned with the investigation of the deformation and fracture of U.V. aged polyethylene under stress-rupture condition. The role of thin brittle surface layer in changing the creep crack initiation behavior during creep deformation is described in term of molecular mechanisms of damage obtained though activation energy and activation volume analysis.

* Illinois Institute of Technology, USA
**L. J. Broutman and Associates Ltd., Chicago, IL USA

EXPERIMENTAL PROCEDURE

The material utilized for this investigation was the ethylene/butene copolymer of medium density polyethylene (PE2306IA). The materials were received in the form of 15.24cm (6") diameter pipe having the standard dimension ratio of 11. The stress-rupture test specimens were obtained from the pipe by cutting, then compression molding (250°F) and air cooling to produce flat plaques. The plaques were then left undisturbed for ten days before the final dimensions were machined. The stress-rupture specimen utilized is the plane-strain grooved tensile (PSGT) specimen, originally developed by Choi and Broutman. The diagram of PSGT specimen is illustrated in Figure 1. The PSGT specimen, although uniaxially loaded, creates a biaxial stress state (approximately 2:1) in the groove root, which simulates the stress state in pressurized specimen.

The thin brittle surface layer on the groove of PSGT specimens was produced by subjecting the sample to an intense UV irradiation (254nm), using cold cathode germicidal sterilamp. During UV aging, thin brittle surface layer thickness of 40μm, 60μm and 160μm were produced for UV exposure times of 25, 50 and 250 hours, respectively. The UV aged surfaces were characterized by their molecular weight, crystallinity, and molecular structures by GPC, DSC, and FTIR methods, respectively.

The stress-rupture test was performed using a pneumatic air cylinder to produce predetermined constant load on the specimen. Battery jars containing distilled water and circulating heaters were used to provide test temperatures of 60°, 70°, and 80°C. The applied load selected produced the characteristic ductile and brittle failures.

RESULTS AND DISCUSSION

The results of stress-rupture test for the UV exposed (25, 50 and 250 hour) and non-exposed PSGT specimens are shown in Figures 1 for 80°C test temperature. Two distinct regions having different slope can be observed. The region characteristic of higher loads and shorter failure times are described by delayed yielding (ductile) failure. The lower loads and longer failure times are characteristic of failures via creep-crack initiation and slow crack growth failures ("brittle" failure). For 25 hour UV aged specimen, there is no change in the failure time compared to that of non-aged specimens. However, for 50 and 250 hour UV exposed specimens, brittle failure curves shifted toward the shorter failure times, while the ductile failure curve is unaffected. The region where two curves meet, known as the ductile-brittle transition, is also affected.

In the brittle failure mode, the total failure time consists of incubation time for initiating creep-cracks and time for the slow crack growth. By comparing stress-rupture curves for 50 hour U.V. exposed samples (Figure 1), it can be observed that sample having the thin brittle surface layer (~60μm) pre-cracked prior to stress-rupture test failed more than 10 times earlier than the non-surface cracked specimens. In other word, the incubation time for crack initiation in PE2306IA takes up more than 90 percent of the total failure time. Hence, the stress-rupture curves obtained can be treated as the creep-crack initiation curves.

To determine the micro-mechanism of deformation leading to creep-crack initiation, the molecular response during sustained loading is examined using the activated rate process analysis. The analysis considers that the creep-crack initiation process is controlled by the bond disintegration dominated process. As a consequence, relationship between the lifetime (t),

applied stress (σ) and temperature (T) can be established using the equation 1 given below (4).

$$\ln t = \frac{\Delta F}{RT} - \frac{\gamma \sigma N_a}{2RT} - \ln \frac{\gamma \sigma N_a}{2RT} - \ln \frac{kT}{h} \qquad \text{(Eqn.1)}$$

where, ΔF and γ are the activation energy and activation volume of the bond disintegration process; k, h, R, and N_a are the Boltzmann's, Planck's, gas-law constants, and Avogadro's number, respectively. By differentiating equation 1 with respect to inverse temperature, the activation energy can be evaluated at zero stress, as shown in equation 2.

$$R\frac{d\ln t}{d(\frac{1}{T})} = \Delta F - \frac{\gamma \sigma N_a}{2} = \Delta F^* \qquad \text{(Eqn.2)}$$

The plot of equation 2 can be obtained from the experimental data of Figure 2a and is shown in terms of apparent activation energy (ΔF^*) and applied stress, in Figure 2b. From equation 2, the activation volume can be evaluated at zero apparent activation energy (Figure 2b) and is given in equation 3. Here, σ^* is the stress at zero apparent activation energy.

$$\gamma = \frac{2\Delta F}{\sigma^* N_a} \qquad \text{(Eqn.3)}$$

Both ΔF and γ were found to increase with UV aging times. The molecular mechanism of bond disintegration leading to creep-crack initiation can be determined by comparing the activation energy to a known molecular process. The ΔF of 150KJ/mole (36Kcal/mole) determined for non-aged specimen can be correlated to the activation energy for a polyethylene chain translation (slippage) through polyethylene crystallites under the combined influence of thermal and mechanical forces exerted on a tie molecule (140KJ/mole), as was theoretically calculated by Kaush and Becht (5). Similarly, for 218KJ/mole (52Kcal/mole) and 267KJ/mole (64Kcal/mole) determined for 50 and 250 hour UV aged specimens, respectively, can be correlated to intercrystalline tie molecular scission. This was established based on the activation energy of 235KJ/mole (56Kcal/mole) for a semi-crystalline polyethylene single chain rupture obtained from the thermal degradation and fracture study of Peterlin (6). The schematic models of intracrystalline chain slip and intracrystalline tie molecule scission are illustrated in Figures 3 and 4, respectively.

For the details of each processes during deformation, leading to creep-crack initiation, a physical interpretation of the activation volume is necessary. The higher activation volumes determined for the UV aged specimens can be correlated to higher local stresses on the tie molecules due to intercrystalline chain scission during UV aging.

REFERENCES

1. Rosenzweig N and Broutman L J, ANTEC Proc (1983) 455
2. So P K and Broutman L J, ANTEC Proc (1985) 639
3. Choi S W, Duvall D E and Broutman L J, ANTEC Proc (1993) 2009
4. Tobolsky A and Eyring H, J of Chem Phys 11 (1943) 125
5. Kaush, H H and Becht J, "Deformation and Fracture of High Polymers", Plenum NY 1973
6. Peterlin A, J of Polym Sci 7 (1969) 1151

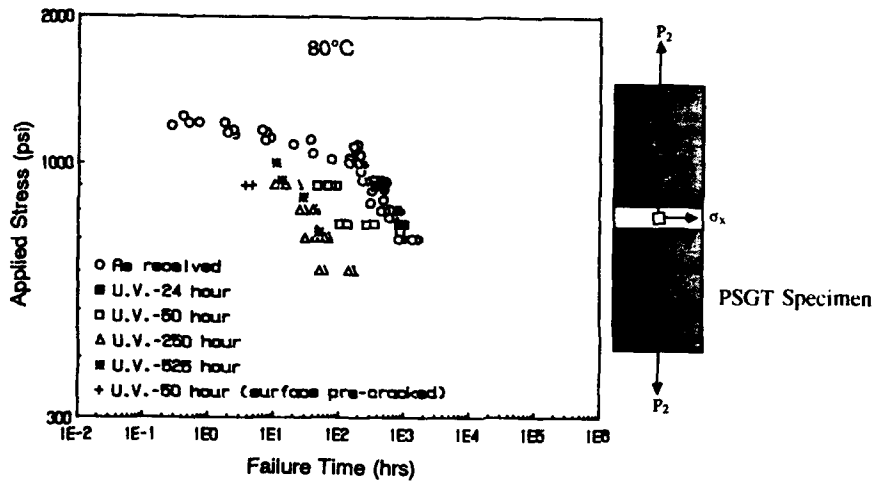

Figure 1. The Effect of UV Exposure on the Stress-Rupture Behavior of PE2306IA at 80°C.

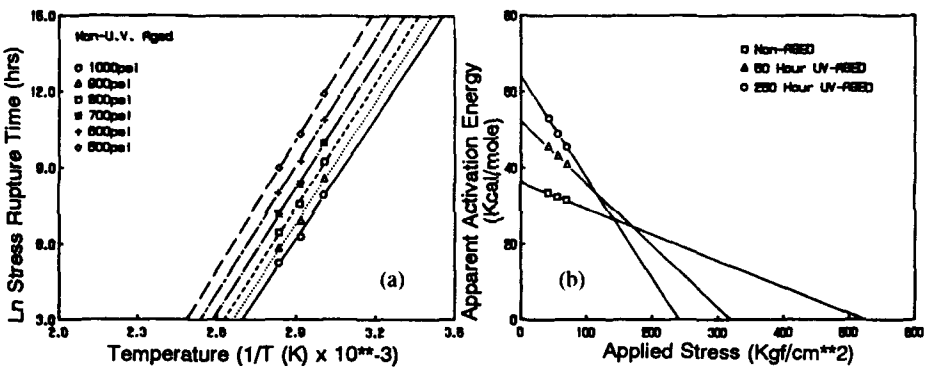

Figure 2. (a) Natural-Log Stress-Rupture Time vs. 1/T for Non-UV aged PE2306IA; (b) Apparent Activation Energy vs. Applied Stress Curve.

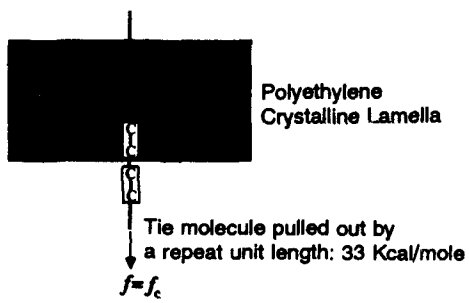

Figure 3. Intracrystalline Chain Slip

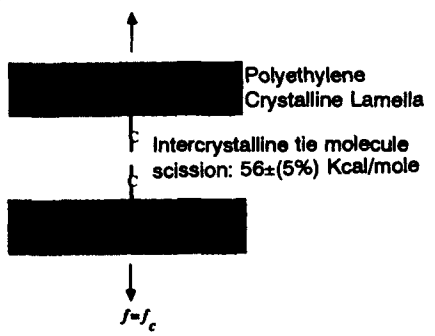

Figure 4. Intercrystalline Tie Chain Scission

PLASTIC DEFORMATION AND STRUCTURE IN ISOTROPIC POLYETHYLENE.

N.W.Brooks*, R.A.Duckett*, A.P.Unwin* & I.M. Ward*

Mechanical experiments carried out on a range of polyethylene materials have shown the existence of two yield points. The behaviour is adequately described by two non-linear Maxwell elements in parallel which yield at different strains. The stress carried by each element was found experimentally at low strains and the strain-rate dependence of each dashpot was determined and then modelled. Parallel structural studies have shown that the first yield point is associated with recoverable interlamellar shear and the second with irrecoverable c-shear.

MECHANICAL BEHAVIOUR

Three polyethylene grades were evaluated described in detail in a previous publication[1] as materials A (low density), B (medium density) and C (high density). Evidence of two distinct yield points can be seen from the stress-strain curves obtained of the materials in tension (Figure 1) and from the plots of the residual strain as a function of the applied strain in compression (Figure 2); in both cases the yield points are indicated by arrows. It has been shown that in tension and compression the first yield point marks the onset of time dependent recovery and the second with the onset of 'permanent' plastic deformation.
The stress-strain curves and the recovery behaviour can be described by two non-linear Maxwell elements in parallel (Figure 3(a)), which below the second yield point can be further simplified (Figure 3(b)). Using this model the stresses carried individually by the two arms can be found experimentally using a strain dip experiment[4]. The materials are loaded to a given test stress, σ_a and then rapidly unloaded and stopped at a new stress, σ_t. If this stress is equal to the stress carried by the strong spring then the stress remains constant for a short time. By trial and error the recovery stress carried by the strong spring can be found: the effective stress is the difference between this and the applied stress. Figure 1 shows a typical separation for a tensile test at a strain-rate of $2.08 \times 10^{-3} s^{-1}$. The yield stresses for each arm can therefore be found as a function of strain-rate. The effective and recovery stresses at the first yield point found for material B as a function of

* IRC in Polymer Science and Technology, University of Leeds, Leeds LS2 9JT

the strain-rate is shown are Figure 4. Similar results were found at different temperatures and at the second yield point. These results were then fitted by:

(I) A single Eyring activated-rate process.

The effective stress results were fitted assuming that the following equation following Truss et al[5] was satisfied:

$$\sigma_e = (2kT/V_1).\mathrm{Sinh}^{-1}((\varepsilon/2a_1).\exp(\Delta H_1/kT)) \qquad (1)$$

The activation volume and energy obtained are shown in Table 1 compared with the previous results obtained for the same material by Truss et al from the total stress-strain-rate curves. The activation volumes are in agreement but the activation energy is smaller, due to variance between sample batches and the fitting procedures employed.

(II) Fotheringham and Cherry co-operative jump model.

Only the effective stress values, σ_e are fitted, the recovery stress is assumed to be strain-rate independent which is in agreement with the results shown in Figure 4. The strain-rate dependence is explained in terms of the activated rate of n chain segments co-operatively; this is interpreted as the motion of regular folds on the lamellar surfaces, leading to recoverable interlamellar shear. It can be shown[4] that:

$$\varepsilon = K_0.\exp(-n\Delta H/kT).\mathrm{Sinh}^{n}(V^*\sigma_e/2kT) \qquad (2)$$

The fitted results are shown in Table 2, compared with results obtained by Fotheringham and Cherry for linear polyethylene. The results show that the activation volume of the medium density material evaluated here is slightly less than for the previous work. The activation energy is in agreement with the result found using a single Eyring activated rate process to fit the data.

STRUCTURAL BEHAVIOUR

Structural studies (T.E.M., optical microscopy and XRD) were carried out on the materials in the isotropic and deformed states. The optical and T.E.M. results showed that the initial morphology of the materials varied markedly. The high and medium density materials were shown to consist of well ordered small spherulites and the low density material of large (20-25μm diameter) less well ordered, banded spherulites.
The XRD patterns obtained during tensile deformation show inhomogeneous spherulitic deformation on drawing as described by Hay and Keller[6]. The first yield point marks the onset of non-linear viscoelastic behaviour after the initial linear response and is associated with inhomogeneous lamellar reorientation leading to a proportion of the lamellae oriented at approximately 45° to the draw direction.

The second yield point is associated with the destruction of the lamellae by c-shear of the reoriented lamellae. The high and medium density materials are fibrillated after the second yield point, but the low density material show deformed spherulites which are still intact.

SYMBOLS USED.

σ	= Stress (MPa).	V^*	= Apparent Activation Volume (A^3).
ε	= Strain.	V	= Activation Volume (A^3).
$\dot{\varepsilon}$	= Strain-rate (Sec^{-1}).	A_1	= Constant.
k	= Botzmann Constant.	n	= Number Of co-operative Chain Segments.
T	= Absolute Temperature (Kelvin).		
ΔH	= Activation Energy ($Jmol^{-1}$).	K_0	= Pre-exponential Factor.

TABLE 1. Single Eyring process.

	Present work	Truss
V_1/A^3	4670	3980
LnA_1	12.1	68.0
$\Delta H_1/Jmol^{-1}x10^{-19}$	0.84	3.01

TABLE 2. Co-operative jump process.

	Present work.	Co-op Jump.
V/A^3	480	570
$n\Delta H/Jmol^{-1}x10^{-19}$	0.856	-
n	3.24	3.1

ACKNOWLEDGEMENTS

Thanks are due to BP Chemicals Ltd, Grangemouth for providing the materials and financial and technical support for the project. Special thanks go to Mr A.D.Channell, Dr Valerie Rose, Dr M.J.Cawood and Dr A.Gray. for their contributions.

REFERENCES

1) Brooks,N.W., Duckett,R.A. and Ward.I.M., Polymer, 1992, 33, 9, 1872.

2) Brooks,N.W., Duckett,R.A. and Ward.I.M., To be published.

3) Brooks,N.W., Duckett,R.A.,Unwin,A.P. and Ward.I.M., To be published.

4) Fotheringham,D.G. and Cherry,B.W., J.Mater.Sci., 1978, 13, 951-964.

5) Truss,R.W., Clarke,P.L., Duckett,R.A. and Ward,I.M., J.Polym.Sci., Polym Phys Ed, 1984, 22, 191-209.

6) Hay,I.L. and Keller,A., Kolloid Z, 1965, 204, 43.

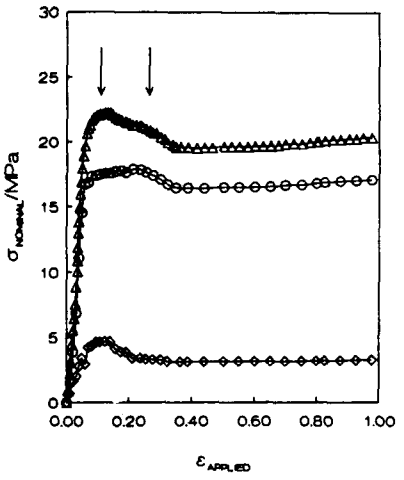

Figure 1. σ–ε Curves In Tension For Material A.
Temp = –50°C, $\dot{\varepsilon}$ = 2.08x10^{-3}s^{-1}
Δ Applied Stress, σ_A, ○ Recovery Stress, σ_R, ◇ Effective Stress, σ_E.

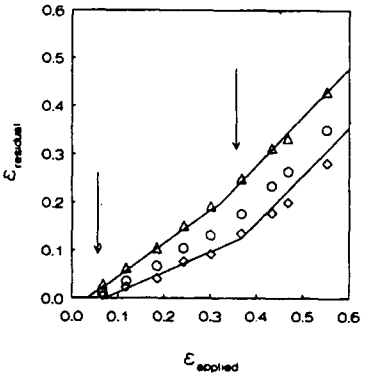

Figure 2. Residual Strain Vs Applied Strain For Material B.
$\dot{\varepsilon}$ = 6.9x10^{-4}s^{-1}
Δ 0 Minutes, ○ 30 Minutes, ◇ 48 Days.

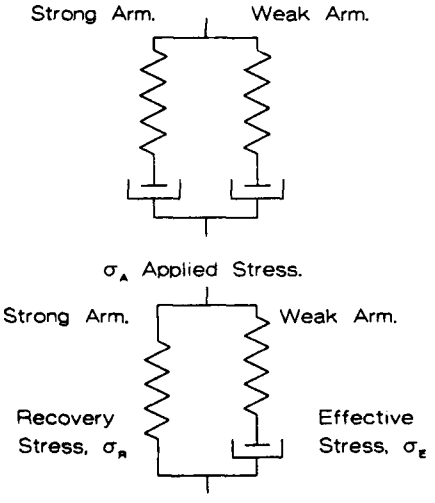

Figure 3(a). (Top) Two Non-Linear Maxwell Elements In Parallel.
Figure 3(b). (Bottom) Simplified Model Used For Transient Dip Experiment.

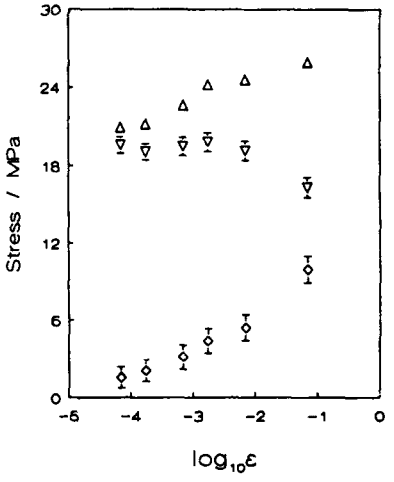

Figure 4. Strain-Rate Dependence Of Material B. Temp = 20°C, ε_{APP} = 0.2.
Δ Applied Stress, σ_A, ▽ Recovery Stress, σ_R, ◇ Effective Stress, σ_E.

PLASTIC DEFORMATION OF HIGH-DENSITY POLYETHYLENE DURING CREEP

J Lai and A Bakker*

In the present paper, an effort is made to interpret the origin of pseudo plastic deformation of HDPE during creep under low stresses in view of the composite structure feature of semi-crystalline polymers. It is suggested that significant shift of the relaxation times of the amorphous region remote from crystals towards shorter times by a stress through the stress-induced change in free volume gives rise to the irreversible part of deformation. The plastic deformation is analysed and determined using a plasto-viscoelastic model. Onset of steady state plastic deformation is found to occur above a critical stress of 12 MPa.

INTRODUCTION

It is generally accepted that the plastic deformation of semi-crystalline polymers results from three yielding mechanisms: crystal slip, twinning and martensitic transformation (1). Recent investigations (2,3) reveal that for some semi-crystalline polymers, such as polyethylene (PE), irreversible deformation can arise from any applied stress, however small. In (3) the experimental results of creep and recovery of high-density polyethylene (HDPE) show that after removal of load, the recovery strain does not decrease to zero but approaches to a plateau value at long times, even the applied stress is very low. The origin and mechanism of the pseudo plastic deformation produced by a stress well below the yield stress of the material is not clear hitherto.

In the present paper, we try to investigate into the origin of the pseudo plastic deformation of HDPE in light of its composite structure feature. The plastic deformation is analysed using a plasto-viscoelastic constitutive model.

EXPERIMENTAL

The raw material for the present investigation is a compression moulded HDPE plate with a density of 0.95 g/cm^3. Specimens were cut from the centre of the plate and heat-treated under a temperature of 85°C for 18 hours, in order to erase previous aging and residual stress during machining, and then aged for 2 weeks at the ambient temperature of 20°C prior to testing.

Tests of creep for 1800 seconds followed by recovery for 3600 seconds were performed at the room temperature of 20°C on an Instron 4505. The stress level under which the creep tests were conducted ranged from 2 to 16 MPa. The strain was measured by an Instron extensometer.

* Laboratory of Materials Science, Delft University of Technology, Rotterdamseweg 137, 2628 AL Delft, The Netherlands.

RESULTS AND DISCUSSION

The experimental data of creep and recovery are shown in figure 1, where the compliance is defined as the strain-to-stress ratio. It can be seen that both the creep compliance and the recovery compliance are stress dependent at all the stress levels concerned, which means that non-linearity of HDPE exists already at a very low stress.

Interpretation of pseudo plasticity

It is known that a semi-crystalline polymer has a spherulitic structure, containing similar lamellar crystals separated by layers of amorphous polymers. The crystals are relatively stable and deform little at a low stress, while the amorphous phase undergoes most of the deformation. It is suggested by Struik (4) that the time-dependent deformation is entirely due to the amorphous region, while the crystals act as inert fillers behaving elasticly and reducing the segmental mobility of the amorphous region adjacent to them. According to this model, a semi-crystalline polymer can be divided into three regions, namely, the crystal region, the amorphous region close to the crystals (region I) with its segmental mobility reduced and thus the glass transition temperature shifted towards the high temperature side, and the amorphous region remote from the crystals (region II) with the segmental mobility and the glass transition temperature undisturbed. Two characteristic glass transition temperatures, T_g^U and T_g^L ($T_g^U > T_g^L$), corresponding to region I and region II respectively, were introduced in (5). For HDPE T_g^L is estimated round -40°C and T_g^U is above 60°C (6). Under room temperature, region I is glassy, while region II has passed its glass transition temperature and is in rubbery state. Obviously, region I and region II will deform in different mechanisms. To this end, we propose the following modified Schapery representation to describe the deformation of HDPE,

$$\varepsilon(t) = g_0 D_0 \sigma + g_1^{(I)} \int_0^t \Delta D^{(I)}\left[\psi^{(I)}(t) - \psi^{(I)}(\tau)\right] \frac{dg_2^{(I)}\sigma}{d\tau} d\tau$$

$$+ g_1^{(II)} \int_0^t \Delta D^{(II)}\left[\psi^{(II)}(t) - \psi^{(II)}(\tau)\right] \frac{dg_2^{(II)}\sigma}{d\tau} d\tau \qquad (1)$$

in which the time-dependent deformations from the two amorphous regions are represented by two hereditary integrals respectively. The stress-reduced times are defined as

$$\psi^{(I)}(t) = \int_0^t ds / a_\sigma^{(I)}, \qquad \psi^{(II)}(t) = \int_0^t ds / a_\sigma^{(II)} \qquad (2)$$

where $a_\sigma^{(I)}$ and $a_\sigma^{(II)}$ are stress-induced time shift factors for region I and region II respectively, and can be evaluated by fitting the following expression for recovery to the experimental data,

$$\varepsilon_r(\lambda) = \varepsilon_r^{(I)}(\lambda) + \varepsilon_r^{(II)}(\lambda) \qquad (3)$$

in which

$$\varepsilon_r^{(I)}(\lambda) = C^{(I)}(\sigma)\left[\left(1 + a_\sigma^{(I)}\lambda\right)^n - \left(a_\sigma^{(I)}\lambda\right)^n\right] \qquad (4)$$

$$\varepsilon_r^{(II)}(\lambda) = C^{(II)}(\sigma)\left[\left(1 + a_\sigma^{(II)}\lambda\right)^m - \left(a_\sigma^{(II)}\lambda\right)^m\right] \qquad (5)$$

$$\lambda = (t - t_1)/t_1 \qquad (6)$$

where t_1 is the time at which load was removed. Power law is introduced for $\Delta D^{(I)}(\psi)$ and $\Delta D^{(II)}(\psi)$ respectively. As a result of curve fitting, $n = 0.2$, $m = 0.5$, $a_\sigma^{(I)}$ is around, while $a_\sigma^{(II)}$ is in the order of $10^{-6} \sim 10^{-5}$. Specifically, for the stress level of 4 MPa, for example, $C^{(I)} = 2.88224 \times 10^{-4}$, $C^{(II)} = 4.08678 \times 10^{-3}$, $a_\sigma^{(I)} = 1.56702$ and $a_\sigma^{(II)} = 1.59066 \times 10^{-6}$. Apparently, the relaxation times of region I is only slightly disturbed by a low stress, the relaxation times of region II, however, is shifted significantly towards shorter times.

The recovery process of the two amorphous regions can be studied by comparing their fractional recovery (FR), a quantity introduced by Turner (7), as follows,

$$FR^{(I)} = 1 - \varepsilon_r^{(I)}(\lambda)/\varepsilon_r^{(I)}(0) = 1 - \left(1 + a_\sigma^{(I)}\lambda\right)^n + \left(a_\sigma^{(I)}\lambda\right)^n \tag{7}$$

$$FR^{(II)} = 1 - \varepsilon_r^{(II)}(\lambda)/\varepsilon_r^{(II)}(0) = 1 - \left(1 + a_\sigma^{(II)}\lambda\right)^m + \left(a_\sigma^{(II)}\lambda\right)^m \tag{8}$$

Plots of $FR^{(I)}$ and $FR^{(II)}$ versus λ for the stress level of 4 MPa in figure 2 show the prediction of recovery process of region I and region II. Region II is seen to recover in a much slower speed than region I. It can be estimated from equations (7) and (8) that to accomplish 98% of the total recovery, i.e. $FR^{(I)} = FR^{(II)} = 0.98$, region I needs about 15 times the creep time, whereas region II needs 10^8 times longer than the creep time. When region I has completed its recovery, region II achieves only 0.5% of its total recovery, and is still in the process of recovery in such a slow speed that the existing extensometer can not detect the decrease of the residual deformation. After removal of load, the deformation from region II seems to be irreversible, a phenomenon observed in the experiment (3) that the recovery strain reaches a plateau at long times.

From the above discussion we can conclude that pseudo plastic deformation of HDPE is from the amorphous region remote from the crystals which has passed its glass transition temperature and whose relaxation times are shifted significantly towards the shorter times by a stress through the stress-induced change in free volume.

Determination of the plastic deformation

It is reasonable to treat the deformation from region II as irreversible plastic deformation. Equation (1) can then be evolved to the following plasto-viscoelastic representation,

$$\varepsilon(t) = g_0 D_0 \sigma + g_1 \int_0^t \Delta D\left[\psi(t) - \psi(\tau)\right] \frac{dg_2\sigma}{d\tau} d\tau + \int_0^t \frac{dP[\sigma(\tau), \hat{t}(\tau)]}{d\tau} d\tau \tag{9}$$

Using the experimental data of creep and recovery in figure 1, all the material properties in equation (9) can be evaluated, and thus the plastic deformation of HDPE during creep can be determined. It is found that the plastic strain ε_p during creep, shown in figure 3, can be expressed as

$$\varepsilon_p(t) = D_{p1}(\sigma)t^{0.5} + \mathrm{H}(\sigma - \sigma^*)D_{p2}(\sigma)t \tag{10}$$

where $\mathrm{H}(x)$ is Heaviside's unit function which is 0 for $x < 0$ and 1 for $x > 0$. The critical stress σ^* is found to be 12 MPa. Below 12 MPa, there is a pseudo plastic deformation from the amorphous region remote from the crystals. Above 12 MPa, the steady plastic flow will occur, duo to the yield mechanisms such as crystal slip, etc.

REFERENCES

1 Bowden, P. B. and Young, R. J., J Mater Sci 25 (1984) 57.

2 Crissman, J. M. and Zapas, L. J., J Polym Sci Polym Phys 23 (1985) 2599.

3 Lai, J. and Bakker, A., Scrip Metall Mater 28 (1993) 1447.

4 Struik, L. C. E., Physical Aging in Amorphous Polymers and Other Materials, Elsevier, Amsterdam, 1978.

5 Struik, L. C. E., Polymer 28 (1987) 1521.

6 Struik, L. C. E., Polymer 30, (1989) 799.

7 Turner, S., Polym Eng Sci 6 (1966) 306.

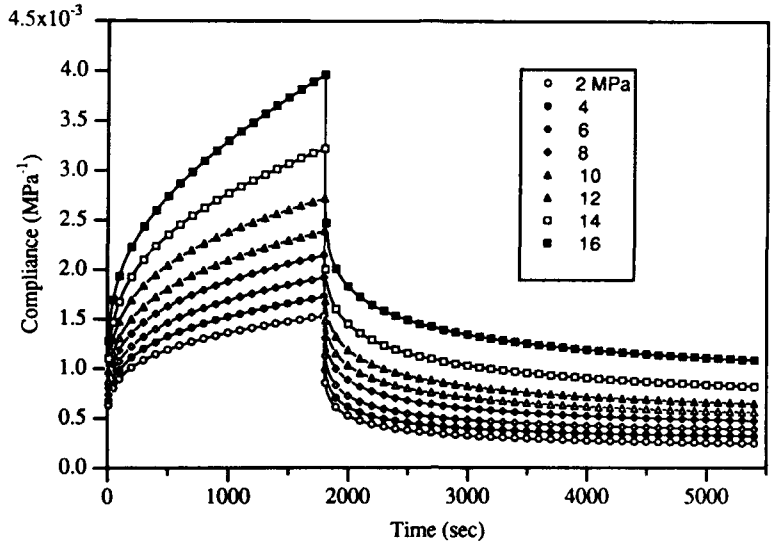

Figure 1 Experimental data of creep and recovery

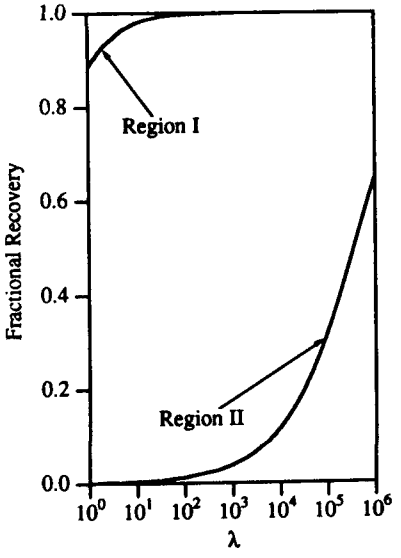

Figure 2 Recovery process

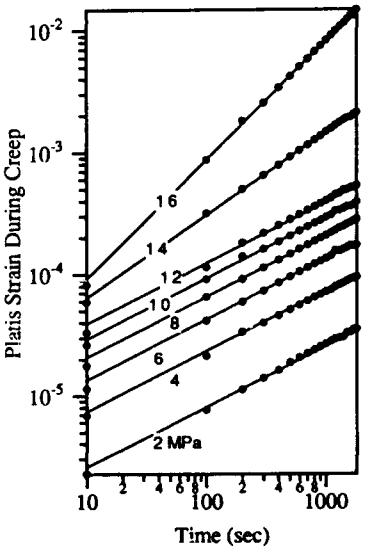

Figure 3 Plastic Strain during creep

IMPACT RESPONSE OF POLYMERIC MATERIALS IN INSTRUMENTED DROP DART TESTING

K. Takahashi and M. Tahara*

Nine kinds of engineering thermoplastics, including five PA6 alloys and two PPE alloys, are tested with an instrumented impact testing apparatus for impact strength E_{3pb} at three-point bending and that E_{pun} at puncturing. E_{3pb} and E_{pun} are correlated on a diagram, which exhibits that the materials can be divided into three groups depending on the slope of E_{pun}/E_{3pb}. The slope is examined also to check the effect of specimen thickness at the puncture testing.

INTRODUCTION

Polymer fracture under impact loading is complicated being influenced by various parameters like flow direction in material processing, temperature and strain rate at testing, specimen thickness, notch length and bluntness, specimen geometry and type of loading, etc.[1, 2] Dynamic mechanical phenomenon in an impacted specimen and a dart involve oscillation and wave propagation, which also makes it difficult to correctly evaluate impact performance of polymers. Nevertheless, industries need to determine impact strength of produced materials which is obtained mostly by Izod impact test because of its simplicity. Materials users, however, need impact performance data obtained under a condition which is closer to an actual situation for materials used. For this reason, impact strength at puncturing has become more important in many cases than the Izod strength. Thus, the correlation of impact strength evaluated by one dimensional impact test like Izod or Charpy and by three dimensional puncture test has been of concern for quality control in the production line and for practical application of polymers. It is recognized, however, to get a good correlation between them is difficult because of the complexity involved in both types of testing as stated above.[3] It seems that no intensive works in this respect have been performed yet.

In the present study, correlation is studied for impact strengths of PA alloys and other engineering thermoplastics at room temperature. Two types of instrumented impact testing were adopted, one being three-point impact bending, i. e., Charpy type test, and others impactive puncture test.

EXPERIMENTAL

Specimen materials tested are listed in Table 1. Geometries of specimens, produced by injection moulding, are shown in Fig. 1a and 1b for the three-point impact bending and the puncture test, respectively. The bend specimens were as-received from injection moulding. Notching was done by machining. The puncture specimens had thicknesses of 2 and 3 mm. For the instrumented

*Research Institute for Applied Mechnaics, Kyushu University, Kasuga-shi, 816 JAPAN

testing, a strain gauge was adhered on an inside wall of the impacting dart (see Fig. 1). Signals from the dart gauge (I) and from a strain guage at the tip of the notch of the three-point bend specimen (II) were compared to decide a frequency suitable for a low-pass filtering of a dart signal processing circuit, and 3 kHz was obtained as a result.

Figure 2 represents examples of the gauge signals from three-point impact bending and puncture tests. In the former tests, signals were likely to become more oscillatory because of much lower levels of force amplitude and of smaller time to fracture under an influence of the dynamic mechanical effects described above. Displacement l was obtained for the dart from time t using the following relationship

$$l = -\frac{1}{m}\int_0^t \int_0^t F(t)\, dt^2 + v_0\, t \qquad (1)$$

where m is mass, $F(t)$ is the gauge signal and v_0 is the impact velocity. Impact energy E was evaluated using the area encompassed by the curve $F(t)$ and the axis l. For each type of loading, impact strength was given as follows,

$$E_{3pb} = E/(B \cdot a_l) \quad \text{(three-point bend)} \qquad (2)$$

$$E_{pun} = E/B \quad \text{(puncture)} \qquad (3)$$

where B is specimen thickness and a_l is the ligament length of the Charpy specimens. To examine the effect of specimen thickness in the puncture test, E was normalized by the thickness to yield E_{pun}.

RESULTS AND DISCUSSION

Experimental results are shown in Figs. 3 and 4, in which E_{3pb} and E_{pun} are correlated for puncture specimen thickness of 3 mm and 2 mm, respectively. From Fig. 3, one may see that data points can be divided into three groups depending on specimen notch embrittlement and other natures of the impact tests. The alloys PA6/EPR and PA6/PPE/SBS/EPR exhibited good performance in the correlation diagram in that both E_{3pb} and E_{pun} are greater, while PBT and PA6 demonstrated much smaller E_{3pb} in spite of their superior performance with E_{pun}. It is noted that PA/EPR was not broken in the bend test and that PA6 was not punctured completely leaving a thin membrane after the dart was stopped by a stopper. PBT/PPE, PPE/SBS, PA6/PPE/SBS are grouped into the intermediate class which comes in between the two groups.

Effect of specimen thickness in the puncture test can be observed in Fig. 4 where results of specimens with the thickness of 2 mm are shown. By comparison with the result in Fig. 3 it is seen that E_{pun} for PA6/EPR is decreased by ca. 20 %, whereas that for PA6/PPE/SBS is increased by similar amount. If one sees the scatter of data designated by bars in Fig. 4, one may see that the changes above are meaningful. Interestingly, values of E_{pun} for other polymers stayed almost uncharged.

Results shown in Figs. 3 and 4 indicate that the diagram to correlate E_{3pb} and E_{pun} would be suitable to characterize impact fracture performance of polymers and to analize the effect of specimen thickness in the puncture test.

CONCLUSIONS

Nine kinds of engineering thermoplastics were tested with an instrumented impact testing apparatus for their three-point impact strength and puncture strength. E_{3pb} and E_{pun} are correlated for each of the specimens. Tested polymers could be divided into three groups on the correlation diagram depending on a slope E_{pun}/E_{3pb}. PA6/EPR and PA6/PPE/SBS behaved oppositely on the diagram when their thickness was decreased.

REFERENCES

1 Impact Tests and Service Performance of Thermoplastics (ed. P. I. Vincent, The Plastics Institute, 1971)
2 Impact Fracture of Polymers –Materials Science and Testing Techniques– (eds. K. Takahashi and A. F Yee, Kyushu University Press, 1992)
3 C. W. Knakal and D. R. Ireland, in *Instrumented Impact Testing of Plastics and Composite Materials*, ASTM STP 936 (1987) pp.44-57.

Table 1 Specimens tested

NO.		1	2	3	4	5	6	7	8	9
Polymer		PBT	PBT/PPE	PPE/SBS	PA6	PA6/EPR	PA6/PPE/SBS	PA6/PPE/SBS/EPR	HIPS	PPE
Thickness (mm)	3pb	4mm	4mm	4mm	4mm	4mm	4mm	4mm	3mm	3mm
	pun	3mm (NO. 1– 9) and 2mm (NO. 8, 9)								
Drop Height (m) / Mass (kg)	3pb	0. 4m (2. 8m/s) / 2.6kg								
	pun	2m (6. 3m/s) / 8kg								

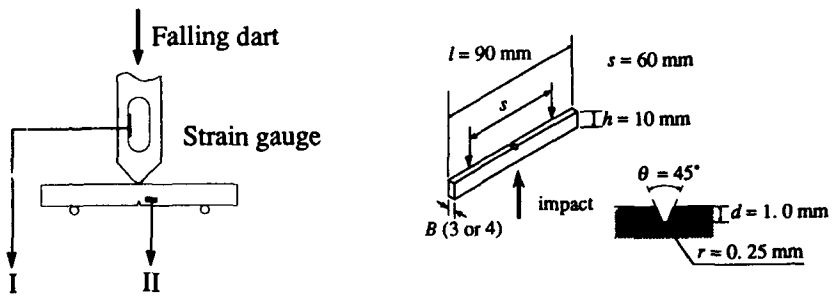

Fig. 1a Three-point bend test

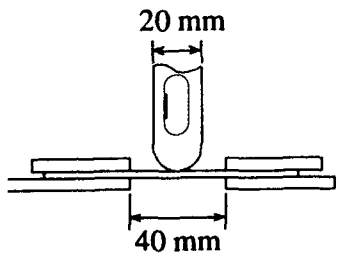

Fig. 1b Puncture test

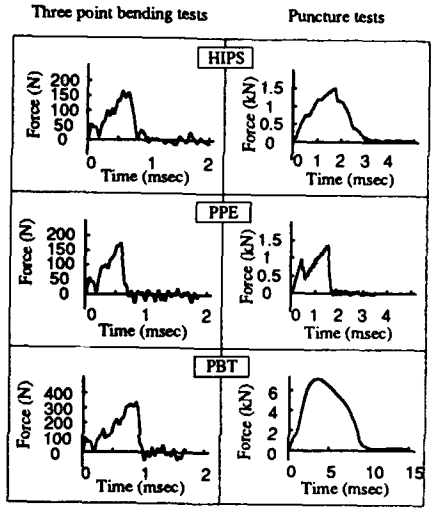

Fig.2 Examples of force-time curve

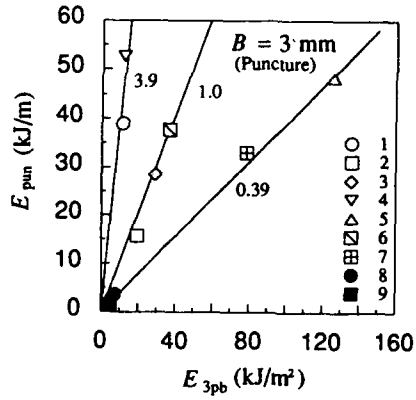

Fig. 3 Relationship between E_{3pb} and E_{pun} for puncture specimen thickness of 3mm

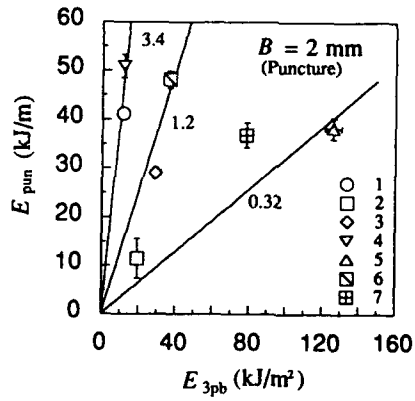

Fig. 4 Relationship between E_{3pb} and E_{pun} for puncture specimen thickness of 2mm

INFLUENCE OF SURFACE TOPOGRAPHY AND MORPHOLOGY ON IMPACT RESISTANCE OF PP-COPOLYMER STUDIED BY FALLING WEIGHT IMPACT TESTING.

K Grøstad, A Syre and T Bach*

Impact resistance of two different PP-copolymers at test specimens with four different surface topographies is studied by instrumented falling weight impact testing. By changing the surface topography, the impact behaviour of the material may vary from ductile to brittle and the impact energy is significantly changed. This phenomena has the largest effect when the topography is coarse. Steep differences of a few microns in height in the surface have little effect on the impact resistance. A material with a high impact resistance is less dependent on surface topography compared to a medium impact PP-copolymer.
Thickness variations of the morphology skin zone in the test specimens do not influence the impact resistance significantly tested by instrumented falling weight impact testing.

INTRODUCTION

PP-copolymers are frequently discussed with respect to impact properties. Our experience is that the preferable test method to predict impact performance of PP-copolymer is instrumented falling weight impact testing. Comparison of materials with this method has been quite successful. The results depend on the test parameters and the geometry of the test specimens. The force-deformation curve obtained is a unique representation of the material. Using high speed film during the impact makes it possible to describe the deformation mechanisms for each type of test parameters and material (1). A high speed film has been used to experience how to interpret the impact performance and the remaining part of the specimens tested.

Processing conditions during injection moulding of test specimens, colour and additives influence the morphology and in turn the impact resistance (2). Industrial products often have surfaces with varying surface topography. This influences the impact performance of the product similar to other effects mentioned and has to be taken into consideration when evaluating the impact resistance of a product. Some topographies cause a brittle fracture though the material itself is ductile as confirmed in this work.

EXPERIMENTAL

Two different PP-copolymers with medium and high impact properties were investigated. The test specimens were injection moulded using an Arburg Alrounder 170MCD injection moulding machine. The moulded test specimens had a thickness of 2 mm and diameter of 60 mm

* BOREALIS, Polymer Research and Development Centre, 3960 Stathelle, Norway.

with four different surface topographies;

- Engraved
- Sand blasted
- Eroded
- Polished

The injection moulding parameters except mould temperature were kept constant with a temperature of the melt of 240°C, injection velocity of 8cm³/s, holding pressure time 10s and holding pressure of 260bar. To investigate the influence of skin zone on the impact resistance, the test specimens were moulded at a mould temperature of 20°C, 40°C and 60°C.

Topography was studied by JEOL JSM-840A scanning electron microscope (SEM). Morphology was studied by polarising microscope.

An instrumented falling weight impact machine from Rosand Precision Ltd., UK, was used to perform the impact tests. The test geometry was according to ISO 6602/3 (3) with a 20mm hemispherical striker head and a mass of 25kg. The test velocity was 4.43m/s and the test specimens were clamped. Test temperatures were 23°C, 0°C an -20°C. Each side of the test specimens were tested since one of the sides had a special topography. The results are given as force as a function of deformation (figure 1). The impact energy is represented by the area of the curve.

RESULTS AND DISCUSSION

The SEM analysis show that the surface topographies differ significantly. The engraved surface has parallel stripes and is anisotropic. The stripes are quite unstructured with respect to width and depth. The largest difference between the top and bottom of the stripes is quantified to approximately 100 microns. Although the surface was rough, there were no steep sides or sharp corners. The sand blasted surface has a larger and a smoother topography compared to the eroded surface. At the eroded surface, the distance between the top and bottom is smaller and sharper. The height difference between the top and bottom was less than 25 microns in the sand blasted surface and less than 10 microns in the eroded surface. The polished surface has some unexpected hollows with a size of 3-10 microns and a depth of not more than 2-3 microns.

The results discussed in the next three sections are with the medium impact PP-copolymer and a mould temperature of 40°C.

Instrumented falling weight impact testing causes a biaxial stress over just a few milliseconds of time. The test specimens obtain the highest stresses and strains on the side opposite to the striking point. The fracture performance may vary from ductile to brittle by respectively testing on the modificated and non modificated (smooth) side of the test specimen. Figure 1 shows how sand blasted material changes in impact resistance as a function of side tested at 0°C. When the modificated surface obtain the highest stresses and strains, the impact performance becomes brittle.

Impact resistance as a function of surface topography is shown in figure 2. The difference in impact resistance is less when the striker point is on the modificated surface. The engraved surface always obtains a brittle impact behaviour and low impact energies. The sand blasted has less impact energy compared to the eroded surface when the striker point is on the opposite side to the modificated surface, and the polished surface has the highest impact energy and most ductile behaviour.

The effect of the reduction in impact resistance with different surface topographies is strongly dependent on the test temperature. The engraved surface always obtains a low impact resistance, and this is even more pronounced at low temperatures. The sand blasted, eroded and polished surfaces are quite comparable with respect to impact resistance when tested at room temperature. At lower temperature the impact energy is differently reduced when the striker hit the smooth surface, as shown in figure 2.

Testing of the high impact PP-copolymer, shows a slightly different behaviour with respect to surface topography and the effect is much smaller than for the medium impact PP-copolymer. The impact resistance is not significantly reduced even when testing at the opposite of the engraved surface when testing at 23°C. At lower test temperatures the general impact resistance of the material increases because of a higher stiffness of the material at these temperatures. The material still keeps ductile behaviour at these low temperatures. The engraved surface obtains a brittle behaviour and low impact resistance at low temperatures and the other surface modifications have no effect on the impact resistance.

The topography of the engraved surface contains no steep sides or sharp corners. From this surface topography, it was not expected that only the engraved surface obtained this very large reduction in impact resistance. The eroded surface with the sharpest topography did not show a large reduction in impact resistance compared to the polished surface. A large difference between the top and bottom of the surface topography seems to have the greatest influence on the impact resistance, even without sharp corners.

The morphology of the injection moulded specimens shows the characteristic zones; skin zone, shear zone, hold pressure zone and core zone. The surfaces with different topographies show as expected the same morphology. All the topographies show β-spherulites in the phase between the hold pressure zone and the core zone. This is probably because of strong shear deformation during the injection moulding. The thickness of the skin zone decreases with increasing mould temperature . Usually this leads to a reduction in impact resistance (2), and especially when testing falling weight impact testing where the fracture starts in the skin and shear zones. These experiments showed no effect on the impact resistance though the skin zone was measured between 1 and 10 microns.

CONCLUSION

Changing surface topography has a great effect on the impact resistance of PP-copolymers and the impact behaviour may vary from ductile to brittle. High impact PP-copolymer is less dependent on surface topography compared to a medium impact PP-copolymer.

REFERENCES

1. F.Polato, G.Paganetto, M.Bramuzzo, E.Marchetti, Deformation, Yield and Fracture of Polymers VI (1985) 84.
2. A.M.Cuhna, A.S.Pouzada, R.J.Crawford, Plastics Rubber and Composites Processing and Applications 18 (1992) 79.
3. ISO 6603/2, Determination of multiaxial impact behaviour of rigid plastics - part 2: Instrumented puncture test, 1989.

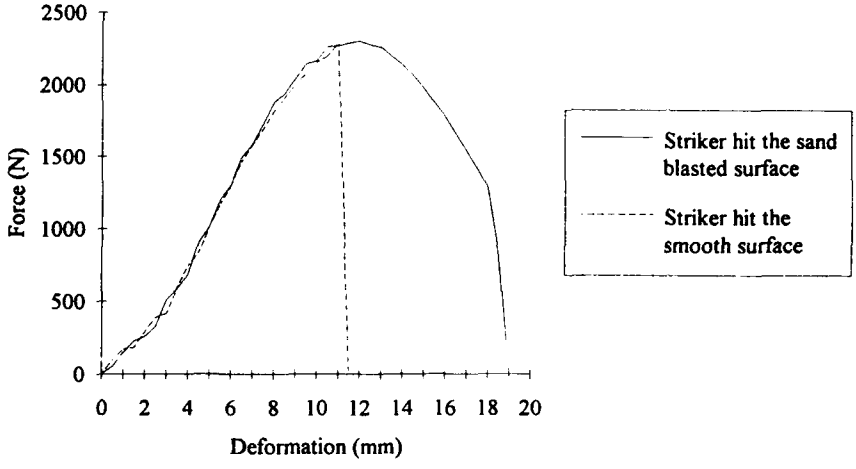

Figure 1.: Force as a function of deformation of a medium impact resistant PP-copolymer when the striker hit the sandblasted surface and the smooth surface opposite to the sand blasted surface. Test temperature 0°C.

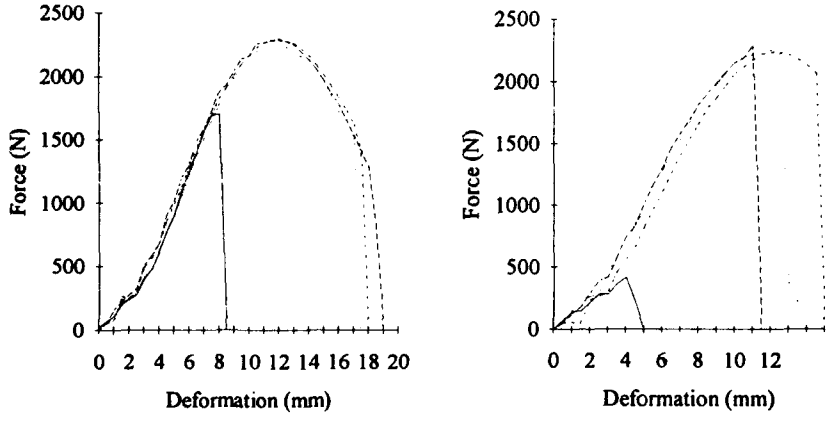

Figure 2.: a) b)
Force as a function of deformation of a medium impact PP-copolymer when a)The striker hit the modificated surface, b) the striker hit the smooth surface (non modificated surface). Test temperature 0°C. (— engraved, — — sand blasted, ---- eroded, — - — polished)

COMPARATIVE STUDY OF THE IMPACT BEHAVIOUR OF DIE-DRAWN POLYETHYLENE AND ULTRA-HIGH-MODULUS POLYETHYLENE FIBRE COMPOSITES

O.E. Darras*, R.A. Duckett*, P.J. Hine* & I.M. Ward*

Die drawn polyethylene and UHMPE/epoxy composites present some similarities in their response to a 3-point bending impact test. They are brittle when the notch is parallel to the fibre or orientation direction and present a mixed brittle-ductile behaviour in the perpendicular direction.
Using a simple parallel model the die drawn polyethylenes can be interpreted as composite with a fibre volume fraction determinated by the elastic modulus. The fracture toughness, Kc, of both kinds of "composite" is proportional to the "fibre volume fraction".

INTRODUCTION

Many authors have proposed that oriented polymers should be considered as *single phase* composites because of the inherently fibrous nature of their morphology. As the die-drawing process enables the production of oriented polymer in large solid sections, the fracture behaviour of polyethylene in the oriented state can now be studied. It has already been established that the fracture properties of die-drawn polyethylene are enormously anisotropic but there is at present no understanding of how the fracture toughness values relate to structure.

The high ductility of ultra-high-modulus polyethylene (UHMPE) fibres, together with their comparatively high strength suggest that composite materials reinforced with these fibres should offer excellent energy absorption characteristics. It is therefore interesting to compare the anisotropy of fracture toughness of these two kinds of materials.

EXPERIMENTAL

The materials. Two die drawn polyethylenes from BP Chemicals Ltd are investigated in this study with grades 002-55 and 006-60, with draw-ratios of 9.4 and 9.6 respectively.
(It was not possible to die-draw to the same draw-ratio as the fibre used in the composites.)

* IRC in Polymer Science and Technology, University of Leeds, Leeds LS2 9JT

0/90 balanced crossply laminates and unidirectional composites of two different volume fractions of fibre i.e. 53% (±3%) and 68% (±3%) were prepared with drawn-high modulus polyethylene fibres and a modified epoxy resin (see table I). Assuming the densities of the epoxy and polyethylene fibre to be 1230 and 967 kg m^{-3} respectively the volume fibre fraction was determinated from density measurements. Some composites were made in which the fibres were plasma treated to improve fibre-matrix adhesion. To achieve a constant thickness for the different composites the laminates were produced with 28 and 20 plies for the low and high fibre fractions.

Impact Testing. The impact behaviour has been investigated through the use of an instrumented falling weight impact tester in a 3-point bend configuration. The high momentum of the striker assures a constant velocity - here 1m/s during impact - so no significant deceleration occurs during penetration. The force exerted by the specimen on the striker during impact is recorded as a function of the displacement of the striker. To stay within the Linear Elastic Fracture Mechanics condition the testing protocol of the European Group on Fracture (1) was used.
A simple servo-hydraulic tester was also used, with the same geometry of sample at approximately the same velocity, which can be stopped accurately at different values of displacement of the striker. So it was possible to follow step by step the initiation and propagation of cracks in the samples.

Modulus Measurements. An ultrasonic technique was used to determine the elastic constants of the different materials. This involves measuring the velocities of ultrasonic waves propagated in various directions through the samples.

RESULTS

The results of the impact tests performed on the different kind of sample are given in Table I. Strong similarities have been found between the failure modes of the composites and the die drawn polymer.

The unidirectional composites tested with the notch direction parallel to the fibres exhibit brittle fracture. The low values of the fracture toughness of those samples ($K_{C\parallel} < 1 MPa\ m^{1/2}$) are of the same order as the epoxy resins. This suggests that the fibres do not actively reinforce the composites in this direction of testing. For the die drawn sample tested in the transverse direction, the fracture is brittle too. In this case the low value of $K_{C\parallel}$ is relevant to the weak secondary bonding between molecules. Cleavage occurs along either lamellar surfaces or planes containing polymer molecules.

For the notch direction perpendicular to the fibre or orientation direction and for the 0/90 crossply laminates, a mixed brittle-ductile fracture behaviour are observed. The samples tested at constant velocity contain small cracks parallel to the fibres and are all buckled. The curves of load versus load point displacement show some non linearity. The fracture toughness, values for this orientation, $K_{C\perp}$, is much higher, in the range 5 - 10 MPa $m^{1/2}$. In order to determine whether the

propagation of a crack or the buckling was responsible for the value of the toughness, it was necessary to know which failure mechanism appeared first. By use of the controlled displacement test it was shown that the propagation of crack along the fibres occurs before the buckling at the point of maximum load, as requied by the testing protocol.

DISCUSSION

As it is well known that composite toughness is always increased by raising the volume fraction of fibre or by using stronger fibres, we made the assumption that $K_{C_\perp}$ is directly related to the volume fraction of the reinforcing agent. In the case of the crossply laminates we assumed that only the half of fibres perpendicular to the notch are effective. With the hypothesis that the die drawn polyethylene acts as a composite during failure, a part of the fibrils plays the same role as the fibres and the remaining part of the polyethylene act as the matrix. Using a parallel model we made the further assumption that E_{33} is proportional to the volume fraction of the reinforcing agent. Assuming that the active fibril part and the fibre have nearly the same modulus we defined a "fibre volume fraction" for the die drawn polyethylene from the values of E_{33} obtained by ultrasonic measurement (see Table I). In order to check those hypothesis we draw the curve of $K_{C_\perp}$ versus the volume fraction of fibre (see Figure 1).

It can be seen that $K_{C_\perp}$ varies linearly with the volume of fibre in this range of concentration for both the untreated and plasma treated fibres. The points corresponding to the die drawn polyethylene fit rather well with the curve of the untreated fibres composites supporting our assumptions regarding this material.

To explain the high values of $K_{C_\perp}$ of this samples we have to emphasise the important part played by the fibres. High modulus polyethylene fibres are classified as tough because they are capable of extensive non-elastic deformation after yielding by plastic necking. So a bundle of such fibres possesses a large fracture energy and a substantial portion of this energy can be transferred into the composites and raises the value of $K_{C_\perp}$.

During fracture, the crack initiated at the notch tip propagates in the matrix phase and is halted by the fibres. As the load increases local stress begins to build up in the fibres which tend to contract. This initiates fibre resin debonding along the fibre in both directions away from the crack plane as clearly seen on the tested samples. Following debonding the fibres are loaded to failure in the debonded length and may break at any point within this region. At this point of the process the plastic necking of the fibre consumes an important part of the energy of deformation. After that frictional work is needed to pull out the fibre from the matrix. This can explain the lower toughness of the plasma treated fibre composites. Improving the fibre matrix bond as with a plasma treatment inhibits debonding. So it tends to reduce the region of fibre plastic necking and the pull out: the value of $K_{C_\perp}$ drops. The plastic deformed zone is more localised and in fact the crack may run through both fibres and matrix without deviation.

SYMBOLS USED

K_C = fracture toughness
E_{33} = elastic modulus along the fibre or orientation direction
$K_{C\parallel}$ = K_C with the notch parallel to the fiber or orientation direction
$K_{C\perp}$ = K_C with the notch perpendicular to the fiber or orientation direction

REFERENCE

1 Williams, J.G. and Cawood, M.J., Polymer Testing 9 (1990) 15

	Composites								Die drawn polyethylene	
	Unidirectional				Cross-Ply 0/90				002 55	006 60
	Untreated		Plasma Treated		Untreated		Plasma Treated			
E_{33} (GPa)	36.0	55.8	32.4	53.0					18.1	24.1
Fibre content (%)	56	67	51	66	54	70	50	69	46	49
$K_{C\perp}$ (MPa $m^{1/2}$)	8.07	9.18	5.27	5.75	4.97	5.78	4.57	4.97	6.61	7.56
$K_{C\parallel}$ (MPa $m^{1/2}$)	0.83	0.87	0.75	0.29	4.97	5.78	4.57	4.97	0.37	0.18

Table I : Results from impact test and ultrasonic modulus measurement

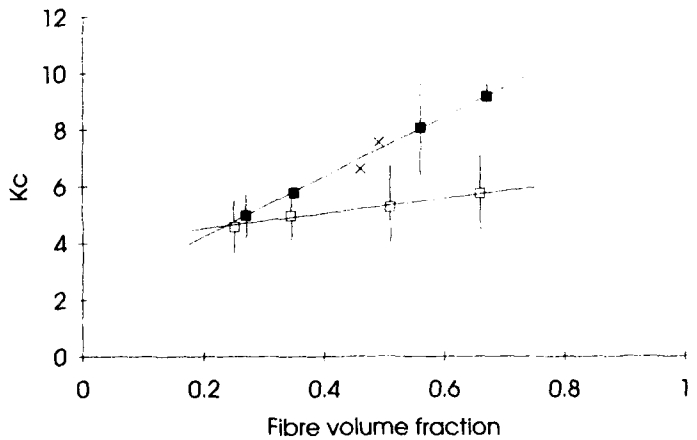

Figure 1 : Variation of K_C (MPa $m^{1/2}$) with the volume fraction of fibre (▪ untreated fibre, ▫ plasma treated fibre and x die drawn polyethylene)

PHASE SEGREGATION AND TOUGHNESS IN LINEAR LOW DENSITY POLYETHYLENE

A.D. Channell, E.Q. Clutton and G. Capaccio*

The impact fracture toughness of three linear low density polyethylenes has been critically assessed. Each material had differing volume fractions of the segregated "rubbery" phase, from 0 to 7%, but similar crystallinity and weight average molecular weight. Total toughness was separated into its component mechanisms using an instrumented impact facility. Previous suggestions of a rubber toughening mechanism in crack initiation in LLDPE were not confirmed. In particular, there was no influence of the "rubbery" phase on the plane strain fracture toughness. However, this phase was found to be responsible for some enhancement of crack propagation energy.

INTRODUCTION

High values of plane strain fracture toughness have been measured (1,2) for linear low density polyethylene (LLDPE). These high levels of toughness have been ascribed to a segregated "rubbery" phase which has been identified by Mirabella et al [3], the presence of which is due to the non uniform branch distribution in these materials. This paper addresses the issue of the supposed rubber-toughening mechanism in LLDPE using instrumented Charpy impact techniques developed in this laboratory. The methodology employed involves the partitioning of the fracture event into the different contributing elements.

EXPERIMENTAL

The materials selected for this study had similar weight average molecular weight (130 000 - 150 000) and density, but a systematic variation in volume fraction of segregated phase from 0% (Sample A) to 1% (Sample B) and 7% (Sample C), as measured by transmission electron microscopy.

RESULTS AND DISCUSSION

Total toughness G_t, i.e. the total energy absorbed during the impact event, varies with test velocity. A comparison at 1 m/s is shown in Table I for all three materials. Material C has the

*BP Chemicals Limited, Research and Development Centre,
P.O. Box 21, Grangemouth FK3 9XH, United Kingdom.

Table I Fracture toughness parameters: Total toughness (G_t) initiation toughness (G_p) and shear lips toughness (G_t - G_p). All values at 1 m/s.

Material	G_t (kJ/m^2)	G_n (kJ/m^2)	G_t - G_n (kJ/m^2)
A	24	18	6
B	19	10	9
C	36	13	23

highest G_t. The difference between **A** and **B**, however, cannot be explained in terms of the different concentration of segregated phase. A more detailed insight into the fracture process can be gained through the partitioning of G_t (Figure 1).

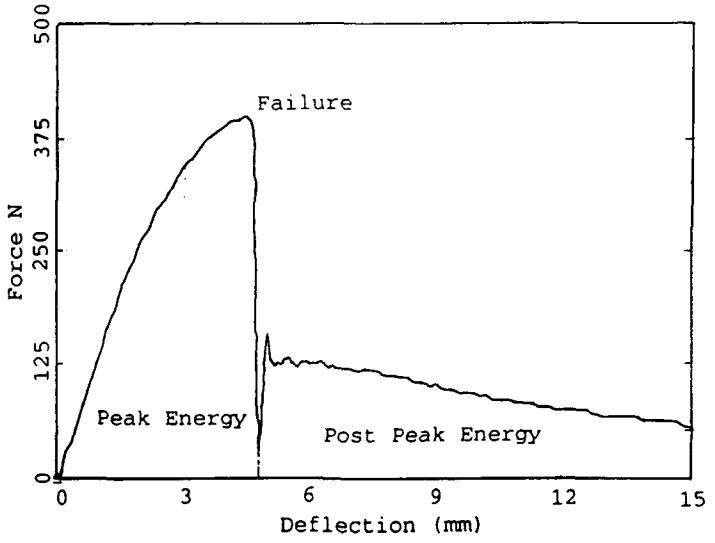

Figure 1 Typical force-displacement curve at impact rate for LLDPE specimens.

The energy required to initiate a crack (normally corresponding to the peak position in Figure 1) is dissipated in two mechanisms. Firstly, the stored strain energy to create new surfaces, referred to as the **intrinsic toughness**. Secondly, craze growth at the root of the notch [5]. Initiation toughness (Gp) varies with test velocity and shows no correlation (Table I) with the volume fraction of segregated phases. In fact material **A**, without any segregated phase, gives the best performance.

A plot of Gp versus craze length r, is shown in Figure 2. Extrapolation of these data to zero craze length provides a value for the intrinsic toughness, $G_{0,}$ which is the same for all three materials, i.e. 6 ± 0.3 kJ/m2.

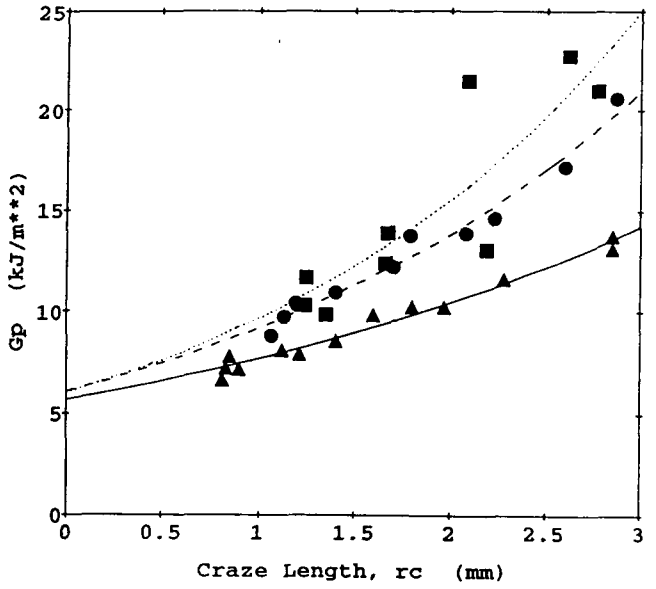

Figure 2 Crack initiation energy (G_p) vs. craze length for different materials: ( )A, ( )B and ( )C.

The slopes of the curves in Figure 2 reflect the difficult ability of the materials to absorb energy in the craze. It seems that the segregated phase in LLDPE has a detrimental effect. It is proposed that this is because the single crazes which form are significantly larger than the domains of segregated phase (~0.2μm) and the latter may become easily incorporated into the craze fibril structure, causing it to be weakened.

The impact energy absorbed after crack initiation ,r post peak energy (G_t - G_p), is consumed in the formation of the shear lips which lead to the arrest of the propagating crack. The values of (G_t - G_p) at 1 m / s are shown in Table I. These rank the materials in the order C, B, and A: The higher the concentration of segregated phase, the higher the the value of (G_t-G_p).

A significant finding of this work is that although the three materials have similar energy absorbing capacity, the size of the shear lips is affected by the segregated phase which promotes deformation over a larger volume.

In summary, no effect of the segregated phase was found on intrinsic toughness G_0. A possibly adverse effect of the segregated phase on the plane strain crazing performance G_p. was detected. However, a positive effect on ductile performance was discovered, which can only be utilised where full shear lips can be developed, i.e. in sections thicker than the shear lips.

REFERENCES

1. Hashemi, S. and Williams, J.G., Polymer, 1986, **27**, 384.

2. Channell, A.D., and Clutton,E.Q., Polymer, 1992, **33**, 4108.

3. Mirabella, F.M., Westphal, S.P., Fernando, P.L., Ford, E.A. and Williams, J.G. J. Polym. Sci., Polym. Phys. Edn. 1988, **26**, 1995.

4. Wilfong, D.L., and Knight, G.W., J.Polym. Sci., Polym. Phys. Edn., 1990, **28**, 861

5. Hemingway, A.J., Channell, A.d., and Clutton, E.Q., Plastics Rubber and Comp. Process. Appl. 1992, **17**, 147

PREDICTION AND ORIGIN OF THE ENVIRONMENTAL STRESS CRACK RESISTANCE OF TOUGH POLYETHYLENE.

L.J. Rose, A.D. Channell, C.J. Frye and G. Capaccio*

It has been shown that a good correlation exists between a single creep parameter and slow crack growth. The existence of such a correlation supports a model in which crack growth is primarily controlled by the creep of fibrils spanning the craze zone. The limit of improvement achievable by increasing molecular weight and the greater effectiveness of short chain branching to improve fibril creep have been highlighted. The effect of density in homopolymers prepared under various cooling conditions, exemplifies a special case in which both yield and creep processes must be considered to interpret slow crack growth performance.

INTRODUCTION

Slow crack growth is an important failure mechanism in polyethylene, relating for instance to environmental stress cracking (ESC). Over the past decade this penomenon has been studied extensively by Brown and co-workers [1-4]. Several processes contribute to and determine crack initiation and growth: yield, yield propagation and drawing are associated with the conversion of isotropic material into highly oriented fibrils; the fibrils in turn, undergo creep deformation and eventually rupture. Whilst the phenomenology of the failure process has been satisfactorily elicidated, a quantitative knowledge of the mechanisms involved is still lacking.

Preliminary results reported by Cawood et al.[5] indicated that the time to initiate a crack may well be controlled by the creep rupture of the fibrils which develop in the crazed zone. This remarkable result would imply a completely new perspective on the study of the failure phenomenon, i.e. the prediction of fracture performance by means of a non fracture parameter. Reported here is an appraisal of the link between crack growth and creep for a comprehensive series of materials, both homopolymers and copolymers.

* BP Chemicals Limited, Research and Development Centre, PO Box 21, Grangemouth, FK3 9XH, United Kingdom.

EXPERIMENTAL

The homopolymers (HP samples) used in this study had M_w's in the range 130,000 - 1.5 x 10^6. The Copolymers used had either Ethyl or Butyl branches with a concentration of up to 5/1000°C. The preparation of the oriented samples, details of the creep test and of the stress crack measurements have been given elsewhere[5].

RESULTS AND DISCUSSION

Plots of creep rate vs. draw ratio (modified Sherby-Dorn plots) are shown in Figure 1. Data of this kind were obtained for all the materials examined, but for clarity, only a selection is shown here. In the majority of cases, the differentiation between short term and long term response is clearly visible as a division of the curves into two regimes of high and low creep rate, respectively. The long term element is significant in the present context. The absolute value of the gradient of the long term component of the curves in Figure 1 will be referred to as the **Creep Rate Decleration Factor (CRDF).**

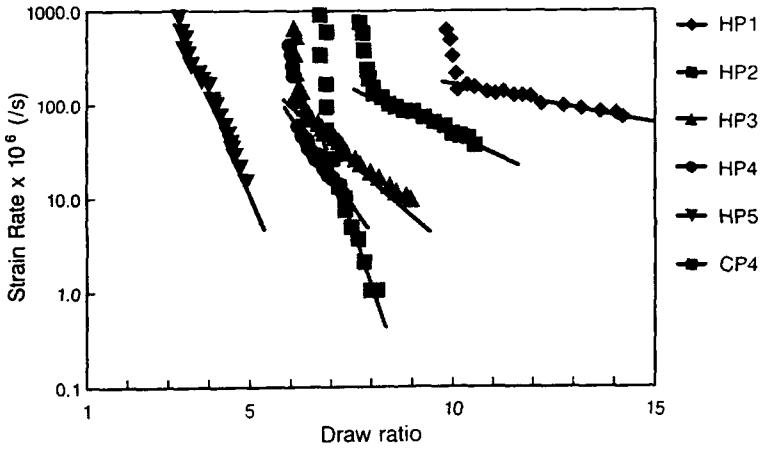

Figure 1 Strain-rate vs. draw ratio plots (derived from creep experiments) for a series of homopolymers (HP) and copolymers) (CP).

Figure 2 shows a plot of Bottle Stress Crack (BSC) performance vs. CRDF. The correlation is astonishingly good. The results for a wide range of materials of very different molecular weight distribution, as well as type and concentration of branching, fall within a very narrow band. The BSC / CRDF correlation suggests that there is a negligible contribution from the yield process in the cases examined. However, all the samples represented had undergone a similar thermal treatment. To probe the role of yielding further, a specific experiment was devised in which the yield stress of the sample was varied at constant molecular weight by variying thermal history.

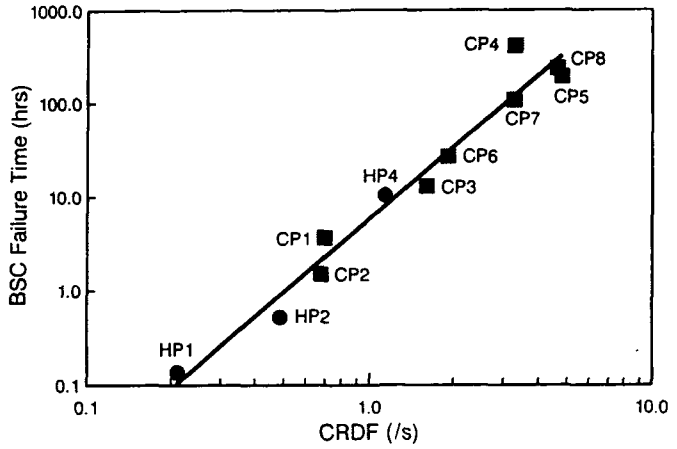

Figure 2 Correlation between Bottle Stress Crack (BSC) failure time at 80°C and the Creep Rate Deceleration Factor (CRDF).

In this case stress crack performance improves with increasing density. This improvement. however, cannot be predicted on the basis of the CRDF values. One way of rationalising the results in the special case of a single material subjected to different thermal treatments, is to invoke the increase in yield stress, and the effect this has on craze zone growth, as the controlling factor. When comparing different materials, on the other hand, molecular weight is a variable and it affects yield stress and creep response in the opposite way. With increasing molecular weight, the rate of creep slows down, giving higher values of CRDF, while the equilibrium crystallinity decreases, resulting in lower yield stresses. In other words, whenever high yield stresses are achieved by decreasing molecular weight, any beneficial effect may be offset by a higher creep rate.

CONCLUSIONS

It has been shown for a wide range of homopolymers and copolymers that the creep rate of drawn specimens correlates with their behaviour in ESCR tests. Such a correlation suggests that fibril creep makes an important contribution to governing crack initiation and growth. The improvement in ESC performance of homopolymers with increased molecular weight relates directly to the enhanced creep resistance of the craze fibrils.

In the specific case of a single material subjected to different thermal treatments, differences in yield stress may contribute more strongly to slow crack growth than creep.

The results presented lay a foundation for a new experimental approach to the understanding of slow crack growth in PE, and the associated phenomenon of environmental stress cracking. The partitioning of the complex fracture phenomenon into a number of fundamental physical processes, yielding, yield propagation, creep of fibrils and their ultimate fracture should provide a deeper understanding of the failure process and enable the influence of molecular structure to be more readily accessed.

References

1. Lu, X., Wang, X., and Brown, N., J. Mater. Sci., 1988, **23**, 643

2. Ward, A.L., Lu, X. and Brown, N., Polym. Eng. and Sci., 1990, **30**, 1175

3. Huang, Y. and Brown, N. J. Polymer Sci. Part B: Polymer Phys., 1990, **28**, 2007

4. Brown, N., Lu, X., Huang, Y.L. and Qian, R., Makromol. Chem., Macromol. Symp. 1991, **41**, 55

5. Cawood, M.J., Channell, A.D., and Capaccio G. Polymer 1993, **34**, 423

BEHAVIOUR OF POLYMERS UNDER CYCLIC FATIGUE WITH REST PERIOD

F. Baltenneck*, J.P. Trotignon*, J. Verdu *

Interrupted flexural fatigue tests on polystyrene samples were compared to continuous ones in order to appreciate the eventual effect of relaxation processes on crack initiation. It appears that the total sample fatigue lifetime can be seven times longer in interruputed than in "one-shot" tests at T>75°C. It is hypothesized that relaxation could favour crack blunting.

INTRODUCTION

In most of the cases, the flexural fatigue of unnotched samples of glassy polymeric materials displays an "induction" period during which there is no measurable change of the macroscopic properties (compliance, damping) of the material.
A possible explanation of this peculiar behaviour consists to assume that loading involves a reversible structural change (for instance build-up of thermodynamically disfavoured conformations) . Crack initiation would then result from the fact that "defects" are accumulated until a threshold concentration where cracking is initiated.

In order to check this hypothesis, it seemed to us interesting to made discontinuous fatigue tests (DFT) where periodical interruptions of loading would favour relaxation and then increase the number of cycles to rupture.

EXPERIMENTAL

The material was a radical polymerized (atactic) amorphous polystyrene (Lacqrene medium grade from ATOCHEM). Samples for tensile testing according to ISO-1 were made by injection molding.
Fatigue tests were carried out on a laboratory made flexural fatigue machine equipped with a thermostated chamber. The loading mode was symmetrical, with constant strain (e=+/-0.55%). The frequency was 10Hz. Tests were made at various temperatures from 20°C up to T_g (105°C).
One-shot fatigue tests (OST) were first performed in order to determine the fatigue lifetime expressed in terms of number No of cycles at rupture. For all DFT (figure 1), loading periods correspond to $N_0/2$. For one DFT, rest time (t_R) is kept constant. The test finishes with the sample failure, or at the decay of strength caused by hysteretic heating. Total fatigue lifetime (N_t : total number of cycles at failure) is defined as the sum of all fatigue periods.

* LTVP , ENSAM Paris , 151 bd de l'Hôpital , 75013 PARIS - FRANCE

RESULTS

Total cycle number versus rest time

For temperatures under 75°C, rest periods have no incidence on fatigue lifetime (figure 2). The total fatigue lifetime N_t is equal to N_0. . For temperatures over 75°C, N_t increased with rest time until 5 minutes. Over 5 minutes rest-time, N_t remains constant (and maximum): N_f (figure 2). Thus, we have :

$0 < t_R < 5$ min $\quad N_0 < N_t < N_f$

$t_R > 5$ min, $\quad N_t = N_f$

For each temperature, N_f is normalised by dividing it by N_0. Then, results are shown on figure 2. Fatigue lifetimes are noticeably improved : At 90°C, fatigue lifetime (for DFT) is 7 times longer than for OST.

In order to get an empirical law, we represented $\log(N_f/N_0)$ versus 1/T (figure 3). Between 75°C and about 100°C, experimental values seem to fit the Arrhenius law.

Microscopic observations

Microscopic observations reveal that :
-On failure surface sample, for T<75°C, two crack initiation sites are observed (that means one for each of the two fatigue sequences)
-Crack propagation begins in a discontinuous way until a threshold at which it accelerates suddenly to give brittle fracture.

-Fringes can be observed in the crack surface. They can be clearly associated to the loading periodicity.

-The role of rest period would be to induce crack blunting and thus, to increase the critical crack length above which dramatical propagation is observed.

-The number of cracks increases with the number of rest periods in a given fatigue test, which seems to indicate that crack blunting during a rest period favours new crack nucleation during the following loading period.

The onset of the increase of the total number of fatigue cycles, in comparison with the OST cycles number seems to be related to the onset of molecular relaxation, corresponding to T_β, which is the first secondary relaxation temperature (80°C for polystyrene), according to McCrum and coworkers (1) and Matsushige & al. (2).

REFERENCES

1 N.G. McCrum, B.E. Read, and G. Williams, Anelastic and Dielectric Effects in Polymeric Solids, Wiley, New York, 1967

2 K. Matsushige, S.V. Radcliff, and E. Baer, J. Appl. Polym. Sc., 20, 1853 (1976)

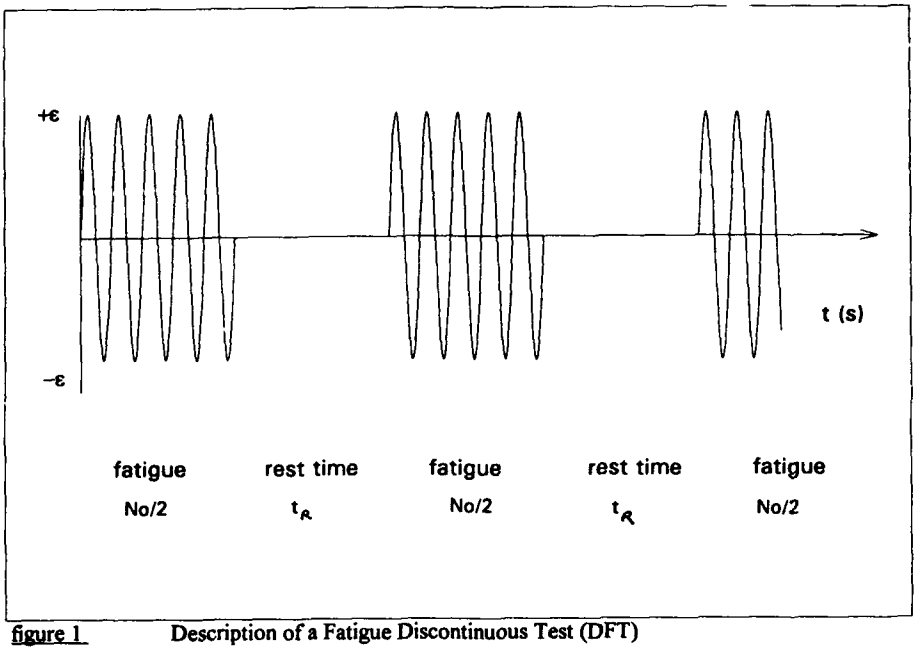

figure 1 Description of a Fatigue Discontinuous Test (DFT)

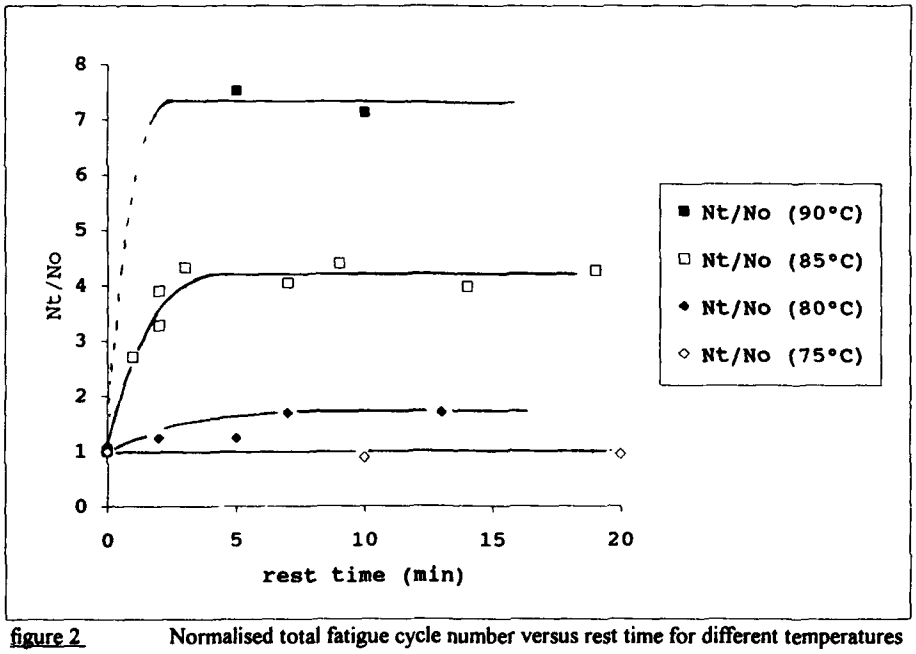

figure 2 Normalised total fatigue cycle number versus rest time for different temperatures

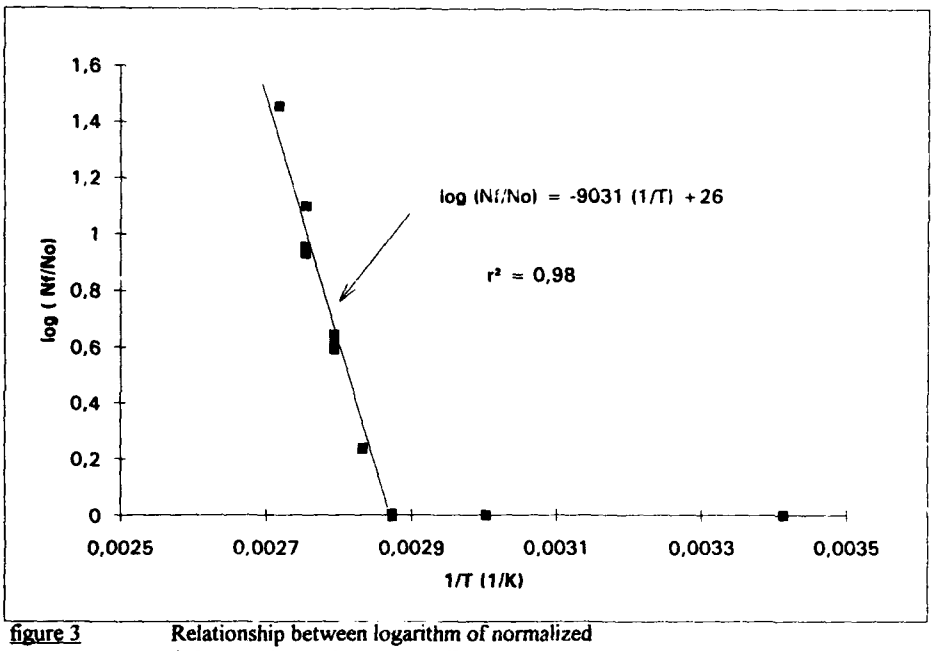

figure 3 Relationship between logarithm of normalized fatigue cycle number versus 1/T

figure 4 SEM fractography of a sample under discontinuous fatigue test (DFT)

IMPACT BEHAVIOR OF POLYPROPYLENE RUBBER BLENDS

A. van der WAL and R.J. Gaymans*

PP-EPDM extrusion blends are made with a rubber particle size of 0.2-0.3 μm. On these materials are studied the notched izod as function of temperature, the notched tensile as function of test speed and the structure of the deformation zone. PP can be toughend with EPDM to very high impact values (50 kJ/m2). The brittle to tough transition decreases strongly with increasing rubber cencentration. The notched tensile data reveal two brittle tough transitions one at low test rates and also one at high test rates. This suggest that at high test rates an other deformation mechanism is operative. The structure of the deformation zone suggest that at high deformation rates a melt blunting process is taking place.

INTRODUCTION

Notched Polypropylene (PP) samples fractures under impact brittle. The impact strength increases with temperature and PP becomes tough at 80° to 140°C (fig 1).

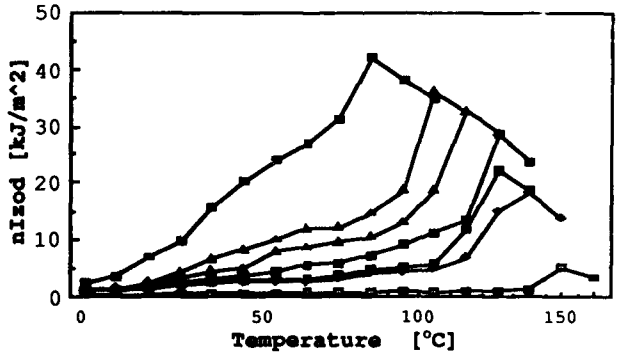

Figure 1 Notched Izod versus temperature of Polypropylene with varying MFI: ■ 0.35, ▲ 1.3, ▲ 2.8, ■ 7, ■ 13, ◆ 20, ■ 40

A strong effect has the molecular weight (MFI) on the impact strength this both in the brittle region as on the brittle to tough transition (BT). The fall in impact strength above the BT transition temperature is due to incomplete fracture of the samples.

PP can be toughened by rubber modification (1-9). Above the Tg of the PP but still in the brittle

* University of Twente, P O Box 217, 7500 AE Enschede, The Netherlands

region a linear increase in toughness with rubber concentration is observed. A lowering of the BT transition temperature both with increasing rubber concentration and decreasing particle size have been observed (6,8). Xie Wu (8) described the BT transition as a transition from multiple crazing to shear yielding. For Polyamide (PA) blends the BT transition has been described as a transition from a unstable to a stable crack propagation (10).
We study the deformation process of PP / EPDM extrusion blends and paid particular attention to the BT transition.

EXPERIMENTAL

Blends were obtained by extrusion blending of PP (Vestolen P9000 with a MFI of 0.35 and Stamylan P 13 E10 with a MFI of 1.0) and EPDM (Keltan 320 and 520). Notched tensile impact (NTI) test were carried out on a Schenck VHS hydraulic tester (11,12). A clamp speed of 1 m/s in the NTI is comparable to the speeds in the notched Izod test.

RESULTS AND DISCUSSION

Rubber concentration

The influence of rubber concentration at nearly constant particle size (0.2 - 0.3 μm) shows a strong shift in the BT transition temperature (fig. 2a).

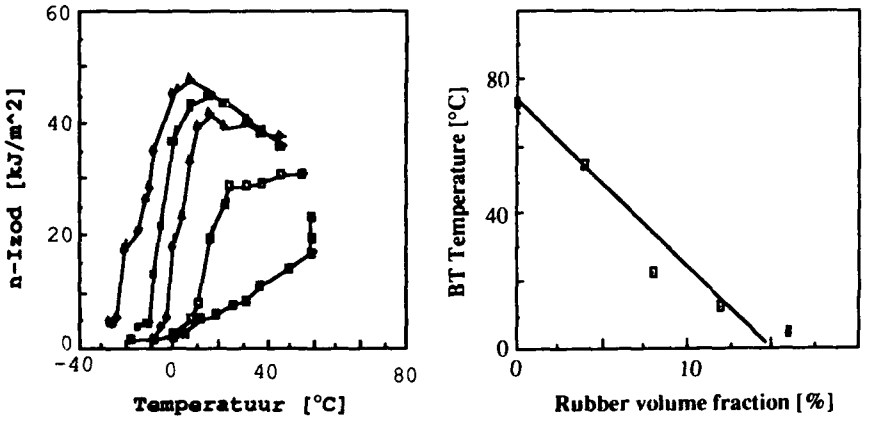

Figure 2 Influence of rubber concentration (%): ■ 0, ■ 5, ◆ 10, ■ 15, ◆ 20

The notched izod values below the BT transition are rather low 2-5 kJ/m^2. The impact values in the tough region seem to depend on the rubber concentration. A problem is that these tough samples are not fully broken. The Izod hammer slips over the samples. This is stronger at higher temperatures (lower moduli of the samples). The 20% blend is already quite tough at -15°C which is below the T_g of the PP (0°C).

The BT temperature decreases gradually with rubber concentration (fig.2b).
This behavior is similar to what has been observed with the polyamide (PA) rubber blends (10).

Influence of test speed

With a notched tensile test the influence of test speed on the fracture toughness was studied and this at several temperatures for samples with varying in particle size. For studying the crack propagation the propagation energy was calculated (11,12). In figure 3 the propagation energy as function of test speed measured at 40°C is given.

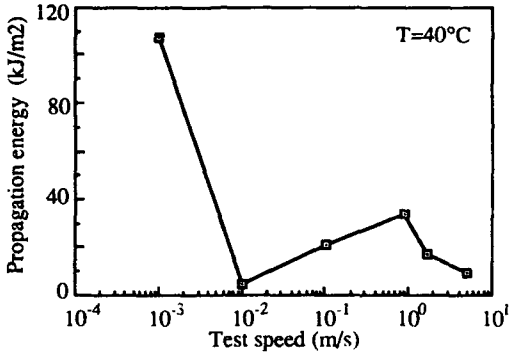

Figure 3 Influencetest speed on propagation energy in NTI-test PP-EPDM (90/10)

A low test speed (10^{-3} m/s) the PP/EPDM blend is tough. At an increased test speed (10^{-2} m/s) the material fractures brittle. Surprisingly at higher test speeds the propagation energy increases again, but at 5 m/s the material fractures brittle again. This unexpected behavior has also been found in PA/rubber blends (11, 12, 13). The fact that a material can become twice brittle suggest that there are two BT transitions. One transition at low speeds and one at high speeds.

Fracture graphics

The structure of the deformed material perpendicular to the fracture surface is studied with SEM. Of a sample broken tough at 1 m/s with the NTI method next to the fracture surface a 10-40 µm thick zone can be observed with only a few round cavities, also a zone (100-200 µm thick) with strongly deformed cavities and a zone 1-2 mm thick with round cavities (figure 4). A similar structure can be observed on samples broken with the notched izod method.
On a sample broken tough at 10^{-3} m/s next to the fracture surface a zone with strongly deformed cavities can be seen and next to that a zone with round cavities thick. The zone without cavities next to the fracture surface on the high speed tested samples are now not observed. A similar structure formation is observed in PA/rubber blends (11,13,14). The zone next to the fracture surface without cavities has been explained as a relaxed layer. During strong deformation under adiabatic conditions the temperature can rises to above the melt and relaxation of the deformed structure can take place. A melt layer in front of a notch, blunts the notch. So the layer without cavities next to the fracture surface suggest that a melt blunting process has taken place.

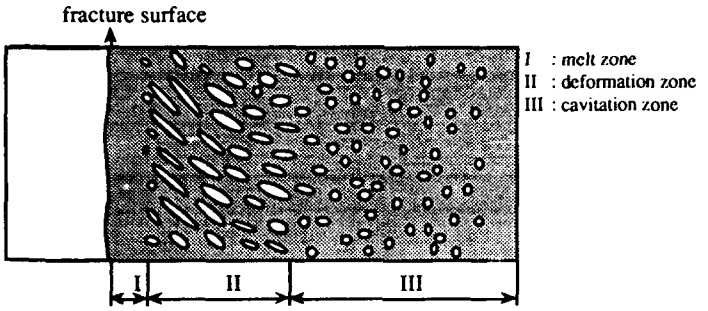

Figure 4 a cartoon of a deformed layer perpendicular to the fracture surface, of a sample fractured tough at 1m/s

CONCLUSIONS

PP is notched brittle at room temperature but becomes tough at a higher temperature. The BT transition is dependent on the MFI of the polymer.
PP/blends show a BT transition too and the BT transition temperature decreases with increasing rubber concentration. From the NTI test it is clear that the PP/blends not only have a BT transition in the high speed region but also a separate one in the low speed region.
The non cavitated layer next to the fracture plane suggests that the high speed BT transition is accompanied with a melt blunting process.

REFERENCES

1 H.K. Asar, M.B. Rhodes and R. Salovey, In Adv. in Chemistry vol 176, "Multi phase polymers", Editors S.L. Cooper and G.M. Estes, ACS, Washington (1979).
2 F. Coppela, R. Greco, G. Raggosta, J. Mat. Sci, **15**, 258 (1980)
3 K.C. Dao, Polymer, **25**, 1527 (1984)
4 J. Karger-Kocsis, Kunststoffe, **74**, 104 (1984)
5 B.Z. Jang, D.R. Ulmann, J.B.Van der Sande, Polym. Eng. Sci., **25**, 643 (1985)
6 C.J Chou, K. Vijayan, D. Kirby, A. Hiltner and E. Bear, J. Mat Sci., **23**, 2521 (1988)
7 C.J Chou, K. Vijayan, D. Kirby, A. Hiltner and E. Bear, J. Mat Sci., **23**, 2533 (1988)
8 Wu, Xie, Zhu, X. Qi, Z., International conference on deformation yield and fracture, Cambridge, April 1991
9 D'Orazio, L., Mancarella, C., Martucelli, E., Polym. Eng. Sci. **32**, 1186, 1991
10 R.J.M. Borggreve, R.J. Gaymans, J. Schuijer and J.F. Ingen Housz, Polymer, **28**, 1489 (1987)
11 K. Dijkstra, PhD Thesis, University of Twente, The Netherlands, February 1993
12 K. Dijkstra, J. ter Laak and R.J. Gaymans, PA 6 Rubber blends, Part 6, Polymer in press
13 R.J. Gaymans and K. Dijkstra, MI Conference; Deformation and Fracture of Polymers, Cambridge April 1994, preprints paper 4
14 A.J. Oostenbrink, K. Dijkstra, A. van der Wal and R.J. Gaymans, PRI Conference; Deformation and Fracture of Polymers, Cambridge April 1991, preprints 50

MECHANICS MODELING OF DEFORMATION AND FRACTURE OF RUBBER-TOUGHENED PLASTICS

J Pan*, H-Y Jeong* and AF Yee‡

A set of macroscopic constitutive laws including a macroscopic yield function and a plastic potential is presented for rubber-modified plastics to take into account the small load-carrying capacity of the rubber particles as well as the pressure-sensitivity and non-normality plastic flow of the plastics matrix. This set of constitutive laws is used to investigate the stress and deformation field near a blunting tip under plane strain, small-scale yielding conditions by finite element methods. The computational results of the shapes and sizes of the cavitation zone and shear plastic zone near the crack tip agree well with experimental observations.

INTRODUCTION

In contrast to the pressure-insensitive yielding assumption in classical plasticity theories, pressure-sensitive yielding has been observed for dense metals, polymers and transformation-toughened ceramics. Pressure-sensitive yielding has been approximately described by Coulomb's yield criterion, where yielding is dependent on a linear combination of the effective shear stress and the hydrostatic stress (Drucker and Prager, 1952). The use of Coulomb's yield criterion is intended to model the intrinsic material flow behavior in metals and polymers, and to model effects of phase transformation in ceramics. On the other hand, inclusions, microvoids or microcracks also result in macroscopically pressure-sensitive yielding. For example, Gurson (1975, 1977) proposed a macroscopic pressure-sensitive yield criterion for porous materials in which the matrices are modeled by the *pressure-insensitive* von Mises yield criterion.

In the plastics industry, it has been known for years that the addition of rubber particles significantly increases the fracture toughness of plastics. The load-carrying capacity of the rubber particles is relatively small when compared to that of the neighboring matrix. Therefore the load-carrying capacity of the rubber particles may be neglected and the volume occupied by the rubber particles can be regarded as the volume of voids in rubber-modified plastics. Based on this viewpoint, Lazzeri and Bucknall (1993) generalized Gurson's yield function to include the pressure sensitivity of the matrix in a porous solid and analyzed the effect of pressure sensitivity on the formation of cavitated shear band (dilatational band) in rubber-modified plastics. We are interested in modeling the constitutive behavior of rubber-modified plastics at large plastic deformations so that the stress and deformation field near the tips of cracks can be simulated by finite element methods.

The plastic zone sizes and shapes near the tips of cracks in pressure-sensitive materials have been studied by Dong and Pan (1990) based on Coulomb's yield criterion. The general effect of the pressure sensitivity under plane strain conditions is to shift the plastic deformation to the front of the crack tip. In rubber-toughened plastics, the cavitation zone and the shear yielding zone under plane strain conditions are also located in front of the tip of a crack (Parker et al., 1990; Pearson and Yee, 1991). Since the pressure sensitivity of the plastics is limited, it is reasonable to speculate that the extensive shear plastic deformation ahead of the tip comes from the additional macroscopic pressure sensitivity due to the small

*Dept. of Mechanical Engineering and Applied Mechanics, ‡Dept. of Materials Science and Engineering, U. of Michigan, Ann Arbor, MI 48109. USA

load-carrying capacity of cavitated particles. In order to use finite element methods to model the observed experimental results on the plastic zone size and shape near a crack tip and to further understand the deformation mechanisms near a blunted crack tip or notch tip, we first formulate a set of macroscopic constitutive relations for rubber-modified plastics. This set of constitutive laws takes account of the small load-carrying capacity of rubber particles and can easily be implemented into a finite element code. It is employed here to investigate the stress and deformation field near a blunted crack tip in a rubber-modified epoxy. The computational results of the sizes and shapes of the cavitation zone and the shear yielding zone for a crack under mode I, plane strain, small-scale yielding conditions are obtained and compared with the experimental results (Jeong, 1992).

A MACROSCOPIC CONSTITUTIVE LAW

We assume that the shear yielding of the matrices along with the cavitated rubber particles in rubber-modified plastics should be mainly responsible for the macroscopic plastic constitutive behavior. Because of the small load-carrying capacity of the rubber particles, we treat the volume fraction occupied by the rubber particles as the void volume fraction. It is well known that Coulomb's yield criterion can be used to model the plastic behavior of plastics. Coulomb's yield criterion can be written as

$$\tau_e + \mu\sigma_m = \tau_o \tag{1}$$

where τ_e is the shear effective stress, μ is a pressure sensitivity parameter, σ_m is the mean stress, and τ_o is the generalized shear effective stress.

We follow the spirit of Gurson (1975, 1977) and propose a macroscopic yield criterion for porous solids with pressure-sensitive matrices modeled by Coulomb's yield criterion. Our modification of Gurson's yield criterion for taking into account the pressure sensitivity of the matrix is based on the solution of the hydrostatic yield stress for a spherical thick-walled shell. It should be noted that it is not uncommon for the volume fraction of the rubber particles to go up to 20% or more in these rubber-modified plastics. Therefore, we adopt a voided cube model to take into account the interaction of voids at large void volume fractions and use finite element methods to compute the macroscopic stresses causing massive plastic deformation of the cube under various multiaxial loading conditions, with the matrix being modeled as an elastic-perfectly plastic material. The yield criterion that fits the finite element results (Jeong, 1992) is

$$\Phi = \left(\frac{\Sigma_e + \mu'\Sigma_m}{\sigma_o}\right)^2 + 2q_1 f \cosh\left[q_2 \frac{3+\mu'}{2\mu'} \ln\left(1 - \mu'\frac{\Sigma_m}{\sigma_o}\right)\right] - 1 - q_3 f^2 = 0 \tag{2}$$

Here Σ_e is the macroscopic tensile effective stress, μ' equals $\sqrt{3}\mu$ of the matrix, Σ_m is the macroscopic mean stress, σ_o is the generalized tensile effective stress of the matrix, and f the void volume fraction. We include three parameter $q_1 = 1.35$, $q_2 = 0.95$, and $q_3 = 1.35$ for fitting the finite element results of the voided cube model.

Experimental results for several steels and polymers (Spitzig et al., 1975, 1976; Spitzig and Richmond, 1979) show much less plastic volume increases than those predicted by the normality flow rule. Therefore, we also model the plastic non-normality of the pressure-sensitive matrix by a plastic potential function. We employ the elastic relation between the elastic strains and the stresses, an evolution rule for the plastic behavior of the matrix, the consistency equation and the void volume evolution equation to complete the constitutive relation for porous solids with rate-dependent pressure-sensitive matrices. Motivated by the experimental results of strain-rate sensitivity in a power-law form for poly(vinyl chloride) and high density polyethylene (G'Sell and Jonas, 1979), we take a simple power law to model the material strain-rate sensitivity from the phenomenological viewpoint. Also we propose an evolution equation for the average flow stress of the matrix with initial strain softening and subsequent hardening. The details of the development of the constitutive laws can be found in Jeong (1992).

NUMERICAL RESULTS

We consider a mode I crack under plane strain, small-scale yielding conditions. We adopt the boundary layer approach by considering a crack in a circular domain where the asymptotic displacement solution of the leading singularity term for linear elastic materials is applied. The crack tip has a finite root radius before the remote load is applied. We use the finite element code ABAQUS with a user subroutine where the set of constitutive laws is implemented (Hibbitt et al., 1992). The finite element program takes into account the finite deformation near the blunting tip. The detailed description of the computational procedure can be found in Jeong (1992).

In general, as the remote load is applied, a steady state solution is obtained when the crack-tip opening displacement is about six times the initial crack tip root radius. We have conducted a study of the plastic zone size and shape as functions of the void volume fraction, pressure sensitivity of the matrix, plastic non-normality, and intrinsic softening and subsequent hardening. In general, when the initial void volume fraction increases, the plastic deformation shifts further towards the front of the tip. Under the assumption of normality, when the pressure sensitivity increases, the normalized plastic zone enlarges and elongates ahead of the tip. With the assumption of non-normality, when the plastic dilatancy decreases, the plastic zone becomes narrower ahead of the tip. When the strain softening and subsequent hardening are considered, the plastic zone becomes even narrower. Here we present the computational results for a representative case where the material parameters are taken for those of the rubber-modified epoxy of Yee and Pearson (1986). We take a stress-controlled void nucleation model for cavitation. We also consider the strain softening and subsequent hardening of the matrix.

Figure 1 shows the normalized opening stress Σ_{yy} / σ_y, the plastic strain E_e^p, and the void volume fraction f as functions of the normalized radial distance ahead of the tip, $x / (K_I / \sigma_y)^2$. Here K_I represents the remote mode I stress intensity factor and σ_y represents the yield stress. Figure 1 shows that the maximum opening stress occurs near the elastic-plastic boundary and the plastic strain and the void volume fraction increase rapidly as the crack tip is approached.

Figure 2 shows the constant plastic strain contours and constant void volume fraction contour in the normalized coordinates. As shown in the figure, the plastic strain becomes very large near the crack plane ahead of the tip. The contours for small void volume fractions appear rounded in front of the tip. The void volume fraction becomes very large near the crack plane ahead of the tip. The load-carrying capacity of the material becomes almost zero in the region of severe crack-tip opening displacements ahead of the tip due to the large void volume fraction as shown in Figure 1.

DISCUSSION AND CONCLUSION

We have developed a set of constitutive laws including a Gurson-type of yield criterion for rubber-modified plastics. With this set of constitutive laws, we are capable of simulating the crack-tip deformation processes by finite element methods. It should be noted that several assumptions have been made in order to arrive at the set of constitutive laws. However, the results of the sizes and shapes of the cavitation zone and plastic zone near the crack tip from the finite element simulation agree well with the experimental observation (Pearson and Yee, 1991).

Acknowledgment

The authors acknowledge the support of this work by a Material Research Group grant funded by the U. S. National Science Foundation under grant no. DMR-8708405.

List of References

Dong, P. and Pan, J. (1991). Elastic-Plastic Analysis of Cracks in Pressure-Sensitive Materials, Int. J. Solids Struct. 28, 1113.

Drucker, D. C. and Prager, W. (1952). Soil Mechanics and Plastic Analysis or Limit Design, Quart. Appl. Math. 10, 157.

G'Sell, C. and Jonas, J. J. (1979). Determination of the Plastic Behavior of Solid Polymers at Constant True Strain Rate, J. Mater. Sci. 14, 583.

Gurson, A. L. (1975). Plastic Flow and Fracture Behavior of Ductile Materials Incorporating Void Nucleation, Growth and Interaction, Ph.D. Thesis, Brown University.
Gurson, A. L. (1977). Continuum Theory of Ductile Rupture by Void Growth: Part I -- Yield Criteria and Flow Rules for Porous Ductile Media, J. Eng. Mater. Tech. 99, 2.
Hibbitt, H. D., Karlsson, B. I. and Sorensen, E. P. (1992). *ABAQUS User Manual, Version* 4-9.
Jeong, H.-Y. (1992). A Macroscopic Constitutive Law for Porous Solids with Pressure-Sensitive Matrices and Its Implications for Plastic Flow Localization and Crack-Tip Behavior, Ph.D. Thesis, The University of Michigan, Ann Arbor, Michigan.
Lazzeri, A. and Bucknall, C. B. (1993). Dilatational Bands in Rubber Toughened Polymers, J. Mat. Sci. 28, 6799.
Parker, D. S., Sue, H.-J., Huang, J. and Yee, A. F. (1990). Toughening Mechanisms in Core-Shell Rubber Modified Polycarbonate, Polymer 31, 2267.
Pearson, R. A. and Yee, A. F. (1991). Influence of Particle Size and Particle Size Distribution on Toughening Mechanisms in Rubber-Modified Epoxies, J. Mat. Sci. 26, 3828.
Yee, A. F. and Pearson, R. A. (1986). Toughening Mechanisms in Elastomer-Modified Epoxies, Part 1, J. Mat. Sci. 21, 2462.

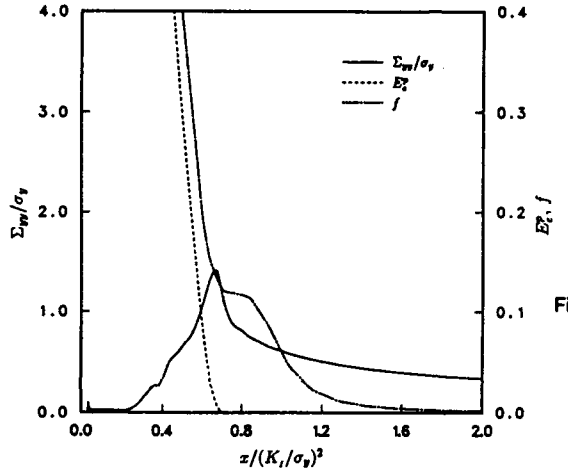

Figure 1
Equivalent tensile plastic strain, Σ_{yy}/σ_Y and void volume fraction along the crack line for a hardening-softening-hardening case with $\mu = 0.13$, $\beta = 0.13$, $f_B = 0.12$, $\sigma_N = 1.0\,\sigma_Y$ and $s = 0.25$

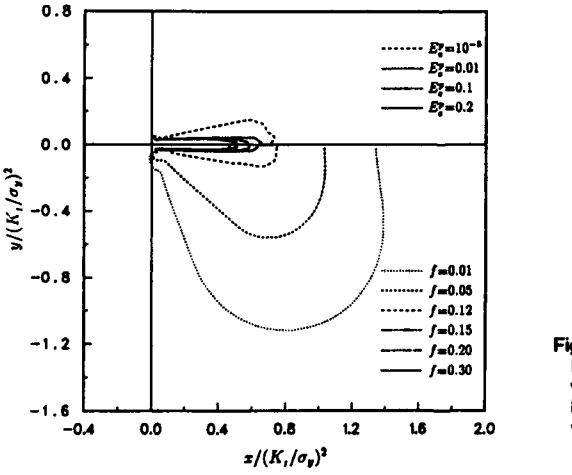

Figure 2
Equivalent tensile plastic strain and void volume distributions for a hardening-softening-hardening case with $\mu = 0.13$, $\beta = 0.13$, $f_B = 0.12$, $\sigma_N = 1.0\,\sigma_Y$ and $s = 0.25$

FACTORS AFFECTING CAVITATION OF RUBBER PARTICLES IN RUBBER-TOUGHENED PLASTICS

C B Bucknall, A M Karpodinis and X C Zhang*

A model proposed recently by Lazzeri and Bucknall [1] is used to calculate critical volume strains at cavitation for the rubber particles in toughened plastics, as a function of particle radius R, shear modulus G_r, and surface energy Γ of the rubber. According to the model, critical volume strains increase as R is reduced or G_r and Γ are increased. These results are supported qualitatively by experimental observations and data from the literature. The model is developed to include energy inputs from the matrix, which give better quantitative agreement with experiment.

INTRODUCTION

There are numerous reports in the literature on cavitation within the rubber particles of toughened plastics, including epoxy resin, nylon, ABS and PVC. Several authors have suggested that cavitation is beneficial, in that it reduces constraint at the crack tip, but there has been no consensus on the subject: it could be argued that cavitation weakens the material. A recent paper by Lazzeri and Bucknall [1] proposes a new model for cavitation, based on a critical stored energy criterion. As small shear strains have little effect on the energy of the rubber phase, the model requires that the available *volumetric* strain energy be greater than the energy to form a void. The void is assumed to be a sphere of radius r formed at the centre of the rubber particle, as illustrated in Fig. 1. Immediately before cavitation ($r = 0$), and the strain energy $U_r(0)$ of the particle is given by:

$$U_r(0) = \frac{4}{3}\pi R^3 W_r^*(0) = \frac{2}{3}\pi R^3 K_r[\Delta V_r(0)]^2 \qquad (1)$$

where $W_r^*(0)$ and $\Delta V_r(0)$ are the stored energy density and volume strain within the rubber phase immediately before cavitation, and K_r is its bulk modulus. Usually, both the radius R and volume strain ΔV_R of the rubber particle (here taken to include both the rubber phase itself and the void) will increase during cavitation. In relation to the rubber particle, the volume fraction of the void cavity is r^3/R^3, and the resulting volume strain within the cavitated rubber phase is $(\Delta V_R - r^3/R^3)$, where in general $\Delta V_R \neq \Delta V_r(0)$.

The formation of a spherical void introduces two additional contributions to the energy of the rubber particle: a surface energy term $4\pi r^2\Gamma$, and the shear strain energy, $\int W_{rs}^* dV$, required to stretch the rubber and allow the cavity to expand. The shear strain energy is $2\pi r^3 G_r F(\lambda_f)$, where λ_f is the extension ratio of the rubber in equi-biaxial extension. The total energy $U_r(r)$ of the cavitated particle is then:

* Advanced Materials Group, Cranfield University, Bedford MK43 OAL

$$U_r(r) = \frac{2}{3}\pi R^3 K_r\left(\Delta V_R - \frac{r^3}{R^3}\right)^2 + 4\pi r^2\Gamma + 2\pi r^3 G_r F(\lambda_f) \quad (2)$$

APPLICATION OF THE MODEL

Figure 2 shows the relationship between $U_r(r)$ and r predicted by this equation for a series of fixed particle volume strains ΔV_R, with R = 0.1 μm, G_r = 0.4 MPa, K_r = 2 GPa, Γ = 0.03 J m^{-2}, and $F(\lambda_f)$ = 1. A critical combination of ΔV_R and R is required to produce cavitation in the rubber phase. Figures 3–6 show how variations in G_r and Γ affect these critical values.

The foregoing results are based on the assumption that the matrix makes no further energy input to the particle during cavitation. To calculate the energy available from the matrix, the rubber-toughened polymer is treated as an assembly of composite spherical elements, each comprising a rubber particle of radius R surrounded by a concentric shell of the matrix polymer, with an external radius Q, as illustrated in Fig. 1. The volume fraction of rubber, ϕ, is therefore R^3/Q^3. The elastic properties of the two phases are defined by shear moduli G_m and G_r and bulk moduli K_m and K_r, where subscripts m and r refer to matrix and rubber respectively.

The elastic behaviour of a shell under uniform internal and external tensile stresses P_R and P_Q, as illustrated in Fig. 1b, is analysed by Reismann and Pawlik [2]. The radial displacement $x(q)$ within the matrix at a distance q from the centre of the sphere is:

$$x(q) = \frac{(P_R R^3 - P_Q Q^3)q}{3K_m(R^3 - Q^3)} + \frac{(P_R - P_Q)R^3 Q^3}{4G_m(R^3 - Q^3)q^2} \quad (3)$$

By substituting rubber volume fraction ϕ for R^3/Q^3 in Eqn 3, we obtain:

$$\Delta V_Q = \frac{3x(Q)}{Q} = \frac{P_Q - \phi P_R}{K_m(1-\phi)} + \frac{3(P_Q - P_R)\phi}{4G_m(1-\phi)} \quad (4)$$

$$\Delta V_R = \frac{3x(R)}{R} = \frac{P_Q - \phi P_R}{K_m(1-\phi)} + \frac{3(P_Q - P_R)}{4G_m(1-\phi)} \quad (5)$$

The stress P_R acting normally at the particle-matrix interface generates a volume strain ΔV_r in the rubber which before cavitation is given by:

$$P_R = K_r \Delta V_r = K_r\left(\frac{4\pi R^2 dR}{V_r}\right) = \frac{3K_r x(R)}{R} \quad (6)$$

where V_r is the volume of the rubber particle. After cavitation, P_R is a function of both r and R. In addition to the mean stress $K_r(\Delta V_R - r^3/R^3)$, which acts over an area $\pi(R^2 - r^2)$ within the rubber phase, there are surface forces acting over a line of length $2\pi r$, and biaxial stretching forces f_r, within the rubber membranes surrounding the void. The total force, f_r, acting on the current cross-section of the rubber particle, πR^2, is therefore:

$$f_r = f_{rs} + 2\pi r\,\Gamma + \pi(R^2 - r^2)K_r\left(\Delta V_R - \frac{r^3}{R^3}\right) = \pi R^2 P_R \qquad (7)$$

By applying the equation for equi-biaxial stretching of a rubber shell, following the method given in reference [1], it can be shown that f_{rs} is:

$$f_{rs} = 2\pi G_r r^2 \int_{\lambda=\frac{R}{R_r}}^{\lambda_r} \left(\frac{\lambda^3 - \lambda^{-3}}{(\lambda^3 - \rho)^{\frac{5}{3}}}\right) d\lambda \qquad (8)$$

In order to calculate energy changes during particle cavitation, the procedure adopted was to fix either ΔV_Q or P_Q, select a series of values for $x(R)$, and find P_R as a function of $x(R)$ and hence R using Eqns 4 and 5. Equations 7 and 8 were then used to obtain allowable values of r. Finally, energies of particle and matrix were calculated as functions of r.

Figures 7 and 8 show typical results of these calculations, relating $U(r)$ to r under conditions of fixed ΔV_R, fixed ΔV_Q, and fixed P_Q. They show that energy input from the matrix is important, and predict critical conditions that are in satisfactory agreement with experiment.

ACKNOWLEDGMENTS

The authors thank the Rohm and Haas Company and the Science and Engineering Research Council (GR/H71130) for financial support of this study.

REFERENCES

1. A. Lazzeri, C.B. Bucknall, *J. Mater. Sci.* **28** (1993) 6799.
2. H. Reismann, P. S. Pawlik, "Elasticity: Theory & Applications", Wiley, NY, 1980.

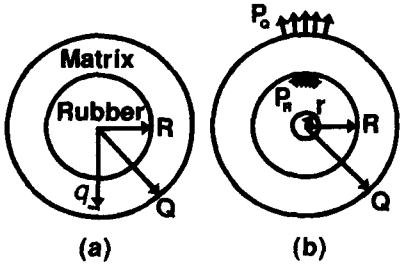

Fig.1. Rubber particle with concentric matrix shell and internal void.

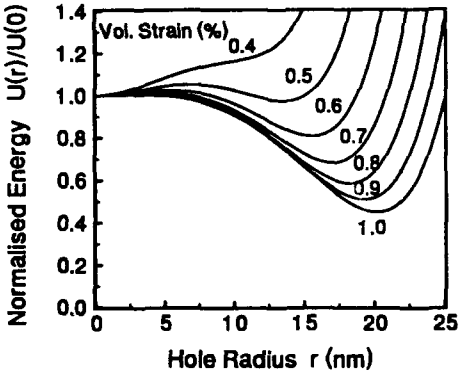

Fig. 2. Calculated energy of cavitated rubber particle

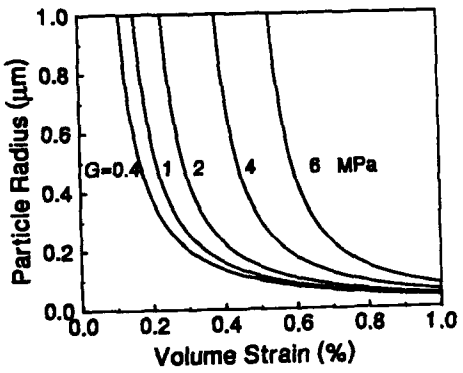

Fig.3. Effect of shear modulus of rubber on particle cavitation. Fixed ΔV_R.

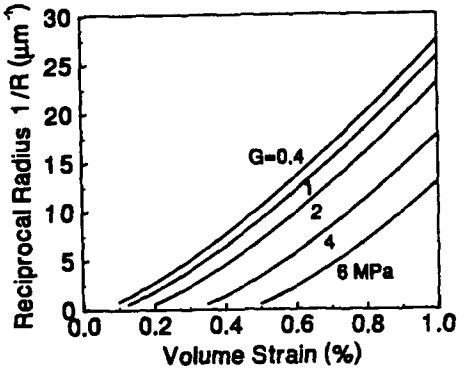

Fig. 4. Results from Fig. 3 replotted in terms of 1/R.

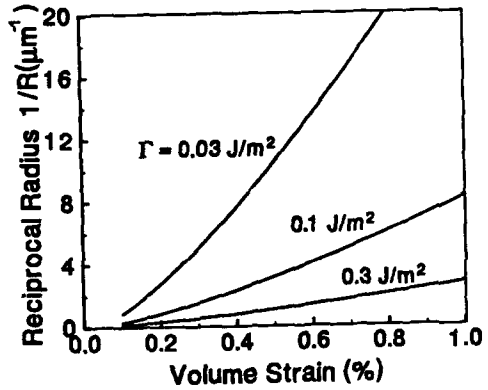

Fig.5. Effect of surface energy on cavitation criterion. Fixed ΔV_R.

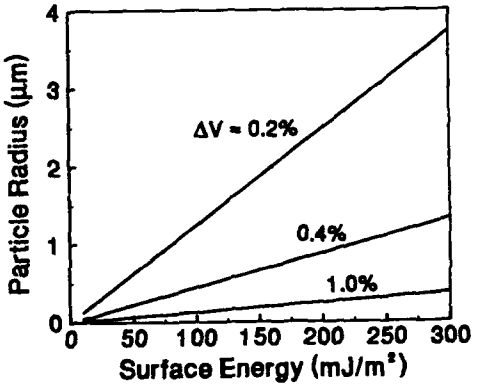

Fig. 6. Relationship between critical radius and surface energy: fixed ΔV_R.

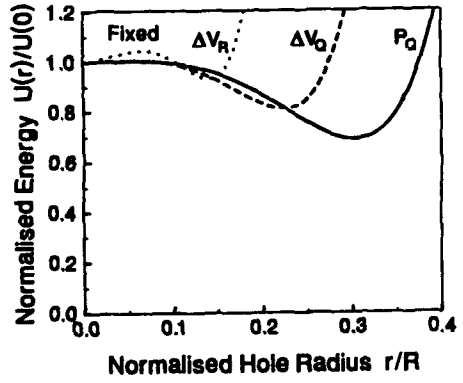

Fig.7. Energy curves calculated with differing boundary conditions.

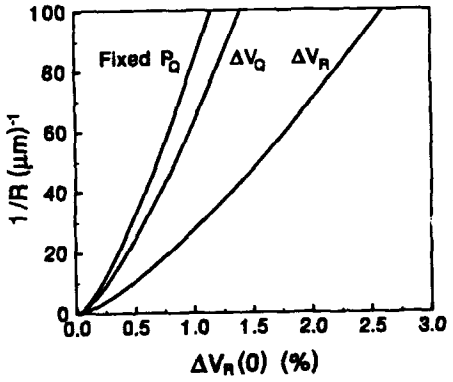

Fig. 8. Critical radius calculated for the three boundary conditions.

DEFORMATION MECHANISMS IN TOUGHENED URETHANE-METHACRYLATE RESINS

X C Zhang*, C B Bucknall*, M L Orton** and G V Jackson**

Deformation mechanisms are investigated in a cross-linked urethane-methacrylate resin toughened with modifier particles consisting of a polybutadiene core and a PMMA shell. Rubber particle cavitation is an important mechanism in this resin. The whitened area ahead of the crack tip defines a zone within which the rubber particles form internal voids on reaching the critical mean stress for cavitation. A relationship is demonstrated between stress intensity factor K_I, cavitation stress σ_{cav} and the radius of the cavitation zone r_{cav}. Plastic deformation in the modified resin is dominated by shear yielding, which is facilitated by cavitation in the rubber phase.

INTRODUCTION

Two main deformation mechanisms, crazing and shearing, are generally recognized as important in rubber-toughened plastics [1]. In some plastics, especially the polystyrene family, plastic deformation occurs essentially through multiple crazing, whereas in the majority of toughened plastics shear deformation dominates. In both cases, the role played by the rubber particles has been a matter of controversy. Some researchers believe that the high tearing energy of the rubber phase is responsible for the increase in fracture resistance [2], while others conclude that rubber particles act simply as holes [3–5]. Recent work at Cranfield has shown that the rubber plays a very positive role in toughening, acting both as a load-bearing strain-hardening component [6] and as the initiator of crazing or shearing in the matrix, which is often a consequence of rubber particle cavitation [7,8]. Cavitation is especially important under conditions that would otherwise cause the matrix to fail in a brittle or semi-ductile manner. It has been found that an increase in the cavitation stress of the rubber leads to an increase in the yield stress of the toughened polymer. Large decreases have been observed in the creep rate of HIPS on increasing the cross-link density of the rubber [9].

The state of stress in the polymer has a strong influence on rubber cavitation. For a thick specimen with a sharp notch, the size of the cavitation zone ahead of the crack tip is much greater in the triaxial stress field at the centre of specimen than in the plane stress region near the surfaces [10]. The radius of the cavitation zone r_{cav}, within which the mean (triaxial) tensile stress reaches a critical value, can be expressed by the following equations:

$$r_{cav} = \frac{2}{9\pi}\left(\frac{K_I}{\sigma_{cav}}\right)^2 (1+\nu)^2 \cos^2\frac{\theta}{2} \qquad (1)$$

* Advanced Materials Group, Cranfield University, Bedford MK43 OAL

** ICI Chemicals & Polymers Ltd, The Heath, Runcorn, Cheshire WA7 4QD

$$\frac{r_{cav}}{r_p} = \frac{4}{9}\left(\frac{\sigma_{yield}}{\sigma_{cav}}\right)^2 (1+\nu)^2 \cos^2\frac{\theta}{2} \qquad (2)$$

where:

$$r_p = \frac{1}{2\pi}\left(\frac{K_I}{\sigma_{yield}}\right)^2 \qquad (3)$$

σ_{yld} = yield stress in uniaxial tension, ν = Poisson's ratio, θ = angle to the crack plane, and r_p is the Irwin plastic zone radius under plane stress conditions. Figure 1 shows the size and shape of the cavitation zone calculated using Eqn 2. It should be noted that this zone is different in shape from the plastic zone of von Mises, and that its dimensions are dependent on the ratio $\sigma_{yld}/\sigma_{cav}$. The factors affecting rubber cavitation are discussed elsewhere at this conference [7]. The current paper proposes a method for measuring the cavitation stress in the rubber, and presents experimental results on deformation mechanisms in a urethane-methacrylate resin toughened with a core-shell modifier.

EXPERIMENTAL

The materials used in this work were: (a) ICI Modar, a urethane-methacrylate resin; and (b) Rohm & Haas Paraloid BTA 753, a rubber-based modifier in which the particles consist of a polybutadiene core and a PMMA shell. The modifier was mixed into the resin for 20 mins at room temperature, before adding 1% benzoyl peroxide initiator and 0.5% N,N-dimethylaniline accelerator and pouring into a glass plates mould. The mixture was cured at room temperature over at least an hour, and post-cured at 115°C for 40 hours.

Observations of the crack tip cavitation zone were made with the aid of a camera, on 6x80x80 mm double-edge-notched tensile specimens. First, 15 mm deep notches were milled centrally into each side with a V-shaped cutter. A fresh razor blade was then pressed into each notch at the minimum possible speed, to extend it by about 1 mm. A constant load was then applied for 30 min to allow equilibrium to be approached. Uniaxial tensile tests were carried out at 23°C at a cross-head speed of 0.5 mm min^{-1}, on dumb-bell specimens measuring 3x6x40 mm in the gauge portion. Volume strains were measured with the aid of Instron longitudinal and transverse extensometers.

RESULTS AND DISCUSSION

Figure 2 is a plot of r_y (max), the maximum observed extent of the cavitation zone along the y-axis (normal to the crack plane), against K_I^2. To a good approximation, the data fall on a straight line passing through the origin. According to Eqn 1, r_{cav} reaches a maximum in the y direction at $\theta = 70°$. Using this value of θ, and the slope of the line in Fig. 2, measurements of whitening give σ_{cav} = 14.8 MPa for the Modar/MBS blend.

The total volume strain ΔV_{tot} in a rubber-toughened polymer can be treated as the sum of the elastic volume strain ΔV_{el} and the contribution due to void formation ΔV_{cav}. Initially, deformation is purely elastic, and the application of uniaxial tensile stress σ gives $\Delta V = \Delta V_{el} = \sigma/3K$, where K is the bulk modulus of the two-phase material. The volume strain due to cavitation is therefore given by:

$$\Delta V_{cav} = \Delta V_{tot} - \frac{\sigma}{3K} \quad (4)$$

Figure 3 is a plot of ΔV_{cav} against ΔV_{tot}. It can be seen that significant cavitation commences at about $\Delta V_{tot} = 0.4\%$. Using the most recent version of the cavitation model, which includes the energy input from the matrix during void formation, the critical cavitation stress σ_{cav} at this volume strain in a material with a rubber content of 15 vol % is 12.4 MPa. This is a little below the figure of 14.8 MPa obtained from observations of the whitened zone, probably because whitening does not become visible until a minimum amount of void formation has taken place. There are difficulties in observing the boundary of the cavitation zone, and more accurate techniques are needed to detect cavitated rubber particles during testing. Viscoelastic recovery adds to the difficulties in observing void formation at a later stage.

An analysis of the observed strains shows that shear yielding becomes the dominant mechanism of deformation as the extension increases, and that cavitation makes only a small direct contribution. This is shown in Figure 4, where ε_{tot} is total longitudinal strain and ε_{el}, ε_{cav}, ε_{sh} are elastic, cavitational and shear strain components respectively. The strain measurements are supported by transmission electron microscopy [10]: cavitated rubber particles can be seen clearly, and there is obvious evidence of shear deformation, but no crazing. However, although cavitation represents only a small proportion of the total strain, its importance should not be underestimated. Relatively small amounts of void formation cause major changes in yield behaviour, as explained in more detail elsewhere [11].

SYMBOLS USED:

ε	=	Longitudinal strain [subscripts: cav = cavitation, el = elastic].
θ	=	Angle to crack plane
ν	=	Poisson's ratio
σ_{cav}	=	Critical stress for cavitation of rubber particles
σ_{yld}	=	Yield stress in uniaxial tension
K_I	=	Mode I stress intensity factor
r_{cav}	=	Extent of cavitation zone, measured from crack tip
r_x, r_y	=	Components of zone size along x and y axes
r_p	=	Irwin plastic zone radius
ΔV	=	Volume strain [subscript cav = cavity]

REFERENCES:

1. Bucknall C B, 'Toughened Plastics', Applied Science, London, 1975.
2. Kunz-Douglass S, Beaumont P W R and Ashby M F, *J. Mater. Sci.* **15** (1980) 1109.
3. Guild F J and Young R J, *J. Mater. Sci.* **24** (1989) 298(Pt 1), 2454(Pt 2).
4. Huang Y and Kinloch A J, *Polymer* **33** (1992) 1330.
5. Bagheri R and Pearson R A, *25th Int. SAMPE Conf.* 26-28 Oct. 1993, PA, USA.
6. Bucknall C B, Correa C A and Soares V L P, Paper 9, this conference.
7. Bucknall C B, Karpodinis A M and Zhang X C, Paper P62, this conference.
8. Lazzeri A and Bucknall C B, Paper 2, this conference.
9. Bucknall C B and Zhang X C, *to be published.*
10. Zhang X C, PhD Thesis, Cranfield University (1993).
11. Lazzeri A and Bucknall C B, *J. Mater. Sci.* **28** (1993) 6799.

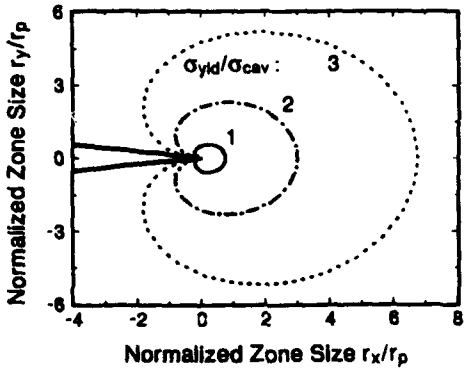

Fig. 1. Cavitation zone profiles calculated using Eqn 1.

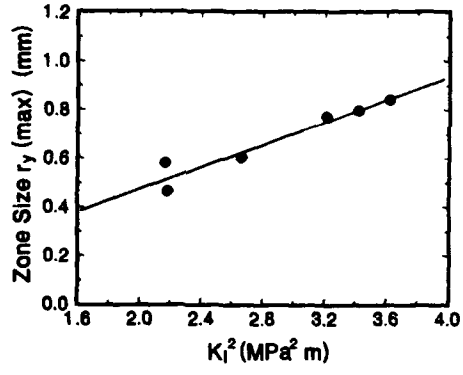

Fig. 2. Observed depth of whitened zone r_y as a function of K_I^2.

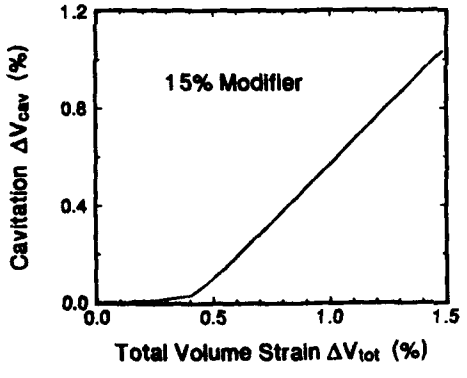

Fig. 3. Volume strain due to cavitation plotted against total volume strain for Modar with 15% modifier.

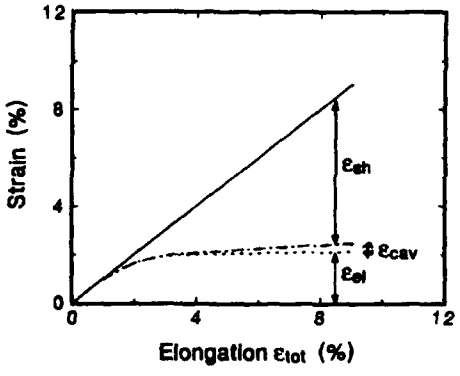

Fig. 4. Contributions of elastic, cavitation and shear components of strain to total elongation.

FRACTURE AND YIELD OF SEVERAL HIGHLY FILLED POLYMERS

D A Wiegand, C Hu, A Rupel and J Pinto*

The mechanical response in compression of five highly filled polymer composites is given as a function of temperature and strain rate. The compressive strength and the apparent modulus increase with decreasing temperature and increasing strain rate, and are proportional to each other above the glass transition temperature. The strain at the maximum stress is approximately constant with variations of temperature and strain rate and can be used as a criterion for failure, and further suggests a critical local strain or displacement for failure.

INTRODUCTION

This paper contains preliminary results and discussion of the mechanical response and in particular the mechanical failure properties of five highly filled polymer composites. Most of the polymers are plastized. The objective is to develop sufficient understanding for predictive capability. The stress versus strain behavior is being studied as a function of temperature, strain rate, density, sample dimensions and mechanically induced damage. In addition, fracture surfaces are being studied by x-ray photoelectron spectroscopy, changes in the areas of various types of internal surfaces are being studied by x-ray and neutron scattering, and finite element calculations are being made to determine stress and strain patterns. Because of space limitations only the stress versus strain behavior as a function of temperature and strain rate is considered here.

EXPERIMENTAL

Each composite is made up of a binder and filler. The binder is a polymer (with plastizer in most cases), the filler is an organic polycrystalline material, and the filler concentration varies from 80 to 95% by weight. Two of the composites differ only in the percentages of the binder and filler while the others have different binders. The binder for composites I and II is cellulose acetate butyrate with bis 2-2 dinitropropyl acetal and bis 2-2 dinitropropyl formal 1:1 ratio as plastizers, for composite III the binder is nitrocellulose with tris(beta chloroethyl) phosphate as plastizer, for composite IV the binder is polyurethane with the same plastizer

*ARDEC, Picatinny Arsenal, New Jersey USA 07806-5000

as for I and II and for composite V the binder is chlorotrifluoro-ethylene/vinylidine flouride copolymer. Composites I through IV have the same filler.

Samples were prepared either by pressing powders or (small cylinders) produced by mixing and extruding into large billets and then cutting and machining to the desired dimensions or by pressing directly to the desired dimensions (1) Wiegand. Samples were right circular cylinders with a length to diameter ratio of one or two and were uniaxially compressed at constant strain rate along the cylinder axis. All samples were loaded using an MTS servo-hydraulic system (2) Wiegand, Pinto and Nicolaides and were coated with graphite on the flat cylinder ends to minimize friction during compression. Complete stress versus strain curves were recorded at temperatures of -45°, -10°, 25° and 65° or 75° C and at strain rates of 0.001, 0.01, 0.1 and 1.0 per second. Between one and five samples were measured at each temperature and strain rate.

RESULTS AND DISCUSSION

With increasing strain the stress initially shows some curvature due to sample end conditions, then increases approximately linearly, curves over and passes through a maximum and decreases for further strain increases. This paper is primarily concerned with the maximum stress, i.e. the compressive strength, σ_m, the slope in the linear region before the maximum stress which is loosely called the modulus, M, and the strain at the maximum stress, e_m. Possible recoverable and non recoverable strain contributions to e_m and M are not separated here.

All samples exhibited brittle like fracture at -45°C and all strain rates as evidenced by an abrupt and significant decrease in the stress with increasing strain. Composites III and V gave the same behavior at -10°C and composites V gave this behavior at 25°C. For all other conditions and samples the stress decreased uniformly with increasing strain beyond σ_m. The strains, e_m, at σ_m are typically in the range of 1 to 5% but the deformations were carried out to at least 10% strain. The condition of the samples after this strain of 10% or more vary with temperature, strain rate and composite. All five composites were fractured at -45° and all strain rates. Composite V was fractured at all temperatures and strain rates while composites I and II were fractured only at low temperatures and were intact and not cracked at the highest temperature. Composites III and IV were fractured at low temperature and were either intact but cracked or fractured at the highest temperature.

With increasing strain rate at constant temperature σ_m and M increase while e_m increases for composites III, IV and V and decreases for the other two composites . However, e_m is much less strain rate dependent than σ_m and M for composites I through IV and for all composites the scatter in the results is greater for M than for σ_m and greatest for e_m. The strain rate dependence of σ_m and M can be best described by noting that both quantities vary as the strain rate to the power m where m is in the range of 0.1 to 0.2. m tends to decrease with decreasing temperature and approach zero at

-45 C°.

Both σ_m and M decrease with increasing temperature at constant strain rate for all five composites and for all strain rates. In contrast, e_m increases with temperature at constant strain rate for composites I and II which have a negative slope with strain rate and decreases for composites IV and V. For the composite III e_m increases with temperature at constant strain rate in the low temperature region but decreases with temperature in the higher temperature region. Thus, σ_m and M increase with strain rate and decrease with temperature for all five composites. e_m also increases with strain rate and decreases with temperature for two of the materials and decreases with strain rate and increases with temperature for two other materials. The fifth composite has anomalous strain rate and temperature behavior. However, it must emphasized that e_m is poorly defined in terms of the stress versus strain curve compared to σ_m and M, and the scatter is much greater. In addition, e_m varies much less with temperature (and strain rate) than σ_m and M for all composites except V.

For the composite for which the data is most complete (at least five samples for each temperature and strain rate) plots of log(M) and log(σ_m) versus the reciprocal of the absolute temperature yield straight lines for each strain rate with apparent activation energies of about 0.2 ev for both σ_m and M. However, the largest values of log (σ_m) and log (M) (low temperature and high strain rate) do not follow this pattern. For the other four composite the data shows similar trends with apparent activation energies between about 0.1 and 0.25 ev. However, the data for these materials is not as extensive and the fit is in some cases over a more limited temperature range.

While a detailed interpretation of these results is not given here a few comments are appropriate. The glass transition temperature T_g is -37°C for composite II and preliminary measurements indicate that the value for composite I is about the same (4) Harris. T_g for composite III is -34°C (5) and the results presented above indicate that T_g for composite VI is in the same temperature range. composite V may have a higher T_g. Therefore, these materials are in a glass like state at the lowest temperature and are expected to be brittle as observed. Relative insensitivity of M and σ_m to temperature and strain rate are then properties of this state. At higher temperatures all five composites exhibit significantly greater sensitivity to and about the same dependence on temperature and strain rate. These properties are characteristic of a (viscoelastic) rubber like state.

Above T_g composites I, II and IV and composite III at all temperatures give linear relationships between σ_m and M which pass through the origin. A straight line can be fit to the data for composite V but the scatter is excessive. M can be approximated by σ_m/e_m so that $\sigma_m \approx M \times e_m$ Thus, the linearity of the curves of σ_m

versus M indicate (approximately) constant e_m. This is not inconsistent with the discussion above regarding the strain rate and temperature dependence of e_m since as noted e_m varies much less with temperature and strain rate than either σ_m of M for composites I through IV. Composite V is anomalous in this group because the variations of σ_m and M with strain rate and temperature are much less than for the others although both of these quantities for this composite do have larger variations than e_m. The constancy of e_m indicates that for practical considerations e_m can be taken as a criterion for failure if the maximum of the stress strain curve is considered to indicate failure. Alternately a fraction of e_m at a point of deviation of the stress versus strain curve from linearity can be used as a yield like criterion for failure. In addition, the constancy of e_m suggests that there are local strains (and displacements) which are the conditions for failure on a local level. While the e_m values are small, i.e. in the range 0.01 to 0.06 for the five composites, the local strains can be much larger especially if they occur primarily in the binder. The binders comprise only 5 to 20% by weight and, perhaps fortuitously, the composites with the higher binder content also have the larger e_m. Thermal activation can yield under appropriate conditions exponential dependencies of M and σ_m on temperature and also yield increases of M and σ_m with strain rate, as observed. These considerations will be addressed in detail elsewhere (3) Wiegand.

SYMBOLS USED

σ_m = compressive strength

e_m = strain at σ_m

M = slope of stress versus strain curve

ev = electron volt

Tg = Glass Transition Temperature (deg C)

REFERENCES

1 Wiegand D A, Materials Research Society Symposium Proceedings Interface Control of Electrical, Chemical and Mechanical Properties, In Press.

2 Wiegand D A, Pinto J J, Nicolaides S, J Energetic Materials 9 (1991) 19

3 Wiegand D A, to be published

4 Harris J, unpublished work

5 Dobratz B M and Crawford P C, LLNL Explosives Handbook, Properties of Chemical Explosives and Explosive Simulants (1985) 19-113

A 3-D stress-strain relation for glassy polymers

T.A. Tervoort, M. Brekelmans and L.E. Govaert

Centre for Polymers and Composites, Eindhoven

Summary.
In constitutive equations for finite elastic-plastic deformation of polymers the elastic part of the deformation is usually formulated by assuming an isotropic relation between the Jaumann rate of the Cauchy-stress tensor and the rate of strain tensor. The Jaumann-stress rate however is known to display aphysical behaviour in the elastic region. In this paper we will derive a "compressible-Leonov model" which reduces to the Jaumann-stress rate in the limit of complete plastic deformation, but is also capable of giving a correct description of the elastic region.

In polymer rheology it is now recognized that constitutive equations are most naturally formulated using evolution equations for state variables [1,2] (the variables that determine the Helmholtz-free energy (A) of the system). Jongschaap[2] derived a formalism which describes how external rate variables (the velocity gradient $\underline{L}$) and external forces (the Cauchy-stress tensor $\underline{\sigma}$) are coupled to the rate of change of the state variables and the internal thermodynamic forces (derivatives of the free energy with respect to the state variables). An important concept in this formalism is that of macroscopic time reversal where one determines to what extend the rate of change of the state variables and the stress tensor $\underline{\sigma}$ are effected by a reversal of the macroscopic external velocity gradient $\underline{L}$. Here it should be noted that any function $f(\underline{L})$ may be decomposed in an even part f^+ and an odd part f^- according to:

$$f(\underline{L}) = f^+(\underline{L}) + f^-(\underline{L}) = \tfrac{1}{2}(f(\underline{L}) + f(-\underline{L})) + \tfrac{1}{2}(f(\underline{L}) - f(-\underline{L})) \qquad \text{(thus } \underline{L} = \underline{L}^- \text{ per definition)}$$

From the notion that the state variables are even per definition and due to the second law of thermodynamics the dissipation function[2] is also even, the formalism describes how a constitutive equation can be decomposed as follows:

$$\begin{pmatrix} \underline{\sigma} \\ \underline{\dot{S}} \end{pmatrix} = \begin{pmatrix} \underline{\underline{\eta}} & -\underline{\underline{\Lambda}}^T \\ \underline{\underline{\Lambda}} & \underline{\underline{\beta}} \end{pmatrix} : \begin{pmatrix} \underline{L} \\ -\underline{M} \end{pmatrix} \quad , \quad \underline{M} = \rho \left(\frac{\partial A}{\partial \underline{S}} \right) \tag{1}$$

Where it is assumed that the state variable determining the free energy is a second order tensor $\underline{S}$ with an associated thermodynamic force $\underline{M}$ (ρ is the density). The fourth-order tensor $\underline{\underline{\eta}}$, $\underline{\underline{\Lambda}}$ and $\underline{\underline{\beta}}$ are even with respect to $\underline{L}$.
One important result is that the reversible (elastic) part of the stress tensor, $\underline{\sigma}^+$, is coupled to the reversible

(odd) part of the rate of change of the state variable, $\underline{S}$:

$$\underline{\sigma}^{rev} = \underline{\sigma}^{\circ} = \underline{\underline{\Lambda}}^{T} : \underline{M} = \underline{M} : \underline{\Lambda}$$

We will now use this formalism to derive a constitutive relation that gives a correct description of the elastic as well as the plastic behaviour of polymers assuming that the volume response remains pure elastic. We will use polycarbonate as a model system to compare some of the existing models.
In the case of isotropic elastic behaviour one can assume that the state variable determining the free energy is the left-Cauchy-Green-deformation tensor $\underline{B}$, $\underline{B} = \underline{F} \bullet \underline{F}^{T}$ ($\underline{F}$ is the deformation gradient).
Because of isotropy we then have:

$$A = A(I_{\underline{B}}, II_{\underline{B}}, III_{\underline{B}}) \qquad I_{\underline{B}} = tr(\underline{B}),\ II_{\underline{B}} = \tfrac{1}{2}(I_{\underline{B}}^{2} - tr(\underline{B} \bullet \underline{B})),\ III_{\underline{B}} = \det(\underline{B})$$

The thermodynamic force therefore equals:

$$\underline{M} = \rho\left(\frac{\partial A}{\partial \underline{B}}\right) = \rho\left(\frac{\partial A}{\partial I_{\underline{B}}}\frac{\partial I_{\underline{B}}}{\partial \underline{B}} + \frac{\partial A}{\partial II_{\underline{B}}}\frac{\partial II_{\underline{B}}}{\partial \underline{B}} + \frac{\partial A}{\partial III_{\underline{B}}}\frac{\partial III_{\underline{B}}}{\partial \underline{B}}\right) = \rho\left(\alpha_1 \underline{I} + \alpha_2 (tr(\underline{B})\underline{I} - \underline{B}) + \alpha_3 \det(\underline{B})\,\underline{B}^{-1}\right)$$

Here, α_i are the derivatives of the free energy with respect to the invariants of $\underline{B}$.
From kinematics we know that the upper convected or Truesdell derivative of $\underline{B}$ equals $\underline{0}$ and this leads us to the evolution equation for $\underline{B}$:

$$\overset{\nabla}{\underline{B}} = \underline{L} \cdot \underline{B} + \underline{B} \cdot \underline{L}^{T} = \underline{\underline{\Lambda}} : \underline{L} \qquad ; \qquad \Lambda_{ijkm} = \delta_{ik} B_{mj} + B_{im} \delta_{jk} \tag{2}$$

Since we have no dissipation $\underline{\eta}$ and $\underline{\beta}$ are $\underline{0}$ and the constitutive equation for elastic behaviour follows directly from (1) and (2):

$$\begin{cases} \underline{\sigma} = \underline{M} : \underline{\Lambda} = 2\rho\left(\alpha_3 \det(\underline{B})\underline{I} + (\alpha_1 + \alpha_2 tr(\underline{B}))\underline{B} - \alpha_2 \underline{B}^{2}\right) \\ \overset{\nabla}{\underline{B}} = 0 \end{cases}$$

This is the well-known expression for Green-elastic behaviour.
Because we want to develop an expression for elastic-plastic behaviour where the volume response is pure elastic, we now consider the case of pure elastic behaviour where the volume deformation is independent of the change of shape. Because of the independent volume deformation we assume that the free energy is determined by two state variables: the relative volume deformation J ($J = \det(\underline{F})$) (for convenience we will use JI instead of J) and the left-Cauchy-Green deformation tensor at constant volume $\underline{B}^{*}$, $\underline{B}^{*} = J^{-\frac{2}{3}}\underline{B}$. In the case of isotropic behaviour we then have[3]:

$$A = A(J, I_{\underline{B}^{*}}, II_{\underline{B}^{*}}) \qquad (III_{\underline{B}^{*}} = \det(\underline{B}) = 1)$$

There are now two conjugated thermodynamic forces, one related to the volume deformation ($\underline{N}$) and one related to the shape deformation ($\underline{M}$):

$$\underline{N} = \rho\left(\frac{\partial A}{\partial J\underline{I}}\right) = \frac{1}{3}\rho\left(\frac{\partial A}{\partial J}\right)\underline{I} \quad \text{and} \quad \underline{M} = \rho\left(\frac{\partial A}{\partial \underline{B}^{*}}\right) = \rho\left(\alpha_1^{*}\underline{I} + \alpha_2^{*}(tr(\underline{B}^{*})\underline{I} - \underline{B}^{*T})\right)$$

From kinematics we have:

$$\dot{J}\underline{I} = J tr(\underline{D})\underline{I} = J\underline{I}\underline{I}:\underline{L} \quad and \quad \overset{\circ}{\underline{B}}^* = \underline{L}^{d^T}\cdot\underline{B}^* + \underline{B}^*\cdot\underline{L}^{d^T} = \underline{\underline{\Lambda}}^*:\underline{L} \quad (\underline{\underline{\Lambda}}^* = \underline{\underline{\Lambda}} - \frac{2}{3}\underline{B}\underline{I})$$

The constitutive equation therefore becomes:

$$\begin{cases} \underline{\sigma} = \underline{N}:J\underline{I}\underline{I} + \underline{M}:\underline{\underline{\Lambda}}^* = \rho_0\left(\frac{\partial A}{\partial J}\right)\underline{I} + \rho\left(2\alpha_1^*\underline{B}^{*d} + 2\alpha_\lambda^*(tr(\underline{B}^*)\underline{B}^*)^d + 2\alpha_2^*(\underline{B}^{*2})^d\right) = \underline{\sigma}^h + \underline{\sigma}^d \\ \overset{\circ}{\underline{B}}^* = \underline{L}^d\cdot\underline{B}^* + \underline{B}^*\cdot\underline{L}^d \\ \dot{J}\underline{I} = J tr(\underline{D})\underline{I} \end{cases} \tag{3}$$

As might be expected the hydrostatic stress is determined solely by the volume deformation, whereas the deviatoric stress is governed by $\underline{B}^*$.
The evolution equation for $\underline{B}^*$ may also be written as:

$$\overset{\circ}{\underline{B}}^* = \underline{D}^d\cdot\underline{B}^* - \underline{B}^*\cdot\underline{D}^d \quad where\ \overset{\circ}{\underline{B}}^*\ is\ the\ Jaumann\ rate\ of\ \underline{B}^*: \quad \overset{\circ}{\underline{B}}^* = \dot{\underline{B}}^* - \underline{W}\cdot\underline{B}^* - \underline{B}^*\cdot\underline{W}^T$$

In case of plastic deformation we now assume that the accumulation of elastic strain (at constant volume) is reduced because of the existence of a (deviatoric) plastic strain rate $\underline{D}_p$[3]. The evolution equation for $\underline{B}^*$ therefore changes to (note that the plastic spin equals 0):

$$\overset{\circ}{\underline{B}}_e^* = (\underline{D}^d - \underline{D}_p)\cdot\underline{B}_e^* - \underline{B}_e^*\cdot(\underline{D}^d - \underline{D}_p) \tag{4}$$

For polymers in general and polycarbonate special it is known[4] that the plastic-strain rate $\underline{D}_p$ is well described by an Eyring-flow process:

$$\underline{\sigma}^d = 2\eta(II_{\underline{\sigma}^*})\underline{D}_p \ ;\ where\ \ \eta(II_{\underline{\sigma}^*}) = A\tau_0\frac{\sqrt{\frac{II_{\underline{\sigma}^*}}{2\tau_0^2}}}{\sinh\left(\sqrt{\frac{II_{\underline{\sigma}^*}}{2\tau_0^2}}\right)}$$

For polycarbonate we have $A = 8.6\ 10^{20}$ s and $\tau_0 = 0.856$ MPa[4].

A constitutive equation for elastic-plastic behaviour with an elastic-volume response is now obtained by combining the equation for elastic behaviour (3) with the new evolution equation for $\underline{B}^*$ (4).We will assume that $\alpha_2^* = 0$ (physical linear elastic behaviour) and identifying $2\rho\alpha_1^*$ with the shear modulus G and $\rho_0(\partial A/\partial J)$ with K(J - 1) (where K is the bulkmodulus) we have (at small volume deformations, $J \approx 1$):

$$\underline{\sigma} = K(J-1)\underline{I} + G\underline{B}_e^{*d}$$

$$\overset{\circ}{\underline{B}}_e^* = (\underline{D}^d - \underline{D}_p)\cdot\underline{B}_e^* + \underline{B}_e^*\cdot(\underline{D}^d - \underline{D}_p)$$

$$\dot{J}\underline{I} = tr(\underline{D})\underline{I}$$

$$\underline{\sigma}^d = 2\eta(II_{\infty})\underline{D}_p$$

We can now compare our model with the widely used Jaumann-stress-rate equation[5]:

$$\frac{\eta(II_{\underline{\sigma}^*})}{G}\overset{\circ}{\underline{\sigma}} + \underline{\sigma}^d = 2\eta(II_{\underline{\sigma}^*})\underline{D} \quad together\ with \quad tr(\overset{\circ}{\underline{\sigma}}) = 3Ktr(\underline{D})$$

and the upper-convected equivalent of this:

$$\frac{\eta(II_{\underline{T}})}{G}\ \overset{\nabla}{\underline{T}}\ +\ \underline{T}^{d}\ =\ 2\eta(II_{\underline{T}})\underline{D}\ \ ;\ \underline{\sigma}^{d}=\underline{T}^{d}\quad \textit{together with}\quad tr(\underline{\sigma})=3Ktr(\underline{D})$$

As an example we will calculate the normal-stress response of the three models for a plane-stress-shear deformation (plane-stress condition in the z-direction). The Young's modulus of polycarbonate E = 2400 MPa and the Poisson constant ν = 0.33.

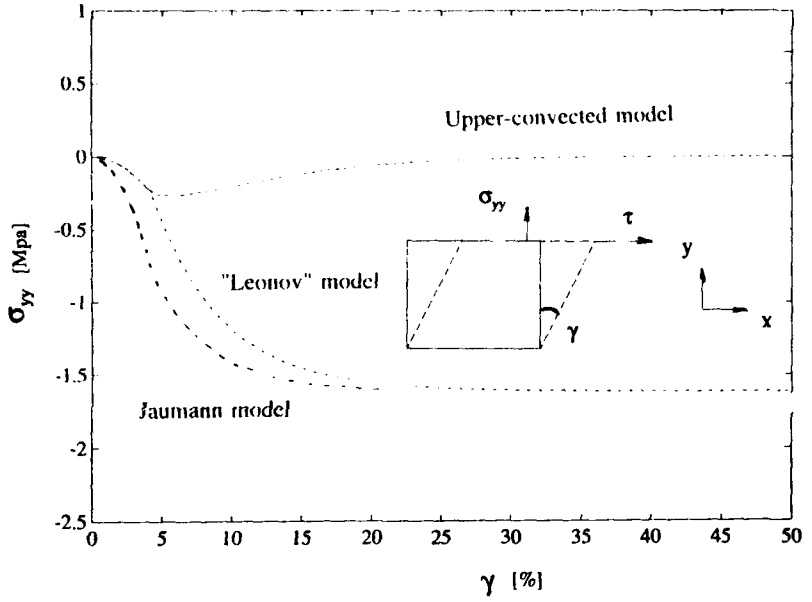

Calculations show that the three models give virtually the same shear-stress response. The normal stresses however differ, as can be seen from the figure.
It is known[6] that the upper-convected model gives a good description of the elastic behaviour, but apparently fails to describe the (experimentally observed) normal stress during plastic deformation. The Jaumann model on the other hand gives a reasonable description of the normal stress, but is not capable of capturing the correct elastic behaviour[6]. Our "compressible Leonov model" provides a natural link between these two extremes.

References:

1. A.N. Beris and B.J. Edwards, J. Rheol.34(4), 503, 1990.
2. R.J.J. Jongschaap, Rep. Prog. Phys., 53, 1, 1990.
3. F.T.P. Baaijens, Philips Internal Report 311/87, 1987.
4. I.M. Ward, "Mechanical Properties of Solid Polymers" sec. ed., Wiley, New York , 1990.
5. K.W. Neale, SM Archives, 6(1), 79, 1981.
6. H. van Wijngaarden and F.E. Veldpaus, Internal WFW-report, ISBN 90-6808-005-9, 1986.

Plastic Instabilities in Glassy Polymers

L.E. Govaert and T.A. Tervoort
Centre for Polymers and Composites, Eindhoven University of Technology
P.O.Box 513, 5600 MB Eindhoven, The Netherlands

In this study it is suggested that the initiation of localized deformation zones in glassy polymers, like crazes or shear bands, is related to the specific flow properties of these materials, where small stress fluctuations lead to large local strain rate differences. This view is supported by a stress optical study on polycarbonate, showing development of inhomogeneous deformation below the yield point. Moreover, it is shown for a commercial grade of polystyrene that the strain rate dependence of craze initiation is equivalent to that of yielding, indicating that both processes originate from the same molecular mechanism.

Introduction

Localized deformation zones, like crazes or shear bands, have a pronounced effect on the macroscopic deformation behaviour of glassy polymers. A prime example is polystyrene which displays a macroscopical strain to break of 1%, whereas, on a microscale, the craze fibrilla extend to their natural draw ratio [1]. Although the exact conditions for craze formation are not yet completely understood, it seems well established that craze initiation involves a local plastic instability leading to lateral stress build-up and incipient cavitation [1,2]. In this study it is suggested that the initiation of localized deformation is inherently related to the specific flow characteristics of these materials. Since the post-yield viscosity displays a strong stress dependence, relatively small stress fluctuations will result in large local strain rate differences: plastic flow instabilities.
In our view the evolution of these plastic instabilities depends on both the strain hardening modulus of the material and the critical stress needed for local cavitation. A high strain hardening modulus (e.g. PC) will stabilize the deformation zone, allowing it to grow slowly with increasing load. A low strain hardening modulus (e.g. PS) will lead to unstable growth, favouring lateral stress build-up and incipient cavitation: craze initiation.
Experimental support for this point of view will be presented in a two step argument. Firstly, the initiation of instable flow will be illustrated by an experimental study on polycarbonate. Secondly, the strain rate dependence of the craze initiation stress and the yield stress of a commercial grade of polystyrene will be compared, giving indicative evidence that for a relation between craze initiation and local plastic flow.

Experimental

The materials used in this study were polycarbonate (Lexan™) and polystyrene (Styron 638™). Polycarbonate tensile and creep specimens were machined in accordance with ASTM D638 III from isotropic sheets of 2 mm thickness. Yield stresses were determined in uniaxial tensile tests at strain rates from 5 10^{-4} to 5 10^{-2} s^{-1}, at temperatures of 20, 40 and 60 °C. Plateau creep rates were determined in creep experiments at stresses from 48 to 60 MPa in the same temperature range. Master curves of stress versus strain rate were constructed for both creep and tensile data by shifting adjacent curves horizontally.

The polystyrene grade (Styron 638™) was specially selected for its extremely brittle behaviour, creating a situation where the craze initiation stress is approximately equal to the breaking stress. The strain rate dependence of the craze initiation stress was studied using biaxial flexure (ball-ring) [3] and three-point bending. In these tests the maximum stress region is limited to a very small volume, thus minimizing the influence of surface flaws and defects on the experimentally determined strength. The biaxial flexure tests were performed on 3 mm thick polystyrene disks with a diameter of 45 mm. The support (ring) consisted of a thrust bearing of 30 mm diameter with balls of 3 mm radius. The load was applied in the centre of the disk with a 3 mm radius ball. As the loading path was linear, tensile strengths and strain rates were evaluated employing the linear elastic theory [3].

Three-point bending experiments were performed according to ASTM D790M-86 on strips of 3x10x70 mm. Since the loading path was observed to be nonlinear, the maximum stress was correct as described in ASTM D790M-86.

To study the strain rate dependence and pressure sensitivity of the yield behaviour of polystyrene two other test methods were employed:

a) Tensile tests under a superimposed hydrostatic pressure (500 MPa), performed on polystyrene specimens with a gauge length of 35 x 10 x 2 mm. The experiments were performed with kind permission at the IRC of Polymer Science & Technology (University of Leeds). The experimental set-up at the IRC has been described extensively in [4].

b) Planar compression tests, performed on polystyrene specimens with a gauge length of 40 x 12 x 3 mm. The specimens were supported by 2 Teflon covered steel plates to create a plane strain condition.

The concept of instable flow

It is well-known that polymers display a significant strain rate dependence of the yield stress. This is demonstrated in Figure 1, where the yield stress of polycarbonate in uniaxial extension is plotted as a function of strain rate. Also represented in Fig.1 are the plateau creep rates obtained from creep experiments at various stress levels. It is obvious that the steady state reached under constant stress conditions and that reached under constant strain rate conditions is equivalent. The consequence of this equivalence is that in a tensile test the onset of plastic deformation already starts at low stress levels, the plastic deformation rate increasing gradually with increasing stress. Once the plastic deformation rate in the sample is in balance with the applied strain rate, a constant stress level is reached: the yield stress.

In an inhomogeneous stress field, small stress variations will have a drastic influence on the plastic deformation rate throughout the sample. This can easily be deduced from figure 1, where is clear

that a stress increase by 2 MPa will increase the strain rate by an order of magnitude. Hence, regions of higher stress will display a much larger plastic deformation rate than its surroundings (a flow instability), which inevitably leads to localisation of deformation. This "concept of instable flow" is supported by a stress optical study of polycarbonate samples which where loaded to different stress levels in a tensile test at 10^{-4} s^{-1}, as indicated in Fig. 2a. When the samples are observed between crossed polarisers, shown in Fig. 2b, it is clear that inhomogeneous plastic flow develops throughout the sample even before the yield point has been reached. Similar observations were made during creep test at high stress levels prior to necking.

Craze initiation

The assumption that craze initiation starts with a local plastic instability inherently implies that the strain rate dependence of the craze initiation stress should be identical to that of the yield stress. The yield and craze initiation behaviour of Styron 638™ was studied using four different loading geometries. For craze initiation biaxial flexure and three-point bending was employed, equivalent to biaxial and uniaxial extension, respectively. Conditions for yielding were successfully achieved in planar compression and uniaxial extension under a superimposed pressure of 500 MPa. A convenient method to compare the results of these different loading geometries is to express the stress state and deformation rate at the yield point in terms of the octahedral shear stress and the octahedral shear rate respectively [5].
The results of the experiments are presented in figure 4, where the octahedral shear stress is plotted as a function of octahedral shear rate for all loading geometries. A detailed analysis of this data, in terms of pressure modified activated flow [5], will be discussed in a forthcoming publication. For the moment we rest in the observation that for the material used in this study the shear rate dependence is the same for yielding as for craze initiation. This is a strong indication that both processes are governed by the same molecular process, in our opinion indicative evidence that craze initiation indeed involves localised plastic flow.

Conclusions

The experimental results are indicative for the assumption that deformation localisations as crazes or shear bands are initiated by local plastic flow instabilities. Further research will have to be performed to investigate the general applicability of this approach to other "brittle" polymers.

References

1. Kramer EJ, Berger, LL, Adv.Polym.Sci., 91/92, 1
2. Argon AS, Hannoosh JC, Phil.Mag., 36, 1195 (1977)
3. de Smet BJ, Bach PW, Scholten HF, Dortmans LJMG, de With G, J.Eur.Ceram.Soc., 10, 101 (1992)
4. Sweeney J, Duckett RA, Ward IM, Proc.Royal soc.london, A420 53-80 (1988)
5. Ward IM, Mechanical properties of solid polymers,John Wiley & Sons, 1983

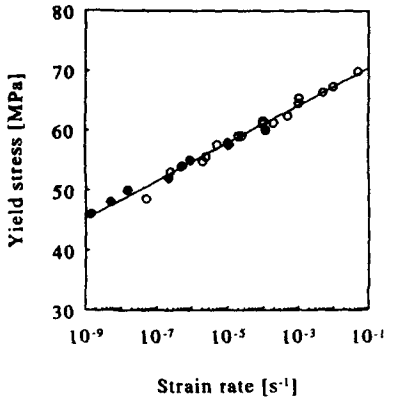

Figure 1. Yield Stress vs. strain rate for polycarbonate; ○: data from tensile experiments, ●: data from creep experiments.

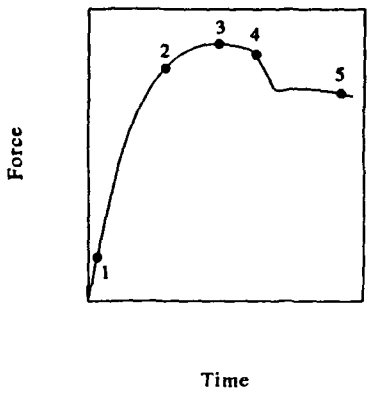

Figure 2a. Loading path for the polycarbonate samples 1 to 5, used in Figure 2b.

Figure 2b. Photograph of the polycarbonate samples 1 to 5 (from Fig. 2a) between crossed polarizers.

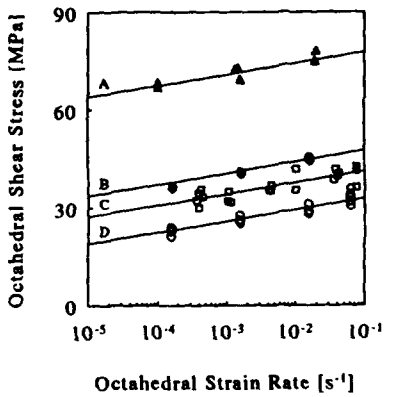

Figure 3. Octahedral shear stress as a function of octahedral shear rate for Styron 638.
A) Hydrostatic tensile (500 MPa): yielding.
B) Planar compression: yielding.
C) Biaxial extension: crazing.
D) Uniaxial extension : crazing.

CHANGES IN GLASSFIBRE REINFORCED INJECTION MOULDED POLYAMIDE DUE TO FATIGUE LOADING

J.J. HORST*

Characterizing the structure of this highly anisotropic material is important to understand better the failure mechanism, especially in fatigue. A new method for measuring the anisotropy and structure was developed and used; thin slices were cut from the material, and subsequently tensile tested. This method makes it possible to obtain profiles of strength, stiffness and fracture strain through thickness, with good reproducibility. Strength profiles were measured for material that had been subjected to fatigue, the layer where the damage or crack initiates can be clearly distinguished. To solve the experimental problem of varying lifetime, the total lifetime of the specimen can be predicted during the fatigue experiment by measuring the elongation.

INTRODUCTION

A characteristic of Fibre Reinforced Plastics (FRP) is their high degree of anisotropy, caused by fibre orientation. An injection moulded FRP plate has a layered structure, each layer having different orientation. These layers have different stiffness, as well as different strength. When a tensile load is applied, a stress distribution through the cross section of the specimen will develop, with stresses higher where the material is stiffer. The location where the stress is high also has higher strength, so prediction of the place where the material will fail is complicated. Residual stresses due to shrinkage further complicate the problem. In unreinforced materials, cracks normally initiate at defects at the surface (scratches) or inside the material (inclusions), for FRP the weakest spot is not easy to identify.

To be able to predict more accurately the fatigue lifetime of FRP products, we want to investigate the influence the anisotropy has on the fracture mechanism, and especially we want to analyze the location where cracks or damage initiates. This has been done by determining the strength profile of specimens, after fatiguing them up to a certain number of cycles, but not until failure. For relating the damage to the fatigue process, we need to know what fraction of the number of cycles to failure was reached, at the moment the fatigue experiment was stopped. The problem is that at a certain fatigue stress, the total number of cycles to failure varies. If an average is used of experimentally determined lifetimes at a certain fatigue load, the percentage of lifetime at the moment the fatigue experiment is stopped can vary with approximately a factor two. We can predict the number of cycles to failure for a particular specimen more accurately by doing measurements while it is being fatigued, especially the elongation (cyclic creep) of the specimen is useful.

*Laboratory for Mechanical Reliability, Delft University of Technology, the Netherlands

EXPERIMENTAL

The material used was Polyamide 6 containing 30%wt. of glassfibres; Akulon K224-G6 provided by Akzo, Holland. Square plates of 100x100 mm and 5.75 mm thickness were injection moulded from this. Earlier experiments indicated the high degree of anisotropy: Although the mould has a line feed, variations in strength and stiffness occur of 40%, measured in mould flow direction. For the fatigue experiments non-standard dog-bone type test specimens were milled from the plate, using a Roland PNC-3000 Computer Aided Modelling Machine. The width of the narrow part was 10mm. The fatigue experiments were executed in a servo-hydraulic MTS bench, at a frequency of 2Hz, to prevent heat build-up in the material. The minimum to maximum load ratio was 0.1. Temperature during testing was 23°C and relative humidity 50%. During the experiment the displacement of the grips was recorded, to obtain a curve of cyclic creep with number of cycles.

The strength profiles were obtained in the following way: First miniature test specimens have to be milled from the location desired, for specimens subjected to fatigue this was the center of the narrow part of the fatigue test specimens. From these miniature samples, with a width of 2 mm, slices are cut using a Leitz microtome. Slices of 85μm thickness were chosen, because at a higher thickness the cutting force was too high, and a lower thickness influences the reliability of results negatively. The fracture strength, fracture strain and modulus can then be measured for each slice, using a miniature tensile test machine. The plotted curves (Figures 1 and 2) were smoothened by averaging over four points. From early results we concluded that cutting and testing must be done the same day, to prevent the foil from absorbing too much water.

RESULTS

The influence of the microtome-cutting was investigated using Scanning Electron Micrography, from which it was concluded that the damage done by the cutting is not deeper than the thickness of one fibre, 10μm. As obvious from strength profiles (Figures 1 and 2) the variations in strength are fairly small and smaller than the variations from layer to layer, through the thickness. The nominal strength of the foils is low, approximately 40% of the strength of a full-thickness test-bar (ca. 120MPa). A similar difference is found for the elastic modulus, and the fracture strain of the slices is a factor 3 - 5 higher as compared to a 5.75 mm test-bar. This thickness-effect can be explained by the loss of coherence in the material. The load cannot be transmitted from the matrix to the fibres, to the same extent as for a thick specimen. Also the stress state will be pure plain stress.

As we can see in the graphs for the unfatigued references, the transitions from layer to layer are very gradual, an effect that was observed also in micrographs of the fibre orientation, by Lang et al (1). The profiles are non-symmetric, as observed by Bay et al (2).

Figure 1 shows the strength profiles for fatigue specimens cut from the side of the plate, in longitudinal direction. At high fatigue loads (60% of UTS) the material shows many cracks towards the end of the fatigue lifetime, which are visible in the slices also. The strength of the slices cut from the shell layers decreases with fatigue, and is lower for the specimen fatigued up to 94% of its predicted lifetime, as compared to the specimen that reached 78%. In both cases also the fracture strain increases (not shown).

For the specimens cut from the middle of the plate, fatigued at low loads (45-50% of UTS, Figure 2), the strength of just a few slices (from the core) decreases, while the fracture strain decreases also. This is the case only for the specimen fatigued up to 100.7% of its predicted lifetime, the specimen that reached 45% doesn't show any significant changes.

Cyclic creep

In Figure 3 the elongation of the specimens is plotted with the number of cycles, for specimens all cut from the same location in the plate, fatigued at a maximum load of 60% of UTS. The specimens with short lifetime elongate very little in the beginning of the experiment, they seem to be rather stiff. With the experiment the creep then increases rapidly, and progressively towards the end of the experiment. The specimens with longer lifetime though, have larger creep in the beginning, but this creep increases far more slowly. To characterize the curve the "creep speed", elongation per cycle, was taken from the secondary creep where the creep is approximately linear with number of cycles. These creep speeds were plotted in Figure 4, against the lifetime of the specimen, on a double log scale. A correlation is apparent, and this method can be used during the fatigue experiment to predict the lifetime of a specimen.

DISCUSSION

This new technique of microtoming and tensile testing of slices makes it possible to get a better view of the material behaviour through thickness. Reproducability is good, considering the fact that the slices were cut to 85μm thickness. Changes in the material that are the result of fatigue can be made visible.

At high loads the material in the shell layers gets weaker, accompanied by an increase in fracture strain. Multiple cracking in these layers is present, maybe accompanied by a process of debonding of the fibres, which makes the material behave more like an unreinforced polymer, with lower strength and higher fracture strain.

At low loads the strength in the shell layers remains the same, and a very local weakening in part of the core layer is present, accompanied by a decrease in fracture strain.

This can be explained by assuming that the mechanism changes from damage in the shell layer at high loads, to crack initiation and growth in the core at low loads.

The correlation that is present between the cyclic creep speed in secondary creep, and the number of cycles to failure, at a maximum fatigue load of 60% of UTS, leads to the conclusion that the variation in the lifetime of the specimens is determined by differences in this specimen that are of global character, as the creep is a global effect. As a consequence of this the variations in lifetime that are the result of local variations in the specimens like scratches at the surface, must be relatively small, at least at this high load.

REFERENCES

1 Lang R W, Manson J A, Hertzberg R W, Org Coatings and Plastics Chem 45 (1981) 778

2 Bay R S, Tucker III C L, Davis R B, ANTEC 89 (1989) 539

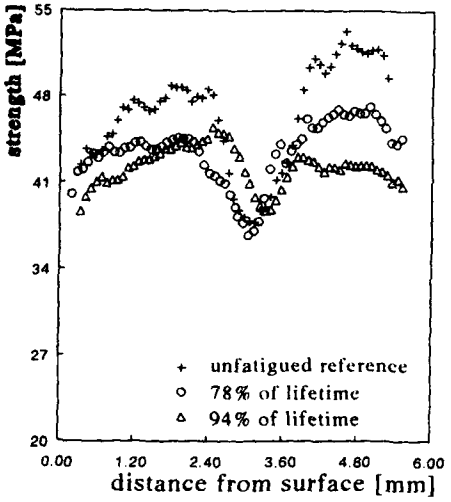

Figure 1 Strength profiles of specimens from the side of the plate, max.stress 60% of UTS.

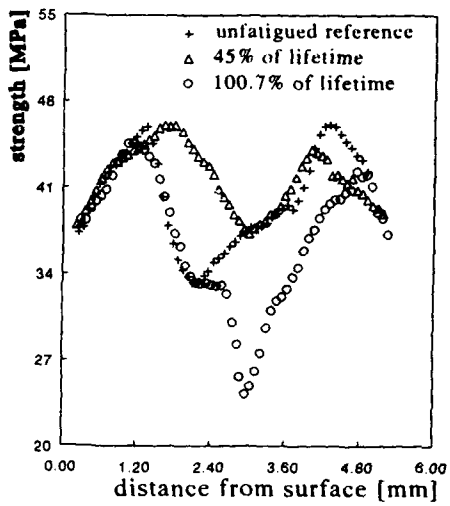

Figure 2 Strength profiles for specimens from middle of the plate, max.load 45-50%

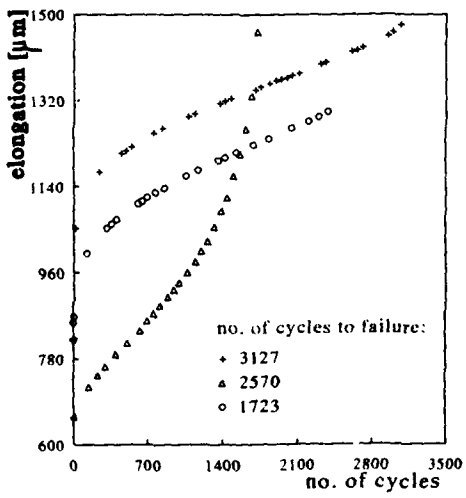

Figure 3 Cyclic creep curves, max.stress 60% of UTS.

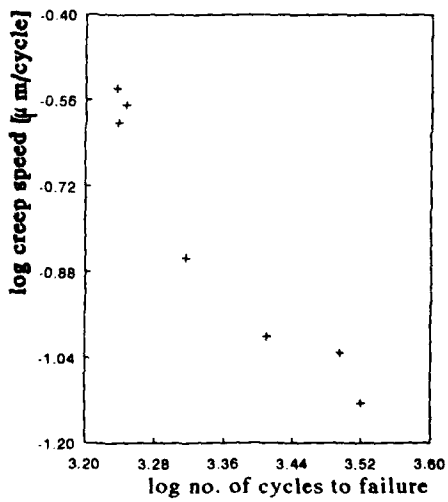

Figure 4 Creep speed in secondary creep to number of cycles to failure.

MECHANICAL PROPERTIES OF A THERMOTROPIC POLYESTER: POLI(TRIETHYLENE GLYCOL *p,p'*-BIBENZOATE)

R. Benavente*, J.M. Pereña*, E. Pérez*, A. Bello*

The mechanical properties of three samples of a thermotropic polybibenzoate with different thermal histories have been determined at two strain rates (1 and 10 cm/min) and two drawing temperatures (23 and 50°C), showing the influence of the thermal and mechanical histories on the stress-strain plots. The phase behaviour and the crystallinity level of the samples also affect the mechanical parameters (Young modulus, yield stress and deformation at break).

INTRODUCTION

Thermotropic behaviour has been observed in many polymers that contain rigid-rod units alternating regularly with relatively flexible spacer units. Several papers have been published by us concerning liquid crystalline polymers, LCP's, derived from bibenzoic acid and oxyalkylene diols (1-4). We have focused our attention in this work on mechanical properties of poly(triethylene glycol *p,p'*-bibenzoate) (PTEB), because the study of macroscopic properties in flexible mesomorphic polymers is of great importance for potential technological applications of these polymers. The best known commercially are lyotropic polymers, and typical values of the tensile parameters are reflected in numerous works (5). However, mechanical properties of thermotropic polymers are less explored.

The effects on modulus in going through the glass transition region have already been discussed (6). Moreover, yield stress, σ_Y, decreases as temperature increases, and the deformation at yield, ϵ_Y, generally decreases with an increase in temperature for amorphous materials, but the opposite effect can be found in some semicrystalline polymers (7). In addition to this, the elongation at break, λ_B, generally decreases for rigid polymers as the rate of testing increases.

The goal of this paper is to present and discuss relevant results on stress-strain behaviour referred to samples of a LCP with different thermal histories, and discuss the effect of the strain rate and the drawing temperature.

*Instituto de Ciencia y Tecnología de Polímeros, Juan de la Cierva 3. 28006-Madrid, Spain.

EXPERIMENTAL

The polyester investigated has been synthesized by melt transesterification of the diethyl ester of *p,p´*-bibenzoic acid and triethylene glycol, using isopropyl titanate as catalyst. The polymer was purified by precipitating into methanol the solution in chloroform. The value of the intrinsic viscosity, measured at 25°C in chloroform, is 1.15 dL/g. The thermal characterization was made with a Perkin Elmer DSC7 calorimeter, and X-ray diffraction patterns were taken with a Philips X-ray diffractometer in the 2θ range between 3° and 36°, using Ni filtered CuKα radiation.

In order to prepare specimens for stress-strain tests, the polymer was placed in a Collin press fitted with smooth polished plates and hot pressed at 1 MPa and 150°C for 1 min. The cooling process was carried out by quenching the molten polymer with water to room temperature under the same pressure (sample PTEB-Q). Part of this film was annealed at 55°C in a thermostatic bath during five days (PTEB-CR) and another one was left at room temperature for about 4 months (PTEB-RT).

Dumbbell specimens for the drawing process were cut with a standardized die and ink marked at 2 mm intervals. The actual draw ratio was determined from the displacement of the parallel marks in the homogeneous stretched portion of the drawn specimen.

An Instron box furnace was used to provide an isothermal test environment accurate to ±1°C. Tests were performed at two drawing temperatures, T_d: ambient conditions (around 23°C) and 50°C. Two crosshead speeds were used in this study (1 and 10 cm/min). For each temperature and crosshead speed, three tests were performed and a mean value obtained. The stress and modulus were calculated dividing the force by initial section. The breaking stress was calculated with the final section.

An Ehringhaus compensator attached to a polarizing microscope (Amplival Pol) was used to measure the optical retardation of the stretched specimens. The birefringences were obtained dividing the optical retardation by each thickness.

RESULTS

The morphology and properties of a semicrystalline polymer are largely determined by the initial rate of cooling or by posterior annealing treatment. However, ageing or slow annealing processes may also occur below or above T_g over long periods of time, respectively. Moreover, in the study of the mechanical properties of a liquid crystal polymer the control of the thermal history is very important because a transformation to a more ordered structure (LC→CR) is possible, changing the mechanical properties. In the case of PTEB-Q film, obtained after melting at 150°C and quenching to room temperature, the DSC traces only show the glass transition (17-20°C) and an endotherm at 114°C, corresponding to the isotropization, T_i, of the mesophase (2). This mesophase is stable at room temperature for several days, and thus PTEB-Q represents a liquid crystalline state. The α relaxation associated with the T_g has been also reported by dynamic mechanical analysis (4). X-ray experiments revealed the diffractions corresponding to the length of the smectic layer (1).

Stress-strain curves corresponding to room temperature drawing of this PTEB-Q sample show homogeneous deformation, similarly to an amorphous polymer (6) and the stress levels are low (Fig. 1). Plastic strain is observed only for stresses greater than or equal to the yield stress and are not recovered on removal of the stress. The yield stress defines the elastic-plastic transition. When a clear load maximum is not observed the yield stress is obtained by intersecting two tangent lines, below and above the yield point in the stress-strain plot. Otherwise, the yield stress is defined as the first maximum in stress on a curve. Obviously, different conditions of the test, such as temperature and strain rate, may produce curves requiring a different definition of yield in the same material (8,9).

A considerable change in the properties is observed when the sample is left at room temperature during a long time (PTEB-RT sample). At temperatures between T_g and T_i, the mesophase of PTEB exhibits a transformation into a crystalline state. This transformation is very slow at any temperature and particularly at ambient conditions, as the temperature is then only a few degrees above T_g. After stretching at room temperature, both the yield stress and the Young modulus increase and the drawing process takes place through necking even though T_d is higher than T_g. In general, a slight increase in the values of different parameters (yield stress, modulus, strain hardening) with the drawing rate is observed. The reason is the presence of a small degree of crystallinity in these specimens, as revealed by the X-ray diffraction pattern.

The influence of the annealing process at higher temperature was also studied. Another sample was annealed at 55°C during 5 days (PTEB-CR sample) and important changes in the properties were observed. The specimens were stretched at 1 and 10 cm/min, but the behaviour was similar in both cases. Typical stress-strain plots are shown in Fig. 1 for samples stretched at 23°C and 50°C. DSC and X-ray results indicate the presence of crystallinity in the samples, which have a clear effect on the mechanical properties. Thus, the Young modulus increases considerably but the elongations at break are small ($\lambda_B = 1.20$) at room temperature, similarly to semicrystalline polymers. When rising the temperature of the drawing process it is possible to increase λ_B up to $\lambda_B = 6$ but the values of modulus decrease, although they remain higher than those of the LC samples (PTEB-Q).

A common feature of the three PTEB samples is that the yield stress decreases as the drawing temperature increases, whereas it does not change significantly with the strain rate. The Young modulus does not change with the strain rate but it decreases as the drawing temperature increases. Moreover, the deformation at break increases with the drawing temperature, while the final birefringence decreases.

The main conclusion is, then, that the behaviour of PTEB-RT is intermediate between the other two samples, with the advantages of a considerable increase in the modulus in relation to sample PTEB-Q without much decrease in the elongation at break.

Acknowledgment The financial support of the Comisión Interministerial de Ciencia y Tecnología (project no. MAT91-0380) is gratefully thanked.

REFERENCES

1 Pérez E, Riande E, Bello A, Benavente R and Pereña J M, Macromolecules 25 (1992) 605
2 Pérez E, Pereña J M, Benavente R, Bello A and Lorenzo V, Polymer Bull. 29 (1992) 233
3 Marugán M M, Pérez E, Benavente R, Bello A and Pereña J M, Eur. Polym. J. 28 (1992) 1159
4 Benavente R, Pereña J M, Pérez E and Bello A, Polymer 34 (1993) 2344
5 Dobb M G and McIntyre J G, Adv. Polym. Sci. 60/61 (1984) 61
6 Benavente R and Pereña J M, Polym. Eng. Sci. 27 (1987) 913
7 Nielsen L E, "*Mechanical Properties of Polymers and Composites*", Marcel Dekker Inc., New York (1974).
8 Ward I M, "*Mechanical Properties of Solid Polymers*", 2nd Ed., J. Wiley & Sons (1985).
9 Duckett R A, in "*Structure and Properties of Oriented Polymers*", Chapter 11, Ed. Ward I M, Appl. Sci. Pub. Ltd., London (1975).

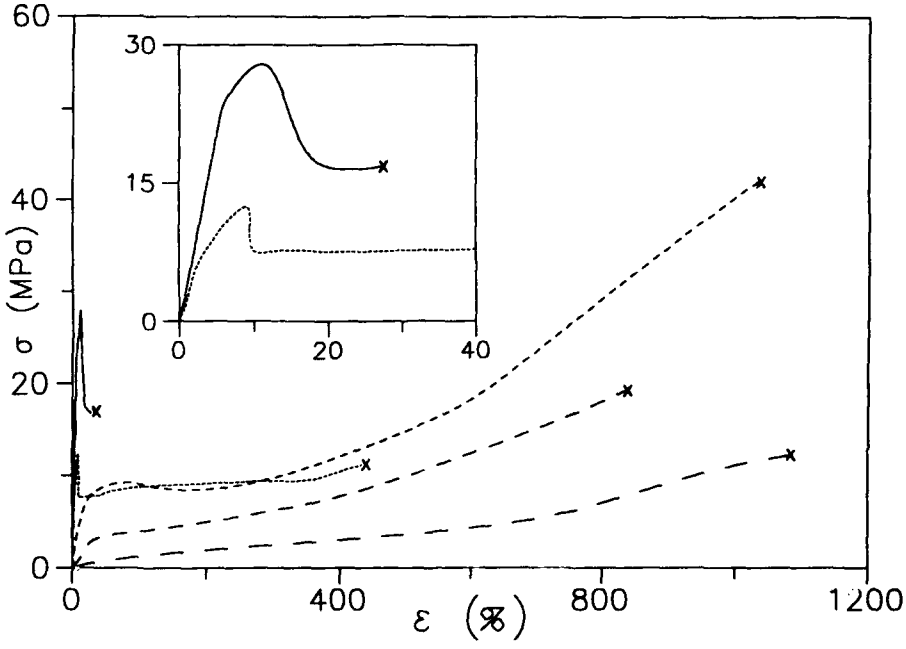

Figure 1 Stress-strain plots of several PTEB specimens, stretched at 1 cm/min and two drawing temperatures : – – – –Q, 50°C; – – – – –Q, 23°C; ------- RT, 23°C; ····· CR, 50°C and —— CR, 23°C. The inset shows the two last specimens at low deformations.

DEFORMATION OF PRESSURE ANNEALED POLYETHYLENE

A.S. Maxwell, A.P. Unwin and I.M. Ward*

Different grades of polyethylene have been annealed in the region of the hexagonal phase and examined in some detail. The annealing process has a considerable impact on the morphology, which in turn affects the mechanical properties of the processed product. In essence there are conflicting requirements in the desire to achieve high moduli. Annealing within the hexagonal phase produces samples with large crystallites and high degrees of crystallinity. This crystal growth occurs at the expense of the molecular network which is required for effective drawing. Too much crystal growth results in friable materials. The response of the polyethylene grade depends on its molecular weight and this role is examined here.

INTRODUCTION

Annealing polyethylene within the hexagonal phase is known to produce a considerable change in the material morphology, but the relevance of this morphology to producing samples of significantly improved mechanical properties upon orientation is unclear. Some laboratories have reported successful deformation of these materials (1,2) whilst others have found friability a major problem (3,4). The exact material grade and annealing conditions clearly have a pronounced influence on the deformation of these materials and there is a need to investigate this systematically, especially if the potential mechanical improvements are to be realised.

In this work we have examined four different grades of polyethylene, with molecular weights M_w in the range 100,000 to 4.5×10^6. Each grade has been pressure annealed under a range of conditions which encompass the orthorhombic hexagonal phase boundary, before subsequently being oriented using hydrostatic extrusion. In this way the effect of annealing conditions on the deformation behaviour and subsequent mechanical properties of each of the different grades could be investigated. The morphologies of these samples have

* I.R.C. in Polymer Science and Technology, Physics Department, University of Leeds, LS2 9JT

been examined before and after extrusion and the role played by the hexagonal phase investigated.

MORPHOLOGY

For a fixed annealing temperature and time, as the annealing pressure drops and the sample enters the hexagonal phase (from the orthorhombic side) considerable changes occur within the sample. Transmission electron microscopy shows that the morphology changes from a basically lamellar structure to the sausage like appearance, characteristic of hexagonal phase annealing. This change does not occur suddenly, but rather over a space of about 20 - 40 MPa annealing pressure, with the position and span of the changeover depending on the molecular weight.

At the same time significant changes still take place within the sample when annealed inside the hexagonal phase. These changes are not so obvious in TEM, but can be detected in other ways. For example, Figure 1 shows the degree of crystallinity developed in each grade as a function of the annealing pressure. At pressures less than 480 MPa all four grades have entered the hexagonal phase, (clearly shown in TEM). As the annealing pressure drops further (below 480 MPa) the crystallinity continues to rise. Other changes are evident in the melting behaviour of the material.

MECHANICAL PROPERTIES

The effect of annealing on the mechanical properties is shown in Figure 2. Here the room temperature three point bend modulus is plotted for samples annealed under identical processing conditions with the exception of the one variable, namely pressure. Each sample has been annealed for 1 hour at 234°C and the pressure shown, before being extruded to a draw ratio of 7. All four grades were found to show an increase in the tensile modulus as the annealing conditions approached the orthorhombic hexagonal boundary from the orthorhombic side. Eventually, however, the modulus begins to decrease, the point at which this occurs depending on the molecular weight, with high molecular weight material surviving to annealing conditions well inside the hexagonal phase.

DISCUSSION

Clearly, both the morphological and physical properties of polyethylene annealed in the vicinity of the orthorhombic hexagonal border are sensitive to the precise annealing conditions and the molecular weight. We intend to show that high modulus samples cannot

necessarily be produced by simply annealing within the hexagonal phase followed by orientation. It is essential to maintain an adequate network in the material to hold the sample together during orientation. Annealing within the hexagonal phase has the effect of reducing the extent of the network as crystallinity and crystal size both develop. Very high molecular weight material can be annealed in the hexagonal phase without losing the effectiveness of the network. The lower crystallinity shown by these grades, however, is a limiting factor in attaining high modulus. For low molecular weight grades annealing within the hexagonal phase produces very brittle friable materials that do not survive the extrusion process. In this case annealing on the edge of the orthorhombic hexagonal boundary is more productive.

REFERENCES

1) Sahari J B, Parsons B & Ward I M, J. Mat. Sci. (1985), 20, 346.

2) Powell A K, Craggs G & Ward I M, J. Mat Sci. (1990), 25, 3990.

3) Mead W T & Porter R S, Int. J. Polym. Mater. (1979), 1, 29.

4) Chuah H H & Porter R S, J. Pol. Sci. Pol. Phys. Ed. (1984), 22, 1353.

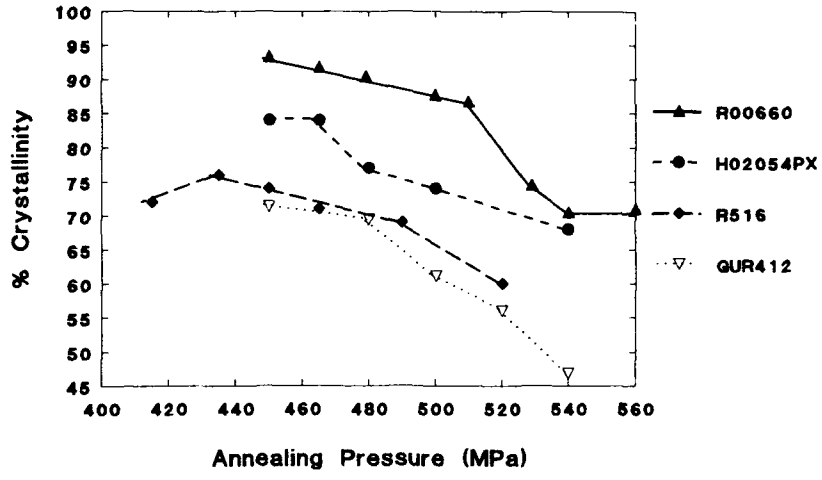

Figure 1 The effect of molecular weight on crystallinity
Samples annealed at 234°C for 1 hour.

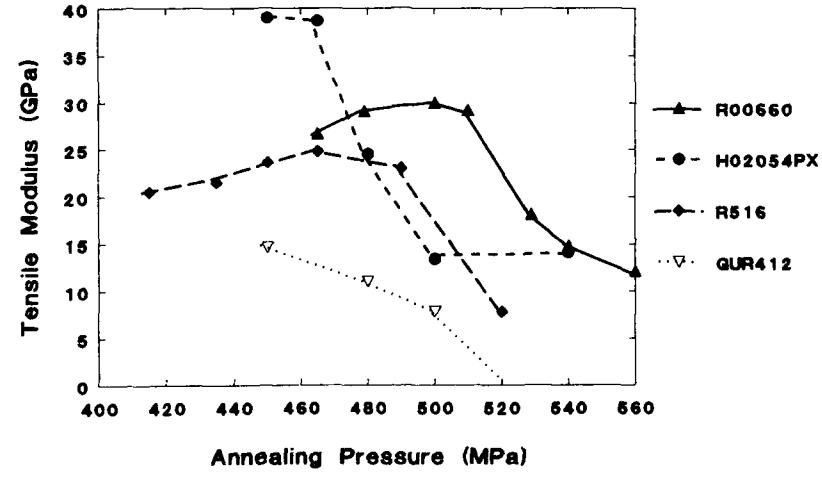

Figure 2 The effect of moleular weight on tensile modulus.
Samples annealed at 234°C for 1 hour, Rn=7

PLASTIC BEHAVIOUR AND STRUCTURAL EVOLUTION OF POLY(OXYMETHYLENE) UNDER LARGE TENSION AND SHEAR STRAINS

A. DAHOUN*, C. G'SELL*, A. MOLINARI, G.R. CANOVA*** and M. J. PHILIPPE******

The plastic behaviour of poly(oxymethylene) was determined under uniaxial tension and simple shear at constant strain rate at a temperature between T_g and T_m. The divergence of the Von Mises equivalent strain-strain curves observed between the two deformation modes for $\varepsilon_{eq} > 0.5$ indicates the effect of the molecular orientation on plastic-hardening. The X-ray diffraction analysis of plastically deformed specimens shows that uniaxial tension induces a fibre-texture with the chains parallel to the tensile axis and simple shear a non-symmetrical texture. It is shown that these results agree with a microscopic deformation model based on the highly anisotropic pencil glide of polymeric chains and on the practical absence of intrinsic plastic hardening for the active glide systems.

INTRODUCTION

Many searchers have acknowledged that the microscopic deformation mechanisms of the individual lamellae play a leading role in the plastic behaviour of semi-crystalline polymers. The papers of Peterlin (1) and Schultz (2), mainly devoted to polyethylene and polypropylene, introduced qualitative concepts showing how the crystalline lamellae deform. However, they could not reproduce the macroscopic behaviour from the microscopic mechanisms, because the mechanical tests conventionally used at that time gave access to the nominal stress-strain behaviour only and not to the true constitutive equation and because no model was available to predict the collective response of a large collection of microscopic events occurring at the scale of single lamellae. Significant progress was achieved recently on both aspects. Firstly the intrinsic stress-strain behaviour of semi-crystalline polymers was determined under uniaxial tension and simple shear at constant true strain rate by means of video-controlled testing devices, as the ones developed by G'Sell et al (3-4). Also, a viscoplastic self-consistent model of polycrystal plasticity originally proposed by Molinari et al (5) was recently adapted to the case of orthorhombic polyethylene and poly(ether ether ketone) (6-9). It is the aim of this paper to apply these new methods to the case of a polymer with a hexagonal crystal structure, namely poly(oxymethylene).

*Laboratoire de Métallurgie Physique & Science des Matériaux (URA CNRS 155) Ecole des Mines, Parc de Saurupt, 54042 NANCY (France)
**Laboratoire de Physique et Mécanique des Matériaux (URA CNRS 1215) Université de Metz, ISGMP, Ile du Saulcy, 57045 METZ (France)
***Génie Physique et Mécanique des Matériaux (URA CNRS 793) INPG, BP 46, 38042 SAINT-MARTIN-D'HERES (France)
****Laboratoire de Métallurgie des Matériaux Polycristallins, Université de Metz, ISGMP, Ile du Saulcy, 57045 METZ (France)

MATERIAL AND MECHANICAL TESTS

The poly(oxymethylene) -POM for short- considered in this work is a commercial grade of molecular weight, M_w = 539 000 g/mol, produced by Hoechst (Ref. Delrin Hostaform C).The thick plates obtained by extrusion were annealed under vacuum for 24 hours at 120 °C. The degree of crystallinity assessed from the density (ρ = 1.40 g/cm^3) and from the DSC (ΔH_F = 162 J/g) is equal to X_c^v = 63 %. The crystalline structure of POM is based on a hexagonal unit cell with axes a = 0.447 nm and c = 1.739 nm (10-11).

The material was subjected to mechanical tests under uniaxial tension and simple shear by means of novel video-controlled materials testing systems called "VidéoTraction" and "VideoShear" respectively (3-4). These systems were designed in such a way that the true strain rate or shear rate can be controlled locally. The deformation or the shear are assessed locally by means of a special videocontrolled extensiometer and a servo-hydraulic testing machine. The comparison of the shear tests with the tensile tests was based on the Von Mises equivalent strain and stress, which write for simple shear $\varepsilon_{eq} = \gamma / \sqrt{3}$ and $\sigma_{eq} = \tau \times \sqrt{3}$. All the tests presented in this paper were performed at 100 °C with an equivalent strain rate equal to $\dot{\varepsilon}_{eq} = 5.10^{-4} s^{-1}$.

As for the microstructural investigation, several specimens were deformed in tension and shear up to different equivalent strain values : ε_{eq} = 0.5, ε_{eq} = 1, ε_{eq} = 1.5 and ε_{eq} = 1.9. Small cylinders, 2 mm in diameter, were carefully machined on a lathe at the precise location where the deformation was measured. The crystallographic texture was characterised from complete pole figures obtained with a X-ray goniometer by rotating the cylinder around its axis and around a perpendicular axis (12). The incident X-ray beam was Cu – Kα_1 (λ = 0.154 nm) and the experimental pole figures were obtained with the $10\bar{1}0$, $10\bar{1}5$ and $11\bar{2}5$ reflections. Microdensitometric analysis was also carried on small fragments of polymer (about 8 mm^3) carefully cut from plastically deformed specimens.

RESULTS AND DISCUSSION

Typical stress-strain curves of POM at 100 °C, obtained under uniaxial tension and simple shear, are shown in figure 1 in term of the Mises work conjugated quantities defined above. It can be observed that for $\varepsilon_{eq} < 0.5$ the curves are nearly superimposed, but they diverge for large plastic deformations : the flow stress remains practically constant after the yield point under shear while a large strain-hardening develops in tension. This dramatic discrepancy from the Von Mises law will be now discussed in terms of the development of orientation textures and of the deformation damage.

Figure 2 shows pole figures of the normals to the crystal planes $(10\bar{1}0)$ for samples deformed at ε_{eq} = 1 under uniaxial tension and simple shear. Unlike the pole figures of the undeformed samples which showed an isotropic distribution (12), it is evident that the deformed samples are highly textured. In uniaxial tension, one observes a fiber texture with the $\vec{c}$ axis (chain direction) parallel to tensile direction : the normals to the $(10\bar{1}0)$ planes (corresponding to $\vec{a}$ axis) are oriented evenly in the plane perpendicular to the tensile axis. In the case of simple shear, the plastic deformation induces a non-symmetrical texture. The $(10\bar{1}0)$ planes are divided in to three groups : one with the normals practically perpendicular to the shear plane and the two others with the normals oriented at 30 degrees apart the shear plane. Subsequently it is deduced from this feature and from the orientation of the $(10\bar{1}5)$ planes (not shown here) that the $\vec{c}$ axis rotates toward the shear direction.

Several works (1, 2, 9, 12-14) have shown that the plastic deformation of the semi-crystalline polymers under uniaxial tension occurs in three steps : i) interlamellar slip and separation affecting the rubber-like amorphous phase, ii) plastic slip of the crystalline lamellae controlled by the glide of dislocations and accompanied by crystal tilting, iii) formation of fibrous structure by chain unravelling, lamella fragmentation and crazing. The curves in figures 3 show the relative variation of the density ρ / ρ_0 during the deformation (ρ_0 is the density of the undeformed material). It appears that the density of the deformed POM under uniaxial tension is reduced by 30 % for $\varepsilon_{eq} \geq 1$, while in

shearing mode it remain almost constant. This microdensitometric analysis shows that the structural damage is active in tension and is negligible in the simple shear case.

A detailed modelling of the viscoplastic deformation in the crystalline lamellae was performed with the viscoplastic self-consistent (VPSC) model introduced by Molinari et al (5) and previously applied to the orthorhombic polyethylene and poly(ether ether ketone) crystals (6-9). For the present material, the VPSC method was adapted to the highly anisotropic behaviour of the POM hexagonal lattice, taking into account both the chain slip and the transverse slip systems on planes parallel to the $\vec{c}$ axis. It predicts the global stress-strain behaviour as well as the texture development due to the progressive rotation for a polycrystalline aggregate subjected to large plastic strains. The model is of the "1-site" type , which means that the interaction between a given lamella and all the others is approached by the interaction of an inclusion with an "equivalent homogenous medium" in which it is embedded. The lamellae are supposed to obey a viscoplastic behaviour controlled by the activation of glide systems on crystallographic planes containing the chain axis. Furthermore, the contribution of the rubber elasticity of the amorphous phase is neglected. In a first approximation, the chain slip systems and the transverse slip systems are supposed to yield under the same critical resolved shear stress (CRSS).

The theoretical stress-strain behaviour of the POM in tension and shear obtained from the VPSC model, are given in figure 4. The adjustment of the overall yield stress with the real curves leads to a CRSS of about 20 MPa. At moderate strains, the model reproduces correctly the main features of the experimental results. However, at very large strains in tension, the simulation overestimates the flow stress. This is because the Schmid factor of the chain slip systems decreases with the plastic strain and the glide of dislocations on these systems becomes more difficult. So the local shear rate ($\dot{\gamma}_s$) of transverse slip systems increase. Furthermore the CRSS of the latter systems is probably underestimated with respect to the values given by the literature (13-14). Experimentally, the chain unravelling and the lamella fragmentation mechanisms do participate to the total deformation. Consequently the variations of Schmid factor for the chain slip systems and the shear rate of the transverse slip systems are less important than predicted by the model in which the strain damage associated with lamellar fragmentation was not introduced to date. This argument is supported *a contrario* by the much better fit in the simple shear case, where the damage was proved to be negligible. Finally in figure 5 are presented the $(10\bar{1}0)$ pole figures obtained from the numerical simulations at $\varepsilon_{eq} = 1$. It is visible from these diagrams that the model reproduces quite correctly the development of the fiber-texture under uniaxial tension and in simple shear, the rotation of the chain axis toward the shear direction.

REFERENCES

1 Peterlin A, J Mater Sci 6 (1971) 490
2 Schultz J, "Polymer Materials Science", Englewood Cliffs (New Jersey), 1974
3 G'Sell C and Shrivastava S, J Mater Sci 18 (1983) 903
4 G'Sell C, Hiver J M, Dahoun A and Souahi A, J Mater Sci 27 (1992) 5031
5 Molinari A, Canova G R and Ahzi S, Acta Met 35 (1987) 2283
6 Ahzi S, Parks D M and Argon A S, Textures and Microstructures 14-18 (1991) 1141
7 Parks D M and Ahzi S, J Mech Phys Solids 38 (1990) 701
8 Dahoun A, G'Sell C, Molinari A and Canova G R, Use of Plastics and Plastic Composites, 1993 ASME Winter Annual Meeting 46 Ed Stokes V K, (New York),1993
9 G'Sell C and Dahoun A, (1993) (to be published)
10 Uchida T and Tadakoro H, J Polymer Sci 5 (1967) 63
11 Wunderlich B, "Macromolecular Physics Vol. 1 : Crystal Structure, Morphology, Defects", Academic Press (New York), 1973
12 Dahoun A, PhD Thesis, Institut National Polytechnique de Lorraine, Nancy, France, 1992
13 Gezovich D M and Giel P H, J Mater Sci 6 (1971) 509
14 Bowden P B and Young R J, J Mater Sci 9 (1974) 2034

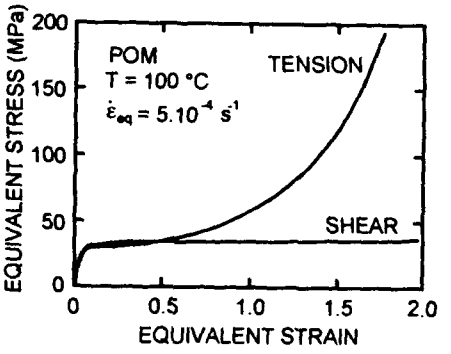

Figure 1 : **Experimental** stress-strain curves obtained from tests under uniaxial tension and simple shear.

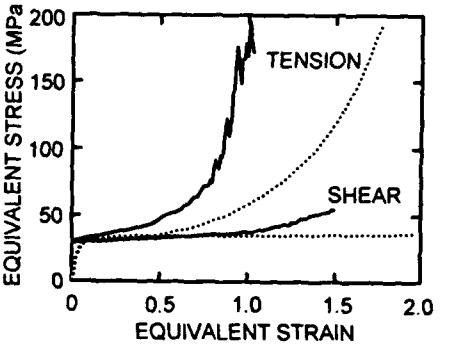

Figure 4 : **Simulated** stress-strain curves from the 1-site viscoplastic self-consistent model for the fully crystallised POM. The experimental curves are displayed in doted line for comparison.

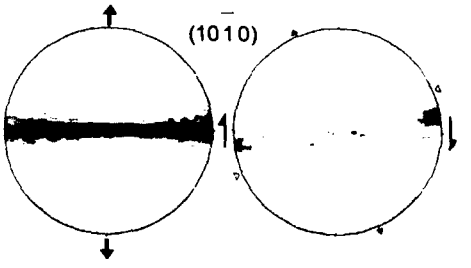

Figure 2 : **Experimental** (10$\bar{1}$0) pole figures obtained at ε_{eq} = 1 under uniaxial tension and simple shear.

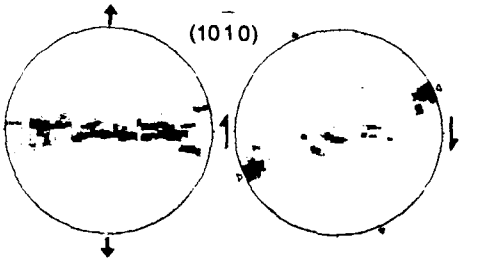

Figure 5 : **Simulated** (10$\bar{1}$0) pole figures obtained at ε_{eq} = 1 under uniaxial tension and simple shear.

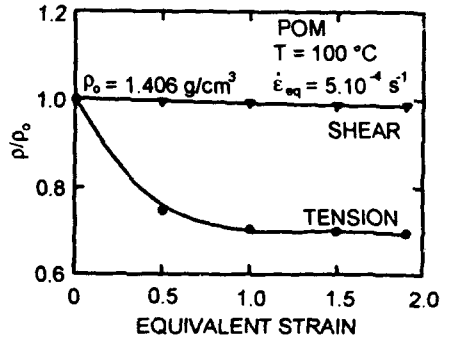

Figure 3 : Relative variation of the density for predeformed POM.

VALIDITY OF THE ACCUMULATED TRUE STRAIN IN THE CONSTITUTIVE EQUATIONS OF GLASSY POLYMERS

C G'Sell, B Dusausoy, M Aboulfaraj and J-M Hiver *

The tensile behaviour of PMMA was investigated with a special videometric system which controls the true stress and the accumulated true strain. Special tests were performed with dual deformation sequences beginning below T_g and ending above T_g (or vice-versa). The corresponding mechanical behaviours were compared to the two constitutive laws at constant temperatures. Although the tensile strain is mostly dependent on the current strain and strain-rate, a significant horizontal shift in the stress-strain curves in observed when the tests are started above T_g and continued below T_g. The shift increases with the prestrain in the rubber-like state. These results show that the accumulated true strain is only valid to a first approximation and should rigorously be corrected by a term taking into account the thermo-mechanical history.

INTRODUCTION

Following pioneer rks (1, 2), the plastic behaviour of amorphous polymers has been the object of a renewed interest d ing the last decade, principally to what is concerned with : i) the microscopic mechanisms which are activated at the yield point (3) and, ii) the processes which control the constitutive equation at large strains under multiaxial loading modes (4, 5). As for the latter point, several arguments co-operatively indicate that the work-hardening at large strain is controlled by the entropic forces which tend to restore the initial shape of the chains between entanglements and/or crosslinks. However, the problem is still open whether the accumulated strain tensor is valid to describe the deformation state or if a more complex function of the thermo-mechanical history of the material should be taken into account to represent the deformation state. The aim of this paper is to check this question in the pure case of uniaxial tension for a crosslinked grade of poly(methyl methacrylate) -PMMA for short- which can be considered as a model amorphous material.

MATERIAL AND METHODS

Thick plates of an industrial grade of PMMA were provided by the Orkem company. It was polymerised in presence of a small amount of trimethylol-1,1,1-propane trimethacrylate (TRIM) which crosslinked the main PMMA chains at fourfold junctions. The microstructure, characterised by swelling in chloroform at 25 °C, corresponds to a rather loose network (molecular weight between crosslinks $M_c = 2840 \pm 230$ g/mole) with a very low fraction of soluble chains (1.5 %). The glass-transition temperature, T_g, is equal to 118 °C. Axisymmetric tensile samples with a hourglass shape were carefully machined out of the plates. They are designed in such a way that the true accumulated strain can be determined at the weakest cross-section from the local diameter, D, according to the relation $\varepsilon = 2\,\mathrm{Log}(D_o/D)$ provided the material is incompressible (which is nearly correct for the large plastic or rubber-like deformations in PMMA). Also the true stress is determined

* Laboratoire de Métallurgie Physique & Science des Matériaux (URA CNRS 155), Ecole des Mines (INPL), Parc de Saurupt, 54042 Nancy, France.

at the same cross-section from the local Kirchoff stress corrected by the Bridgman triaxiality factor $F_T(D, R_c)$ through the equation $\sigma = (4F/\pi D^2) \times F_T(D, R_c)$. The geometric parameters (diameter D, radius of curvature R_c) were assessed in real time by a 2-dimensional videometric extensometer and the local true strain-rate was set at a constant value, $\dot{\varepsilon} = 5 \times 10^{-4}\ s^{-1}$, by means of a computerised servo-hydraulic regulation system described elsewhere in details (6).

EXPERIMENTAL RESULTS

The reference behaviours of the PMMA was determined from monotonous tensile tests at 100 °C and 140 °C, respectively (Fig 1). The true stress-strain curve below T_g is characterised by an abrupt yield stress followed by a transient strain-softening stage and eventually a long plastic regime with an increasing strain-hardening. It should be noticed that the yield drop is fully intrinsic since the geometric artefacts associated with the necking process are avoided by the testing method employed. By contrast, the curve above T_g is representative of a rubberlike material with no yield and a progressive construction of the stress as the accumulated strain (and hence the chain orientation) increases.

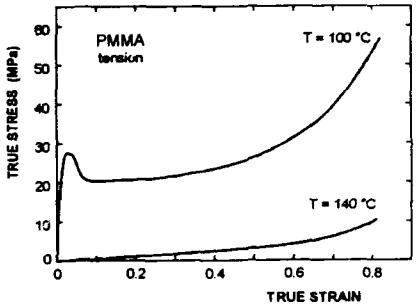

Figure 1
Reference stress-strain curves for the PMMA below T_g (100 °C) and above T_g (140 °C)

Now we examine the results of tests performed with dual-temperature conditions. In some tests the deformation was first run at 100 °C up to a tensile prestrain ε_p and then continued after a temperature jump to 140 °C. In others, the test was started at 140 °C and finished at 100 °C. In both cases, the accumulated strain was strictly held at ε_p during the time necessary for the temperature to stabilise precisely at its new value (30 minutes). The curves corresponding to these thermo-mechanical histories are displayed in figures 2 and 3 respectively, for the same prestrain $\varepsilon_p = 0.4$.

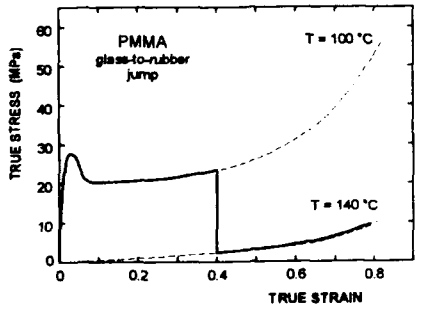

Figure 2 Stress-strain curve observed for a jump from 100 °C to 140 °C

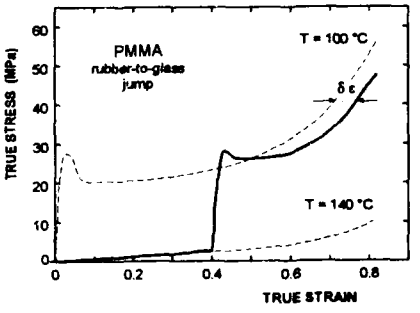

Figure 3 Stress-strain curve observed for a jump from 140 °C to 100 °C

In the case of the glass-to-rubber jump, the behaviour at large strains fits to a very good approximation with the reference stress-strain curve at 140 °C. This means that, for this case, the accumulated strain ε is a quite valid state variable, the constitutive relation $\sigma(\varepsilon,\dot{\varepsilon})$ being independent of the conditions at the beginning of the test.

As for the rubber-to-glass jump, two sources of discrepancy are observed. First, after the strain-rate is switched on again at 100 °C, a marked stress overshoot is recorded at yield. This phenomenon is of the same vein as the transient effects described in a previous paper for various glassy polymers subjected to sudden changes in their plastic regime (7). It corresponds to the onset of plastic deformation from an annealed glassy state, and rapidly disappears after a new steady-state structure is established (within about 0.1 of strain). However, in the present case, the stress-strain curve does not rejoin the reference curve, after the latter transient is passed. Although it is evident that a certain strain-hardening is restored, the true stress lags somehow below the stress corresponding to the reference loading at 100 °C. Consequently, the accumulated strain should be utilised cautiously for the modelling of complex loading histories since, as in this rubber-to-glass jump experiment, the current response of the material may be influenced by the previous loading conditions. Furthermore, in the latter case, it is interesting to note that the discrepancy of the stress-strain curve with respect to the reference curve increases with the prestrain ε_p. Since the attention is focused on the strain variable, we quantify the discrepancy through the horizontal shift $\delta\ \varepsilon$ which separates the actual curve and the reference curve (see Fig. 3 for this construction). The variation of $\delta\varepsilon\ (\varepsilon_p)$, plotted in figure 4, appears to be nearly linear, with an equation which writes $\delta\varepsilon = 0.147\ \varepsilon_p$.

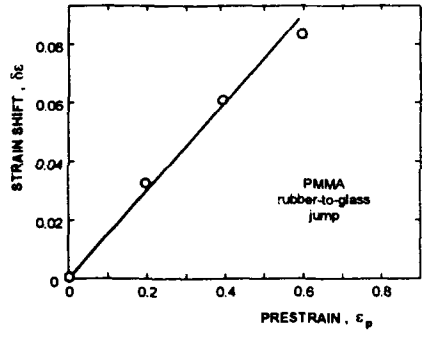

Figure 4 Influence of the amount of prestrain in the rubberlike state on the strain shift in the glassy state

The last type of thermo-mechanical history addressed in this study corresponds to a tensile test run entirely in the glassy state, except for a period of relaxation in the rubbery state. In other words, the material is deformed at 100 °C, stopped at a given prestrain ε_p , heated at 140 °C for 30 minutes, cooled back to 100 °C while the prestrain is still maintained for 30 extra minutes, and finally deformed again up to rupture at 100 °C. Interestingly, the stress-strain curves recorded after the relaxation period is quite similar to the tests performed with a rubber-to-glass jump (Fig. 3). In this case, we observe both the transient yield overshoot when the tension is resumed in the glassy state, and the strain shift of the curve as well. Furthermore, it is found that the influence of the prestrain on the shift follows the linear relation illustrated in Fig. 4 with the same regression coefficient.

DISCUSSION AND CONCLUSIONS

As illustrated by the various experiments above, the validity of the total accumulated strain ("true strain") for the analysis of constitutive relations in amorphous polymers may be questionable if the thermo-mechanical history includes drastic deformation path changes, temperature jumps and/or relaxation periods. However, through the cases reported in the present work, it is evident that some

types of perturbations are more severe than others. In particular it was shown that an escape into the rubbery state (above T_g) results in "erasing out" partially the memory of the previous deformation history. This effect is particularly noticeable in the cases when the ultimate tensile behaviour is recorded in the glassy state, the horizontal shift of the strain-strain curve meaning that the strain memory "lost" during the stay above T_g is about 15 % of the prestrain. In critical cases, serious errors might be committed in the constitutive equation, if this memory erasure were neglected.

In terms of the microstructure, this effects discussed here are to be connected with the different orientational states induced by a deformation above or below T_g. Although the entropic origin of the work-hardening in the glassy state is acceptable, it is clear that the consolidation at large strains is much higher for a glassy polymer than for the corresponding rubbery network, even in the case (as here) when the chains are crosslinked and thus cannot be affected by extensive slip-flow. The latter fact indicates that the network model applicable for predicting the constitutive equations should take into account to some extent the short range van-der-Waals interactions (when they are active) and not only the long-range configurational statistics. By many aspects, this problem corresponds to classical models introduced many years ago for describing the behaviour of glasses and rubbers, particularly the so-called "pseudo-affine" and "affine" schemes (8). In the first one, the macroscopic strain was supposedly undergone by each individual macromolecular bond, while in the second the strain is applied to the extremities of the polymer coils (typically the chemical junctions in a crosslinked network). Although the basic ideas of these models seem rather sound, the differentiation between the two schemes is certainly too drastic if one considers (9) the very gradual transition from the rubberlike to the glassy behaviour while the temperature is lowered across T_g. It should rather be envisaged that inter-chain entanglements become more and more active, the effective end-to-end distance of the sub-chains decreasing progressively as the temperature decreases in the glassy state. By applying an entropy-based constitutive equation for such a finite-length chain network (10, 11), the experimental strain-hardening variations can be readily reproduced.

In this approach, the rubberlike behaviour above T_g constitutes a stable reference basis for the discussion of stress consolidation effects at large strains in amorphous polymers. By contrast, the larger hardening observed in the glassy state is unstable and can be relaxed if the material is re-heated. It is now clear that maintaining the network in the rubberlike state at a given strain for some time tends to loosen the pre-existing entanglements and keeps only the orientation state corresponding to the entropic coils deformed under the macroscopic strain field between the crosslinks. If the deformation is then resumed in the glassy state, this relaxed configuration should be taken as the new starting point of the microstructure.

Acknowledgements

The authors are grateful to Drs. J-Cl Robinet and C Wrotecki, formerly at the Orkem Co., for kindly providing the material and for valuable discussions.

REFERENCES

1 Argon A S, Phil Mag 28 (1973) 839
2 Bowden P B, Raha S, Phil Mag 29 (1974) 149
3 Mangion M B M, Cavaillé J Y, Perez J, Phil Mag A66 (1992) 773
4 Boyce M C, Parks D M, Argon A S, Mech Mater 7 (1988) 15
5 Souahi A., Thèse de Doctorat, INPL, Nancy (France), 1992
6 G'Sell C, Hiver J-M, Dahoun A, Souahi A, J Mater Sci 27 (1992) 5031
7 G'Sell C, Jonas J J, J Mater Sci 16 (1981) 1956
8 Ward I M, Br J Appl Phys 18 (1967) 1165
9 G'Sell C, Souahi A, in this volume, paper # 29
10 Arruda E M, Boyce M C, J Mech Phys Solids 41 (1993) 389
11 Wu P D, van der Giessen E, J Mech Phys Solids 41 (1993) 427

ESSENTIAL WORK OF FRACTURE FOR LLDPE AND PA/PPE BLEND

X C Zhang* and I K Partridge*

Fracture essential work w_e was investigated for linear low density poly thylene (LLDPE) and nylon/polyphenylene ether blend (PA/PPE) using deeply double edge notched tension (DDENT) specimens. Non-linear relationship between total fracture work w_f and ligament length l was noticed. w_e obtained by linear regression, which is normally used in this kind of work, is always higher than that obtained by non-linear regression. Variation of plastic work in the outer region within the ligament is probably the main cause responsible for the non-linearity, due to a change of plastic constraint experienced ahead of the crack tip.

INTRODUCTION

Essential work of fracture for ductile and semi-ductile polymers has been explored recently. The basic idea was originally suggested by Broberg (1). Total energy W_f dissipated in the fracture process consists of two parts: (a) **essential work of fracture** w_e, which is the work directly involved in the fracture process at the crack tip, and (b) the plastic work or **non-essential work** w_p, which is the work done in the outer region where gross plastic deformation occurs. W_f can be expressed by:

$$W_f = w_e A_f + w_p V_p \tag{1}$$

where A_f is fracture surface and V_p the plastic zone volume. Consider a pre-cracked sheet of thickness t and ligament l. Equation (1) can be equally expressed by:

$$w_f = w_e + w_p \alpha h \tag{2}$$

or alternatively

$$w_f = w_e + w_p \beta l \tag{3}$$

where w_f ($=W_f/tl$) is normalized total energy of fracture, h the maximum plastic zone height, and α and β the shape factors of the zone, presumed ellipse-shaped.

Equation (3) is widely used in literature for w_e measurement. Linear relationship between w_f and l has been reported by several authors (2 - 6). w_e is a

* Advanced Materials Group, Cranfield University, Bedford MK43 OAL, England

material constant for a given sheet thickness. A transition region of plane stress - plane strain is set up at the ratio $l/t = 3$. This transition, however, was not observed by Parisi et al (7) in the nylon/polyphenylene ether blend, although linear relationship between w_f and l was observed. In this research, non-linear relationships between w_f and l are found for the two materials investigated. The deviation from linearity is probably due to change in non-essential work w_p and, possibly, the shape factor β with variation of the l/t ratio .

EXPERIMENTAL

Materials used in this research are: (1) linear low density polyethylene (LLDPE) in the form of 0.3 mm thick blown film; (2) nylon - polyphenylene ether blend (PA/PPE) as 1 mm and 4 mm thick sheet. Deeply double edge notched tension (DDENT) specimens, of width W = 75 mm and height H = 150 mm, were made as follows. The LLDPE film specimen notches were shaped centrally on both side with a razor blade, whereas the initial notch in the PA/PPE blend specimens was milled with a V-shaped cutter. In both cases, the notch was sharpened further by pressing in a new razor blade. The test was conducted on an Instron Model 6025 machine at cross-head speed 2 mm min^{-1} and 20 mm min^{-1} for PA/PPE blend sheet and LLDPE film respectively.

RESULTS AND DISCUSSION

Figure 1 shows a plot of fracture energy w_f against ligament l, where points are experimental results, solid lines are non-linear regression lines and the dotted line is linear regression line (only one is shown). Essential work of fracture w_e obtained from both methods is collected in Table I. It appears that the essential work of fracture w_e obtained by linear regression is significantly higher than that obtained by non-linear regression for the materials investigated.

Stress state experienced ahead of the crack tip will affect the fracture. Energy consumed during the process is normally lower in plane strain than in plane stress fracture due to the high plastic constraint for the former. Both essential work w_e and non-essential work w_p will be affected by this factor. Total normalized fracture energy w_f is expected to be lower for a thicker specimen, as should be the fracture initiation stress. This is confirmed by the results in Figures 1 and 2, where the maximum nett section stress σ_{max} is taken as the fracture initiation stress. However, there is no clear indication of transition from plane stress to plane strain fracture when l decreases through the point where $l/t = 3$, as indicated in Figures 1 and 2 for 4 mm thick PA/PPE sheet. It can be seen that σ_{max} increases gradually with decreasing ligament l for increasing plastic constraint as l/t decreases.

The non-linear relationship of w_f against l found in this research may be caused by two factors: (a) non-essential work w_p; and (b) plastic zone shape factor β in Equation (3). They are possibly variables rather than constants, changing with variation of stress state, which is affected by both thickness and the ratio l/t. Assuming an ellipse-shaped plastic zone gives $\alpha = \pi/2$ and $\beta = \alpha hl$. According to Equation (2), a straight line would be expected for a plot of w_f against h if w_p is a constant. This is not true as shown in Figure 3, where the non-linearity relating to

w_f and h indicates that w_p may not be a constant but may increase with increasing h. This behaviour should be expected because of less plastic constraint ahead of the crack tip at large ligament l and, therefore, more plastic deformation work involved before fracture. In addition, non-linear relation between h and l also exists as shown in Figure 4, indicating that β might not be a constant either.

It is worth noticing that w_p increases with increasing h (Figure 3) while β decreases (Figure 4). These two effects may lead to $w_p\beta$ being a constant or only slightly variable, which might give an approximately linear relationship of w_f and l at the plane stress/plane strain transition. It is understood that the crack tip stress state will change as l/t decreases, especially approaching zero. However, for sheet 3 - 6 mm thick, normally used in the research (references 2 - 7), it is not easy to approach plane-strain-dominated fracture. This requires very thick specimens, about 50 mm as found by Yap et al (8) in HIPS, for most ductile or semi-ductile plastics. As a result, gradual changing in the stress state ahead of the crack tip with variation of l will be expected, which probably leads to variation of w_p in the same way. Nevertheless, the concept of fracture essential work is clearly defined and the method is easy to use, particularly for those plastics which fail in ductile manner, such as the thin sheet used in this research. However, further research is needed to clarify whether or not non-essential work w_p is a constant under presumably plane stress conditions at $l/t > 3$ or under near plane strain conditions when $l/t < 3$.

TABLE I Fracture essential work w_e (kJ m^{-2}) of LLDPE and PA/PPE

Materials	LLDPE t = 0.3 mm	PA/PPE t = 1 mm	PA/PPE t = 4 mm
Linear R+	50	26	21
Non-linear R+	33	15	15

+ R stands for regression.

ACKNOWLEDGEMENTS

The authors thank the VAMAS (Versailles Project on Advanced Materials and Standards) TWA4 group for providing PA/PPE material and the ESIS (European Structural Integrity Society) Task group 4 for supplying LLDPE film and the test protocol.

SYMBOLS USED:

α/β = plastic zone shape factor
h = plastic zone height (mm)
l = ligament (mm)
t = thickness (mm)
w_e = essential work (kJ m^{-2})
w_f = normalized total energy (kJ m^{-2})
W_f = total energy (kJ)
w_p = non-essential work (kJ m^{-3})

REFERENCE:

1 Broberg K B, J. Mech. Phys. Solids 23 (1975) 215.
2 Mai Y-W and Cotterell B, Int. J. Fract. 32 (1986) 105.
3 Vu-Khanh T, Polymer 29 (1988) 1979.
4 Saleemi A S and Nairn J A, Polym. Eng. Sci. 30 (1990) 211.
5 Mai Y-W and Powell P, J. Polym. Sci., Part B: Polym. Phys. 29 (1991) 785.
6 Wu J, Mai Y-W and Cotterell B, J. Mater. Sci. 28 (1993) 3373
7 Parisi L, Marchetti A, Lazzeri A and Levita G, Polymer Processing Society IX Annual Meeting, Manchester 5-8 April 1993, page 281.
8 Yap C F, Mai Y W and Cotterell B, J. Mater. Sci. 18 (1983) 657.

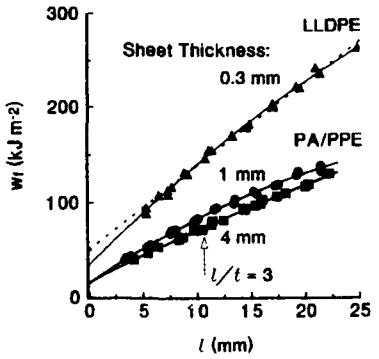

Figure 1 Fracture energy w_f as a function of ligament l.

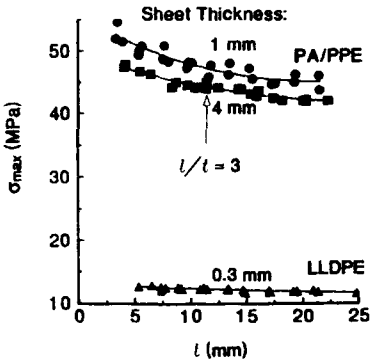

Figure 2 Maximum nett section stress σ_{max} as a function of ligament l.

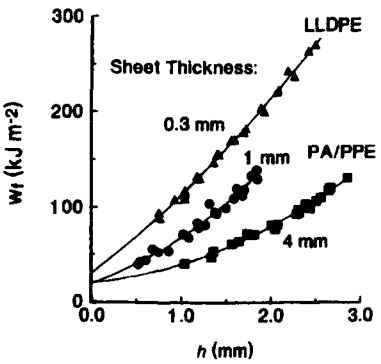

Figure 3 Fracture energy w_f as a function of maximum plastic zone depth h.

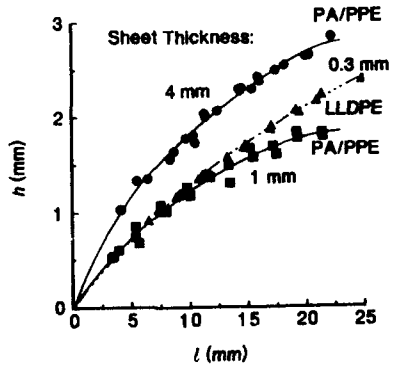

Figure 4 The influence of ligament l on maximum plastic zone depth.

TOUGHENING OF EPOXY CASTING MATERIALS

T. Shimizu*, M. Kamino*, M. Miyagawa*, N. Nishiwaki**, S. Kida**

Epoxy casting materials are usually filled with rigid particles like silica flours and their fracture toughness is also improved by the crack pinning effect. Epoxy resin is also toughened by adding soft silicone gel particles. The toughness is influenced by the size and amount of dispersed silicone gel particles. The maximum effect is obtained for hybrid system filled with both particles. This material also shows an excellent balance of mechanical, electrical and thermal properties for insulating and structural materials.

INTRODUCTION

Epoxy casting materials are used widely in heavy apparatuses because of their excellent properties. They are usually filled with inorganic fillers, like silica flour, to control their thermal expansion coefficient and modulus. Their fracture toughness is also increased by crack pinning effect of rigid silica. However, epoxy casting materials are still brittle and their resistance to thermal shock or small defects is poor. To improve their fracture toughness, furthermore, it is effective to use soft particle dispersion. The toughening mechanism of rigid particles is different from that of soft particles, so it is possible to obtain the maximum effect by using the hybrid system of both particles(1,2).
In this report, the effect of a hybrid system of rigid silica flours and rubbery soft particles on the fracture toughness and on other properties was investigated for epoxy casting materials.

EXPERIMENT

Materials Bisphenol epoxy resin was used with a curing agent (phthalic anhydride) and two types of fillers were added. About 400 phr (per hundred of resin by weight) of silica flour was filled as a rigid particle. Silicone gel was filled up to 30 phr as a soft particle.
Each filler was added to the resin and mixed completely. The size of dispersed silicone gel particle was controlled by changing mixing conditions. After the de-aeration, a curing agent (phthalic anhydride) was added and mixed thoroughly. This mixture was degassed again and poured into a preheated mold and then cured in an oven. Then specimens were cut to a suitable testing geometry.

* Toshiba Corporation, Tokyo, Japan
** Toshiba Silicone Corporation, Gunma, Japan

Testing The fracture toughness (K_{IC}) was measured with SENB (single edge notch bending) according to the testing method recommended by the EGF (European Group of Fracture) (3). As typical static mechanical properties, flexural strength and flexural modulus were determined using three point bending specimens. Electrical properties of volume resistivity and dielectric breakdown strength were also determined. An important thermal index, Tg (glass transition temperature) was determined by DSC (differential scanning calorimetry). The morphology of fracture surfaces were observed by using an SEM (scanning electron microscope).

RESULTS AND DISCUSSION

Mechanical Properties The flexural properties are shown in Figure 1 and Figure 2. The flexural strength did not change much by adding silica flours, but it decreased in the presence of silicone gel and decreased with the increase of silicone gel. This drop was moderated by filling silica flours. The modulus was increased dramatically with silica flours, but decreased more with the increase of silicone gel amount.

The fracture toughness K_{IC} also increased by adding a rigid silica flours as shown in Figure 3. The K_{IC} was increased by increasing the silicone gel content and the maximum value was observed between 10 to 30 phr. The average diameter of silicone gel particles was between 0.2 to 1 μm. This effect was more remarkable for a hybrid system filled with silica flours and silicone gel. Rigid particles seemed to change the stress field around crack tip and promote the shear deformation effect of the soft particles .

By changing mixing conditions, the particle size of the silicon gel was controlled. Figure 4 shows an influence of the average diameter of silicone gel particles on K_{IC}. The amount of silicone gel was a constant 15 phr. The maximum value of K_{IC} was obtained between 0.1 to 1 μm of the average diameter. Finer particles decreased the distance between particles and optimized the shear deformation effect caused by their stress concentration(4), however, gel particles that were too fine no longer cause the stress concentration.

Figure 5 shows the fracture surface of silicone gel filled system without silica flours. It is relatively smooth. On the other hand, the fracture surface of the hybrid system of silica flours and silicone gel was very rough by crack pinning effect of rigid silica as shown in Figure 6. Because the adhesion between epoxy resin and silicone gel was poor, most of the gel particles were pulled out from semi-spherical holes. The strong adhesion around soft particles was not always necessary to improve fracture toughness.

Electrical and Thermal Properties The properties are summarized in Table I. The hybrid system filled with silica flours and silicone gel have a higher toughness and minimized the decrease of static strength.

The volume resistivity was increased slightly by adding silica flours. Silicone gel decreased the volume resistivity even in hybrid systems, but the system's value was still high enough for insulating materials. The dielectric breakdown strength was improved slightly by silica flours and silicone gel. A typical thermal index, Tg, did not change in the presence of silica flours and/or silicone gel. The hybrid system is expected to be thermally stable.

The toughened material of hybrid system had good mechanical, electrical and thermal properties, and showed relatively lower viscosity before curing. It is suitable for insulating, structural and casting materials.

CONCLUSION

From our study, we conclude the following:
(1) The fracture toughness of epoxy resin is dramatically improved by using rigid and/or soft particulate dispersion. The hybrid system is the most effective way to improve the fracture toughness.
(2) The fracture toughness is influenced by the diameter and the content of the dispersed silicone gel particles. The optimum size and content exist to obtain the maximum toughness.
(3) Silicone gel is effective as a soft dispersed particle material and gives a good balance of mechanical, electrical, and thermal properties.

REFERENCES

1 Moloney A C, Kausher H H, Kaiser T and Beer H R, J. Mater. Sci. 22 (1986) 381
2 Kinloch A J, Maxwell D L and Young R J, J. Mater. Sci. 20 (1985) 4169
3 EGF Task Group on Polymers, Testing Protocol (1990)
4 Huang Y and Kinloch A J, J. Mater. Sci. 27 (1992) 2763

Table I Properties of epoxy casting materials

Filler	K_{IC} (MPa-$m^{0.5}$)	Flexural strength (MPa)	Modulus (GPa)	Volume resistivity ($\times 10^{16}$ Ω·cm)	Breakdown strength (kV/mm)
Neat resin	0.64	122	3.0	4.60	25.7
Silica(400phr)	2.47	118	12.1	8.20	27.8
Silicone(15phr)	1.75	88	2.6	0.28	26.5
Hybrid	4.65	109	10.3	1.98	29.4

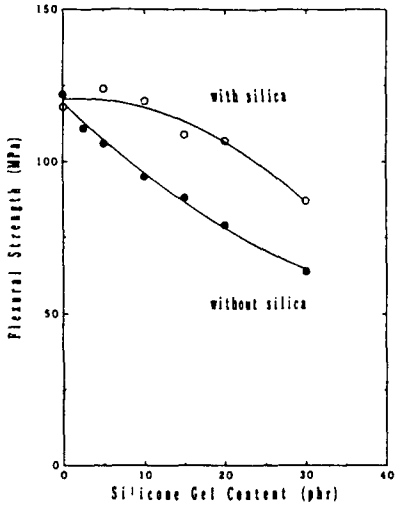

Fig.1 Flexural strength vs silicone gel content

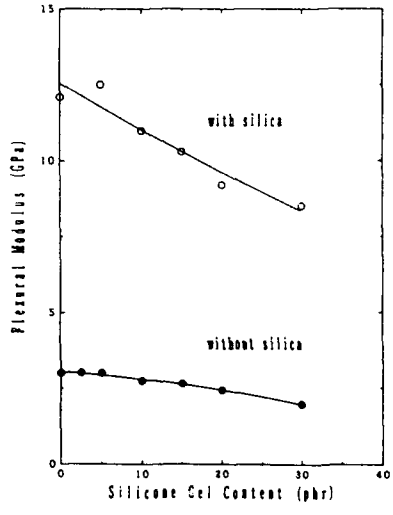

Fig.2 Modulus vs silicone gel content

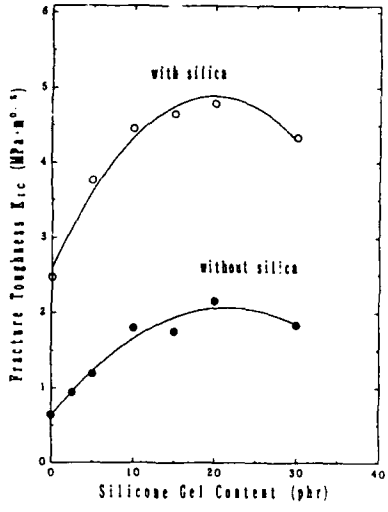

Fig.3 K_{IC} vs silicone gel content

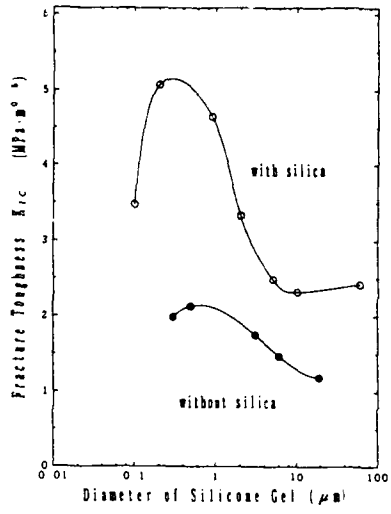

Fig.4 The influence of silicone gel particle size on K_{IC}

Fig.5 Fracture surface of the silicone gel-filled epoxy resin

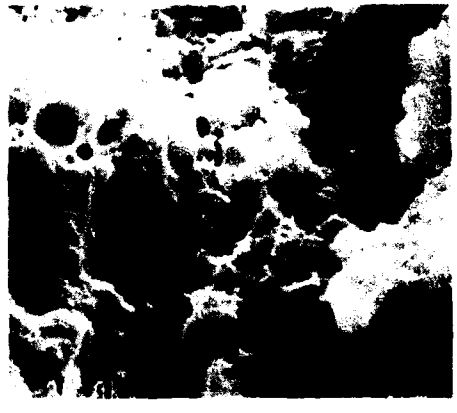

Fig.6 Fracture surface of the hybrid system

INFLUENCE OF CROSSLINK DENSITY OF DIEPOXY/DIAMINE/MONOAMINE NETWORKS ON VISCOELASTIC AND MECHANICAL PROPERTIES

J Galy, J F Gérard, G Reffo and H Sautereau*

R Frassine and A Pavan**

Model epoxy networks with various crosslink densities are prepared using mixtures of diamine and monoamine.

The fully cured networks are studied by means of dynamic mechanical spectroscopy: the glass transition region is characterized by the WLF equation; in the secondary relaxation zone two sub-T_g relaxations, denoted β and ω, are evidenced and discussed. Yielding properties are measured and it is shown that the plastic deformation is favoured by a low crosslink density. A linear relationship is found between K_{Ic} (at 25°C) and $T_{g\infty}$ of the various networks.

INTRODUCTION

The aim of this paper is to describe and analyse the mechanical behaviour of networks and especially the effect of crosslink density. Many ways have been investigated to modify the crosslink density (1). One consists in changing the molecular weight of the epoxy prepolymers (2-3); a second one is to change the stoichiometric ratio (4,5,6); a third one is to regulate the cure schedule (7,8). In these cases dangling chains and/or unreacted monomers are still present in the final networks which are not perfect.

The best way to change the molecular weight between crosslinks seems to be the introduction of a primary monoamine, with a structure similar to that of the diamine comonomer (9,10), which plays the role of chain extender. The stoichiometric ratio is kept constant for all systems.

EXPERIMENTAL

Materials

Pure diglycidyl ether of bisphenol A (DGEBA) from Dow Chemical (DER332) was cured with a cycloaliphatic diamine, 4,4'-diamino-3,3'-dimethyldicyclomethane (3DCM or Laromin C260) from BASF (11). A third component, methylcyclohexylamine (MCHA) from Aldrich was used as a chain extender. The mixtures were prepared with a stoichiometric ratio, a/e, aminohydrogen [NH] to epoxy groups [E] equal to 1, in order to reach the ultimate glass transition temperature. A range of materials, noted MX, with X varying from 0% to 100%, was synthetized, X representing the per cent ratio of $2[NH]_0$ belonging to the monoamine MCHA to the total number of $2[NH]_0$ functions, where the subscript $_0$ means the initial concentration.

* Laboratoire des Matériaux Macromoléculaires, URA CNRS n° 507
Institut National des Sciences Appliquées de Lyon, F-69621 Villeurbanne Cedex, France
** Dipartimento di Chimica Industriale e Ingegneria Chimica
Politecnico di Milano, Piazza L. da Vinci 32, I-20133 Milano, Italy

In order to avoid a loss of monoamine, mixtures having more than 30% of MCHA were cured at 90°C for 1 hour, then at 150°C for 14 hours. Mixtures having less than 30% of MCHA were cured at 130°C for 1 h and then at 190°C for 14 h (11). The final curing temperatures were chosen so as to obtain fully crosslinked networks with T_g equal to $T_{g\infty}$.

Testing

Dynamic mechanical spectroscopy (DMS) of all networks was carried out in the temperature scanning mode at some selected frequencies by means of a dynamic mechanical analyser RDA700 from Rheometrics. The Young modulus at 25°C (E_{25}) was obtained from tensile tests. The uniaxial compressive yield stress, σ_{yc}, was determined for all materials, at different temperatures and strain rates. The fracture properties were measured according to linear elastic fracture mechanics with various geometries [C(T), SE(B), DT], at 25°C and different rates.

RESULTS AND DISCUSSION

Crosslink densities

The experimental values of molecular weight between crosslinks ($\overline{M_c}$) and crosslink density are obtained from the rubber elasticity theory applied to the shear modulus at $T_{\alpha+50°C}$ (Table I).

Table I Characteristics of the networks

Network	T_α [a] (°C)	$\tan\delta_{max}$ [a]	$\overline{M_{c}}_{exp}$ (g mol^{-1})	n_{exp} (mole kg^{-1})	E_{25} (GPa)
M0	207	0.6	245	2.72	2.36
M10	190	0.78	357	1.87	2.65
M30	165	1	540	1.23	2.60
M50	137	1.35	926	0.72	2.67
M60	132	1.41	979	0.68	2.73
M70	126	1.55	1041	0.64	2.77

[a] DMS at 11 Hz at the maximum of the tan δ peak.

Relaxations

The study of the main, α, relaxation leads us to compute the W.L.F. coefficients C_1^g and C_2^g for all the networks. These coefficients decrease as the amount of chain extender is increased. In agreement with previous works, the free volume fraction at T_g increases as the crosslink density decreases.

Other relaxations are evidenced at lower temperatures:

- a relaxation, noted ω, located at 70°C (at 11 Hz), which could be attributed to the motions of parts of the macromolecular chains including the cycloaliphatic groups of the diamine;
- the typical secondary relaxation of the epoxies, noted β, located at -50°C (at 11 Hz), commonly associated to the motion of the hydroxyether units;
- in the case of the epoxy networks synthetized with the cycloaliphatic monoamine, MCHA, as a chain extender, an additional relaxation, denoted ω', is observed between the secondary relaxations β and ω. By changing the amount of MCHA, this relaxation becomes more and more pronounced. Thus, ω' could be associated with the motion involving the dangling cycloaliphatic groups of the chain extender.

The amplitude of the β-relaxation peak increases with increasing the crosslink density. This effect could be explained by the required rearrangements of the surrounding chains to accommodate the conformational changes. Thus, the level of damping depends on the crosslink density. For the highest amounts of chain extender, the amplitude of the β-peak is constant: this effect is attributed to the superposition of the ω-relaxation peak which contributes to overestimate the amplitude of β.

The apparent activation energy of the β relaxation, $E^{\neq}_{a\beta}$, slightly increases with increasing amount of chain extender, and reaches a plateau over 30% of MCHA. The $E^{\neq}_{a\beta}$ values are very close to those obtained for epoxy networks based on similar epoxy series. The slight dependence of the apparent activation energy on the amount of monoamine could be explained by the overlapping of the ω and β relaxations above pointed out, which contributes to the increase of $E^{\neq}_{a\beta}$

As indicated in Table I, the Young modulus (E_{25}) decreases as the crosslink density is increased. This phenomenon, called "antiplasticization", is related to the characteristics of the β relaxation peak. According to the increased β-motions (i.e., higher amplitude of the β-peak), the Young modulus at room temperature is lower for the more crosslinked network.

Yielding

Attempts at determining the onset of plastic deformations under a number of states of stress (uniaxial tension, simple shear, plane-strain compression) were unsuccessful due to the limited ductility of the materials: they generally fractured before yielding. Only the yield stress in uniaxial compression, σ_{yc}, could be determined for all samples.

At 25°C and a strain rate of 3×10^{-4} s^{-1} the compressive yield stress was found to decrease linearly with MCHA content. This result reflects the increasing mobility of the chain segments as the length of the chain sections between crosslinks increases. Since the glass transition temperature, T_α, of the networks decreases when the amount of MCHA is increased, and these yield measurements were carried out at the same temperature (25°C), the observed trend in σ_{yc} vs MCHA content is likely to reflect, mainly, the different depression of the test temperature below the sample glass transition temperature.

On the contrary, the values of σ_{yc} measured at 77°K (-196°C) are constant with MCHA content, showing that below T_β the deformation mechanism which governs the yielding process does not depend on the degree of crosslinking.

Fracture

The double-torsion (DT) testing technique was used to study the effect of varying crack speed (obtained by varying the displacement rate) on fracture toughness, G_{Ic}, at 25°C. Two materials were tested: M0 and M60. Depending on displacement rate, the material M0 displayed either stick-slip or continuous crack propagation. In the former case, the G_{Ic} values at crack initiation, G_{Ici}, are observed to decrease as displacement rate increases up to the point where the propagation mode changes from unstable to stable; on the contrary, the G_{Ic} values at crack arrest, G_{Ica}, are substantially constant with displacement rate. The material M60, on the other hand, displayed stable crack propagation for all displacement rates tested and G_{Ic} values very close to the arrest values obtained with the material M0.

The influence of crosslink density was studied more extensively in three-point bending [SE(B)] by testing the whole series of networks, though at a single displacement rate and room temperature.

Stick-slip crack propagation was only observed for the M0 and M10 networks. The transition to stable crack propagation at higher MCHA contents, i.e. lower crosslink densities, appears to be related to the decrease in glass transition temperature and the associated decrease in yield stress.

The values of the critical stress intensity factor measured at fracture initiation, K_{Ici}, are strongly improved (from 0.76 MPa$\sqrt{m}$ for M0 to 1.37 for M70) by the insertion of increasing amounts of monoamine, while the values measured at crack arrest, K_{Ica}, are nearly the same for the M0 and M10 networks. The fracture energy values obtained with this geometry for the M0 and M60 networks compare well with those obtained in DT.

The increase in K_{Ici} correlates with the decrease in σ_y. In the case of thermosets a simple calculation shows that chemical bond breakage may contribute to the fracture energy only for about 1 J m^{-2}, which is less than 1% of the experimental G_{Ic} value. Thus, in the case of high-T_g crosslinked materials the main source of energy absorption before failure is shear plastic deformation at the crack tip. A linear relationship (with negative slope) between K_{Ici} and σ_{yc} is found up to about 130 MPa.

Linear relationships are also obtained between K_{Ici} and T_g and K_{Ici} versus crosslink density n. The latter one obeys the equation $K_{Ici} = K_{Ico} - 0.28n$, n being expressed in mole kg^{-1} and K_{Ic} in MPa$\sqrt{m}$. A linear relationship such as this one has already been reported (12) and is, here, clearly ascertained because of the introduction of a monoamine of the same structure for the same stoichiometric ratio. Extrapolation of this relationship to n=0 gives K_{Ico} = 1.5 MPa$\sqrt{m}$ for the critical stress intensity factor of the uncrosslinked polymer.

CONCLUSION

The choice of a model system obtained by using a monoamine as a chain extender made it possible to prepare well-characterized networks of various crosslink densities. The glass transition and the secondary relaxations were characterized and discussed in connection with the network structure. The antiplasticization effect was explained. We demonstrated clearly that fracture toughness is related to T_g or crosslink density by a linear relationship.

REFERENCES

1 Lemay J D, Swelin B J, Kelley FN, ACS Adv. Chem. Ser. 243 (1984) 165.

2 Misra S C, Manson J A, Sperling L H, ACS Adv. Chem. Ser. 114 (1979) 137.

3 Vaskil U M, Martin G C, J. Appl. Polym. Sci. 46 (1992) 2089.

4 Gupta V B, Drzal L T, Lee C Y C, Polym. Eng. Sci. 25 (1985) 812.

5 Palmese G R, McCullough R L, J. Appl. Polym. Sci. 46 (1992) 1863.

6 Ilavsky M, Zelenka J, Spacek V and Dusek K, Polym Networks Blends 2(2) (1992) 95.

7 Jordan C, Galy J and Pascault J P, J. Appl. Polym. Sci. 46 (1992) 859.

8 Amdouni N, Sautereau H, Gérard J F and Pascault J P, Polymer 31 (1990) 1245.

9 Charlesworth J M, Polym. Eng. Sci. 28 (1988) 221.

10 Won Y G, Galy J, Gérard J F, Pascault J P, Bellenger V and Verdu J, Polymer 31 (1990) 1787.

11 Verchere D, Sautereau H, Pascault J P, Riccardi C C, Moschiar S S and Williams R J J, Macromolecules 23 (1990) 725.

12 Verdu J, Bellenger V, Morel E in 'Developments and design with advanced materials', G.C. Sih, S.V. Hoza, J.T. Pindera eds., Elsevier (1990) p. 249.

THE EXPERIMENTAL STUDY ON TIME-TEMPERATURE SUPERPOSITION PRINCIPLE FOR INJECTION MOULDED PC/ABS AND PC/PBT BLENDS

G.O. Shonaike*, H. Hamada*, S. Miyaji* and Z. Maekawa*.

An investigation on the effects of temperature and strain rates on mechanical properties of injection moulded PC/ABS and PC/PBT blends have been conducted through bending test over a range of temperature and strain rates. The bending modulus reduces with increasing temperature and strain rate had no significant effect in both cases. The time-temperature master curves indicated that the modulus can be predicted over a wide range of temperatures and strain rates.

INTRODUCTION

Blending of two or more polymer components creates materials with unique properties at low cost. Blend components selected for various reasons must provide stable and reproducible properties which may involve incorporation of a compatibilizer, a chemical reaction or high shear mechanical re-entanglement (1). Some of the properties improved by suitable blending include stiffness, impact resistance, heat distortion temperature, thermal stability and chemical resistance (2-4).

Due to the experimental limitations, the time-temperature curve provides information on modulus in a wide range of temperature, strain rate and time. Therefore, the objective of this investigation is to superimpose data taken from the above variables by shifting.

EXPERIMENTAL

The PC/ABS and PC/PBT blends with trade names of Cycoloy C1000 and Xenoy 1101 were supplied by the General Electric Co. Ltd. The blends were injection moulded using TOYO Plaster T1-30F6 injection moulding machine. The moulding conditions were cylinder temperature = 270^{o}C, mould temperature = 85^{o}C and injection pressure = 77 MPa. The thickness of the injection moulded sample was 3.1mm. Three-point bending test was carried out on by using Instron Tensile Testing Machine, Model 4206 with span length of 48mm at cross-head speeds of 1, 10 and 100mm/min. Test temperature was varied between -40 and 150^{o} C.

*Faculty of Textile Science, Kyoto Institute of Technology, Matsugasaki, Sakyo-ku, Kyoto 606, Japan.

RESULTS AND DISCUSSION

The bending modulus as a function of temperature at different strain rates are presented in Fig.1 for PC/ABS and PC/PBT blends. In PC/ABS blend shown in Fig.1(a), the modulus which was not affected by strain rate remains fairly constant until the temperature approaches the glass transition temperature (Tg) of ABS (Tg = 112°C in this study). In this case, a rapid drop of modulus occurred around 95°C, and towards the highest test temperature, the sample manifests an apparent state of liquid flow. The modulus of PC/PBT irrespective of strain rate (Fig.1(b)) also reduces with increasing temperature but without clear transition from leathery to rubbery state. The reduction of bending modulus of PC/PBT occurred linearly with a certain deviation near the glass transition temperature of PBT, taken to be 73°C (5).

Crazes were observed in PC/ABS tested at 120 and 130°C. They were not detected in other test temperatures and PC/PBT blend. Since PC has a propensity to crazing (6,7), the presence of semi-crystalline PBT in PC/PBT blend suppresses craze formation.

The modulus of the blends can be predicted over a wide range of temperatures and strain rates by superposition. The "master" or reduced curves were constructed by shifting the strain rate scale of each measurement by a factor a_{T_o} with reference temperature been 25°C. The shift factor was obtained by using a well-known Arrhenius equation

$$\log_{10} a_{T_o}(T) = \beta \frac{\Delta H}{R}\left(\frac{1}{T} - \frac{1}{T_o}\right) \qquad (1)$$

where a_{T_o} is the shift factor, β is constant, R is gas constant, ΔH_a is the activation energy, T is the test temperature and T_o is the reference temperature.
The obtained master curves are shown in Fig.2. Both PC/ABS and PC/PBT blends can be superimposed. Although, superposition of semi-crystalline polymers are difficult due to their structures which are rather sensitive to temperature changes (8) but the presence of PC made superposition of the blends possible. The amounts of curve shifting required for the blends at different temperatures are shown in Fig.3. Since the value of the slope is known to be

$$\beta \frac{\Delta H}{R}$$

the activation energies were estimated at low and high temperatures. In both cases, the activation energy was higher in the high temperature region. In the low temperature region, the activation energies of PC/ABS and PC/PBT were almost the same but in the high temperature region, the value for PC/ABS was higher. This indicates that the presence of entanglements in amorphous-amorphous polyblends may lead to high energy barrier which needs to be overcome during deformation.

CONCLUSION

It is established that through the bending test, the modulus of PC/ABS and PC/PBT blends can be predicted over a wide range of temperature and strain rates. The bending modulus, however, reduces with increasing temperature irrespective of strain rate.

REFERENCES

1. Utracki, L., SPE Techn. Pap. 33 (1987)1339.
2. Robeson, L.M., Polym. Eng.& Sci. 24 (1984) 587.
3. Keitz, J.D., Barlow, J.W. and Paul, D.R., J. Appl. Polym. Sci. 29 (1984) 3131.
4. Shonaike, G.O., Europ. Polym. J. 28 (1992) 777.
5. Takashi, M. and Kunio, T., Japan J. Mat. Syst. 10 (1988) 21.
6. Shonaike, G.O. and Reed, P.E., Mat.Sci.& Eng. A119 (1989) 231.
7. Shonaike, G.O. and Reed, P.E., Polym. Inter. 29 (1992) 17.
8. Utracki, L.A., Polymer Alloys and Blends, Hanser Pub. N.Y (1989) Chapter 3.

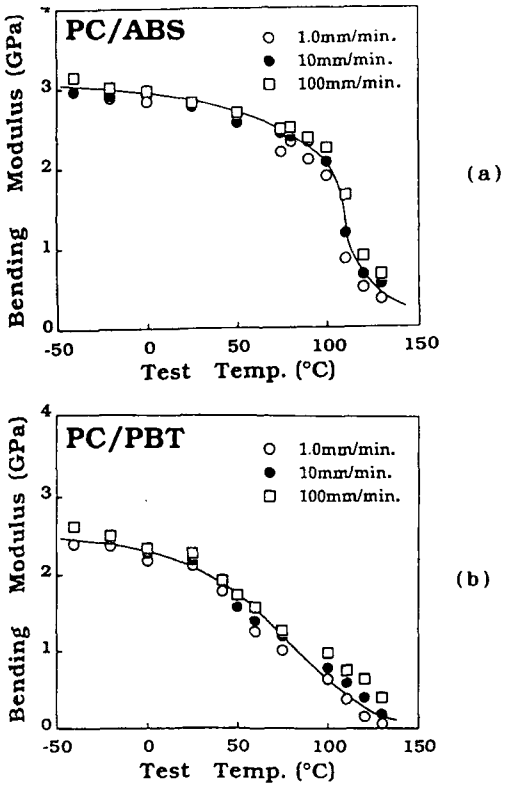

Fig.1. Bending modulus vs temperature (a) PC/ABS (b) PC/PBT.

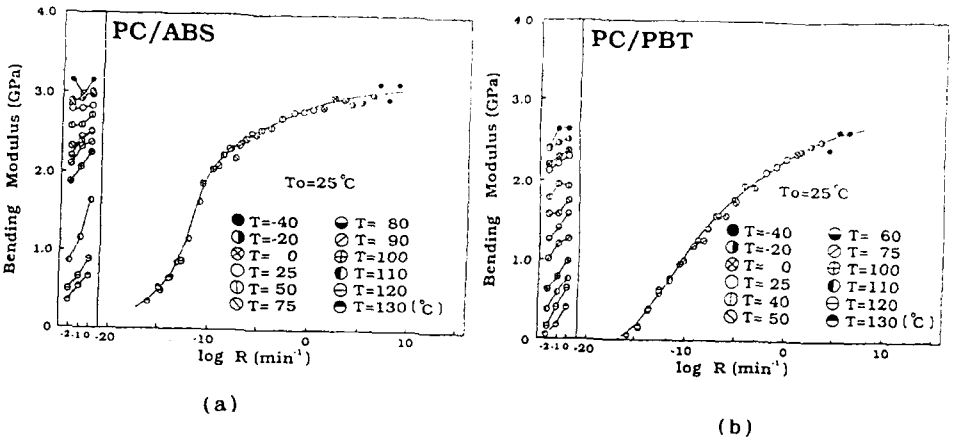

Fig.2. Construction of master curves at different strain rates (a) PC/ABS (b) PC/PBT

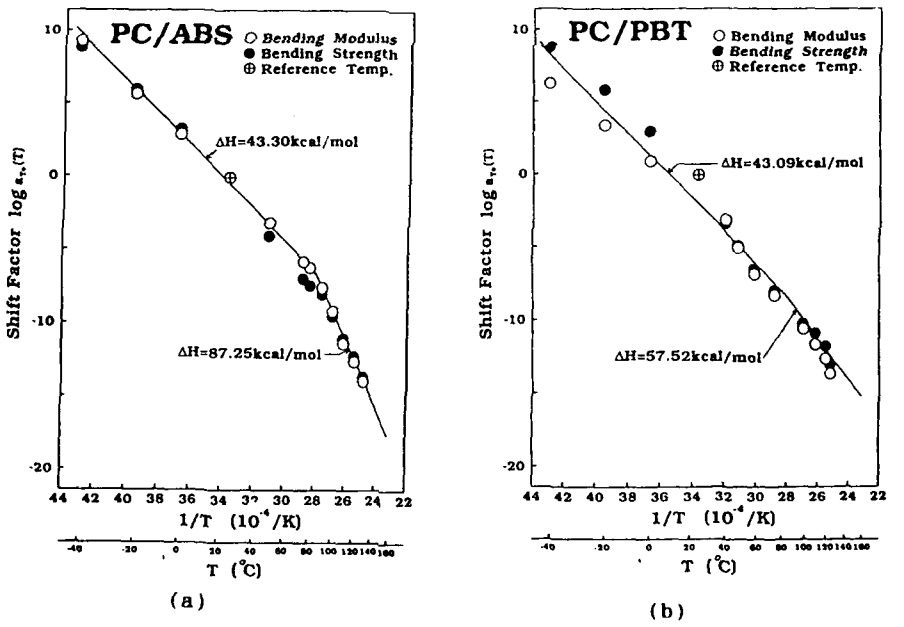

Fig.3. Shift factors for the master curves (a) PC/ABS (b) PC/PBT

THE INFLUENCE OF LCP ON MECHANICAL PROPERTIES OF PPS/LCP BLEND

C.O. Shonaike*, H. Hamada*, S. Yamaguchi* and Z. Maekawa*

The effect of liquid crystalline polymer (LCP) on blend containing polyphenylene sulphide (PPS) and LCP has been studied by bending testing at various temperatures. The increase of bending modulus and reduction of bending strength with increasing LCP content was related to skin-core morphology. The experimental results of bending modulus were in good agreement with calculated values based on rule of mixture.

INTRODUCTION

Inorganic fibres such as glass and carbon fibres are traditionally used as reinforcements for thermoplastics. However, processing of carbon and glass fibre reinforced thermoplastics is somehow difficult and recycling is not easily accomplished. LCP may be regarded as a good reinforcement comparable with carbon and glass fibres (1-3). Depending on processing conditions, the shape of LCP can be changed from spherical to rod-like structure which serves as good reinforcement. This work is directed towards the experimental investigation of the influence of LCP component on deformation and fracture behaviour of PPS/LCP blend. Bending properties were examined at various temperatures and the thermal properties of the two components were checked by using differential scanning calorimetry. The skin-core morphology at various blend compositions was examined by scanninig electron microscopy.

EXPERIMENTAL DETAILS

The linear PPS with $\bar{M}_w$ = 42040 and T_m = 277^oC was supplied by Idemitsu Petrochemical Company. The commercial grade LCP was purchased from dealer and the melting temperature was also 277^oC. Both homopolymers were mixed to give compositions (PPS/LCP) 90/10, 75/25, 50/50, and 25/75. Blending was carried out using a Toshiba TEM35B-10/IV double-screw blender. The blends were extruded, pelletized and dried for about 24hr at 150^oC.

*Faculty of Textile Science, Kyoto Institute of Technology, Matsugasaki, Sakyo-ku, Kyoto 606, Japan.

The injection moulding was carried out on Toyo TI-30F6 injection moulding machine. The moulding conditions were: cylinder temperature = 300°C, mould temperature = 100°C and the injection pressure was 30kg/cm^2. Three-point bending test was carried out on injection moulded samples at testing speed of 2.0mm/min. The fractured surface was examined by scanning electron microscopy.

RESULTS AND DISCUSSION

One of the general attractive features of LCP/thermoplastic blend is the improved stiffness. Plots of bending modulus as a function of LCP content (Fig.1(a)) showed that the bending modulus increased monotonically with increasing LCP content. In Fig.1(b), however, the bending strength falls with increasing LCP content whereas the pure PPS and LCP had identical values. The improved bending modulus and reduction of bending strength is suggested to be related to the skin-core relationship of LCP. The observed morphologies of the skin and core regions of 75/25 blend are shown in Fig.2. The skin region contain fibrils or rodlike structures of LCP about 1-3 μm(4) embedded in PPS matrix. The core region indicates the formation of fine droplets of LCP in the PPS matrix.

The effect of temperature on bending properties are shown in Fig.3. The mode of failure ranges from brittle to ductile depending on test temperature and blend composition. In (PPS/LCP) 100/0, 90/10, 75/25 and 50/50 samples, the brittle-ductile (B-D) transition point was accompanied by a rapid load drop. The B-D transition temperature was not observed in neat LCP and 25/75 blend. Similar situation occurred in bending strength versus temperature curves shown in Fig.3(b). The failure mechanism in this high performance blends involves breaking of the entanglements in the brittle region, stretching and fibre pullout in the ductile region. The enhancement of modulus as a result of LCP fibrils indicates that the rule of mixture applicable to unidirectional fibre-reinforced composite can be used to evaluate the modulus (1).

$$E_c = E_1 V_1 + E_2 V_2 \quad (1)$$

where E_c is the composite modulus, E_1 and E_2 are the moduli of the reinforcing LCP and matrix respectively. V_1 and V_2 are their volume fractions.
Fig.4 compares the experimental and calculated values of bending modulus in the brittle, B-D transition and ductile regions. Good agreement between the experimental and calculated values may be attributed to the alignment of LCP microfibrils as confirmed by SEM observation.

CONCLUSION

It is evident from the above results that LCP is a good reinforcing agent comparable with inorganic reinforcements. The

morphological observation of the blends indicates that the enhancement of bending modulus with increasing LCP component was due to the alignment of LCP fibrils.

REFERENCES

1. Dutta, D., Fruitwala, H., Kohli, A. and Weiss, R.A., Polym. Eng.& Sci. 30 (1990) 1005.
2. Budgell, R.D. and Day, M., Polym.Eng.& Sci. 31 (1991) 1961.
3. Dole, J.R. CHEMTECH, 17 (1987) 242.
4. Shonaike, G.O., Hamada, H., Maekawa, Z., Yamaguchi, S., Nakamichi, M. and Kosaka, W., submitted to J. Mat. Sci.
5. Shonaike, G.O., Yamaguchi, S., Ohta, M., Hamada, H., Maekawa, Z., Nakamichi, M., Kosaka, W. and Toi, K., Polymer Eng.& Sci. (in press).

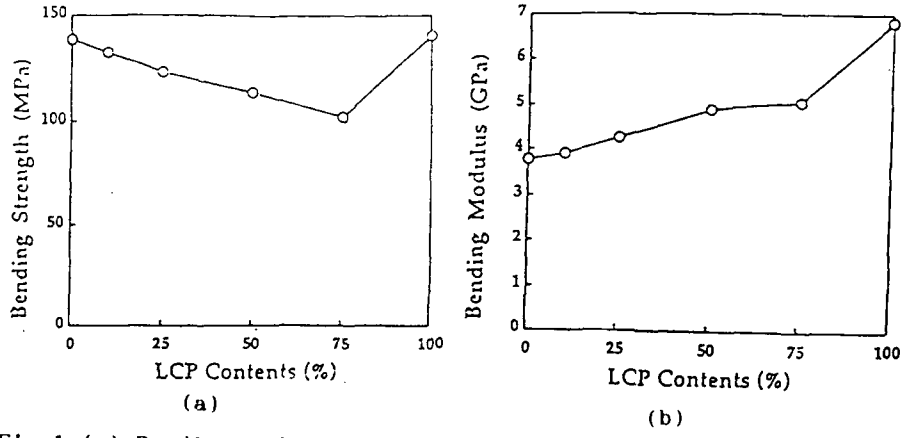

Fig.1.(a) Bending modulus as a function of LCP content
(b) Bending strength versus LCP content (PPS/LCP).

Fig.2. SEM micrographs of fractured surface of 75/25 PPS/LCP blend (a) skin region (b) core region.

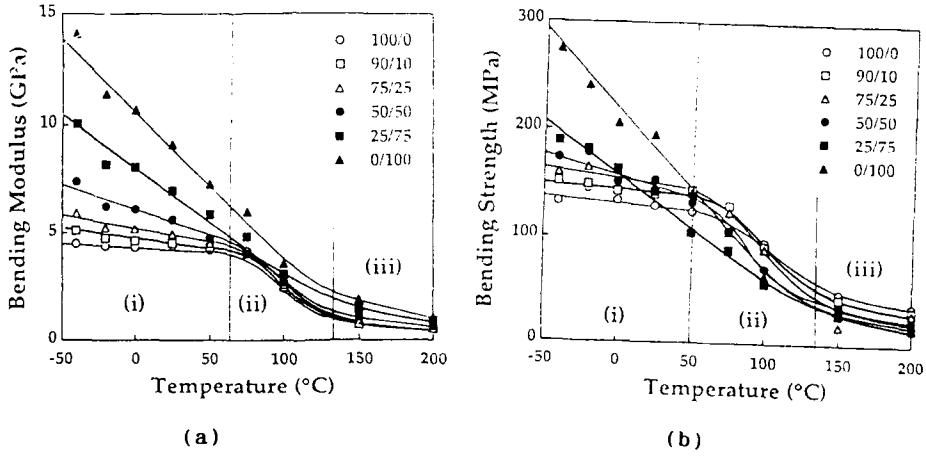

Fig.3.(a) Bending modulus vs temperature (b) Bending strength as a function of temperature.

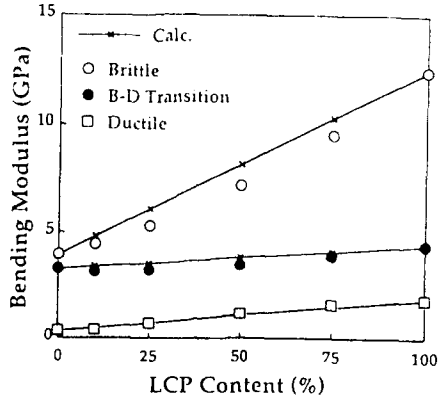

Fig.4. Comparison between experimental and calculated values of bending modulus against LCP content in PPS/LCP blends.

APPROACHES TO DIRECT CALCULATIONS OF SOLID-STATE PROPERTIES: MOLECULAR DYNAMICS SIMULATIONS OF SILOXANE-BASED LIQUID CRYSTALLINE MACROMOLECULES

B. L. Farmer*, R. Pachter§, S. S. Patnaik*, E. P. Socci*, R. L. Crane§ and W. W. Adams§

In our continuing efforts towards developing new materials with controlled optical properties, we focus our studies on a liquid-crystalline siloxane-based ordered matrix for incorporating $\chi^{(2)}$ nonlinear optical (NLO) chromophores. To obtain an estimation of the orientational order parameter from atomistic simulations, molecular clusters of a system based on a cyclic pentamethyl siloxane (D5) core with biphenyl-4-allyloxybenzoate mesogens (BCS) were modeled, with the extensive computational effort enabled by utilizing a massively parallel processing supercomputing capability. In addition, results on a chromophore based on a cyclic tetramethyl siloxane (D4) backbone are presented.

INTRODUCTION

As part of an ongoing effort to complement the understanding of the structure-to-property relationships in siloxane-based liquid crystals, a series of molecular simulations were performed, for example, by Pachter at al (1,2), Socci et al (3), and Patnaik et al (4). These computational studies offered an initial understanding of the influence of molecular structure on the intramolecular interactions and especially the intermolecular arrangements of the mesogens pendant on the cyclic siloxane ring. In this paper molecular dynamics (MD) simulations of BCS (Figure 1a), particularly of molecular clusters with and without periodic boundary conditions, are summarized. Since molecular shape and size are important in determining the mesophase behavior, the overall shape of the molecule was estimated by approximating an ellipsoid around the molecule and also the mesogens. The orientational order could then be calculated by defining the molecular axis to be along the major principal axis. In addition, simulations of the NLO chromophore 3'-methyl-4'-allyoxybenzoate nitrostilbene (MONS) (Figure 1b) that is covalently bonded to D4 along with a cholesteryl-4-vinylbenzoate (C4VB) mesogen (Figure 1c) are reported. The C4VB mesogen initiates liquid crystal phase formation, providing an ordered matrix for the MONS NLO chromophore. Although the glass transition temperature of this material is relatively low for many practical purposes (ca. 80°C), this system holds promise as a model for future NLO materials. These investigations offer an initial step towards the derivation of a general modeling strategy to be used in molecular design studies of $\chi^{(2)}$ materials that exhibit well-defined interlayer order.

* University of Virginia, Charlottesville, Virginia, U.S.A.
§ Materials Directorate, Wright Laboratory, Wright-Patterson AFB, Ohio, U.S.A.

Molecular Dynamics Calculations

Methods

MD calculations were performed with the CHARMM (5) force-field and the parallel molecular simulation code Parbond (6), applying a heating, equilibration and simulation protocol. The large scale simulations were run on an nCUBE 2 machine, a 1024-processor distributed-memory parallel computer capable of 1-2 Gflops. Full molecular flexibility was allowed as no geometric constraints were enforced on the molecular model. In all the simulations a 0.001 picosecond (ps) integration time step was used. An approximate measure of the shape of the mesogens was obtained by describing an ellipsoid around the mesogens. The major symmetry axis of the ellipsoid, which gives a measure of the molecular length (*a*), was considered as the molecular director. The two minor axes of the ellipsoid estimate the molecular width (*b*) and breadth (*c*), and the ratios *a/b* and *a/c* were evaluated to estimate various molecular shapes. The orientational order of the system was predicted by calculating the uniaxial order parameter S:

$$S = \frac{1}{2}(3 < \cos^2\theta > -1)$$

where θ is the angle between any molecular axis and the mean molecular director for all the molecules in the system. Such a calculation is expected to provide a basis for comparison with the calculated orientational order parameter of the higher temperature nematic phase.

BCS. Simulations were carried out on a cluster of 27 molecules (6750 atoms) with 135 mesogens arranged in a box of size X=69 Å, Y=34.5 Å and Z=49.5 Å, with the long axis of the molecules along X, as based on earlier results (4). The relevant correlation length (λ) in the system is assumed to be ca. 15 Å, as indicated by conservation of energy with a 15 Å cutoff, so that the smallest dimension of the cluster is larger than 2λ. The effect of the finite system size is expected to be minimal by using an appropriate lattice size. However, these cutoffs were studied for isolated molecules and may not account for all long range interactions. Results from simulations with free boundaries were therefore compared with those using periodic boundary conditions (pbc). A tilted layer structure evolves for the molecular cluster without pbc, which is consistent with experimental data reported by Ober et al (7), and possibly due to intermolecular electrostatic interactions. However, no such development is observed when pbc were included in the simulation, indicating that the shape of the simulation box is critical and should be consistent with the periodicity of the phase being studied. In the absence of any knowledge on the periodicity in the system, it may be appropriate to use free boundaries and a large cluster so that the system size effects are small. A detailed study of the molecular shape is also presented, with the large variations observed. It is shown that molecular shapes associated with low energy conformations are not cylindrically symmetric but more splayed like. The orientational order during the simulation with respect to the mean molecular director is shown in Figure 2.

D4 Substituted Siloxane. The flexibility of the D4 siloxane substituted with 75% C4VB mesogen and 25% MONS chromophore, which is important for determining its ability to form a liquid crystalline phase, is assessed in this study, as well as its possible response to alignment techniques such as poling. The results are also compared with those obtained previously on a (D5) substituted with cholesteryl-4'-allyloxybenzoate and biphenyl-4'-allyloxybenzoate mesogens (3). Figure 3 indicates a larger dihedral angle range of the mesogens during the simulation for the D5-based material.

REFERENCES

1. Pachter, R., Bunning, T.J., Socci, E.P., Farmer, B.L., Crane, R.L., and Adams, W.W., 1993, Die Makromolekulare Chemie, Theory & Simulations 2, 337.

2. Pachter, R., Bunning, T.J., and Adams, W.W., 1991, Computational Polymer Science 1, 179.

3. Socci, E.P., Pachter, R., Farmer, B.L., Bunning, T.J., and Adams, W.W., 1993, Liquid Crystals 13, 811.

4. Patnaik, S.S., Pachter, R., Bunning, T.J., Crane, R.L., and Adams, W.W., Liquid Crystals, in press.

5. B.R. Brooks, R.E. Bruccoleri, B.D. Olafson, D.J. States, S. Swaminathan and M. Karplus, 1993, J. of Comp. Chem. 4, 187.

6. Plimpton, S.J., Hendrickson, B.A., and Heffelfinger, G.S.,1993, Proceedings of 6th SIAM Conference on Parallel Processing for Scientific Computing, 178.

7. Ober, C.K., McNamee, S.G., McHugh, C.M., Bunning, T.J., Patnaik, S.S., and W.W. Adams, presented at the APS March meeting, Seattle, WA, 1993 (unpublished).

(a)

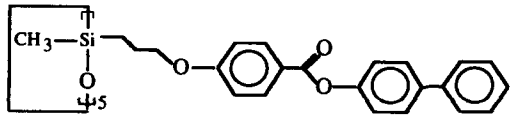

(b)

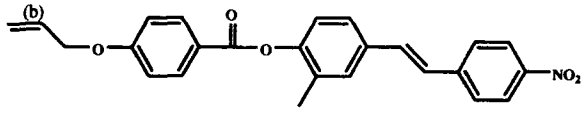

(c)

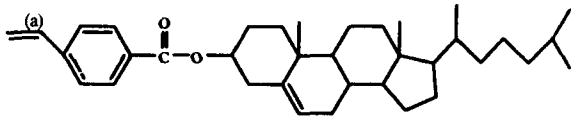

Figure 1: Schematic of (a) cyclic siloxane with a D5 core and biphenyl-4'-allyloxybenzoate mesogens, (b) MONS, and (c) C4VB

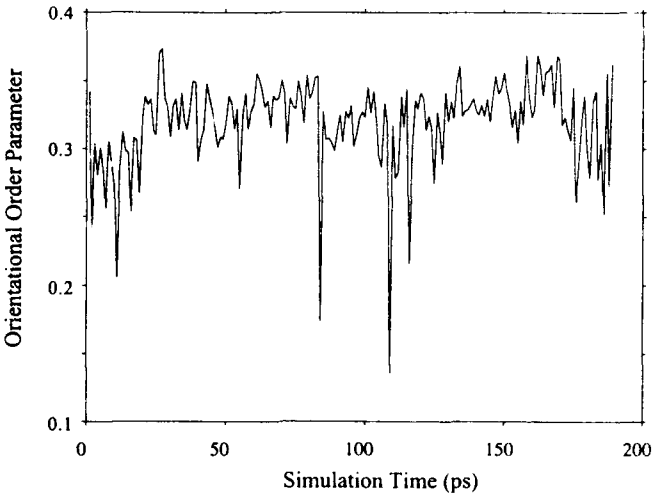

Figure 2: Uniaxial order parameter S at 300 K during 200 ps simulation time

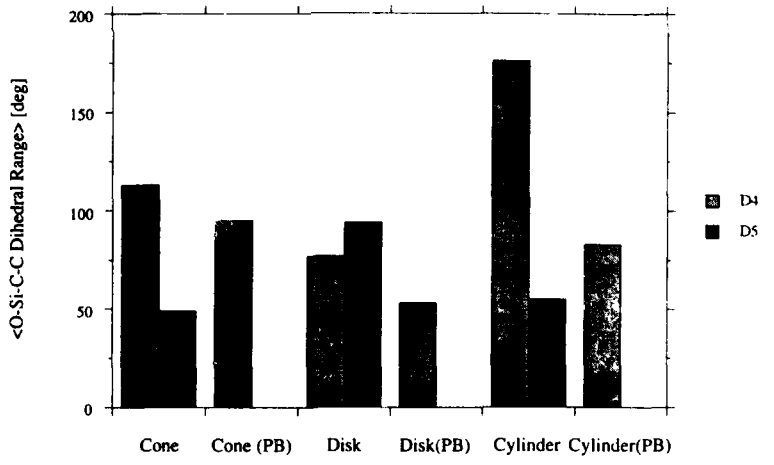

Figure 3: Dihedral range for D4 and D5-based siloxanes, for the cone, disk, and cylinder models (2), excluding and including (BC) periodic boundary conditions

A MODEL FOR CREEP OF POLYMERS IN THE AGEING RANGE

S Hellinckx, N Heymans and J-C Bauwens*

A model has been proposed for describing the creep behaviour of amorphous and semi-crystalline polymers. This model can be generalised to account for physical ageing prior to and during creep, for stress activation and for rejuvenation induced by deformation. The generalised equations are compared with low-strain creep measurements performed on PP samples aged for various times prior to testing and with non-linear creep data obtained on PVC samples.

MODEL

Deformation has been considered as a random walk diffusion process (1). The retarded creep extension ϵ_r was expressed by a differential equation

$$d\left(\frac{\epsilon_r}{J_0\sigma}\right)=\frac{1/(n+1)}{\left(\frac{\epsilon_r}{\sigma J_0}\right)^n}\frac{dt}{\tau} \tag{1}$$

where τ, the retardation time, depends on temperature and thermal and mechanical histories of the polymer and where n, σ and J_0 are the order of the diffusion process, the applied stress and the instantaneous compliance respectively. Integration of equation (1) gives

$$\epsilon_r=\sigma J_0\left(\frac{t}{\tau}\right)^{\beta} \tag{2}$$

where β has been substituted for $1/1+n$.
Therefore the total creep strain is given by

$$\epsilon=\sigma J_0\left(1+\left(\frac{t}{\tau}\right)^{\beta}\right) \tag{3}$$

* Physique des Matériaux de Synthèse 194/8, Université Libre de Bruxelles, 1050 Bruxelles, Belgium

Effect of physical ageing prior to and during creep

The ageing effect can be simply expressed by assuming that the characteristic time increases with total ageing time $t+t_a$ following

$$\tau=\tau_0\left(\frac{t+t_a}{\tau_0}\right)^{\mu} \tag{4}$$

where t_a denotes ageing time prior to testing and μ is Struik's exponent (generally close or equal to unity) (2).
Taking equation (4) into account, integration of equation (1) gives

$$\epsilon_r=\sigma J_0\left[\ln\left(1+\frac{t}{t_a}\right)\right]^{\beta} \qquad \text{if } \mu=1 \tag{5}$$

and

$$\epsilon_r=\sigma J_0\left[\frac{\tau_0^{\mu-1}}{(1-\mu)}\left((t+t_a)^{1-\mu}-t_a^{1-\mu}\right)\right]^{\beta} \qquad \text{if } \mu\neq 1 \tag{6}$$

Effect of stress activation

When high stress creep tests are performed, the behaviour of the polymer becomes non-linear. It can therefore be assumed that the deformation behaviour depends on temperature and applied stress through an Eyring-type equation (1)

$$\frac{1}{\tau}=C\ \exp\left(\frac{\sigma}{\sigma_0}-\frac{Q}{RT}\right) \tag{7}$$

where $\sigma_0=AT$ (A, C and Q being contants) and R denotes the universal gas constant. Equation (7) may be rewritten as $\tau=\tau_0\exp(-\sigma/\sigma_0)$ and equation (3) becomes

$$\epsilon=\sigma J_0\left[1+\left(\frac{t}{\tau_0}\ \exp\left(\frac{\sigma}{\sigma_0}\right)\right)^{\beta}\right] \tag{8}$$

Effect of rejuvenation

In non-linear creep experiments, large deformations induce rejuvenation of the sample giving rise to an acceleration of the kinetics and to an inflection in the creep curve (1). If the structural changes are assumed to be proportional to the retarded extension, the retardation time can be rewritten as $\tau=\tau_0\exp(-B\epsilon_r)$ where B is a constant. Therefore equation (3) becomes

$$\epsilon=\sigma J_0\left[1+\left(\frac{t}{\tau_0}\ \exp\left(B(\epsilon-\sigma J_0)\right)\right)^{\beta}\right] \tag{9}$$

COMPARISON OF THE MODEL WITH THE DATA

Effect of physical ageing on low-strain creep of PP

It has been shown that the fraction of amorphous phase which relaxes in the α (upper glass transition) range increases with ageing time (3). The retarded creep compliance associated with the α-process can then be expressed by

$$J_{r\alpha}=Dt_a^{\beta(1-\mu)}[(t+t_a)^{1-\mu}-t_a^{1-\mu}]^{\beta} \qquad (10)$$

obtained by considering that the α-fraction increase results from a diffusion process similar to creep. Equation (10) is compared on figure 1 with Read et al.'s (4) results obtained on PP.
The theoretical curves are obtained taking $\beta=0.25$, $\mu=0.8$ and $D=3.63.10^{-10}Pa^{-1}s^{-0.1}$.
A vertical shift is applied to the calculated curves to take into account the retarded compliance related to the lower glass transition.

Effect of high stress on PVC creep experiments

On figures 2a and 2b, the shear creep data due to Mallon et al. (5) on PVC are compared with

$$\epsilon=\sigma J_0[1+(\ln(1+\frac{t}{t_a})\frac{t_a}{\tau_0}\ \exp(\frac{\sigma}{\sigma_0})\ \exp(B(\epsilon-\sigma J_0)))^{\beta}] \qquad (11)$$

taking B=0 and B=35 respectively i.e. accounting or not for rejuvenation. The effect of physical ageing prior to and during creep is shown in both cases : the dashed lines are obtained when ageing is not taken into account ($t \ll t_a$) and the full lines are calculated taking an ageing time $t_a=600000s$. It can be seen that, to improve fitting, both acceleration of the kinetics caused by rejuvenation and physical ageing during creep must be considered. For all the curves, stress activation (see equation (8)) is taken into account.
The values of the different parameters are $J_0=8.73.10^{-10}Pa^{-1}$, $\beta=1/3$, $\tau_0=\exp(24.3)s$ and $\sigma_0=1.95.10^6Pa$. This latter is close to the value obtained previously from yield stress measurements on PVC (6).

REFERENCES

1 Bauwens J-C, Colloid Polym Sci 270 (1992) 537
2 Struik LCE, 'Physical aging in amorphous polymers and other materials', Elsevier, Amsterdam (1978)
3 Hellinckx, submitted for publication in Colloid Polym Sci
4 Read BE, Dean GD and Tomlins PE, Polymer 29 (1988) 2159
5 Mallon PJ and Benham PP, Plastics and Polym 40 (1972) 22
6 Bauwens-Crowet C, Bauwens J-C and Homes G, J Polym Sci A-2 7 (1969) 735

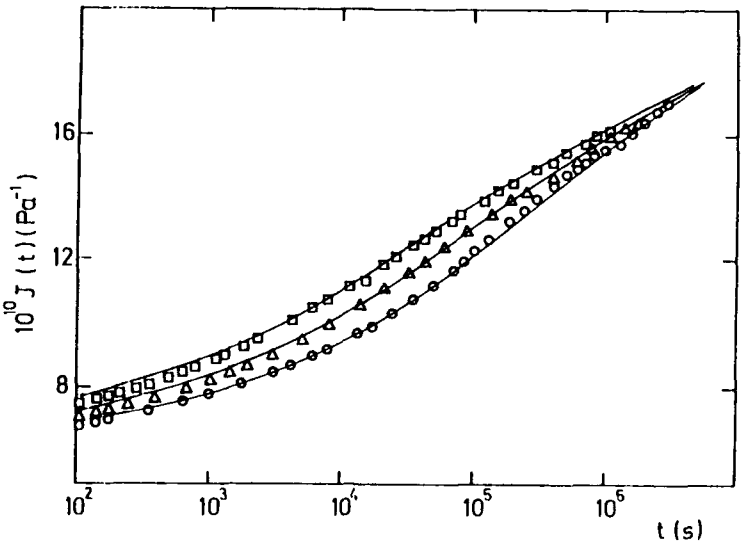

Figure 1 Creep compliance of PP aged □:8h, △:24h, ○:72h at 23°C. The data are taken from (4) and the curves are calculated from equation (10).

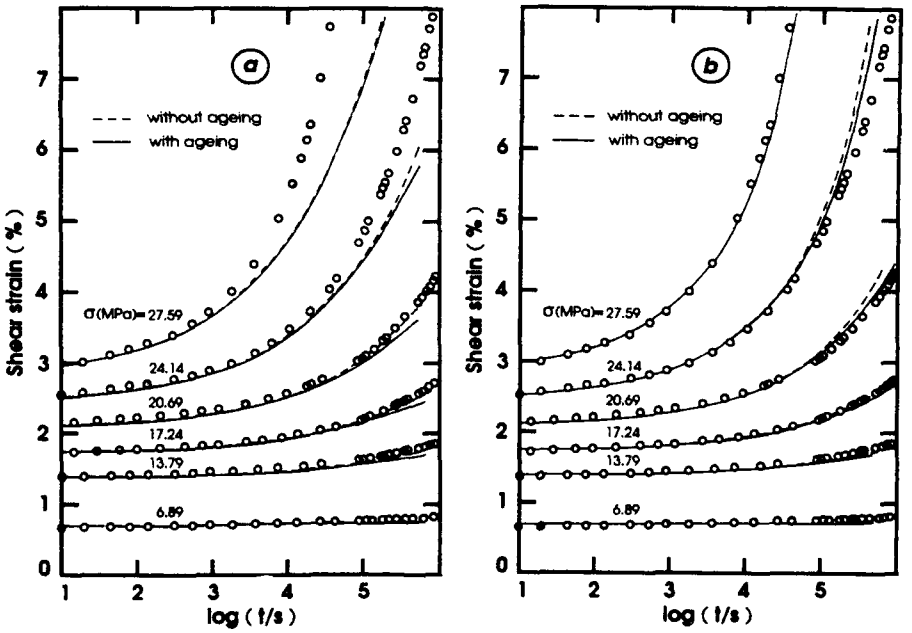

Figures 2 Shear creep data of PVC taken from (5). The curves on figures a and b are calculated with equation (11) taking B=0 and B=35 respectively.

DESCRIPTION OF VISCOELASTIC BEHAVIOUR BY HIERARCHICAL RHEOLOGICAL MODELS

N. HEYMANS and J.-C. BAUWENS*

The constitutive equation describing hierarchical rheological models can be expressed in terms of a fractional differential equation leading to concise formulation of complex rheological behaviour. In certain cases, in particular in creep, the fractional differential formulation is equivalent to an ordinary differential. This latter approach lends itself to extensions incorporating aging effects and non-linearity.

INTRODUCTION

It has been shown recently (1) that a constitutive equation for viscoelastic behaviour containing time derivatives of stress and strain to fractional order can be obtained from a hierarchical self-similar rheological model. Equivalence between tree and ladder fractal models at long times was also demonstrated. The fractional differential equation was shown to be equivalent to ordinary differential formulations in the case of a simple power-law response, e.g. in creep; the adequacy of such formulations to describe non-linearity has been demonstrated previously. The model gives a good description of viscoelastic behaviour under all stress modes and has been extended to include aging effects.

GENERALIZED RHEOLOGICAL MODELS

Tree model

The complex modulus **X** of the tree model shown on fig. 1 fulfils the equation :

$$\mathbf{X} = \left(\frac{1}{\mathbf{E}} + \frac{1}{\mathbf{X}}\right)^{-1} + \left(\frac{1}{i\omega\eta} + \frac{1}{\mathbf{X}}\right)^{-1} \qquad (1)$$

or

$$\mathbf{X} = \sqrt{i\omega\eta\mathbf{E}} = \mathbf{E}\sqrt{i\omega\tau} \qquad (2)$$

* Physique des Matériaux de Synthèse 194/8, Université Libre de Bruxelles, 1050 Bruxelles, Belgium

Since the symbolic operator $(i\omega)^\beta$ represents the fractional derivative d^β/dt^β, the constitutive equation of the tree model is :

$$\sigma = E\tau^\beta \frac{d^\beta}{dt^\beta} e \qquad \text{or} \qquad e = \frac{1}{E\tau^\beta} \frac{d^{-\beta}}{dt^{-\beta}} \sigma \tag{3}$$

with $\beta = 0.5$ for the model given on fig. 1. The model may be generalized (1) to give any value $0<\beta<1$. The fractional differential has also been found (2) to describe the long-term behaviour of a hierarchical ladder model with coordinate-dependent spring and dashpot coefficients. These models can therefore be considered as representing viscoelastic elements whose response is described by equation (3). These elements will be represented by a dashpot denoted β. they may be introduced into classical models to describe general rheological behaviour in a concise manner. The fractional differential automatically introduces complex behaviour including non-exponentiality and memory effects.

Generalized Maxwell model

The Maxwell model may be generalized by replacing each of its elements by a β element. If the larger exponent is β and the lower is γ, the constitutive equation becomes :

$$\sigma + \tau^\alpha \frac{\partial^\alpha \sigma}{\partial t^\alpha} = \tau^\beta E_1 \frac{\partial^\beta e}{\partial t^\beta} \tag{4}$$

where $\alpha = \beta-\gamma$. The condition for thermodynamic compatibility (3) is $\alpha \leq \beta$ and is automatically fulfilled by construction of the model. If $\gamma = 0$ one of the elements is purely elastic and $\alpha = \beta$. If $\beta = 1$ one of the elements is purely viscous. As noted by Friedrich (3), equation (4) only shows viscous flow at long times if $\beta = 1$.

Generalized Zener model

Generalization of the Zener model by replacing the viscous element by a β element yields the fractional differential equation :

$$\sigma + \tau^\alpha \frac{\partial^\alpha \sigma}{\partial t^\alpha} = E_0 e + \tau^\beta E_1 \frac{\partial^\beta e}{\partial t^\beta} \tag{5}$$

shown (3) to display non-thermodynamic behaviour (non-decreasing relaxation modulus at long times) unless $\alpha = \beta$. This condition is automatically fulfilled if the viscous element in the Zener model is replaced by a viscoelastic element having an exponent ß. Equation (5) was shown by Friedrich to give a valid solution if a derivative of strain to order α is added to the r.h.s. This corresponds to replacement of the spring in the Maxwell element by a β element of exponent $\gamma<\beta$.

In conclusion, all forms of constitutive equations using fractional derivatives which have been shown to give thermodynamically acceptable rheological behaviour can be connected with simple rheological models. These models are extremely concise, as they require only a limited number of parameters while being able to describe complex material behaviour.

CREEP RESPONSE

The response of a β element can be obtained under extremely general conditions using the general relation for fractional differentiation of a power of time :

$$\frac{d^q t^p}{dt^q} = \frac{\Gamma(p+1)}{\Gamma(p-q+1)} t^{p-q} \tag{6}$$

In creep, strain is found by integration of the constant stress ($\sigma_0 t^p$ with p=0) to order β, hence in equation (6) p = 0 and q = $-\beta$, and since $\Gamma(1) = 1$, the strain response is :

$$e = \frac{\sigma_0}{E} \frac{1}{\Gamma(1+\beta)} \left(\frac{t}{\tau}\right)^\beta \tag{7}$$

For a generalized Maxwell element, the response can be written :

$$J = J_0 \left(1 + \left(\frac{t}{\tau_0}\right)^\beta\right) \tag{8}$$

This is also the solution under creep conditions (constant total strain ϵ_0 for t>0) of the ordinary differential equation :

$$\frac{de}{d(t/\tau)} = j \left[\frac{\Gamma(j-\beta+1)}{\Gamma(j+1)}\right]^{1/\beta} \left(\frac{\sigma}{E}\right)^{1/\beta} \frac{1}{e^{1/\beta - 1}} \tag{9}$$

Thus the ordinary differential formulation, equation (9) is equivalent to the fractional differential formulation, equation (4) in creep. It has been shown that this equivalence extends to all cases where the response is a power law (1).

AGING

Aging effects can be very simply expressed by assuming that the characteristic time τ increases with aging time t_a :

$$\tau = \tau_0 (t_a/\tau_0)^\mu \tag{10}$$

where μ is Struik's exponent (approximately 0.8). If stress aging continues during creep, the total aging time is simply $t + t_a$ and the creep equation becomes

$$d e_r = \frac{1}{e_r^n} \frac{d(t/\tau_0)}{[(t+t_a)/\tau_0]^\mu} \tag{11}$$

where n has been substituted for $1/\gamma - 1$. Integration of this equation gives

$$e_r = K[(t+t_a)^{1-\mu} - t_a^{1-\mu}]^\gamma \tag{12}$$

where

$$K = \left[\tau_1^\mu / \{\gamma \tau_0 (1-\mu)\}\right]^\gamma \tag{13}$$

Equation (12) predicts that in the early stages of creep, no aging effects appear since $t + t_a \approx t_a$ and the characteristic time of the process is therefore a constant. In this case creep follows a power law with exponent γ.

Creep in aged or aging polymers has been shown (4,5) to be very well described by equation (12). The generalized Maxwell model can be used to describe mechanical behaviour of polymers when two processes are active, i.e. in the aging range.

NON-LINEAR BEHAVIOUR

In the non-linear range, the characteristic time τ becomes stress- and strain-dependent through stress activation of the deformation process and through increase in entropy with strain. Assuming the entropy to vary linearly with plastic strain in the low strain region, and writing the enthalpy of deformation as $V_0\sigma$, the characteristic time becomes :

$$\tau = \tau_0 \exp\left(\frac{Q - V_0\sigma}{RT} - B\varepsilon_r\right) \tag{14}$$

Equation (14) accounts both for strain softening and for stress activation of creep. It is shown (5) to give an excellent description of literature data on creep of PVC in the non-linear range.

REFERENCES

1. N.HEYMANS and J.C.BAUWENS, submitted to Rheol. Acta
2. H.SCHIESSEL and A.BLUMEN (1993) J.Phys A: Math.Gen. 26: 5057-5069
3. Ch.FRIEDRICH (1991) Rheol. Acta 30: 151-158
4. N.HEYMANS, S.HELLINCKX and J.-C.BAUWENS, accepted for publication in J. Non-Crystalline Solids
5. S.HELLINCKX, N. HEYMANS and J.-C. BAUWENS, paper P81, this issue.

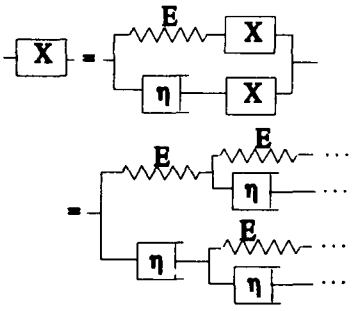

Figure 1 Hierarchical tree model

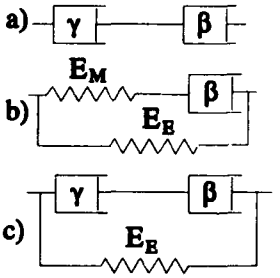

Figure 2 a) Generalized Maxwell model; b) generalized Zener model; c) fully generalized Zener model

INSTRUMENTATION TECHNIQUES FOR IMPACT AND OTHER FRACTURE TESTING OF POLYMERS

P A Ibru* and J P Dear*

Useful when evaluating the fracture properties of polymers is detailed information about the transient and other forces acting at the tip of the propagating crack. Instrumentation methods have been devised to obtain these data for both impact and static loading of specimens.

INTRODUCTION

Charpy is a widely used test method to measure the fracture toughness of materials. This is to subject a small rectangular bar specimen to rapid three-point bending using an impacting striker. Care is needed in interpreting the information obtained as it can be affected by a number of factors. These include the dimensions of the specimen, pre-notching and other preparation, viscoelasticity of the material and the striker impact velocity used. A problem is that the specimen can be excited into different and complex modes of vibrations as it is fractured. Also, the results are a mixture relating to both crack initiation and propagation. In this study, large three-point bend specimens have been used as these are not only easier to instrument but the important point is that the dynamic loading conditions can be more precisely controlled using a high-rate servo-hydraulic test machine(1).

Different test methods are often required to study the continuous propagation of long cracks in materials supporting a steady load. A method has been developed to achieve steady state crack propagation in small specimens and this is descibed in this paper(2). An interesting feature of this method is that the material can be loaded and allowed to stress relax before a crack is launched into the specimen without disturbing the established steady state conditions. Specimens for both rapid three-point bending and steady state fracture have been instrumented to research the forces acting about the propagating crack tip.

*Department of Mechanical Engineering, Imperial College.

EXPERIMENTAL

Figure 1 shows the instrumentation arrangement for studying three-point bend polyethylene specimens of dimensions 200mm x 40mm x 25mm. For two different loading rates, Figures 2 and 3 show force-time traces obtained from the sensor on the striker and the strain gauges (SG1 and SG2) on the specimen. With a low loading rate of 0.5 m s^{-1}, the rising ramp of the saw-tooth from the sensor in the striker showed only small transient oscillations as the striker interacted with the specimen. SG1 monitoring strains normal to the crack path, showed a smooth saw-tooth profile as did SG2. When the loading rate was increased to 1.1 m s^{-1}, the interaction between striker and specimen produced large transient forces as shown in Figure 3. SG1 shows that the initial fracture of the specimen was erratic with oscillations on the loading ramp of the saw-tooth and the fracture of the specimen was interrupted and was not a clean break. The second strain-gauge output from SG2 was disturbed to a lesser extent. It was found that the transient forces, due to the impact of the striker and fast bending of the specimen, increased with striker velocity to produce wide variation in the outputs obtained from the striker sensor and strain gauges on the specimen. Figure 4 shows the type of fracture surfaces obtained. These show a crack initiation zone, a varying texture of the crack surface as the crack propagates through the specimen with partial arrest lines and the hinge zone which in some cases was not severed.

For the steady state crack propagation, the specimens were rectangular in shape as shown in Figure 5. The protruding tongue on one side of the specimen extended the intended crack path. After loading the main section of the specimen normal to the crack path and allowing the material to stress relax, a crack was initiated in the tongue so that it propagated into the main section of the specimen. In the case of polyethylene, starting the crack in the tongue was a simple matter after it had been freeze-cooled with liquid nitrogen. Validation of the tongue method showed that because of the good thermal insulation properties of polyethylene, the cooling of the tongue section of the specimen was confined to a small zone at the beginning of the crack path into the main section. Also, it was found that the tongue only disturbed the stress distribution for a small distance along the crack path into the main section of the specimen. Figure 6 shows the outputs from the two strain gauges adjacent to the crack path. From these traces, which show the rise and fall of strain about the crack tip, the crack velocity can also be obtained. Crack velocity was also determined from the breaking of conducting strips at the beginning and end of the crack path. Figure 7 shows the fracture surface generated using the tongue specimen technique. These fracture surfaces are a product of crack propagation only and the same pattern is obtained along the whole length of the crack.

CONCLUSIONS

The techniques used in this study usefully provide for obtaining a wide variety of data when studying the fracture behaviour of polymers and other materials.

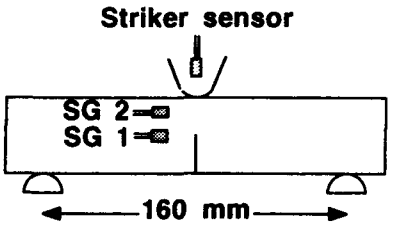

Figure 1 Three-point bend test. Support span is 160 mm.

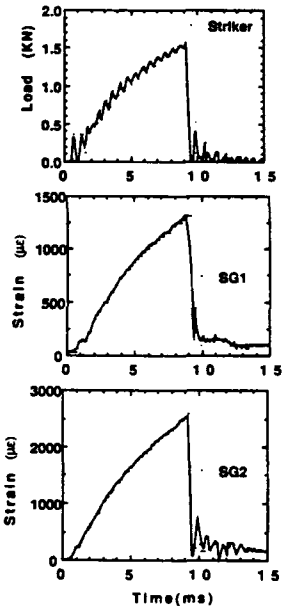

Figure 2 Outputs for rate of loading of 0.5 m s^{-1}.

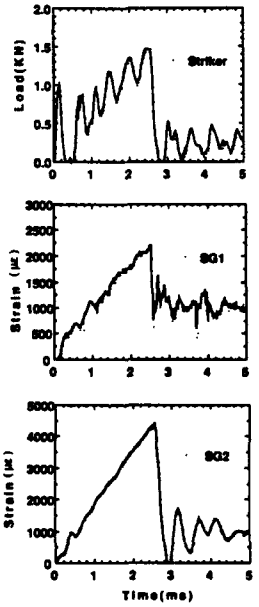

Figure 3 Outputs for rate of loading of 1.1 m s^{-1}.

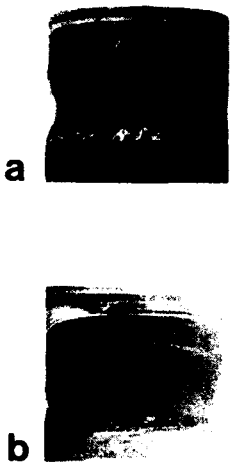

Figure 4 Fracture surfaces (a) 0.5 m s^{-1} (b) 1.1 m s^{-1}.

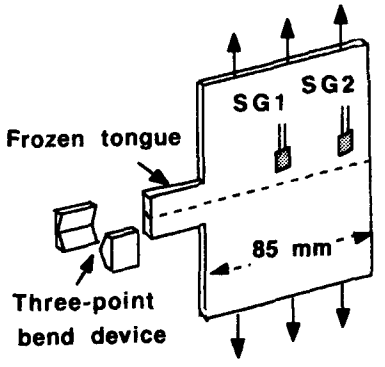

Figure 5 Frozen-tongue test.

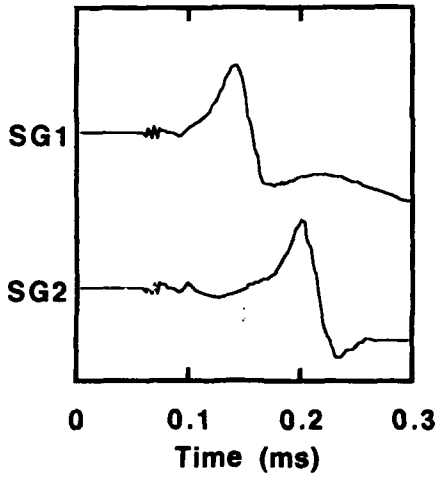

Figure 6 Outputs from SG1 and SG2 strain gauges.

Figure 7 Fracture surface for frozen-tongue test.

ACKNOWLEDGEMENTS

The authors appreciate the interest and support they have received from SERC and the supply of materials from BP Chemicals.

REFERENCES

1 Ibru P A, PhD Thesis , University of London, 1994.

2 Dear J P, J. Mater. Sci. 26 (1991) 321-327.

CRACK TIP HEATING DURING RAPID CRACK PROPAGATION in TOUGH THERMOPLASTICS

M A Wheel* and P S Leevers†

Polyethylene (amongst other 'tough' crystalline thermoplastics) can be triggered into a Rapid Crack Propagation (RCP) mode characterised by low fracture resistance and a 'brittle' fracture surface. RCP tests on medium and modified high density polyethylene specimens instrumented with fast-response thermocouples have shown that RCP generates a significant local temperature rise, whose magnitude corresponds to complete conversion of the dynamic fracture resistance (as measured by High Speed Double Torsion tests) into heat. Modelling of the running crack tip craze as a Dugdale-Barenblatt cohesive zone suggests that the fracture resistance of these PEs can be *predicted*, on the criterion that both cohesive surfaces melt to a depth sufficient to liberate all chains up to and including those which are fully extended.

INTRODUCTION

Characteristically tough crystalline polymers can fail unexpectedly by brittle crack propagation. For polyethylene, conditions known to precipitate a ductile-brittle transition include both long-duration static loading (promoted by increasing temperature), and impact loading (promoted by reducing temperature). For long-time failure, some progress has been made in relating the competing kinetics of yield and slow crack propagation to viscoelastic properties. For impact, however, progress seems unlikely until the mechanism of Rapid Crack Propagation (RCP) is understood.

As part of a project on RCP in pressurised plastic pipe, the dynamic fracture resistance, G_D, of several very tough pipe grade polyethylenes has been measured using the High Speed Double Torsion (HSDT) test [1]. For crack speeds exceeding about 100 m s^{-1}, G_D bottoms out at a few kJ m^{-2}, which is an order of magnitude less than the resistance to slow ductile tearing. RCP fracture surfaces have a smooth, silky appearance, lacking the stress whitening typical of ductile tearing. There has been little speculation concerning the underlying fracture mechanism.

We believe that the RCP in tough crystalline polymers involves local fusion of the crystalline phase, due to heating within an adiabatic process zone. The direct measurements of heat generated at a fast-running crack tip which are reported here can serve two objectives. Firstly, they offer direct, evaluation of G_D, free from uncertainties about bulk dynamic elastic properties which affect the crack extension force G (from which G_D is usually inferred). Secondly, they provide an insight into the mechanism by which increasing crack speed promotes the separation process, and could thereby suggest material development strategies to counteract it.

The study described here therefore consists of two parts: experimental determination of the temperature rise near a fast-running crack; and modelling of a process by which such a temperature rise could *cause* RCP.

* Mechanics of Materials Department, Strathclyde University, Glasgow UK
† Mechanical Engineering Department, Imperial College, London UK

EXPERIMENTAL WORK

Dynamic fracture tests were carried out on statically loaded specimens, using a variant of the 'glass duplex' technique developed by Genussov [2]. Each specimen consists of an edge-notched and side-grooved PE plate whose notch mouth is restrained by a PMMA strip bonded across it. When loaded axially in tension at room temperature, the PMMA strip fractures, rapidly loading the PE notch tip and precipitating RCP. Uniformly brittle fracture surfaces are produced. The fracture load can be controlled by varying the initial notch depth.

In these tests, T-type rapid-response foil thermocouples, bonded to the primed PE surface in one side-groove using cyanoacrylate adhesive, were used to measure the temperature rise as the crack passed. The voltage signal from each junction was stored using a transient recorder. Experiments were carried out on both a medium density (MDPE) and a modified high density (HDPE) resin for which G_D data were already available: about 3.0 and 6.0 kJ m^{-2} respectively [3] at 0°C.

MEASURED AND PREDICTED TEMPERATURE PROFILES

Thermocouples whose junctions were centred a few hundred μm from the crack path recorded a rapid rise of about 1 K over about 1 s, followed by a slower decay. These times greatly exceed both the time taken for the crack to cross the specimen (<0.5 ms) and the thermocouple response time (<10 ms). A thermocouple placed 15 mm from the crack plane on a similar specimen recorded no change in temperature. It seems clear that (a) the source of the heat flux is the crack, and that (b) this method can resolve neither the dynamics of the source nor its local temperature distribution .

Fuller *et al.* [4] and Döll [5], studying PMMA, treated the fracture surface as an instantaneous plane heat source. Alternatively, the crack front can be treated as a moving line heat source [6] (which induces a temperature singularity) or as a moving plane source plane source (which does not), each having equivalent intensity per unit area. For these experiments, however, because the thermal diffusivity of the material is so low and the crack speed so high, all three models yield indistinguishable temperature histories unless the crack runs directly under a thermocouple. All three models neglect latent heat absorbed by local melting, but this too will have little effect if recrystallisation is relatively rapid.

Fig. 1 shows temperature histories, computed using measured thermal diffusivity data, which provide the best fit to those recorded in one fracture test on HDPE and for two on MDPE. The corresponding heat intensities, 7 kJ m^{-2} and 3.25 for MDPE, agree well with the measured G_D..

MODELLING of the PROCESS ZONE

Having shown that the heat evolved from the crack surface during RCP in PE is approximately equivalent to the fracture resistance, G_D, we consider the possibility of *predicting* G_D from a criterion of critical thermal 'damage' inflicted by it. The essentials of the argument are presented here; the mathematical details will be presented elsewhere [7].

The Dugdale-Barenblatt cohesive line zone model has proved its value for modelling the crack-tip craze in amorphous polymers [8], the assumed constant cohesive stress representing the craze stress. The zone length c and crack tip opening displacement δ are related to each other and to the crack extension force; the crack resistance is determined by a criterion which imposes a critical δ or c .

In PE, craze fibrils are relatively large, and the cohesive surface can be regarded as a drawing front, propagating into the bulk material, at which all deformation, and thus all heat generation, is localised. The cohesive stress can be identified as the flow stress. The flow stress for each PE grade was measured in compression at similar mean plastic strain rates, using a Split Hopkinson Pressure Bar method — in which, as in our model, the plastic strain rate is averaged across a propagating

plastic wavefront. 5% flow stress data for temperatures of −20°C, 0°C and 23°C are reported in [9]. Within the elastic region *outside* the cohesive zone, strain rates are much lower, but still high enough to require use of a dynamic modulus to characterise the energy flux. We have derived modulus data both from 1 MHz ultrasonic tests and from dynamic torsional impedance tests: they agree well [3].

It is now possible to estimate the cohesive zone dimensions and, given the minimum RCP speed of 100 m s^{-1}, the depth to which conduction from the cohesive surface can influence the material in the time taken for the zone to traverse any point. This turns out to be so small that the two cohesive surface conduction layers can influence neither the bulk properties, nor each other.

PREDICTION of BRITTLE FRACTURE RESISTANCE

The lowest-energy way to inflict structural damage on a crystalline polymer by heat is to melt it. It is proposed that separation occurs, determining the zone length c and thus G_D, when the heat flux conducted from each cohesive surface is sufficient to heat the material to its fusion (i.e. peak endotherm) temperature to a depth of one-half of a mean chain contour length. One end of every chain passing through the cohesive surface lies within this zone. Further work equivalent to the latent heat of fusion of the crystalline phase liberates each fibril at both ends — one of which is then easily uprooted. The heat flux needed to attain the required fusion layer thickness at the crack tip can be calculated from the conduction analysis for a moving plane source c long. The thermal parameters needed were determined for us using Differential Scanning Calorimetry.

Predicted G_D results for MDPE and HDPE (Fig. 2) agree encouragingly well with HSDT data. Note that G_D for pure 'brittle' mode fracture is expected to *fall* with increasing temperature, a counter-intuitive prediction which may subject the model to a severe test.

SYMBOLS USED

G	= Crack extension force (kJ m^{-2})	G_D	= Dynamic fracture resistance (kJ m^{-2})
c	= Dugdale-Barenblatt zone length (m)	δ	= Crack tip opening displacement.

REFERENCES

1 Wheel M A and Leevers P S, *Int J Fracture* 61 (1993) 349

2 Genussov R M S and Williams J G, *Int J Fracture* 38 (1988) R9

3 Wheel M A and Leevers P S, *Int J Fracture* 59 (1993) R47

4 Fuller K N G, Fox P G and Field J E, *Proc Roy Soc* Series A, 341 (1975) 537

5 Döll W, *Int J Fracture* 12 (1976) 595

6 Carslaw H S and Jaeger J C, *Conduction of Heat in Solids*, 2nd Ed., Oxford University Press (1959) 267

7 Leevers, P S *A Model for Rapid Crack Propagation in Polyethylene by Fusion at a Dugdale-Barenblatt Zone Surface*, submitted to *Int J Fracture* (1994)

8 Williams J G, *Fracture Mechanics of Polymers*, Ellis Horwood, Chichester, U.K. (1987).

9 Dioh N N, Leevers P S and Williams J G, *Polymer* 34 (1993) 4230

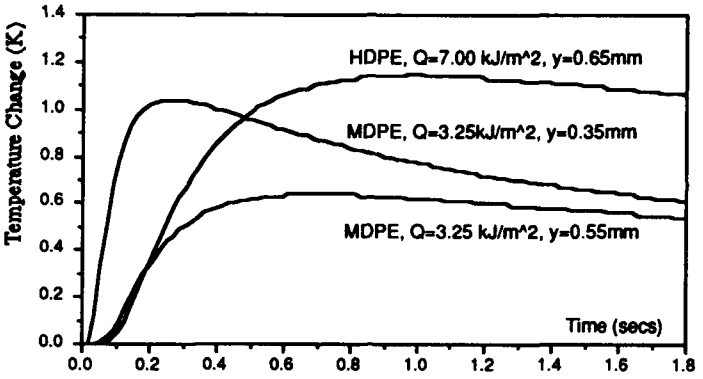

Figure 1 Predicted temperature histories for HDPE and MDPE for heat intensities Q as shown

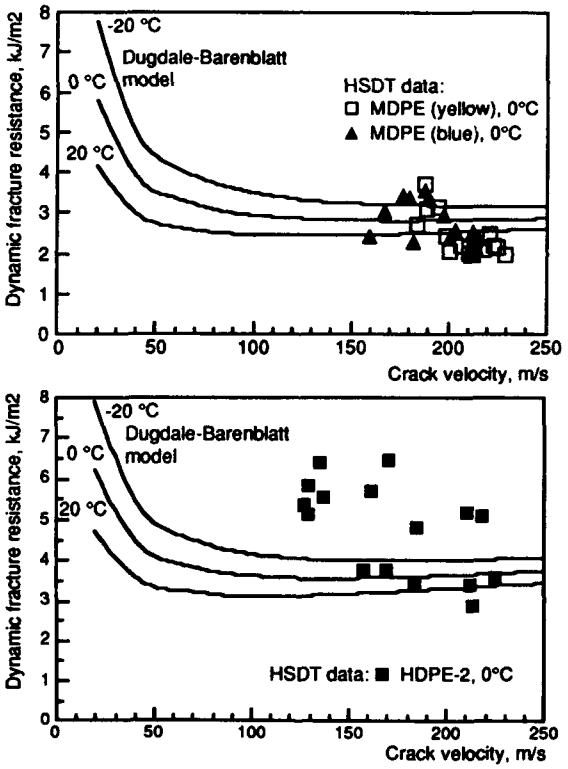

Figure 2 Plane-strain dynamic fracture toughness of two pipe grade polyethylenes predicted from the fusion model, compared with data measured using the HSDT test

THE LOGARITHMIC CREEP AT A BEGINNING OF THE CREEP DEFORMATION OF PMMA UNDER LOW STRESSES

J.M. Cherière, L. Belec and J.L. Gacougnolle*

The physical ageing of PMMA is studied by means of torsional microcreep tests. An accurate anlysis of the creep data reveals that a brief logarithmic creep precedes the well known KWW creep. This logarithmic creep is perfectly recoverable with exactly the same logarithmic kinetics. The duration of this logarithmic creep increases with the ageing time nevertheless its amplitude remains constant. It is attributed to an enthalpie internal back stres σ_i which is proportional to the torsional strain γ.

INTRODUCTION

The creep under low stresses of amorphous polymers between T_β and T_α is generally described by the KWW law (1). It is attributed to α molecular jumps which are supposed to be randomly distributed. Using accurate experimental data it is shown in this paper that the KWW creep is preceded by a logarithmic transient creep. The recovery of this creep follows the same logarithmic kinetics, this suggests that it is due to an enthalpic internal back stress. The classical models of logarithmic creep in metals (2) assume that this internal back stress is generated by local shear strains. In the case of polymers the KWW creep is supposed to be due to the spread of these local shear strains by the α molecular jumps.

EXPERIMENTAL

PMMA (M_n = 49200, M_w/M_n = 2.12) has been kindly supplied by CdF Chimie. The glass transition temperature determined by DSC is 111°C. Each specimen is maintained at 80°C under vacuum for 12 h in order to eliminate water, then it is fixed on the torsion pendulum and annealed at 135° for 30 mn. During this heat treatment no stress, neither longitudinal nor torsional, is applied.

After cooling from 135°C the specimen is kept for several days at 55, 70, 84 or 90°C. Owing to the experimental procedure proposed by Struik (3) a torsional microtorque is applied from time to time to the specimen inducing a maximal shear stress lower than 0.02 MPa. The duration of each microcreep test is the tenth of the ageing time, Figure 1.

* Laboratoire de Mécanique et de Physique des Matériaux, URA 863 CNRS, ENSMA, Chasseneuil du Poitou, BP 109, 86960 Futuroscope Cedex.

ANALYSIS OF CREEP DATA

For each test both the creep strain and the recovery are recorded, Figure 2. Whereas the creep strain is entirely recovered at 55 and 70°C it is only partly recovered at 84 and 90°C. In order to take into account this recovery it is attempted to fit the creep curves by the KWW law,

$$J(t) = J_u + \Delta J\left[1\text{-}\exp - \left(\frac{t}{\tau}\right)^{\beta}\right]$$

since $t << \tau$ this relation can be reduced

$$J(t) = J_u + b\, t^{\beta}$$

At 84°C two different numerical methods have been used to determine directly the 3 parameters J_u, b and β, obviously J_u is not measured on the recorded creep curve.

The first method requires 3 experimental values of J, namely J(t), J(10t) and J (100t). Each of the 3 parameters is given by a relation between these 3 values of J, for instance

$$\beta = \log \frac{(100t) - J(10t)}{J(10t) - J(t)}$$

Unfortunately the calculated value of β depends strongly on the magnitude of the chosen time t. Figure 3 shows the increase of β for the short times t up to a constant value which is reached beyond a time t_c. This time t_c increases with ageing time, t_c is 30 s and 110 s for ageing times of respectively 1035 and 4225 mn.

The second method is a classical linear regression which supposes the knwoledge of β. For each given value of β the values of J_u and B as well as the error with the experimental data are determined. The accepted value of β is that corresponding to the minimal error.

For the first microcreep test performed after 80 mm of ageing Figure 4 shows that the best fit is reached when all the experimental plots are taken into account. For longer ageing times the best value of β is obtained by neglecting the first experimental plots, for an ageing time t_e = 16025 mn Figure 5 shows that only the data beyond 384 s must be considered.

So it is clear that the KWW creep is preceded by a transient logarithmic creep occuring from the application of the microtorque till the time t_c. Moreover it must be noticed that the logarithmic creep and its recovery follow exactly the same kinetics as shown on Figure 2 while the KWW creep rate is higher than the recovery rate.

During the ageing at 84°C J_u diminishes very little, the duration t_c increases and the slope b decreases so that the compliance $J(t_c)$ remains nearly constant, Figure 6, as well as the amplitude of the logarithmic creep, $\Delta J_L = J(t_c) - J_u$.

INTERPRETATION

The logarithmic creep has been explained in metals by Mott (2) and in polymers by Escaig (4) assuming the raise of an internal back stress σ_i which is proportional to the creep strain γ, $\sigma_i = \alpha G \gamma$ where G is the shear modulus. The torsion rate can be written

$$\dot{\gamma} = \dot{\gamma}_o \exp - \frac{\Delta H - (\sigma - \alpha G\gamma)\, V^*}{kT}$$

where ΔH is the activation enthalpy, σ the applied stress and V^* an activation volume.

In this model the origin of σ_i is enthalpic, thus localised. It can be due to the build up of microsheardbands under the influence of the applied stress σ. During the further KWW creep the localisation of this internal stress is spread to a more extended volume because of the molecular α jumps.

REFERENCES

1 Dean G D, Read B E and Small G D, Influence of physical ageing on creep in the α-and β-relaxation regions in PMMA" Plastics and Rubber Processing and Applications 9 (1988) 173-179.

2 Mott N F, Phil Mag. 44 (1953) 742.

3 Struik LC, Physical Ageing in Amorphous Polymers and other Materials, Elsevier, 1978.

4 Escaig B, Plastic Deformation of Amorphous and Semi-crystalline Materials, Editions de Physique, 1982, 187.

Fig. 1 MICROCREEP IN TORSION AT 84°C
σ=1,455e^{-2}MPa; β=0,46

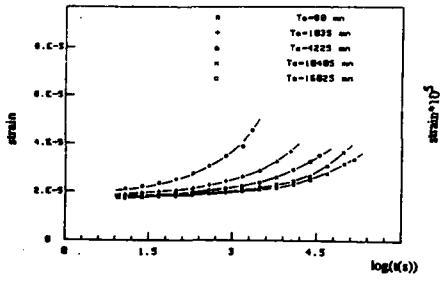

Fig. 2 MICROCREEP AND RECOVERY AT 84°C
σ=1,455e^{-2}MPa; t_c=961500s

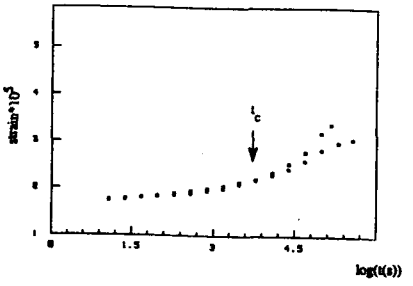

Fig. 3

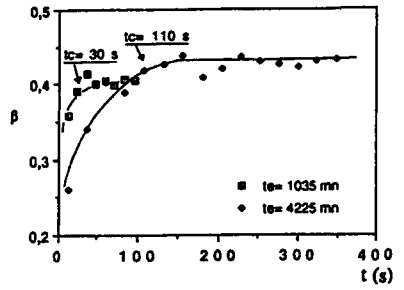

Variation of β versus time for the tests with t_e=1035mn and t_e=4225mn at 84°C

Fig. 4

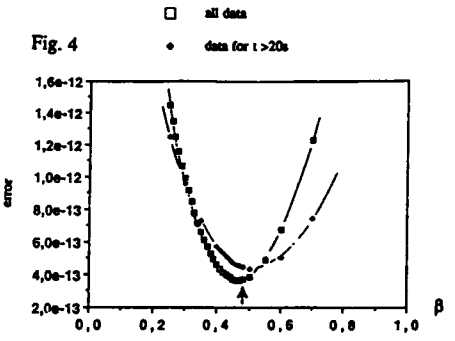

Determination of β for the test with t_e=80mn at 84°C; β=0,47 for t >0s

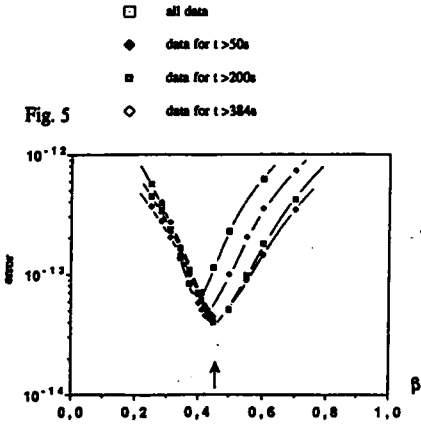

Fig. 5

Determination of β for the test with t_e=16025mn at 84°C; β=0,46 for t >384s

Fig. 6

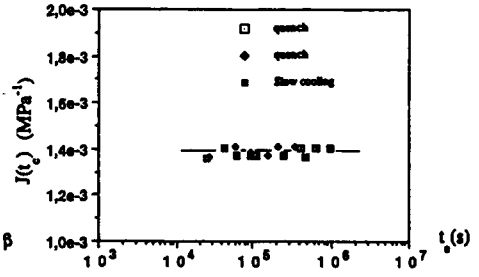

Variation of $J(t_c)$ with the ageing time at 84°C

DESIGN FOR RELIABILITY OF PLASTICS PRODUCTS UNDER COMPRESSIVE LOADING

ir. E.W.G.Zweers*

Compressive tests have been performed on strips and U-profiles representing popular types of crate-constructions. Different material models are used to describe the buckling behaviour of these specimen in numerical simulations.
Strips show that predictions by Euler's formula are valid to lower slenderness values than commonly used for metal columns.
An experimental algorithms for optimisation is used on models showing physical and geometrical non-linear behaviour. The model is capable to optimise problems with many parameters and converges more quickly on a solution compared to ANSYS 5.

Introduction

Early use of plastics has mostly been restricted to unloaded or lightly loaded products. Improving mechanical properties have caused an increasing use of plastics as engineering materials in a wide range of applications, often replacing metals or other classical engineering materials. Some properties of plastics cause that it should be treated different by engineers than for instance metals (2):

- The time and temperature dependent non-linear material behaviour.
- The relatively low stiffness
- Large diversity in shapes made possible by the injection moulding production process

This project is focussed on deriving rules for design and optimisation of plastics crates and boxes, usually made out of High Density PolyEthylene (HDPE). The most severe load on crates occurs during the stacking on pallets, several pallets high. This stacking results in a substantial compressive load especially on the lower crates. Because of the compressive load (local)buckling of the lower crates often occurs. Users demand of the producers of crates that they are constructed in such a way, that they can withstand the compressive loadings during stacking for a certain specified amount of time usually at an elevated temperature. The larger part of the construction of crates is dedicated to withstanding this compressive load. At the moment two types of constructions for crates are popular. The first type is a thin plate construction forming a box with a number of ribs attached near the corners forming a "corner column".

*Laboratory for Mechanical Reliability, Delft University of Technology, the Netherlands.

The accompanying figure 1 shows results of short term tests on HDPE strips exhibiting Euler buckling. Of each specimen the maximum stress reached during the test is measured. Further we can introduce an effective slenderness defined by:

$$\lambda_e = \frac{l_e}{r}$$

where r is the radius of gyration and l_e "effective length" is the halve wavelength of the buckled strip.
The maximum stress with the effective slenderness yield one point in figure 1
Theoretically the buckling load is given by (1):

$$P_{cr} = \frac{\pi^2 EI}{l_e^2}$$

Using the effective slenderness it is possible to rewrite the equation into

$$\sigma_{cr} = \frac{\pi^2 E}{\lambda_e^2} \tag{1}$$

Using the initial modulus measured in tensile tests a line is drawn in figure 1. The graph then shows a curve predicting maximum buckling stresses as a function of slenderness according to Euler's theory.
The result shows that the specimen behave as predicted when the slenderness ratio exceeds 40-50, which is a much lower value commonly used for columns out of metals. Below this value non-linear behaviour decreases the peak stress value. Other models are necessary to describe specimen behaviour in this region.

Plate buckling

Figure 2 shows the load-displacement curve of a simulated compressive test on a HDPE U-profile exhibiting local and global buckling. The model can buckle in two opposing shapes where buckling starts at the same load for both cases. The numerical simulation gives an accurate prediction of the onset of local buckling but overestimates the forces in the post-buckling region.
One can see that the two paths differ in the post buckling region which leads to the conclusion that especially for a complex construction all shapes have to be examined to find the shape with the lowest load carrying ability.
Again the modulus of elasticity has been taken from a tensile test at the same nominal strain rate. The overestimation can be reduced largely by using more appropriate material models.
As can be seen from figures 3 and 4 the shape of the buckled FEM-model is very similar to the shape of a real specimen in compression.
The same FEM-model has been used with an optimisation algorithm that is capable of solving this non-liner problem.

References:

(1) S.P. Timoshenko and J.M. Gere, *Theory of elastic stability*, 2nd edition, McCraw-Hill, New York, 1961.

(2) J.G. Williams, *Stress analysis of polymers*, Longman Group Ltd, London, 1973.

The second, more modern, type is an open construction, leaving the contents visible, where the load carrying construction consists of a number of (hollow) columns. This leads to our choice of U-profiles and strips for specimen.

Goals

The aim is to establish a model describing the failure of plastics constructions under compressive loads and to find design rules accordingly. The model(s) will be used in Finite Element Method (FEM) calculations and will have to be verified experimentally.
The material we focus on is HDPE since this is one of the most used materials in crates and in injection moulding in general.
Once a model for the buckling behaviour is established a further goal is to be able to optimize automatically a plastics construction with respect to the buckling behaviour and weight. Experiments are conducted with several algorithms and strategies for automatic optimization (with FEM calculations) of plastics constructions with respect to buckling behaviour.
With the results it must be possible to design lighter crates which are able to withstand the compressive loading. Since material costs determine the larger part of the product costs, weight savings can give considerable cost reductions for manufacturers since roughly 60% of the cost is directly related to weight.

Experimental

Since two types of constructions are considered there will be two basic types of specimen: columns showing eulertype buckling and thin plate constructions showing plate (local) buckling.
Plastics products behave differently under compressive loads compared to for instance metal or concrete constructions. The behaviour of the plastics constructions can be described using formulae and computer simulations. Most important is the used material behaviour, for which several models can be used:

- linear elastic
- elasto plastic
- multilinear model (provided by ANSYS)
- linear- and non-linear visco-elastic.

The experimental verification of the different models is, of course, very important. For this reason many experiments are being conducted: firstly short-term compressive tests on columns, secondly on plates and panels and finally on entire or partial crates. The short-term tests are, of course, followed by long term tests.
The influence of temperature on the buckling behaviour is not within the scope of this research.

Eulertype buckling

A simple specimen for Eulerbuckling is a strip. Strips of two thicknesses have been used where both thicknesses have been tested as simply supported and clamped specimen.

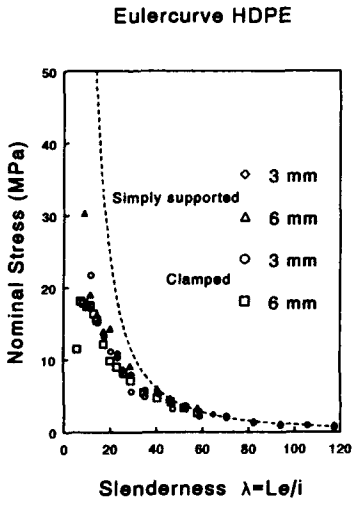

Figuur 1: Eulercurve from HDPE strips

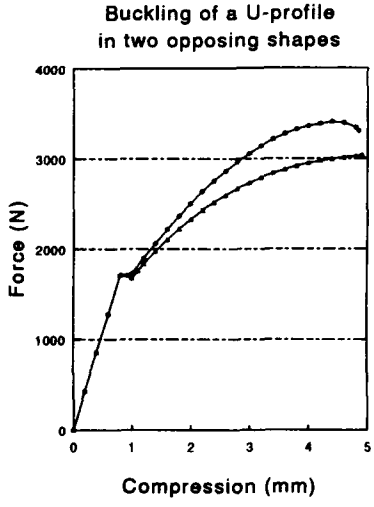

Figuur 2: Different postbuckling behaviour of opposing shapes

Figuur 3: Digitised picture of specimen

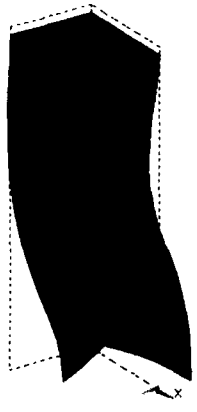

Figuur 4: Deformation calculated by ANSYS of a quarter model

INFLUENCE OF PLASTIC DEFORMATION ON PHYSICAL AGEING OF PMMA

J.L. GACOUGNOLLE, J.J. MARTINEZ*, Y.A. BERTIN
ENSMA Laboratoire de Mécanique et de Physique des Matériaux (CNRS URA 863)
Poitiers, France.

The aim of this study is the comparison between the rates of physical ageing of PMMA in 3 successive states: first when the specimen is maintained at constant temperature after cooling from the rubbery state, second during a creep elongation at this temperature and finally during the spontaneous contraction after the creep elongation load has been removed. The accuracy of the specially designed creep machine (1) for the measurements of the torsion deformation of the specimen is $5x10^{-8}$ allowing microcreep torsion tests of a total strain less than 10^{-4}. In each of the 3 states physical ageing is determined by means of repeated microcreep torsional tests (2). The torsional microstress $\tau<0.1$ MPa is so low that it doe. not modify the structure of the specimen and it is much lower than the longitudinal stress ($\tau/\sigma < 1/40$) so that it has no detectable influence on the longitudinal creep rate.

INTRODUCTION

A microcreep curve can be considered as reflecting the momentary molecular mobility of the specimen in the experimental conditions.
The important parameter for the creep strain of polymers is the contribution of the α relaxation, therefore in the case of PMMA the temperature range which has been investigated extends from 42°C where the α relaxation is nearly negligible up to 100°C, near Tg. The applied creep stresses were high at low temperature, 26 MPa at 42°C, but low at high temperature, 4 or 8 MPa at 100°C.

EXPERIMENTAL PROCEDURE

The specimens, after mounting, are heated at 140°C (Tg + 30°C) for 30 mm then cooled down to the test temperature. The temperatures of the tests were 42°C, 61°C, 68°C, 82°C, 90°C and 100°C (3). In order to characterize the physical ageing at the test temperature the specimen is first kept 100h at this temperature before the longitudinal creep test.
The microcreep tests are done by following the procedure used by Struik, the torque is applied for a duration less than 10% of the ageing time, then the specimen is released until it recovers 95% of its strain. The longitudinal creep stress is applied after this preliminary ageing and removed either when the creep rate is very low or when the creep strain is high enough, say 10%.
The torsional microcreep curves are fitted by the stretched exponential function $\gamma=\gamma_i\exp(t/t_o)^m$. The three parameters γ_i, t_o and m are graphically adjusted for each curve.
In this paper we will focus mainly on the variation of t_o at 42°C and 100°C this parameter being directly related to the shift factor which is generally used to characterize the physical ageing.

* Permanent address: UPS-Physique des Solides, 31062 Toulouse, France.

The variation of the exponent m and the initial shear strain γ_i for all test temperatures will be analysed in a next paper.

EXPERIMENTAL RESULTS

Longitudinal creep at 42°C under 26 MPa.

Figure 1 shows the evolution of the relaxation time t_0 in the 3 successives stades.
After cooling (Fig. 1a) from the rubbery state the relaxation time t_0 increases during the 100 h at 42°C. During the longitudinal creep (Fig. 1b) the first microcreep test is performed 2 hours after the application of the longitudinal stress, the value of t_0 is $1.8 \cdot 10^6$ s. This corresponds to a vigorous deageing since at this moment of the creep t_0 is lower than just after cooling from the rubbery state. The preliminary ageing has been completely erased. The other 5 first values of t_0 determined during the longitudinal creep increase slow but beyond 100h of creep t_0 increases linearly with the time creep exactly like during the preliminary physical ageing. At this time the high longitudinal stress seems to have no more influence on the ageing rate of PMMA.
After the removal of the longitudinal stress (Fig 1c) the relaxation time of torsional microtests t_0 behaves exactly like after the loading of the specimen. The initial drop of t_0 is followed by a slow increase for 100 h and then the enhancement of t_0 becomes a linear function of the ageing time t_e as during the preliminary ageing and during the longitudinal creep.

Longitudinal creep at 100°C under 4 MPa

During the preliminary physical ageing at 100°C the relaxation time t_0 of the torsional tests increases with the ageing time t_e (Fig. 2a). The longitudinal stress applied after 140 h of ageing is only 4 MPa. All the torsional microcreep tests made during the longitudinal creep are apparently identical (Fig. 2b) and there is no drop of t_0 just after the application of the longitudinal stress like for 26 MPa at 42°C.
The mathematical analysis shows that t_0 keeps all along the creep elongation. The constant value of t_0 suggests that the physical ageing is only stopped, but the natural tendency of a system to go to its thermodynamical equilibrium can not be controlled and the physical ageing continues.
The microcreep tests made during the recovery (Fig. 2c) reveal the great influence of the new molecular arrangement due to a very small elongation of only 3%.
After about 200 h the ageing ceases suddenly, for the last 100 h t_0 remains nearly constant, the specimen of PMMA seems to have reached an equilibrium state. It is surprising that a small irreversible creep strain of 2% can accelerate such a decrease of the molecular mobility.

Longitudinal creep at 100°C under 8 MPa

The preliminary ageing of this specimen is identical with the physical ageing of the above specimen (Fig. 3a). The total longitudinal elongation is 10.5%, no striction is observed on the specimen there are many crazes of about 0.3 mm of length.
The first microcreep tests (Fig. 3b) is nearly identical with the last test of the physical ageing, as for 4 MPa the relaxation time t_0 does not vary while the longitudinal creep rate decreases. This confirms the similarity of the strain mechanisms during the first hours.
Beyond the minimum creep rate the parameter t_0 decreases deeply from $5 \cdot 10^4$ s down to 1400 s. The bypassing of the obstacles by the jumping segments creates a specific molecular arrangement different from the arrangement detected under 4 MPa where the minimum creep rate is not reached.

During the first hours after the removal of the stress the specimen contracts very rapidly up to 1.5%, then the recovery rate reduces and beyond 25 hours the recovery remains nearly to 2.2%. This value of recovery is about twice the recovery of the previous specimen after creep under 4 MPa, this ratio is perhaps fortuitous nevertheless it can be simply interpreted as the existence within the specimen of local back stress which are twice as high as in the previous specimen As for 4 MPa the microcreep tests reveal an acceleration of the ageing after the creep (Fig. 3c).

CONCLUSION

These results show the importance of the contribution of α relaxation and internal stresses even near Tg in creep experiments. Physical ageing rate after plastic deformation can be either the same or higher than physical ageing rate after cooling from rubbery state. It is depending of the strain amplitude and ageing temperature.

REFERENCES

1. GACOUGNOLLE J.L., PELTIER J.F. and de FOUQUET J., Mechanical testing for deformation model development (ASTM 1982).
2. STRUIK L.C.E., Physical aging in amorphous polymers and other materials. Elsevier Amsterdam (1978).
3. J.J. MARTINEZ VEGA, Thèse ENSMA-Poitiers, France (1986).

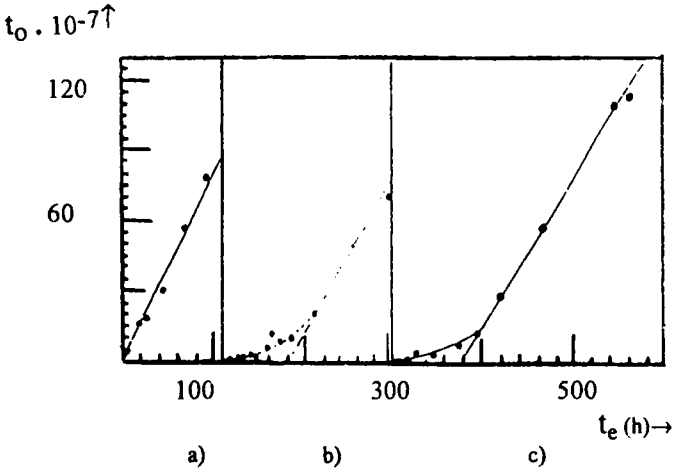

Figure 1

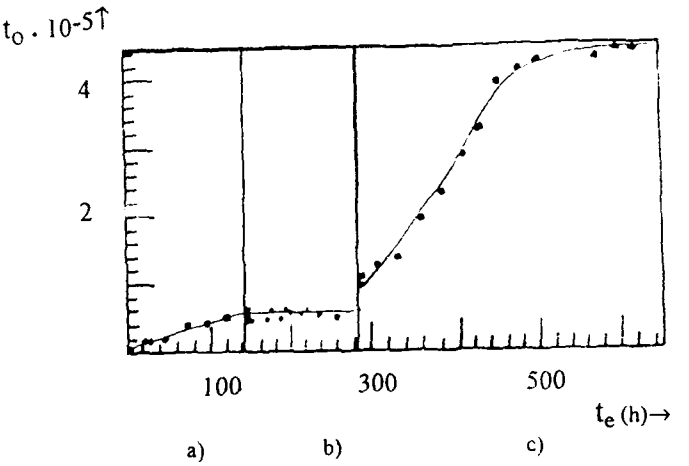

Figure 2

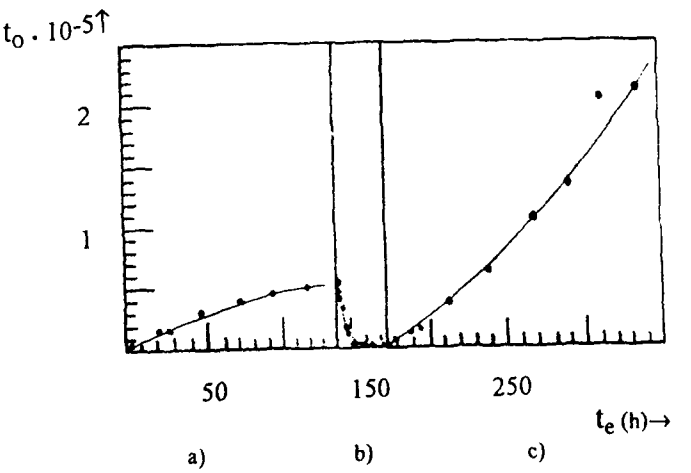

Figure 3

INFLUENCE OF CROSSLINKING ON MECHANICAL RETARDATION MODES OF LOW DENSITY POLYETHYLENE

M. GRIMAU, J.J. MARTINEZ, C. LACABANNE
Solid State Physics Laboratory, Paul Sabatier University
Toulouse, France

The purpose of this work is to improve the molecular understanding of the specific mechanical retardation phenomena observed in crosslinked polyethylene. So a comparative study of a low density polyethylene (LDPE) and the same low density polyethylene but crosslinked with the peroxides (XLPE) has been performed by thermally stimulated creep (TSCr) spectrometry and by differential scanning calorimetry (DSC). LDPE and XLPE are characterized by three mechanical retardation modes: α, β and γ in the order of decreasing temperatures. In both samples the classical endothermic melting peak in DSC experiments is observed around 100°C for LDPE and 103°C for XLPE. Moreover DSC thermograms display for both samples a endothermic peak around 38°C. The comparison of DSC thermograms and the complex TSCr spectra show that the onset of this peak coincide with the maximum of α retardation mode.

INTRODUCTION

The crosslinked low density polyethylenes (XLPE) have been largely used in the insulation of energy distribution cables. The main difference with the uncrosslinked low density polyethylenes (LDPE) is their higher thermal stability. This feature is its most important characteristic because the work temperature in cables is usually about 75°C. Recent works (1) about the dynamic (non-isothermal) crystallization of crosslinked polyethylenes do not reveal major differences between XLPE and LDPE. This implies that the crystallization is more dependent upon branching than upon crosslinking for relatively low crosslink densities.

EXPERIMENTAL

The Thermostimulated Creep (TSCr) spectrometry has been used for characterizing these materials. The TSCr principle and the torsion pendule used for this work have been extensively described elsewhere (2). However, the general outlines are mentioned below.

The sample is subjected to a static torsional stress σ at a given temperature T_σ for 2 min., allowing complete orientation of the mobile units that one whishes to consider. The resulting viscoelastic strain ($\gamma<10^{-3}$) is then frozen in by quenching the sample to a temperature $T_0 << T_\sigma$ and the stress is removed. Next, the sample is warmed up at a linear rate so that the mobile units can return to equilibrium. The strain γ, its time derivative $\dot{\gamma}$, and the temperature T are simultaneously recorded as function of time t. The plot of the normalized magnitude $|\dot{\gamma}/\sigma|$ versus T constitues the TSCr complex spectrum. This spectrum is characterized by a distribution of mechanical retardation times and can be resolved into elementary retardation process by using the fractional stresses method (2). Each elementary retardation process is characterized by a single retardation time:

$$\tau_i = \tau_{0i} \exp(\Delta H_i/kT) \qquad (1)$$

The retardation parameters, τ_{0i} and ΔH_i, are obtained from the semi-logarithmic plot of $\tau(T) = |\gamma(T)/\dot{\gamma}(T)|$ versus 1/T (2).

RESULTS AND DISCUSSION

Figure 1 shows the variation in the heat capacity of LDPE and XLPE at a scanning rate of 10 °C/min. First and second thermograms are showed, the second one has been obtained immediately after slow cooling from 150 °C down to -10°C. For both polymers two endothermic peaks appear in the first thermogram. The higher temperature one (≈100°C) corresponds to the classical melting of crystallites. The peak located at about 38°C is obtained only in the first running for both polymers. It should be noted that a room temperature annealing during half an hour makes it to reappear. This low temperature endothermic transition implies the disappearance of some order in the crystal structure. Moreover its dissappereance in the second heating cycle implies a time dependent phenomenon at room temperature.

Figure 2 shows the TSCr spectrum obtained for XLPE in the temperature region of the α retardation mode. The maximum of this mode coincides with the onset of the low temperature endothermic peak showed in the DSC traces.

The experimental resolution of this complex spectra and those corresponding to γ and β modes has been carried out by using the fractional stresses procedure (2). The relaxation map of the elementary spectra isolated in each mode are presented in figure 3. No major differences have been found in the γ and β retardation modes between LDPE and XLPE. Contrarily, the activation parameters (τ_0, ΔH) in the α mode region and above show important differences. Because of a better "structural" stability, the analysis of XLPE by fractional stesses was possible at higher temperature than for LDPE. The main difference between XLPE and LDPE in the α retardation mode temperature is the linear relationship between logτ and ΔH for the XLPE. This behaviour is called a *Compensation* Phenomenon and is associated with an important increase of molecular mobility (2).

Accordingly to the most recent interpretations (3), the α retardation mode in polyethylene should correspond to the chain segments diffusion in the crystallites, and to the consequently surface adjusting. Thus, we believe that this high-temperature compensation phenomenon is associated with an important increase of molecular mobility in crystalline regions; this molecular mobility could be associated with a conformational evolution inside and at the surface of crystallites. This evolution in the crystalline phase would be responsible for the endothermic phenomenon found in the DSC experiments.

The difference found between XLPE and LDPE relaxation map in the temperature domain of α retardation mode and above is a consequence of the higher thermal stability of the XLPE, but also possibily of the defects -branchs and crosslinks- ability to stabilize the crystalline structure at high temperature.

REFERENCES

(1) J.Y. Kao and P.J. Phillips, Polymer, **27**,1669 (1986)
(2) C. Lacabanne, D. Chatain and J.C. Monpagens, J. Macromol. Sci. Phys., **B13**, 537 (1977)
(3) R.H. Boyd, Polymer, **26**, 1123 (1985)

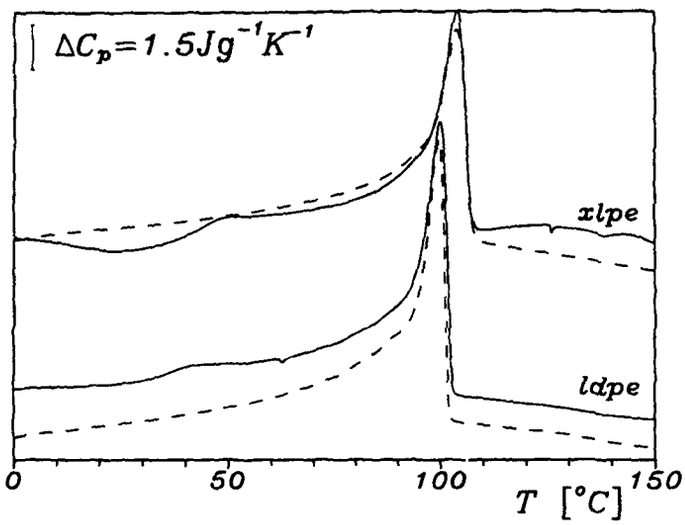

Figure 1. DSC melting thermograms for XLPE and LDPE: solid line= first heating; dashed line= second heating.

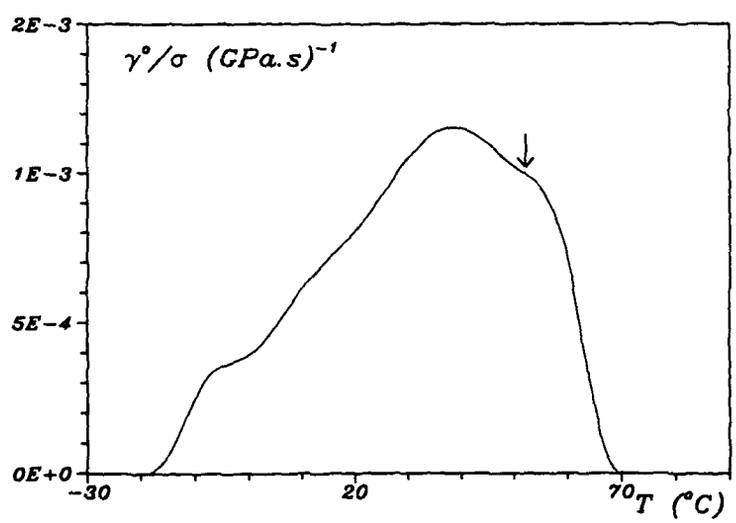

Figure 2. TSCr spectrum of XLPE, arrow indicates the temperature at which the torsional stress σ was applied.

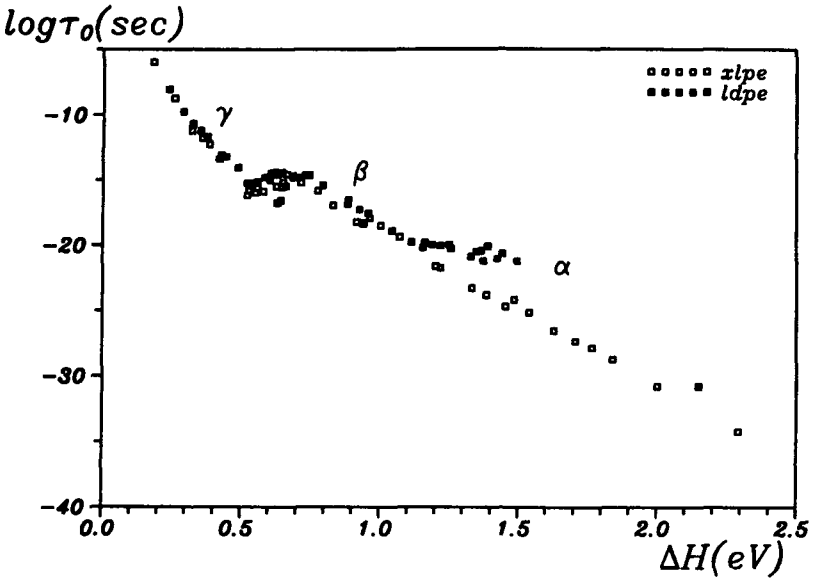

Figure 3. Semilog diagram of τ_0 versus ΔH deduced from the analysis of the elementary TSCr peaks.

RETARDATION MODES AND PHYSICAL AGEING IN PMMA BETWEEN Tβ AND LIQUID STATE

J.J. MARTINEZ*, M. DIFFALAH*, J.L. GACOUGNOLLE**, C. LACABANNE*

The anelastic properties of PMMA have been studied by thermally stimulated creep (TSCr) spectrometry, dynamic mechanical analysis (DMA), differential scanning calorimetry (DSC) and isothermal microcreep (Struik technique).

New retardation modes (α_1, α_1', α_3, α_4) around the main process α_2 (associated to the manifestation of the glass transition) have been detected.

INTRODUCTION

The aim of this study is to improve our understanding of the unstable non-equilibrium state characteristic of amorphous polymers between T_β and T_α and the post-T_α behaviour of PMMA. So, molecular mobility and retardation phenomenon in PMMA have been characterized between T_β and the liquid state.

EXPERIMENTAL PROCEDURE

Thermally Stimulated spectrometries.

We briefly recall the principle of ThermoStimulated Creep (TSCr) spectrometry (1). The sample is subjected to a static shear stress σ at a given temperature $T\sigma$ for 2 min. allowing some orientation of the mobile retardation units. The temperature is then lowered to $To << T\sigma$ at which molecular motions are frozen. At To σ is removed and the sample is heated at 7 K/min so that mobile units can disorientate. The recovery of the frozen-in strain (γ), its time derivative ($d\gamma/dt$) and the temperature are recorded as a function of time.

In the case of ThermoStimulated Currents (TSC), the mechanical stress is replaced by an electric field.

Dynamic Mechanical Analysis (DMA)

Samples were characterized by using a Perkin-Elmer DMA7 analyzer. The measuring system used was 3-point bending at 1 Hz.

* Université Paul Sabatier, Physique des Solides (CNRS URA 74) Toulouse, France.
**ENSMA Mécanique et de Physique des Matériaux (CNRS URA 863) Poitiers, France.

Differential Scanning Calorimetry (DSC)
The transition spectra were recorded (10K/min) on a DSC7 calorimeter from Perkin-Elmer. 15/20 mg samples were used.

Isothermal microcreep
The accuracy of the specially designed creep machine (2) for the measurements of the microtorsion deformation of the specimen is $5 \cdot 10^{-8}$ allowing microcreep torsion tests of a total strain less than 10^{-4}. The torsional microstress $\tau < 0.1$ MPa is so low that it does not modify the structure of the specimen.

RESULTS

Figures 1 and 2 show the complex TSCr and TSC spectra of PMMA respectively. These spectra show 4 retardation submodes labelled α_1 (157°C), α_2 (127°C), α_3 (110°C), α_4 (60°C) in the order of decreasing temperatures.
Note the tendency of α_4 submode to vanish during the second and third scan.
By applying the technique of fractional stresses the complex spectra can be experimentally resolved into elementary spectra and allow us to obtain the compensation diagram (1). Figure 3 show the PMMA compensation diagram between 70°C and 170°C, we can observe two compensation phenomenon associated to α_2 and α_3 submodes.
The experimental conditions in the high temperature domain associated to α_1 submode avoid us to obtain all the elementary spectra. So until now we do not know if this submode is characterized or not by a compensation phenomenon.
Figure 4 shows the DMA spectrum (1Hz) of PMMA only aged at room temperature during about 3 months. This spectrum shows the existence of β relaxation (~ 0°C), α_4 submode (~ 60°C) and α_2 submode (~ 129°C).
In figure 5 we show the DMA spectrum for the second scan. We can observe the existence of a higher temperature submode (~ 150°C) and as in TSC experiments (Fig. 1) the vanishing of α_4 submode.
Figure 6 shows the DSC thermogram (time derivative of enthalpy vs. temperature) obtained for PMMA during a first (Fig. 6a) and a second scans (Fig. 6b).
Further the classical phenomenon associated to the glass transition (~ 110°C), DSC thermogram display a slope change in the α_1 temperature domain (157°C).

DISCUSSION

α_2 submode
TSCr, TSC, DMA and DSC experiments show clearly that this mode is associated to the glass transition of PMMA.
α_4 submode
TSC and DMA experiments show that α_4 is associated with physical ageing. In effect this submode disappears in the second or third scan (Figure 1 and 5).
Moreover isothermal microcreep experiments display two different physical ageing kinetics in PMMA for temperatures lower and upper than 60°C (3). So, α_4 submode has been associated to a kind of boundary temperature of the two physical ageing process.
α_3 submode
The complex TSCr spectra (Figure 2) and mainly the nearly continuity in the compensation diagram of α_3 and α_2 submodes (Figure 3) show that α_3 submode is a precursor of the main process α_2 (4).

α_1 submode

The explanation for α_1 is less clear. The temperature position of α_1 in TSCr experiments depends of the application stress temperature (4). That means that there is another relaxation phenomenon at higher temperatures. Diffalah results (4) allowed us to define for PMMA a rubber-liquid "relaxation/transition" temperature which is a function of the number average molecular weight (Mn) and verify the ratio $T\alpha_1/Tg \approx 1.2$. This will be discussed in a next paper.

The α_1 behaviour in TSCr experiments let us to think that the high temperature relaxation phenomenon (~ 150°C) in DMA experiments and the slope change (157°C) in DSC experiments are not associated to the same phenomenon that the α_1 TSCr submode.

That means that before the rubber-liquid "transition" temperature ($T\alpha_1/Tg \approx 1.2$) there is a kind of soft rubber to rigid rubber transition (α_1' submode).

CONCLUSION

Ours results show that even for a classical amorphous polymer like PMMA the relaxation phenomenon is very complex. New retardation modes (α_1, α_1', α_3, α_4) around the main process α_2 (associated to the manifestation of the glass transition) have been detected in PMMA samples.

REFERENCES

1) J.C. Monpagens, D. Chatain, C. Lacabanne, P. Gautier, J. Polym. Sc. Phys. Ed. 15 (1977) 767.

2) J.L. Gacougnolle, J.F. Peltier et J. de Fouquet, Mechanical testing for deformation model development, ASTM (1982).

3) J.J. Martinez-Vega, Thesis ENSMA-Poitiers, France (1986).

4) M. Diffalah, Thesis UPS-Toulouse, France (1993).

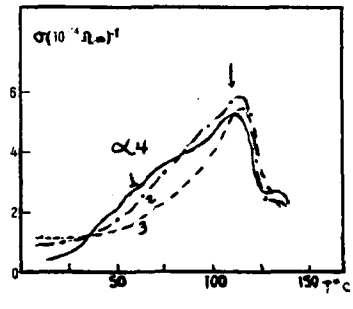

Figure 1

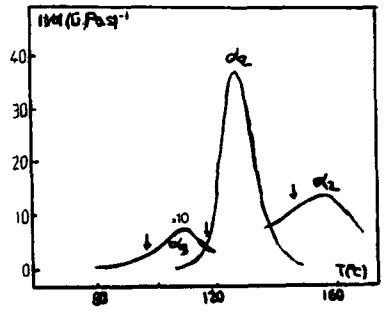

Figure 2

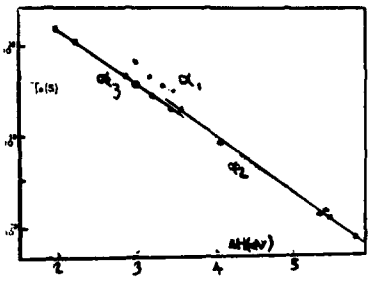

Figure 3

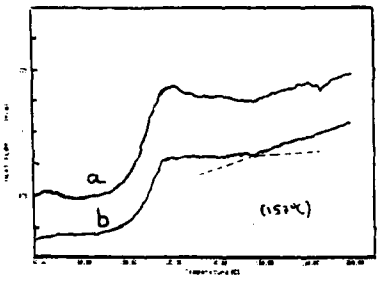

Figure 4

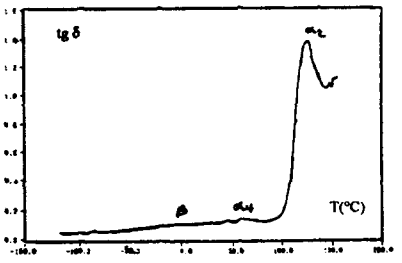

Figure 5

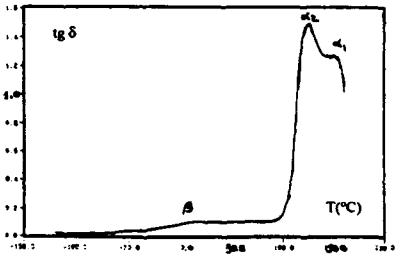

Figure 6

THE EFFECT OF INJECTION MOULDING AT GEOMETRY CHANGES IN PLASTICS PRODUCTS

Marcel J. M. van der Zwet*

The combined effect of orientation due to injection moulding and geometry changes on the load carrying capacity has been examined in tensile tests and fatigue tests for six different thermoplastics. Although the used materials have different deformation and yield behaviour, similar effects were found. Due to orientation at locations of stress-concentrations, injection moulding can lead to a pronounced increase in load carrying capacity.

INTRODUCTION

Plastics products often fail due to stress concentrations near geometry changes. Often a plastics product will be injection moulded in its final shape with geometry changes included. Injection moulding will then have an additional influence at locations of stress concentrations, which runs via orientation, internal stresses and variations in density. Depending on the way of injection moulding, either an increase or a decrease of the load carrying capacity can be found.

As a part of our research program, we examine advantageous effects due to orientation around geometry changes. Similar effects have been reported before by Crawford et al. [1] for fatigue experiments on an acetal copolymer. We studied the effect of orientation and stress concentrations in both tensile and tensile-fatigue tests in various thermoplastics. The aim of this research is to obtain insight in the load carrying capacity and the failure mechanism of injection moulded plastics products with complex shape.

EXPERIMENTAL

Experiments were carried out on injection moulded tensile specimens containing a circular hole (figure 1). Both specimens with a moulded hole and with a machined hole were used and the results were compared to the results of specimens without a hole. The applied materials were PMMA, PS, RTPMMA, HIPS, ABS and PP. PMMA and PS are mainly brittle while the other materials are more ductile, each having its own typical deformation behaviour. The tensile tests were carried out at various cross-head speeds (5 to 20,000 mm/min), the fatigue tests at various stresses. We used specimens both annealed and as-moulded.

In order to describe the failure mechanisms, fracture surfaces have been examined using optical microscopy and scanning electron microscopy (SEM). Important aspects are the type and location of craze-/fracture-initiation. The initiation point was compared to the stress and strain field as obtained from finite element analysis. Birefringence measurements were carried out on the PMMA, RTPMMA and PS specimens to determine the distribution of orientation around the hole.

*Delft University of Technology, Delft, The Netherlands

RESULTS AND DISCUSSION

Tensile tests The tensile tests revealed that the strength reduction due to a circular hole was much less than the theoretical elastic stress concentration factor (see table 1). This holds not only for moulded holes, but also for drilled holes. Especially in RTPMMA, HIPS, ABS and PP there was mostly a notch strengthening effect even for drilled holes. This means that the nominal stress based on the net cross section was higher than for specimens without a hole. The notch strengthening effect can be explained by a higher yield stress around the hole due to constraint.

The specimens with a moulded hole were always stronger than those with drilled holes. Especially PMMA and PS showed a considerable increase in strength due to the orientation around the hole. The other materials showed a less pronounced effect. Here it was not possible to find higher values, because the specimens with drilled holes already showed notch strengthening. However, substantial increases in strain to fracture were found. An example is shown in figure 2 for HIPS. The reduction of the cross section is nearly overcome by the increase in loadability due to the orientation. The material further away from the moulded hole will therefore largely contribute to the energy storage during loading. Comparing the moulded and drilled holes, increases of energy storage up to five times were found.

Fatigue tests In fatigue tests again a substantial effect of the orientation around the hole was found. The specimens with a moulded hole have endurances up to ten times more than those with a drilled hole. An example is shown in figure 3 for RTPMMA. Similar values were found for all materials.

The strengthening effect of the orientation at a certain number of cycles becomes more pronounced at higher lifetimes, where the materials behave less ductile.

Fracture surfaces An explanation of the improved strength due to orientation around the hole can be found on the fracture surfaces in comparison with the stress state as calculated in finite element analysis. This has primarily been studied on PMMA specimens with a drilled hole and tested in a tensile test [2]. It was found that the location of craze initiation, that is the distance to the hole surface, depends on the testconditions, temperature and straining rate. The initiation site corresponds to the location of the highest peak stress as was found in finite element calculations. At higher temperatures or lower straining rates the material behaves more ductile, leading to more redistribution of stresses before crazing. The location of the peak stress and of craze initiation is then located further away from the hole.

The PMMA specimens with a moulded hole also showed crazes on the fracture surfaces with similar structure as for drilled holes, but at other locations on the fracture surface. These locations are shown in figure 4. From the calculations it could be concluded that the location of crazing and fracture initiation does not coincide with the location of the peak stress or peak strain.

Similar results were found for PS specimens with a moulded hole. Crazing and fracture initiation in the middle of the cross section next to the hole was found especially in fatigue tests. Near the hole surface multiple crazing was found, leading to local craze yielding. In the very skin around the hole even shear yielding was found. According to [3] this will only occur at a high amount of orientation.

Orientation distribution As could be expected from the fracture surfaces of PS, the birefringence measurements (figure 5) showed a high amount of orientation in the skin layer. It was also found that the orientation (due to shear flow and packing pressure) around the hole was higher than elsewhere in the specimens. According to [3] the degrees of orientation indeed could cause shear-yielding and craze-yielding around the hole. The sites of fracture initiation corresponded to the locations, where minima of orientation were found.

The PMMA and RTPMMA specimens showed a distribution of orientation similar to that of PS. The measured distribution, maxima due to fountain- and shearflow and holding pressure, also

corresponds to the literature. It could therefore be assumed that the other materials also have a similar distribution of orientation.

CONCLUSIONS

The testresults showed that orientation can have a considerable advantageous effect at locations of stress concentrations. If the material behaves brittle a pronounced increase in strength is found. If the material behaves more ductile, especially an increase in strain and thereby energy uptake is found.
From the results it can be concluded that the strengthening effect of orientation, for materials that show crazing, is caused by shifted deformation behaviour. With increasing orientation first the crazing stress is elevated, then multiple crazing can occur and finally shear yielding. Materials that already show shear yielding while not being oriented, have a higher yield stress and a higher strain at fracture with increasing orientation. Finally, the load carrying capacity depends on the combination of the stress- and strain-field and the orientation distribution.

REFERENCES

[1] R.J. Crawford, V. Klewpatinond and P.P. Benham, Polymer, May 1979, Vol 20, p. 649-652.
[2] M.J.M. van der Zwet, European Conference on Fracture no. 9 papers, 1992.
[3] L. Hoare and D. Hull, Polymer Engineering Science, March 1977, Vol 17, No 3, p. 204-212.

Table 1
Notch factors measured in tensile tests at 23°C and 5 mm/min on annealed specimens. Right column shows strength increase due to injection moulding.

	drilled	moulded	strengthening effect [%]
PMMA-1	1.290	1.028	25.5
PMMA-2	1.480	1.058	39.9
RTPMMA	0.897	0.846	6.0
PS	1.057	0.841	25.6
HIPS	0.883	0.798	10.7
ABS	0.942	0.856	10.1
PP	0.923	0.863	6.9

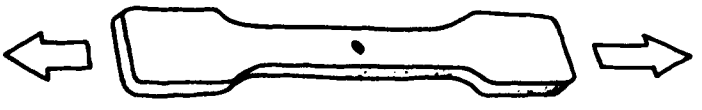

Figure 1
Used tensile specimen with central hole. Dimensions: effective length: 100 mm, width: 10 mm, thickness 4 mm, hole diameter 2 mm.

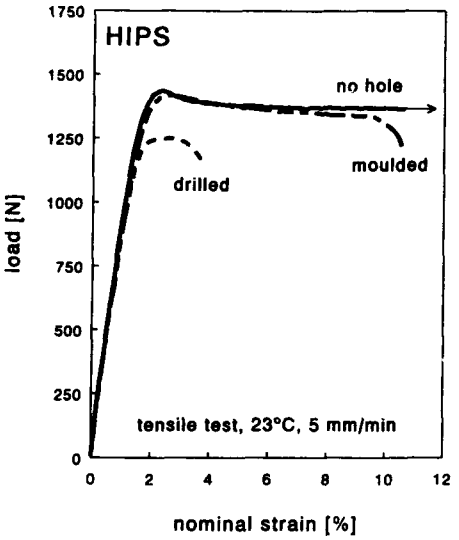

Figure 2
Tensile behaviour of HIPS specimens containing a circular hole, showing the increase in load carrying capacity and energy uptake of moulded vs. drilled holes.

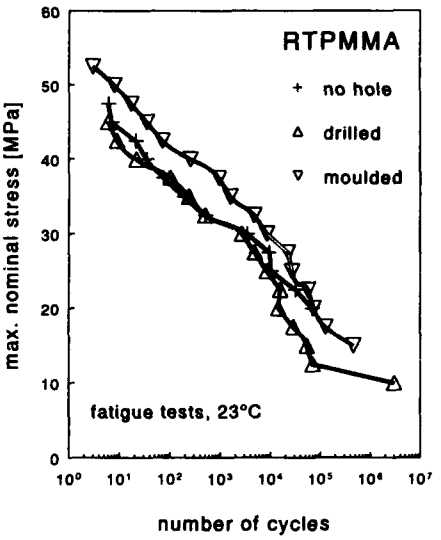

Figure 3
Fatigue behaviour of RTPMMA specimens containing a circular hole

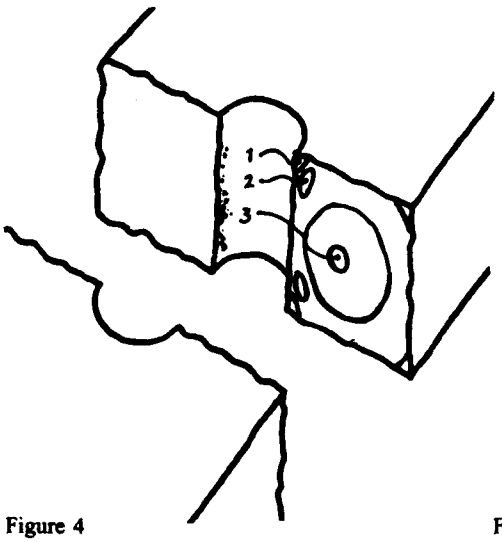

Figure 4
Schematic representation of the fracture surfaces of PMMA and PS specimens with a moulded hole. Arrows indicate craze- and fracture initiation sites.

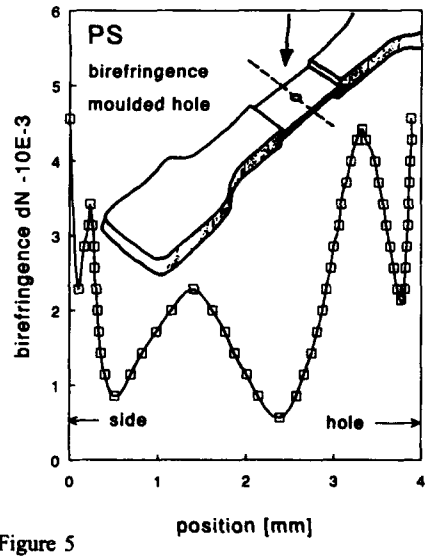

Figure 5
Orientation distribution in a PS specimen next to the moulded hole. The sample was taken from the centre in thickness as indicated.

DEVELOPMENTS IN THE STUDY OF LARGE DEFORMATIONS IN THERMOPLASTICS

R N Haward*

The further application of the Gaussian equation for high strains in thermoplastics is described. The treatment make it possible to derive expressions for the underlying properties which lead to the localisation of strains in a tensile test. It is also possible to calculate the rates of strain as the materials pass through the neck. An approximate expression for predicting the natural draw ratio is also given.

INTRODUCTION

Over an extended period an increasing number of true stress-strain curves have been reported in the literature with the result that it is now possible to study large deformation processes in a quantitative manner (1,2). It has been found that most of the measurements can be well represented by a spring and dashpot model in parallel (3) where the spring complies with the Gaussian theory of rubber elasticity (4,5,6,7,8). The equation takes the form shown below:

$$\sigma_{True} = Y + G_p\left(\lambda^2 - \frac{1}{\lambda}\right) \qquad \ldots\ldots (1)$$

Examples are given in Figures 1 and 2.

Extended application of the Gaussian equation

The application of this equation may be extended by combining it with any suitable viscosity equation relating strain rate to stress as provided by the model. For example, the Eyring equation may be used to describe the behaviour of the dashpot and the constants of the Eyring equation may be determined at low strains when $\lambda \rightarrow 1$. Isothermal deformation in tension may then be represented by the formulae:-

* Department of Engineering Science and New College, Oxford.

$$\frac{1}{\lambda} \cdot \frac{d\lambda}{dt} = K \exp kV\left(\sigma_o \lambda - G_p\left(\lambda^2 - \frac{1}{\lambda}\right)\right) \quad \ldots\ldots (2)$$

Then,

$$\ln\left(\frac{1}{\lambda} \cdot \frac{d\lambda}{dt}\right) = \ln K + kV\left(\lambda\sigma_o - G_p\left(\lambda^2 - \frac{1}{\lambda}\right)\right) \quad \ldots\ldots (3)$$

and so,

$$\frac{d}{d\lambda}\left(\ln\left(\frac{1}{\lambda} \cdot \frac{d\lambda}{dt}\right)\right) = kV\left(\sigma_o - G_p\left(2\lambda + \frac{1}{\lambda^2}\right)\right) \quad \ldots\ldots (4)$$

It is now proposed that the differential, represented by Equation (4), determines the bias between uniform and localised deformation in a tensile test. Further, as the mode of deformation is set at the beginning of the test we can again put $\lambda = 1$ and so that the differential Eqn.(4) now equals:

$$kV\,(\sigma_o - 3G_p)$$

Qualitative conclusions

Since K & k are constant under isothermal conditions, the expression given above contains only two material constants V and G_p. Both are therefore significant in determining the type of deformation (9). The ratio between σ_o, the yield stress under the conditions of the test and the constant G_p is of particular importance. If $\sigma_o < 3G_p$, then the rate of strain falls as deformation takes place under a constant nominal stress and uniform extension results, as with the cellulosics and certain polyimides (8). The condition $\sigma_o = 3G_p$ corresponds to the Considere principle. When $\sigma_o > 3G_p$, which is the most common situation with thermoplastics, strain localisation is favoured and where the product $kV\,(\sigma_o - 3G_p)$ is sufficiently large, necking may be expected. Once the necking process is established, with a constant load or drawing stress, the rate of strain of any section of the test piece passing through the neck first accelerates and then slows down as strain hardening takes over. At this point the mode of deformation becomes uniform again but still continues slowly as provided by the Gaussian equation (10). Here an important feature of the equation is that it provides for two tangents from the origin and a minimum in the true nominal stress strain curve as required by Vincent's adaptation of the Considere principle to thermoplastics (11). Further, if we assume that the termination of the necking process coincides with the point where the strain rate is the same as that at the yield point, then the draw ratio λ_D will be given by the following equation:

$$\frac{\sigma_o}{G_p} = \frac{\left(\lambda_D - \frac{1}{\lambda_D^2}\right)}{\left(1 - \frac{1}{\lambda_D}\right)}$$

Examples will be given of the application of these equations to illustrate the behaviour of thermoplastics under tension.

SYMBOLS USED

σ_{True}	=	true stress
Y	=	yield stress
G_p	=	strain hardening modulus
λ	=	extension ratio
K,k	=	constants of the Eyring viscosity equation
σ_o	=	nominal or engineering stress
λ_D	=	natural draw ratio

REFERENCES

1. Meinel, G and Peterlin, J, J. Polm. Sci., 9, (1971), 67.
2. G'Sell, C and Jonas, J J, J. Mat. Sci., 16, (1981), 1956.
3. Thackray, G and Haward, R N, Proc. Roy. Soc. London, A302, (1968), 453.
4. Arruda, E M and Boyce, M C, Proc. Plasticity 91, Grenoble, France, 483.
5. Argon, A S, J. Macromol. Sci. (Phys.), B38, 4, (1973), 573.
6. Cross, A and Haward, R N, Polymer, 19, (1978), 677 and 21, (1980), 1226.
7. Haward, R N, Polymer, 28, (1987), 1485.
8. Haward, R N, Macromolecules, 26, (1993), 5860.
9. Tervoort, T (private communication).
10. Mills, P J, Hay, J N and Haward, R N, J. Mat. Sci., 20, (1985), 801.
11. Vincent, P I, Polymer, 1, (1960), 7.

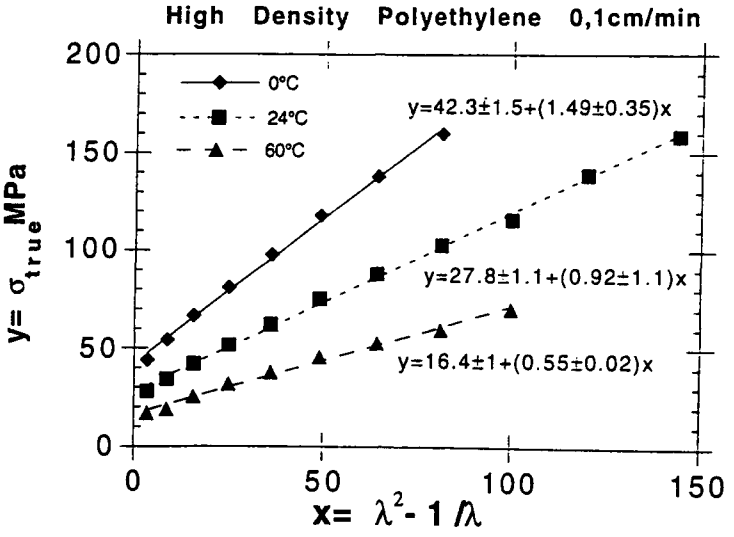

Figure 1 Gaussian plots for HDPE from the work of Meinel and Peterlin (1)

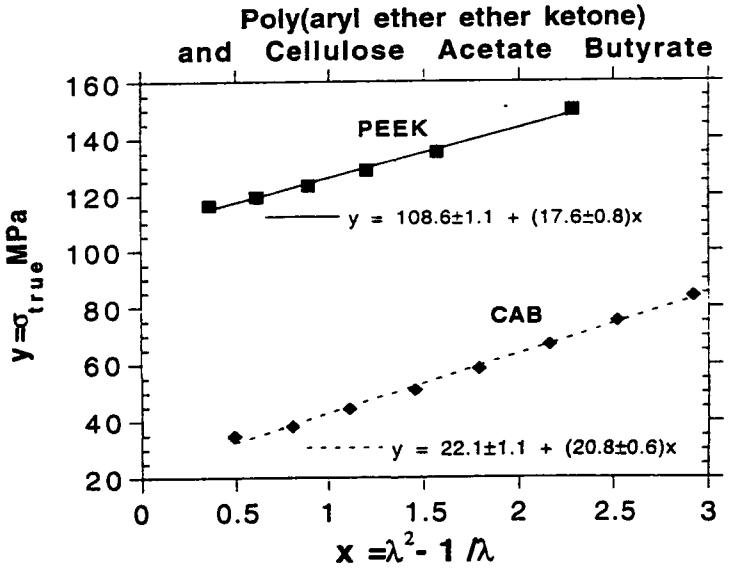

Figure 2 Gaussian plots for poly(ether ether ketone) and cellulose acetate butyrate (7)

IMPACT STRENGTH OF ACRYLONITRILE-BUTADIENE-STYRENE

S. Akkurt*

The impact strength of two ABS grades (general purpose ABS and glass fibre reinforced ABS) and effect of annealing on the impact strength were investigated. ABS specimens were annealed at 80°C for 24 h, 100°C for 1 h and 100°C for 24h. The impact strength of general purpose ABS are more affected by annealing and this is significant at higher test temperature.

INTRODUCTION

Acrylonitrile-butadiene-styrene (ABS) is one of the most important commercial polymers used widely in applications requiring substantial levels of toughness. The studies of the variables affecting their mechanical properties have been the subject of a number of reviews and articles (1). Also in some previous studies the toughening process has been discussed by Parvin et al (2) . A useful feature of ABS resin is its ability to be blended with a variety of polymers such as PC, PP, LDPE, PVC and nylons. Variation of impact strength and the fracture surface morphology with blend composition for PP/ABS and PP/ABS/LDPE was examined and interpreted by Gupta et al (3). Furthermore Jong-Han Chun et al (4) studied the miscibility and synergistic effect of impact strength in PC/ABS blend.

In this study the impact strength of two grades of ABS and effect of annealing temperature and time on the impact strength were investigated.

EXPERİMENTAL DETAILS

Two commercial grades of ABS: general purpose ABS (Sinkral A02, MFI 10, density 1.06 gm^{-3}, supplied by Enichem, IT) and 25% glass fibre reinforced ABS (MFI 8, density 1.15 gcm^{-3}, made by Teknopolimer, TR) were used in these experiments. The polymers weredried before processing by injection molding. Molding of ABS to obtain impact

*Istanbul Technical University, Faculty of Mechanical Engineering, Istanbul-Turkey.

specimens was carried out in an Imbat 160/1000 injection molding machine. A softening temperature of 260°C, an injection pressure about 90 MPa and a mold temperature of 60°C were used. The dimensions of the specimens were 130 mm length, 12.7 mm width and 3.43 mm thickness.

The impact strength of the specimens were tested with a CEAST 6545/000 pendulum impact tester by Charpy impact test method on notched (notch depth. 2.54 mm; notch radius : 0.25 mm; angle: 45°) specimens. The two grades of ABS specimens were annealed in an air oven at 80°C for 24 h, 100°C for 1 h, and 100°C for 24 h. The specimens were tested at room temperature and 50°,70°,90°,110°C. At each test temperature 5 or 7 specimens were tested to have the average impact energy. Impact strength was calculated from impact energy and cross sectional area under the notch according to:

$$I = \frac{E}{B(W-s)} \qquad (1)$$

where I: impact strength [KJ/m^2]; E: Fracture energy [kJ] and s is notch depth [m].

The melt flow indexes were determined according to ASTM D 1238 (220°C/10 kg) and Vicat softening temperatures according to ASTM 1525(10N/120°C/h)

RESULTS AND DISCUSSION

Impact strength values versus annealing temperature and annealing time of 24 h for all test temperatures were shown in figures. In general, impact strength of both ABS grades decreased with the increasing annealing temperature and time. This gives an indication of that annealing temperature produces a change in the rubbery phase of ABS as it comes crosslinked / oxidized. Furthermore as the temperature increases impact strength of both ABS increased. This increase can be explained taking in consideration that elastomeric behaviour of butadiene phase increases with the increasing test temperature (5).

Figure 1 shows the impact strength of glass fibre reinforced ABS as a function of annealing temperature. As it is seen in this figure, annealing has a little effect on the impact strength of glass reinforced ABS. In spite of this, the effect of annealing at the test temperature of 70°C was relatively excessive. By rising the test temperature from room temperature to 110°C, the impact strength of this ABS increased about 65 percent.

The effect of annealing temperature on the impact strength of general purpose ABS at room temperature and 50°C was shown in Figure 2. It is clearly seen that impact strength decreases linearly with temperature. It is seen from the experiments performed at 50°C and room temperature that annealing at the temperature of 100°C for 24 h decreases the impact strength of the material about 15 percent. When unannealed polymers are compared at room temperature the impact strength value of general purpose ABS is 6.6 times the value of glass reinforced ABS. The comparison of

polymers annealed at 100°C for 24 h shows that general purpose ABS has 5.2 times the impact strength of glass reinforced ABS.

An examination of MFI values after annealing gives an indication of that crosslinking takes place during annealing. However annealing temperature has no effect on Vicat softening point of two ABS grades.

CONCLUSIONS

General purpose ABS has higher impact strength than glass fibre reinforced specimen. Glass fibre reinforcement eliminates the effect of rubber phase and thus annealing has a little effect on the impact strength of this ABS. The effect of annealing temperature on general purpose ABS becomes important at higher test temperature.

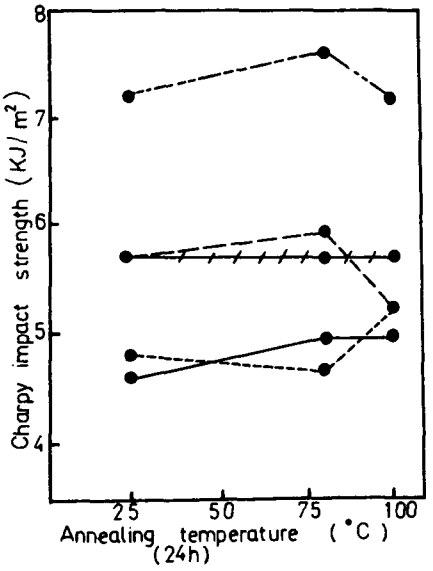

Figure 1. Effect of annealling temperature on the impact strength of glass reinforced ABS. (——): room temp., (- - - -): 50°C, (— —): 70°C, (//): 90°C, (— · — —): 110°C.

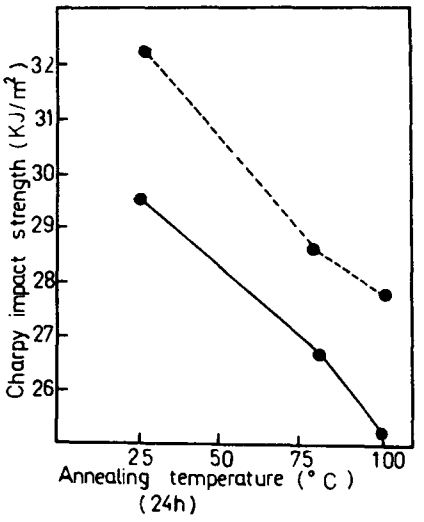

Figure 2. Effect of annealling temperature on the impact strength of general purpose ABS (——): room temp., (- - - -): 50°C.

REFERENCES

1 Paul D R, Barlow J W, Keskula H, "Encyclopedia of Polymer Sci and Eng" 12 Wiley, New York 1988.

2 Parvin M and Williams J G, J Mat Sci 11 (1976) 2045

3 Gupta A K, Jain A K, Ratnam B K, Maiti S N, J Mat Sci 39 (1990) 515

4 Chun J H, Maeng K S, Suh K S, J Mat Sci 26 (1991) 5347

5 Eguiazabal J I and Nazabal J, Polymer Eng Sci 30, (1990) 527

EVOLUTION OF MECHANICAL PROPERTIES OF ULTRAFILTRATION HOLLOW FIBRES WITH AGEING

M. Galop*, A. Lamure*, C. Lacabanne*, P. Aptel* and N. Abidine†

The thermostimulated techniques (T.S.Cr., T.S.C and D.S.C.) have been used to characterize the structure of ultra filtration hollow fibres. Origins of retardation/ relaxation modes of the fibre have been precised. First, the plasticizer effect of water and relaxation modes due to fibre structure have been studied. Second, the effect of natural ageing has been analysed.Influence of natural ageing has been completed by artificial ageing stresses (hydrolysis or chain cutting).

INTRODUCTION

Ultra filtration hollow fibres are working under mechanical and chemical stresses that could induce ageing phenomena. Then, structural changes appear in the fibre. The aim of this study is to underline these evolution. The Thermally Stimulated Creep (T.S.Cr.), Thermally Stimulated Current (T.S.C.) and Differential Scanning Calorimetry (D.S.C.) have been chosen for this study. In this paper, the relaxation modes of ultra filtration hollow fibre will be presented first. In the second part, the effect of natural ageing phenomenon will be discussed and compared with artificial ageing.

METHODS

Thermally Stimulated Creep (T.S.Cr.) and Current (T.S.C.)

The principle of these techniques is the following :
A static shear stress(1 MPa in T.S.Cr) or an electrical field(250V/mm in T.S.C.) is applied to a solid state sample at a given temperature. Then, the corresponding strain reaches an equilibrium value. This configuration is frozen by decreasing the temperature to T_o, where the stress/field is cut off. The return to equilibrium of the sample is induced by a controlled increase in temperature (7°C/min). The temperature T, the strain γ, the strain rate $\gamma' = d\gamma/dt$ in T.S.Cr. or the current in T.S.C. are simultaneously recorded versus time.

* Paul Sabatier University, 118 Route de Narbonne 31062 Toulouse, France
† Tech-Sep 5 chemin du Pillon St Maurice de Beynost 01703 Miribel Cedex

In order to compare the samples, the spectra are normalized towards the applied mechanical stress σo: a reciprocal viscosity has been defined $\eta^{-1}=\gamma/\sigma_o$.
The peaks of $\eta^{-1}(T)/I(T)$ curves indicate mechanical or electrical energy losses due to molecular movements in the sample. Any modification of those movements, like interaction with water, will induce a modification of T.S.Cr./T.S.C. spectra.

RESULTS

The ultra filtration asymmetric hollow fibres have been provided by the "Laboratoire Membranes. Lyonnaise des Eaux-Dumez". They are constituted by cellulose derivatives.
In T.S.Cr. and T.S.C, the retardation/relaxation modes have been investigated between -150°C to 200°C. Above 200°C, which is the glass transition temperature determined by D.S.C., the global porosity decreases, the sample turns black on surface and begins to degrade.
Figure 1 shows the complete retardation modes of the fibres. They can be classified in three ranges of temperature : low, room and high temperatures.

Low temperature relaxation modes

In literature concerning cellulose or derivatives(1-4), localised relaxations are generally attributed to the movements of substituted groups and hydroxyl groups. The 2 peaks observed at -110 and -85°C on the T.S.C. spectra of the fibre (5) have the same origin.

Bertran and Dale (6) have observed that water molecules are fixed on the OH groups of amorphous phase of cellulose. The evolution of the peak at -110°C, upon hydration of the di substituted sample, confirms that the peak -110°C could be associated with the movement of OH groups under the electrical field.

As for the second peak at -85°C, it is associated with the return to equilibrium of the substituted groups.

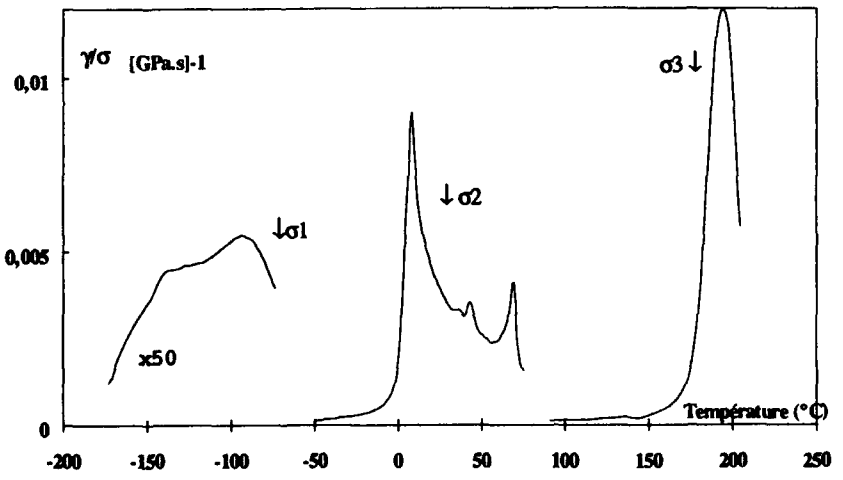

Figure 1 retardation modes of the fibre

Room temperature retardation modes

Previous D.S.C. and T.S.Cr. studies and works of Kim and al. (2) have permitted to associate peak around room temperture with the motion of water.

In order to precise the origin of room temperature retardation modes, a particular experimental procedure has been used. The stress is applied at 27°C, three peaks are observed at 10, 50, 70°C. After an annealing of two minutes at 47°C, the spectrum only shows the existence of a broad peak at 20°C. The same behavior is obtained with a dehydration at 100°C for 20 minutes under secondary vacuum. Then, the differences observed between the two spectra are due to water.

The first peak at 10°C can be attributed to the melting of water. Below 0°C, water, in solid state, blocks long range motions of fibre. When water becomes liquid, the mobile polymeric sequences will release accumulated stress and give a mechanical retardation peak.

For explaining the two other relaxation modes at 50 and 70°C, complementary thermogravimetric measurements have been made. 2 kinetics of evaporation could be seen. The evaporation of the porous zone is driven by the external skin of the fibre. During evaporation, water creates cavities which permit movements of polymeric chains in the direction of accumulated stress. The mechanical retardation mode traduces this increase of mobility. So the existence of the two peaks can be explained by a selective loss of water. The peak at 53°C has been associated with the evaporation of water in the porous zone and the peak at 70°C with the evaporation of water in the dense skin.

High temperature transitions

The T.S.Cr. and T.S.C. spectrometry can be generally applied above the glass transition temperature. But in cellulosic materials, at this temperature, the inter-chains linkages decrease drastically and the fibre can release the internal stresses accumulated during the spinning process. Then, there is an irreversible compression of the porous zone. In that case, D.S.C. is the more suitable technique to study this temperature zone.

The standard polymer (in powder) has been analysed from room temperature to 350°C and compared with the spun polymer.

Three main events have been shown :

- a broad peak between 50 to 120°C. This endothermic transition disappears after an annealing at 120°C. It is associated with the water evaporation.
- a weak step near 200°C, characteristic of the glass transition of the polymer.
- several endothermic peaks near 300°C. These are associated with the melting of the crystalline zones before degradation.

Comparatively with the standard polymer, the spun fibre presents some differences. First, the glass transition appears at lower temperatures (190°C). Second, it presents a exothermic peak at 210°C characteristic of crystallisation. During the spinning process, the polymeric chains are oriented. When their mobilities are sufficient (at the glass transition), the polymeric chains can move to a new equilibrium state (increase of local order).

EFFECT OF NATURAL AGEING

Natural three years aged fibres have been analysed and compared with a reference new synthesised fibre.

If the samples are taken in particular places of the filtration module, the dispersion decrease again but the two peaks at 50°C and 70°C shift to 55 and 65°C. This result indicates structural evolutions in the skin and in the porous zone. The shift is more important where the filtration pressure is applied.

In typical place of the module, a new peak at -30°C could appear on T.S.C. spectra of natural aged fibre (figure 2). The same peak can be created by a reaction of the fibre with Sodium Hypochlorite. So, the fibres have be degraded by the sodium hypo chloride injections used to sterilise water. The chlorine is a powerful oxidant, and it responsible of the chain cutting of cellulosic polymer.

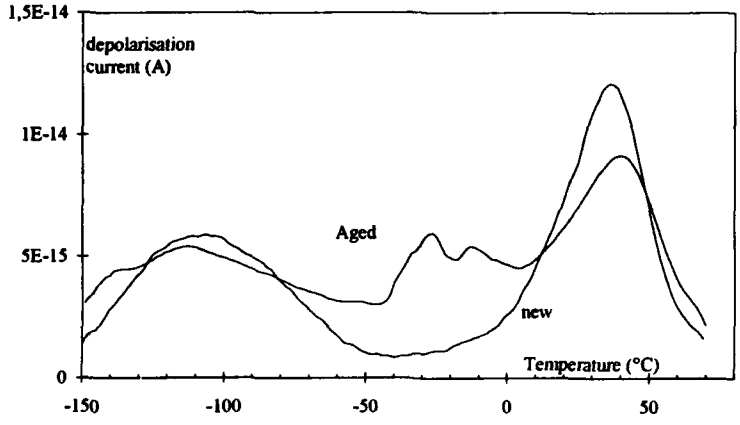

Figure 2 TSC spectra of new and aged fibres

CONCLUSION

Relaxation modes and transitions of an ultra filtration hollow fibre have been precised to have a reference for ageing study. The chlorine etching and the pressure fatigue have been underlined. The effet of the hydrolisis of substituted groups during ageing are now in progress.

References

1. Sawatary A., in "Charge storage, charge transport and electrostatics with their applications" ed. by Wada, Perlman and Kokado, 347-351, (Kodansha-Elsevier 1979).
2. Kim K.Y., Kim N.H., Nishinari K., Carbohydrate Polymers,16, 189-198, (1991).
3. Bradley S.A., Carr S.H., J. of Polym. Sci., 14, 111-124, (1976).
4. P. Pissis J PHYS D : Appl P 16 (1983) pp 915-925
5 M. Galop, A Lamure, C.Lacabanne, P. Aptel, N. Abidine Proceding of Euromembrane 92. Paris France. October 5-8 1992 p 99-104
6. Bertran M.S., Dale B.E., J. Appl. Polym. Sci, 32, 4241-4253, (1986)

MICROSTRUCTURE AND CONTOURS OF CRACK TIP CRAZES IN PVC CREATED UNDER DIFFERENT LOADING CONDITIONS

L Könczöl[1], W Döll[1], G H Michler[2], M Ensslen[2]

Crack tip crazes in rigid PVC were investigated by optical interferometry and subsequently microtomed for investigation in an high voltage electron microscope. A good agreement in craze length measured by both means has been found. A craze created under fatigue loading exhibits fibrillar structure whereas the craze matter from static load is found to be almost structureless, even at highest resolution. In a craze first created under fatigue and than enlargened under static load both types of craze structure can be found according to the regimes of different loading histories.

INTRODUCTION

Crazing is the predominant plastic deformation process in many thermoplastics. Crazes are highly localized narrow deformation bands perpendicular to the main tensile stress direction, containing highly stretched polymeric material. The formation and failure of crack tip craze zones, which may be single crazes or craze bundles, governs also crack formation and growth in many thermoplastics.

Size and shape of crazes at the tips of stationary and propagating cracks in different thermoplastics, such as PMMA, PVC, PS, PC, have been measured by different authors [1-4] under both static and fatigue loads by the method of optical interferometry. Micromechanics of crazing was evaluated on the basis of fracture mechanics by analytical and numerical means [4, 5]. The results exhibit large differences between crazing behaviour under the different loading conditions indicating also structural differences.

Internal structure as well as dimensions the of crazes in thin films or in sections of several thermoplastics are investigated by electron microscopy [6-7]. A large variation from regular fibrillation to almost structureless crazed material has been found in different polymers. However, since the crazes investigated by electron microscopy were created stretching thin films, they differ due to both stress state and loading history from crazes in bulk specimens.

Therefore, it was attempted to perform interference and electron microscopical investigations of the identical craze.

1 Fraunhofer-Institut für Werkstoffmechanik (IWM), D-79108 Freiburg, Germany
2 Martin-Luther-Universität Halle/Wittenberg (MLU),FB Werkstoffwissenschaft, D-06217 Merseburg, Germany

EXPERIMENTAL

The experiments were performed on a commercial grade of unplastisized PVC (Vestolit 3869 B, supplied by Chemische Werke Hüls, Marl, Germany) with molecular weight $M_n = 1.37 \cdot 10^4$ g/mol and $M_w = 3.43 \cdot 10^4$ g/mol. In miniature compact specimens (CT) with dimensions 4x8x10 mm^3 the machined cracks were sharpened by introducing a razor blade and subsequently lengthened by tensile fatigue at approximately 50 Hz. The fracture mechanics experiments under static as well as under fatigue loads in combination with optical interferometry were performed in specially constructed set-ups [8, 9] and evaluated as described in [4].

Thereafter these specimens were microtomed and semi-thin sections (around 1 μm thickness) of the crack tip area with craze zone were prepared. The subsequent electron microscopic investigations have been performed in a high-voltage electron microscope (1000 kV, HEM).

SOME RESULTS

Interferometric investigation of crack tip crazes is usually performed taking micrographs of both the loaded and the unloaded craze. This enables for the evaluation of craze dimensions for some well defined loading states making possible subsequent micromechanical analyses. The thin sections of polymer investigated by HEM can be stretched somewhat, however, an exactly measurable load cannot be applied. Therefore, unloaded crazes are investigated to get comparable results with both methods.

The contour of a crack tip craze in PVC which has been created during fatigue crack propagation at a slow rate (≈ 1 μm/cycle) and measured by interferometry after unloading is shown in Fig. 1. It exhibits the typical shape of a narrow wedge with length $s \approx 40$ μm and maximum width at the crack tip ($x = 0$) $2v \approx 0.6$ μm. The same craze was investigated in HEM after microtoming thin sections of the crack tip region with the craze zone. Fig. 2 shows the micrograph of the entire craze with the same magnification as in Fig. 1. Whereas the craze length in both figures is almost the same there are significant differences in craze width. The maximum width is on the micrograph about twice as large as interferometrically measured while in the centre part of the craze its width seems to be smaller on the micrograph than evaluated from interferometric measurements. This becomes reasonable taking into account that a crack tip craze in an unloaded CT specimen is compressed near to the crack tip and under some tensile stress in the interior of the specimen [5]. On the other hand the craze may be unstressed in a thin section (perhaps due to preparation strained somewhat in the crack tip region).

Micromechanics of fatigue crack propagation in rigid PVC has been investigated intensively [4, 10]. Retarded crack growth has been observed at different frequencies over a wide range of loading amplitudes and, thus, crack propagation rates. During retarded crack growth (RCG) under fatigue the crack front is stationary for a large number of loading cycles during which the crack tip craze zone grows from an initial to a final size and subsequently during a particular cycle the crack jumps through the major part of its craze. Hence, the RCG process is governed by alternating formation and growth of stretched craze material and its failure.

The craze growth occurs by both additional fibrillation of bulk material and stretching of

already formed fibrils up to some critical extension ratio. This stretching has been found to be connected with fibril coalescence causing increasing fibril thickness [11]. The craze shown in Figs. 1 and 2 was investigated just after crack jump and, thus, should exhibit a structure stretched only a little. Structural details of this craze can be seen at a higher magnification in Fig. 3. The craze exhibits a network of fibrils without an evident preferential direction in the unloaded state. The major holes may be artefacts of the preparation.

Under static load the size of crack tip craze zones in PVC increases similarly as in other thermoplastics [4]. If the load increases, however, no slow crack growth was observed in the present type of PVC. Crack growth occurs in an uncontrolled manner when the enlargened craze starts to fail mostly causing immediate failure of the specimen. A craze zone in another specimen of PVC created similarly to the previous one by fatigue and subsequently enlargened under static load (K_I = 1.8 MPa·√m) was measured by interferometry before and after growth. Fig. 4 exhibits the craze width 2v along the unloaded craze after both fatigue and static loading. The craze grew in length from almost 70 μm to about 100 μm, in maximum width from 0.7 μm to 1.8 μm. An even more significant change occured in craze shape.

The electron micrograph in Fig. 5a shows a section of the craze in the area created under static load as marked in Fig. 4. The almost homogeneous structure differs remarkably from the fibrillar structure of the fatigue craze in Fig. 3. These different structures can be found together in the area closer to the crack tip, where the interior craze layer was created under fatigue and the exterior under static load. These different features are also found on the fracture surfaces observed in the SEM.

LITERATURE

1. H R Brown, I M Ward, Polymer 14, 469 (1073)
2. R Schirrer, C Goett, J Mat Sci 16, 2563 (1981)
3. Y Imai, T Takase, K Nakano, J Mat Sci 24, 3289 (1989)
4. W Döll, L Könczöl, in: "Crazing in Polymers", Vol.2, H H Kausch (Ed), Adv Polym Sci 91/92, Springer Verlag Berlin Heidelberg 1990, p 137
5. L Bevan, W Döll, L Könczöl, J Polym Sci, Polym Phys 24, 2433 (1986)
6. E J Kramer, in: "Crazing in Polymers", Vol.1, H H Kausch (Ed), Adv Polym Sci 52/53, Springer Verlag Berlin Heidelberg 1983, p 1
7. G H Michler, Colloid Polym Sci 263, 462 (1985)
8. M G Schinker, W Döll, Inst Phys Conf Ser 47, 224 (1979)
9. R Schirrer, M G Schinker, L Könczöl, W Döll, Colloid Polym Sci 259, 812 (1981)
10. L Könczöl, W Döll, L Bevan, Colloid Polym Sci 268, 814 (1990)
11. H R Brown, Mater Sci Reports 2, 315 (1987)

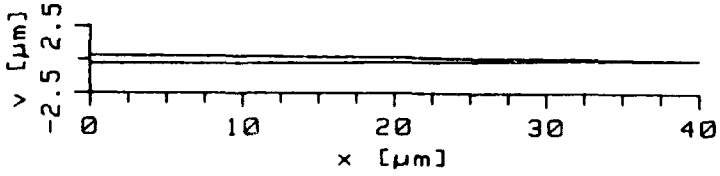

Fig. 1: Contour of an unloaded fatigue Craze in PVC as measured by interferometry

Fig. 2: HEM micrograph of the same craze as in Fig. 1 (same magnification)

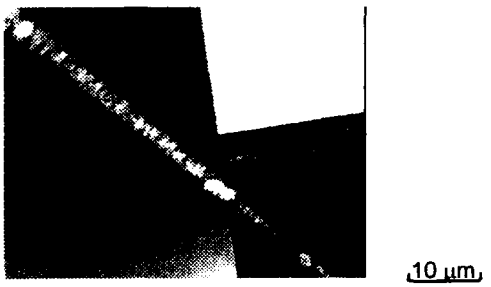

Fig. 3: Fibrillar structure in a fatigue craze in PVC (detail of Fig. 2)

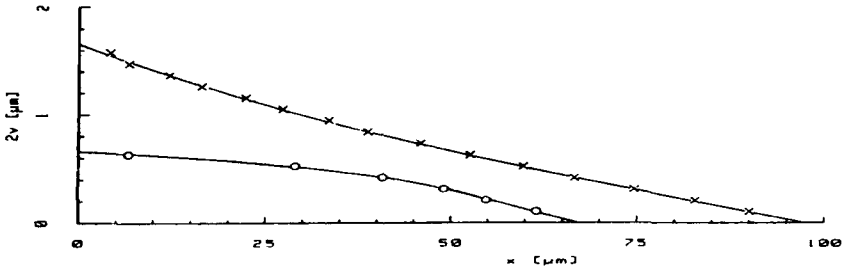

Fig. 4: Craze width as function of the distance from crack tip of an unloaded PVC craze crea ted under fatigue before and after extension under constant load

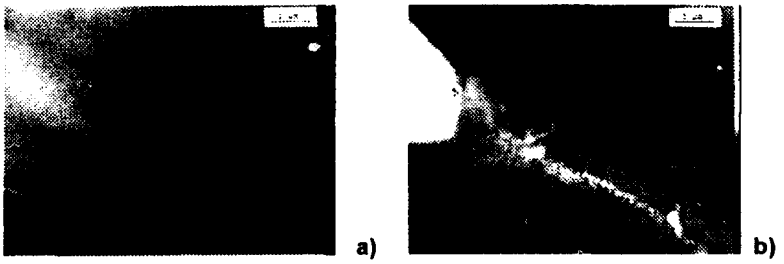

Fig. 5: Structural details of the PVC craze shown in Fig. 4: **a)** Nearly homogeneous craze area created under static load and **b)** Fibrils from fatigue load and almost homogeneous craze matter from craze extension under static load near to the crack tip

DAMAGE PROCESSES IN FILLED AND RUBBER TOUGHENED EPOXY ADHESIVES

I N Bysh*, A D Crocombe* and P A Smith†.

The damage occurring on the microstructural level in both filled and filled and rubber toughened epoxy adhesives have been investigated. Scanning electron microscopy of loaded bulk compact tension specimens have provided quantitative data about the size and distribution of the damage. Finite element analyses have then been carried out on a unit cell of the damaged material. These provided properties for the base epoxy adhesive which were used to determine the macroscopic properties of the damaged material. Additional finite element analyses of the compact tension specimen are carried out using these macroscopic properties to represent the damaged material enabling the effect of the damage on the response of the specimen to be assessed.

1. INTRODUCTION

Epoxy resins form the basis of many modern structural adhesives. Neat epoxy is brittle, however, and a second phase of rubber is often added to toughen it. Unfortunately, the addition of rubber can cause a significant reduction in stiffness and to combat this, the adhesive is frequently filled as well with a rigid third phase. During the formulation stages adhesive manufacturers have found that certain morphology and volume fraction combinations of rubber and filler have a significantly greater toughening effect than others. It is only recently that various mechanisms of toughening have been identified in detail, and attempts been made to model them, notably by Kinloch et al [1, 2] and Pearson et al [3, 4]. This paper is concerned with experimental investigations of damage and associated mechanical modelling in two commercially available adhesive systems; a two part adhesive, consisting of an epoxy resin filled with an inorganic second phase; and a three part adhesive, containing an additional third phase of CTBN type rubber.

2. DETERMINATION OF MORPHOLOGY

In the systems under investigation, rigid inorganic filler is introduced in powdered form. Determining the volume fraction and average particle size and shape from scanning electron microscope (SEM) micrographs (see figure 2.1 for example) of polished samples was therefore necessary in order to analyse the damage. Obtaining a micrograph of the rubber phase, however, was more complicated, and involved staining samples of the adhesive with osmium tetroxide before microtoming them, and viewing in a transmission electron microscope (TEM) (figure 2.2).

Photographs of the adhesive were digitised using an Epson GT-8000 scanner, and image processed to find, count and measure the particles. The size of the particles is calculated by

* Department of Mechanical Engineering
† Deparartment of Materials Science and Engineering, University of Surrey

drawing a best fit ellipse through the particle boundary and finding the major and minor axis lengths. The area fraction of particles in a micrograph could be found easily by dividing the total area of cross sectioned particles by the overall micrograph area. Assuming the particles to be randomly distributed, the volume fraction can be set equal to the area fraction.

Figure 2.1: A SEM micrograph to show damage on the surface of a polished compact tension specimen of the two phase adhesive. Note the extent of the damaged zone and the two types of filler particle failure.

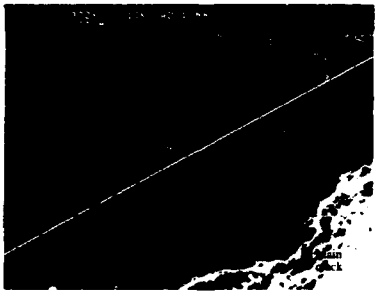

Figure 2.2: A TEM micrograph of the three phase adhesive, magnified about 10 000 times. The inset shows the matrix magnified a further ten times, and in it can be seen several rubber particles. The specimen was stained with osmium tetroxide and microtomed to a thickness of approximately 100 nm.

3. DAMAGE OBSERVED IN COMPACT TENSION TESTS

Compact tension specimens of bulk adhesive, 6 mm x 24 mm x 25 mm, were tested using an Instron tensile testing machine and on a special straining stage designed to fit within the vacuum chamber of an SEM. In each case, the damage observed in the specimens prior to catastrophic failure was similar. For the two phase adhesive, the main crack is banded on each side by a region of approximately 30 μm. Apart from the main crack, the epoxy in the damaged region shows no sign of cracking, and the only microcracking present is to be found in the filler particles. They have either fractured through their bulk or debonded. The in situ SEM tests showed that cracking and debonding of the particles preceded the main crack growth which proceeds by the linkage of these defects.

The zone containing damaged particles in the three phase adhesive is an order of magnitude greater in size than that in the two phase adhesive, and is more diffuse with increasing distance from the main crack. The larger extent of plastic deformation within the matrix can be gauged by this phenomenon, as well as by the increase in the amount of crack tip blunting shown by the specimens. Once more, however, cracking, apart from the main crack, is limited to the filler particles. In order to understand the effect of the filler particle cracking on the macro material behaviour near the main crack tip, finite element analyses have been used to determine the ensuing reduced elastic properties for the adhesive.

4. EFFECTIVE MATERIAL PROPERTIES

Damage does not exist in a uniform way in the three phase adhesive. Cracking becomes more sparse, with increasing distance from the crack tip. Plasticity within the damaged zone is also believed to be present, and the result is a relatively compliant damage zone. In contrast, damage in the two phase adhesive appears to be uniform within the damaged zone, and the effect of localised plasticity would seem much less. For these reasons it was decided to begin by modelling the damage in the simpler, two phase system.

The first task was to establish the material properties of the neat epoxy. A unit cell of matrix containing a filler particle was modelled using finite element techniques both in two and three

dimensions (figure 4.1). The diameter of the particle was chosen to make the volume fraction in the unit cell the same as that found from the morphology study. Conventional tensile tests had determined the composite modulus and Poisson's ratio as 3265 MPa and 0.4204 respectively. The tests could be reconstructed numerically by straining the model in one direction whilst allowing the material to contract freely in the other (figure 4.2). By assuming properties for the filler and taking the actual adhesive system properties as the target value, the problem could be solved iteratively to give the neat epoxy material properties.

Figure 4.1: The unit cell of a cracked filler particle within epoxy matrix. The quarter model can be used as a base for either a two dimensional solution (cylinder in a box) or a three dimensional solution (sphere in a cylinder)

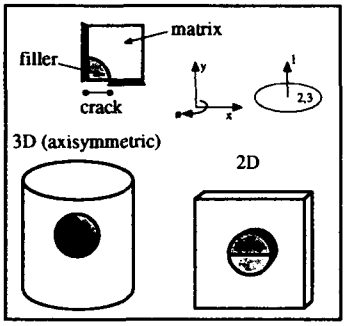

Figure 4.2: The loading regime for the unit cell in order to obtain the elastic properties of the base epoxy matrix.

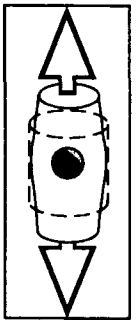

Spectrum analysis of emitted electrons under an SEM beam had indicated the chemical composition of the filler. Reference texts indicate that a Poisson's ratio of 0.3 and a tensile modulus in the range 10000 MPa to 17000 MPa would not be unreasonable for these particles. The difference in the results derived using the maximum and minimum values of the filler modulus was 3.6% and 0.48% for the epoxy modulus and Poisson's ratio respectively. The disparity between the two and three dimensional analyses was 0.44% and 0.82% for the modulus and Poisson's ratio respectively.

Figure 4.3: Three typical ways in which the unit cell is loaded in order to obtain the effective damaged material properties.

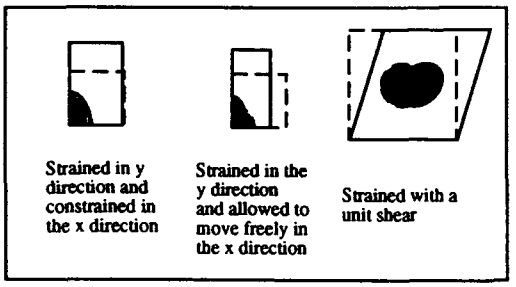

With the material properties of the constitutive materials established, a finite element model for a unit cell of damaged material could be constructed. It was decided to model first a cracked particle (figure 4.1) as a debonded particle model would involve contact elements, introducing a non-linear solution. The composite material emerging from the axisymmetric model is cylindrically orthogonal (in the plane of the micro-crack it is isotropic), whilst the two dimensional model exhibits plane stress orthotropy. The general compliance matrix is:

$$\begin{bmatrix} S_{11} & S_{12} & S_{13} & 0 & 0 & 0 \\ S_{21} & S_{22} & S_{23} & 0 & 0 & 0 \\ S_{31} & S_{32} & S_{33} & 0 & 0 & 0 \\ 0 & 0 & 0 & S_{44} & 0 & 0 \\ 0 & 0 & 0 & 0 & S_{55} & 0 \\ 0 & 0 & 0 & 0 & 0 & S_{66} \end{bmatrix}$$

Taking "1" as the direction perpendicular to the micro-crack, then for the axisymmetric model:

$S_{12} = S_{13} = S_{21} = S_{31}$; $S_{22} = S_{33}$; $S_{23} = S_{32}$; $S_{55} = S_{66}$

Two finite element solutions for the unit cell employing two separate load cases (figure 4.3) are sufficient to find all the direct stress coefficients. The remaining shear terms are found by applying a shear strain to the unit cell (figure 4.3). For the plane stress orthotropic model, only the in-plane coefficients are of interest, and so the same unit cell approach with two separate load cases can be adopted.

5. FINITE ELEMENT MODELLING OF A DAMAGED STRIP IN A COMPACT TENSION SPECIMEN

With the effective material properties of the damaged material found they may be used in a finite element analysis of the original compact tension specimens. Micrographs of damage in the specimens indicate that damage extends a distance of 30 μm each side of the main crack, and a similar distance in front of it. Using a suitably refined mesh, material this distance from the main crack in a model of the compact tension specimens may be given the effective damaged material properties. A numerical analysis of the model then gives a value for the strain energy release rate and allows the shielding effect the damaged material has on the stress distribution to be assessed.

The procedure may be refined by applying the load in steps, and modifying the material properties only of elements satisfying a certain criterion. So far, the criterion used has been a simple maximum principal stress value, but others could be implemented. In this way, it is possible to simulate the build up in the damage zone as the load increases.

6. FURTHER WORK

In due course, it is intended to extend the work to account for plastic behaviour of the epoxy matrix, in particular to give the effective properties for material damaged by rubber particle induced shear yielding. Coupled with experimental observations, it should be possible to establish bulk material failure criteria from which the design of adhesive joints may sensibly proceed. Possible criteria may involve the size of the damaged zone, be stress based or employ fracture mechanics parameters such as the strain energy release rate.

7. REFERENCES

1 Kinloch AJ, Shaw SJ and Hunston DL; Polymer, 24 (1983) 1355

2 Kinloch AJ, Shaw SJ, Tod DA and Hunston DL; Polymer, 24 (1983) 1341

3 Pearson RA and Yee AF; Journal of Material Science, 26 (1991) 3828

4 Pearson RA, Smith AK and Yee AF; Proc.2nd Int. Conf. on Deformation and Fracture of Composites, Manchester, March 1993, pp.9.1-9.10

MOLECULAR DEFORMATION PROCESSES IN POLYESTER FIBRES

W.-Y. Yeh* and R.J. Young*

An investigation has been carried out on the molecular deformation processes of poly(ethylene terephthalate) (PET) fibres using Raman spectroscopy. It has been found that the fibres have well-defined Raman spectra and that the Raman bands of the fibres tend to shift to lower wavenumber on the application of tensile strain. In particular, it was found that the bands at 1616 cm^{-1} and 1730 cm^{-1} behaved similarly implying that macroscopic deformation of the fibres resulted in 'chain stretching' of the molecules in the fibre. The results obtained were then compared with the tensile properties of the fibres and it is shown that the shift in the Raman band wavenumbers for PET is related to the macroscopic stress on the fibres rather than the strain.

INTRODUCTION

The aim of this study was to analyse deformation processes in poly(ethylene terephthalate) fibres (PET) at the molecular level using Raman Spectroscopy. This technique has been employed by many researchers to study molecular deformation in a variety of high-performance materials such as aramid fibres [1], rigid-rod polymer fibres [2] and gel-spun polyethylene fibres [3] etc. An important finding was that for all of these fibres the Raman bands shift in wavenumber on the application of stress or strain. In our previous work on PET fibres [4], a significant shift of up to approximately 2.5 cm^{-1} for the Raman band at 1616 cm^{-1} (which involves phenyl ring stretching) for PET fibres was found during deformation up to fracture. It was shown that by analogy to the deformation of aramid fibres [1], this result could be related to chain stretching in the molecules in the PET fibres.

EXPERIMENTAL

Two experimental PET fibres (namely P1 and P2) and one commercial grade (P3), Diolen 855T, 1100 dtex f210 were studied. They were supplied by Akzo Research. The fibre P3 is a technical yarn with a tenacity of 80 cN/tex and full details of its physical properties are given elsewhere [5]. The experimental fibres P1 and P2 both had a similar initial modulus to P3 but had been processed such that they either had a narrow (P1) or wide (P2) orientation distribution. For the Raman deformation studies, single PET fibres with a gauge length of 50 mm were fixed using aluminium foil tabs and a cyanoacrylate adhesive on a manual straining rig. The fibres were then loaded to failure in steps of the order of 0.5% strain. The 632.8 nm red line of a 7 mW He-Ne laser was used to excite the spectra in the samples using a Raman microprobe system [4]. This consisted of

* Manchester Materials Science Centre, UMIST and University of Manchester, Grosvenor Street, Manchester, M1 7HS, UK.

an Olympus microscope, a SPEX 1000M single monochromator and a liquid N_2 cooled charge-couple device (CCD) camera.

For tensile testing, randomly selected PET fibres were tested to failure using a Model 1121 Instron universal testing machine following the testing procedure given in ASTM D3379-75. A fibre gauge length of 50 mm was employed with an initial strain rate of 1.6×10^{-3} s^{-1}. Full details of equipment used and experimental procedure were given in the previous publication [4].

RESULTS AND DISCUSSION

A typical Raman spectrum for P3 fibre is shown in Figure 1. Most of the Raman active bands, ie. those at 1730, 1616, 1310, 1286, 1120, 1001, 861 and 632 cm^{-1}, have been assigned by Bower [6], and Beorio et al [7,8]. However, in this work, discussion has been confined only to the bands at 1730, 1616, 857 and 632 cm^{-1}. The band at 1730 cm^{-1} is known to involve the C=O stretching vibration [7,8]. It was found that the intensity of the band decreased and its width broadened during deformation as shown in Figure 2. Both the unloaded and loaded bands were found to be asymmetric. It is convenient to quantify the degree of Raman band asymmetry by means of the asymmetry index, (SI, see [9]). The undeformed P3 fibre had an SI value of 1.3. After deformation to 13% strain, the SI value had risen to 1.5, an increase of 15%. Thus the C=O stretching band had become more asymmetrical during tensile deformation. Similar broadening was also observed for the band at 1616 cm^{-1} [4].

Similar behaviour was found for many of the Raman bands seen in Figure 1. Figure 3 shows the behaviour of the Raman bands for the fibre P3 subjected to tensile deformation. The bands at 1730, 1616 and 857 cm^{-1} shifted to lower frequencies when the applied stress or strain on the single fibre was increased until fracture occurred. The band at 857 cm^{-1} has been assigned to the benzene ring and ring-ester stretching vibration [6]. It was also noted that the band at 632 cm^{-1}, which involves a benzene ring vibration [6], did not shift during deformation. The reasons for this are not clear but it is likely to be significant, giving an important insight into the molecular deformation processes in the material, and it is currently the subject of further study.

The stress-strain curves for the P1 and P2 fibres are shown in Figure 4 and it can be seen that the behaviour at low strains is very similar but that the curves deviate form each other at high strains (>8%). The curves are non-linear and the Young's modulus and ultimate tensile strength (UTS) of P1 and P2 were 14.5 GPa, 0.87 GPa and 15.8 GPa, 0.74 GPa respectively. Figure 5 shows the change in the 1616 cm^{-1} Raman band position with strain for fibres P1 and P2. It can be seen that the curves in Figure 5 are essentially a mirror image across the x-axis of the stress-strain curves in Figure 4. This suggests that the shift in the Raman band is related to the fibre stress rather than the fibre strain, i.e. the deformation if the fibre is controlled by a uniform stress, series model [10]. This is confirmed in Figure 6 which combines the data of Figures 4 and 5 and show the dependence of the Raman band peak upon stress for fibre P1 and P2. The two curves are now much closer to each other than in Figure 5 supporting the series model.

CONCLUSIONS

It had been demonstrated that Raman spectroscopy is a powerful technique which can aid in the study of deformation processes of PET fibres at molecular level. Some of the Raman bands shift to lower frequency under the action of applied stress or strain whereas others do not shift significantly. It has been shown that the Raman band shifts follow stress rather than strain which indicates that the deformation of the materials may be analysed by a series model.

ACKNOWLEDGEMENTS

This research is part of a program of work supported by the SERC through a research grant. The fibres used in this work were kindly supplied by Dr. R. Huijts of Akzo Research. The authors are also grateful to Dr. Huijts and Dr. M.G. Northolt of Akzo Research for valuable discussion. RJY is also grateful to the Royal Society for support in the form of the Wolfson Research Professorship in Materials Science.

REFERENCES

1. Young, R.J., Day, R.J., Dong, L. and Knoff, W, 1992, *J. Mater. Sci.*, **27**, 5431.
2. Young, R.J. and Ang, P.P., 1992, *Polymer*, **33**, 975.
3. Grubb, D.T. and Li, Z., 1992, *Polymer*, **33**, 2587.
4. Young, R.J. and Yeh, W.-Y., *Polymer*, in press.
5. Heuvel, C.J.M.v.d., Heuvel, H.M., Fassen, W.A., Veurink, J. and Lucas, L.J., *J. Appl. Polym. Sci.*, in press.
6. Purvis, J. and Bower, D.I., 1976, *J. Polym. Sci. Polym. Phys.*, **14**, 1461.
7. Beorio, F.J., Bahl, S.K. and McGraw, G.E., 1976, *J. Polym. Sci. Polym. Phys.*, **14**, 1029.
8. Bahl, S.K., Cornell, D.D. and Beorio, F.J., 1974, *Polym. Lett.*, **12**, 13.
9. Suffolk, B.R. and Gilpin, R.K., 1985, *Anal. Chem.*, **57**, 596.
10. Northolt, M.G., Private communication.

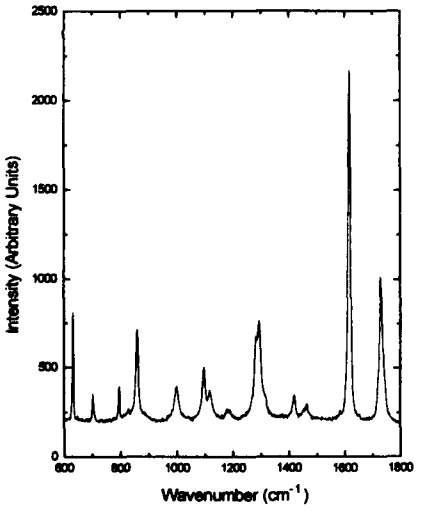

Figure 1 Raman Spectrum for a single PET (P3) fibre.

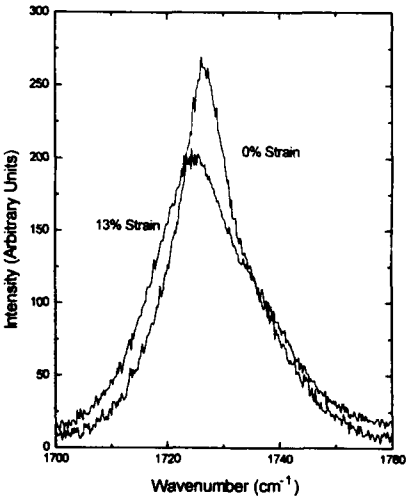

Figure 2 The Raman band at 1730 cm^{-1} for the P3 fibre unstrained and at a strain of 13%.

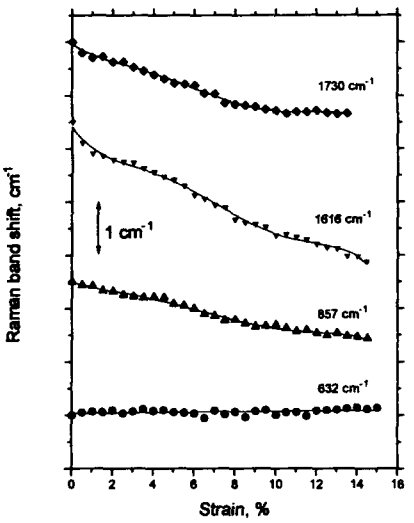

Figure 3 The variation of wavenumber at 1730, 1616, 857 and 632 cm^{-1} with strain for the P3 fibre.

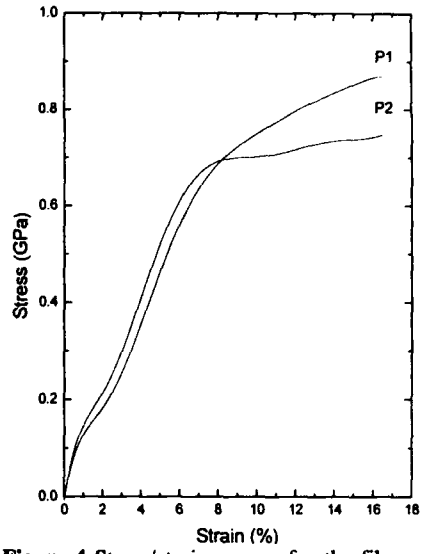

Figure 4 Stress/strain curves for the fibres of P1 and P2.

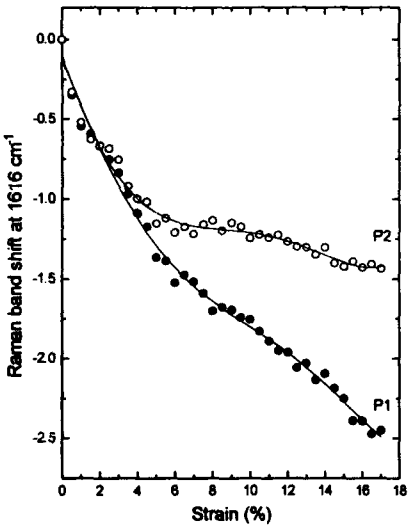

Figure 5 The variation of wavenumber at 1616 cm^{-1} with strain for P1 and P2 fibres. The curves are the fit of the data points to a 5th-order polynomial.

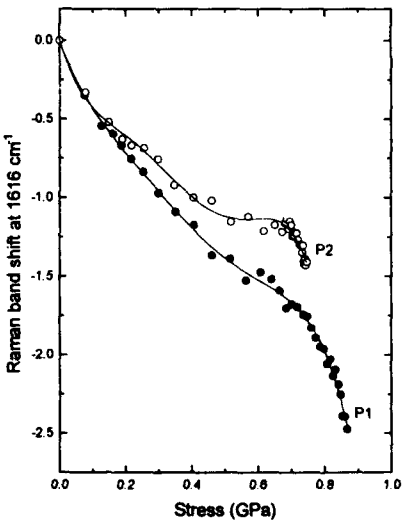

Figure 6 The variation of wavenumber at 1616 cm^{-1} with stress for P1 and P2 fibres. The curves are the fit of the data points to a 5th-order polynomial.

THE RELATIONSHIP BETWEEN STRUCTURE AND MECHANICAL PROPERTIES OF POLYPROPYLENE FILMS

W J O'Kane*, R J Young* and A J Ryan*

The structure and mechanical properties of two PP films, one displaying the monoclinic α-modification and the other the quenched structure, have been investigated after annealing at elevated temperatures for various times. In particular it is found that heat treating films with the quenched structure results in a dramatic increase in mechanical properties. This improvement in properties is paralleled by the development of a well-defined structure through a quenched-to-monoclinic structural modification. The properties of the monoclinic α-modification are also improved by annealing this being due to an increase in the perfection of the crystalline regions. The yielding behaviour of both films has been interpreted in terms of a model involving the thermal activation of screw dislocations.

INTRODUCTION

The structure of the different crystal modifications of PP has been known for many years [1-4]. Upon rapid cooling from the melt a quenched phase is obtained, the structure of which has still not been fully resolved. This quenched phase is stable at room temperature but transforms to the monoclinic α-modification upon heating at temperatures above 60-70°C [5-8]. Although this transition has been studied by a variety of techniques, the accompanying changes in mechanical properties have not previously been studied in detail. The object of this paper therefore is to provide preliminary results obtained from mechanical testing of samples which have been heat treated at different temperatures for various times and to correlate them to the development of crystallinity attained through the quenched-to-monoclinic α-modification structural transition.

EXPERIMENTAL

Two 50 μm thick cast PP films were used for the purposes of this investigation:-

(i) Film A which exhibited the monoclinic α-structural modification, and

(ii) Film B which exhibited the quenched structure of PP.

The films were annealed by placing them in ovens at temperatures ranging from 60-120°C for times of up to 24 hours. After heat treating the samples were conditioned for 72 hours in a controlled environment laboratory (T=23°C±1°C, RH=50%±2%). After this time the samples were cut into strips 100 mm long by 25 mm wide and mounted onto window cards to ensure that they were of the correct gauge length (~50 mm). The samples were deformed on an Instron 1122 tensile testing machine fitted with a 0.5 kN load cell at a rate of 50 mm/min until they had yielded.

* Manchester Materials Science Centre, University of Manchester and UMIST, Grosvenor Street, Manchester, M1 7HS, UK.

As-cast heat-treated samples were also analysed by wide- (WAXS) and small-angle x-ray scattering (SAXS, using the SRS at the Daresbury laboratory) in order to determine the effect of heat treatment on the structure of the films.

RESULTS AND DISCUSSION

The data obtained from mechanical testing of films A and B are illustrated graphically in Figure 1. From the results it can be seen that annealing both films at temperatures $>60°C$ results in an improvement in their mechanical properties. It is clear that at each annealing temperature a significant increase in yield stress is attained in a relatively short time; the magnitude of the increase depending upon the annealing temperature. The highest yield stresses are attained by annealing at higher temperatures. In addition the time that it takes to reach this maximum plateau value decreases as the annealing temperature is raised. The results obtained from SAXS analysis of undeformed heat treated samples (Figure 2) reveals that the development of long period closely mirrors the improvement in mechanical properties. The relationship between crystallinity and mechanical properties is well established and by estimating the crystal thickness to a first approximation as the product of the long period and the volume fraction of crystals (which can be determined from the WAXS patterns) the dependence of the yield stress upon the crystal thickness can clearly be observed (Figure 3).

Theories to explain the yielding behaviour of polymers can be divided into two schools of thought. One theory pictures deformation to occur by a "partial melting and recrystallisation" process resulting in a transformation of the polymer structure into a new morphology which is not related to the original microstructure [9]. As yet no equations have been developed to describe the dependence of this process on factors such as temperature or crystal thickness. The second more popular belief is that the deformation process at least at small extensions occurs by mechanisms such as chain slip, tilting and martensitic transformations [10]. Yielding itself is believed to occur by the thermal activation of screw dislocations and equations have been developed to quantify the process [11-14]. Although rather simplified they have proved remarkably accurate in describing the effect of parameters such as crystal thickness and temperature on the yielding process in polyethylene. In particular, it is predicted [14] that at a given temperature the yield stress will be controlled by the crystal thickness and should increase with increasing crystal thickness. This has been found experimentally and Figure 3 shows that for each type of film, the yield stress correlates with the crystal thickness. Hence, it appears that the dislocation mechanism may be valid to describe the deformation of semicrystalline polymers such as the polypropylene films studied here. The data for each type of film fall on a single curve although it is not clear why the curves for the two types of films are displaced relative to each other. This is currently the subject of further investigation.

CONCLUSIONS

In summary it can be seen that the mechanical properties of quenched PP films can be improved significantly by annealing at elevated temperatures. This improvement in mechanical properties is caused by a quenched-to-monoclinic structural modification which results in an increase in the crystal size and perfection of the samples. The process by which the crystalline lamellae themselves deform can be explained by a mechanism involving the thermal activation of screw dislocations.

ACKNOWLEDGEMENTS

WJO'K is grateful to the Royal Society for financial support. RJY is also grateful to the Royal

Society for support in the form of the Wolfson Research Professorship in Materials Science. Thanks are also extended to the Four Square Division of Mars (GB) Ltd for financial support and supplying the materials used in this study.

REFERENCES

1. Natta, G. Corradini, P. 1955, *Nuovo Cimento*, **15**, 40
2. Kieth, H. Padden, F.J. Walter, N.M. Wyckoff, H.W. 1959, *J. Appl. Phys.* **20**, 1485
3. Turner-Jones, A. Aizlewood, J.and Beckett, D. 1964, *Makromol. Chem.* **75**, 134
4. Addinck, E. and Bientema, J. 1961, *Polymer*, **2**, 185
5. Grebowicz, J. Lau, I.F. Wunderlich, B. 1984, *J. Polym. Sci. Polym. Symp.* **71**, 19
6. Glotin, M. Rahalkar, R. Hendra, P. Cudby, M. Willis, H. 1981, *Polymer*, **22**, 731
7. Vittoria. I. 1989, *J. Macromol. Sci. Phys. Edn.* **B28(3,4)**, 489
8. O'Kane, W.J. Young, R.J. Ryan, A.J. Bras, W. Derbyshire, G.E. Mant, G.R. *Polymer*, in press
9. Popli, R. Mandelkern, L. 1987, *J. Polym. Sci. Phys. Edn*, **25**, 441
10. Bowden, P.B. Young, R.J. 1974, *J. Mat. Sci.* **9**, 2034
11. Young, R.J. 1974, *Phil. Mag.* **30**, 85
12. Shadrake, L.G. Guiu, F. 1976, *Phil. Mag.* **34**, 565
13. Crist, B. Fisher, C. Howard, P.R. 1989, *Macromolecules*, **22**, 1709
14. Young, R.J.,1988, *Materials Forum*, **11**, 210

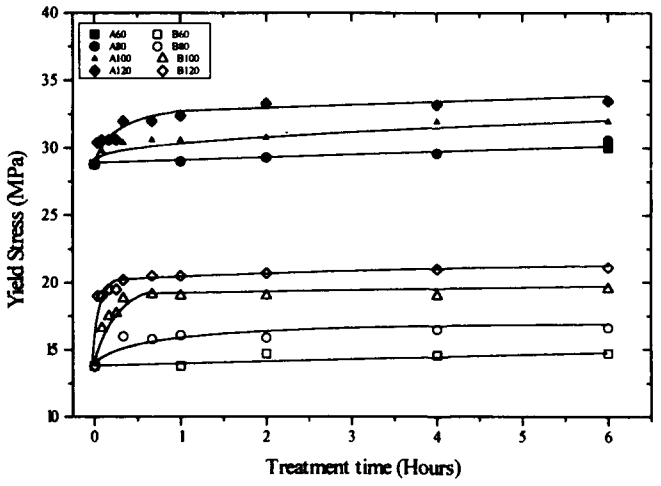

Figure 1 Effect of heat treatment on the yield stress of polypropylene films. The letter refers to the film type and the number the annealing temperature in°C.

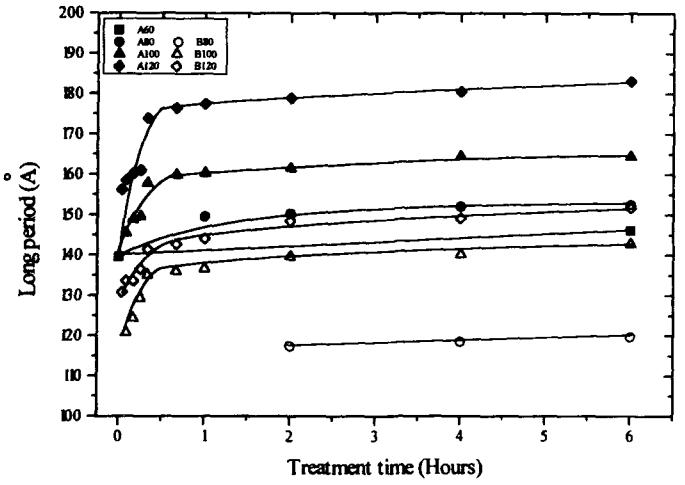

Figure 2 Effect of heat treatment on the long periods of films A and B.

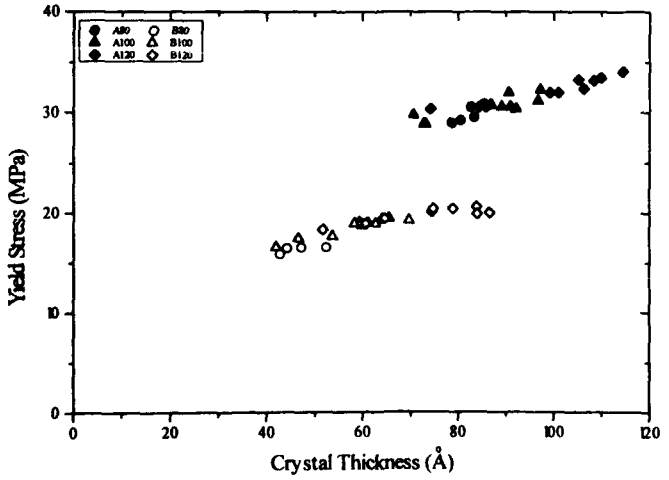

Figure 3 Effect of crystal thickness on the yield stresses of films A and B.

MECHANICAL PROPERTIES OF RUBBER-TOUGHENED ACRYLIC POLYMERS

A.C. Archer, P.A. Lovell, J. McDonald, M.N. Sherratt* and R.J. Young

Rubber-toughened poly(methyl methacrylate) (RTPMMA) materials are produced by extrusion blending PMMA with separately-prepared toughening particles. This permits independent control of the properties of the matrix PMMA, the composition, morphology and size of the dispersed rubbery phase, and the level of inclusion of the toughening particles. This paper presents results from mechanical testing of a range of RTPMMA materials with systematic changes in particle composition, size and morphology.

INTRODUCTION

Rubber-toughened poly(methyl methacrylate) (RTPMMA) materials are produced by blending PMMA with separately-prepared toughening particles [1]. Emulsion polymerisation is used to prepare the toughening particles which typically comprise two to four radially-alternating rubbery and glassy layers, the outer layer always being of glassy polymer. The particles are crosslinked during their formation in order to ensure that they retain their morphology and size during subsequent blending. This route has the advantage of allowing independent control of the composition, morphology, size and the level of inclusion of the toughening particles. This paper presents results from mechanical testing of a range of RTPMMA materia's with systematic changes in particle composition, size and morphology.

EXPERIMENTAL

Materials

The matrix PMMA used was Diakon LG156 (ICI plc) which is poly[(methyl methacrylate)-*co*-(n-butyl acrylate)] with 8 mol% n-butyl acrylate repeat units and has M_n = 47 kg mol^{-1} and M_w/M_n = 1.7 (GPC, polystyrene calibration).

The two-, three- and four-layer (i.e. 2L, 3L and 4L) toughening particles are represented schematically in *Figure 1* and were prepared by sequential emulsion polymerisation [1,2]. The compositions of the rubbery and glassy phases of the particles were chosen such that their refractive indices match that of the matrix PMMA. The rubbery and glassy layers consist of poly[(n-butyl acrylate)-*co*-styrene] and poly[(methyl methacrylate)-*co*-(ethyl acrylate)] respectively, the inner glassy layers being crosslinked. Each layer is graftlinked to the adjacent layer(s). With the exception of the 3LAI and 3LAII particles, allyl methacrylate (ALMA) was used at constant levels for both crosslinking and graftlinking. For the 3LAI particles, ALMA was used at higher-than-normal levels in the interfacial regions. For the 3LAII particles ALMA was replaced by identical molar quantities of ethan-1,2-diol dimethacrylate and hexan-1,6-diol diacrylate to crosslink the glassy and rubbery phases respectively.

* Polymer Science and Technology Group, Manchester Materials Science Centre, University of Manchester & UMIST, Grosvenor Street, Manchester, M1 7HS, United Kingdom

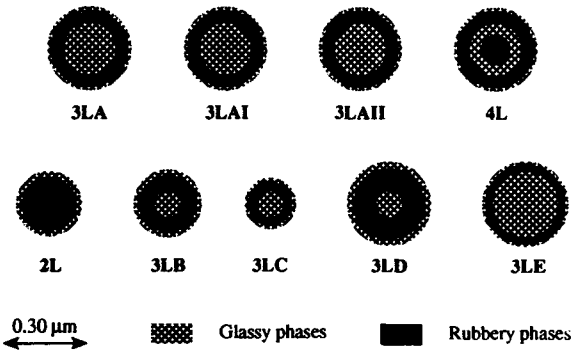

Figure 1. Schematic diagrams of sections through the equators of the toughening particles showing their sizes and internal structures.

Dried aggregates of toughening particles were extrusion blended with the matrix PMMA at 220 °C. For each type of particle, four blends containing different weight fractions (w_p) of particles were produced. Complete dispersion of the of the particles was confirmed by transmission electron microscopy (TEM).

Mechanical Testing

The matrix PMMA and each of the RTPMMA materials were compression-moulded into plaques of 3 mm thickness (for tensile testing) and 6 mm or 12mm thickness (for impact and low-rate fracture testing respectively). Tensile tests were carried in accordance with ASTM D638-84 employing a nominal strain rate of 2×10^{-3} s^{-1}. *Three-point* bend fracture tests were conducted in accordance with ASTM D5045-91 with loading times in the range 0.8-2.0 ms for impact testing and 3-8 s for low-rate testing. All tests were conducted at 20 °C

RESULTS AND DISCUSSION

Tensile testing revealed that, with the exception of 3LAII particles, each type of toughening particle is capable of inducing extensive shear yielding in the matrix leading to much greater fracture strains (up to 30-50%, compared to 3% for the unmodified matrix PMMA) and correspondingly increased energies to fracture. The poor performance of the 3LAII materials (ca. 8% ultimate elongation for $w_p > 0.20$) results from the change in the chemistry of crosslinking in 3LAII particles which leads to a substantial increase in crosslink density [3]. With the exception of the 3LC and 3LAII type materials tensile yielding is accompanied by stress whitening which occurs as a consequence of cavitation within the rubbery layers of the particles[4]. For the 3LC type materials yielding is accompanied by particle cavitation, however, the voids are to small to scatter light. For the 3LAII materials cavitation appears to be suppressed and unstable yielding is rapidly succeeded by fracture.

The values of Young's modulus (E) and yield stress (σ_y) from tensile testing are shown in *Figure 2* . In each case, the data are plotted against the volume fraction of rubber (V_r), which excludes the particles outer and internal glassy phases. For the 4L particles the central rubbery core is not included in the calculation of V_r. Inspection of *Figures 2a and 2b* shows that E and σ_y are determined by V_r .

Figures *3a* and *3b* show the variation of critical strain energy release rate (G_{Ic}) with V_r, for all materials under low-rate and impact loading respectively. The data presented for low rate testing are for the observed onset of crack growth while the data for impact testing are for energy absorbed to peak load. The trends observed in the variation of G_{Ic} with V_r are markedly different for the two situations. Under low-rate loading G_{Ic} is independent of particle size and morphology for all but the 3LC and 3LAII materials, while under impact loading G_{Ic} is strongly dependent upon both particle size and morphology.

The 3LAII and 3LC type materials perform poorly at both loading rates. For the 3LC type materials this apparently arises from the small particle size (150 nm rubbery layer diameter) and/or from the abnormal particle morphology. TEM reveals that the outer rubbery layer is not continuous but is present as lobes surrounding the glassy core. The poor performance of the 3LAII type particles arises from the high level of crosslinking within the particles rubbery layers which elevates the glass transition temperature of the rubbery phase. The rubbery phase glass transition is indestinct but occurs in the range 5 - 10 °C (tan δ) for the 3LAII particles compared to -5 - 0 °C for all other toughening particles.

Figure *3a* shows that, under low rate loading, G_{Ic} increases rapidly with increasing V_r reaching a maximum for V_r in the range 0.1-0.2. As the particle content is increased further G_{Ic} begins to decrease. Mechanistic studies indicate that the particles prevent the formation and subsequent breakdown of mature crazes by cavitating and generating a multiplicity of small fine crazes [4]. It appears that the materials generate a saturation density of crazes at the maximum in G_{Ic}. Further increases in particle concentration do not increase the extent of crazing and reduce the load bearing capacity of the material. For the tougher RTPMMA materials the magnitude of G_{Ic} is principally determined by V_r and is not strongly dependent upon particle size, morphology or level of interfacial graftlinking.

Figure *3b* shows the variation of G_{Ic} with V_r under impact loading. A general increase in G_{Ic} with increasing particle size is apparent for a given V_r. The particle size effect is most clearly seen by comparing the data for the 3LC, 3LB and 3LD materials. These materials contain particles with 100nm diameter glassy cores, but with rubbery layer diameters of 152 nm, 202 nm and 252 nm respectively. The particle size effect is also evident in the further increase in G_{Ic} between the 3LD and 3LA materials. The latter contain particles with an outer diameter of approximately 290 nm. However, this marked increase may not be due to the increase in particle size alone, since, the glassy core size is also increased to approximately 200 nm.

Comparing the data for the 2L and 3LB materials suggests that introduction of a glassy core into a homogeneous rubber particle leads to a small increase in fracture resistance for a given V_r. This effect may be due partly to the corresponding increase in the volume fraction of particles at a given V_r. The effect of the glassy core is also demonstrated by the data for the 3LA and 3LE materials. These materials contain particles with equivalent rubbery layer diameters. However, the core size in the 3LE materials is increased to 244nm. This reduction in the rubber content of the particle allows much higher particle volume fractions to be achieved for a given V_r.

Comparing the data for the 3LA materials with the data for 3LAI materials demonstrates that the level of interfacial graftlinking has little effect on the magnitude of G_{Ic} at a given V_r.

Finally comparison of the data for the 3LA materials with that for the 4L materials demonstrates that the introduction of a 100 nm diameter rubbery core into the glassy core of the 3LA particle also has no significant effect on the fracture resistance.

ACKNOWLEDGEMENTS

The authors express their thanks to the Science and Engineering Research Council and ICI plc for funding this research programme. The assistance of Mike Chisholm and Bill Jung of ICI plc is gratefully acknowledged.

REFERENCES

1. (a) Rohm and Haas Company, Brit. Patent No. 1 340 025 (1973);
   (b) Rohm and Haas Company, Brit. Patent No. 1 414 187 (1975);
   (c) E.I. Du Pont de Nemours and Company, Gt. Brit. Patent Appl. No.2 039 496A (1979)
2. P.A. Lovell, J. McDonald, D.E.J. Saunders and R.J. Young, *Polymer*, **34**, 61 (1993)
3. F.Heatley, P.A. Lovell and J. McDonald, *Eur. Polym. J.*, **29**, 255 (1993)
4. P.A. Lovell, A.J. Ryan, M.N. Sherratt and R.J. Young, Paper 3, Deformation Yield and Fracture of Polymers, Churchill College, Cambridge, 11-14 April 1994.

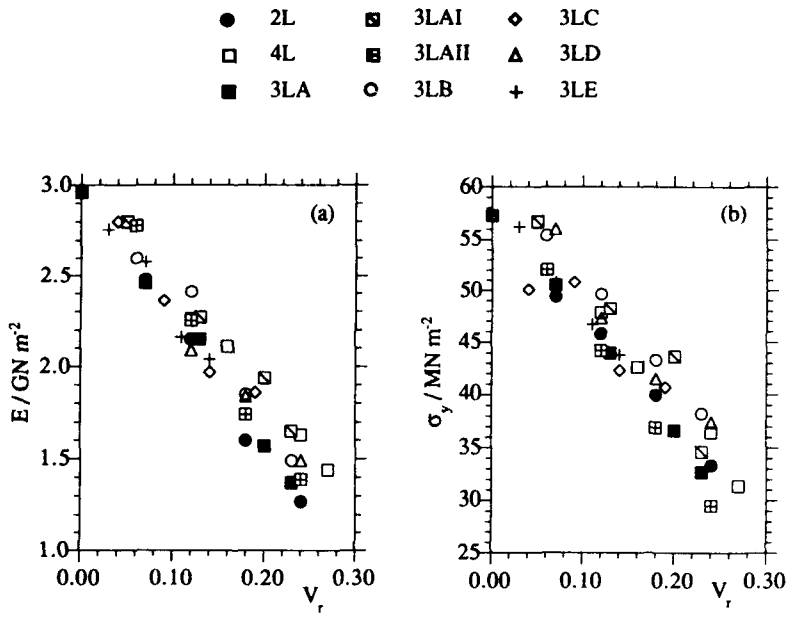

Figure 2. Variation of (a) Youngs modulus and (b) tensile yield stress with rubbery phase volume fraction (V_r) for all RTPMMA materials.

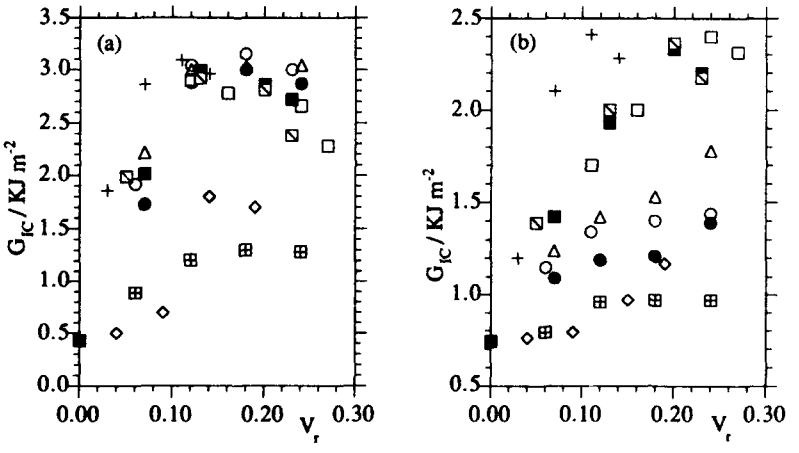

Figure 3. Variation of critical strain energy release rate (G_{Ic}) with rubbery phase volume fraction (V_r) for all RTPMMA materials under (a) low-rate loading and (b) impact loading.

WELDING OF POLYOLEFINE MATERIALS - EVALUATION OF THE OPTIMAL WELDING PARAMETERS AND TEST METHODS

T Christensen*

The weld factor of polyolefine pipes is calculated on the basis of failure times from accelerated creep tests with specimens taken from welded and unwelded materials. The investigation is done on HDPE, MDPE and PP pipe materials, and includes a literature study of test methods and an evaluation of the optimal welding parameters.

INTRODUCTION

This paper is mainly based upon results from Nordic joint projects supported by the Nordic Fund for Technology and Industrial Development, raw material producers and pipe manufacturers. The following items were investigated:

* A literature study on welding parameters and test methods of welded pipes
* Evaluation of the optimal welding parameters of polyolefine pipes
* The influence of the welding parameters on the weld quality
* The reciprocal weldability of different materials

THE PRINCIPLE OF WELDING PIPES

In principle, the butt welding process is a simple one, and can be divided into the following steps, see Figure 1.

I. The pipes are cut straight and the surfaces are carefully cleaned.

II. The pipe ends are heated by a welding mirror. The heating is done in two, steps:
During the first step (1) the pipe ends are pressed against the mirror with a pressure of 0.10-0.18 MPa . The pressure is maintained until the prescribed bead is formed.
In the second step (2), the pressure is reduced to nearly zero, still ensuring that the welding surfaces have full contact with the mirror.

III. After heating (3), the mirror is removed and the melted surfaces are brought together as quickly as possible . The weld is then cooled under pressure (4).

*SINTEF Production Engineering, Trondheim

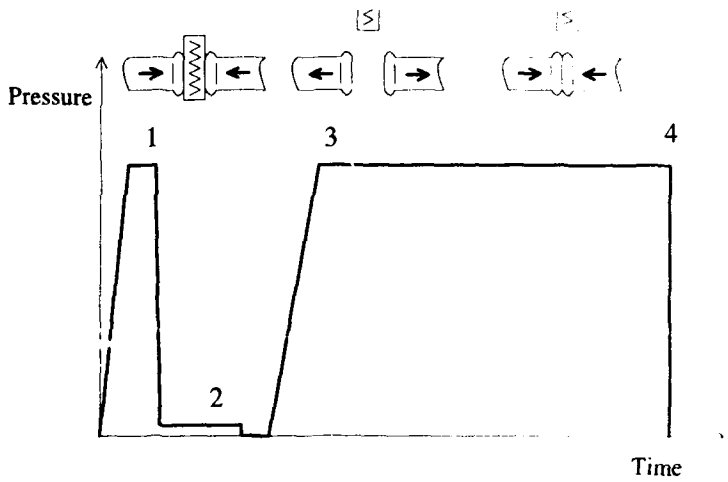

Figure 1 Principal pressure/time course for the welding of pipes

On basis of the results from the nordic joint projects, the welding times are to be calculated by the following fomulas:

Heating time in seconds: 15· wall thickness in mm
Cooling time in minutes: 10 + 0.5· wall thickness in mm

TEST METHODS FOR WELDED PIPES

There are several current test methods for pipe welds; the most common are listed below:

1. Destructive tests, short term	2. Destructive tests, long term	3. Non-destructive tests
a. Internal pressure test	a. Internal pressure test	a. Visual control
b. Tensile test	b. Creep test	b. Ultrasonic test
c. Bending test	c. Penetrating pin test	c. X-ray inspection
d. Impact tensile test		

The short term test methods may only reveal very poor welds. For pressure pipes, the long term behavior is of interest. So far, there is no reliable correlation between the short and long term quality of welds.

The only reliable test method giving a long term welding factor is accelerated creep test (method 2b mentioned above). The tests are done with unwelded and welded bars from the pipe. The long term weld factor is determined according to figure 2. Only brittle failures are taken into consideration.

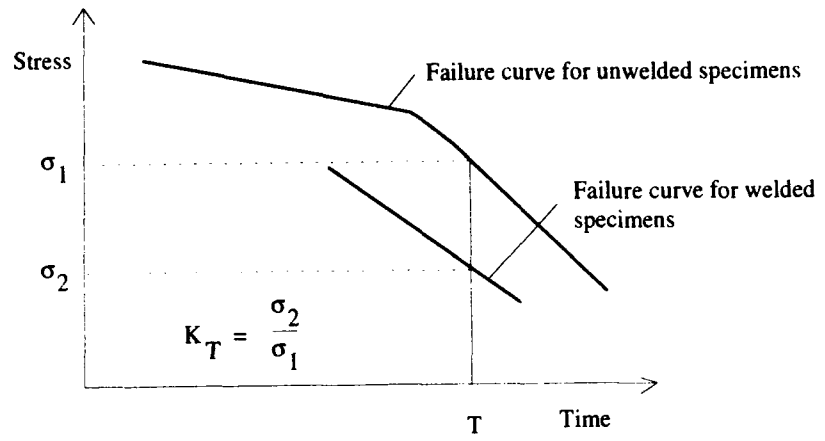

Figure 2 *The principle of calculating the weld factor* K_T

CREEP TESTS

The tests were carried out in water with detergent on six types of welded polyolefine pipes.

The results are shown in figure 3.

Mat.	Temp (° C)	σ (MPa)	Bar type	Time to failure (h)
HDPE80	80	5.4	Welded	
			Unwelded	
HDPE100	80	5.4	Welded	
			Unwelded	
HDPE80/ MDPE	95	3.0	Welded	
			Unwelded	
MDPE	95	3.0	Welded	
			Unwelded	
PP homopol.	95	5.0	Welded	
			Unwelded	
PP copol.	95	4.5	Welded	
			Unwelded	
				10 100 1000 10000

Figure 3 Failure times from creep tests with bars taken from welded and unwelded polylefine pipes.

On basis of these results, HDPE80 gave a weld factor of 0.9. The long term properties for the HDPE100-material is a great deal better than the HDPE80, but only a slight improvement of the weld failure time was observed. The long term factor is about 0.5. The factor for the MDPE-material was about 0.75, corresponding to one decade reduction in the failure time. The welding of PP materials gave a weld factor close to 1.0.

REFERENCES

1 Christensen T, The weldability of polyolefine materials, SINTEF report STF16 F 89013 (1989)

2 Christensen T, Nordisk fellesprosjekt - undersøkelse av sveisbarheten av polyolefinrør, SINTEF report STF20 F89051 (1989)

3 H. Böcker, Rheinberg, und R. Dewitt, Brüssel, 'Hochleistungs-PE gibt mehr Sicherheit bei Rohrleitungen', Kunststoffe 82 (1992)

4 Wolters M, Venema B, Specification of butt welding for pipes and fittings of polyethylene with a density of at least 930 kg/cm^2, VEG Gaasinstituut (1985)

EPOXIES TOUGHENED WITH HOLLOW LATEX PARTICLES

Reza Bagheri and Raymond A. Pearson †

The addition of rubber particles can toughen brittle epoxy polymers through a rubber particle cavitation and concomitant shear banding mechanism. It is hypothesized that pre-cavitated particles should be able to play similar scenario. Indeed, preliminary finding by Huang and Kinloch suggests that microvoids produced by unreactive liquid rubber can be used to toughen epoxy polymers. Our investigation examines the use of hollow latex particles to toughen epoxies. Surprisingly, it is shown that small hollow plastic spheres are equally as effective as conventional rubber tougheners!

INTRODUCTION

Rubber modification, i.e. addition of a rubbery particulate phase to a glassy polymer, has been found a very successful approach to overcome the inherent brittleness of many epoxy resins. The origin of this improvement in crack growth resistance is believed to be cavitation of rubber particles and concomitant shear deformation of the matrix [1-4]. It is agreed that the major contribution in toughening is due to the plastic deformation of the matrix. Controversy, however, exists on the role of particle cavitation in toughening. Some researchers treat rubber particle cavitation as a pre-cursor to massive shear banding in the epoxy since it may relieve the plane strain constraint from the matrix [2,3]. Some other researchers, however, believe that rubber particles contribute in shear yielding of the matrix through concentrating stress in the surrounding matrix and that cavitation is not required and may even be detrimental [4,5].

This controversy has yielded some interests in studying the concept of hole toughening, since rubber particles and holes may play very similar function(s). Fukui et al. [6] conducted an elastic-plastic analysis using a two dimensional finite element model with five rubber/hole inclusions. This study showed that rubber particles provide a more favorable situation for toughening than voids, since the latter causes cracking at lower strain levels. Huang and Kinloch [7] created holes in an epoxy using unreactive liquid rubber. This technique improved the fracture toughness of their neat resin significantly and showed a great potential for voids to toughen brittle polymers. Despite having no rubber modifier to compare with the holes in that particular matrix, Huang and Kinloch [7] predicted higher fracture toughness for a rubber modified epoxy due to the bridging efficiency of rubber particles. More recently, Huang et al. [8] studied the influence of adhesion at the rubber particle/matrix interface using liquid rubbers with different degree of reactivity. No conclusive comparison between strongly and poorly adhered rubber particles was made in that study since the volume fraction and size of the precipitated phases varied in different cases; a common problem in using liquid rubbers.

† *Department of Materials science and Engineering, Lehigh University*

An alternative approach to elucidate the concept of hole toughening in a systematic fashion based on using hollow latex particles is selected in this study. These particles act as pre-cavitated rubber particles and have the benefit of controlled size comparable with that of the conventional rubber modifiers. Understanding the mechanism of toughening in epoxy polymers modified with hollow plastic micro-spheres should provide further insight about the role cavitation in rubber toughened epoxies.

EXPERIMENTAL PROCEDURE

The system selected for this study is based on a diglycidyl ether of bisphenol A (DGEBA) epoxy with an epoxy equivalent weight of 187 g/mol. The curing agent used is aminoethyl piperazine (AEP). Stoichiometric ratio of curing agent was mixed with resin at room temperature and poured into an aluminum mold. The cast material was allowed to gel for one hour at room temperature and then post-cured for two hours at 100°C. Toughening agents used are listed in Table I.

The cured materials were characterized using a variety of techniques. Glass transition temperatures of cured materials were determined using a DSC unit at a heating rate of 10°C/min. The ASTM D5045 guideline was followed to measure the plane strain fracture toughness in this study. Fracture toughness values were determined using pre-cracked, single edge notched (SEN) specimens in three point bending (3PB) geometry. Fracture surfaces were examined using a scanning electron microscope. The double-notched four-point bend method in conjunction with transmission optical microscopy [2] was employed to study the crack tip damage zone of modified materials.

RESULTS

The DSC analyses revealed glass transition temperatures of 105±1°C for all modified and unmodified materials indicating no change in the chemical structure of the epoxy matrix via rubber/void modification. As shown in Table II, the results of the fracture toughness evaluations showed a significant increase in the crack growth resistance of the neat epoxy by incorporation of either rubber particles or voids. SEM micrographs of the fracture surfaces taken from the stress whitened zone of the modified epoxies showed uniformly distributed second phase particles and very similar features in all modified materials. Fracture surfaces of epoxies modified with 10 vol% CTBN and small hollow particles (HLP-62) are shown in Figure 1. Transmission optical microscopy (TOM) of thin sections of double-notched four-point bend specimens revealed massive shear banding at the crack tips of modified materials. Figure 2 represents the TOM micrographs of the crack tip damage zone in the epoxies modified with 10 vol% of CTBN and HLP-62 under crossed polars.

DISCUSSION

Observation of shear bands at the crack tip damage zone of both rubber and hole-modified materials indicate a similar toughening mechanism operating in both systems. Similarly, fracture toughness values shown in Table II indicate no essential difference between a rubber particle and a hole in inducing shear deformation in the epoxy matrix. In the other words, microvoids toughen the present matrix in the same way and almost the same magnitude that rubber modifiers do. Modest differences observed among the fracture toughness data can be attributed to the particle size effect. Although modifiers used are nearly the same size, the smaller particles are capable to induce higher fracture toughness at a given volume fraction. An exception is found when 10 vol% of HLP-62 is employed. This material is about 7% tougher than the material modified with MBS rubber particles.

Results of this study refute the idea of Huang and Kinloch [7] in bridging efficiency of rubber particles as an additional toughening mechanism compare to that of voids. These results

also disagree with the hypothesis of Pearson and Yee [2] in superiority of high cavitation resistance rubber particles. These researchers claimed that later cavitation, due to higher cavitation resistance, results in build up of a larger elastic energy prior to shear yielding of the matrix which accelerates shear band propagation and induces higher fracture toughness. Based on this hypothesis MBS latex particles with the highest cavitation resistance should yield the maximum toughness followed by CTBN particles and microvoids, respectively. Results of this study, however, indicate that the cavitation resistance of rubbery phase has no value in determining the fracture toughness of the blend. It should be also noted that both rubber modifiers used in this study cavitated at the crack tip; other wise different results might have been observed. Also the epoxy polymer used in this study is not the piperidine cured epoxy studied by many researchers. The importance of cavitation resistance may indeed be matrix dependent.

CONCLUSIONS

Based on the preliminary results, the conclusions are:

1) Hollow plastic micro-spheres can toughen brittle epoxies in the same manner that rubber particles do.

2) Within the concentration range examined, no superiority of rubber particles than that of the voids was found.

3) Cavitation resistance of rubber particles has no value in determining the fracture toughness of the rubber modified blend.

ACKNOWLEDGEMENTS

Financial support of the Polymer Interfaces Center at Lehigh University is greatly appreciated.

REFERENCES

1. C. B. Bucknall, P. S. Heather, and A. Lazzeri, J. Mater. Sci., 16, (1989) 2255.
2. R. A. Pearson and A. F. Yee, J. Mater. Sci., 26, (1991) 3828.
3. A. F. Yee, D. Li, and X. Li, J. Mater. Sci., 28, (1993) 6392.
4. Y. Huang and A. J. Kinloch, J. Mater. Sci. Lett., 11, (1992) 484.
5. F. J. Guild and R. J. Young, J. Mater. Sci., 24, (1989) 2454.
6. T. Fukui, Y. Kikuchi, and T. Inoue, Polymer, 32, (1991) 2367.
7. Y. Huang and A. J. Kinloch, Polymer, 33, (1992) 1330.
8. Y. Huang, A. J. Kinloch, R. Bertsch, and A. R. Siebert, in Advances in Chemistry Series, 233, C. K. Riew and A. J. Kinloch (Eds), ACS, Washington, (1993) 189.

TABLE I. Description of the Toughening Agents used

Modifier	Description of Modifier
CTBN Rubber	Carboxyl terminated liquid copolymer of butadiene and acrylonitrile (AN=18%) from BF Goodrich [Hycar CTBN 1300X8].
MBS Rubber	Structured core/shell latex particles comprised of a methacrylated butadiene-styrene copolymer with acid functionality from Rohm & Haas Co [Paraloid EXL-2611].
HLP-62	Hollow latex particles with a styrene-acrylic shell from Rohm & Haas Co [Ropaque OP-62].
HLP-91	Similar to HLP-62 but larger in size [Ropaque HP-91].

TABLE II. Fracture Toughness of Neat and Modified Epoxy Blends

No.	Modifier	Particle Size† (μm)	Volume Fraction of Modifier‡ (%)	Fracture Toughness ($MPa.m^{0.5}$)
1	None	None	None	0.85
2	CTBN	0.6	10	2.05
3	MBS	0.2	10	2.15
4	HLP-62	0.4	10	2.30
5	HLP-91	1.0	10	1.95
6	CTBN	0.75	15	2.00
7	MBS	0.2	15	2.20
8	HLP-62	0.4	15	2.05

† Particle size for solid modifiers are reported based on the producers catalogues. Particle size of CTBN modified materials were measured using SEM micrographs taken from the fast fracture region.
‡ Volume fraction in case of CTBN is actually the weight percent of rubber per hundred resin.

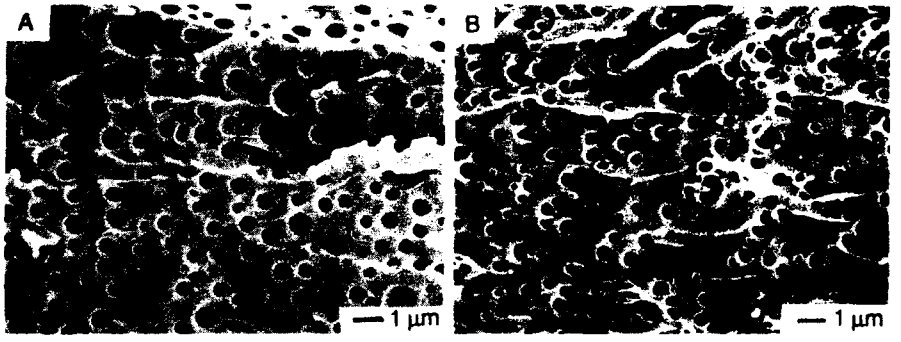

FIGURE 1. SEM micrographs of the fracture surface of epoxies modified with 10 vol% of (a) CTBN and (b) HLP-62 particles.

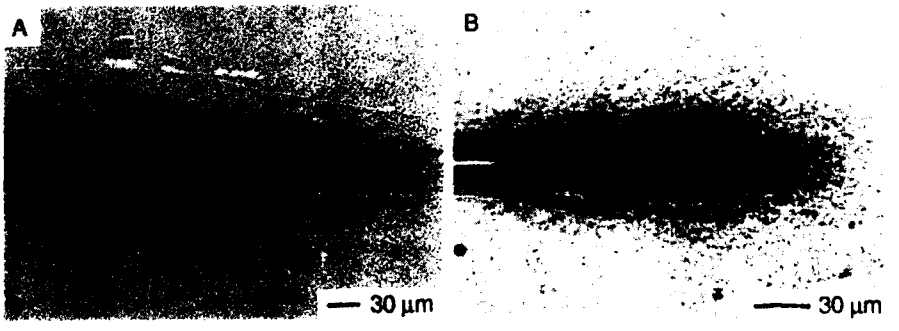

Figure 2. TOM micrographs of the crack tip damage zone of the same materials as Figure 1 taken in the mid-plane of double-notched four-point bend specimens.

SHEAR STRENGTH OF GLASSY POLYMERS, DEDUCED FROM THEIR THERMAL PROPERTIES

Michael Fischer *

Shear strength of glassy polymers at various temperatures can be estimated from (c_p-c_v), the difference of the heat capacity at constant pressure and at constant volume. (c_p-c_v) is accessible by purely thermodynamic arguments if the thermal expansivity and two elastic moduli of the polymer are known in the relevant temperature range. An example is presented using results on the adhesive Araldite AV 3131.

1. BACKGROUND

Shear yielding of polymers is a familiar subject in literature and textbooks [1,2]. Usually, yielding is treated either phenomenologically in classical failure criteria or in molecular models along the lines of Eyring viscosity theory [3,4,5].

A different and novel approach to shear yielding is based on the internal energy of the glassy polymer. The internal energy depends on details of the molecular structure as well as on intermolecular forces. Therefore, the shear strength of glassy polymers is linked to the internal energy.

2. ENERGY BALANCE

Polymers exhibit almost no shear strength at temperatures above the glass transition ($T > Tg$), since they behave like melts. However, as the polymer passes through the glass transition during the cooling process, the molecular chains approach each other. At temperatures below the glass transition ($T < Tg$), the chains are still randomly orientated in space but they are packed tightly. They are frozen up.

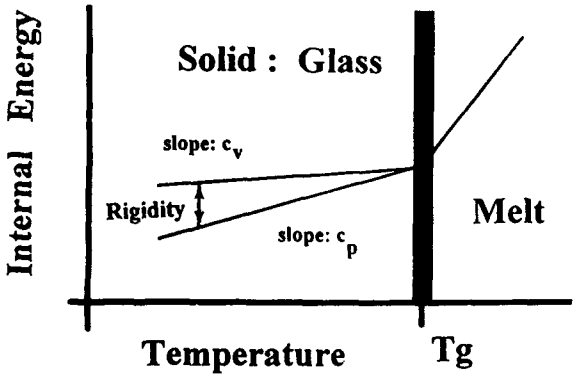

Figure 1:
Origin of rigidity: Internal energy is plotted schematically against temperature

* Materials Research, Ciba-Geigy SA , CH-1723 Marly, Switzerland

During the cooling, the polymer shrinks and gains rigidity. Simultaneously, its internal energy U is reduced as indicated schematically in Fig. 1. If, hypothetically, the polymer were cooled at constant volume V (Fig. 1, upper branch) instead of constant pressure p (Fig. 1, lower branch), the molecules would keep their volume and they would not close up to each other. On these conditions, the polymer could not gain strength at temperatures below Tg, as it actually does.

Apparently, the difference ΔU of internal energy between the two states is responsible for the solidification of the polymer (the difference is represented by the arrow in Fig. 1).

$$\Delta U_{(T)} = \int_{\vartheta=T}^{\vartheta=T_g} (c_p - c_v)\, d\vartheta \qquad (1)$$

If the polymer is loaded by the shear stress σ, the stored energy amounts approximately to

$$W = V \frac{\sigma^2}{2G} \qquad (2)$$

V : volume σ : shear stress G : shear modulus

Yielding of the polymer will take place if the energy W stored in the polymer equals the energy required to overcome the molecular forces that solidify the polymer

$$W \geq \Delta U \qquad (3)$$

Combining the three equations yields the shear strength σ_y

$$\sigma_{y(T)} = \sqrt{\frac{2G}{V} \int_T^{T_g} (c_p - c_v)\, d\vartheta} \qquad (4)$$

The difference in heat capacities (c_p-c_V) can be evaluated by purely thermodynamic arguments [6].

$$c_p - c_v = \frac{9\alpha^2 V T}{\beta} \qquad (5)$$

V : volume α : thermal expansivity (linear)
T : temperature β : isothermal compressibility

Measured quantities such as the Young's modulus E and the Poisson's ratio μ are introduced [7].

$$\beta = \frac{3(1-2\mu)}{E} \qquad (6) \qquad G = \frac{E}{2(1+\mu)} \qquad (7)$$

Putting together the equations (4,5,6,7) yields the shear strength ($V \approx V_{(T)}$)

$$\sigma_{y(T)} = \left[\frac{3E}{1+\mu} \int_T^{T_g} \frac{\alpha^2 E\, \vartheta}{1-2\mu}\, d\vartheta \right]^{1/2} \qquad (8)$$

3. EXAMPLE

The shear strength of the adhesive Araldite AV 3131 was determined by torsion tests [3] on joints of aluminium parts in the temperature range between -196°C and 160°C. The shear strength of torsion tests equals the yield strength of the adhesive according to our experience, if the bonded surfaces have been well treated.

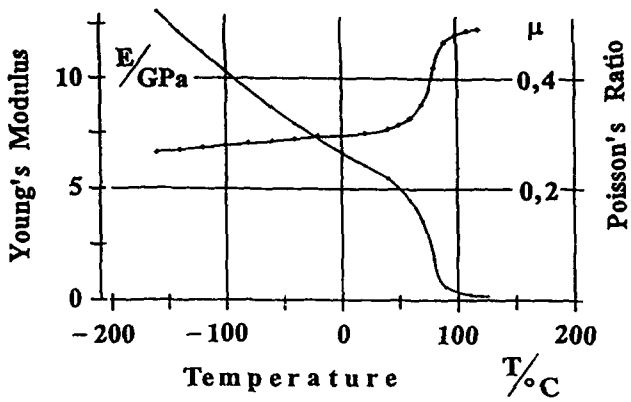

Figure 2:
Young's modulus E and Poisson's ratio μ of a bulk sample of Araldite AV 3131 are plotted against temperature (tensile tests with strain gauges, strain rate $10^{-4}\,s^{-1}$)

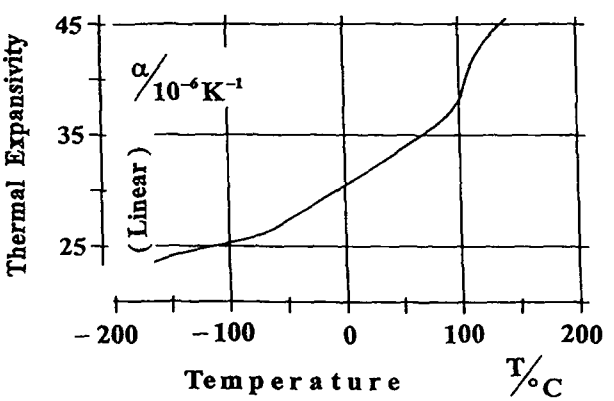

Figure 3:
Linear thermal expansivity (averaged) of a bulk sample of Araldite AV 3131 against temperature (DIN 53762)

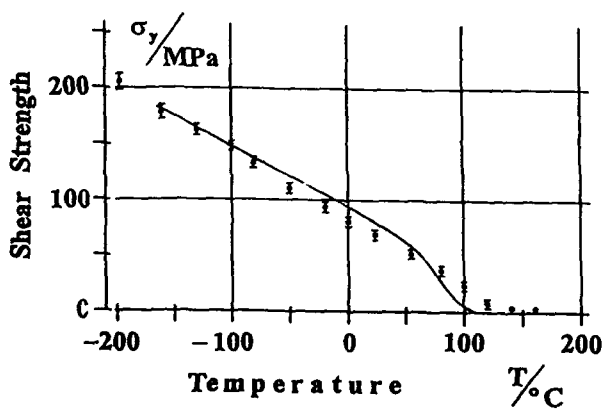

Figure 4:
Comparison between experiment and calculation in the temperature range -196°C to 160°C
Solid line: shear strength calculated according to equ. (8)
Symbol: average of five results (± s) of shear tests on aluminium joints bonded with Araldite AV 3131

Tensile tests on bulk polymer (4mm x 15mm x 150mm) provided Young's modulus E and Poisson's ratio μ. Strain was measured by means of two times two strain gauges bonded to both sides of the test piece. The results on E and μ are presented in Fig. 2. Results on thermal expansivity are shown in Fig. 3.

The solid curve in Fig. 4, representing shear strength against temperature, was calculated by inserting the data of Fig. 2 and Fig. 3 into equ. (8) (Tg = 110°C). The averaged results of five torsion tests are presented in the same figure in order to facilitate the comparison. The agreement between the shear strength values derived from experiments and from calculation is quite remarkable, particularly, as no adjustable parameters are involved.

4. REFINED DISCUSSION

- Non-linearity

Diagrams of shear stress against shear strain deviate frequently from linearity. Proportionality between stress and strain was assumed in equ. (2) for the sake of simplicity. Shear yielding requires therefore often more energy than calculated according to equ. (2). Equ. (4) should be corrected for this additional energy. The amendment will further improve the agreement of calculated and experimental shear strength values.

- Rate effects

Shear strength depends on testing rate to some extend. However, rate effects cannot be dealt within the frame of thermodynamics.

5. CONCLUSION

Shear strength of glassy polymers can be deduced from thermodynamic arguments if the thermal expansivity and the elastic behaviour (E, μ) are known in the relevant temperature range. No parameters are adjustable.

Correction for non-linear stress strain diagrams will further improve the agreement between experiments and calculations.

6. REFERENCES

[1] H.-H. Kausch, "Polymer Fracture" 2nd ed., Springer-Verlag, Berlin, Heidelberg, New York, 1987, p. 58 and p. 268

[2] I.M. Ward, "Mechanical Properties of Solid Polymers" 2nd ed., John Wiley & Sons, Chichester, New York, 1983, p. 337 and p. 377

[3] M. Fischer, F. Lohse, R. Schmid, Makromol. Chem. **181** (1980) 1251

[4] X.X. Zhu, G.R. Zhu, Polymer **33** (1992) 4968

[5] M.B.M. Mangion, J.Y. Cavaillé, J. Perez, Philos. Mag. A. **66** (1992) 773

[6] W.J. Moore, "Physical Chemistry", Longman, London, 1972, p. 103

[7] see [2] p. 25

The valuable support of Mr. Denis Martin for the mechanical tests is gratefully acknowledged.

CRACK INITIATION BEHAVIOUR OF POLYMERS

S Seidler and W Grellmann *

The paper demonstrates that there are differences in crack tip behaviour after blunting between amorphous and semi-crystalline thermoplastics. On example of ABS and a PC/ABS blend can be shown that initiation in amorphous polymers starts with the translation of the entire crack front. In semi-crystalline polymers (for example PP) the blunting process occurs without translation of the crack tip and the initiation starts with the opening of the crack tip. It is the same process like metals show. The blunting process is quantified and a physical crack initiation value and a physical blunting line are determined. These results are compared with the ASTM standard and a testing protocol of the ESIS TC4 group.

INTRODUCTION

The toughness of a material sets limits both on design and safety of engineering components and structures. Therefore, the questions of a criterion for toughness in fracture of polymer solids have been extensively investigated from both scientific and practical viewpoints.
The toughness characterization of polymers is generally accomplished by means of conventional impact tests (Charpy or Izod). Therefore the instrumented Charpy impact test was used as a testing method.

EXPERIMENTAL

ABS (acrylonitrile-butadiene-styrene) and PP (polypropylene) were chosen for this study. The specimens were produced by injection moulding. The dimensions of the single edge notched three point bend specimens were: length L = 80 mm, width W = 10 mm and thickness B = 4 mm. The specimens were notched with a razor blade. The notch depth, a, was 4.5 mm and the notch tip radius was 0.2 μm. For the toughness measurements, a Charpy impact tester with 4 J work capacity was used and load(F)-deflection(f) diagrams were recorded. The experimental conditions were:

pendulum hammer speed $v_H = 1.5\ ms^{-1}$ and
support span $s = 40\ mm$, i.e. $s/W = 4$.

The multiple specimen stop-block technique was used for R-curve determination. Stable crack growth, Δa, was quantified on the fracture surface by light microscopy. The fracture

* Department of Materials Science, Martin-Luther-University Halle-Wittenberg, Germany

surfaces were produced by breaking the specimens at liquid nitrogene temperature and high pendulum hammer speed. The value of J for each specimen was determined from the area under its F-f curve (Eq. 1) [1,2].

$$J = \eta_{el} \frac{A_{el}}{B\,(W-a)} + \eta_{pl} \frac{A_{pl}}{B\,(W-a)} \left\{ 1 - \frac{(0{,}75\ \eta_{el} - 1)\ \Delta a}{(W-a)} \right\} \qquad (1)$$

with

$\eta_{e,p}$ geometry functions

$A_{e,p}$ elastic/plastic part of total deformation energy up to maximum impact load

This equation includes a crack length correction. So the restriction of Δa, which is contained in the standards and drafts [1-3] for the determination of valid J-integral values will be irrelevant [4].

The SEM observations were done with the scanning electron microscop Tesla BS 343 with integrated loading device. This apparatus enables in-situ experiments with the same specimen geometry as described above.

RESULTS

The fracture behaviour of materials with high toughness properties is characterized by dominant stable crack growth. In this case toughness characterization has to be done by crack resistance curves (J or δ versus Δa curves). This curves include the processes crack tip blunting and crack growth.

A description of J-crack growth resistance curve tests on plastics is possible using a testing protocol from the ESIS TC 4 group [2]. These are the only testing instructions for polymer materials. But, small Δa values ($\Delta a < 0{,}05$ mm) and crack tip blunting processes are not considered in this procedure. This is due to many reasons, for example:

- small amounts of crack growth are difficult to measure and they are subject to error
- crack tip blunting processes are not clear.

It is well established that before the initiation of crack propagation the initially sharp crack tip is more or less blunted depending not only on the properties of the material and the geometry of the specimen, but also on the mode of loading of the precracked plate.

Under conditions of plane strain for metals the crack initiation process is quite clear. The crack growth processes in metals and polymers are presented schematical in [5].

Compared to the metals, the only difference is in the location of crack advance. In the initial stages of crack growth, the starter cracks in metals, amorphous and semi-crystalline polymers blunt and than resharpen. However, the blunting in the semi-crystalline polymers occurs without translation. For metals and semi-crystalline polymers, crack advance occurs from the thin resharpened point of the blunt crack [6,7].

For amorphous polymers, the entire resharpened crack front appears to translate [8].

First in-situ SEM observations agree with this model (see Fig. 1 and 2).

The blunting process is a plastic deformation process on crack tip and the result of this plastic deformation is the stretch zone which is evident on fracture surface. The stretch zone has two dimensions: in crack growth direction the stretch zone width (SZW) and perpendicular to this the stretch zone hight (SZH). If the crack growth mechanism occurs like described the stretch zone must be evident at the end of the starter crack for semi-crystalline

polymers and at the end of stable crack growth for amorphous polymers.
The quantification of the stretch zone can be used to determine a physical crack initiation value if there are data points in the blunting range and it can be used to determine a physical (experimental) blunting line. Fig. 3 shows the comparison of the blunting line using ASTM 813 [3] and the experimental blunting line and their influence on the $J_{0.2}$ value of ABS.

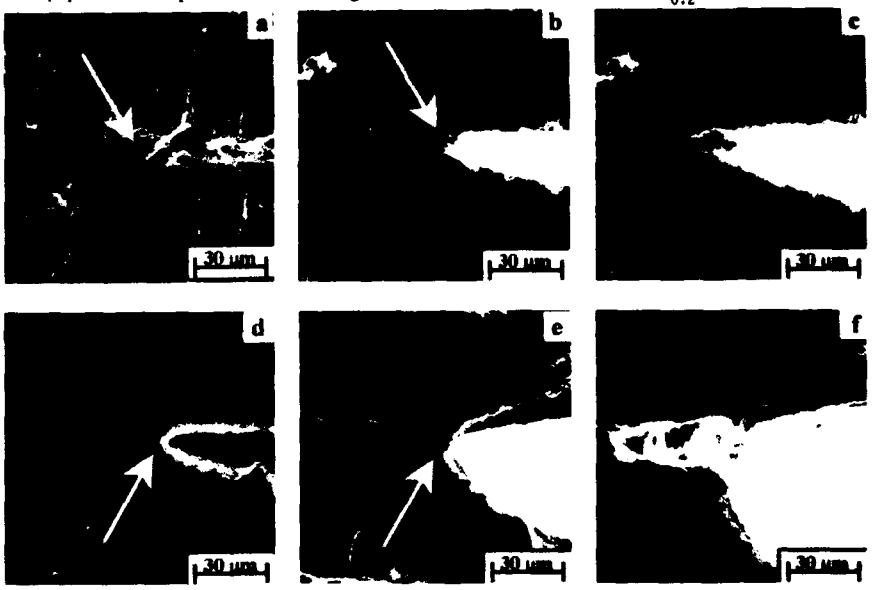

Fig. 1: In-situ SEM-observations of ABS (a-c) and PP (d-f); a,d unloaded crack tip; b,e blunted crack tip before initiation; c,f crack tip after initiation

Fig. 2: Crack front of a PC/ ABS blend after initiation

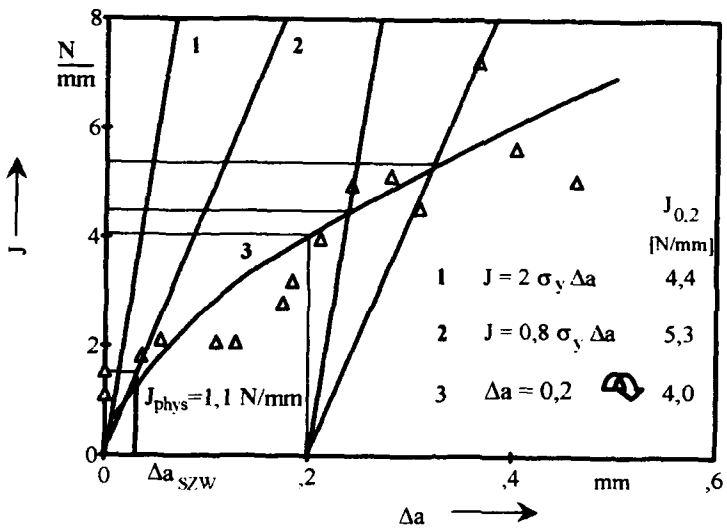

Fig. 3: Physical crack initiation value, J_{phys}, and determination of technical crack initiation values, $J_{0,2}$

The stretch zone width of this material is SZW = 30 μm.
From Fig. 3 is evident, that

1. A physical crack initiation value is very small in comparison to the technical values. Under the aspect of stretch zone dimensions of < 50 μm in 1 m/s tests the determination of a technical crack initiation value at Δa = 0.2 mm and more if a blunting line is used must be revised.
2. The ASTM blunting line does not represent the blunting process in the ABS material.
3. The ESIS TC4 determination of $J_{0,2}$ is a conservative estimation criteria. In practice it is very useful because the quantification of the stretch zone is very expend in doing and subject to error.

REFERENCES

[1] ESIS Procedure P2-91, EGF Recommendations for Determining the Fracture Resistance of Ductile Materials
[2] ESIS TC4-91, A Testing Protocol for Conducting J-Crack Growth resistance Curve Tests on Plastics
[3] ASTM 813-89, Philadelphia, PA, 1989
[4] Zerbst U and Will P, Neue Hütte 33 (1988) 7, 269
[5] Seidler S and Grellmann W, Proc Europ Symp Impact and Dynamic Fracture of Polymers and Composites, Porto Cervo, Italy, 1993
[6] Garwood S J and Turner C E, Int J of Fracture 14 (1978) R 195
[7] Narisawa I and Takemori M T, Polym Eng Sci 29 (1989) 671
[8] Huang D D, Proc 8th Intern Conf on Deformation, Yield and Fracture of Polymers, Cambridge, 1991

FATIGUE LIFE ESTIMATION OF A POLYMER MATRIX COMPOSITE HIP JOINT PROSTHESIS

M AKAY and N ASLAN*

A fracture mechanics approach is applied to estimate the life of a prosthesis made from thirty percent short carbon fibre reinforced PEEK composite. Fracture toughness, fatigue crack growth rate and threshold stress intensity factor were determined by using single-edge notched bars in bending and the data was used to estimate fatigue life of the prosthesis. An elliptical slit crack was assumed to exist within the prosthesis. It was shown by fracture mechanics approach that a fatigue failure due to crack propagation would be unlikely for a crack length smaller than 2.7 mm.

INTRODUCTION

The long term complications of loosening and calcar resorption of total hip joint replacement confine the application to elderly people, although many young people also suffer from it. The bone resorption is believed to occur because of the stress shielding of the bone by the stiff metallic implants. Bone, as a living material, adapts itself to this reduced stress distribution by bone resorption (1). The use of less stiff materials with elastic moduli close to that of the bone would restore bone stresses up to normal levels and prevent the bone resorption. Thirty percent carbon fibre reinforced PEEK (CF/PEEK) with a modulus of elasticity between 13 and 20 GPa, depending on its microstructure, offers an elastic modulus which is comparable to that of bone (~17 GPa). CF/PEEK also has excellent chemical resistance and is biocompatible (2).

CF/PEEK is a difficult material to process by injection moulding in thick cross-sections. The differential solidification of the melt in the mould can cause voids in the core of the component which weakens the mechanical properties. The hip joint implant is continuously subjected to repetitive external cyclic loading during daily activities. Therefore, presence of voids in the component will be very detrimental in terms of fatigue life. Fatigue in terms of ordinary S-N curve can overestimate the life of the component, since it accounts for both the initiation and propagation of cracks. Therefore, fracture mechanics approach which considers the presence of defects and cracks in the component would be a safer procedure to estimate the life of the implant.

*Mechanical and Industrial Engineering Dept, Univeristy of Ulster at Jordanstan, Co. Antrim, UK.

The purpose of this paper is to determine the fracture properties of the composite and apply the data in the fatigue life estimation of the implant under loading conditions simulating daily activities.

MATERIALS AND METHODS

CF/PEEK (ICI grade 450CA30) test specimens in the form of flat bars of 6.4x13x130 mm^3 were produced by injection moulding. The dimensions were chosen so that it matched the dimensions of the prosthesis. Specimens had two distinct regions of fibre orientation: the outer shear zone where the fibres are oriented predominantly longitudinal to the mould fill direction and the core where the fibres are randomly oriented.

Fracture toughness (K_{Ic}) tests were conducted at room temperature according to ASTM 399 and the recommendation of the European Group on Fracture (3). Single edge notched bending (SENB) specimens were loaded in three point bending mode with a support span of 52 mm. The notches were initially machined to a length of 6 mm and then sharpened by tapping a razor blade producing an overall crack length of approximately 6.5 mm ($0.45 \leq a/W \leq 0.55$). The load vs. COD curves were obtained at a loading speed of 10 mm/min. The intersection of the 5% secant line with the curves was designated as the conditional load, P_Q. The ratios of P_{max}/P_Q and minimum thickness requirement ($B \geq 2.5(K_Q/\sigma_{ys})^2$) were in accordance with ASTM recommendation.

Fatigue crack propagation tests, to determine the crack growth rate (da/dN) and threshold stress intensity factor (K_{th}), were also performed by using SENB specimens. Specimens with a notch length of approximately 3.2 mm were prepared same as fracture toughness test specimens. Notches were further fatigue precracked to a length of approximately 4.5 mm. Two specimens (A and B) were tested according to K-increasing procedure to obtain the crack growth rate and another specimen (C) was initially tested according to K-decreasing method to determine K_{th} and further tested under K-increasing conditions to obtain a crack growth rate for comparison with the other specimens. The crack lengths were computed from the compliance values using COD and also measured with a travelling microscope. Tests were performed on an Instron 8502 servo hydraulic testing machine and controlled with a personnel computer running the Instron software of 'Advance Fatigue Crack Propagation'. The frequency of the test was 1 Hz simulating normal walking speed and load ratio was 0.1.

RESULTS

In accordance with ASTM standard, the ratio of P_{max}/P_Q was less than 1.10 and specimen thickness (6.4 mm) was greater than the minimum required thickness of 2.5 mm. The fracture toughness was found to be 8.6±0.2 $MPa.m^{1/2}$. This value is comparable with the published data. Friedrich et al. (4) have reported a fracture toughness value of 6.9 $MPa.m^{1/2}$ and Pao et al. (5) a value of 8.9 $MPa.m^{1/2}$. The discrepancy can be attributed to the microstructural differences of fibre orientation and fibre length distribution (6) and crystallinity (7).

Fatigue crack growth curves obtained from three specimens are presented in Figure 1 and the constants of the Paris equations are presented in Table 1. Although specimens A and B produced close results, specimen C resulted in a smaller slope. The reason for this discrepancy was that the regions where crack growth data were obtained for specimens A and B were

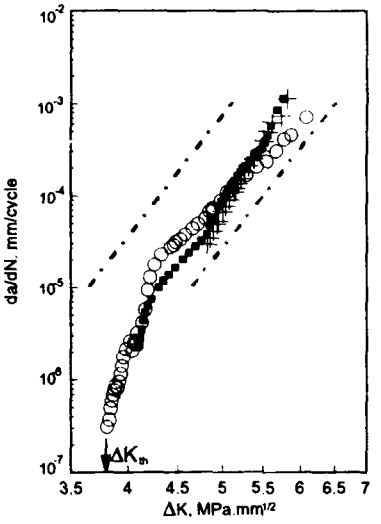

Figure 1 Fatigue crack growth curve of 30% short carbon fibre reinforced PEEK for specimens A (■), B (+) and C (○). Upper and lower limits reported by Friedrich et al. [4] (· · · ·).

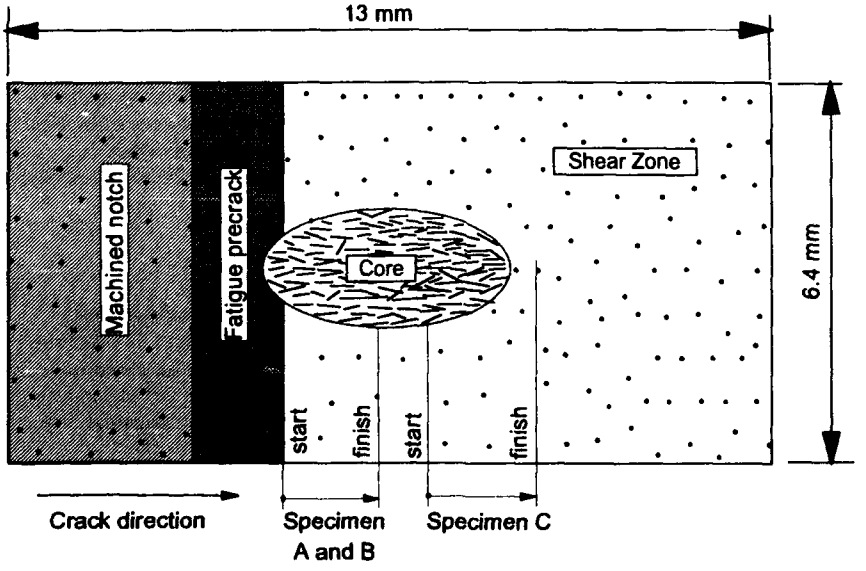

Figure 2 Fibre orientation distribution across the specimen and the regions of fatigue testing for different specimens

different than that for specimen C (Figure 2). Specimens A and B were tested in a region which contained both shear zone and core whereas specimen C was tested starting in a region containing both shear zone and core, but ended in a region which contained only the shear zone. It is a well known fact that crack grows faster along the fibre direction than perpendicular to it. Therefore, the crack growth in specimen C was faster initially and slowed down when it reached the shear zone.

Table 1. Constants of Paris equation ($da/dN = C\Delta K^m$)

	m	C
Specimen A	18.9	$3.7X10^{-21}$
Specimen B	15.7	$9.1X10^{-19}$
Specimen C	10.9	$2.0X10^{-15}$
Friedrich et al. [4]	13.4	-

The threshold stress intensity factor range, ΔK_{th}, was determined to be approximately 3.8 MPa.$m^{1/2}$ at a growth rate of 10^{-7} mm/cycle.

FATIGUE LIFE ESTIMATION

A three-dimensional finite element analysis was employed to calculate the stress distribution on the prosthesis (8). Accordingly, a load of 3 kN at angle of 20° to the shaft of the femur produced a maximum tensile stress, σ_{max}, of 83 MPa at the spigot of the prosthesis and normal to the cross-section.

The average size of the voids measured in the prosthesis were approximately 1 mm. In a dynamic application like hip joint replacement, K_{th} is an important design parameter. Therefore, in order to ensure that the prosthesis will not fail due to crack growth, the stress intensity factor must be smaller than K_{th}.

An elliptical slit crack, embedded in a three dimensional body was considered to simulate a void in the prosthesis subjected to uniform tensile stress. The stress intensity factor at any location in the crack boundary (defined by the angle φ) is given as (9):

$$K_I = \frac{\sigma\sqrt{\pi a}}{\frac{3\pi}{8} + \frac{\pi a^2}{8c^2}}\left(\sin^2\varphi + \frac{a^2}{c^2}\cos^2\varphi\right)^{1/4} \quad (1)$$

K_I becomes maximum when the crack is elliptical and the angle φ is 90°. Therefore, for a/c of 1/2, the maximum stress intensity factor is:

$$K_I = 0.784\sigma\sqrt{\pi a} \quad (2)$$

Rearranging Equation (2) and expressing it in terms of threshold stress intensity range gives:

$$a = \frac{1}{\pi}\left(\frac{\Delta K_{th}}{0.784\Delta\sigma}\right)^2 \qquad (3)$$

Substituting into Equation (3) ΔK_{th} 3.8 MPa.m$^{1/2}$ and the stress range corresponding to the maximum tensile stress predicted in the prosthesis (i.e. $\Delta\sigma$=74.7 MPa) produces a threshold crack length of 2.7 mm. Therefore, under these fatigue conditions, the growth of sharp voids of 1 mm dimension is very unlikely.

REFERENCES

1 Oh I and Harris WH, J. Bone and Joint Surg. 60-A, (1978) 75.

2 Williams DF, McNamara A. and Turner RM, J. Mat. Sci. Let. 6 (1987) 188.

3 Williams JG and Cawood, Polymer Testing 9 (1990) 15.

4 Friedrich K, Walter R, Voss H and Karger-Kocsis J, Composites 17 (1986) 205.

5 Pao PS, O'Neal JE and Wolf CF, Polym. Mat. Sci. Eng. 53 (1985) 677.

6 Karger-Kocsis J, in: Friedrich K (ed), Application of Fracture Mechanics to Composite Materials, (1989) 189.

7 Saib KS, Evans WJ and Isaac DH, Polymer 34 (1993) 3198.

8 Aslan N, PhD. Thesis, Polymeric Composite Hip Joint Prosthesis, University of Ulster, UK, 1994.

9 Ewalds HL and Wanhill RJH, Fracture Mechanics, Edward Arnold Pty Ltd. 1986.

EFFECTS OF MEAN STRESS ON FATIGUE CRACK PROPAGATION IN EPOXY ADHESIVE

H. Y. Ahmad* and L. Edwards*

The effects of the stress intensity factor range ΔK and the load ratio, R on fatigue crack propagation in a rubber toughened epoxy has been investigated. Direct crack observation and subsequent fractography showed that crack branching was prevalent when the crack encountered filler particles. Under these circumstances, unstable or "Stick-Slip" crack propagation where the crack divides into separate branches one or more of which is arrested before one of the branches continues to propagate at a retarded rate was observed.

INTRODUCTION

A number of studies have been conducted to evaluate the effect of mean stress on the rate of Fatigue Crack Propagation (FCP) in Epoxy adhesives at different ΔK levels and load ratio ($R = \frac{K_{min}}{K_{max}}$). Manson *et al* (1) reported that the crack growth rate in polycarbonate decreased with increasing mean stress level when the fatigue data correlated well if the $2\Delta K\ K_{mean}$ parameter proposed by Arad *et al* (2) was used. On the other hand, Mai et al (3) suggested that such fatigue data were better correlated by using ΔK rather than $2\Delta K\ K_{mean}$. They found that the FCP rate in polystyrene increased at a given ΔK level when the load ratio R increased from 0 to 0.6. Similarly, Sauer et al.(4) found that the fatigue life of polystyrene samples decreased at fixed stress range when the mean stress was increased.

In the present work, the influence of both the alternating stress intensity factor range ΔK and mean stress, R on fatigue crack growth has been examined and the role of local filler particle geometry and mean stress on the mechanism of stick-slip crack propagation is discussed.

EXPERIMENTAL DETAILS

As part of work investigating interfacial failure in bonded aluminium structures, fatigue crack growth behaviour of a monolithic adhesive material has been studied using Compact Tension and Shearing (CTS) specimens (5) loaded in mode I. The adhesive is a rubber toughened epoxy system based on a diglycidyl ether of Bisphenol-A with a dicyandiamide curing agent. This latter system is designed for high cross linkage of polymeric groups to improve long term creep behaviour. The

* Fracture Research Group, Materials Discipline, The Open University, Milton Keynes, MK7 6AA, UK.

microstructure of this epoxy system consists of an epoxy matrix containing a dispersion of rubber toughening particles, and calcium silicate particles which are used to control the rheology of the adhesive during setting. The fracture toughness of this epoxy system was measured to be K_{IC}=4.12 MPa$\sqrt{m}$.

All tests were performed in laboratory air, at room temperature using a sinusoidal wave form at the relatively low frequency of 6Hz in order to prevent the local temperature rises due to viscoelastic hysteresis. Fatigue tests were carried out under constant ΔK control for the range ΔK= 0.3MPa$\sqrt{m}$ to 2MPa$\sqrt{m}$ and using load ratios of R= 0.1, 0.5 and 0.8. The stress intensity factor K for CTS specimen was calculated as given in reference (5) in terms of the crack length to the specimen width ratio a/W and the angle θ between the applied load and the perpendicular axis of the crack, which is 0^o in mode I:

$$K=Y\,\sigma\sqrt{\pi\,a} \qquad (1)$$

where

$$Y=\frac{\cos\theta}{1-\frac{a}{w}}\sqrt{\frac{0.26+2.65\,\frac{a}{w-a}}{1+0.55\frac{a}{w-a}-0.08\left(\frac{a}{w-a}\right)^2}} \qquad (2)$$

Crack lengths were measured on the surface of the specimen using a travelling microscope capable of a resolution of 0.02 mm.

RESULTS AND DISCUSSION

Fatigue crack growth behaviour in epoxy CTS specimens loaded in tension pure mode I were correlated using a linear elastic fracture mechanics approach, since epoxies are normally brittle and display approximately linear elastic deformation behaviour with very little plastic deformation.

The fatigue crack propagation data are presented in Figure 1. These data have been obtained using decreasing ΔK loading, starting with high values and decreasing ΔK to just above the threshold. This figure shows the crack growth rate da/dN plotted as a function of the stress intensity factor range ΔK for three different load ratios. The overall average crack growth rates at any given ΔK obtained followed the classic Paris-Erdogan power law for crack propagation and the results show that for a given ΔK, the crack growth rate increases markedly with load ratio R.

Although loading occurred under constant applied ΔK pronounced local variations in crack growth rate were observed. A typical example is shown in Figure 2 which plots local crack growth rate at ΔK=0.7 and R=0.8. This behaviour is typical of epoxies which are prone to crack propagation by crack jumping, i.e. unstable or "stick slip" modes (6).

The effect of the filler particles on this crack growth mechanism was explored in some detail. As shown in Figure 3a the crack often kinked when it encountered a filler particle. Sometimes the crack branched (see Figure 3b) on reaching a filler particle and typically, in this situation, one branch, which saw the greatest the driving force, subsequently propagated whilst the remainder arrested.

Examination of the fracture surfaces in the Scanning Electron Microscope (SEM) provided evidence of two distinct types of crack/particle interaction. In Figure 4a. it can be seen that the particle has cleaved showing that the crack grew through the filler particle. In contrast the particles in Figure 4b are smooth suggesting that the crack grew in the epoxy around the filler particle.

CONCLUSIONS

1) The crack growth rate in epoxy followed the classic Paris power law for crack propagation and increased with load ratio R at a given ΔK.

2) Cracks propagated by an or "stick slip" mechanism.

ACKNOWLEDGEMENTS

The authors gratefully acknowledge The Open University, the Science and Engineering Research Council (UK) and Alcan International Ltd for supporting this research.

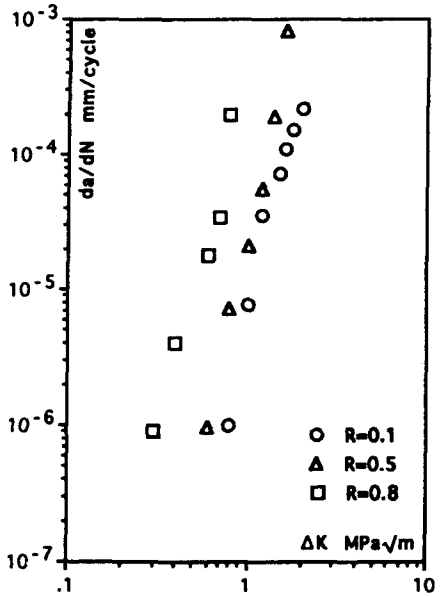

Figure 1, Fatigue Crack Growth Rates

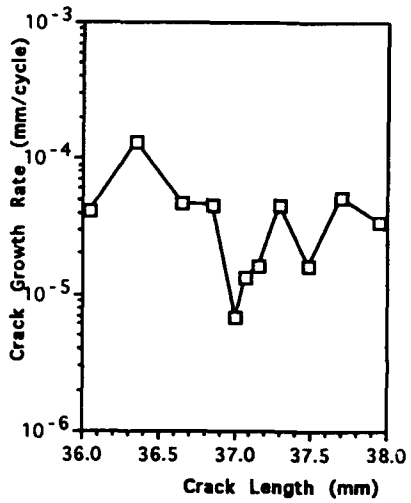

Figure 2, Local Crack Growth Rate

SYMBOLS USED

R = load ratio
ΔK = stress intensity range
K_{mean} = mean stress intensity factor
K_{IC} = fracture toughness
θ = angle between the applied load and the perpendicular axis of the crack
a = crack length
W = specimen width
σ = applied stress
Y = geometry correction factor
FCP = Fatigue Crack Propagation

CTS = Compact Tension and Shearing

REFERENCES

1 Manson J A and Hertzberg, CRC Crit. Rev. Macromol. Sci. 1, (1973) 433
2 Arad S, Radon J C, Culver L E, J. Mech. Eng. Sci. 13 (1971) 75
3 Mai Y M and Williams J G, J. Mater. Sci. 14 (1979) 1933
4 Sauer J A, McMaster A D, Morrow D R, J. Macromol. Sci.-Phys. B12 (1976) 535
5 Buchholz F G, Pirro P J M, Richard H A, Dreyer K H, 'Numerical and experimental mixed-mode analysis of a compact tension-shear-specimen', 4th Int. Conf. on Num. Method Fract. Mech. Proc., Swansea, UK, 1987.
6 Kinloch A J and Williams J G, J. Mater. Sci. 15 (1980) 587

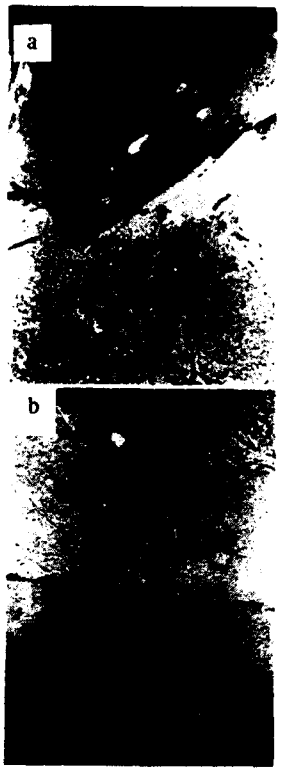

Figure 3, Crack Growth Configurations

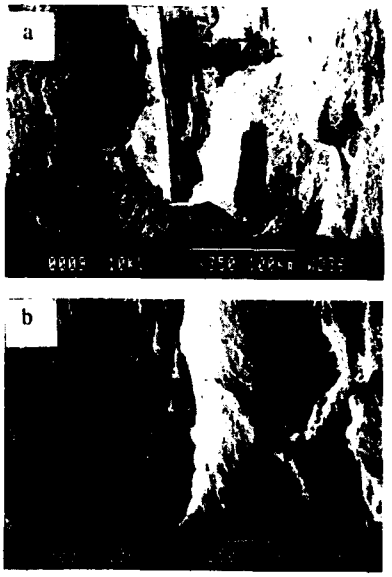

Figure 4, Fracture Surface of a Rubber Toughened Epoxy with Filler Particles.

Swelling of Elastomers in Sub- and Super-Critical Fluorocarbons

Gregory B. McKenna, William K. Waldron Jr., Ferenc Horkay
Polymers Division
NIST
Gaithersburg, MD 20899 USA

Vapor sorption measurements were performed on several cross-linked and uncross-linked elastomers in different fluorocarbon fluids in the temperature range 35 to 150 °C, from below to above the critical temperature of the diluents, T_c. It was found that below T_c the experimental data can be interpreted in the framework of the Flory-Huggins lattice theory using a temperature and concentration dependent interaction parameter. Above T_c the fluid uptake of the elastomers drastically decreases.

INTRODUCTION

Environmental considerations are leading to searches for substitutes for brominated fire suppressant fluids which are found to be deleterious to stratospheric ozone. Since brominated chemicals will not be available in the near future, there is a great demand to test the alternative agents regarding their compatibility with vessel containment materials. Thermodynamic measurements provide useful information on the compatibility of elastomeric seals with potential candidates for replacement of the current fluid in fire suppression systems.

In the present work the vapor sorption of fluorocarbon fluids in different elastomers has been investigated. Measurements were carried out over a wide range of temperatures and pressures, from below to above the critical temperature of the fluids. The experimental results were analyzed using the Flory-Huggins theory and Flory's equation-of-state theory.

THEORY

Swelling of Elastomers

Swelling is a relatively simple method to characterize the affinity of an elastomer to a solvent. The driving force of swelling is the change in the free energy of mixing.

According to the Frenkel-Flory-Rehner hypothesis[1] at swelling equilibrium we have

$$\Delta\mu_1^{gel} = \Delta\mu_1^{mix} + \Delta\mu_1^{el} \qquad (1)$$

where $\Delta\mu_1^{el}$ and $\Delta\mu_1^{mix}$ are the elastic and mixing components of the change in chemical potential of the diluent in the gel. The total change in the solvent chemical potential, $\Delta\mu_1^{gel}$, is related to the vapor pressure of the solvent in the partially swollen network p and the saturation vapor pressure p^o of the pure solvent by

$$\Delta\mu_1^{gel} = RT\ln(p/p^o) \qquad (2)$$

The Flory-Huggins lattice theory[1] describes $\Delta\mu_1^{mix}$ as a function of the volume fraction v_2 of the polymer

$$\Delta\mu_1^{mix}=RT[\ln(1-v_2)+v_2+\chi v_2^2] \quad (3)$$

where χ is the Flory-Huggins polymer-solvent interaction parameter. In general χ depends on the volume fraction of the polymer ($\chi=\chi_o+\chi_1 v_2+\ldots$).

Flory's Equation of State Theory

Corresponding state theories imply that the thermodynamic properties of a fluid are determined by two scale factors: one for the distance of separation of molecular centers and the other for the magnitude of the intermolecular potential. These factors are embodied in a characteristic temperature T^* and a characteristic pressure p^*. In the case of polymers the third important parameter is the number of intermolecular degrees of freedom.

Flory[2,3] formulated the partition function of liquids by combining a rudimentary factor for hard spheres with an intermolecular energy of the van der Waals form. The reduced equation of state of a pure liquid is

$$\tilde{p}\tilde{v}/\tilde{T} = \tilde{v}^{1/3}/(\tilde{v}^{1/3}-1)-(\tilde{v}\tilde{T})^{-1} \quad (4)$$

where $\tilde{v}=v/v^*$, $\tilde{T}=T/T^*$, $\tilde{p}=p/p^*$ are the reduced variables and v^* is the characteristic (hard core) volume. The values of v^*, T^* and p^* can be determined from pvT (pressure-volume-temperature) data.

The application of the equation of state theory for a binary mixture also requires the knowledge of the interactions in the mixture defined by an interaction enthalpy parameter, X_{12}, and an interaction entropy parameter, Q_{12}. The chemical potential of mixing is given by

$$\begin{aligned}\Delta\mu_1/RT=&\ln(1-\varphi)+(1-1/P)\varphi\\&+p_1^*v_1^*/RT\{3\tilde{T}_1\ln[(\tilde{v}_1^{1/3}-1)/(\tilde{v}^{1/3}-1)]+1/\tilde{v}_1-1/\tilde{v}\\&+\tilde{p}_1(\tilde{v}-\tilde{v}_1)\}+v_1^*X_{12}\theta_2^2/RT\tilde{v}-v_1^*Q_{12}\theta_2^2/R\end{aligned} \quad (5)$$

where φ is the segment fraction and θ_2 is the site fraction of the polymer.

Eq. 5 allows the calculation of the chemical potential both below and above the critical temperature of the diluent, and can be used to describe the solubility of supercritical gases in polymers. (The simple Flory-Huggins lattice theory discussed above can only be used below the critical temperature of the fluid because p^o is not defined under supercritical conditions.)

EXPERIMENTAL PART

Vapor sorption measurements were performed on crosslinked and uncrosslinked silicone, fluorosilicone, neoprene and fluorocarbon polymers. The cross-linked samples were prepared from the corresponding high molecular weight uncross-linked polymers by standard vulcanization procedures at elevated temperatures. The ratio of the monomer units of the polymer to the molecules of the cross-linking agent was approximately 100 in each case.

Three fluids were chosen for vapor sorption measurements: decafluorobutane (T_c=113.2°C), perfluoropropane (T_c=71.9°C) and chlorodifluoromethane (T_c=96.0°C).

Special pressure vessels were constructed for measuring the fluid uptake of the elastomers as a function of the solvent vapor pressure. Elastomer samples (30-40 mg) were placed on quartz pans suspended from quartz springs. The sensitivity of the quartz springs was approximately 1mg/mm. After pressure and temperature equilibrium were achieved, the displacements of the calibrated springs were measured using a cathetometer.

Swelling measurements were carried out at 35, 70, 105 and 150 °C in the pressure range of

0-5.86 MPa.

RESULTS AND DISCUSSION

In Figure 1 typical plots of solvent weight fraction, w_1, vs. vapor pressure, p, are shown for the uncross-linked silicone sample in three different diluents at 35 °C. It is apparent that the solvent uptake of the polymer significantly increases with the vapor pressure. The vertical arrows in the figure show the saturation vapor pressures of the diluents, p^o.

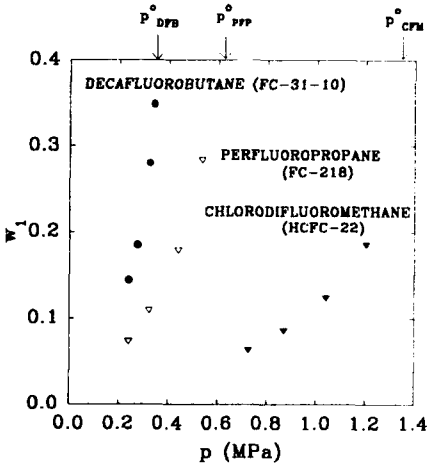

Figure 1. *Swelling of uncrosslinked silicone* in various fluids as a function of the pressure at 35 °C.

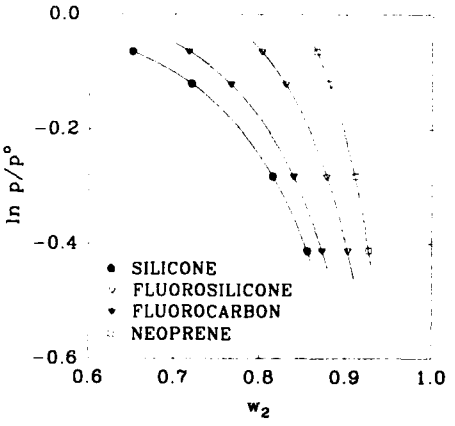

Figure 2. *Solvent activity in various* uncrosslinked polymers in decafluorobutane as a function of polymer weight fraction at 35 °C.

In Figure 2 similar experimental data are displayed according to the Flory-Huggins representation. (Although the Flory-Huggins theory is formulated in terms of volume fractions the results are given in mass fraction w_2 because it is the directly measured quantity. This substitution is arbitrary, but the functional form of eq. 3 remains unchanged.) The continuous curves in the figure were calculated by least squares fitting of the data to the equation

$$\ln(p/p^o) = \ln(1-w_2^2) + w_2^2 + \chi_o w_2^2 + \chi_1 w_2^3 \qquad (6)$$

In Figure 3 the swelling of the uncrosslinked silicone is compared with that of the corresponding cross-linked silicone in decafluorobutane at 35 °C. The cross-linked polymer exhibits considerably lower affinity to the solvent than the uncross-linked one. The values of the interaction parameters calculated from the solubility data are $\chi_{x\text{-linked}} = 0.99$ and $\chi_{uncross\text{-linked}} = 1.04$, respectively. This result is in qualitative agreement with previous data[4-8] obtained for different polymer/solvent systems, i.e., the Flory-Huggins interaction parameter for the network polymer exceeds that of the corresponding uncross-linked polymer solution.

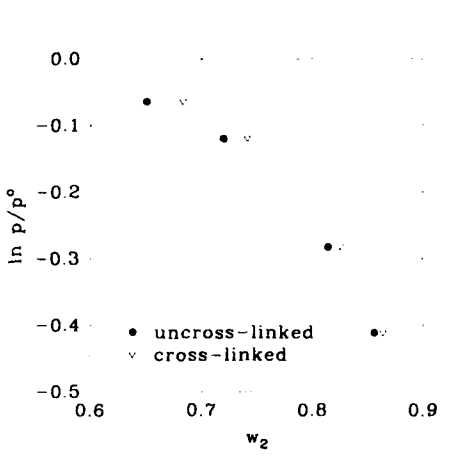

Figure 3. Comparison between the swelling of the crosslinked and uncrosslinked silicones in decafluorobutane at 35 °C.

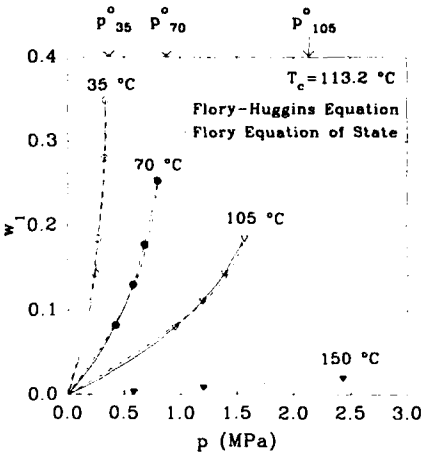

Figure 4. Measured and calculated values of decafluorobutane weight fraction dissolved in uncrosslinked silicone.

Figure 4 shows that the swelling degree of silicone in decafluorobutane significantly decreases with increasing temperature. At 150 °C, i.e. above the critical temperature of decafluorobutane (T_c = 113.2 °C) the fluid uptake dramatically decreases (it is approximately one order of magnitude smaller than at 105 °C). The dotted lines show the fits of eq. 5 to the swelling data. (The values of the equation-of-state parameters used in this calculation were taken from Refs.9,10). In the figure the fits to the Flory-Huggins expression (eq.3) are also displayed. It can be seen that the experimental data can be reasonably described by Flory's equation-of-state theory both above and below the critical temperature of the diluent.

ACKNOWLEDGEMENT

This work has been supported by the U.S. Air Force, Flight Dynamics Laboratory, WPAFB, Ohio.

REFERENCES

1. Flory, P.J., "Principles of Polymer Chemistry"; Cornell, Ithaca, New York, 1953.
2. Flory, P.J., Orwoll, R.A., and Vrij, A., *J. Am. Chem. Soc.*, 86, 3515 (1964).
3. Flory, P.J., *Disc. Faraday. Soc.*, 49, 7 (1970).
4. Gee, G., Herbert, J.B.M., and Roberts, R.C., *Polymer*, 6, 51 (1965).
5. McKenna, G.B., Flynn, K.M. and Chen, Y., *.Macromolecules*, 22, 4507 (1989).
6. McKenna, G.B., Flynn, K.M. and Chen, Y., *Polymer*, 31, 1937 (1990).
7. Horkay, F. and Zrinyi, M., *Macromolecules* 15, 1306 (1982).
8. Horkay, F., Hecht, A.-M. and Geissler, E., *J.Chem.Phys.*, 91, 2706 (1989).
9. Shih, H., Flory, P.J., *Macromolecules*, 5, 758 (1972).
10. Wilson,L.C., Wilding,W.V., and Wilson,G.M., "Thermo-Physical Properties of Perfluorobutane", Wiltech Research Company, 1992.

CRITICAL STRUCTURAL PARAMETERS IN TOUGHENING OF POLYMERS

G H Michler, G M Kim, J U Starke*

Of particular interest in heterogeneous polymers with a semicrystalline matrix is the possible existence of critical maximum and minimum distances (A_{max}, A_{min}) for producing a high local plasticity. The micromechanical deformation processes in rubber modified and particulate-filled polyamide and polypropylene have been studied by different techniques of electron microscopy. The experimental results are compared with theoretical analyses of the stress concentration in the polymer matrix strands between particles dependent on the thickness of these strands.

INTRODUCTION

Toughness is a very important mechanical property for many applications of polymers. There are several routes of enhancing the toughness, including a route of particular interest: modification of a relativly stiff and strength material in such a way that lots of local yield events appear above a relativly high stress. This concept of combining stiffness and plasticity was initially utilized in the well-known rubber-modified polymers, as in the classical HIPS or ABS polymers. Here, rubber particles distributed in a matrix of polystyrene or styrene- acrylonitrile copolymer initiate the formation of lots of crazes at the rubber particles. Meanwhile, other polymers have been modified with various elastomers or modifiers. In these systems several other mechanisms of toughening appear, including shear yielding or local plastic yielding of matrix strands between particles.
In these heterogeneous systems there are several structural details important for toughness, including the shape and the internal structure of modifier particles, the interface between polymeric components, the morphology of matrix material and others. Many investigations have shown that the reaching of a maximum toughness requires an optimum morphology, taking into account the same critical structural parameters [1,2].
It has been found that local yielding processes comparable with those in toughened polymers also exist in particulate-filled thermoplastics [3].

* Department of Materials Science, Martin-Luther-University Halle-Wittenberg, D-06217 Merseburg, Germany

EXPERIMENTAL

Different techniques of electron microscopy, including scanning- and high voltage electron microscopy in connection with in situ-methods, were used to study the influence of structural details on the micromechanical processes of deformation and fracture and, therefore, on toughness.
Polyamide and polypropylene were used as matrix materials which were modified with several types of rubber or filler particles. The diameter and the volume content of the rubber and filler particles were changed, enabling it to vary the interparticle distance in a large range from below 10 nm up to a few μm.

SOME RESULTS

The results of the electron microscopic investigation of the micromechanical processes are summarized in a three-stage-mechanism:

Stage 1 - stress concentration:
Stress concentrations are built up at and between the rubber particles or filler particles (after debonding). At places with a maximum shear stress component weak shear bands are formed between the particles under an angle of about 45° (Fig. 1).
Stage 2 - void formation:
Owing to stress concentration and formation of shear bands, larger hydrostatic stresses are built up inside the particles, giving rise to the cracking of the particles and the formation of micro-voids inside (Fig. 2).
In composites, however, void formation occurs between particles and matrix (at the interfaces, Fig. 3). In both cases, the result of void formation is a higher local stress concentration between the particles and the formation of shear bands.
Stage 3 - induced shear deformation:
Owing to high local stress concentration, shear processes are initiated in the matrix bridges between the particles (or voids). The shear deformation proceeds simultaneously at numerous adjacent matrix bridges and thus takes place in fairly large polymeric volumes.

This mechanism through shear deformation requires interparticle distances smaller than a critical value A_{max}. If the interparticle distances are too large (i.e. the matrix strands are too thick), the matrix material between the particles is under triaxial stress including a strong hydrostatic component. This stress state is not effective to initiate local plastic deformations. If the distance between the particles (i.e. the thickness of the matrix strand) is small enough, a plastic response of the matrix material is reasonable. As a result, the hydrostatic stress component in the matrix can be reduced in favour of a uniaxial stress component parallel to the load direction. An intense plastic yielding of the matrix strands can occur. This decisive role of the interparticle distance A has been explored first by WU [4] and later by BORGGREVE et al. [5].

Although the reason of the stress concentration is different in both cases, the result of local yielding of matrix strands is comparable. In both cases the interparticle distance plays the decisive role of plasticity:

- There is a critical maximum interparticle distance A_{max} , which describes the brittle-tough-transition of the material.
- There is an optimum interparticle distance A_{opt} , defining an intense plastic yielding of the matrix strands.
- There is a critical minimum interparticle distance A_{min} , correlated with the inability of very small zones to yield

REFERENCES

1 G H Michler, Kunststoff-Mikromechanik, Morphologie, Deformations- und Bruchmechanismen, Carl Hanser Verlag München 1992

2 G H Michler, Acta polymerica 44 (1993) 113-124

3 G H Michler, J M Tovmasjan, W A Topolkarajev, I L Dubnikova, V Schmidt, Mechan. Kompos. Mat. 2 (1988) 221-226

4 S Wu, Polymer 26 (1985) 1855

5 R J M Borggreve, R J Gaymans, Polymer 29 (1988) 1441

Figure 1 Deformation structure of high impact polypropylene, HVEM

Figure 2 Void formation inside the rubber particles of impact polyamide, HVEM

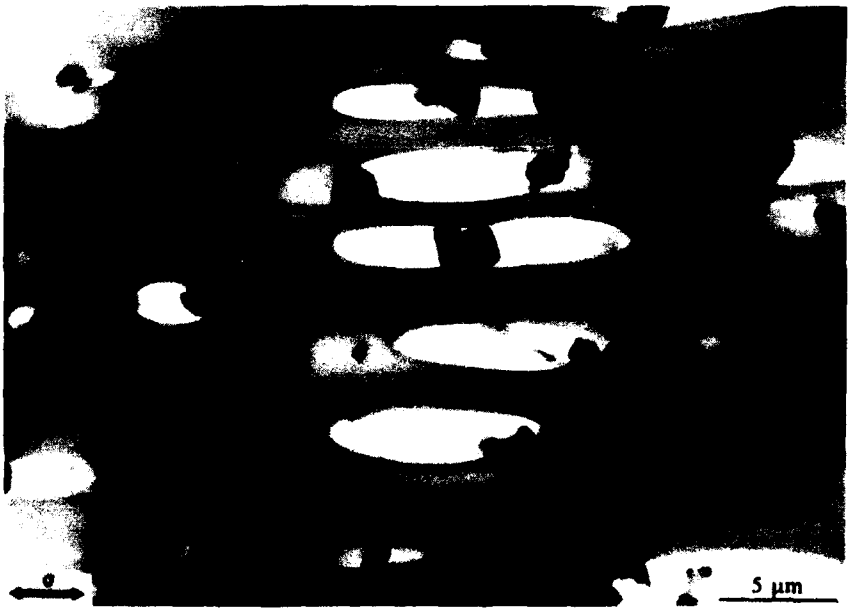

Figure 3 Deformation structure of particulate-filled polypropylene, HVEM

FRACTURE TOUGHNESS RELATED TO PLASTIC PROPERTIES UNDER IMPACT

J. Parisot*

Several factors such as yield stress level, strain hardening capacity and ductility, influencing plastic energy dissipation in fracture, were varied on Polycarbonate, through preliminary unidirectional cold-rolling, and different rates and temperatures of testing. At lower rates, the highest toughness is obtained when loading in the rolling direction, owing to a wide plastic zone and blunting. Under impact, fracture becomes brittle in the rolling direction, while ductile propagation continues to act when loading in the transverse direction, where yield stress is lower, dissipating much more energy.

INTRODUCTION

A small preliminary plastic deformation of glassy Polycarbonate by unidirectional cold rolling leads to important changes of mechanical properties. Two features can be emphasized. On the one hand, it induces molecular orientation and anisotropy of properties, in the same manner as prestraining in the rubber state followed by quenching. On the other hand, mobility is increased and further plastic deformation becomes easier and stable. This last aspect, which may be seen as a plasticizing effect, was not analysed enough in the literature, as it differs deeply from prestraining in the rubbery state.

Such changes were previously shown through tensile and fracture properties at low rates /1, 2/. The aim of this paper is to see what happens at impact rates /3/.

EXPERIMENTAL PROCEDURE

Material was taken from 3, 6 or 10 mm thick sheets of Polycarbonate from Röhm (Makrolon). Some pieces were unidirectionally cold rolled by 40 %, thicknesses becoming about 2 and 6 mm respectively for tensile and fracture specimens. Specimens were cut following two orientations, for loading respectively in rolling and transverse direction.

Impact tensile tests were performed on a falling weight device, recording load vs time.

For low rate fracture tests, CT 40 specimens were used, with measurement of 3 parameters : load, displacement and crack length /4/. They were notched then precracked by fatigue. For impact, SEN bending specimens were used, on a Charpy pendulum with a 40 mm span, at ambient or liquid nitrogen temperature. They were prenotched at 60° by milling and then by gliding a razor blade on about 0,1 mm depth, with a tip radius $25 < \rho < 200$ µm. Two parameters were measured : the loss of energy of the pendulum U and the initial notch length a_o (or the

* Lab Mécanique et Physique des Matériaux, CNRS/ENSMA, Chasseneuil du Poitou, BP 109, 86960 Futuroscope cedex.

ligament length). In linear elastic fracture mechanics, the energy release rate is given as $G = U/(BW\Phi)$, where B is the thickness (6 mm) of the specimen, W the width (5 or 10 mm) and $\Phi(a/W)$ the calibration factor /5/ : in the present case, a range of three values of Φ was obtained, with W = 0.5 or 3 mm, and G_c was deduced from the slope of the plot U vs $BW\Phi$, providing experimental dots lie on a right line passing through the origin.

TENSILE PROPERTIES

Stability of plastic flow at yield is, with anisotropy, the most striking feature of cold rolled glassy PC : neither stress peak, nor necking occur as they do for as-received material, whatever the direction of loading, transverse or longitudinal. Such stabilization results from the fact that yielding occured during prestraining : molecular mobility is then easier and further plastic deformation may act at lower stresses. Two types of tensile curves are obtained depending on the direction of loading. Rolling direction corresponds to high yield stress level and strain hardening, owing to molecular orientation, but lower deformability and energy at fracture. Conversely, loading in the transverse direction leads to lower yield stress level and strain hardening, but keeps higher deformability and energy at fracture.

The same features are kept at impact rates. The only change concerns values of flow stresses which are raised for both directions of loading, due to the rate sensitivity of the material : in this way, yield stress passes from 57 to 101 MPa for loading in the rolling direction, and from 44 to 90 MPa for the transverse direction.

CRACK PROPAGATION

In static tests, as-received material behaves close to brittle with successively two stages of stable and unstable propagation. During the stable propagation, the plastic zone is restricted to a slight lateral contraction on the faces of the specimen, between two shear bands initiated at about $\pm 45°$ from the initial crack tip. The crack tip is stopped by those shear bands on the surfaces and propagates only in the bulk, its front line bowing more and more, and the tearing resistance $\partial J/\partial a$ is close to zero /2/.

Conversely, cold rolled PC exhibits stable propagation with a several millimeters wide plastic zone propagating ahead the crack tip. The critical J value becomes particularly high when loading in the rolling direction (15 kJ/m^2 against 3 for as-received PC), while the tearing resistance $\partial J/\partial a$ is strongly increased for both directions (18 and 16 kJ/m).

Under impact, the energy of fracture is strongly increased after cold rolling compared to the as-received material. However, unlike the low rates, the highest energy is now obtained when loading in the transverse direction. All those energies are decreased when changing the temperature from ambient to liquid nitrogen (Fig. 1).

That inversion of U corresponding to the two directions is due to a brittle behaviour in longitudinal direction. The fracture surfaces are very rough when made at liquid nitrogen temperature, without any mark of plastic deformation on lateral faces, while they are smooth for room temperature and exhibit only small marks of shear deformation at the initial notch tip and a few penny shaped cracks in delamination plane. Plots of U_e *vs* $BW\Phi$ form right lines like as-received material (Fig 2), but the slopes give surprisingly high values of G (respectively 9 and 36 kJ/m^2 at liquid nitrogen and ambient temperature, to be compared with Jc previously determined).

In the transverse direction, the LEFM analysis is obviously not valid, as the dots are not on a right line on the U_e *vs* $BW\phi$ diagrams : a more involved approach is needed /6/. Moreover, strong

marks of plastic deformation are visible on cracked specimens, at least at room temperature : the fracture surfaces are deeply ploughed while lateral contraction gives rise to a wide plastic wake.

It is seen finally that the influence of plasticity under impact is obvious for loading in the transverse direction but uncertain in the longitudinal one. In the latter case, the yield (or flow) stress may be thought to be too high to allow significant strains to occur beyond the crack front : increase of toughness may result from the increase of stress at fracture rather than from plastic deformation (which occur only at a microscopic scale). Secondly, the question remains in the present case of the validity of LEFM models giving toughness from the only measurements of fracture energy and initial crack length a. It should be interesting to compare, at the same rate, values of toughness respectively obtained from such models, or from three parameter measurements (load, displacement and crack propagation), in order to define limits of validity.

CONCLUSION

Among factors influencing plastic energy dissipation in fracture, yield stress level, strain hardening capacity and ductility play important role. Those factors were varied on polycarbonate through preliminary cold rolling and different rate and temperature of tests.

A remarkable fact resulting from the analysis above is, for loading in the rolling direction, the apparent transition from ductile to brittle when passing from low rate to impact. The same is not true in the transverse direction where the contribution of plasticity remains significant in both cases. That results in an inversion in the order of the energy levels of the two orientations, when passing from static to impact fracture.

REFERENCES

1 Belcadi M, Comportement Mécanique d'un Polycarbonate Prédéformé par Laminage, *Thesis*, Université de Poitiers (France), 1990.

2 Parisot J, Cocchi F, 8th International Conference on Deformation, Yield and Fracture of Polymers, Cambridge, The Plastics and Rubber Institute, London, p 110 1-4, 1991.

3 Parisot J, Aubert P, Belcadi M, Cocchi F, Impact and Dynamic Fracture of Polymers and Composites, ESIS, Sardinia, 1993.

4 Landes J D, Begley J A, Fracture Analysis, ASTM STP 560, American Society for Testing and Materials, pp. 170-186, 1974.

5 Williams J G, Fracture Mechanics of Polymers, Ellis Horwood Ltd Publ. Chichester, 1987.

6 Hashemi S and Williams J G, Polym. Eng. Sci. 26, 760-767, 1986.

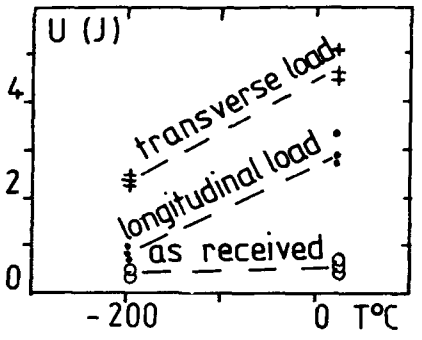

Figure 1. Loss energies of the Charpy test ($BW\Phi=83mm^2$) : from top to bottom, cold rolled PC loaded in the transverse and longitudinal (rolling) directions, as-received PC.

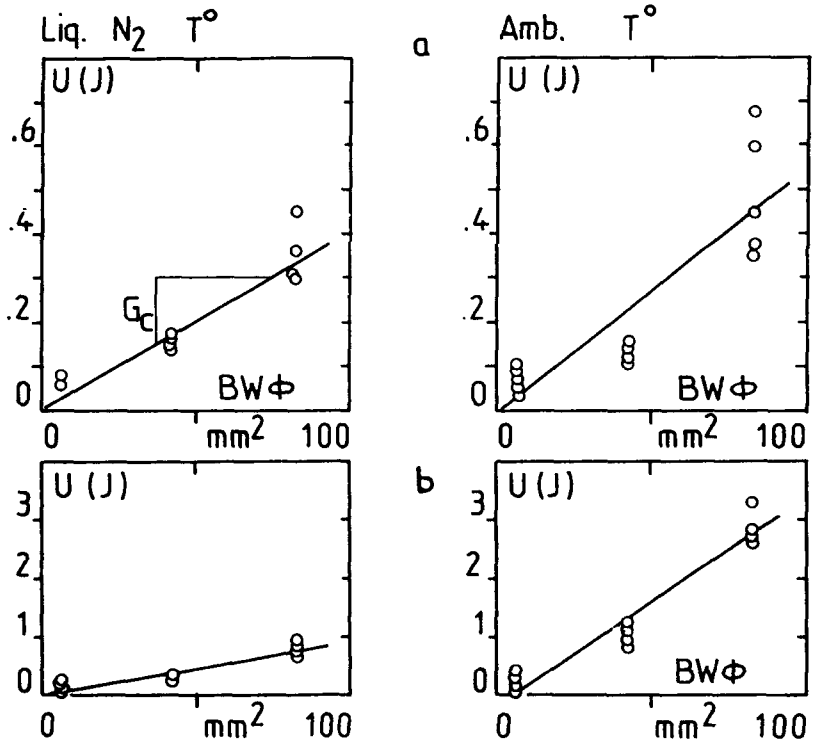

Figure 2. LEFM analysis of Charpy tests
Left : Liquid Nitrogen Temperature .../... Right : Room temperature
a) as received PC, b) cold rolled PC loaded in the longitudinal direction.

THE LOADING RATE DEPENDENCE OF THE FRACTURE TOUGHNESS OF RUBBER MODIFIED POLY(METHYL METHACRYLATE).

O. Julien * Ph. Béguelin **, L. Monnerie *, H.H. Kausch **

The mode I fracture resistance of neat and rubber-toughened PMMA modified by incorporating 15%, 30% and 45% by volume core-shell latex particles has been investigated at room temperature over a wide range of testing velocities (from 10^{-4} to 10 ms^{-1}). Notched compact tension specimens were tested by using a servo-hydraulic testing apparatus.
Whereas the neat material remains brittle over the whole range of testing velocities, the toughened PMMA materials undergo two successive transitions. The first corresponds to a transition from stable to unstable crack propagation. The second is the result of the progressive disappearance of the toughening mechanisms.
Together with an energetic approach, a fractographic study is used to investigate these transitions.

INTRODUCTION

Since it allows investigation of the deformation mechanisms involved in fracture, the characterisation of engineering polymers over a wide range of loading rates is currently of great interest. Moreover, the use of different test methods to cover several decades of test speed often fails to provide consistent data, and at impact testing rates the analysis of data by fracture mechanics is complicated by the dynamic nature of the tests [1-2]. A new testing procedure based on the reduction of the initial acceleration during the test by damping the contact stiffness is applied here [3-5]. Rather than determing the impact behaviour of polymeric materials, this test procedure allows the measurement of properties at high loading rates, under quasi-static conditions. Using this technique, the fracture behaviour of neat and rubber-toughened Poly(methyl methacrylate) - RTPMMA- is investigated over five decades of test speed, up to those used in impact characterisation. Mechanical transitions are identified by means of an energetic approach, together with post-mortem surface analysis on macroscopic scale. The shift of these transitions to higher testing speeds with the content of modifying particles is discussed.

EXPERIMENTAL

Test equipment

Fracture tests in mode I opening are performed with a high-speed servo-hydraulic testing apparatus made by Schenck. In order to avoid any loss of contact at high testing rates between the tested specimen and the adjacent parts, a compact tension CT geometry is used. Details on the experimental procedure can be found in references 4 and 5.

Material

A PMMA matrix of molecular weight M_W= 130'000 has been toughened with core-shell latex. The materials were synthesised by ATOCHEM [6]. The core component is based on Poly(*n Butyl Acrylate-co-Styrène*). The average particle diameter is 160 nm. Toughened PMMA granulates were prepared by mechanical blending the neat matrix with 15%, 30% and 45% volume fractions of latex. The neat PMMA used as the matrix has also been investigated.

* Laboratoire PCSM, Ecole Supérieure de Physique et de Chimie Industrielles, 75231 Paris Cedex 05, France.
** EPFL Laboratoire de Polymères, MX-D, CH 1015 Lausanne, Switzerland.

Testing conditions and analysis

The fracture behaviour is investigated at room temperature over a wide range of piston velocities, from 10^{-4} ms^{-1} to 10 ms^{-1}. For testing speeds higher than 10^{-1} ms^{-1} the damped test procedure described in reference 5 is used. Thus, quasi-static stress conditions prevail in the specimen, even at high loading rates. This allows the apparent critical fracture toughness (K_{Ic}) and the critical energy release rate at initiation (G_{Ic}) to be calculated by the static approach. Standard linear elastic fracture mechanics analysis (LEFM) is performed [7]. However, the size and linearity criteria are not always fully satisfied, in particular for RTPMMA at low testing speeds. The energy is calculated by integration of the load versus displacement curves. In sub-critical crack growth, the energy for initiation and for propagation are calculated separately. Integration of the load-displacement curve up to the maximum force (P max) is associated with initiation, since the occurrence of the crack growth at this point has been verified.

For the post-mortem analysis of plastic deformation, associated with stress-whitening, a numerical image of each fracture surface was taken under identical lightning condition using a video camera. Computer analysis of these images allowed us to quantify the macroscopic damaged area. For each concentration of latex, a constant grey-level threshold was used to obtain a binary image of the stress-whitened zone of the fractured ligament. The relative surface of this zone was then measured.

RESULTS AND DISCUSSION

General results.

The plot of figure 1 shows the stress intensity factor K_{Ic} versus the testing speed for all the materials tested. The test speed in the horizontal axis is the opening displacement rate of the specimen when fracture occurs. It is measured by the optical device, and can be up to 14 ms^{-1}.

The neat PMMA behaves in a brittle manner over the whole range investigated. At the lowest test speed, stable or partially stable crack propagation can occur. At higher test speed the crack propagation is always unstable. All the RTPMMA grades remain rate insensitive over three decades of test speed, and exhibit decreasing fracture resistance at rates higher than about 1 ms^{-1}. Increasing the rubber content improves the fracture toughness, in particular in the high speed regimes where the transition occurs.

In order to consider the whole fracture process (initiation and propagation), an energetic approach is considered below.

Determination of transitions in the fracture process

It has already been shown that these RTPMMA grades exhibit two successive mechanical transitions with respect to temperature [8]. Similar transitions can be expected when the test speed is increased. In order to determine these transitions, different fracture parameters can be considered together: K_{Ic}, G_{Ic} at initiation, initiation and propagation energies, as well as the macroscopic stress-whitened zone. Figures 2-5 show the example of RTPMMA modified with 15% of particles.

At low testing speed, the crack propagation is fully stable, and the whitened zone covers the entire fracture surface (Fig. 5). Then, as the test speed increases, the whitened zone area and the energy of propagation decrease continuously: the fracture becomes partially unstable. Notice that such a transition from stable to unstable crack propagation depends on the geometry and the size of the specimen used.

Since the crack changes from partially unstable to fully unstable propagation, the energy required for fracture propagation drops drastically. Above this transition, the propagation energy cannot be separed from the initiation energy since the driving force of the crack is the elastic energy stored in the specimen. The crack velocity is high and the whitened zone is restricted to the process zone developed ahead of the pre-crack during the initiation process. This transition which we term 'Transition I' occurs at about $2x10^{-2}$ ms^{-1}.

Another transition (Transition II) occurs, at a test speed about two decades above that at which Transition I is seen (4 ms^{-1}). This transition is related to the total disappearance of toughening effect of the particles (figures 3 ant 5). It is thus relevant that the K_{Ic} and G_{Ic} values measured for this system are even lower at high testing speeds than those measured for the neat PMMA.

A similar analysis has been applied to the RTPMMA grades with 30% and 45% particle contents in order to determine positions of their transitions. The results, as well as the crack velocity measured are summarised in table I.

Volume content of modifier [%]	*Fully stable to partially unstable crack propagation* [ms^{-1}]	**Transition I** *Partially unstable to fully unstable crack propagation* [ms^{-1}]	**Transition II** *Complete loss of toughening properties* [ms^{-1}]	Crack speed measured at piston velocity 1 ms^{-1}
0	0.001	0.01	-	120
15	0.001	0.02	4	540
30	0.009	0.2	~13	550
45	0.05	0.8	>14 (if occurs)	not meas.

Table I: Transitions and crack speed for neat PMMA and RTPMMA

Discussion

The major result is that all the transitions are shifted simultaneously when the rubber content is increased.

Since the highest piston velocity of our experimental set-up is 10 ms^{-1}, it is not clear whether the transition II for 30% and 45% RTPMMA is completed at the highest velocity used here. If not, further decrease of the fracture resistance may occur at higher velocities.

From the crack velocity measurement performed by means of a graphite gauge [9] at a piston speed of 1 ms^{-1}, it appears that the crack speeds in the toughened materials are higher than those measured in the neat material. This could be explained as being a consequence of the crack tip blunting occurring in RTPMMA [10]: as the fracture is delayed, the elastic energy stored in the specimen before fracture is increased. Notice that the crack velocities measured here are close to the maximum speeds generaly measured in polymers [11].

CONCLUSION

The two mechanical transitions observed in the RTPMMA are shifted to higher testing speeds when the particle content is increased. The stable to unstable crack propagation (toughening mechanisms associated to the propagation stage: Transition I) and the total disappearence of the toughening mechanisms acting at initiation (Transition II) occur at higher speeds. It is postulated to be related to the change of the inter-particle distance. Kinetics of micro-mechanisms growth in the matrix between particles may be involved as suggested by Bucknall [11].

Acknowledgement: Financial support by ELF ATOCHEM is gratefully acknowledged.

1 W. Böhme, J. F. Kalthoff, *Journal de Physique, Colloque C5*, Supplément No 8, 46 (1985) 213-218
2 J.G. Williams, G.C. Adams, *Internat. Jour. of Fract.* **33**, (1987) 209-222.
3 Ph. Béguelin, M. Barbezat, *Journal de Physique III France* **1** (1991), 1867-1880
4 Ph. Béguelin, H.H. Kausch, *J. of Mat. Sci.* **29** (1994) 91-98.
5 Ph. Béguelin, H.H. Kausch, *ESIS European Symposium on Impact and Dynamic Fracture of Polymers and Composites.* Porto Cervo (Sardinia), Italy, September 20-22, 1993
6 C. Wrottecki, P. Heim, P. Gaillard, *Polym. Eng. and Sci.*, **31**, No 4, 213 (1991)
7 ESIS Technical Commitee 4, "A Linear Elastic Fracture Mechanics (LEFM) Standard for Determining Kc and Gc for Plastics - *Testing Protocol 1990* -"
8 O. Julien, *MPhil thesis,* CIT Crandfield, UK, (1991)
9 B. Stalder, Ph. Béguelin, A.-C. Roulin Moloney, H.H. Kausch, *J. Mat. Sci.*, **24**, 2262, (1987)
10 P. A. Lowell, J. McDonald, D. E. J. Saunders, M. N. Sherratt, R. J. Young, *Plast. Rub. and Comp. Process. and Appl.*, **16**, No1, 37 (1991)
11 C. B. Bucknall, *Makromol. Chem., Macromol. Symp.*, 16, 209, (1988)

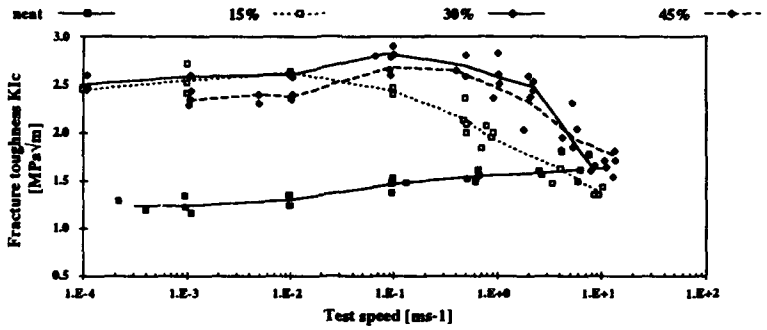

Fig. 1: Critical stress intensity factor KIc versus the log of the test speed. Neat PMMA and toughened grades

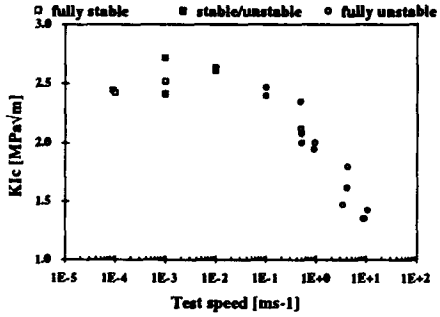

Fig. 2: RTPMMA modified with 15% of particles. Critical stress intensity factor KIc versus test speed.

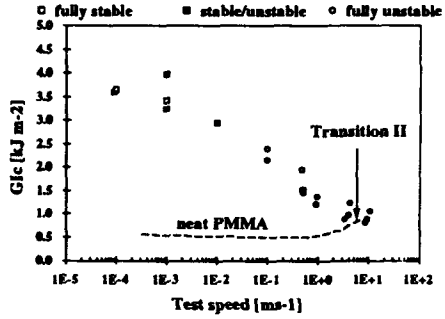

Fig. 3: Critical energy release rate GIc versus test speed.

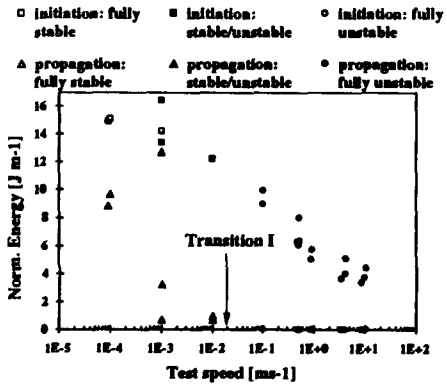

Fig. 4: Normalized energy for initiation and for propagation versus test speed.

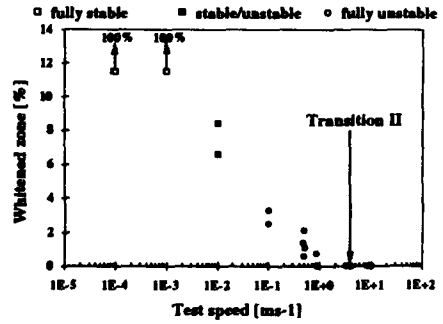

Fig. 5: Relative stress-whitened surface of the ligament versus test speed.

THE EFFECT OF STRAIN RATE ON THE UNSTABLE FRACTURE OF ABS

A.C. Steenbrink, R.J. Gaymans *, E. van der Giessen ‡

Extrusion blends of a styrene-acrylonitril copolymer (SAN) and a SAN-grafted polybutadiene (PB) were prepared to obtain ABS materials. The PB-content was varied between 15 and 30 % . Fracture toughness in ABS is studied by means of a notched Izod test in a temperature range from −45 to +80 °C. A notched tensile test with a speed range of 10^{-5} - 10^{1} m/s was used to study the influence of deformation rate. Over the whole speed range the propagation energy was low, so that crack propagation was unstable. In the impact regime, above loading rates of around 1 m/s the energy dissipation shows a marked increase. This is caused firstly by a sudden increase of the maximum load. Secondly, the energy dissipation during crack propagation is somewhat enhanced.

INTRODUCTION

The enhancement of toughness by the incorporation of rubber particles in a brittle matrix has been the subject of many studies. Much research has been devoted to the toughening mechanisms in HIPS [1–4] and ABS [5–7]. Due to considerable microstructural differences in the materials, the results are difficult to put into perspective, and many questions about the micromechanisms of plastic deformation and fracture are still open. The present research is concentrated on some of these micromechanisms within a micromechanics approach.

In this study, blends of a styrene-acrylonitril copolymer (TYRIL 790, supplied by the Dow Chemical Company) and a SAN-grafted polybutadiene (GRC 310, supplied by Dow) were prepared in a Berstorff ZE 25 corotating twin screw extruder. The rubber content was 15–30 % vol. and the particle size 0.1 μm. Injection moulded bars (100 × 10 × 4 mm) with a 2 mm sawed notch were used for Izod tests with varying temperature and tensile tests on a Schenck VHS servo-hydraulic tensile tester. The speed of the clamps ranged from 10^{-5} m/s up to 10 m/s. The distance between the clamps was 41 mm and accordingly the macroscopic strain-rate ranged from 0.0002 to 250 s^{-1}.

RESULTS AND DISCUSSION

Notched Izod test. The fracture toughness of Izod specimen is studied as a function of temperature between −45 °C and +80 °C (see figure 1). At very low temperatures (below −30 °C), the rubber behaves glassy at the high deformation rates applied here. Any toughening effects are absent then. Above this temperature the rubber becomes effective. The toughness increases slightly with increasing temperature, and has an optimum at about room temperature. From the notched Izod test it is not clear if crack propagation is stable or not.

It is noticed that there are two distinct zones that show whitening as a result of plastic deformation. Firstly, there is a circular zone of diffuse whitening around the fracture surface which is associated with cavitation of the rubber particles. In specimens fractured at low temperatures, the diffuse zone is relatively large. At high temperatures (close to T_g) the diffuse zone is very small. This can be explained by the effect of internal stresses due to the thermal expansion mismatch between rubber

*. University of Twente, P.O. Box 217, 7500 AE Enschede, the Netherlands

‡. Delft University of Technology, P.O. Box 5033, 2600 GA Delft, the Netherlands

and matrix. Secondly, there is a zone of intense whitening along the fracture surface which is associated with yield processes. The thickness of the zone of intense whitening correlates well with the fracture toughness. When toughness is low the zone is very thin, conversely when toughness is relatively high the zone is thicker. The distinction between zones of intense whitening and diffuse whitening, as regions of rubber particle cavitation and yield processes respectively, has been made previously by Ni et al. [8] and by Newmann et al. [9].

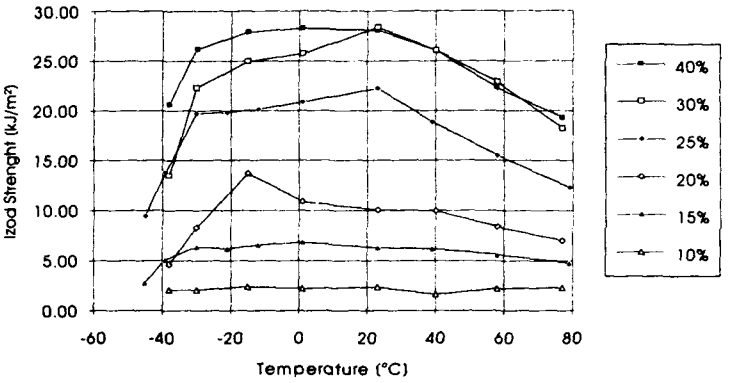

Figure 1. Notched Izod strenght for ABS having a rubber content of 10 - 40 % vol, all blends have a particle size of approximately 0.1 μm.

Notched tensile test. Force-displacement curves from notched tensile tests that are typical for materials with a relatively high rubber content are shown in figure 2. They indicate that crack propagation is unstable. The maximum load increases with increasing test speed for materials with a high rubber content (figure 3). This effect is quite pronounced at very high speed (7.5 m/s).

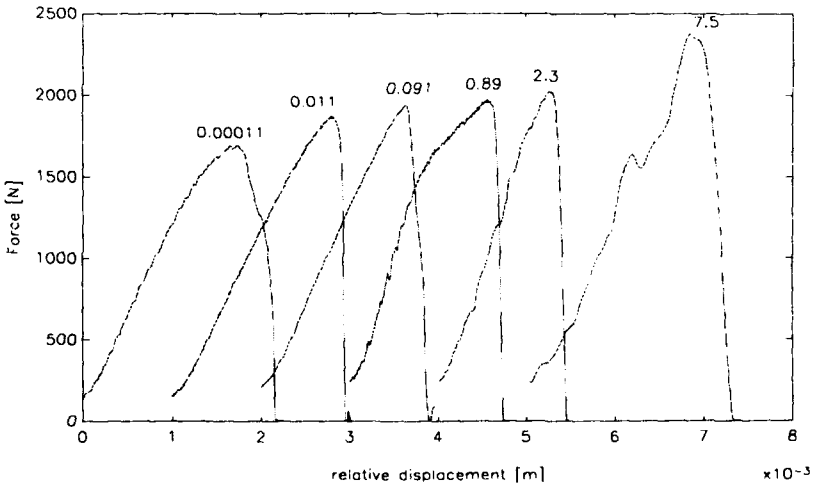

Figure 2. Typical plots of force versus relative displacement at different speeds for ABS containing 30 % vol. rubber. The tensile speed (in m/s) is indicated at the top of each curve.

When the rubber content is low, the maximum force decreases with increasing speed, and the crack is initiated already at a lower stress level. Materials having a high rubber content show an increase of maximum load. However, the sudden increase at high deformation rate cannot be explained by the increase of the yield stress alone. In ABS this is the main reason for the large increase of the total energy dissipation at high deformation rate (figure 4)

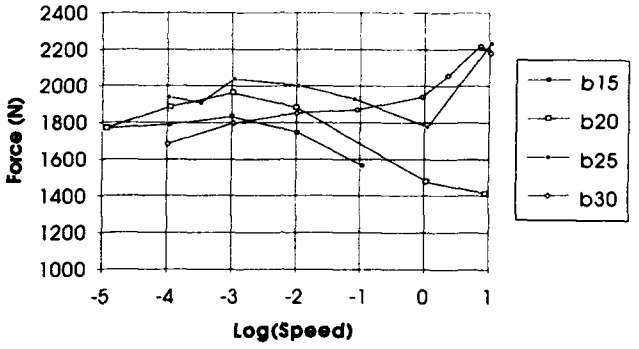

Figure 3. Maximum load as a function of tensile speed for materials having a rubber content as indicated in the legend by bxx, where xx is the volume fraction of the rubber.

On increasing the deformation rate, it can be seen that the energy dissipation decreases. From figure 2 it is clear that crack propagation is unstable, even at low speeds. At high speeds, the total energy dissipation shows a marked increase (figure 4). This is primarily the result of the increase in maximum load.

In figure 4 it can be seen that there is also a small contribution of the increase in the propagation energy, which is defined as the area under the force-displacement curve after maximum load. Furthermore, the thickness of the intense whitened zone was larger at high speed. This indicates that the plastic deformation during crack propagation is somewhat enhanced.

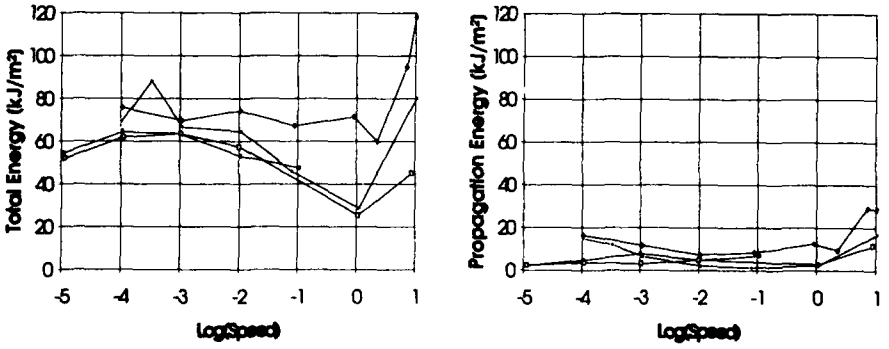

Figure 4. Total energy dissipation at fracture and propagation energy as a function of tensile speed. The materials are indicated in the same way as in figure 3.

The observations discussed here are similar to that for rubber toughened nylon [10,11] and polypropylene [12]. However, in those studies crack propagation was stable which makes the enhanced energy dissipation in the propagation phase (attributed to melt blunting) more important. In the ABS under the test conditions considered here, crack propagation is unstable and the enhanced energy dissipation is primarily caused by the ability to increase the maximum load.

CONCLUSIONS

Crack propagation in ABS materials is unstable in the temperature and speed range under consideration. The fracture toughness in the Izod test has an optimum at about room temperature. Below 30 °C the rubber behaves glassy and looses its effectiveness. In the notched tensile test, the fracture energy decreases on increasing the strain rate. However, when the global strain-rate is in the impact regime (i.e. > 1 m/s), a marked increase of the fracture energy occurs. This is primarily caused by an increase of the maximum load which raises the initiation energy. At the high deformation rates the enhanced energy dissipation during crack propagation has also a small contribution.

REFERENCES

[1] Donald AM, Kramer EJ, J Mat Sci, **17**, 1982,2351

[2] Bucknall CB, Côte FFP, Partridge IK, J Mat Sci, **21**, 1986, 301

[3] Bucknall CB, Makromol. Chem. Macromol. Symp. **16**, 1988, 209

[4] Cook DG, Rudin A, Plumtree A, J Appl Pol Sci, **48**, 1993, 75

[5] Donald AM, Kramer EJ, J Mat Sci, **15**, 1982, 1765

[6] Kim H, Keskulla H, Paul DR, Polymer, **32**, 1991 1447

[7] Kim BK, Shin GS, J Appl Pol Sci, **48**, 1993, 945

[8] Ni BY, Li JCM, Polymer, **32**, 1991, 2766

[9] Newmann LV,Williams JG, J Mat Sci, **15**, 1980, 773

[10] Dijkstra K, *Deformation and fracture of nylon6-rubber blends*, Ph D Thesis, University of Twente, 1993

[11] Gaymans RJ, Dijkstra K, Janik H, MI Conference ; Deformation and Fracture of Polymers, Cambridge 1994, Preprints paper 4

[12] Van der Wal A, Gaymans RJ, MI Conference ; Deformation and Fracture of Polymers, Cambridge 1994, Preprints poster 60

CAVITATION IN RUBBER MODIFIED THERMOPLASTICS.

Krijn Dijkstra*, Reinoud J. Gaymans†

ABSTRACT.

In this paper the cavitation behaviour of rubber modified thermoplastics is studied. It is found that the cavitation strain is independent of particle size and rubber properties in case the rubber particle size is above a certain critical particle size (~ 0.2 μm). Below this critical particle size the cavitation strain increases with decreasing particle size. A hypothesis is put forward to explain the observed behaviour.

INTRODUCTION.

An important step in the deformation mechanism of many rubber modified thermoplastics is cavitation of the rubber phase. Due to cavitation, the high hydrostatic tension ahead of a notch or cracktip is relieved to a biaxial stress state. Because of this transition, the deviatoric component of the stress tensor increases locally and yielding becomes possible.

The consequence of the mechanism described above is that a rubber that cavitates at low strains is more effective than an impact modifier with a high cavitation strain. It was demonstrated by Borggreve et. al. [1] that nylon 6 - rubber blends with different types of impact modifier but identical morphology showed large differences in impact behaviour. This was attributed to differences in cavitation behaviour.

More recently it was shown that nylon 6 - rubber blends with an extreme small particle size (d_{crit} ~ 0.2 μm) had a relatively low impact strength [2]. As a possible explanation for this behaviour it was proposed that these small particles are unable to cavitate.

In this paper a new technique is described to measure the cavitation stress of blends directly. The cavitation stress is measured as a function of the rubber particle size and the rubber modulus.

* DSM Research, P.O. Box 18, 6160 MD Geleen, The Netherlands.
† University of Twente, P.O. Box 217, 7500 AE Enschede, The Netherlands.

MEASUREMENT OF THE CAVITATION STRESS.

Recently a new technique to measure cavitation stresses in blends over a broad range of strain rates was developed [3]. The underlying principle of the method is that cavitation in a blend is accompanied by a change in transparency (stress whitening). This transparency can be quantified by measuring the intensity of the transmitted light of a strong light source (e.g. a laser). At the onset of cavitation this intensity will suddenly decrease. The test set-up used is shown in Figure 1. A typical test result, and the definition of the cavitation stress/strain, is shown in Figure 2. With the test described here it is only possible to measure the start of cavitation. No information is obtained about the growth of the number and/or size of the cavities.

The relation between the cavitation strain as measured with this technique and the actual volumetric strain in the particle can be found using the analysis of Goodier [4]. Also a correction is made in order to incorporate thermal stresses in the blend (due to a mismatch in thermal expansivity of the components) in the model.

EXPERIMENTAL

The blends were prepared on a Berstorff co-rotating twin screw extruder with a screw diameter of 25 mm and a L/D of 33. Dumbbell shaped specimens (according to ISO R527-1) were injection moulded on an Arburg Allrounder 221-55-250. Before testing the specimens were dried at 110 °C under vacuum overnight.

The particle size of the dispersed phase was varied by varying the extrusion conditions. In order to determine the blend morpholgy a sample was taken from an injection moulded specimen. This sample was cryotomed and from the surface the rubber was extracted in boiling m-xylene. From these samples micrographs were taken using SEM.

Mechanical testing was done on a Schenck hydropuls 25 VHS high speed hydraulic tensile tester with a maximum piston velocity of 12.5 m/s. The data in this paper were measured using a piston speed of 1 m/s.

RESULTS AND DISCUSSION.

Recently a model was proposed by Lazerri and Bucknall [5] to model the cavitation of rubber particles as a function of particle size and rubber properties. This model is based on the concept that cavitation will occur if the process is energetically favourable. This means that cavitation starts when the internal elastic energy release upon cavitation is greater than the energy required for the creation of new surface. Using the model of Lazerri and Bucknall a relation between the cavitation strain and rubber particle size can be derived (equation 1). This relation is given in Figure 3.

$$\Delta_c = 2\left(\frac{4\Gamma}{K \cdot d}\right)^{3/4} + \frac{9}{4}\frac{1-2\nu}{1+\nu}\rho F(\lambda_f) \qquad (1)$$

In this equation Δ_c is the volumetric cavitation strain, K is the bulk modulus, Γ is the energy necessary to create new surface, d is

the rubber particle size, ν is the Poisson's ratio, ρ is the density ratio of the uncavitated and the cavitated rubber and $F(\lambda_f)$ is function to take into account the strainhardening behaviour of the rubber and chain scission effects. Lazerri et.al. assume ρ and $F(\lambda_f)$ to be equal to 1. For normal rubber properties and small particle sizes, the second term can be neglected. When the particle size gets very large, the first term can be neglected and the equation reduces to a form very similar to the solution given by Gent [6].

Very recently Dompas et.al. [7] modelled the cavitation strain using a similar approach as Lazerri et.al. (equation 2). In contrast to Lazerri et.al., Dompas et.al. incorporate the energy necessary for chain scission in the surface energy term. This means that the value for Γ given by Dompas is slightly higher than the one given by Lazerri (0.07 N/m resp. 0.03 N/m).

$$\Delta_c = \left(\frac{12\Gamma}{K \cdot d}\right)^{3/4} \qquad (2)$$

In Figure 3 the experimentally determined volumetric cavitation strains are given versus particle size for the blends tested. Dompas et.al. did similar experiments on the cavitation behaviour of PVC/MBS blends with very small particle sizes. Using their raw data cavitation strains can be calculated using the same corrections as described in this paper. These data are also given in Figure 3.

It appears that for particle sizes below d_{crit} the increase in cavitation strain with decreasing particle size is well predicted by equation 1 and 2. However, when the particle size is above d_{crit} the measured cavitation strain clearly does not follow the predicitons. In this region the cavitation strain is independent of particle size and rubber type ($\Delta_c \sim 0.75\%$). Considering the assumptions made, the scatter of the data around this average value are quite small.

In order to explain the observed discrepancies between theory and experiment the following hypothesis is put forward. Fracture processes generally can be divided in an initiation and a propagation phase. Griffith-type criteria (like the model of Lazerri/Dompas) are typically crack propagation criteria; i.e. it is calculated whether it is energetically favourable to propagate a crack. For crack initiation a different criterion may be in order (e.g. a critical stress or strain). Crack initiation and propagation only will occur when both criteria are fullfilled.

Cavitation can also be subdivided in the intitiation of the cavity and the growth of this cavity to dimensions in the same order of magnitude as the particle size. The data suggest that the initiation of cavitation is governed by a critical volumetric strain ($\Delta_c = 0.75\%$). If propagation of cavitation is dependent on the energy release, the model of Lazerri et.al. predicts that for particle sizes above the critical particle size the propagation criterion always is fullfilled when the critical volumetric strain is reached. This means that indeed the critical cavitation strain is independent of particle size.

When the particle size is smaller than the critical particle size the situation is reversed, such that the propagation criterion is fullfilled after the initiation criterion. In this region the cavitation strain can be described by the model of Lazerri/Dompas.

At this moment the model presented in this paper is based on a limited amount of data, calculated on the basis of some rough assumptions. It is therefore still hypothetical and intended to open perspective on the description and the understanding of cavitation (and fracture in general) rather than to give definite answers.

REFERENCES.

1 Borggreve, R.J.M., Gaymans, R.J., Schuijer, J., Polymer, **30**, 71 (1989)
2 Oostenbrink, A.J.M., Dijkstra, K., Wal, A. van der, Gaymans, R.J., PRI conf. Cambridge, april 1991, paper 50
3 Dijkstra, K., Wal, A. van der, Gaymans, R.J., J.Mater.Sci., accepted for publication.
4 Goodier, J.N., ASME Appl.Mech.Trans., **55**, 39 (1933)
5 Lazerri, A., Bucknall, C.B., J.Mater.Sci., **28**, 6799 (1993)
6 Gent, A.N., Tompkins, D.A., J.Appl.Phys., **40**,2520 (1969)
7 Dompas, D., Groeninckx, G., Isogawa, M., Hasegawa, T., Kadokura, M., Polymer, submitted.

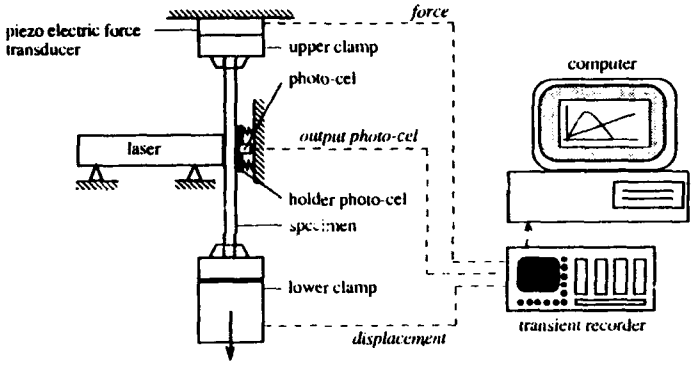

Figure 1 Test set-up for measuring the onset of cavitation.

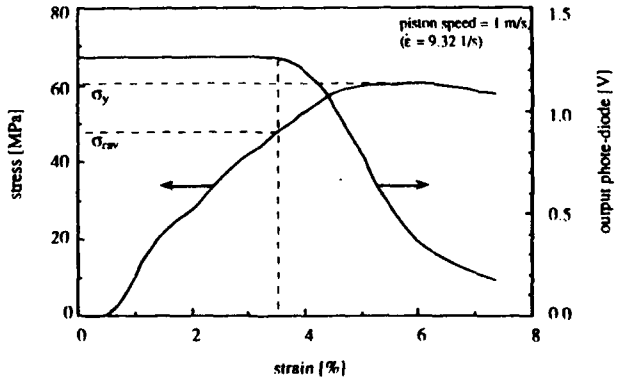

Figure 2 Example of stress/output voltage-strain curve. The material tested is nylon-6/BR.

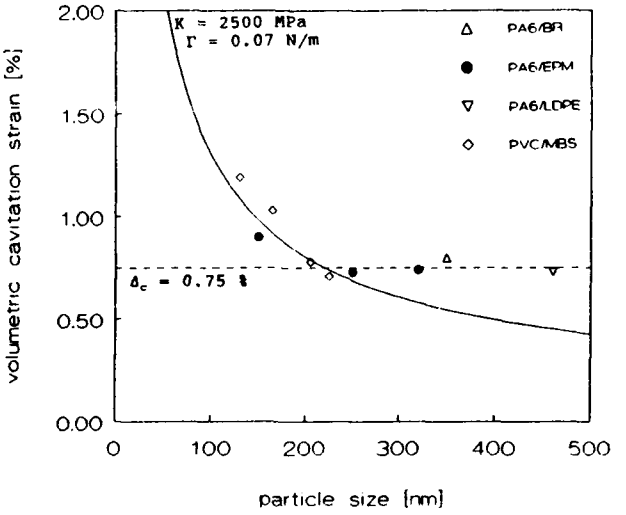

Figure 3 Volumetric cavitation strain vs. rubber particle size for different rubber modified thermoplastics.

MODELLING THE ELASTIC MODULUS OF HDPE IN TERMS OF STRESS DEPENDANT THERMALLY ACTIVATED RATE PROCESS

F. Daver* and B. W. Cherry#

If a three element mechanical model incorporating a stress dependant thermally activated rate process is used to predict the instantaneous and anelastic components of elastic modulus of HDPE (high density polyethylene), it is suggested that the measured elastic modulus determines the anelastic response rather than an instantaneous response and furthermore it is related to an interlamellar shear rather than a slip process in the crystalline region.

INTRODUCTION

Mechanical analogues are commonly used to analyse the stress-deformation behaviour of polymers. However the relationship between the elements of the model and the mechanical properties measured by standard methods is not always entirely obvious and it is the aim of this paper to relate the modulus of elasticity as determined in a standard constant strain rate test to the appropriate portion of the three-element mechanical model. Figure 1 shows a model which is widely used to represent stress relaxation results.

The Eyring dashpot in the model represents a stress dependant thermally activated process (SDTAP) associated with slip in crystalline and/or interfacial regions. Anelasticity is provided in the model by a linear spring in series with the dashpot and this spring may be associated with amorphous chains linking portions of deforming crystallites. The stress acting on this branch of the three-element mechanical model is termed the effective stress. The instantaneous deformation which stems from the entropic elasticity of amorphous regions, is represented by another linear spring in parallel with the anelastic component. An internal stress, which is associated with the stretched tie molecules, is assumed to act on this branch of the model. In a stress relaxation experiment the internal stress is the stress level reached when all the relaxation processes have been exhausted.

If the stress relaxation arises as a result of internal deformation, that is, the flow in the Eyring dashpot, SDTAP theory can be applied to this process and the variation of the effective stress with time calculated. When in a stress relaxation experiment the total rate of change of strain is equated to zero, the effective stress can be obtained in terms of the initial applied stress, activation energy, activation volume, temperature, time and the elastic and anelastic components of elastic modulus.

*Department of Manufacturing Systems Engineering, RMIT, Bundoora, Vic 3083, Australia

#Department of Materials Engineering, Monash University, Clayton, Vic 3168, Australia

$$\ln(-\dot{\sigma}^*) = \ln\left(\frac{E_a K}{2}\right) + \frac{V\sigma^*}{2kT} \qquad (1)$$

Equation (1) can also be integrated using the relationship that at at t = 0,

$$\sigma_0^* = \frac{(\sigma_{app})_0 E_a}{E_c + E_a}$$

to yield

$$\sigma^* = \frac{1}{\alpha} \ln \left| \frac{\exp\left(\alpha \frac{(\sigma_{app})_0 E_a}{E_c + E_a}\right) + \tanh\left(\frac{\alpha K E_a}{2} t\right)}{1 + \exp\left(\alpha \frac{(\sigma_{app})_0 E_a}{E_c + E_a}\right) \tanh\left(\frac{\alpha K E_a}{2} t\right)} \right| \qquad (2)$$

Equation (2) gives the effective stress as a function of the initial applied stress, activation energy, activation volume, temperature, time, elastic and anelastic components of elastic modulus. If equation (2) is fitted to stress relaxation curves then the instantaneous (E_c) and anelastic (E_a) component of elastic modulus can be obtained and compared with the values for the elastic modulus which might be measured by standard methods.

EXPERIMENTAL

The polymer used was high density polyethylene supplied in powder form without additives by Hoechst Pty Ltd and designated GA7260 (M_w = 97,900 and M_n = 10,000). The polymer was subjected to a number of heat treatments in order to produce a series of samples with a range of structures. Daver (1). Samples 0.5x6.4x45.7 mm were used for subsequent experiments. Both elastic modulus and stress relaxation experiments were performed using a dual cantilever bending fixture on a Rheometrics Solid Analyser (RSAII) at two different temperatures, T= 28 ^oC and T = 48 ^oC. The sample extension at elevated temperatures was compensated by the spring loaded clamps in the fixture. Elastic modulus was recorded for both groups at static strain sweep mode at a strain of 0.1%. Stress relaxation experiments were conducted at a strain of 0.1%. The strain was held for a sum of four time zones over a duration of 4164 s.. In each time zone, 16 equally timed measurements were taken. The existence of four different time zones enabled the recording of sufficient data over a narrow range of time when the sample was undergoing a great deal of change at the beginning of the experiment and the recording of less frequent data points over a longer period of time when the sample was undergoing considerably less change.

σ^* was equated to the difference between the instantaneous applied stress at any time and the equilibrium stress at long times and then V/2kT and (E_aK) were calculated from equation (1) by determining the instantaneous decay rate at every point as shown in figure 2. Using the values of V and E_aK thus obtained the values of the other constants were calculated through a least squares minimisation program utilising Marquardt-Levenberg algorithm to fit equation (2) to the obtained stress relaxation curves.

RESULTS AND DISCUSSION

Internal stress calculations

In order to distinguish between the two types of internal stresses, stress relaxation experiments were conducted at four different strains (0.6%, 0.1%, 1.5% and 2%) by using samples made from the same microstructure. The internal stress values were calculated for each stress relaxation experiment. As initial applied stress approaches zero, internal stress also approaches zero; the disappearance of internal stress with zero initial applied stress suggests that the samples which were used for the stress relaxation experiments were virtually free of any residual internal stresses and all the internal stresses present in the samples were due to the deformation preceding the stress

relaxation experiments.

Elastic modulus, instantaneous and anelastic modulus results

Typical values obtained from one series of experiments were as follows:

At T = 28 ^{0}C, Elastic modulus = 4.1 GPa, E_e = 2.4 MPa, E_a = 3.4 GPa.

At T = 48 ^{0}C, Elastic modulus = 3.4 GPa, E_e = 4.8 MPa, E_a = 5.2 GPa.

It can be seen that the anelastic modulus increases while measured elastic modulus decreases with temperature. E_e increases with temperature as might be expected for entropic elasticity. These results suggest that the elastic modulus is not controlled by E_e or E_a but is controlled by the slip in the interfacial region. The instantaneous component of elastic modulus has a very small value, whereas the anelastic component is of the same order of magnitude as the measured elastic modulus. Relative magnitudes of instantaneous elastic modulus and anelastic modulus suggest that the measured elastic modulus is actually the anelastic modulus. This implies that in an elastic modulus measurement what is measured is probably the anelastic component of the elastic modulus rather than the instantaneous component.

The relationship between the elastic modulus and activation volume

If the elastic modulus as measured in a constant strain rate experiment is in fact a function of the slip processes occurring in the body of the polymer, then the "elastic" modulus should be a function of the activation volume for that slip process. According to the SDTAP theory, in a constant strain deformation for which $\sigma = K_2 t$,

$$\dot{\varepsilon} = K_1 \exp\left(\frac{V\sigma}{2kT}\right)$$

the elastic modulus, E is given as

$$E = \frac{K_2}{K_1}\left[1 + \frac{K_1 2kT}{VK_2\varepsilon}\right]$$

or

$$E \approx \frac{1}{V} \qquad (3)$$

Equation (3) suggests an inverse relationship between the measured elastic modulus values and the calculated activation volume results.

Samples were prepared in which the structure was modified by a range of heat treatments. The activation volume and the measured modulus of activity were determined. The inverse relationship between the elastic modulus and the activation volume is observed very clearly if the elastic modulus and the inverse of the activation volume are plotted together. Figure 4 shows this inverse relationship at T = 48 ^{0}C. It seems likely therefore that the measured value of the elastic modulus in experiments carried out in a constant strain rate experiment should be related, not to the elastic processes which take place within the body of the polymer, but to the reversible plastic processes associated with slip.

REFERENCE

1. Daver F, Ph.D. Thesis, Monash University, Clayton, Vic., Australia, (1993)

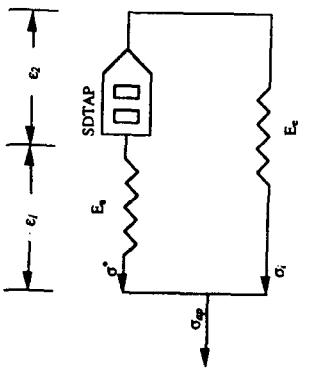

Figure 1.
Three-element model

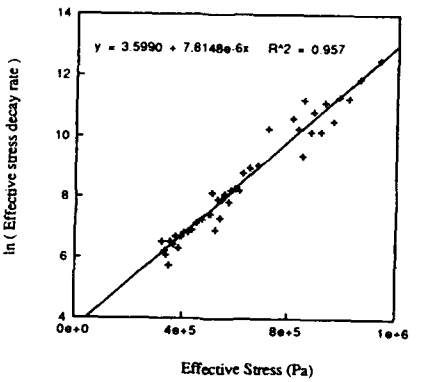

Figure 2.
Stress decay vs. effective stress

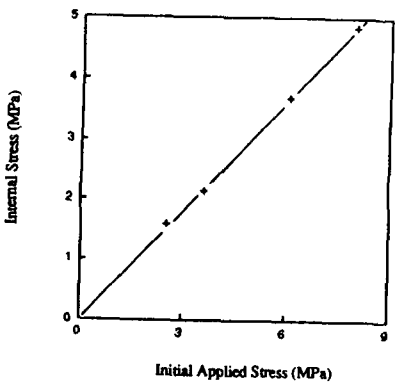

Figure 3.
Internal stress vs. initial applied stress

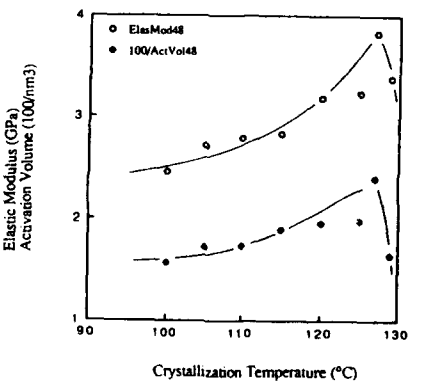

Figure 4.
The relationship between elastic modulus and activation volume at T = 48 °C

AXIAL COMPRESSION AND FATIGUE IN POLYMER FIBRE ROPES

J.W.S. Hearle*, R.E. Hobbs* and P. Noone#

Polyester and the new high-performance polymer fibres provide opportunities for uses as ropes in structural engineering. In addition to quasi-static strength and stiffness, long life is needed. Six fatigue mechanisms have been identified. Axial compression is a potential killer in highly oriented linear polymer fibres. A new analysis describes the mechanics of buckling. Observations of fibres from fatigued ropes show the formation of kinkbands across fibres, bending of fibres into sharp kinks, angular breaks along kinkbands, axial splitting, fibrillar breaks and surface wear.

INTRODUCTION

Ropes are a scene of competition between materials. Natural cellulose fibres were traditional. Later steel wire ropes and cables came to dominate the serious engineering applications. Then came the challenge of the first and second generation of synthetic polymer fibres. Not only the high-performance polymers but also polyester fibres are candidates for uses such as mooring large oil rigs in deep water. Carbon or glass fibres can be employed as pultrusions with a polymer matrix.

The use of continuous filaments led to many new low-twist constructions, in addition to the familiar three-strand rope. The range of choice is enormous. Furthermore there are interactions between material, construction and application. The forces developed depend on the responses of the fibre and the structure as well as on the external factors; and economics must reflect not only direct costs but also effects on the rest of the design and on erection and maintenance. Relevant data on quasi-static and dynamic strength and stiffness is mostly available. For example, both para-aramid and other liquid crystal polymers (LCP) and high-modulus polyethylene (HMPE) give strength/weight ratios more than five times greater than steel, and polyester provides the strength at about half the cost and half the weight of steel.

Many structural engineering applications are looking for lifetimes of ten, twenty or more years. This poses much

* TTI Ltd, 2A, Lloyds Wharf, 2, Mill St, London, SE1 2BD
# Department of Textiles, UMIST, Manchester, M60 1QD

greater problems. Although scientific understanding of long-term effects in metals and polymers is not so very different, steel has a long history of experience in use, so that reliable codes of practice are available. For engineers to select polymer fibre ropes, we need assurances on long-term performance, which requires more knowledge of fatigue.

FATIGUE IN ROPES

External abrasion and environmental damage can usually be avoided, but Parsey and others [1,2] have described six internal "fatigue" mechanisms. Lifetimes can be predicted by computer models [3], though for some of the mechanisms the experimental input data is inadequate. Pictures of failures have been published [4].

Creep rupture is always a factor, if only as a terminal cause of failure. Strength falls off logarithmically with time, but there is a big difference between materials. It would take thousands of years for the strength to fall to 50% of the one-minute value in LCP fibres, but the time would be measured in hours in polyethylene. **Hysteresis heating**, due to the dynamic losses of the material and to friction between rope components, can be severe particularly in large ropes subject to dynamic loading. Rise in temperature weakens fibres, but may increase or decrease rates of fatigue. The **tensile fatigue** mechanism in nylon and polyester fibres cycled to zero load occurs infrequently in ropes. **Structural fatigue** is a is a complicated and poorly documented large-scale effect, involving disturbance of the rope structure. **Internal abrasion** gives shear stresses, axial cracks, peeling and surface wear, which is serious in wet nylon. However, with correct design, these mechanisms are not usually a great problem in the LCP fibres or polyester. A potential killer mechanism in the highly-oriented highly-crystalline linear-polymer fibres is **axial compression fatigue**. A bad example occurred ten years ago with Kevlar ropes in the Gulf of Mexico in ropes attached to buoys, which failed at 20% of rated strength when they were picked up.

AXIAL COMPRESSION OF FIBRES IN ROPES

It is perhaps not immediately obvious why fibres should be subject to axial compression in ropes, since ropes buckle under low compressive stress in a mild curvature, which is not damaging. However, even in tension-tension cycling, rope components can go into axial compression. One cause is a differential response of components of the rope; if some yarns or strands are put in at a higher tension than others, or respond differently, they will contract when the rope is under low tension and force the slacker components into axial compression. The other cause is rope twisting. Increased twist tensions the outer yarns, and causes core yarns to go into compression; and reducing twist has the reverse effect, bringing outer yarns into compression. In ropes that are not strictly torque-balanced, tension can lead to twist when there is a differential torsional response of rope and termination or variability along the rope. In the Gulf of Mexico failure, there was a system interaction with wave motion on the buoys, which caused the ropes to twist.

Starting with the classical work of Euler on columns, there have been many analyses of beam buckling, some of which involve multiple and localised buckles, but these have assumed elastic behaviour in bending, whereas fibres yield. Suppose that a particular yarn or strand in a rope experiences an axial compressive force. There is then a choice of what buckles. The first form does not involve fibre bending: buckling may occur directly along the fibres at their compressive yield stress (about 0.35 Gpa in para-aramids), with kinkbands at the molecular or fine-structure level running right across the fibres. If fibre slip is possible, the kink bands may concentrate at particular positions along the fibre. At the other extreme, the yarn or strand may buckle as a whole in a moderate wavy curvature, which is not very damaging. However, the most interesting case involves the formation of sharp kinks (bends) in the fibres, either individually or, more likely, cooperatively across a yarn.

The fibre bending moment-curvature relation is nonlinear, and turns over from an initial elastic value to an asymptotic value derivable from the fibre compressive yield stress. In a new analysis, this was approximated as elastic-plastic. Smooth curvature elastic buckles turn into plastic hinges at sharp zig-zag kinks. The restraints involved are frictional resistance to axial slip, which is needed if the kinks are to localise at intervals along the fibres, and lateral pressure from the surrounding components, which can be taken as constant during kinking (equivalent to a plastic restraint). Differential equations for the mechanics can be formulated. The form of buckling is established in the elastic mode. There is a whole set of solutions, not very different in critical criteria: the infinite case has buckles continuously along the yarn; alternatively the buckles can localised into a single buckle, or groups of two or more buckles, separated by straight sections. When a critical compressive load is reached, the plastic hinges form at the points of maximum curvature, and the plastic solution of the equations peels off from the elastic solution. Imperfections may also influence the mechanics and modify the behaviour. The predicted appearance is a smooth elastic bend leading to the first sharp kink, with the zig-zag continuing along the fibres.

Fibre bending leads to two fatigue effects. Firstly, the structural changes at the kinkbands, which are formed on the inside of a bend, gradually become more severe and eventually break down into cracks. This will be severe at the sharp kinks and, in para-aramid fibres might cause rupture in about 1000 cycles; in HMPE it would take longer, and in polyester longer still. Shear stresses associated with variable curvature cause axial splitting to occur; when this becomes severe, it leads to fibrillar breaks in the material.

OBSERVATIONS OF FAILURE

A considerable programme of tension-tension fatigue of high-performance ropes made from aramid (Kevlar, Twaron, Technora), LCAP (Vectran), HMPE (Dyneema, Spectra) and polyester ropes has been carried out at NEL as a part of a joint industry project

FIBRE TETHERS 2000 managed by Noble Denton with TTI Ltd as consultants. We were able to obtain samples of these ropes in order to investigate the damage occurring. Several techniques were used. Visual observation or macrophotography shows gross effects. High-power optical microscopy was the most effective technique for showing the detail of damage, though scanning electron microscopy was also used. Finally, the location of both kinkbands and abrasion damage can be identified by dyeing aramid fibres, in yarn or rope form. A collection of pictures will be shown in the poster.

The observations confirm the theoretical predictions made above, most clearly in the aramid ropes. Spaced-out groups of kinks in fibres, running across yarns, were observable either directly or in dyed samples. Some core yarns had broken or partially broken into pieces, a few millimeters long, separated by a few centimeters. The microscopic views showed portions of fibres with rounded curvature leading to sharp kinks. There were also many examples of kink bands right across unbent fibres, either at random intervals of a few fibre diameters or concentrated in a length of dense kinkbands. Some breaks showed in a simple form the characteristic angle of kinkbands, whether from uniform compression or on the inside of bends. Others were more complicated, possibly due to cracks along more than one kinkband or to fibrillar break-up of the fibre end after rupture. There were also many examples of axial splitting and some long fibrillar breaks. Peeling and surface wear occurred to a small extent.

In HMPE fibres, which have a non-round cross-section, the kinking takes more complicated forms but can be severe. In polyester, there is much less effect.

REFERENCES

1 HEARLE J W S and PARSEY M R , 'Fatigue Failures in Marine Ropes and their Relation to Fibre Fatigue', Polymers in a Marine Environment Conference, IMarE, June 1983.

2 PARSEY M R, BANFIELD S J and HEARLE J W S, 'Life of Polymeric Ropes in the Marine Environment', Polymers in a Marine Environment Conference, IMarE, October 1987.

3 HEARLE J W S, PARSEY M R, OVERINGTON M S and BANFIELD S J, 'Modelling the Long-Term Fatigue Performance of Fibre Ropes', Proc. 3rd Int. Symp. Offshore and Polar Engg., Vol. 2, 377-383, 1993.

4 HEARLE J W S, LOMAS B, COOKE W D, and DUERDEN I J, 'Fibre Failure and Wear of Materials', Ellis Horwood, 1989.

BLENDS OF EPOXY RESIN AND POLYPHENYLENE ETHER AS A MATRIX MATERIAL FOR HIGH-PERFORMANCE COMPOSITES

R.W. Venderbosch, H.E.H. Meijer and P.J. Lemstra
Centre for Polymers and Composites, Eindhoven University of Technology
P.O. Box 513, 5600 MB Eindhoven, The Netherlands

Poly(2,6-dimethyl-1,4-phenylene ether), PPE, has been introduced as a matrix material in carbon fabric reinforced composites, using epoxy resin (DGEBA) as a reactive solvent. After impregnation the epoxy resin solvent is converted into non-solvent and phase separation is initiated. The resulting thermoplastic composites reveal an unique morphology of epoxy coated fibres in a pure PPE matrix. The epoxy interphase provides a high level of interfacial adhesion. Additionally, it is shown that multiple brittle failure of the epoxy interphase during mode-II loading (impact) is effective in delocalizing damage. This could be a new toughening mechanism for thermoplastic composite materials.

INTRODUCTION

An interesting polymer to apply as matrix material for high performance composites is poly(2,6-dimethyl-1,4-phenylene ether) or PPE. PPE is a relatively low cost amorphous thermoplastic with a high T_g, of approximately 220 °C and excellent mechanical properties e.g. in terms of toughness. However, as a result of its limited thermal and oxidative stability PPE can not be melt processed. The high temperatures required for melt processing (300 °C à 350 °C) will yield severe degradation and therefore PPE is usually classified as intractable. Consequently, a solution impregnation route has to be considered. However, solution impregnation techniques will introduce additional problems related to the complete elimination of residual solvent from the composite material.

A challenging solution to these problems can be found in the use of reactive solvents. In a previous study [1], a reactive processing technique was explored for PPE, based on the use of standard bisphenol A epoxy resin as reactive solvent. In contrast to the literature [2-4] on blends of epoxy resins and engineering plastics, which mainly aims at toughened epoxy systems or hybrids of thermosets and thermoplastics, in this processing technique, basically, the epoxy resin is only introduced in order to tune the processability of PPE. In accordance with conventional solvent techniques this results in enhanced flow and reduced processing temperatures. However, instead of the complicated solvent recovery step required in conventional solvent techniques, the homogeneous solution is cured after processing and consequently the epoxy resin solvent is converted into non-solvent. At the high PPE contents of interest, > 40wt.%, phase separation is accompanied by phase inversion. Consequently, neat PPE is regained and the solvent is converted into a dispersed phase. Due to this morphology the properties of the final material are dominated by PPE.

In this investigation [5,6] the reactive processing technique is studied as a route to introduce PPE in high performance composite structures. Attention is mainly aimed at the composite morphology and toughness.

RESULTS AND DISCUSSION

The epoxy/PPE system (Epikote 828EL, Shell, PPE 803, 30 $kg \cdot mol^{-1}$, GE plastics) was applied as a matrix material in continuous carbon fibre reinforced composites. Using epoxy resin as a reactive solvent, the viscosity of PPE at an impregnation temperature of 225 °C could be reduced to 30 and 500 Pa.s for 40 and 60 wt.% PPE, respectively. These medium viscosity compounds can be relatively easily used in a film-stacking technique to prepare carbon fabric (CD168, Ten Cate) reinforced composites with a fibre volume percentage of 50 % under low pressure conditions. Optical microscopy studies demonstrated that the reactive processing technique resulted in PPE based composites exhibiting a low void content and an excellent degree of impregnation.

A more detailed study of the morphology of the carbon fabric laminates revealed a pronounced influence of the presence of fibres on the matrix morphology. In composites epoxy resin preferentially accumulates at the fibre surface resulting in an epoxy 'interlayer' around the fibre. This effect is shown to be dependant on the fibre volume fraction. In contrast to the phase inverted morphology of epoxy spheres dispersed in a PPE matrix as observed in the unreinforced epoxy/PPE system (*Figure 1a*), in fibre-rich areas of the composite, in the PPE-rich matrix no epoxy spheres are distinguished (*Figure 1b*). Consequently, the majority of epoxy resin is migrated to the fibre surface resulting in an unique composite morphology of epoxy coated fibres in a nearly pure PPE matrix. Based on these morphological results it is concluded that epoxy resin is not only effective as a solvent enabling the preparation of PPE based composites, but additionally provides an important structural part of the final composite, i.e. the interphase, resulting in excellent adhesion.

a) b)

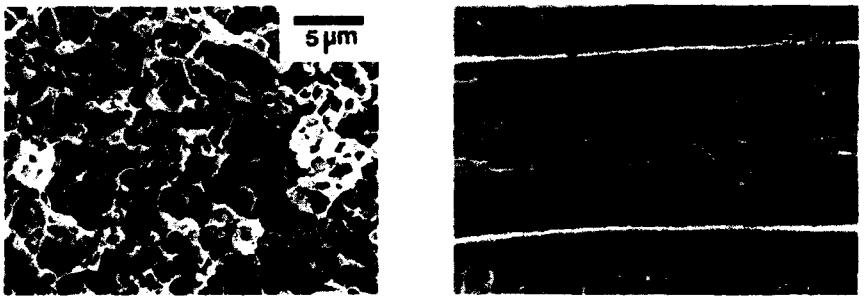

Figure 1: SEM micrograph of fracture surface of cured epoxy/PPE (60 wt% PPE) blend; a) in the pure material and b) in a carbon fabric reinforced composite (50 vol.% fibre). A: fibre(imprint), B: epoxy interphase, C: PPE matrix.

In *Figure 2* the mode-I and mode-II interlaminar fracture toughness, G_{Ic} and G_{IIc}, obtained for the composites based on the neat constituents and the blends are presented together with the G_{Ic} of the pure matrix materials. As shown by Bradley *et al*[7] no linear correlation exists between matrix and composite mode-I fracture toughness. For ductile matrix materials the neat resin fracture toughness is only partly translated into the composite fracture toughness and an 'upper limit' for G_{Ic}^{C} is found of approximately 2 à 3 $kJ \cdot m^{-2}$. The low G_{Ic}^{C} values are related to the high volume fraction of high modulus fibres which constrain the development of a large plastic zone at the crack tip. For the epoxy/PPE based composites this limit is reached already at low PPE contents. A positive consequence is that the penalty in matrix toughness due to the use of epoxy resin as a reactive solvent is negligible and barely affects the composite performance. The mode-II tests, however, reveal a remarkably strong synergy in G_{IIc} for the epoxy/PPE based laminates. In contrast to the pure PPE composites where mode-II tests yield only a minor increase in G_c ($G_{IIc}=1.6 \times G_{Ic}$), the pure epoxy as well as the epoxy/PPE composites reveal in mode-II test conditions pronounced higher G_c values compared to mode-I test conditions ($G_{IIc}=4 \times G_{Ic}$ and $G_{IIc}=3.3 \times G_{Ic}$, respectively). In the basically brittle epoxy resin composites this is the result of a deformation mechanism involving extensive microcracking ahead of the crack tip, referred to in the literature [7] as 'hackling'. This cracking mechanism is very effective in increasing the amount of energy absorbed. Obviously, such a change in deformation mechanism has also to occur in the epoxy/PPE composite. Taking into account the unique composite morphology this may give the explanation for the synergy observed. Provided that cracks in the epoxy interlayer can initiate yielding in the PPE-rich phase, multiple brittle fracture of the epoxy interlayer during mode-II loading can effectively delocalize yielding of the PPE-rich phase and subsequently increase the deformation volume and G_{IIc}^{C}. A schematic presentation of the influence of brittle interphases on the mode-II deformation mechanism in ductile thermoplastic composites is shown in *Figure 3*.

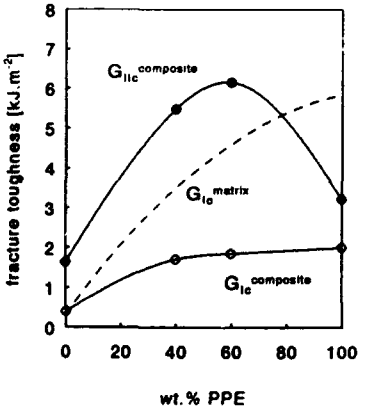

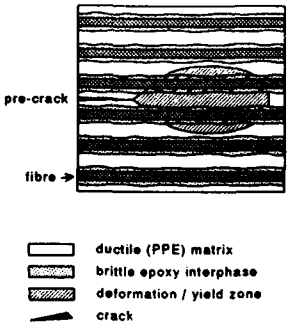

Figure 2: *Matrix mode-I fracture toughness and composite (50 vol.% fibre) mode-I and mode-II fracture toughness versus matrix composition.*

Figure 3: *Schematic presentation of the mode-II deformation mechanism in ductile thermoplastic composites including brittle epoxy resin interphases.*

In order to evaluate the toughening effect observed, a new epoxy resin solvent system is applied, based on a range of homogeneous blends of bisphenol A and polypropylene oxide epoxy resins (Epikote 828 and Epikote 877, Shell). By means of this reactive solvent system, the strain at break of the in-situ polymerized glassy interphase can be varied from 5% up to 80 %. In *Figure 4* the mode-I and mode-II fracture toughness of an epoxy/PPE (60 wt% PPE) composite as a function of the ductility of the interphase is presented. With increasing ductility, G_{Ic} increases slightly while a pronounced drop in G_{IIc} is observed. The results clearly support the toughnening effect of brittle interphases: Upon increasing the interphase ductility, multiple fracture of the interphase and the consequent increase in G_{IIc} is suppressed, yielding in the end a deformation mechanism which is independant of the loading conditions and corresponds with the deformation of a composite based on a homogeneous ductile matrix material.

Surprisingly, the results reveal that a brittle interphase is effective in increasing the toughness of a ductile thermoplastic composite. This observation is of particular interest, since in the existing literature attention is mainly directed towards the introduction of ductile or rubbery interphases [8]. In future, more results will be presented on this intriguing feature.

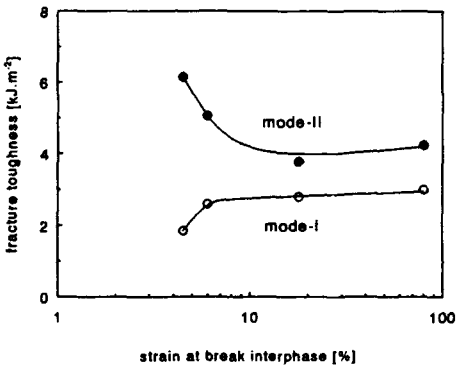

Figure 4: Mode-I and mode-II fracture toughness of an epoxy/PPE (60 wt% PPE) carbon fabric reinforced composite versus the strain at break of the interphase.

REFERENCES

1: Venderbosch, R.W. *et al Polymer* 1994 accepted
2: Recker, H.G. *et al SAMPE Journal* 1990, **26** No 2, 73
3: Hedrick, J.L. *et al Polymer* 1991, **32** (11), 2020
4: Sefton, M.S. *et al* in 'Proc 19th Int SAMPE Symp., 13-15 October 1987', p. 700
5: Venderbosch, R.W. *et al Makromol. Chem., Macromol. Symp.* 1993, **75**, 73
6: Venderbosch, R.W. *et al Polymer* 1994 submitted
7: Bradley, W.L. in *Composite Materials Series, vol 6, Application of Fracture Mechanics to Composite Materials* Friedrich, K. (Ed.), Elsevier Science Publishers, 1989, p. 159
8: McGarry, F.J. in *Advances in Chemistry Series* **222**, American Chemical Society, 1989, p. 175

X RAY SCATTERING STUDIES OF IN SITU DEFORMATION OF POLYETHYLENE

M F Butler*, A J Ryan†, W Bras‡, A M Donald*

Combined small and wide angle X ray scattering from real time deformation of commercial grade polyethylene was investigated using a combined SAXS/WAXS area/area detector setup. The experiments were carried out at the SRS Daresbury on station 8.2. Preliminary analysis has shown the existence of a martensitic phase transformation in both HDPE and LLDPE at early stages of the deformation. The transformation occurs at lower strains for the HDPE. Changing thermal history was also shown to have some effect on the strain at which the transformation occurs.

INTRODUCTION

Much attention has been directed towards understanding the deformation of polyethylene. Most work has, however, been performed on samples with specified textures such as single, or pseudo-single, crystals, or highly oriented fibres. Previous time resolved X ray scattering studies (1) (2) (3) have concentrated on highly oriented UHMW samples, so there is an absence of knowledge on the scattering of X rays from ordinary commercial grade polyethylene with a random texture. It is advantageous to perform real time scattering studies, since this removes the possibility of stress relaxation inherent in previous scattering studies, where the sample was first deformed to a predetermined extent and then examined. Previous real time studies have also been conducted at elevated temperatures.

The deformation of polyethylene has been shown to proceed via a combination of mechanisms, some or all of which will be activated in the course of deformation. Peterlin's micronecking model (4) is widely used as a basis for describing the deformation of polyethylene, whereby the structure undergoes a transformation from a lamellar to an oriented fibrillar structure.

The initial response to stress is deformation of the amorphous component (5).

* Department of physics, University of Cambridge
† Materials Science Centre, UMIST
‡ SERC Daresbury Laboratory

Further deformation proceeds via deformation of the crystalline regions, mainly due to crystallographic mechanisms i.e. chain and transverse slip (5). Chain slip occurs in the (100)[001] and (010)[001] slip systems and transverse slip occurs in the (100)[010] and (010)[100] slip systems when the critical resolved shear stress (CRSS) in that system is reached. In addition to the crystallographic mechanisms, deformation can also proceed via twinning and a martensitic transformation, whereby the orthorhombic structure of the crystalline polyethylene is transformed to a monoclinic structure. The monoclinic phase is metastable and probably only exists under stress (5). It has been shown to be unstable above 110°C (5). Twinning and martensitic transformations are important because they provide a means for plastic deformation even if slip is geometrically unfavourable, and provide a supplementary means of deformation when slip can occur. The existence of martensitic transformations in bulk material has been shown before (5).

Commercial grade melt crystallised samples have a spherulitic morphology and compatibility of the different parts must be maintained with the different deformation mechanisms coexisting.

EXPERIMENTAL

High density polyethylene (HD6007EA) and linear low density polyethylene (LL7209AA) were kindly supplied by BP Chemicals Ltd. Tensile testing samples were made from sheets approx. 1mm thick. The samples were cut with a gauge length made containing two semicircular cut-outs (of radius 8mm) to ensure that the yielding region remained in the X ray beam during deformation. The samples were 50mm long and 20mm wide.

The samples were deformed at room temperature *in situ* using a Polymer Laboratories Minimat. Small and wide angle scattering patterns were detected using area detectors. Two extension rates were used; 0.5mm/min and 5mm/min. Data was collected over approximately eighty frames for each run. The duration of each frame was fifteen seconds.

Combined measurements of SAXS and WAXS patterns during deformation were made from samples that had received no treatment after manufacture. Annealed samples were also used, in which the samples were annealed at a certain temperature followed by either quenching in liquid nitrogen or allowing to cool slowly.

To compensate for fluctuations in incident beam intensity, both small and wide angle data were normalised with respect to the readings on the ion detectors placed in front of and behind the sample. Corrections were made for sample thickness, sample transmission and detector non linearity. The background scattering was subtracted from the SAXS data. The necessity for desmearing the SAXS data was removed by

the point collimated size of the beam compared to the pixel size of the area detector. The combined SAXS/WAXS data was analysed using software (BSL) developed by G.R. Mant of the Daresbury Laboratory.

RESULTS AND DISCUSSION

Preliminary analysis of the WAXS data shows the appearance of extra reflections indicating the presence of a new crystalline phase. Initially the WAXS pattern shows the strong (110) and (200) reflections from the orthorhombic crystal structure of polyethylene. During tensile deformation these reflections become less isotropic as the polyethylene chains (parallel to the c axis of the orthorhombic unit cell) become aligned with the draw direction, as expected. More interestingly, new reflections appear in the scattering pattern. These are attributed to the stress induced formation of a monoclinic phase (5). During deformation these reflections become stronger (especially the one below the orthorhombic 110 reflection) indicating the increasing formation of monoclinic material as the strain increases.

The orthorhombic to monoclinic transformation occurred at lower strains for the HDPE. Since deformation is accomodated by a combination of mechanisms, it is reasonable to assign the delayed appearance of the martensitic transformation in LLDPE to the greater contribution of deformation within the amorphous component.

The SAXS data shows an increase in scattering at small angles as deformation progresses. This can be attributed to the formation of microvoids in the material, as predicted by Peterlin's micronecking model.

CONCLUSIONS

The feasibility of real time SAXS/WAXS deformation studies has been proven, yielding interesting results regarding the occurrence of a martensitic transformation at low strains in commercial grade high density and linear low density polyethylene

REFERENCES

1. N.A.J.M. van Aerle, A.W.M Braam Coll and Poly Sci. 267 (1989) 233
2. N.A.J.M. van Aerle, A.W.M Braam Makromol Chem 189 (1988) 1569
3. W. Wilke, M. Bratrich, J.Appl. Cryst 24 (1991) 645
4. A. Peterlin, J. Mater. Sci 6 (1971) 490
5. L. Lin, A.S. Argon J. Mater. Sci 29 (1994) 294

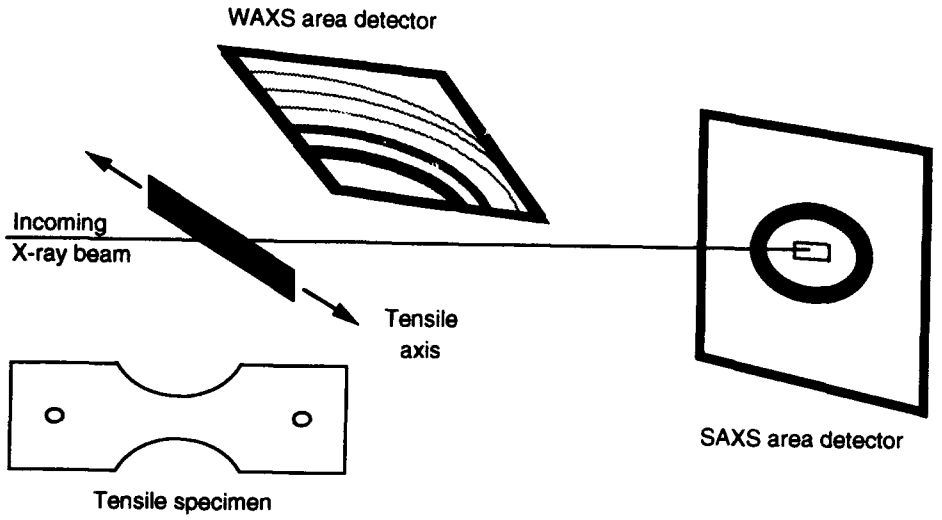

Figure 1 Schematic diagram of experimental setup, with the sample geometry shown inset

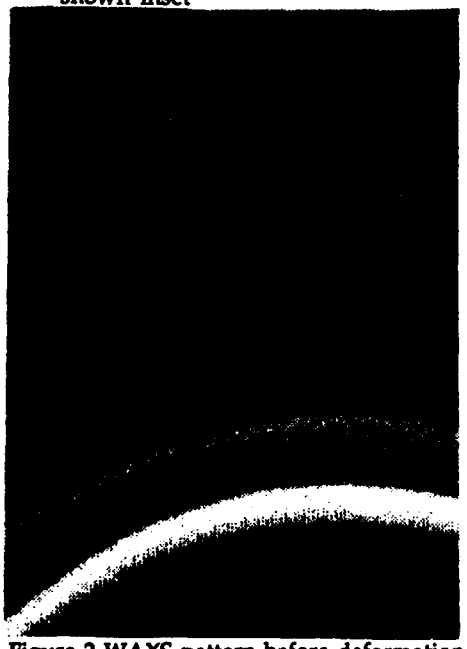

Figure 2 WAXS pattern before deformation showing (110) and (200) reflections

Figure 3 New monoclinic reflection (arrowed) after 25mm extension of sample